Lecture Notes in Mechanical Engineering

Ladislav Ševčík
Petr Lepšík
Michal Petrů
Ivan Mašín
Rudolf Martonka *Editors*

Modern Methods of Construction Design

Proceedings of ICMD 2013

Springer

Lecture Notes in Mechanical Engineering

For further volumes:
http://www.springer.com/series/11236

About this Series

Lecture Notes in Mechanical Engineering (LNME) publishes the latest developments in Mechanical Engineering - quickly, informally and with high quality. Original research reported in proceedings and post-proceedings represents the core of LNME. Also considered for publication are monographs, contributed volumes and lecture notes of exceptionally high quality and interest. Volumes published in LNME embrace all aspects, subfields and new challenges of mechanical engineering. Topics in the series include:

- Engineering Design
- Machinery and Machine Elements
- Mechanical Structures and Stress Analysis
- Automotive Engineering
- Engine Technology
- Aerospace Technology and Astronautics
- Nanotechnology and Microengineering
- Control, Robotics, Mechatronics
- MEMS
- Theoretical and Applied Mechanics
- Dynamical Systems, Control
- Fluid Mechanics
- Engineering Thermodynamics, Heat and Mass Transfer
- Manufacturing
- Precision Engineering, Instrumentation, Measurement
- Materials Engineering
- Tribology and Surface Technology

Ladislav Ševčík · Petr Lepšík
Michal Petrů · Ivan Mašín
Rudolf Martonka
Editors

Modern Methods of Construction Design

Proceedings of ICMD 2013

Springer

Editors
Ladislav Ševčík
Petr Lepšík
Michal Petrů
Ivan Mašín
Rudolf Martonka
Department of Design of Machine
Elements and Mechanism
Faculty of Mechanical Engineering
Technical University of Liberec
Liberec
Czech Republic

ISSN 2195-4356 ISSN 2195-4364 (electronic)
ISBN 978-3-319-05202-1 ISBN 978-3-319-05203-8 (eBook)
DOI 10.1007/978-3-319-05203-8
Springer Cham Heidelberg New York Dordrecht London

Library of Congress Control Number: 2014934141

Printed on acid-free paper

Springer is part of Springer Science+Business Media (www.springer.com)

Preface

The book "Modern Methods of Construction Design" has been created on the basis of contributions of the 54th International Conference of Machine Design Departments.

This conference is one of the oldest central conferences, dealing with methods and applications in the machine design. The main aim of the conference is to provide an international forum where experts, researchers, engineers, and also industrial practitioners, managers, and Ph.D. students can meet, share their experiences, and present the results of their efforts in the broad field of machine design and related fields.

In the year 2013, the Department of Design of Machine Elements and Mechanisms of Technical University of Liberec, whose members deal above all with machine design, tribology, experimental methods and measuring, engineering analyses and products innovation, organized the 54th International Conference of Machine Design Departments on the occasion of 60th anniversary of Technical University of Liberec. The mountain town of Hejnice in Northern Bohemia was chosen for this celebratory event.

Since 1960, when the first conference was organized in Mělník by Brno University of Technology, more than 50 years have passed. The main aim of the conference was providing an opportunity for professional experiences sharing in the field of machine design, gears and transmission mechanisms. The heads of Mechanical Design Departments decided to organize these conferences annually first at the national and later at the international level. The significance of the conference has grown. Historically, the conferences were organized in different places by different mechanical design departments of Czech and Slovak technical universities:

1960	Brno University of Technology	Mělník
1961	Brno University of Technology	Brno
1962	University of West Bohemia	Plzeň
1963	Slovak University of Technology in Bratislava	Bratislava
1964	Technical University of Liberec	Liberec
1965	Technical University of Kosice	Košice

1966	Czech Technical University in Prague	Praha
1967	VŠB-Technical University of Ostrava	Ostrava
1968	University of Zilina	Žilina
1969	University of West Bohemia	Plzeň
1970	Brno University of Technology	Brno
1971	Technical University of Zvolen	Zvolen
1972	Slovak University of Technology in Bratislava	Bratislava
1973	Technical University of Liberec	Liberec
1974	Technical University of Kosice	Košice
1975	Brno University of Technology	Brno
1976	Czech Technical University in Prague	Praha
1977	Czech University of Life Sciences Prague	Praha
1978	University of Zilina	Kysucké Nové Mesto
1979	Technical University of Liberec	Liberec
1980	Slovak University of Technology in Bratislava	Smolenice
1981	Brno University of Technology	Brno
1982	Technical University in Zvolen	Šachtičky
1983	Technical University of Kosice	Michalovce
1984	VŠB-Technical University of Ostrava	Podolánky
1985	Czech Technical University in Prague	Kladno
1986	University of West Bohemia	Plzeň
1987	Slovak University of Technology in Bratislava	Bratislava
1988	Brno University of Technology	Brno
1989	Technical University of Liberec	Liberec
1990	University of Zilina	Papradno
1991	Technical University of Kosice	Herl'any
1992	VŠB-Technical University of Ostrava	Těšínské Beskydy
1993	Technical University of Zvolen	Zvolen
1994	Czech Technical University in Prague	Praha
1995	Brno University of Technology	Brno
1996	University of West Bohemia	Plzeň
1997	Slovak University of Technology in Bratislava	Gabčíkovo
1998	Technical University of Liberec	Liberec
1999	University of Zilina	Belušské Slatiny
2000	Technical University of Kosice	Herl'any
2001	VŠB-Technical University of Ostrava	Ostrava
2002	Technical University of Zvolen	Bienska dolina
2003	Czech Technical University in Prague	Praha
2004	Brno University of Technology	Blansko
2005	Technical University of Liberec	Sedmihorky
2006	Czech University of Life Sciences Prague	Praha
2007	Slovak University of Technology in Bratislava	Smolenice
2008	University of West Bohemia	Srní
2009	University of Zilina	Terchová
2010	Technical University of Kosice	Slovenský Ráj
2011	VŠB-Technical University of Ostrava	Sepetná
2012	Brno University of Technology	Mikulov
2013	Technical University of Liberec	Hejnice

The long history shows that meeting and exchange of views of experts from universities, research institutions, and companies contribute significantly to problems solving in a scientific field of machine design.

We firmly believe the tradition of ICMD will continue in the coming years.

Members of conference organizing committee

International Scientific/Programme Committee of the 54th ICMD 2013

L. Ševčík—Chairman, Czech Republic
P. Lepšík—Secretary, Czech Republic
M. Petrů—Secretary, Czech Republic
Z. Matuszak, Poland
J. Machado, Portugal
E. N. Mohammadali, Iran
A. Ahameedi, Iraq
Y. Takeichi, Japan
M. Vereš, Slovakia
V. Dynybyl, Czech Republic
V. Lasova, Czech Republic
H. Haberhauer, Germany
M. Bozca, Turkey
M. Rackov, Serbia
J. Homišin, Slovakia
H. Mickoski, Macedonia
M. Bošanský, Slovakia
S. Medvecky, Slovakia
M. Malý, Czech Republic
V. Arakelyan, France
M. Hartl, Czech Republic
L. Pesik, Czech Republic
W. Toisuta, Australia
J. Bronček, Slovakia
S. Popescu, Romania
E. Coatanea, Finland
M. Abdulgadir, Libyan Arab
Jamahiriya S. Logvinov, Russia
M. Němček, Czech Republic
Z. Dejl, Czech Republic
S. Simanjuntak, Indonesia
D. Bakti, Indonesia
J. Boamah, Ghana

L. Prasil, Czech Republic
D. Herak, Czech Republic
P. L Nbah, Cameroon
L. Yaoming, China
S. Hosnedl, Czech Republic
I. Mašín, Czech Republic

Review Committee of the 54th ICMD 2013

S. Logvinov, Russia
W. Toisuta, Australia
O. Novak, Czech Republic
J. Petřík, Czech Republic
S. F. Chowdhury, USA
J. Bronček, Slovakia
M. Komarek, Czech Republic
S. Popescu, Romania
V. Arakelyan, France
D. Herak, Czech Republic
P. Hrabe, Czech Republic
R. Choteborsky, Czech Republic
J. Machado, Portugal
E. Coatanea, Finland

Organizing Committee of the 54th ICMD 2013

L. Ševčík—P. Lepšík—M. Petrů—I. Mašín—R. Martonka

Contents

Part IV Products Innovation

Part V Optimization and Design

Part VII Tribology

Contributors

P. Alipur Dicle University, Diyarbakir, Turkey

J. Andruš Czech Technical University in Prague, Prague, Czech Republic

A. Atar Dicle University, Diyarbakir, Turkey

O. Ayer Dicle University, Diyarbakir, Turkey

L. Bartoň University of West Bohemia, Pilsen, Czech Republic

R. Bašťovanský University of Zilina, Zilina, Slovakia

S. Bingol Dicle University, Diyarbakir, Turkey

P. Bocko IDIADA CZ a.s., Mladá Boleslav, Czech Republic

M. Bošanský Slovak University of Technology in Bratislava, Bratislava, Slovakia

T. Bouda Czech Technical University in Prague, Prague, Czech Republic

M. Bozca Yildiz Technical University, Istanbul, Turkey

P. Brabec Technical University of Liberec, Liberec, Czech Republic

J. Brandejs Brno University of Technology, Brno, Czech Republic

J. Bronček University of Zilina, Zilina, Slovakia

V. Brozová VUTS Liberec, a.s., Liberec, Czech Republic

J. Bucala University of Zilina, Zilina, Slovakia

M. Burián VŠB-Technical University of Ostrava, Ostrava, Czech Republic

O. Burucu Dicle University, Diyarbakir, Turkey

Ü. H. Büyükalgan Yildiz Technical University, Istanbul, Turkey

J. C. Campos Minho University, Braga, Portugal

J. Chmelař Czech Technical University in Prague, Prague, Czech Republic

O. Dajbych Czech University of Life Sciences Prague, Prague, Czech Republic

M. Diblík Technical University of Liberec, Liberec, Czech Republic

T. Donič University of Zilina, Zilina, Slovakia

M. Druckmüller University of Technology Brno, Brno, Czech Republic

M. Dub Czech Technical University in Prague, Prague, Czech Republic

J. Dvorak University of West Bohemia, Pilsen, Czech Republic

V. Dynybyl Czech Technical University in Prague, Prague, Czech Republic

M. Dzimko University of Zilina, Zilina, Slovakia

H. B. Elem Dicle University, Diyarbakir, Turkey

J. Fábera VUTS Liberec, a.s., Liberec, Czech Republic

V. Fliegel Technical University of Liberec, Liberec, Czech Republic

P. Florian University of West Bohemia, Pilsen, Czech Republic

Z. Folta VŠB-Technical University of Ostrava, Ostrava, Czech Republic

I. Gajdac University of Zilina, Zilina, Slovakia

T. Gajdošík University of Zilina, Zilina, Slovakia

M. Galbavý University of Zilina, Zilina, Slovakia

M. Galda Brno University of Technology, Brno, Czech Republic

J. Gavačová Slovak University of Technology in Bratislava, Bratislava, Slovakia

R. Grega Technical University Kosice, Kosice, Slovakia

H. Haberhauer Hochschule Esslingen, Esslingen, Germany

J. Hanuš Technical University of Liberec, Liberec, Czech Republic

M. Hartl University of Technology Brno, Brno, Czech Republic

J. Havlík Technical University of Ostrava, Ostrava, Czech Republic

D. Herak University of Life Sciences Prague, Prague, Czech Republic

J. Homišin Technical University Kosice, Kosice, Slovakia

S. Hosnedl University of West Bohemia, Pilsen, Czech Republic

S. Hrček University of Zilina, Zilina, Slovakia

M. Hrudičková VŠB-Technical University of Ostrava, Ostrava, Czech Republic

J. Ilčík Brno University of Technology, Brno, Czech Republic

L. Janik University of West Bohemia, Pilsen, Czech Republic

A. Kabutey University of Life Sciences Prague, Prague, Czech Republic

K. Kaláb VŠB-Technical University of Ostrava, Ostrava, Czech Republic

P. Kamas University of Zilina, Zilina, Slovakia

J. Kamenický Czech Technical University in Prague, Prague, Czech Republic

M. Kanovic University of Novi Sad, Novi Sad, Serbia

P. Kaššay Technical University Kosice, Kosice, Slovakia

M. S. Keskin Dicle University, Diyarbakir, Turkey

M. Khidhair Al-Mustaqbal College University, Hillah, Iraq

U. Kınıt Yildiz Technical University, Istanbul, Turkey

V. Klouček VUTS Liberec, a.s., Liberec, Czech Republic

P. Kochmański Szczecin University of Technology, Szczecin, Poland

R. Kohár University of Zilina, Zilina, Slovakia

O. Kohl Technical University of Liberec, Liberec, Czech Republic

M. Konečný Technical University of Liberec, Liberec, Czech Republic

M. Kopecky University of West Bohemia, Pilsen, Czech Republic

B. Kopiláková Slovak University of Technology in Bratislava, Bratislava, Slovakia

D. Koutný University of Technology Brno, Brno, Czech Republic

M. Kovalíček University of Zilina, Zilina, Slovakia

R. Kovář Technical University of Liberec, Liberec, Czech Republic

J. Kratky University of West Bohemia, Pilsen, Czech Republic

P. Kříbala Czech Technical University in Prague, Prague, Czech Republic

J. Křička Czech Technical University in Prague, Prague, Czech Republic

E. Kronerova University of West Bohemia, Pilsen, Czech Republic

I. Křupka University of Technology Brno, Brno, Czech Republic

V. Kubec University of West Bohemia, Pilsen, Czech Republic

Ľ. Kučera University of Zilina, Zilina, Slovakia

O. Kult Czech Technical University in Prague, Prague, Czech Republic

M. Leitman University of Zilina, Zilina, Slovakia

P. Lepšík Technical University of Liberec, Liberec, Czech Republic

A. Lufinka Technical University of Liberec, Liberec, Czech Republic

J. Machado Minho University, Braga, Portugal

R. Madaj University of Zilina, Zilina, Slovakia

P. Malý Czech Technical University in Prague, Prague, Czech Republic

O. Marada IDIADA CZ a.s., Mladá Boleslav, Czech Republic

P. Maršálek Technical University of Ostrava, Ostrava, Czech Republic

R. Martonka Technical University of Liberec, Liberec, Czech Republic

I. Mašín Institut prumysloveho inzenyrstvi, Liberec, Czech Republic

M. Matuszak Szczecin University of Technology, Szczecin, Poland

M. Mazac Technical University of Liberec, Liberec, Czech Republic

I. Mazínová University of West Bohemia, Pilsen, Czech Republic

P. Mossóczy Czech Technical University in Prague, Prague, Czech Republic

J. Mrázek Czech Technical University in Prague, Prague, Czech Republic

J. Mudrák University of Zilina, Zilina, Slovakia

D. Nečas Brno University of Technology, Brno, Czech Republic

M. Němček VŠB-Technical University of Ostrava, Ostrava, Czech Republic

P. Němeček Technical University of Liberec, Liberec, Czech Republic

J. Nevrlý Brno Technical University, Brno, Brno, Czech Republic

G. Nicewicz Maritime University of Szczecin, Szczecin, Poland

O. Novak Technical University of Liberec, Liberec, Czech Republic

M. Omasta Brno University of Technology, Brno, Czech Republic

İ. M. Palabıyık Yildiz Technical University, Istanbul, Turkey

D. Paloušek Brno University of Technology, Brno, Czech Republic

L. Pesik Technical University of Liberec, Liberec, Czech Republic

K. Petr Czech Technical University in Prague, Prague, Czech Republic

J. Petřík Technical University of Liberec, Liberec, Czech Republic

M. Petrů Technical University of Liberec, Liberec, Czech Republic

J. Pitoňák University of Zilina, Zilina, Slovakia

S. Poljak University of Zilina, Zilina, Slovakia

J. Popelka Technical University of Liberec, Liberec, Czech Republic

B. Powałka Szczecin University of Technology, Szczecin, Poland

J. Prokop Skoda Auto Mlada Boleslav, Mlada Boleslav, Czech Republic

S. Prýl VUTS Liberec, a.s., Liberec, Czech Republic

M. Rackov University of Novi Sad, Novi Sad, Serbia

P. Rydlo Technical University of Liberec, Liberec, Czech Republic

K. Sarikaya Dicle University, Diyarbakir, Turkey

L. Ševčík Technical University of Liberec, Liberec, Czech Republic

A. Sevinç Yildiz Technical University, Istanbul, Turkey

A. Skarolek Technical University of Liberec, Liberec, Czech Republic

P. Skládal Masaryk University, Brno, Czech Republic

R. Slanina VŠB-Technical University of Ostrava, Ostrava, Czech Republic

D. Smejkal Brno University of Technology, Brno, Czech Republic

P. Sniehotta VŠB-Technical University of Ostrava, Ostrava, Czech Republic

P. Šperka Brno University of Technology, Brno, Czech Republic

P. Srb Technical University of Liberec, Liberec, Czech Republic

P. Štarha University of Technology Brno, Brno, Czech Republic

F. Starý Czech Technical University in Prague, Prague, Czech Republic

P. Syrovátka Czech Technical University in Prague, Prague, Czech Republic

Y. Takeichi Toyohashi University of Technology, Toyohashi, Japan

E. Tomeh Technical University of Liberec, Liberec, Czech Republic

M. Trochta Technical University of Ostrava, Ostrava, Czech Republic

R. Uhlíř Czech Technical University in Prague, Prague, Czech Republic

V. Vanek University of West Bohemia, Pilsen, Czech Republic

D. Vejrych Technical University of Liberec, Liberec, Czech Republic

R. Voženílek Technical University of Liberec, Liberec, Czech Republic

M. Vrbka Brno University of Technology, Brno, Czech Republic

J. Zápotočný Slovak University of Technology in Bratislava, Bratislava, Slovakia

M. Žarnay University of Zilina, Zilina, Slovakia

A. Zatočilová Brno University of Technology, Brno, Czech Republic

Part I
Machine Design

S. Bingol, M. S. Keskin, O. Ayer, K. Sarikaya, O. Burucu, P. Alipur, J. Bucala, J. Mudrák, M. Žarnay, M. Burián, J. Havlík, Z. Folta, M. Trochta, P. Maršálek, M. Galbavý, J. Pitoňák, Ľ. Kučera, M. Galda, J. Brandejs, R. Grega, J. Hanuš, P. Rydlo, L. Ševčík, M. Konečný, D. Vejrych, M. Diblík, J. Homišin, P. Kaššay, S. Hrček, J. Bucala, M. S. Keskin, S. Bingol, H. B. Elem, A. Atar, M. Khidhair, U. Kınıt, M. Bozca, İ. M. Palabıyık, A. Sevinç, Ü. H. Büyükalgan, V. Klouček, J. Fábera, S. Prýl, V. Brozová, Ľ. Kučera, I. Gajdac, P. Kamas, Ľ. Kučera, T. Gajdošík, R. Madaj, J. Machado, J. C. Campos, M. Mazac, R. Martonka, V. Fliegel, M. Mazac, I. Mazínová, P. Florian, M. Němček, J. Nevrlý, K. Petr, V. Dynybyl, J. Chmelař, J. Prokop, L. Ševčík, P. Srb, V. Fliegel, P. Syrovátka, V. Dynybyl, J. Andruš, E. Tomeh, V. Vanek, R. Voženílek and P. Brabec

Part I—Machine Design consists of 31 scientific papers dealing mainly with designing, machine parts, equipments, mechanisms, and functional units. Design is a creative activity using theoretical knowledge and practical experience and is focused on the creation of a technical documentation for manufacturing of certain equipment. An equipment design must be based not only on functionality and durability, but also easy manufacturing, low cost and low energy, and environmental performance. In most construction branches computer technology is applied. It greatly facilitates not only routine calculations and virtual modeling, but also allows analyzing and simulating of operating conditions of designed parts and whole mechanisms. The study and research leading to further knowledge about the unknown effects, parameters, mechanical properties and character of the individual parts, and complete assemblies of machinery are therefore very important not only for understanding the problem substance, but above all for achieving the subsequent optimization.

FE Analyzing of Layout Types for Multi-hole Extrusion Dies

S. Bingol, M. S. Keskin, O. Ayer, K. Sarikaya, O. Burucu and P. Alipur

Abstract Extrusion method is an important bulk-forming process to transform materials into semi-finished products in the form of bar, strip, and solid section as well as tubes and hollow sections. One of the basic considerations of die design is to determine the number of die openings based on the shape and size of the profile. In this study, variation of the extrusion load and temperature is investigated for different number and layout of die openings by finite element analysis. Three types of layouts, radial layout of a multi-hole die, flat layout of a multi-hole die and orientation of a shape around its center of gravity, were simulated with four openings in the dies. Moreover, the most commonly used type of them was also simulated for different number of openings in the die to compare the effect of the openings number on the extrusion.

Keywords Extrusion · Multi-hole die · Finite element analysis · Aluminum

1 Introduction

Extrusion is a metal forming method in which a metal block, named as billet is forced by the stem and formed through a die opening that is smaller than the billet's cross-section. Extrusion process can be realized as cold or hot metal forming depending on the material and the used method.

S. Bingol (✉) · M. S. Keskin · K. Sarikaya · O. Burucu · P. Alipur
Engineering Faculty, Dicle University, Diyarbakir, Turkey
e-mail: sbingol@dicle.edu.tr

O. Ayer
Engineering Faculty, Trakya University, Edirne, Turkey
e-mail: onderayer@trakya.edu.tr

L. Ševčík et al. (eds.), *Modern Methods of Construction Design*,
Lecture Notes in Mechanical Engineering, DOI: 10.1007/978-3-319-05203-8_1,

In the extrusion process, one of the most important stages is design of the extrusion dies. In the die design, primarily evaluation and requirement to be decided key criterions are as below;

1. How many profiles will be produced at the same time depending on the shape and sizes of the product in a die (the number of die openings)
2. Location of the die openings with respect to the billet axis,
3. Optimum die bearing length to increase manufacturing speed.

Design of a die with single-hole is simpler than a die with multi-hole. During the designing of a multi-hole die, it is required to decide the number of the openings and how to be placed a geometric layout on the surface of the die (Saha 2000).

In the multi-hole dies, the distance between the die openings should be large enough to withstand the die pressure at these points. Essentially, there are three methods of layout for the multi-hole dies; flat, radial, and around the center of gravity. In radial layout, major axis of each shape lies along a radius and same points on the channel of each opening are in the same position according to the center of the die. The advantage of this method is that the openings are uniform and die corrections are easy. The disadvantage can be listed as the difficulty in controlling twisting and handling on runout table. Radial layout is not in use for the aluminum extrusion due to difficulty in handling (Saha 2000).

Major axis of each shape in flat layout is perpendicular or parallel to a line passing through the center of the die. The advantage of a flat layout is that products can easily be pulled keeping in runout table for a quick production. The disadvantage is known as difficulties in die correction and controlling uniform extrusion length on the runout table.

In the multi-hole dies, material flow is quite complex structure. Material flow is dependent on the number of parameters such as shape, number and layout of die openings. To obtain a regular metal flow in the die, some of the rules are decided by the die designers. In a single-hole die, the center of gravity of the section should be close to the center of the billet or the die. In the multi-hole dies, the center of gravity of each section should be more or less coincident with the center of gravity feeding the opening portion of billet. Another parameter is to decide the number of holes in the die. This parameter is determined by some factors such as existing tooling to fit the number of holes, movement ease of products in runout table, profile length and the metal flow.

A brief review of the research on multi-hole extrusion is as follows. Ulysee and Johnson have presented analytical and semi-analytical upper bound solutions for plane-strain extrusion through an eccentric hole and unsymmetrical multi-hole dies. It is validated the upper bound results with the literature and with the finite element method results (Ulysse and Johnson 1998). The flow behavior of metal in the extrusion of a pipe into a porthole-die was investigated by Xie et al. A kind of visioplasticity method employed in the study (Xie et al. 1995). Sinha et al. presented a methodology for the preliminary design of the multi-hole extrusion

process. The estimation of the ram force is carried out using upper bound method by considering the process as a single-hole extrusion (Sinha et al. 2009). In the last two decades, computer simulation based on the finite element method (FEM) has been increasingly applied to the aluminum extrusion process. FEM allows geometrical complexities to go beyond the capabilities of the conventional analytical methods. A developed FEM program (Press Form) based on the mixed Eulerian–Lagrangian approach by Tong (Tong 1995) was applied to extrusion dies with two double-hole flat layout. It was demonstrated that velocity non-uniformity as affected by hole size and position (Tong 1995). Another FEM model was developed by Van Rens. It was demonstrated that the possibility of revealing velocity fields in the case of extrusion through a two-hole flat die with varied bearing length (Van Rens 1999). Fang et al. attempted to investigate the effect of steps in the die pocket on metal flow to produce two chevron profiles with unequal thicknesses through two-hole dies, by means of 3D FEM simulation of extrusion in the transient state. The results showed that the pocket step could be effectively used to balance metal flow. Extrusion experiments also validated the predictions of metal flow, extrudate temperature and the pressure required for extrusion through the pocket dies with three different designs (Fang et al. 2009).

In recent years, the finite element modeling has been started rather an intense interest to minimize the cost of extrusion and loss of labor. The finite element modeling provides a great advantage for designer to prevent the errors in the design stage which may effect to production. In this study, in extrusion method, extrusion loads which are consisted as a result of different layouts in multi-hole dies were examined. For that purpose, the simulations of three different layout geometries in the dies (flat, radial, and around the center of gravity) were performed and consisting of the results were compared. Thus, the most suitable geometric layout was tried to detect by FE analyzing. After detecting the die has the most suitable layout geometry, an additional simulation was performed changing the numbers of the die openings in that same layout geometry type.

2 Finite Element Modeling of Multi-hole Dies

As it is seen in the Fig. 1, geometries of dies were designed in three different layout geometries that are flat, radial, and around the center of gravity settlement. In the modeling, AA6061 have been selected as the billet material because 6xxx series aluminum alloys are used extensively in extrusion industry. As it is seen in the Fig. 2, billet temperature of 460 °C, die temperature of 420 °C, and stem temperature of 70 °C were assigned for three different simulations. The geometries of billet and tools were drawn in a CAD-based software and saved as *.STL formats. Then, the geometries were transferred to the pre-processor unit of DEFORM 3D software. Mesh density of billet material was kept high and it has been selected the range of 30,000 and 50,000 elements. As it is seen in the Fig. 3, in the modeling step, structure of high density mesh was used in sections

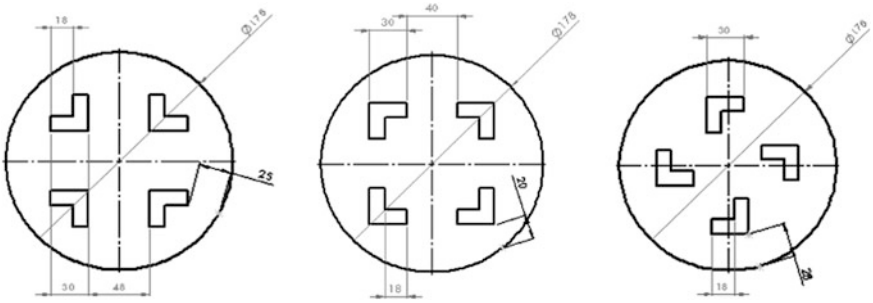

Fig. 1 Technical drawing of the multi-hole dies (from *left* to *right*): flat layout, around the center of gravity layout, radial layout

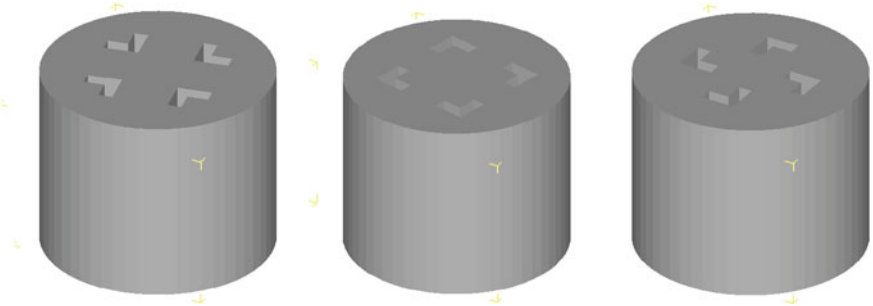

Fig. 2 Multi-hole die design used in the modeling (from *left* to *right*): flat layout, around the center of gravity layout, radial layout

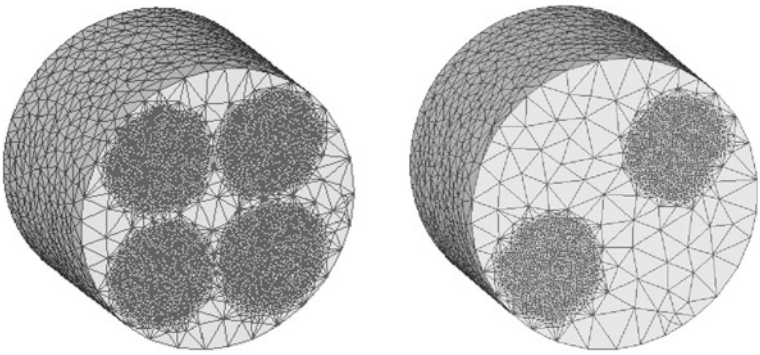

Fig. 3 Different mesh density for four holes and two holes dies (from *left* to *right*): four holes die, two holes die

corresponding to the openings of die because of the billet is that the front surface of the main deformation region. Dies and ram materials were defined as rigid bodies. Therefore, non-mesh structures were used in their geometries. Ram speed

was kept constant for all the simulations and regulated as 5 mm/s. The coefficient of friction between the dies and the work piece was appointed as 0.4 by the software library. Modeling was completed in light of these parameters and established database required for the initiation of the simulation.

In the study conducted, as well as the above given shapes of dies, an additional simulation of the die with two-holes was performed (Fig. 3). The aim in this case is to determine the effect of the number of holes in the die.

3 Results of FE Analyses and Discussion

After modeling, obtained results with simulations were compared. The simulations were performed for three different layouts in the dies with four holes. They can be seen in the Fig. 4. The extrusion loads occurring for each layout type are seen in the Fig. 5. When analyzed Fig. 5, extrusion loads consisting during the stroke are observed that a typical such as load—ram travel diagram consisted in a direct extrusion. It is observed from the figure that there is no significant difference between the three die types. The possible reason for this case, the extrusion rate which is calculated as the ratio of cross sectional area of billet to opening area of the die, is same for each of the three die types. However, the extrusion load consisted for the flat layout die can be seen that relatively a bit low according to the type of the other two die layouts. The reason is that as can be understood from Figs. 1, 2 and 4, the flowing metal in the flat layout is near the center of the die. As it is well known in extrusion process, the central area of billet according to the surrounding area shows a more easily and quickly flow. One of the reasons of this flow difference is existence of friction between the container and the billet the surrounding area, while the other reason is that the center area is directly in front of the opening of die. Consequently, due to the fact that profile openings on the flat layout in the die is located closer to the center, occurred of a material flow is more comfortable than the other layouts in the die and thus, less extrusion load is occurred.

After it was determined that extrusion load was lower for flat layout die according to other layouts of die, a new simulation was performed for the flat layout die type. Only the number of output profiles was reduced two keeping the same as all other modeling parameters in this simulation. Thus, the effect of the same die type of settlement and the number of output obtained for extrusion parameters were simulated on the extrusion load. The load versus stroke diagram obtained from as a result of the simulation can be seen in the Fig. 6. As can be seen easily in the figure a large increase was occurred in the extrusion load. As is might be expected that the reason for this is the change of the extrusion rate. The extrusion rate was increased doubled because the number of profile (die openings) was reduced from four to two. The extrusion rate can be seen to be highly effective on the extrusion load in the composed load-stroke diagrams.

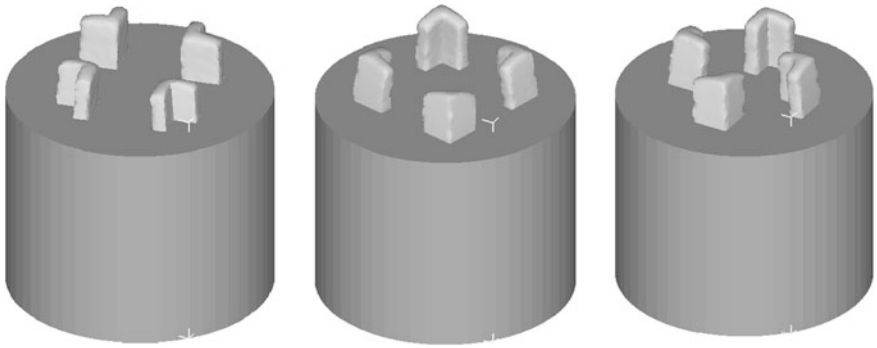

Fig. 4 Simulations for different layouts (from *left* to *right*): flat layout, around the center of gravity layout, radial layout

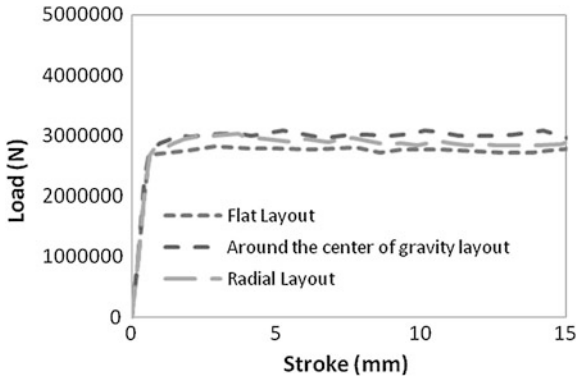

Fig. 5 The extrusion loads versus stroke occurred for each layout type

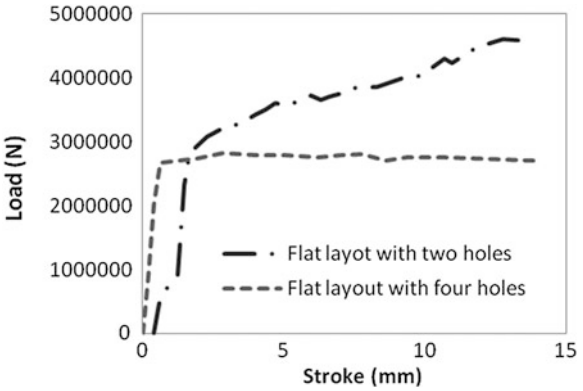

Fig. 6 The extrusion loads versus stroke occurred for flat layout types with two holes and for holes

4 Conclusions

In the same extrusion process conditions, extrusion loads for the different layout of profile form in the multi-hole dies were examined. However, extrusion load changing were examined by changing of the number of die openings. With this study, the following results were obtained;

- As compared the three different layouts in the die, extrusion load which occurring for a flat layout was found to be slightly lower according to the other two layouts in die. Due to the fact that profile openings of flat layout in the die are located closer to the center of die, a more comfortable material flow occurred and so that less extrusion load was occurred.
- As a result of performed a simulation as two openings in addition to the four openings in the flat layout in die, extrusion load was found quite rise. The reason for this is two times increase in the extrusion rate.

Acknowledgments A commercial FEM code DEFORM-3D v10.2 was used for simulations in this study. DEFORM-3D developed by Scientific Forming Technology Corporation (SFTC)® in the US. Authors wish to thank Trakya University for the support of DEFORM-3D simulations under the license of SFTC®.

References

Fang G, Zhou J, Duszczyk J (2009) FEM simulation of aluminum extrusion through two-hole multi-step pocket dies. J Mater Process Technol 209:1891–1900

Saha PK (2000) Aluminum extrusion technology. ASM International, Ohio

Sinha MK, Deb S, Dixit US (2009) Design of a multi-hole extrusion process. Mater Des 30:330–334

Tong L (1995) FE simulation of bulk forming processes with a mixed Eulerian–Lagrangian formulation. Ph.D. thesis, Swiss Federal Institute of Technology Zurich, pp 89–91

Ulysse P, Johnson RE (1998) A study of the effect of the process variables in unsymmetrical single-hole and multi-hole extrusion processes. J Mater Process Technol 73:213–225

Van Rens BJE (1999) Finite element simulation of the aluminum extrusion process. Ph.D. thesis, Eindhoven University of Technology, pp 77–79

Xie JX, Murakami T, Ikeda K, Takahashi H (1995) Experimental simulation of metal flow in porthole-die extrusion. J Mater Process Technol 49:1–11

Development of the Testing Device for Simulation of Contact Between Plasmabit's Locking System and the Surface of the Geothermal Well

J. Bucala, J. Mudrák and M. Žarnay

Abstract This article is focused on design of innovative systems for locking mechanisms used for geothermal wells up to 10 km deep. The article contains design of the testing device, which will be constructed in order to confirm proper function of the locking system. The testing device is currently under development at Department of Design and Mechanical Elements of University of Žilina.

Keywords Plasmabit · Locking system · Testing device

1 Introduction

The Plasmabit is unique device which should be able to work under extreme conditions up to 10 km beneath Earth surface effectively. It is an autonomous system for drilling able to move on its own and withstand temperatures up to 400 °C and pressure of 100 MPa. There are not any known manufacturers of such devices or any other similar systems already working anywhere around the world. The device consists of many subsystems, such as systems for motion, rock disintegration, control systems, cooling systems and backup systems.

The locking system is currently under development, but so far we are able to state that the idea of the locking system itself is possible to design. Locking to the surface of the geothermal well is possible because of two horizontally mounted linear hydromotors orientated against each other. Locking to the surface of the

J. Bucala (✉) · J. Mudrák · M. Žarnay
University of Žilina, Žilina, Slovakia
e-mail: jan.bucala@fstroj.uniza.sk

J. Mudrák
e-mail: jozef.mudrak@fstroj.uniza.sk

M. Žarnay
e-mail: martin.zarnay@fstroj.uniza.sk

L. Ševčík et al. (eds.), *Modern Methods of Construction Design*,
Lecture Notes in Mechanical Engineering, DOI: 10.1007/978-3-319-05203-8_2,

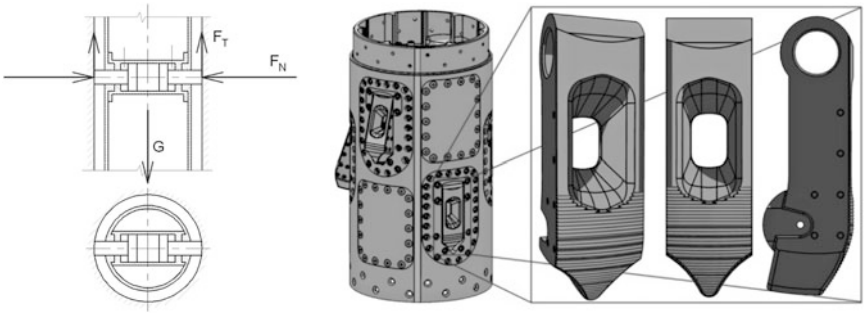

Fig. 1 The principle of the locking system, part of the locking subsystem and detail view on the locking element

geothermal well is accomplished by pushing out locking elements towards the surface of geothermal well and by generating normal force $\boldsymbol{F_N}$ high enough for safe lock. In this case, vertical force which needs to be locked has magnitude according to Eq. (1).

$$\mathbf{G} = 2.F_T = 2.F_N.f \tag{1}$$

where **G** is the force of gravity of the plasmabit, F_T is the friction force between locking elements and the surface of the geothermal well, F_N is generated normal force on the surface of the geothermal well f is the friction factor (Fig. 1).

After one of plasmabit's locking subsystems is fixed, another part can move in vertical direction. Vertical motion is similar to one of the earthworm and it is allowed by the linear hydmomotor which is oriented vertically.

It is possible to minimize dimensions and mass of whole device by next development, research and optimisation of the locking system or whole device at once. That's why it is necessary to have geothermal well surface data measured and verified for further development of the locking system. The key goal is to know real contact conditions between the locking element and the surface of the geothermal well. In order to solve this task, the testing device is being developed. The device will simulate normal force and tangential motion of locking element on the rock specimen (Medvecký et al. 2012).

Measurements will take place in a laboratory of Faculty of Mechanical Engineering of University of Žilina. It is required to use materials and technologies available directly at the university.

2 The Testing Device

It is device designed to simulate contact between locking elements and the surface of the geothermal well. The device is designed to simulate real load of whole device with two locking elements in simultaneous contact with the surface of the

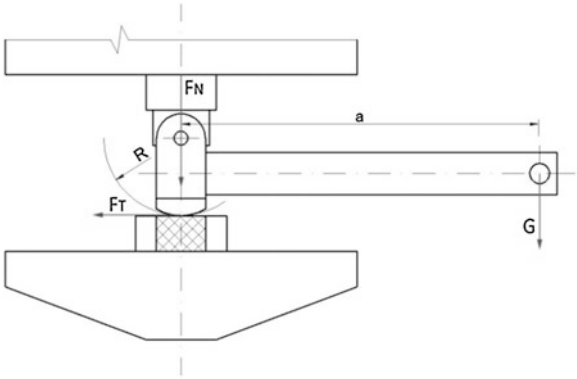

Fig. 2 Variant with one friction surface

geothermal well. Main reason of developing the testing device is to verify system's ability to carry out required functions. Main goal to be achieved is to find out whether it comes to movement of locked locking elements or not under given load and normal forces. In other words, what will the friction factor value for different materials of friction coupling be. The measurement of normal forces is planned in order to verify proper function of the locking system.

The testing device consists of a hydraulic press, which is available in one laboratory of Faculty of Mechanical Engineering. The hydraulic press is suitable for given task because it can generate adequate force and this force can be measured and recorded. However there is only one hydraulic press available. That means one force has to be generated by any other way. Devices such as levers, pulleys and motion screws were taken into an account. Some variants are described in following text.

We took into an account solution with one friction surface as well as solution with two friction surfaces (which represents real load more accurately) while creating new variants. Variant with one friction surface is shown in Fig. 2. Normal force F_N is drawn by the hydraulic press and friction force F_T is drawn by the lever mechanism. The locking elements are located at the very end of lever, the rock specimen is hatched.

Variant with two friction surfaces and the lever mechanism is shown in Fig. 3. Normal force is drawn by the hydraulic press and friction force by the lever mechanism.

Variant with two friction surfaces is designed to draw normal force by hydraulic press and mass of Plasmabit by the motion screw. Plasmabit's mass represents force which is able to move the device, especially the locking elements, vertically. Device is shown in Fig. 4.

Variant, which is shown in Fig. 5, uses extra weight to simulate Plasmabit's mass. Weight is attached to tightened rope through the pulley. The force inside the rope is axial with rest of the device. Weight can be added or removed according to current demands.

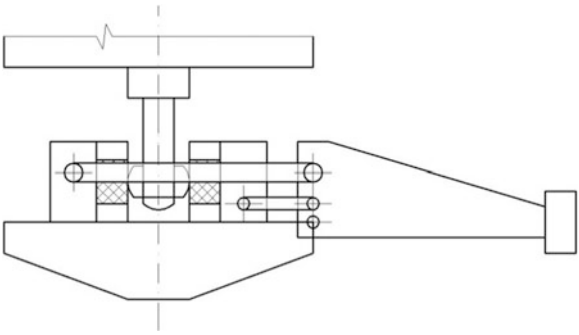

Fig. 3 Variant with two friction surfaces and lever mechanism

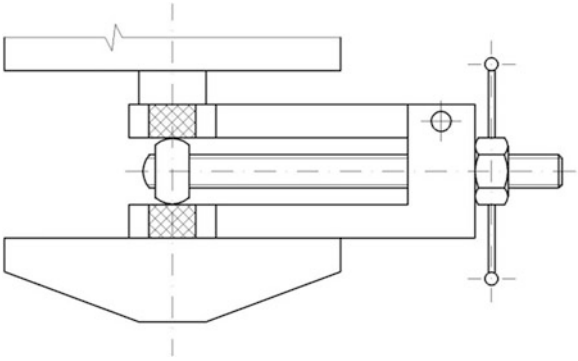

Fig. 4 Variant with two friction surfaces and motion screw

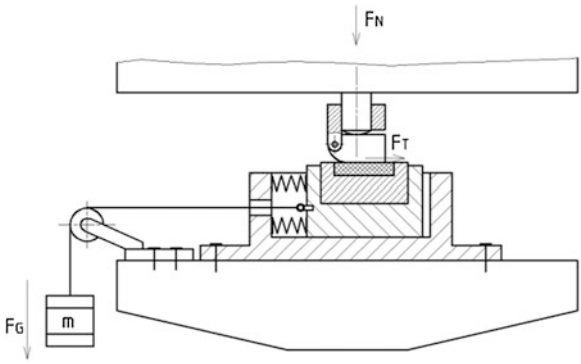

Fig. 5 Simulation of Plasmabit's mass with extra weight and the pulley

The reel is used to generate adequate axial force inside the rope and simulates Plasmabit's mass this way, as is shown in Fig. 6.

Another variant, which is shown in Fig. 7, uses short stroke, manually operated hydromotor to simulate Plasmabit's mass.

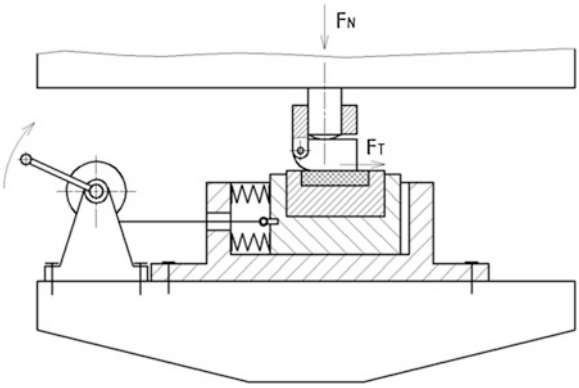

Fig. 6 Simulation of Plasmabit's mass with the reel

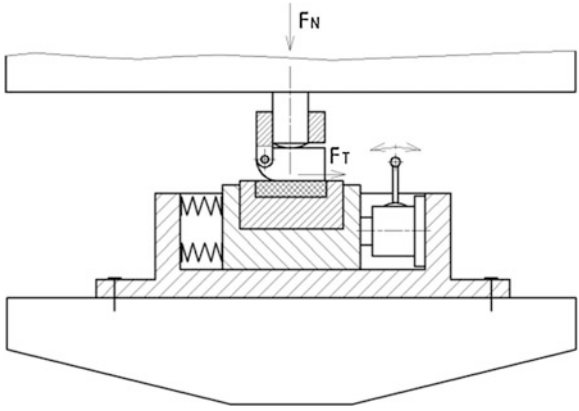

Fig. 7 Simulation of Plasmabit's mass with manually operated hydromotor

Plasmabit's mass is simulated by piston ejection of the linear hydromotor as is shown on Fig. 8. The normal force towards the surface of the geothermal well is simulated by turning the motion screw with a trapezoidal thread. Whole system is attached to the hydraulic press. The locking element has two operational surfaces and is pressed towards two rock specimens.

All variants (including those not mentioned in this article) were compared to each other by many criteria: similarity of force conditions with reality, possibility to apply motion sensors and load cells, compatibility of dimensions with the hydraulic press, manufacturability of whole testing device and manufacture cost. The most suitable system for our purpose is one shown in Fig. 8. All experiments will take place on this variant.

Selected variant of the testing device is currently under development and early stage 3D model can be seen in Fig. 9. (Žarnay et al. 2013)

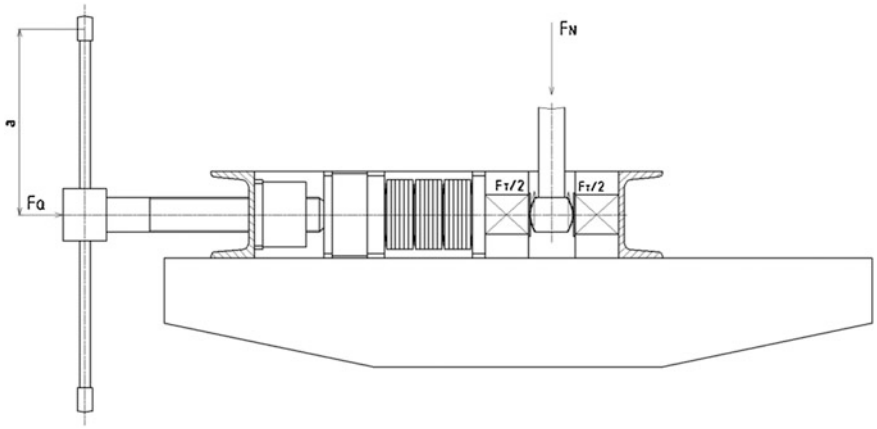

Fig. 8 The force of gravity is drawn by the hydraulic press and the normal force on the locking elements is drawn by the motion screw through the load cell and system of disc springs

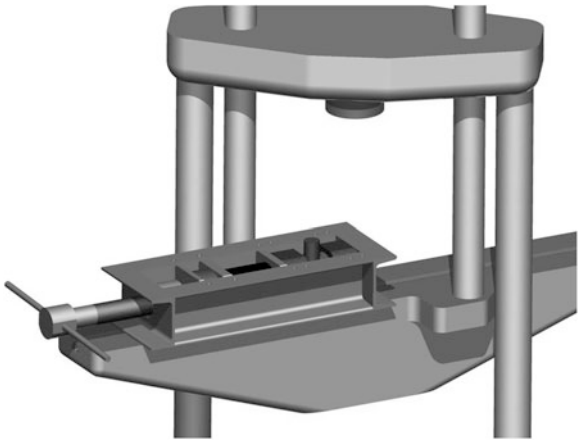

Fig. 9 Early stage 3D model of the testing device

3 Conclusions

The data measured during the simulation can be used directly for project "Autonómne robustné mechatronické systémy pre ultrahlboké geotermálne vrty". There are other subjects to be verified during the tests, such as properties of rocks under high contact pressure, experimental verification of the friction factor on selected surfaces and measurement of wear of locking elements. Measured data will be preliminary only because simulation in the real conditions (very high pressure and temperature) would be very expensive and difficult solution.

Acknowledgments The research work reported here was made possible by the scientific grant agency of the Ministry of Education of the Slovak Republic (VEGA), project numbers 1/1049/11 and 1/0582/12.

References

Medvecký Ľ, Žarnay M, Gajdáč I, Sokol, M, Mudrák J, Drdol K, Kamas P (2012) Konštrukčný návrh funkčného vzoru pohybového systému plazmabitu. Štúdia k výskumnej správe KKČS-2012-139-04, Žilina

Žarnay M, Medvecký Ľ, Sokol M, Kamas P (2013) Systém pohybového systému plazmabitu. Základné informácie pre vývoj hydraulického a elektrického systému (Výskumná správa), Žilina

Solution the Drive Lifting Scissor Platforms

M. Burián, J. Havlík, Z. Folta, M. Trochta and P. Maršálek

Abstract Scissor platforms are used for vertical transport of loads or persons to keep them at the requested height of the load device. Lifting platforms, both mobile and stationary, are nowadays used almost with no limitation, e.g. in the production, storage, handling (for loads, equipment or people transport). Drive scissor lift platform is an important part of scissor platform. Lifting device is a mechanism that raises scissor construction and the platform to specific height.

Keywords Scissor platforms · Lifting device · Hydraulic piston · Telescopic push chain Serapis

1 Introduction

There are many solutions and options the platform can be lifted. Decisions are made according to three main criteria: the lifting height, weight lifting equipment and lifting equipment according to the drive (ČSN EN 1494 + A1; ČSN EN 280 + A2).

M. Burián (✉) · J. Havlík · Z. Folta · M. Trochta · P. Maršálek
VŠB—Technical University of Ostrava, Ostrava, Czech Republic
e-mail: miroslav.burian@vsb.cz

J. Havlík
e-mail: jiri.havlik@vsb.cz

Z. Folta
e-mail: zdenek.folta@vsb.cz

M. Trochta
e-mail: miroslav.trochta@vsb.cz

P. Maršálek
e-mail: petr.marsalek@vsb.cz

L. Ševčík et al. (eds.), *Modern Methods of Construction Design*,
Lecture Notes in Mechanical Engineering, DOI: 10.1007/978-3-319-05203-8_3,

According to (ČSN EN 1494 + A1), page 11, Sec. Drive 3.2 these drives are used:

- Manual—human power drive,
- Pneumatic—compressed gaseous substances drive,
- Hydraulic—compressed hydraulic liquid drive,
- Electric—electrical energy drive.

There are described the most commonly used drives of lifting device by using hydraulic piston and a telescopic push chain Serapis.

2 Hydraulic Piston

Most often, it is a hydraulic piston in the Fig. 1 which is used for scissor platforms drive.

Lifting is based on the principle of pressure energy and physical properties of the incompressibility of liquids. The principle is in the circulation of working liquid in the closed circuit and of mineral oil in the tank of hydraulic unit. Pressure of the liquid is ensured by hydroelectric generator. Pipeline, connections and pressure hoses are used for joining the individual parts.

In the hydraulic mechanism, there are losses caused by liquid friction, therefore there must be used short hoses and a little amount of knees (Kopáček and a Pavlok 2009).

The benefits are simplicity, large force and accuracy in small dimensions, and a high efficiency.

Disadvantages of this mechanism are expensive service, maintenance, risk of liquid leakage at the failure, commissioning by a specialized person.

Possibilities of the scissor platforms 'hydraulic piston locations are in the Fig. 2. Individual placement of hydraulic piston has an impact on its size.

3 Electric Drive with Push Serapid

It is a mechanical way of lifting. The principle is based on locking or unlocking the connecting elements. During lifting a load, specially shaped chains join together and formate a solid column. When folding the chains are gradually unlocked and composed in the lower part. Serapid combines the advantages of hydraulic mechanisms which are reliable and safe, and removes restrictions of lift height. It is possible to construct Serapid by achieving higher heights of strokes height while Serapid is on the same hight but at the expense of larger rack type area.

Other benefits include lift to the nearest millimeter at high speed, high speed of lift, lift up to 10 tons at high altitudes, easy construction, minimal maintenance.

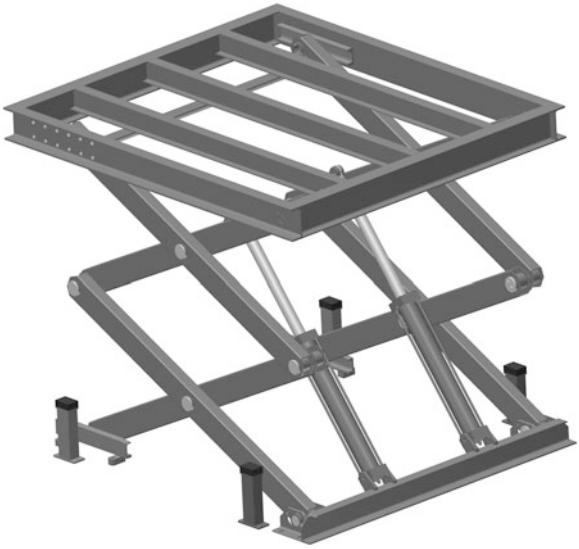

Fig. 1 Hydraulic piston by scissor platforms

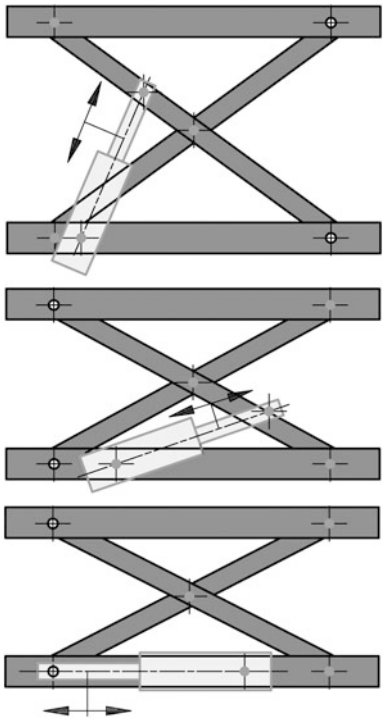

Fig. 2 Possibilities of the hydraulic piston by scissor platforms

Fig. 3 Location by scissor platforms

The disadvantage is that the load must lie at right angles to conduit, the power unit must be horizontally attached to the base. It must be ensured to prevent working of axial force to a fixed column of linear telescopic push chain. Location of linear telescopic push chain Serapide at the scissor structure is in the Fig. 3 (Serapid 2013).

4 Pivots Load When Using a Hydraulic Piston or Serapid

Various forces affect the hydraulic piston in its different location (see this chapter).

This location affects size of the hydraulic piston. There was made a static calculation of scissor construction for placing of hydraulic piston, which is shown in Fig. 1. Method of the scissor structure individual elements replacement, see Fig. 4, was used for the calculation. This method is based on the principle of removing one element of the scissor structure, implementation of relevant responses, influencing the body, and building equilibrium conditions.

A similar calculation was performed for linear telescopic push chain Serapide which is shown in Fig. 3. Method of the scissor structure individual elements replacement for Serapide is shown in Fig. 5.

The calculation was performed for the same conditions, which are load capacity of the device 500 kg/m^2, 6.3 m^2 platform area, the same distance of pivots in the shoulder (1 m), etc.

Individual pins arrangement for scissor structure is illustrated by Arabic numerals, see Figs. 4 and 5. In the calculation using the push chain Serapide it was

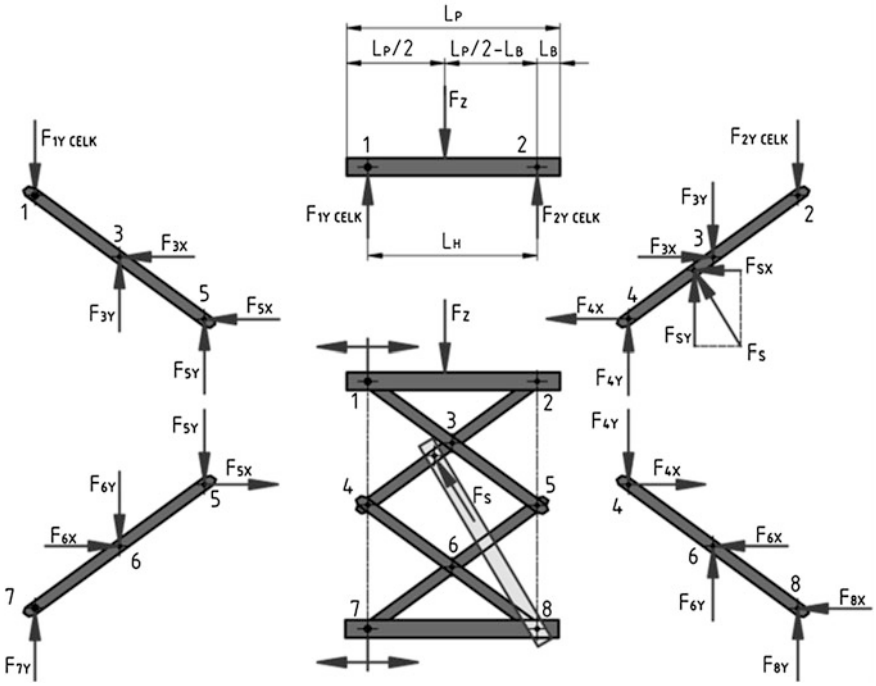

Fig. 4 The effect of individual forces in the shoulder when lifting with hydraulic piston

found out that the same loading force act on the pivots in paragraphs 2, 4, 5, 8. The pins 3 and 6 have a double power than pins 2, 4, 5, 8. These forces the pins 3 and 6 are the same size. Calculation is therefore conducted to pin 2, see Fig. 6 and to pin 3, see Fig. 7.

A similar calculation was made for the hydraulic piston, except that usually different strengths act in the pins. Most of them are not the same as when using the push chain Serapide. The same load forces are at the loading platforms, where the load forces from the weight of the platform and platform capacity act.

Example of maximum bending moment calculation according to the Eqs. (1), (2) and pin gauge specification according to the Eq. (3):

Maximum bending moment for maximum force F_i, for Fig. 6.

$$M_{Oi} = \frac{\left|\sqrt{F_{iY}{}^2 + F_{iX}{}^2}\right|}{2} \cdot l_{\check{C}iM} \tag{1}$$

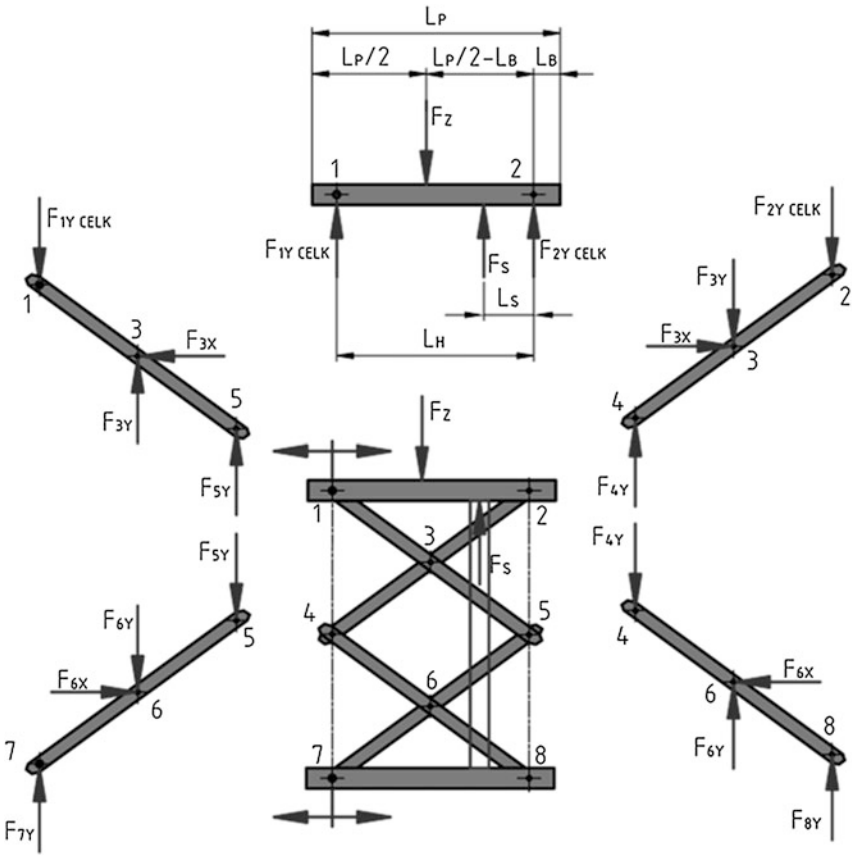

Fig. 5 Acting of individual shoulder forces at lifting by Serapid

Maximum bending moment for maximum force F_i, for Fig. 7.

$$M_{Oi} = F_{3Y} \cdot l_{\check{C}iM} \tag{2}$$

Diameter pin

$$d'_{\check{C}i} = \sqrt[3]{\frac{M_{Oi} \cdot 32 \cdot k_S}{\pi \cdot Re}} \tag{3}$$

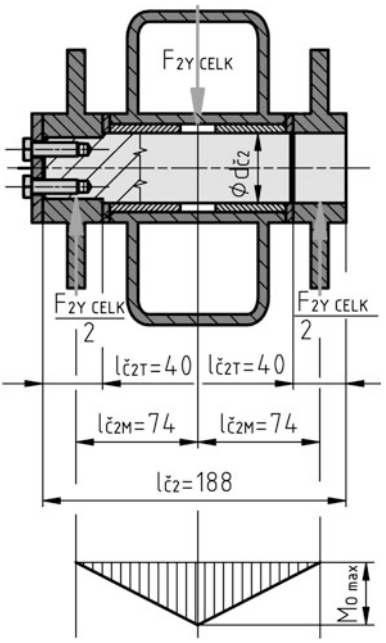

Fig. 6 Pin storage 2

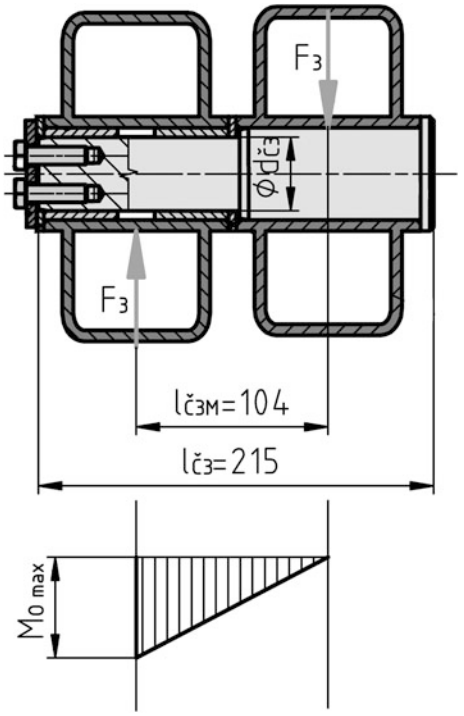

Fig. 7 Pin storage 3

5 Conclusions

The advantage of using pushed chain Serapid is in using push chain as a lifting device while scissors ensure only platform stability. In case of using hydraulic piston, scissors are loaded directly. These scissors form a lifting element and at the same time fulfill a function of platform stability. By calculation it was found out that when using hydraulic piston, the forces based on the pines are approximately 20 % bigger then using Serapid. Scissors size and the location of hydraulic piston which lifts scissors construction are very important for it. Size of both profiles and individual pins can be influenced by these parameters.

References

ČSN EN 1494 + A1. Mobilní a přemístitelné zvedáky a souvisící zdvihací zařízení. Praha: Úřad pro technickou normalizaci, metrologii a státní zkušebnictví, Třídící znak 270810, 2010, pp. 40

ČSN EN 280+A2. Pojízdné zdvihací pracovní plošiny – Konstrukční výpočty – kritéria stability – konstrukce – přezkoušení a zkoušky. Praha: Úřad pro technickou normalizaci, metrologii a státní zkušebnictví, Třídící znak 27 5004., 2010, pp. 72

Kopáček J. a Pavlok B (2009) Tekutinové mechanismy. VŠB – Technical University of Ostrava, 2009, pp.151

Serapid (2013) Serapid lift products applications and Advantages. 2013, Available via Serapid.com, http://serapid.com/gb/theatre/th_app_av_gb.html

Powershift Differential Transmission with Three Flows of Power for Hybrid Vehicles

M. Galbavý, J. Pitoňák and L. Kučera

Abstract In near future hybrid vehicles will by very popular, because of its ecology and efficiency. Using electric power with light transmission these benefits can increase. Differential transmissions enable us to achieve by its construction to split the power into more flows, so they offer higher number of speed gears at lower count of gears and control components. A planetary set, working as a gear at several speed gears, in other speed gears as a differential represents the base of the transmission. The principle is a base of the described powershift differential transmission with three flows of power.

Keywords Hybrid vehicle · Transmission · Differential transmission · Matlab

1 Introduction

The request of fluent start and smooth running of vehicle, as well as energy and fuel consumption eventuated into the design of gearboxes enabling the powershift. This option offers a higher number of gearbox concepts. Many transmissions include planetary gearboxes and shaft gearboxes with powershift, where the synchronizing elements are replaced by the most frequently used lamellar frictional components (brakes and clutches) (Naunheimer et al. 2011).

M. Galbavý (✉) · J. Pitoňák · L. Kučera
University of Žilina, Žilina, Slovakia
e-mail: galbavym@fstroj.utc.sk

J. Pitoňák
e-mail: pitonakj@fstroj.utc.sk

L. Kučera
e-mail: kuceral@fstroj.utc.sk

L. Ševčík et al. (eds.), *Modern Methods of Construction Design*,
Lecture Notes in Mechanical Engineering, DOI: 10.1007/978-3-319-05203-8_4,

2 Transmission Working Principle

The basic of the described powershift transmission is a differential with four shafts—combined planetary mechanism, consisting of two simple planetary gears. This differential includes three input shafts and one output shaft. In the case if there are inserted several countershaft gears before the differential, it is possible to create the configuration (Fig. 1) with a possibility to split the power into three flows and subsequently merged into the four-shaft-differential (Pitoňák et al. 2012, Málik et al. 2007; Ikrinský 2003; Málik and Kučera 1999).

Accordingly, between the gearbox input shaft and the four-shaft-differential, there are implemented countershaft gears. Each from these countershaft gears is connected to a corresponding differential shaft by a frictional lamellar clutch and each of them can be blocked by the frictional lamellar brake. There holds that if the clutch of the shaft is on, the brake of the same shaft is off and vice versa too; these components are ergo associated and, combining the of engaged and disengaged associated control components, it is possible to achieve seven ways of power flow in the gearbox, thus seven different gears.

3 Transmission Requirements

The main design includes definition of minimal and maximal transmission ratio and option of all other transmission ratios. Its application is conditioned by a correspondent designing of transmission ratios, resulting from direct requirements to vehicle capacities, in particular in its operating conditions. It is possible to set the minimal and maximal transmission ratio according to the known definitions. In order to achieve a regular gears layout and to prevent changing short and long gear differentiations φ between individual gears, it is necessary to design all adjacent transmission ratios φ approximately the same (Naunheimer et al. 2011; Ikrinský 2003).

If ω is angular velocity of component and u_v is internal transmission ratio of planetary set, for the aforementioned transmission with four-shaft-differential, there are defined the following equations (Málik et al. 2007; Málik and Kučera 1999), whereby all the significations of equation parameters and transmission components are the same according to the Fig. 2 (it equals $R_2 = Q_1$):

$$\omega_{P1} - \omega_{Q1} \cdot u_{v1} = (1 - u_{v1}) \cdot \omega_X \tag{1}$$

$$\omega_{P2} - \omega_{Q2} \cdot u_{v2} = (1 - u_{v2}) \cdot \omega_{R2} \tag{2}$$

$$\omega_A = \omega_{Q2} \cdot i_3 \tag{3}$$

$$\omega_A = \omega_{P2} \cdot i_2 \tag{4}$$

$$\omega_A = \omega_{P1} \cdot i_1 \tag{5}$$

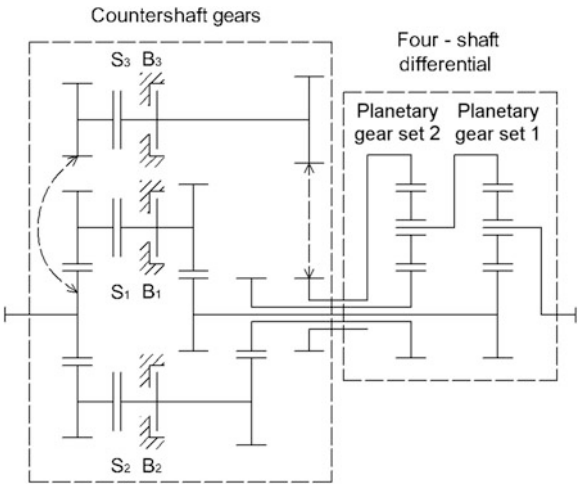

Fig. 1 Flow diagram of the powershift differential transmission with three flows of power for hybrid vehicles

Overall transmission ratio i_{AX} between input and output shaft is defined:

$$i_{AX} = \frac{\omega_A}{\omega_X} = \frac{(1 - u_{v2}) \cdot (1 - u_{v1}) \cdot i_1 \cdot i_2 \cdot i_3}{(1 - u_{v2}) \cdot i_2 \cdot i_3 - u_{v1} \cdot i_1 \cdot (i_3 - u_{v2} \cdot i_2)} \tag{6}$$

If the transmission ratio of the first gears is signed i_{AX1}, ratio of the second gear is i_{AX2} and the ratio of nth is i_{AXn}, we can set the gear differentiation φ (Naunheimer et al. 2011; Málik et al. 2007; Ikrinský 2003) between two adjacent gear steps:

$$\varphi_{(n-1)} = \frac{i_{AX(n-1)}}{i_{AXn}} \tag{7}$$

4 Basic Transmission Parameters and Achieved Values

The transmission consists of countershaft gears and four-shaft-differential—schematically drawn and signed on Fig. 1. For described concept with potential exploitation in hybrid vehicle, etc., the transmission ratios of countershaft gears i_1, i_2, i_3 and internal transmission ratios of both planetary sets in differential u_{v1}, u_{v2} are: $i_1 = 1,\ 8;\ i_2 = 2;\ i_3 = 1,\ 8;\ u_{v1} = -2;\ u_{v2} = -2$. If speaking about an application in a specific vehicle, it is necessary to set these values so that the output values of overall gearbox gear ratios and its differentiation would match to the machine drive train. In this case, the individual clutches and brakes are engaged and disengaged in order to reach the gear ratios exactly according the Table 1.

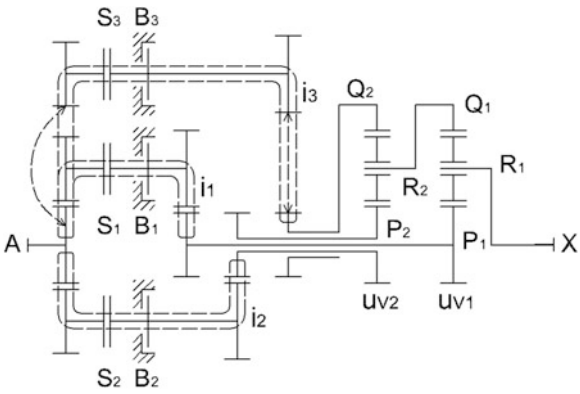

Fig. 2 Schematic signing of transmission components of differential gearbox for hybrid vehicle with three flows of power. Countershaft gears $i_{1,2,3}$, internal transmission ratios $u_{v1,2}$, *A* input shaft, *X* output shaft, *S* clutch, *B* brake

Table 1 Gearshift pattern of differential transmission with three flows of power for hybrid vehicles

Speed gear nr.	Engaged shifting element						Transmission ratio	Gear differentiation
	S1	S2	S3	B1	B2	B3		
1		×		×		×	9	1.67
2	×				×	×	5.4	1.33
3			×	×	×		4.05	1.2
4	×	×				×	3.375	1.21
5		×	×	×			2.793	1.21
6	×		×		×		2.314	1.26
7	×	×	×				1.841	

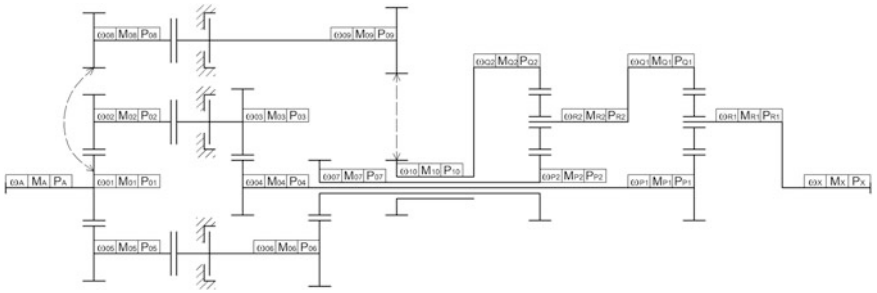

Fig. 3 The scheme of the solved differential transmission with significations of angular velocities ω, torques *M* and powers *P* at all components

The values of gear ratios of countershaft gearbox and internal gear ratios of four-shaft-differential are defined so that the transmission would achieve the ratios according the Table 1.

Table 2 Relative values ω, M and P at individual components of differential transmission with three flows of power for construction machines

Gear nr.	Element	A	01	02	03	04	05	06	07	08	09	10	P2	Q2	R2	P1	Q1	R1	X
1	ω	1	1	−0.83	0	0	−0.71	−0.71	0.5	−0.83	0	0	0.5	0	0.17	0	0.17	0.11	0.11
	M	1	−1	0	2	3	−1.41	1.41	2	0	2.67	4	−2	−4	6	−3	−6	9	−9
	P	1	−1	0	0	0	1	−1	1	0	0	0	−1	0	1	0	−1	1	−1
2	ω	1	1	−0.83	−0.83	0.56	−0.71	0	0	−0.83	0	0	0	0	0	0.56	0	0.19	0.19
	M	1	−1	−1.2	1.2	1.8	0	0.85	1.2	0	1.6	2.4	−1.2	−2.4	3.6	−1.8	−3.6	5.4	−5.4
	P	1	−1	1	−1	1	0	0	0	0	0	0	0	0	0	−1	0	1	−1
3	ω	1	1	−0.83	0	0	−0.71	0	0	−0.83	−0.83	0.56	0	0.56	0.37	0	0.37	0.25	0.25
	M	1	−1	0	0.9	1.35	0	0.64	0.9	−1.2	1.2	1.8	−0.9	−1.8	2.7	−1.35	−2.7	4.05	−4.05
	P	1	−1	0	0	0	0	0	0	1	−1	1	0	−1	1	0	−1	1	−1
4	ω	1	1	−0.83	−0.83	0.56	−0.71	−0.71	0.5	−0.83	0	0	0.5	0	0.17	0.56	0.17	0.3	0.3
	M	1	−1	−0.75	0.75	1.12	−0.53	0.53	0.75	0	1	1.5	−0.75	−1.5	2.25	−1.12	−2.25	3,37	−3,37
	P	1	−1	0.62	−0.62	0.62	0.38	−0.38	0.38	0	0	0	−0.38	0	0.38	−0.62	0.38	1	−1
5	ω	1	1	−0.83	0	0	−0.71	−0.71	0.5	−0.83	−0.83	0.56	0.5	0.56	0.54	0	0.54	0.36	0.36
	M	1	−1	0	0.62	0.93	−0.44	0.44	0.62	−0.83	0.83	1.24	−0.62	−1.24	1.86	−0.93	−1.86	2.79	−2.79
	P	1	−1	0	0	0	0.31	−0.31	0.31	0.69	−0.69	0.69	−0.31	−0.69	1	0	−1	1	−1
6	ω	1	1	−0.83	−0.83	0.56	−0.71	0	0	−0.83	−0.83	0.56	0	0.56	0.37	0.56	0.37	0.43	0.43
	M	1	−1	−0.51	0.51	0.77	0	0.36	0.51	−0.69	0.69	1.03	−0.51	−1.03	1.54	−0.77	−1.54	2.31	−2.31
	P	1	−1	0.43	−0.43	0.43	0	0	0	0.57	−0.57	0.57	0	−0.57	0.57	−0.43	−0.57	1	−1
7	ω	1	1	−0.83	−0.83	0.56	−0.71	−0.71	0.5	−0.83	−0.83	0.56	0.5	0.56	0.54	0.56	0.54	0.54	0,54
	M	1	−1	−0.41	0.41	0.61	−0.29	0.29	0.41	−0.54	0.54	0.82	−0.41	−0.82	1.23	−0.61	−1.23	1.84	−1.84
	P	1	−1	0.34	−0.34	0.34	0.21	−0.21	0.21	0.45	−0.45	0.45	−0.21	−0.45	0.66	−0.34	−0.66	1	−1

Table 3 Theoretically described transmission efficiency on individual gears

Speed gear nr.	1	2	3	4	5	6	7
Transmission ratio	9	5.4	4.05	3.375	2.793	2.314	1.841
Transmission efficiency	0.9128	0.9128	0.9221	0.9255	0.9307	0.9328	0.9401

5 Kinematic and Torque Conditions of Individual Transmission Components

Methodology from Naunheimer et al. (2011) and Ikrinský (2003) is suitable for this analysis. For calculation of individual velocities ω and torques M, there we use well known relations between kinematic and torque parameters of spur and planetary gears (Fig. 3). We can set the transmission efficiency $\eta_{AX} = 100$ % into the calculation, the parameters were thus examined by theoretical lossless power transmission.

In order to simplify it, it might be reasonable to calculate with relative parameters. So it is applied $\omega_A = 1$, $M_A = 1$, $P_A = 1$ and other values ω (angular velocities), M (torques) a P (powers) of random transmission component are the multiples of input shaft parameters A. In the Table 2, there are listed all relative values of ω, M and P on individual transmission components for all speed gears and they are accordingly multiples of the input shaft values.

6 Transmission Efficiency

Algorithm for calculation of the parameters solves the theoretical transmission efficiency, too. The efficiency of outer gear mesh was set 0.98 (efficiency of countershaft gears), internal efficiency of planetary set was 0.97 and all remaining power losses were neglected. Table 3 shows the overall transmission efficiency at each speed gears.

7 Conclusions

Differential transmissions offer large-scale possibilities if required a of higher number of speed gears. For example, the combination of two planetary sets provides 36 possible structures and each structure enables different speed gears redistribution. The chosen concept has been proven as being suitable for application in hybrid vehicle, as it provides a number of available speed gears and its differentiation.

The described transmission renders a powershift meeting actual requirements for the vehicle transmissions. To achieve seven gears, six control components are needed. The advantage of this type of the transmission is that it does not require the same number of gear meshes in comparison with countershaft transmission in order to achieve the same number of speed gears. The result is that the transmission efficiency of differential transmission is higher too.

Acknowledgments This paper has been elaborated with the support of the project VEGA 1/0721/13, Energy balance of electromobiles and hybrid vehicles

References

Ikrinský A (2003) Mechanické a hydraulické prevody. Vydavateľstvo STU Bratislava. ISBN: 80-227-1855-6

Málik L, Kučera Ľ (1999) Mechanické, hydraulické a hydromechanické prenosy. Žilina, EDIS—vydavateľstvo ŽU. ISBN 80-7100-513-4

Málik L, Chrzová J, Šoška M (2007) Konštruovanie III. Žilina, EDIS—vydavateľstvo ŽU. ISBN 978-80-8070-733-0

Naunheimer H, Bertsche B, Ryborz J (2011) Automotive transmissions: fundamentals, selection, design a application. Springer, Berlin Heidelberg. ISBN: 978-3-642-16213-8

Pitoňák J, Galbavý M, Prodaj J (2012) Powershift differential transmission with three flows of power. MECCA—J Middle Eur Constr Des Cars. ISSN: 1214-0821

Active Bonnet Hinge

M. Galda and J. Brandejs

Abstract With the increasing demands on traffic safety, car manufacturers concentrates besides safety of the crew during a collision with another vehicle also on minimization of injuries of the pedestrians during accidents in urban traffic. Conducted studies show, that the construction of the bonnet has a large influence on the resulting injury. One of the possibilities of the active pedestrian protection is to increase the space between the bonnet and the rigid parts of the engine compartment in the event of a collision with a vehicle. The resulting space allows a greater deformation of the bonnet and thereby absorption of a greater part of the energy. This paper deals with the design of the active bonnet hinge including hinge kinematics and appropriate dimensioning of the individual parts of the hinge.

Keywords Active · Bonnet · Hinge · Pedestrian · Protection

1 Introduction

Car manufacturers are nowadays rushed to produce cars on high technical level in the great production volume. However, with increasing number of cars on the road, also the number of traffic accidents increase. Worst accident statistics come from developing countries and from countries with a high population density and large concentration ratio of cyclist and pedestrians, such as China and India. For this reason, car manufacturers also focus on the safety of pedestrians.

M. Galda (✉) · J. Brandejs
Brno University of Technology, Brno, Czech Republic
e-mail: michalg@centrum.cz

J. Brandejs
e-mail: brandejs@fme.vutbr.cz.cz

L. Ševčík et al. (eds.), *Modern Methods of Construction Design*,
Lecture Notes in Mechanical Engineering, DOI: 10.1007/978-3-319-05203-8_5,

Vehicles' designers focused on passenger safety in cars already in the 60 s of the last century. However, the issue of pedestrians' protection has not been solved. Pedestrian' protection at that time was adjusted by the decree of design of the front of the vehicle. However, the sharp features such as logos were still allowed. The first accurate description of pedestrian movement during the car crash was based on the examination of real-life situations (Mclean 2005).

This study (Mclean 2005) of collision of pedestrian with a car clearly shows, that the structure of the bonnet has a large influence on the resulting injuries, mainly to head injuries, which are often the cause of death.

The deceleration characteristics of the pedestrian head significantly depends on the part of the bonnet where the head hits. This may be influenced by the distribution of elements in the engine compartment or by the bonnet structure. If the pedestrian's head hits the area of the bonnet hinge or the bonnet lock, these elements does not allow deformation of the bonnet. This leads to an enormous increase in deceleration and thus to worse consequences of collision (Gandhi and Trivedi 2007; Marjoux et al. 2008). One of the ways how to minimize the effects of head impact at the bonnet lock, is the active bonnet hinge. The active bonnet, after its activation into the upper position, allows springing and thus absorption of impact energy.

The aim of designers is to reduce the stiffness of the bonnet and allow a sufficient deformation during impact with pedestrian. The energy required for deformation of the bonnet is obtained from the kinetic energy of the pedestrian. Thus, converted energy is absorbed in the bonnet, instead of destructive acting on the pedestrian's head. At the modern cars the engine area is almost completely filled. Enlargement of this area can lead to interference with the design of the vehicle and to increase of the aerodynamic drag, weight and fuel consumption.

These disadvantages can be reduced by using active bonnet hinge, which is in the event of accident intended to lift the rear part of the bonnet and thereby increase the space between the engine and the bonnet.

Our aim was to design a simple kinematic mechanism of the bonnet hinge, which would also allow the return of bonnet after the accident to its original position and transportation of the car to the service.

2 Design of Active Hinge

The basis of the active bonnet hinge is kinematic single pivot or pantographic mechanism, which uses as a driving force of particular actuator type. This driving unit can be pyro-cartridge, spring, electro-mechanism, hydraulic or pneumatic unit (KIA Motors 2009; Nadeau et al. 2005; Park et al. 2009; Salmon et al. 2011; Landholm et al. 2010; Karlsson 2012). Each type of actuator for active hinge must achieve lifting of the rear part of the bonnet in a very short time, before the pedestrian's head hits it. The common used active bonnet hinge is usually hook-shaped, when the rotation center of the hinge is placed in the

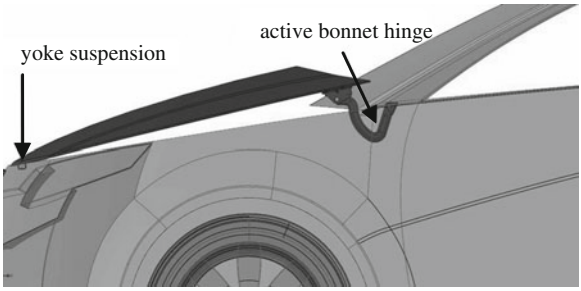

Fig. 1 Active bonnet

A-pillar of the car frame. Location of the rotation center behind the back edge of the bonnet allows the lifting of the bonnet above the engine area on the side of the front window (Fig. 1).

The aim of the producers are the lowest costs and the final price of the product. This is also the reason for choice of single-pin hinge with shear rivet in comparison with multi-pin mechanisms. The disadvantage could be a larger required installation space for the proper function of the hinge.

2.1 Design of Hinge Mechanism

The basis of the hinge (Fig. 2—pos. 2) is attached to the car bodywork. The hinge arm (pos. 1) and hinge basis are connected by the main pin (pos. 4), which is placed in the sliding bearing and axially secured by riveting of the end of the pin. The hinge arm is attached by a pin (pos. 5) to bonnet console and axially secured by riveting of the end of the pin. On the bonnet console, there is an emboss around the rivet hole, which eliminates the clearance between the hinge arm and bonnet console.

The aim was to reduce the contact area between the hinge and bonnet console. Once the activation of the hinge is launched, during the accident, it won't be necessary to overcome the frictional force between these surfaces, and all the energy of the actuator will be used for cutting of the rivet (pos. 7) and lifting of the rear part of the bonnet.

2.2 Maximal Position of Bonnet Opening

In case of the opening of the bonnet, it is necessary to adjust the position of maximum hinge extension. For the determination of this position is not possible to use the car bodywork. The stopper is therefore integrated into the hinge basis (Fig. 3). It is located on one side of the hinge basis as a bent nose and allows easier assembly. The disadvantage of this design is the bending of the stopper. Therefore

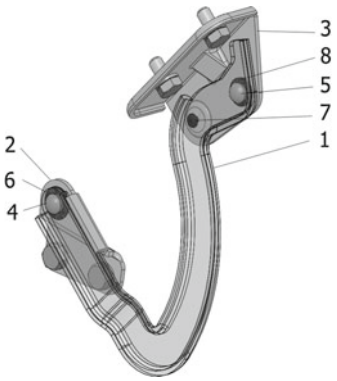

Fig. 2 Description of individual parts. *1* Hinge arm, *2* Hinge basis, *3* Bonnet console, *4* Main pin (rotation axis), *5* Active hinge pin, *6* Insert, *7* Shearing rivet, *8* Washer

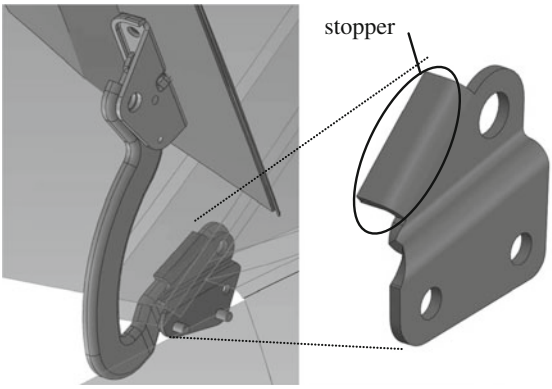

Fig. 3 The stopper for limitation of maximum extension

it has been designed so that the bolts are placed below the A-pillar. This allows an easier replacement.

2.3 The Stopper for Top Position of Activated Hinge

Lever mechanism of the active hinge is not firmly connected to the actuator. When activated, the piston of actuator will impact to bonnet console. The place of impact is shown at Fig. 4a. Because the hinge opens in larger angle in comparison to the activation of the hinge during an accident, it is necessary to place a stop position into the mechanism. For the definition of the upper position a shape-fit between the hinge arm and firming beading of the bonnet console was used. This shape-fit is shown on Fig. 4b.

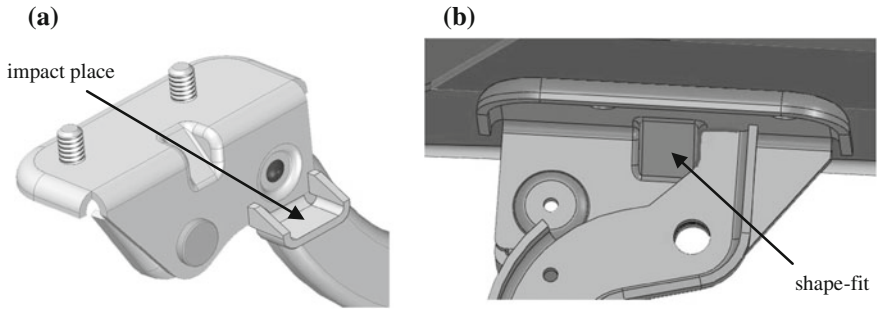

Fig. 4 **a** Impact place. **b** The stopper for the *top* position of activated hinge

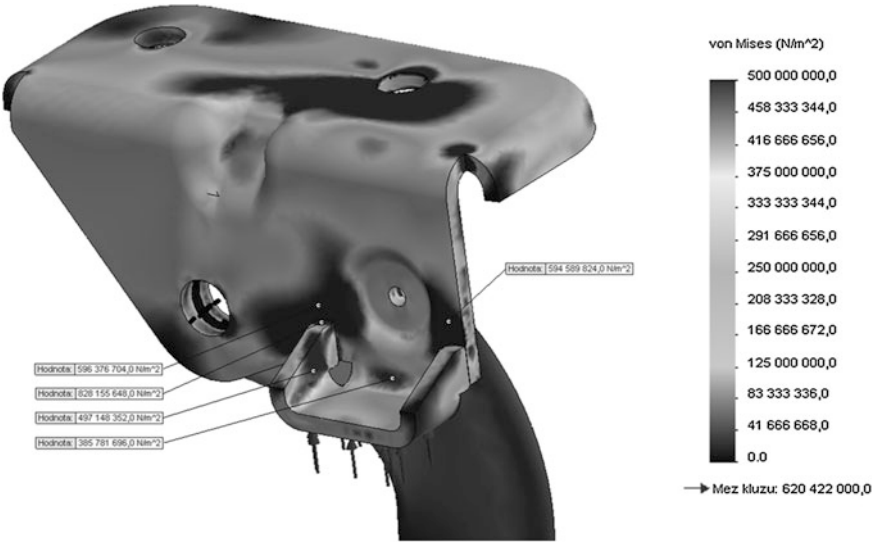

Fig. 5 FEM analysis of the impact place of the actuator

2.4 Impact Place of the Actuator

Impact place of the actuator was selected within the engine compartment on the outer side nearer to the mud guard. This allows implementation of the actuator within the area of mud guard.

The stiffness of the impact place was verified using FEM analysis for the bonnet weight of 17 kg and force of 3,800 N during ejection of the actuator (Fig. 5).

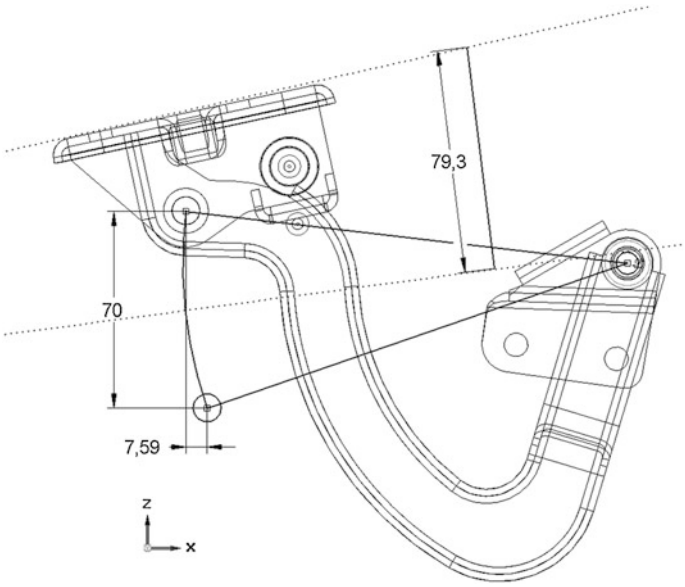

Fig. 6 Activation of the hinge

3 Description of Active Hinge Function

During a collision of the car and pedestrian, sensors transmit the information about the impact to the control unit, which evaluates the situation whether to activate or not activate the actuator. When activated, an igniter in gas is initiated and gas pressure shoots piston of the actuator against the impact place on the bonnet console. Therefore the hinge arm cuts the shearing rivet lifts up the rear part of the bonnet.

4 Conclusions

Active hinge was designed on the principle of single pin mechanism with hook shape. The hinge mechanism has independently placed actuator, which is implemented into the side of the mudguard wall. In case of accident with pedestrian, the hinge is able to lift the rear part of the bonnet about 70 mm (Fig. 6).

For this bonnet hinge a gas actuator type was chosen. The use of gas actuator is advantageous in terms of the overall simplicity of the system. It also meets the requirement for lowering of the bonnet after the accident for transportation to the authorized service center. This follow-up height reduction is caused by release of combustion products from the gas actuator.

Acknowledgements The work was supported by European Regional Development Fund in the framework of the research project NETME Centre under the Operational Programme Research and Development for Innovation. Reg. Nr. CZ.1.05/2.1.00/01.0002, id code: ED0002/01/01, project name: NETME Centre—New Technologies for Mechanical Engineering and project of specific research FSI-S-11-30/1454.

References

Gandhi T, Trivedi MM (2007) Pedestrian protection systems: issues, survey, and challenges. doi:10.1109/TITS.2007.903444

Karlsson M, Saab Automobile AB (2012) Hood hinge assembly for a motor vehicle (patent). EP 249 514 0 A1. Granted 5 Sept 2012. Registered 1 Mar 2011

KIA Motors (2009) Lift device of active hood system (patent), United States. Utility model, US 2009/0289474, A1, Granted 26 Nov 2009

Landholm R, Fredriksson A, Lindmark P, Volvo Car Corporation (2010) Hinge mechanism (patent), SE. EP 2 380 787 A1. Granted 26 Oct 2011. Registered 21 Apr 2010

Marjoux D, Baumgartner D, Deck C, Willinger R (2008) Head injury prediction capability of the HIC, HIP, SIMon and ULP criteria. Accid Anal 40(3):1135–1148. ISSN 00014575

Mclean AJ (2005) Vehicle design for pedestrian protection. Centre for Automotive Safety Research, Adelaide, p 22. ISBN 1 920947 39 6

Nadeau JP, D′emmanuelle L, Laspesa E (2005) Safety device for lifting a bonnet of a motor vehicle in the event of a collision (patent), France. Utility model, US 6,942,056 B2. Granted 13 Sept 2005

Park DW, Hyundai MOBIS CO., Ltd (2009) Pedestrian protecting apparatus of vehicle hood (patent), KR. Utility model, US 6,637,344 B2. Granted 29 Dec 2009

Salmon J, Crowder K, Multimatic Inc (2011) Pedestrian protection automotive hood hinge assembly (patent), Ontario. EP 1 922 241 B1. Granted 21 Dec 2011. Registered 18 Apr 2006

The Chance for Application of the Pneumatic Dual: Mass Flywheel in Drive Combustion Engine

R. Grega

Abstract In order to reduce the vibrations of diesel engines it is necessary to apply a dual-mass flywheel as an unavoidable part of the piston combustion engine. The dual-mass flywheel replaces the classic flywheel in such way that it is divided in two masses (the primary mass and the secondary mass), which are jointed together by means of a flexible interconnection. This kind of the flywheel solution enables to change resonance areas of the engine with regard to the engine dynamic behaviour what leads to a reduction of vibrations consequently. There was projected a new type of the dual-mass flywheel in the framework of our workplace in order to eliminate disadvantages of the present dual-mass flywheels, i.e. we projected the pneumatic dual-mass flywheel, taking into consideration our experiences obtained during investigation of vibrations.

Keywords Combustion engine · Vibrations · Dual-mass flywheel

1 Introduction

Reduction of gaseous emissions together with effort to reach the highest engine power outputs and torques are most recent trends in development of the piston combustion engines. It is possible due to application of the mechatronic system in order to manage the combustion process with the aim to minimalise the exhaust gas emissions and to increase efficiency of the fuel mixture combustion. The regulation of the combustion process in the individual cylinders is bringing negative consequences as well, in the form of occurrence and extension of vibrations

R. Grega (✉)
Technical University of Košice, Košice, Slovakia
e-mail: robert.grega@tuke.sk

L. Ševčík et al. (eds.), *Modern Methods of Construction Design*,
Lecture Notes in Mechanical Engineering, DOI: 10.1007/978-3-319-05203-8_6,

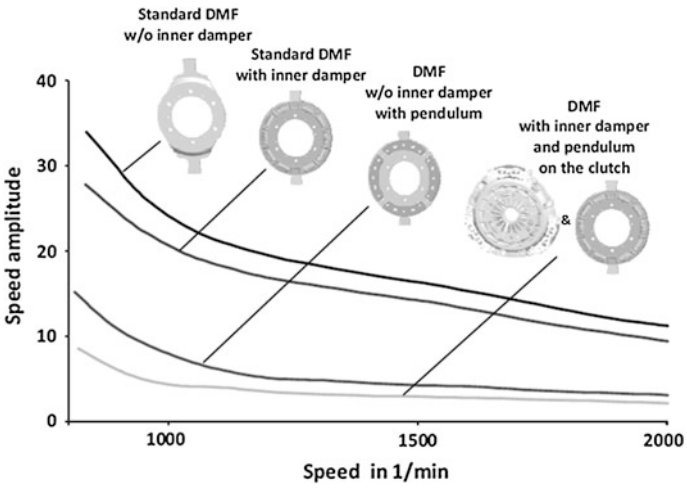

Fig. 1 The impact of dual-mass flywheel on vibrations

in the combustion engine. In case of a controlled combustion process there is a typical occurrence of amplitudes of the secondary harmonic vibration components (Hlavňa 2007). The torsional vibrations arising in the combustion engine are transmitted into the whole driving system. Afterwards these vibrations cause negative impacts on the tooth-wheels in gearboxes, on the connected shafts and on other components of the driving mechanism as well. A very negative consequence is transmission of the vibrations and noisiness into the surrounding (Grega 2002; Grega et al. 2006).

In 1985, the company LuK presented a new solution of the dual-mass flywheel. The main role of the dual-mass flywheel is reduction of torsional vibration amplitudes Fig. 1 (Kroll et al. 2010). Such reduction can be reached by using separation of the flywheel on two individual masses that are joined to each other by means of a flexible connection. Application of the dual-mass flywheels in the diesel engines has also disadvantages with regard to their durability. The durability of the flywheel depends predominately on loading regime. The flexible connection between both masses is realized with a metal spring, which is stressed due to repeated dynamic impacts during starting-up of coupling, which is connected with one of both masses. The starting phase is characterised by a low speed and high loading. This kind of fatigue of the connecting spring causes higher noisiness and higher level of vibrations (Homišin 2005).

Nowadays, the dual-mass flywheels are designed in such way that they are able to transmit the torque up to 300 Nm with the angle of twist 40° at least. Concerning spatial dimensions, it is important to say that the new flywheel has to be similar to the classic flywheel and must be able to be mounted to the coupling lamella (Homišin 2006).

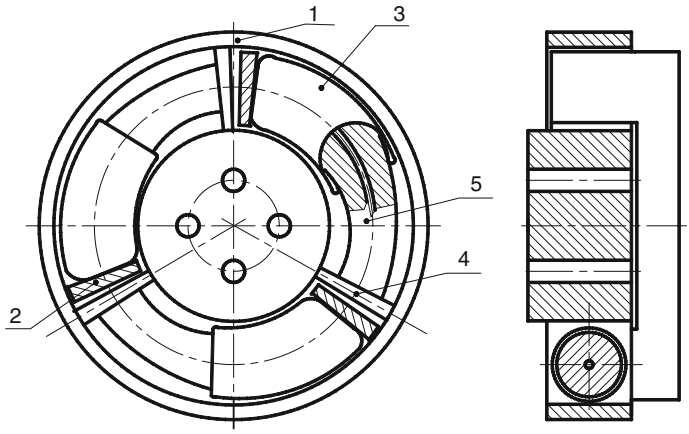

Fig. 2 Pneumatic dual-mass flywheel

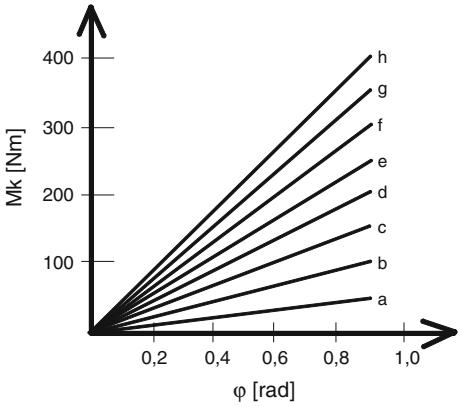

Fig. 3 Loading characteristics of the pneumatic dual-mass flywheel

2 The Pneumatic Dual-Mass Flywheel

Our research team obtained a great amount of experiences in the development area of machineries and systems projected at our workplaces for reduction of torsional vibrations. Therefore we developed also a new pneumatic dual-mass flywheel, Fig. 2, which consists of the primary mass (1) and the secondary mass (2). The secondary mass is pressured with the pneumatic flexible chambers that are shaped like half-moons and are filled with the air (3). The primary mass is joined to the carrier (4), which is equipped with the compression pistons (5). The pistons are linked with the pneumatic flexible chambers. The chambers are compressed towards the pistons when they are loaded. The pneumatic dual-mass flywheel is attached to the pneumatic accumulator situated out of the combustion engine. The main task of the pneumatic accumulator is keeping of a constant air pressure in the pneumatic flexible chambers (Grega and Kaššay 2007; Grega 2002).

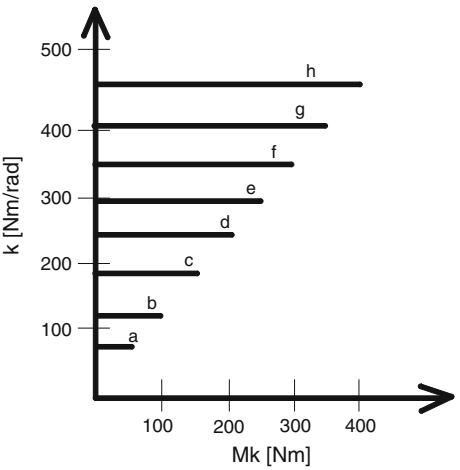

Fig. 4 Characteristics of torsional stiffness of the pneumatic dual-mass flywheel

There were defined the basic loading characteristics according to the performed theoretical analysis, Fig. 3 and it was specified the static torsional stiffness of the designed pneumatic dual-mass flywheel, Fig. 4. The air pressure in the pneumatic dual-mass flywheel can be changed from the 100 up to 800 kPa. The behaviours signed with the letters from a to h in the Fig. 3 are the loading characteristics and in the Fig. 4 are presented the courses of static torsional stiffness of the pneumatic dual-mass flywheel operating at the pressure levels from the 100 up to 800 kPa (Němeček 2008).

3 Conclusions

The pneumatic dual-mass flywheel was projected on the basis of experiences gained at our department in the area of the torsional oscillation tuners. This new construction of the pneumatic dual-mass flywheel is able to fulfil the required parameters, namely the angle of twist 40° minimally and the transmitted torque 300 Nm. The given new pneumatic dual-mass flywheel reaches the angle of twist 50° with the maximum torque 400 Nm at the pressure level 800 kPa. A very important advantage of this pneumatic flywheel is a fact that its flexible elements are not subjected to the fatigue process because they are developed in the form of the flexible chambers filled with the air. The constant air pressure is maintained by means of the pneumatic accumulator. The pneumatic dual-mass flywheel is a suitable technical solution for reduction of the combustion engine vibrations.

Acknowledgments This paper was written in the framework of Grant Project VEGA: "1/0688/12—Research and application of universal regulation system in order to master the source of mechanical systems excitation".

References

Hlavňa V.a kol (2007) Dopravný prostriedok jeho motor., EDIS Žilina

Grega R (2002) Prezentácia výsledkov dynamickej torznej tuhosti pneumatickej pružnej spojky s autoreguláciou na základe experimentálnych meraní. Acta Mechanica Slovaca, roč. 6, č. 2, 2002, s. 29–34

Grega R, Kaššay P (2007) Porovnanie teoreticko-experimentálnych výsledkov extrému účelovej funkcie extremálnej regulácie. 48. Medz. konf. KČSaM 2007, Smolenice,12 – 14.9. 2007, Bratislava, STU, 2007. s. 372–377

Grega R, Homišin J, Kardoš F (2006) Porovnanie účelovej funkcie pri bezporuchovom a poruchovom chode mechanickej sústavy. Acta Mechanica Slovaca, roč. 10, č. 4-b, 2006, s. 39–42

Grega R, Medvecká S, Kardoš F (2008) Napäťové rozloženie na pneumaticko-pružnom elemente. Budowa i eksploatacja maszyn, nr 25, 2008, s. 33–38

Homišin J (2005) Spôsoby ladenia mechanických sústav aplikáciou ladičov torzných kmitov. Acta Mechanica Slovaca, roč. 9, č. 3-b, 2005, s. 5–12

Homišin J (2006) Súčasné trendy optimalizácie strojov a zariadení. C–Press, Košice

Kroll J, Kooy A, Seebacher R (2010) Torsional vibration damping for future engines, Schaeffler symposium

Homišin J (1992) Mechanická sústava vhodná pre realizáciu jej plynulého ladenia. Patent nr. 276926/92

Homišin J (1986) Pneumatická pružná hriadeľová spojka. Patent nr. 222411/86

Hal'ko J, Vojtko I (2008) Diferenciálny harmonický prevod a jeho simulácia. Acta Mechanica Slovaca, roč. 12, č. 3-c, 2008

Němeček P (2008) Diagnostika strojů s vibračním principem činnosti. Acta Mechanica Slovaca, roč. 12, č. 3-c, 2008

Pešík L, Vančura M (2009) Values identification of kinematic quantities during a mechanical shock. ACC JOURNAL, XV 1/2009, s. 30–35

Ságа M, Vaško M, Kopas P, Handrik M (2008) Príspevok k napätostnej analýze napätosti prútových a rámových konštrukcií. Acta Mechanica Slovaca, roč. 12, č. 3-c, 2008,s. 351–360

Tolerance Analysis: Future Prospects

H. Haberhauer

Abstract Poor dimension and tolerance practices are a significant quality issue. It is estimated that 80 % of all manufacturing issues are directly related to improper use of GD&T. Therefore it is very important to define the permissible deviations from the ideal geometry as clearly as possible. That means suitable dimensional and geometrical tolerance indications in technical drawings are necessary. But the determination of optimal tolerances is not easy. Firstly, tolerances must always have a relation to function. Secondly, the indicated tolerances have to be produced. Thirdly, unambiguous and reproducible measurements of all given tolerances must be able. Functional tolerances need tolerance studies and knowledge about manufacturing and measuring is also required for design engineers.

Keywords Dimensional tolerance · Geometrical tolerance · Geometrical Product Specification · GPS · Tolerance analysis

1 Introduction

It is not possible to produce perfect workpieces. Each manufactured component has dispersions in geometrical characteristics about the optimum and form. To ensure function and compatibility tolerance entries on technical drawings are necessary. Typically, the requirements for specific geometrical characteristics will be expressed at this stage as maximum permissible errors which set an acceptable limit on how far each geometrical characteristic is permitted to deviate from nominal without leading to detrimental product quality. A simple rule says: "As accurate as necessary, not as accurate as possible". But daily experience shows that tolerances normally will be defined as accurate as possible and not as accurate as necessary.

H. Haberhauer (✉)
Hochschule Esslingen, Esslingen am Neckar, Germany
e-mail: horst.haberhauer@hs-esslingen.de

L. Ševčík et al. (eds.), *Modern Methods of Construction Design*,
Lecture Notes in Mechanical Engineering, DOI: 10.1007/978-3-319-05203-8_7,

One reason is: It is easier to ask the manufacturing department about their machine accuracies than to make a tolerance study. Another reason could be the lack of knowledge about geometrical tolerances and measuring in design departments.

In the past in-house production depth was very deep and the production mainly limited to the local region. Consequently the know-how in the manufacturing was very high. Therefore indications of tolerances were normally restricted to dimension tolerances. Geometrical tolerances were only sparely used in old drawings.

Today the in-house production depth in companies decreases more and more. Global production increase and development engineers often do not know where their components will be produced in the future. That means the know-how regarding function in production diminish more and more. To avoid problems during the production process an unambiguous and complete product specification is necessary.

2 GPS-Strategy

The aim of developing a Geometrical Product Specification (GPS) is to define the shape (geometry), dimensions and surface characteristics of a workpiece on an engineering drawing to ensure optimum functioning. Thereby will be determined with the principle of duality that only the designer is responsible for functionality and production and quality assurance are responsible for correct interpretation of the indicated specifications.

2.1 GPS-Matrix

The ISO GPS Matrix (Fig. 1) given in ISO/TR 14638 contains *fundamental*, *global*, *general* and *supplementary* GPS-standards. The standard concept of GPS creates integrated and compatible chains of standards and specifies the necessary context between the workpiece defined by development/design, produced by manufacturing and measured by quality assurance.

The geometry of a workpiece is defined by 18 geometrical properties (e.g. size, distance, form …). One chain link includes all standards with same geometrical properties. Chain link 1 contains the *drawing indications*, chain link 2 the *theoretical definitions*, chain link 3 the *definitions of real workpiece properties*, chain link 4 the *determination of deviations*, chain links 5 and 6 *contain requirements of test equipments and calibration*.

2.2 ISO 14405

The new ISO 14405 tries to eliminate ambiguities which have been in previous drawings. In this standard dimension characteristics are assigned to dimension

General GPS standards Chain link number	1	2	3	4	5	6
Size						
Distance						
Radius						
Angle						
Form of line independent of datum						
Form of line dependent of datum						
Form of surface independent of datum						
Form of surface dependent of datum						
Orientation						
Location						
Circular run-out						
Total run-out						
Datums						
Roughness profile						
Primary profile						
Waviness profile						
Surface imperfections						
Edges						

Fig. 1 GPS matrix of general GPS standards (ISO 1101 2012)

elements. This is necessary for an unambiguous definition and measuring of form elements. So this standard contains 14 new modification symbols for sizes. If the drawing does not contain an indication, the two-point size is valid. That means the dimension is defined as distance between two points. Because a two-point size does not include information about geometry the principle of independency is valid for this drawing.

Accordingly to DIN 7167 in Germany the *envelope principle* was valid up to 2012 when the drawing had no indication with respect of the tolerance principle. Using the principle of envelope, all form and parallelism tolerances are included inside the envelope which is defined by maximum material size. Today the indication "Size ISO 14405 Ⓔ" is necessary for the envelope principle.

The *principle of independency* says that dimensional tolerances and geometrical tolerances are independently. The drawing indication "Size ISO 14405" is recommended to define this tolerance principle. This indication can be supplemented with a size characteristic symbol to avoid ambiguous measurement results.

3 Geometrical Tolerancing

Geometrical tolerances are distinguished between form and orientation, location and run-out tolerances. For orientation, location and run-out tolerances, datums are required (Fig. 2).

Unambiguous measurements of geometrical tolerances require often datum systems. The correct application of geometrical tolerancing is more complex and

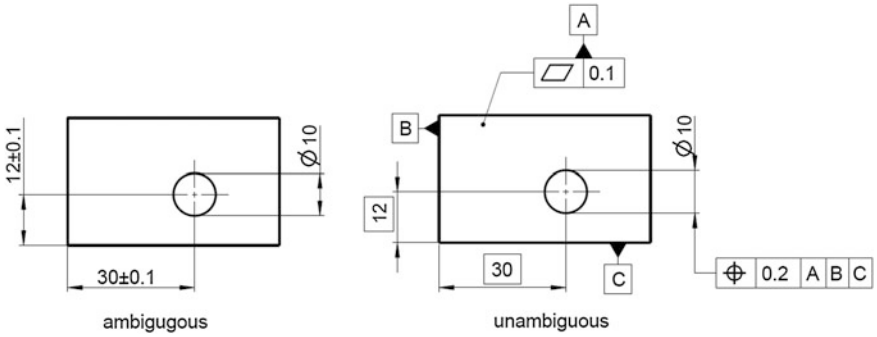

Fig. 2 Ambiguous distance tolerancing and unambiguous position tolerancing

difficult than the indication of dimension tolerances. Because of education neglect of geometrical tolerances, engineers in industry frequently have problems to define correct datums or datum systems.

In the future tolerances will be linked to 3D-CAD-models. But for this functionality CAD systems have to increase. Today the complete tolerancing on 3D-models are still limited. Suitable software will support CAD user and compensate insufficient knowledge regarding geometrical tolerances. An example for such support is the GD&T advisor from Sigmetrix (Fig. 3). It helps user to define unambiguous and complete tolerancing.

4 Tolerance Calculations

Arithmetical tolerance calculations (worst case) and statistical tolerance calculations which consider only dimensional tolerances are state-of-the-art. Tolerance analyses with linear dimension chains (one-dimensional) are easy to use. For statistical analyses production distributions must be considered. Nonlinear dimension chains (multi-dimensional) are more difficult. But a lot of problems can be reduced to linear dimension chains.

For a complete analysis, geometrical tolerance must also be considered. Although this could be very complicated (multi-dimensional) the principle is very easy: The geometrical tolerance have to convert into a dimensional tolerance. After this is it no problem to consider this size in a dimension chain. But the determination of influence is difficult. Besides, the tolerance principle is to consider, too. With a simple example this context should be shown in Fig. 4.

Using the principle of envelope, flatness deviations must always be within maximum material size. When the principle of independency is valid flatness tolerances could add up to dimensional tolerances in worst case. But how big is the

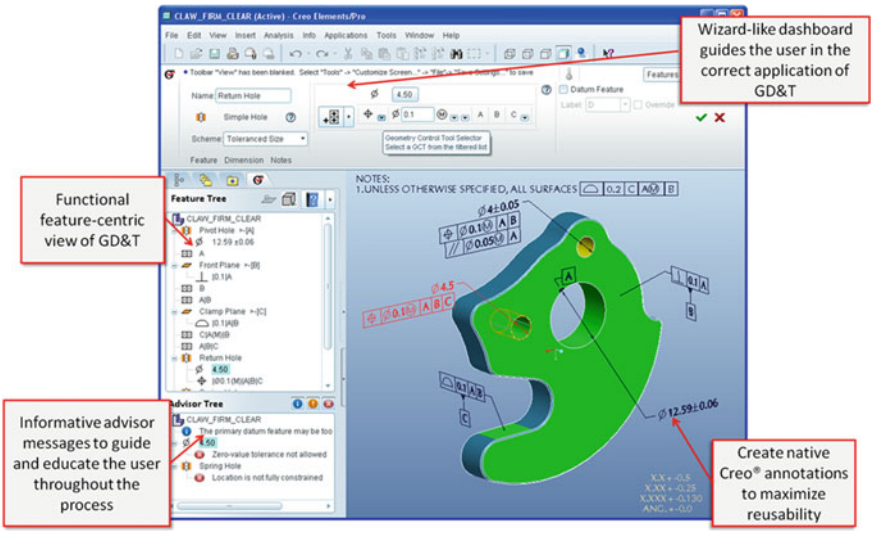

Fig. 3 GD&T Advisor creates and places annotations automatically (Sigmetrix 2013a)

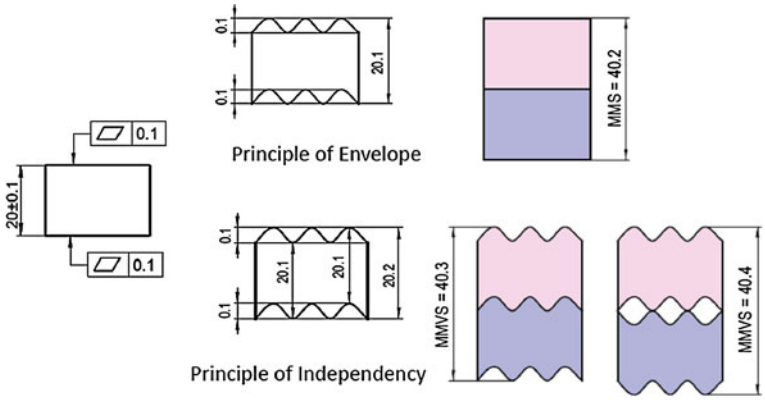

Fig. 4 Influence of tolerance principle

probability that the extreme cases "phase-conform" and "phase-delayed" occur? This probability is depending on the existing production distribution.

In the future, tolerance calculations will be supported by software, too. More than 250 assembly conditions can exist. The tolerance analysis software CETOL (Sigmetrix 2013b), for example, can every one of these constraints automatically recognize through the integration with the CAD system. CETOL then automatically generates the equations for use in the tolerance study.

5 Conclusions

With Geometrical Product Specification (GPS) should it be possible to design any shaped components, unambiguous and independent of locations. Furthermore, verification according to the specifications of the design engineer must be ensured. The GPS matrix shows what is covered today by standardization or what is still to do. It is estimated that only about 50 % of needed requirements are currently covered. That means changes and new standards are expected in the near future.

Consideration of geometrical tolerances in tolerance calculations leads quickly to nonlinear dimension chains. Because of their complexity it will not be possible to calculate it without software support. The determination of tolerances is an important expanse factor. Therefore tolerances should be as big as possible without leading to detrimental functionality.

Extensive knowledge about tolerancing will be needed in the future. Universities and industry have to invest more in education than in the past. Tolerancing is not only important for design engineers but also for all involved persons in the product emergence process.

References

ISO 1101:2012. Geometrical tolerancing—Tolerances of form, orientation, location and run-out

Sigmetrix (2013a) GD&T Advisor. http://www.sigmetrix.com/gdt-software/

Sigmetrix (2013b) CETOL 6σ Tolerance Analysis. http://www.sigmetrix.com/tolerance-analysis-software-cetol/

The Design of the Folding Device for the Production of 3D Textile Products

J. Hanuš, P. Rydlo, L. Ševčík, M. Konečný, D. Vejrych and M. Diblík

Abstract The contribution describes a system of mechanical forming 3D textile products of thickness 4–18 mm made from thin (2D) nonwoven fabric whose thickness is from 0.2 to 2 mm. System that forms thin nonwoven fabric into waves of specific shape and the desired height and wave number consist of a suitably arranged series of gears and tape conveyors. Basic working elements of that device and basic relationship between the parameters of the 3D textile product structure (thickness, weight, wave number) and between parameters of system is described. It is shown on the specific of the side gear teeth processing and of the tape conveyor.

Keywords Gear assembly · Mechanical forming · Non-woven textile

J. Hanuš (✉) · P. Rydlo · D. Vejrych · M. Diblík
Technical University of Liberec, Liberec, Czech Republic
e-mail: jaroslav.hanus@tul.cz

P. Rydlo
e-mail: pavel.rydlo@tul.cz

D. Vejrych
e-mail: david.vejrych@tul.cz

M. Diblík
e-mail: martin.diblik@tul.cz

L. Ševčík · M. Konečný
Department of Design of Machine Elements and Mechanism, Faculty of Mechanical Engineering, Technical University of Liberec, Liberec, Czech Republic
e-mail: ladislav.sevcik@tul.cz

M. Konečný
e-mail: martin.konecny@tul.cz

L. Ševčík et al. (eds.), *Modern Methods of Construction Design*,
Lecture Notes in Mechanical Engineering, DOI: 10.1007/978-3-319-05203-8_8,

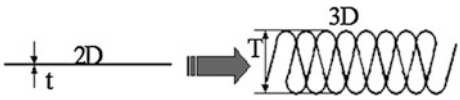

Fig. 1 Principle machine (Hanuš et al. 2008)

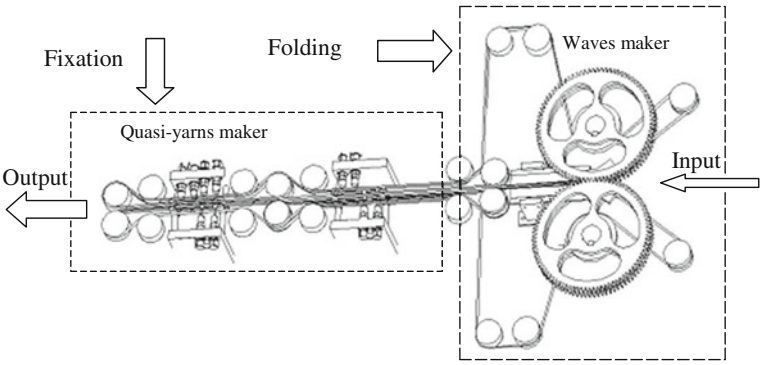

Fig. 2 Scheme of device

1 Introduction

If the requested thickness and/or mechanical properties of a product are beyond technological possibility of manufacturing textile fabrics, the requested thickness can be obtained by pleating thin fabrics Fig. 1.

The schematic diagram of a device for the vertical pleating of thin nonwoven textiles is shown in Fig. 2. The device consists of two basic assemblies; in the first assembly the pleats are formed by means of a forming gear set. A conveyor being moved at a control speed passes through the forming gear set. In the second assembly the formed pleated structure is fixed.

2 A System for Forming of Waves

The basic unit is a series of gears and a series of conveyors arranged in accordance with Fig. 2 (Hanuš and Ševčík 2009).

Unusual gearing see Fig. 3. Wheel was produced with module 6 mm, number of teeth 32 and is interesting that the angle is 0.05 rad. For create a wave is more important that the press angle was near 0°. The axial distance is changed from 210 to 227 mm depending on the desired thickness of the 3D product. Teeth were produced in the laser burn center. Surface after firing is smooth and does not

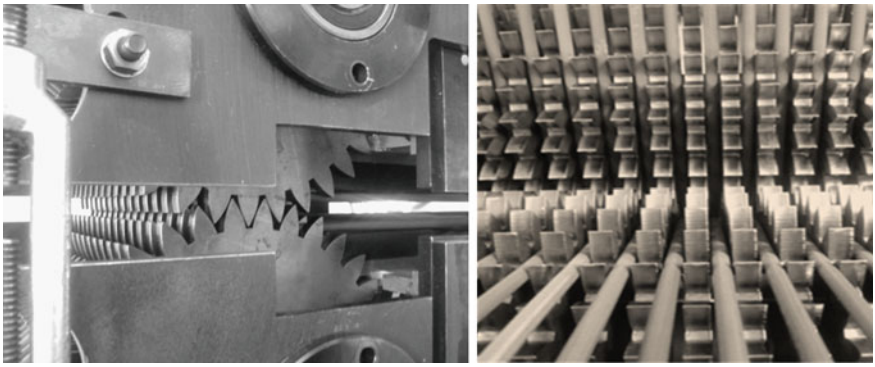

Fig. 3 The mechanism of formation of waves

capture the fiber on the leaf. The system of conveyors uses circular belts by company Habasit a diameter of 5 mm. Pitch of belts conveyor is 16 mm. For mutual adjustment gears and conveyor speed can be used the following formulas.

3 System Parameters and Their Relation to the Parameters of the Product

The relations between the technological parameters of the pleating (system parameters) and product parameters can be described as follows:

(A) ***Technological parameters:***

v_1 Input speed of semi-product (ms^{-1}); (given the previous device)
v_2 Remove speed of semi-product (ms^{-1}); (given speed of forming wheels)
v_3 Output speed of the product (ms^{-1}); n_2 = speed of forming wheels [s-1];

(B) ***Parameters of gears:***

p pitch tooth of forming wheels (mm);
z number tooth of forming wheel;
P intersection tooth of forming wheel (mm);
Δ height of circle segment;
a distance top of the two teeth on the line (mm) (difference from of tooth pitch p);
l length of the join (lines) between the peaks of three teeth (mm);
O width between centres of forming wheels;
ra radius of crown circle of forming wheels;

(C) ***The parameters of the conveyor:***

R_d speed of conveyor;
U_d distance of conveyor;

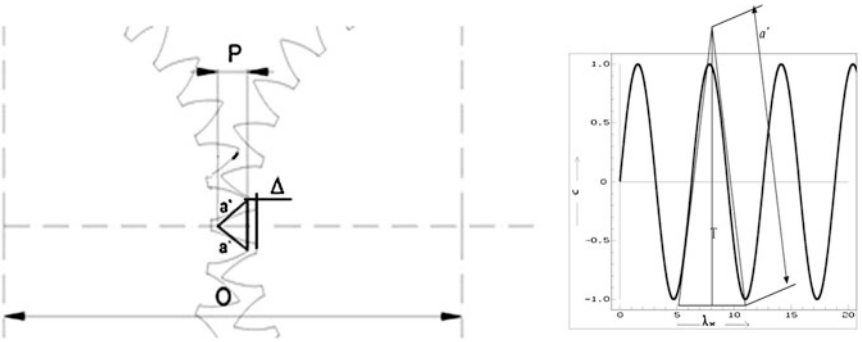

Fig. 4 Relations between the parameters of the gearing and the geometric parameters of the product

(D) ***Parameter of semi-product:***

t thickness of semi-product (mm);
g surface density of semi-product (gm^{-2});

(E) ***Parameter of product:***

T thickness of product (mm);
G surface density of product (gm^{-2});
k compression of product;
ρ wavenumber (number of wave on 1 m of semi-product) (m^{-1}).

To formulate the following formulars simplified geometry of shaping space and of wave as show in Fig. 4 where used.

Geometry of shaping space is on the left, the geometry of shaped wave is right. It follows from Fig. 4

$$a' = \left(\frac{l}{2}\right); \quad a'^2 = \left(\frac{a}{2}\right)^2 + (P - \Delta)^2 \tag{1}$$

$$a' = \sqrt{\left(\frac{a}{2}\right)^2 + (P - \Delta)^2} \tag{2}$$

$$\Delta = r_a - \frac{1}{2}\sqrt{4 * r_a^2 - a^2} \tag{3}$$

Simplifying assumptions:

1. Δ is so small that it can be neglected in practical calculations
2. l does not vary much from the curve length being curved by the semi-product in the forming space.

Then

$$a' = \sqrt{\left(\frac{a}{2}\right)^2 + P^2} \tag{4}$$

It is valid for the product compactness:

$$k = \frac{G}{g} = \frac{v_2}{v_3} \tag{5}$$

The wave number per 1 m of the product is

$$\rho = \frac{zn_2}{v_3} \tag{6}$$

Then

$$v_3 = \frac{v_2}{k} = \frac{zn_2}{\rho} \tag{7}$$

It also valid that the wave length in the semi-product is

$$\lambda = \frac{1}{\rho} \tag{8}$$

The length *á* (Fig. 3) is

$$a' = \sqrt{T^2 + \left(\frac{\lambda}{2}\right)^2} \tag{9}$$

There is possible to determine P from Eqs. (4) and (9) for the given thickness T or to determine T when the penetration of the forming gears P has been set, all that at the given semi-product weight. The semi-product thickness is neglected in the calculation (it is about 0, 1–0, 5 mm).

$$P = \sqrt{T^2 + \left(\frac{\lambda}{2}\right)^2 - \left(\frac{a}{2}\right)^2} \tag{10}$$

Or

$$T = \sqrt{P^2 + \left(\frac{a}{2}\right)^2 - \left(\frac{\lambda}{2}\right)^2} \tag{11}$$

It is valid for the product weight G that

$$G = \rho 2a'g = \frac{1}{\lambda}2a'g; \quad \frac{G}{g} = k$$

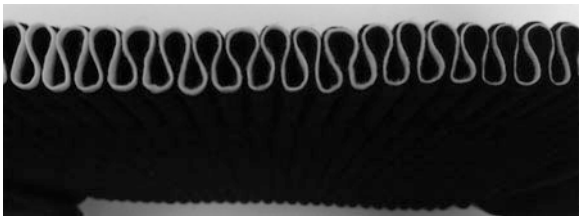

Fig. 5 The result set is applied to product

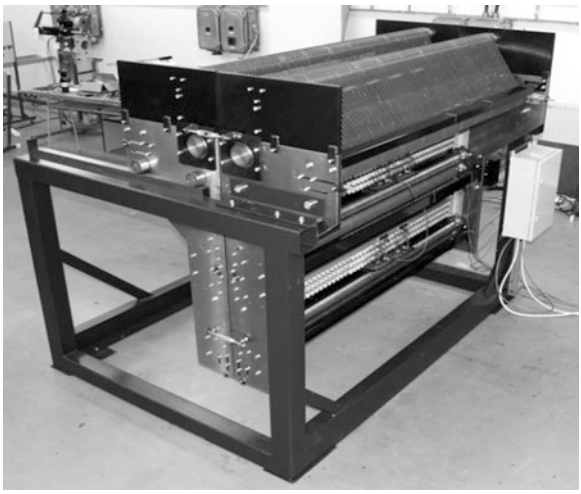

Fig. 6 Functional model of machine

Hence, it is possible to derive for the wave length in the semi-product

$$\lambda = \frac{2a'}{k} \tag{12}$$

Using Eqs. (4) (9) and (12), T and P can be estimated as follows:

$$\mathrm{T} = \sqrt{\frac{\mathrm{P}^2k^2 + \left(\frac{a}{2}\right)^2k^2 - \left(\frac{a}{2}\right)^2 - P^2}{k^2}} \tag{13}$$

$$P = \sqrt{\frac{-\left(\frac{a}{2}\right)^2k^2 + \left(\frac{a}{2}\right)^2 + T^2k^2}{k^2 - 1}} \tag{14}$$

where a is given by the forming gear construction. In the device model there is $a = 21$ mm.

These two parameters are used to set the machine. In most cases P, is calculated according to the desired thickness T of the final product. Product example 16 mm thick, is show in Fig. 5 are automatically calculated and set. Parameter T—thickness sets the distance conveyors, P parameter sets the space between the gears. The result of set is shown in Fig. 5 (Konečný et al 2008).

View of the functional model of the machine is shown in Fig. 6.

Described technology allows production of special filter medium and sorption medium suitable for producing different types of filters and sorbents. Products are characterized due to its larger surface by higher filtration efficiency, higher absorption capacity, and longer service life. Described technology enables the production of multi-layer filter and sorption media in one manufacturing operation allowing managing the properties of the resulting products. The machine is designed so that the input section allows the establishment of several different materials, such as different types of textiles, paper, plastic, plastic films, including layers of nano-fibres. The structure of the product is fixed mechanically only.

The novelty lies in the way of composing more layers of different types of materials into waves and mechanical fixation of the product structure. Then principle isn't commonly used in the word and against other principles has high production efficiency and low operating costs. Heat or chemicals are not needed to fix the structure. The structure of the products is fixed by kvazi-yarns, i.e. a way that is not subject of this post.

4 Conclusion

Approximate machine settings can be done via the control computer with the required parameters of the product. The exact parameters will need to be found experimentally. The calculation does not include the properties of the used materials.

Acknowledgments This work resulted from the OP Research and Development for Innovation (support pre-seed activities) "New Technologies and Special Machine Components", CZ.1.05/3.1.00/13.0291 funded by Ministry of Education, Youth, and Sports of the Czech Republic.

References

Hanuš J, Ševčík L (2009) New Quasi-Yarn application. In: 14th international conference STRUTEX, Nov 2009, Liberec

Hanuš J, Ševčík L, Rydlo P, Konečný M (2008) Nové textilní 3D produkty; In: Textilie v novém tisíciletí VI, duben 2008, Liberec

Konečný M, Ševčík L, Hanuš J, Rydlo P (2008) Device for manufacture of nonwoven textiles, 10. mezinárodní konference o teorii strojů a mechanismů, září 2008, Liberec

Optimal Tuning of Torsional Oscillating Mechanical Systems

J. Homišin and P. Kaššay

Abstract According to more authors the most convenient method for system tuning is application of flexible element, which can be a flexible shaft coupling. By means of correct chosen flexible coupling based on detailed dynamic calculation it is possible to tune torsional oscillation of mechanical system.

Keywords Torsional oscillation · Control of dangerous torsional oscillation · Detailed dynamical calculation

1 Introduction

According to several authors (Zoul 1982; Böhmer 1983; Homišin and Jurčo 1997; Homišin 2000) the most appropriate way of optimal tuning of the system is the application of a suitable elastic element, which can be flexible shaft couplings.

By an appropriate selection of flexible shaft couplings based on *detailed dynamic calculation* it is possible considerably tune torsional vibration of mechanical system without enlarging the diameter of the shaft, or using dampers and eliminators of torsional oscillations.

The main aim of this paper is to present, on the results of solved examples, the inappropriate and appropriate tuning of torsional oscillating mechanical system by applying two proposed flexible couplings. Particularly, flexible coupling selection based on *operating coefficient K*, and flexible coupling selected on the basis of *detailed dynamic calculation* of the system.

J. Homišin (✉) · P. Kaššay
Technical University of Košice, Košice, Slovakia
e-mail: Jaroslav.Homisin@tuke.sk

P. Kaššay
e-mail: Peter.Kassay@tuke.sk

L. Ševčík et al. (eds.), *Modern Methods of Construction Design*,
Lecture Notes in Mechanical Engineering, DOI: 10.1007/978-3-319-05203-8_9,

2 Results of Tuning the Torsional Oscillating Mechanical Systems by Application of Flexible Couplings

To illustrate the control of torsional vibration of the system is presented in the form of its tuning on solved example. This will be an example of an inappropriate method of tuning, which is unfortunately currently used and the correct method of tuning the system by application flexible coupling. In the first case the proposal of flexible coupling is made based on operation coefficient K, while in the second case, the proposal of flexible coupling was carried out on the basis of a detailed dynamic calculation.

- Example assignment

Make a selection of flexible coupling for a torsional oscillating mechanical system according to Fig. 1. Compare the optimization results from the view of its proper tuning by selected couplings and also the size of dangerous torsional vibration. Mechanical system will work by operating speed $n = 600\ \text{min}^{-1}$ by 100 % fuel supply of diesel engine, thus 100 % power $P = 98$ kW and with idle speed $n_v = 380\ \text{min}^{-1}$.

Realized torsional oscillating mechanical system consists of a piston engine *(1)*, formed by six-cylinder four-stroke diesel engine type *6S160PN*, driving a DC generator type *DN 1144-4 (2)* trough a flexible coupling *(3)*.

2.1 Proposal of Flexible Shaft Coupling Based on the Operation Coefficient K

- Computation of nominal load torque:

$$\begin{aligned} P &= M_N \cdot \omega. \\ M_N &= 1,560\,\text{Nm} \end{aligned} \tag{1}$$

- Computation of load torque transmitted by flexible coupling based on operation coefficient:

$$\begin{aligned} M_{KS} &= K \cdot M_N. \\ M_{KS} &= 4,368\,\text{Nm}. \end{aligned} \tag{2}$$

where: $K = 2, 8$—operation coefficient determined by the construction of mechanical system.

On the basis of calculated load torque transmitted by flexible coupling ($M_{KS} = 4{,}368$ Nm) we choose from a catalog of flexible couplings for the next higher $M_{KS} = 5{,}000$ Nm a linear flexible coupling, because the mechanical system will operate at a constant speed.

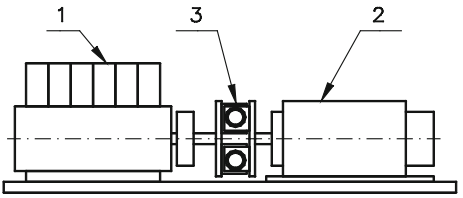

Fig. 1 Realized torsional oscillating mechanical system

2.2 Proposal of Flexible Shaft Coupling on the Basis of a Detailed Dynamic Calculation

2.2.1 Proposal of Flexible Shaft Coupling

- Computation of nominal load torque:

$$P = M_N \cdot \omega.$$
$$M_N = 1,560\,\text{Nm}. \tag{3}$$

- On the basis of calculated nominal load torque $M_N = 1{,}560$ Nm, and therefore also the load torque transmitted by flexible coupling we choose from a catalog of flexible couplings for the next higher $M_{KS} = 2{,}200$ Nm linear flexible coupling wit following parameters:

$M_{KS} = 2{,}200$ Nm;	maximum operating torque,
$M_{KM} = 5{,}000$ Nm;	maximum short term torque,
$M_{KW} = 640$ Nm;	dynamic component by alternating symmetrical load,
$k_d = 24.6$ kNm rad^{-1};	dynamic torsional stiffness of flexible coupling,
$\psi = 1.13$;	relative damping,
$I_{SP} = 0.041$ kg m^2;	mass moment of inertia of flexible.

2.2.2 Implementing the Dynamic Calculation of Torsional Oscillations for Mechanical System with Applications of Proposed Flexible Coupling

Based on the Campbell diagram (Fig. 2) it can be concluded that the resonance of the main harmonic component will be at speed $n_{r3} = 272$ min^{-1}; while the lower harmonic load torque resonances ($i = 2.5$; 2; 1.5; 1 and 0.5) take values:

$n_{r2.5} = 327$ min^{-1}; $n_{r2} = 408$ min^{-1}; $n_{r1.5} = 544$ min^{-1}; $n_{r1} = 816.5$ min^{-1}; $n_{r0.5} = 1{,}633$ min^{-1}.

Computation and representation (Fig. 3) of dynamic component M_d and total load torque M_{KC} of torsional oscillating mechanical system from the main

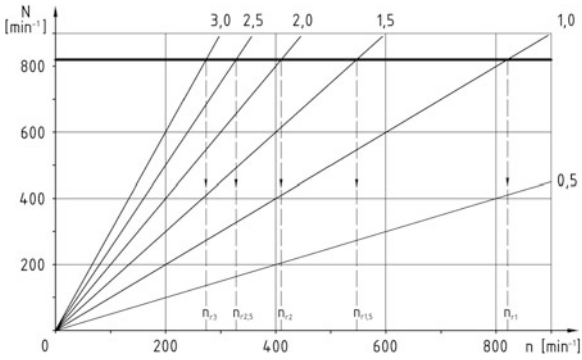

Fig. 2 Campbell diagram of torsional oscillating mechanical system

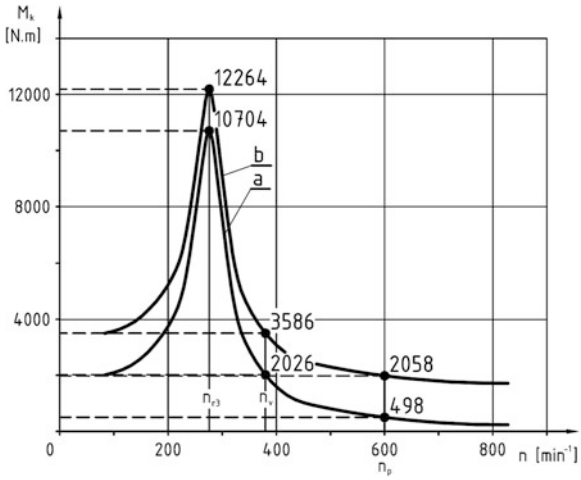

Fig. 3 Graphs of the dynamic M_d and the total M_{KC} load torque from the main harmonic component ($i = 3$) at working mode of mechanical system

harmonic component ($i = 3$) at its various dynamic states and different operating modes:

Resonance ($n_r = 272$ min^{-1}), operating mode ($n_p = 600$ min^{-1}), idle speed ($n_v = 380$ min^{-1}).

3 Implementing the Dynamic Calculation of Torsional Oscillating Mechanical System by the Application of Flexible Couplings Selected Based on the Operation Coefficient K

Dynamic calculation of mechanical system will be realized, as previously by application of flexible coupling catalogue parameters:

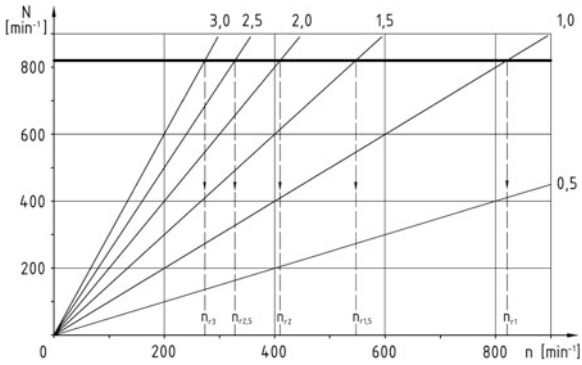

Fig. 4 Campbell diagram of torsional oscillating mechanical system by application of flexible coupling selected on the basis of operating coefficient K

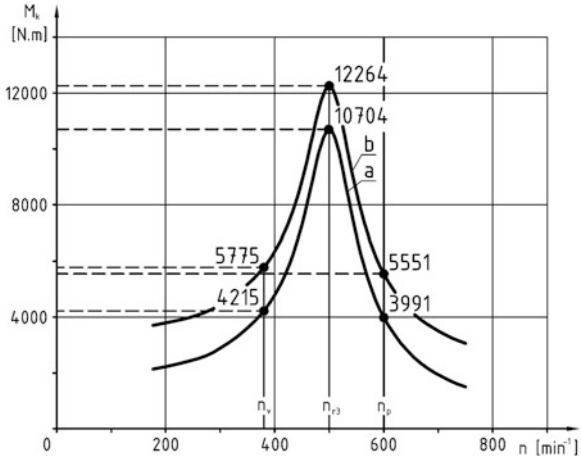

Fig. 5 Graphs of the dynamic M_d and the total M_{KC} load torque from the main harmonic component ($i = 3$) at working mode of mechanical system

$M_{KS} = 5{,}000$ Nm; maximum operating torque,
$M_{KM} = 15{,}000$ Nm; maximum short term torque,
$M_{KW} = 2{,}000$ Nm; dynamic component by alternating symmetrical load,
$k_d = 83$ kNm rad^{-1}; dynamic torsional stiffness of flexible coupling,
$\psi = 1.13$; relative damping,
$I_{SP} = 0.08$ kg.m^2; mass moment of inertia of flexible.

Based on the Campbell diagram (Fig. 4) it can be concluded that the resonance of the main harmonic component will be at speed $n = 499$ min^{-1} $\approx$ 500 min^{-1}, thus $n_{r3} = 500$ min^{-1}; while the lower harmonic load torque resonances ($i = 2.5$; 2; 1.5; 1 and 0.5) take values:

$n_{r2.5} = 600$ min^{-1}; $n_{r2} = 748$ min^{-1}; $n_{r1.5} = 998$ min^{-1}; $n_{r1} = 1{,}496$ min^{-1}; $n_{r0.5} = 2{,}992$ min^{-1}.

Computation and representation (Fig. 5) of dynamic component M_d and total load torque M_{KC} of torsional oscillating mechanical system from the main harmonic component ($i = 3$) at its various dynamic states and different operating modes:

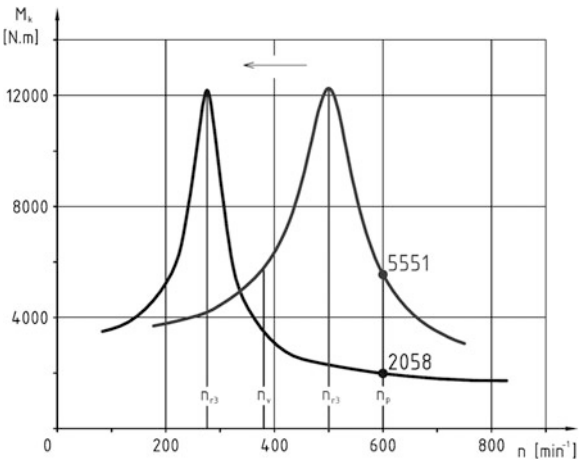

Fig. 6 The result of optimal tuning of torsional oscillating mechanical system

Resonance ($n_r = 500\ \text{min}^{-1}$), operating mode ($n_p = 600\ \text{min}^{-1}$), idle speed ($n_v = 380\ \text{min}^{-1}$).

4 Evaluation of Tuning of Torsional Oscillating Mechanical System with Flexible Couplings

From the results of the dynamic calculations of mechanical of system in case of application of the proposed flexible couplings it is possible to confirm the fact that a properly chosen flexible shaft coupling, in this case proposed on the basis of detailed dynamic calculation, shifts its natural angular frequency of torsional oscillation, and thus the critical speeds of the individual load torque harmonics to the area of the lower rotational speeds.

That fact is presented by courses of the main harmonic component of load torque (Fig. 6) for both selected flexible shaft couplings:

$$\Omega_0 = 85.5\,\text{rad s}^{-1} < \Omega_0 = 156.68\,\text{rad s}^{-1}$$
$$\text{n}_{\text{r3}} = 272\,\text{min}^{-1} < \text{n}_{\text{r3}} = 500\,\text{min}^{-1}.$$

Due to that fact there is a load reduction of flexible shaft coupling and hence the overall mechanical system for balanced excitation of each cylinder engine: $M_{KCp} = 2{,}058$ Nm $< M_{KCp} = 5{,}551$ Nm.

5 Conclusions

Based on the contents of the article can be declared and also confirm the fact, that a properly chosen flexible shaft coupling, serves as a simple and relatively

inexpensive way of reducing resonance formation in the range of operating speed and reducing the additional dynamic torsional load of all members of the system.

Acknowledgments This paper was written in the framework of Grant Project VEGA: "1/0688/12—Research and application of universal regulation system in order to master the source of mechanical systems excitation".

References

Böhmer J (1983) Einsatz elastischer Vulkan – Kupplungen mit linearer und progressiver Drehfedercharakteristik. MTZ, 44/5

Homišin J (2000) Ovládnutie torzného kmitania v mechanických sústavách. Acta Mechanica Slovaca, 1/2000, p 83

Homišin J, Jurčo M (1997) Aplikácia diferenčných pneumatických spojok s autoreguláciou a bez autoregulácie v torzne kmitajúcich mechanických sústavách. Strojnícky časopis, 48/2, p 116

Zoul V (1982) Některá hlediska vývoje pružných spojek pro soustrojí s naftovými motory. Strojírenství, 32, 6/7

Thermal Simulation of Plasmabit Electronic System Protective Housing

S. Hrček and J. Bucala

Abstract This article deals with temperature stabilization within the electronic system protective housing of the Plasmabit device, employed in ultra-deep geothermal wells. Device description, boundary conditions of geothermal wells and simulation results are also presented. Simulations have been carried out using finite element method (FEM) approach.

Keywords Plasmabit · Protective housing · Electronics · Thermal analysis · FEM

1 Introduction

Electricity consumption and dependence thereon is constantly increasing. In view of the said increase, new and more effective means of energy development are necessary, all while minimizing negative impact on the environment, in accordance with the "20/20/20" plan of the European union aiming to reduce emissions to 30 % by the year 2020. Long term plans include the substitution of fossil fuels by other means of energy, most notably from sustainable resources such as geothermal energy. Although already utilized, geothermal wells are limited only to a few locations offering high temperatures in relatively small depths. The Geothermal Anywhere Corporation plans to harvest geothermal energy on a worldwide basis.

S. Hrček (✉) · J. Bucala
University of Žilina, Žilina, Slovakia
e-mail: slavomir.hrcek@fstroj.uniza.sk

J. Bucala
e-mail: jan.bucala@fstroj.uniza.sk

L. Ševčík et al. (eds.), *Modern Methods of Construction Design*,
Lecture Notes in Mechanical Engineering, DOI: 10.1007/978-3-319-05203-8_10,

In view of the above, the Plasmabit device (working title) is being developed, capable of operation in depths up to 10 km beyond the Earth surface, with temperatures reaching up to 280 °C and pressure of 100 MPa. Plasmabit is an autonomous system capable of self-movement and includes various subsystems responsible for movement, rock disintegration, coordination and control thereof.

2 Description of Boundary Conditions

Geothermal wells and their properties change with depth and also vary based on local core composition and presence of various anomalies. Most notably the temperature increases with increasing depth. However, when taking into account the average geothermal gradient of 3, 6 °C/100 m, the temperature of a 10 km deep well is approximately 360 °C (Heuze 1983).

The Plasmabit device includes protective housing for the control and power electronic systems which are a source of waste heat. Given the current components, the average thermal radiation is approximately 4 kW. This waste heat must be conducted away from the protective housing in order to assure proper functioning of the electronics, which have a maximum working temperature of 150 °C. In order to achieve this, water must be supplied from the well surface, whose temperature reaches a maximum of 105–120 °C before entering the Plasmatron (rock disintegrating system), which represents an additional heat source. The Plasmatron operates on the principle of contact arcing and the resulting plasma generating process disintegrates rocks along the well path. The said technology is compatible with aqueous environments. Water, combined with particles stemming from disintegrated rocks, is part of the borehole fluid, reaching a temperature of 280 °C after passing through the Plasmatron. The borehole fluid returning to the surface interacts with both the well wall and the Plasmabit hull (Chan et al. 1980).

Simulations are of utmost importance to assure sufficiently low temperature within the protective housing. Additional details obtained from simulations will help prevent electronics malfunction or destruction thereof and to obtain further information pertaining to possible thermal scenarios.

3 Simulation Setup and Results

Finite element method simulations have been performed using Ansys Workbench ver. 14.0 and the Transient Thermal module. The main task was to obtain correct material data because thermal variations cause significant changes in key properties of materials used in the construction: thermal conductivity, thermal capacity and density. Coolant properties are dependent not only on temperature but also largely on pressure conditions.

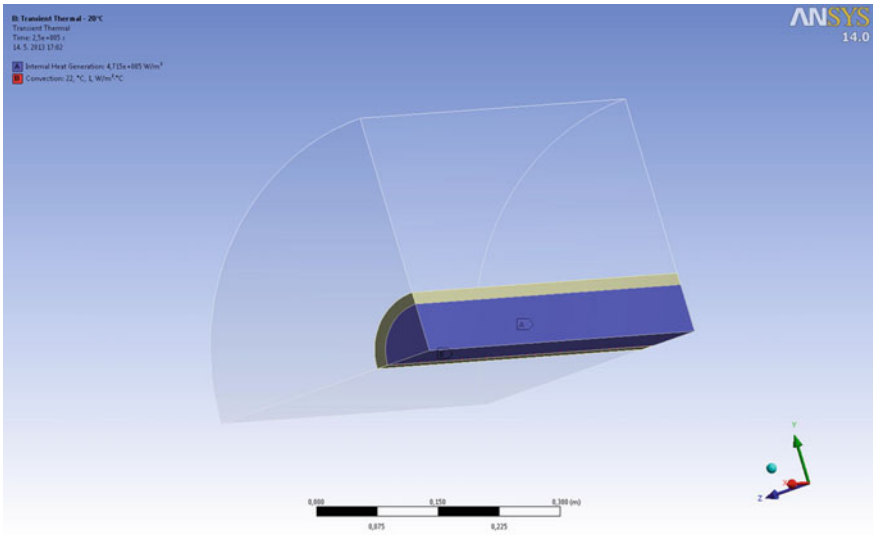

Fig. 1 Simplified Plasmabit simulation model

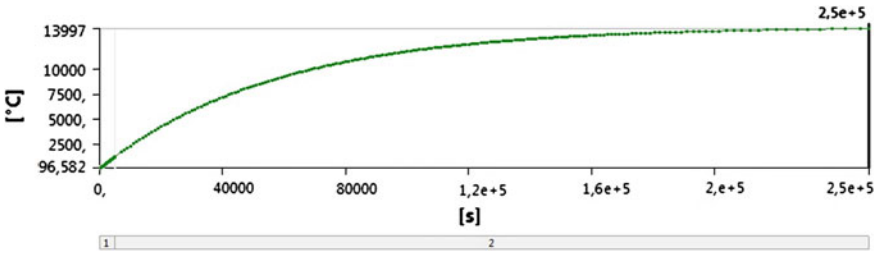

Fig. 2 Thermal analysis in the time domain

The simplified model used in the first batch of simulations is shown in Fig. 1. Symmetry has been defined based on XY and XZ planes to reduce calculation complexity. This model considers only an air-filled protective housing made of steel 1.4545 and an initial background temperature of 20 °C. The goal was to find out whether a steady state could be reached and at what temperature.

Figure 2 shows the thermal steady state has been reached after approximately 250,000 s, with a steady temperature of 13,997 °C. However, the said temperature is not possible and the simulation has confirmed that effective cooling is necessary in order to prevent the malfunction and eventually the destruction of internal electronic components due to excessive heat within the protective housing.

Subsequent simulations included a more complex model containing all important elements. The current development phase considers the well wall to consist of granite. The hull of the protective cover and Plasmabit are defined as corrosion and heat-resistant steel 1.4545. The protective housing contains

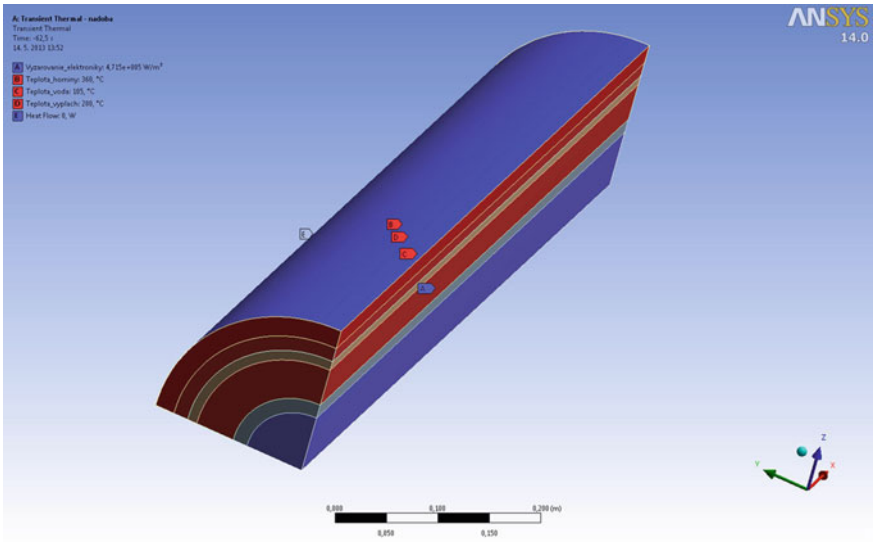

Fig. 3 Complex model with boundary conditions

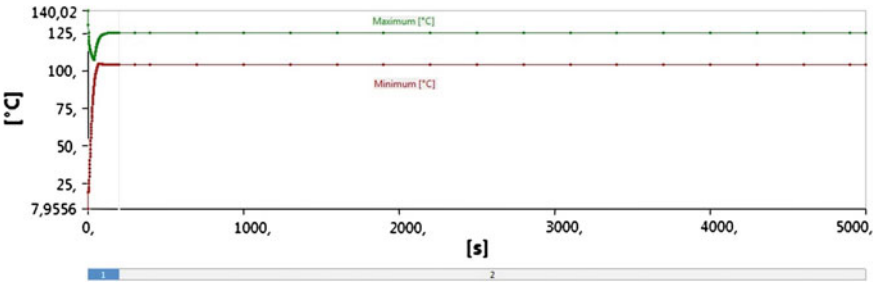

Fig. 4 Thermal analysis of the protective housing using the complex model

electronic components and air. Water, borehole liquid and air within the protective housing are defined as liquids, while the Plasmabit hull and protective housing are defined as solid materials.

Thermal radiation of electronics in the model has been defined as Internal Heat Generation within the protective housing. The well wall temperature can change from 10 °C at the surface up to 360 °C at a depth of 10 km. The model with boundary conditions and thermal effects is shown in Fig. 3.

Highest thermal stress within the protective casing has been observed at the maximum expected well depth of 10 km, wherein the maximum temperature of the protective casing has stabilized at 125, 26 °C ± 5 %, conforming to thermal limits for proper operation of the Plasmabit electronic systems (Fig. 4) (Medvecký et al. 2012).

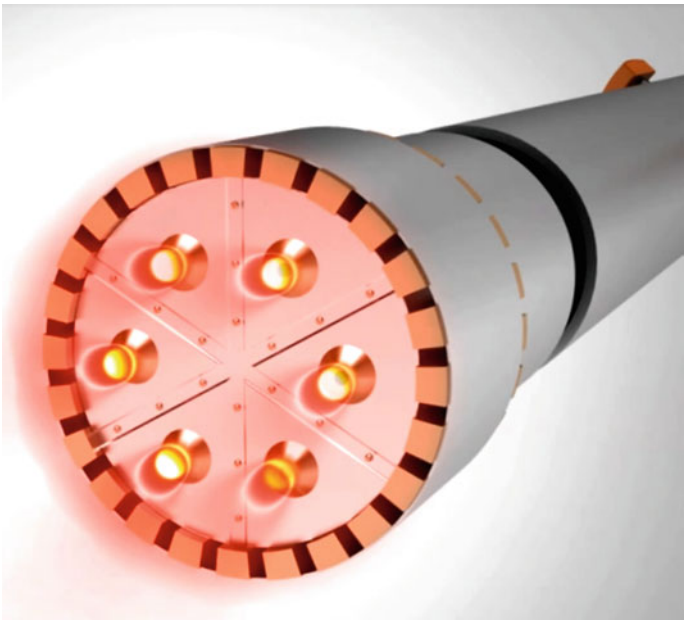

Fig. 5 Plasmabit prototype visualization

Obtained results are only valid for conditions and material properties used in the simulations. Rock properties can vary significantly within the same rock type. This is due to different chemical composition and other properties such as porosity. Additional precision can be achieved using a more complex model which will be considered in further development of the protective housing (Fig. 5).

4 Conclusion

Simulations conducted thus far using FEM-based software have enabled us to evaluate thermal conditions within the electronics protective housing without the need to construct and evaluate the actual device prototype under real-life conditions, which would be financially much more expensive. The project is still in R&D phase and more precise and detailed analyzes and simulations will be conducted in future works.

Acknowledgments This work was created by the implementation of the "Applied research and development of innovative sources of energy for ultra-high pressure pulses", "ITMS: 26220220088" to support the Operational Programme Research and Development financed by the European Fund for Regional Development.

References

Medvecký Ľ;, Žarnay M, Gajdáč I, Sokol M, Mudrák J, Drdol K, Kamas P (2012) Konštrukčný návrh funkčného vzoru pohybového systému plazmabitu. Štúdia k výskumnej správe. KKČS-2012-139-04, Žilina

Heuze FE (1983) High-temperature mechanical, physical and thermal properties of granitic rocks. Int J Rock Mech Min Sci Geomech 20(1):3–10

Chan T, Javandel I, Witherspoon PA (1980) Heat transfer in underground heating experiments in granite, Stripa, Sweden. In Technical session on heat transfer in nuclear waste disposal. Chicago, Illinois

Finite Element Modeling of a Torque Rod Forging Process

M. S. Keskin, S. Bingol, H. B. Elem and A. Atar

Abstract Aluminum forging products has been increasingly used in automotive and aerospace industry due to their lightness and strength. Torque Rod is a connection part used for tying of the axle to the chassis frame. In this study, torque rod part from two different aluminum alloys (AA7075 and AA6061) were analyzed by finite element method. Three different initial temperatures of the workpiece; 300, 400 and 500 °C, have been used in simulations. Finally, the load-stroke and effective stress-stroke diagrams were examined according to forging of the mentioned aluminum alloys at different temperatures.

Keywords Torque rod · Hot forging · Finite element method · Metal forming

1 Introduction

Forged aluminum alloys have high strength properties and light weight. These properties provide a wide range of applications. Torque rod is used in heavy commercial vehicles for connecting the axle to chassis frame. Uncontrolled movement on tires through the road according to the road conditions is transmitted to the axle. Most of these uncontrolled movements are transmitted to the axle, but the rest of that movement is damped by suspension system and tires. The inertia of vehicle, negative effects of the wheels' traction, and centrifugal forces transferred to chassis frame of vehicle via suspension system, and torque rod.

In recent years, usage of aluminum forging products especially in automotive industry has been increased because of their lightness, strength and formability. The necessities to make modern vehicles lighter, safer and friendlier with

M. S. Keskin (✉) · S. Bingol · H. B. Elem · A. Atar
Dicle University Engineering Faculty, Diyarbakir, Turkey
e-mail: keskinms@gmail.com

L. Ševčík et al. (eds.), *Modern Methods of Construction Design*,
Lecture Notes in Mechanical Engineering, DOI: 10.1007/978-3-319-05203-8_11,

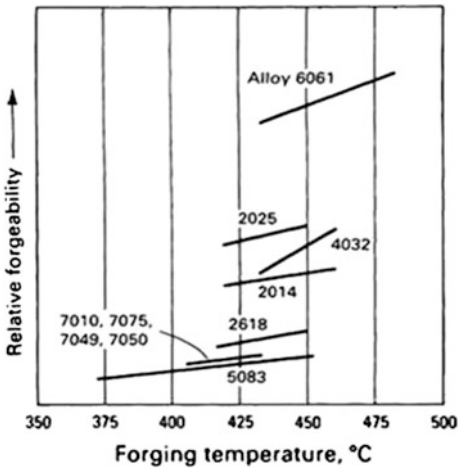

Fig. 1 Forgeability of various aluminum alloys (ASM 1988)

environment, these products are used in automotive industry. It is required to use more products from aluminum alloys in automotive industry because of increasing demand for low fuel consumption cars (Ozturk 2008; Nagaumi et al. 2004).

ASM Handbook Committee's Metals Handbooks Volume 5 and 14 explain the aluminum forging process and its properties fully (ASM 1988, 1970). The forging heat interval is determined after examining Fig. 1.

In some previous studies; Kim et al. (2002) used aluminum casting/forging to produce aluminum tie-rod ends for the steering systems of automobiles. The effect of additives, Ti+B, Zr, Sr, and Mg was investigated on mechanical properties of casting products. They also determined the heat treatment condition suitable for the cast forged product and compared it with conventionally forged product for hardness. Tanner and Robinson aimed to reduce the residual stress in AA2014 forged aluminum alloy products. For that, warm water and boiling water methods were used for quenching the aluminum alloy. Finally, occurring residual stresses by two methods were compared (Tanner and Robinson 2007).

In this study, a forging process has been designed and analyzed to produce a particular AA6061 and AA7075 aluminum alloy parts. Finite element method has been used for modeling and analyzing this process. The load-stroke and effective stress-time diagrams have been compared for 300, 400 and 500 °C of initial workpiece temperature.

2 Modeling of the Torque Rod Forging Process

The Forging simulations of the torque-rod production are performed with using the Deform 3D program. Many materials' properties are available in DEFORM 3D library. Between these materials AA7075 and AA6061 were chosen as workpiece materials. Tooling (upper and lower dies) was assigned as rigid while the billet material

Table 1 The used parameters in the modeling

Modeling no	Velocity (mm/s)	Forging temperature (°C)	Material	Product
1	50	300	Al6061	Torque rod
2		400		
3		500		
4	50	300	Al7075	
5		400		
6		500		

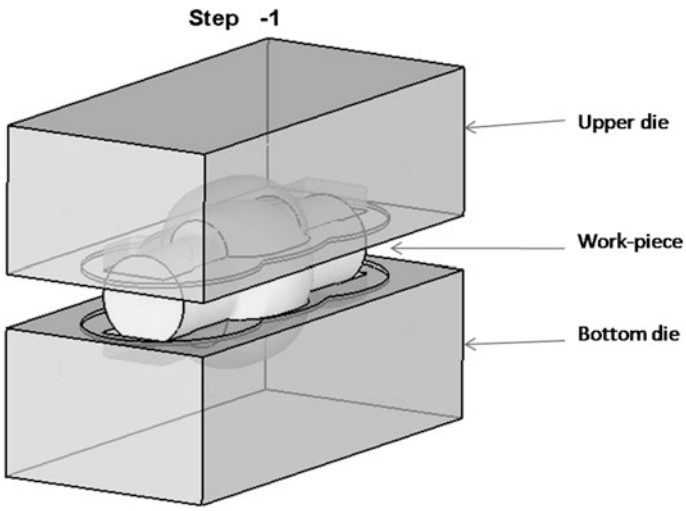

Fig. 2 The modeling of the forging process for torque rod production

was selected as plastic. In order to obtain more sensitive results, the number of element and nodes were assigned 40000 and 8448, respectively. The speed of the upper die was valued as 50 mm/s. Friction between dies and workpiece is determined as 0.4 by the DEFORM software. The used parameters in the modeling can be seen in Table 1.

The finite element modeling of the forging process including upper die lower die and workpiece (Fig. 2) was set. The workpiece designed as a pre-form to improve the forgeability. In literature, it was noticed that the pre-form should be designed for sufficient deformation (Kim et al. 2002).

3 Simulation Results and Discussions

The obtained model for torque rod forging process was successfully simulated (Fig. 3). After simulation, the load requirement and effective stress values were obtained by using the post-processor unit in DEFORM 3D software. The simulations

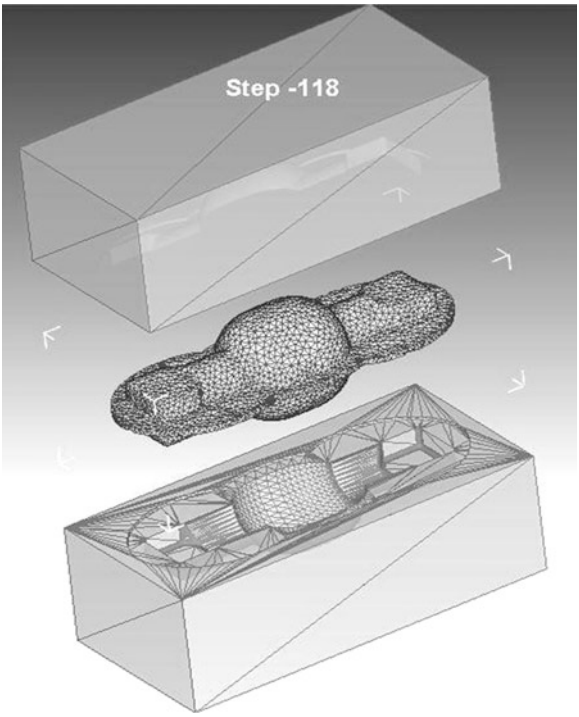

Fig. 3 The simulation of the forging process for torque rod production

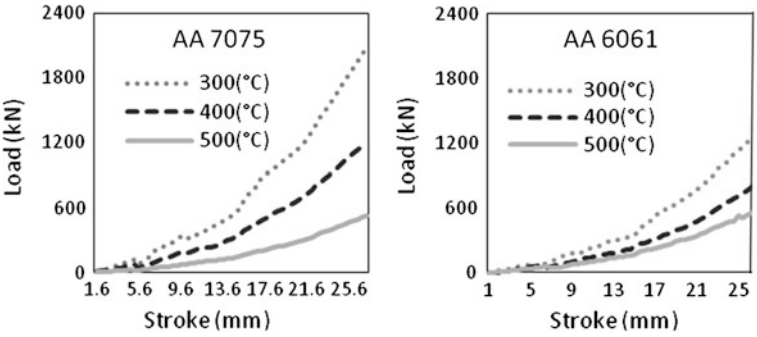

Fig. 4 Load versus stroke AA6061 (graph at *left*) AA7075 (graph at *right*) at 300, 400 and 500 °C

in this study have been run for the forging temperatures of 300, 400 and 500 °C. Figures 4, 5, 6 give the simulation results.

In Fig. 5, the loads occur in forging process are compared for AA6061 and AA7075 at the different temperatures. The maximum die load was found at 300 °C

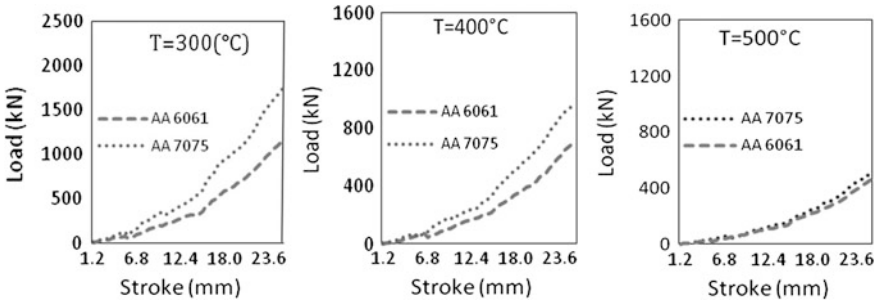

Fig. 5 The load-stroke diagrams of AA6061 and AA7075 at 300, 400 and 500 °C

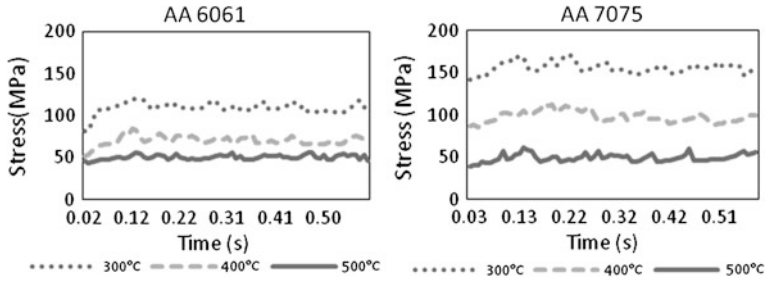

Fig. 6 The effective stress-time diagrams for AA6061 and AA7075 at 300, 400 and 500 °C

Table 2 Maximum load and effective stress for different temperatures of aluminum alloy

Initial temperature of workpiece (°C)	Max. die load for AA6061 at 27.6 mm ram travel (kN)	7075 Max. die load for AA7075 at 27.6 mm ram travel (kN)	Max. effective stress for AA6061 (MPa)	Max. effective stress for AA7075 (MPa)
300	1396	2088	142	163
400	902	1247	102	109
500	629	569	70.9	73.8

both AA6061 and AA7075. The forging loads were occurred lower with higher initial workpiece temperatures.

It is known that the effective stress increases during deformation under high force. As mentioned above figures, load requirement for AA7075 is higher than AA6061. In Fig. 6, the effective stresses occurring as a result of the forging analysis of AA6061, and AA7075 with different temperatures are given. Maximum effective stress for AA6061 and AA7075 were given for different temperatures in Table 2. As seen from Table 2, effective stress decreases by increasing temperature.

In Table 3, temperature increase in forged pieces of AA6061, and AA7075 materials at different temperatures are seen. It is seen from Table 3 that increasing

Table 3 Maximum workpiece temperatures for different forging temperatures

Initial temperature of workpiece (°C)	Max. workpiece temperature (°C) for AA6061	Max. workpiece temperature (°C) for AA7075
300	380.2	450.3
400	427.2	467.2
500	513.1	526

in temperature for AA7075 is more than AA7075 in forging process. The reason of this is that the effective stress in deformation of AA7075 is more than of AA6061. Another effect of increased stress is increase of maximum die force and this situation makes forging difficult. Also this state is compatible with literature (ASM 1988).

4 Conclusions

In this study which is based on producing the torque rod made AA6061 and AA7075 materials by forging method with using Deform 3D software, the following results were obtained.

- In the same forging temperature higher forging load was occurred for AA7075 according to AA6061.
- By increasing initial workpiece temperature, forging loads and effective stress for both AA6061 and AA 7075 materials were decreased.

References

ASM (1970) Metals handbook-forging and casting. vol. 5, 8th edn. ASM Handbook Committee

ASM (1988) Metals Handbook-Forming and Forging. vol. 14, 9th edn. ASM Handbook Committee, USA

Kim HR, Seo MG, Bae WB (2002) A study of the manufacturing of tie-rod ends with casting/forging process. J Mater Process Technol 125–126:471–476

Nagaumi H, Takeda Y, Pongsukiwat S, Umeda T (2004) Hot tear and its prevention of irregular near net shape D.C. Billet of high strength Al-Mg-Si alloy. Nippon Light Metal Company Ltd., Kambara, Japan

Ozturk H (2008) Analyses and design for aluminum forging process. MSc Thesis Natural and Applied Sciences of Middle East Technical University

Tanner DA, Robinson JS (2007) Reducing residual stress in 2014 aluminum alloy die forgings. J Mater Des 2:84–96

Influence of Heat Treatment on the Mechanical Properties of Steel Type (40X)

M. Khidhair

Abstract This work includes in its theoretical review, some information about such type of constructural alloyed steel which has wide range of applications, referring to its chemical composition, hardness, UTS, yield point and ductility (elongation) in the hot rolled case. However in the practical part, several specimens were made in two forms, circular discs for hardness test after each heat treatment process, and specimens for mechanical test, machined to dimensions near the final standard dimensions in order to complete machining to accurate size after heat treatments to use them in testing UTS, yield point, elongation and contractions in cross section area.We used in this work the following heat treating: Full annealing, normalizing, oil quenching hardening, high and low tempering. These were done to determine the tested properties of this steel to enable the choose of suitable properties to demand or in case of looking for replacement material in production of given parts to help both designer and producer. The research included many tables and graphs and discussion of results.

Keywords Engineering materials · Heat treatment · Steel 40X

1 Introduction

The purpose of heat treatment is to cause desired changes in metallurgical structure, and thus in the properties of metal parts (Totten 2009).

The mechanical properties of carbon—alloy steel could be changed widely by heat treatment. Medium carbon—alloy steel such as steel (40X) are used in general purpose, because of low coast, good range of strength and toughness, which could

M. Khidhair (✉)
Al-Mustaqbal College University, Hillah, Iraq
e-mail: Khidhair_aljuboury@yahoo.com

L. Ševčík et al. (eds.), *Modern Methods of Construction Design*,
Lecture Notes in Mechanical Engineering, DOI: 10.1007/978-3-319-05203-8_12,

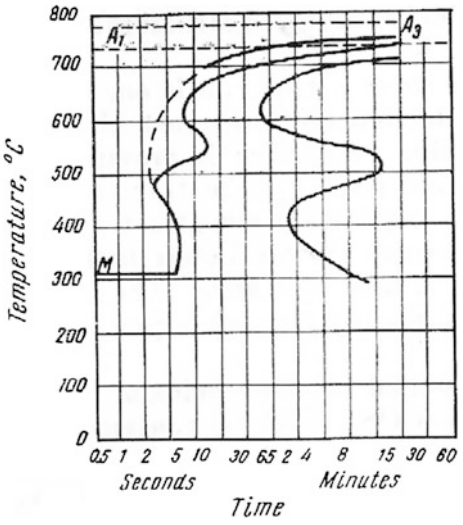

Fig. 1 Isothermal transformation (TTT) diagram for steel (40X) (Prof. Lakhtin)

be achieved by various heat treatment. The effect of heat treatment on steel properties, could be used to decide the required treatment to provide the desired properties (Callister 2003a, b). Alloying additions in steels—such as Cr—may give higher strength and deeper hardening. They generally heat treated before use to achieve the desired properties.[1] Cr—Steels are used in wide field of industry and steel (40X) is used mostly after structural improvement heat treatment [Prof. Lakhtin 1968]. St-40X as referred to in the [Gost 4,543–57] could have different properties according to the requirements, therefore improvement treatment used to provide those requirements .According to isothermal austenite decomposition (TTT-diagram) of mentioned steel Fig. 1, it could be ferritic, pearlitic, bianitic or martensitic structures depending on cooling rate from austenitic range [Prof. Lakhtin 1968]. Investigations in this work had done for estimation of its properties after each heat- treating so as to choose the suitable one to requirements.

2 Aim of Research

The main goal of this work is to determine the basic mechanical properties of steel type (40X) after each heat treatment used, in order to choose the suitable case of them to satisfy the requirements in the designing, production and using of given parts.

[1] Adobe Research—Chap. 2, 1998

Table 1 Chemical composition in wt. % of steel (40X) used

C	Si	Mn	Cr	P	S	Ni	Cu
0.40	0.23	0.58	1.07	0.016	0.018	0.11	0.16

Table 2 Mechanical Properties of steel (40X) in hot rolled case

UTS-MPa	Elongation (%)	Contraction in area (%)	Hardness HB
790	12.6	44.5	219

3 Practical Part

Many actions were done in this work, mainly; testing chemical composition of the steel used, using spectro—analiser type; ARL-34000-OE, Brinel hardness test, microstructure check by using simple microscope and tensile properties test by using universal testing machine . The results of tests were listed in Tables 1 and 2. The microstructure in hot rolled case as could be seen by looking through microscope was mainly alloyed ferrite with about 20 % of pearlite, its mechanical Properties were shown in Table 2.

4 Heat Treatments Used

Electrical chamber furnaces were used in heat treatment processes. Specimens for hardness tests were discs of Ø 25 mm, and for mechanical tensile properties were normally of d° = 6 mm. The following processes were done

1. Full annealing: By heating at a rate of 200 °C/h to (850–870) °C, holding 1 h, then furnace cooling (closed) till °C and then still air cooled to room temperature.
2. Normalizing: By heating as in (1) above, holding also one hour then still air cooling to room temperature.
3. Hardening: By putting specimens in the available furnace of 600 °C, heating to (850–870) °C at a rate of 200 °C/h and then oil quenching.
4. Tempering: By heating hardened specimens to specified temperatures holding one hour then cooling as follow.

Note: in each case 3 specimens were used.

(a) Heating to 600 °C and cooled in oil to room temperature.
(b) Heating to 500 °C and cooled in oil to room temperature.
(c) Heating to 400 °C and cooled in still air to room temperature.
(a) Heating to 300 °C and cooled in still air to room temperature.

Table 3 Mechanical properties of steel (40X) after oil quenching and tempering

Hardening temperature (°C)	Tempering temperature (°C)	UTS (MPa)	Elongation (%)	Reduction in area (%)	Hardness HB	Yield point (MPa)
850–870	Without	1146	6.2	23.4	350	800
850–870	500/oil cooled	1050	13.0	40.0	313	840
850–870	400/air cooled	1104	10.5	44.6	316	820
850–870	300//air cooled	1263	6.7	29.8	345	860
850–870	600/oil cooled	935	17.5	60.9	272	828

Table 4 Mechanical properties of steel (40X) after all heat treatment processes

Metal condition	UTS (MPa)	Yield Pt. (MPa)	Elongation (%)	Contraction in area (%)	Hardnes HB
As rolled	790	600	12.6	44.6	219
Full annealed	637	470	13.1	27.0	187
Normalized	840	620	11.0	61.0	234
Oil quenched	1146	800	6.2	23.4	350
600 Coil tempered	935	828	17.5	60.9	272
500 Coil tempered	1050	840	13.0	40.0	313
400 Castile air tempered	1104	820	10.5	44.6	316
300 Castile air tempered	1263	860	6.7	29.8	345

Note: in cases (a) and (b) oil cooled to avoid embrittlement at that temperature ranges.

The results of mechanical tests after oil cooling hardening and then tempering were shown in Table 3.

All results of mechanical tests after heat treatments were listed in Table 4.

5 Results Obtained

The results of tests after heat treatments obtained in this work were as follow.

1. The highest (UTS) was (1,263) MPa after oil hardening and 300 °C/air tempering.
2. The lowest (UTS) was (637) MPa after full annealing and furnace cooling to 260 °C, then still air cooling to room temp. That result was about one half the highest one
3. Brinell hardness decreased and ductility (E) increased as tempering temperature after quenching increased (as shown in Table 3).

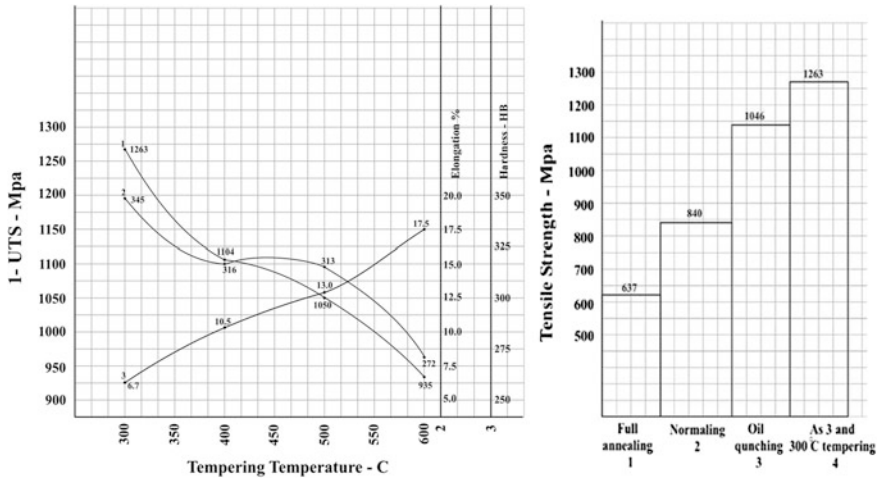

Fig. 2 Effect of tempering temperature on some properties of steel (40X). *1* Tensile strength. *2* Hardness. *3* Elongation

4. Moderate (UTS)—840 MPa and elongation (11 %) and high contaction in area—61 % were obtained after normalizing.
5. In all cases except full annealing—UTS and hardness were higher than that in hot rolled case.

6 Discussion of Results

From the above mentioned results we can conclude that general mechanical properties could be improved widely by using heat treatment. However in case of easy machining, full annealing could be used as lowest hardness was obtained due to soft ferrite microstructure as could be noted from Fig. 1. While in other heat treatments, the high mechanical properties achieved due to the formation of martensite in highest (UTS) and hardness. This was revealed mostly due to the decomposition of retained austenite during tempering at 300 °C—martensitic range—as shown in Fig. 1.

In case of lower (UTS) and hardness, the structure might be martensitic, or bianitic or pearlitic formes, depending on their temperatures ranges shown in Fig. 1. Those structures were the results of decomposition of austenite formed after heating the steel above the austenite start point and depending on the cooling rate of austenite below that point. The (Cr) in this steel acts on the construction of (TTT) curve so as the shape of the curve look like Fig. 1.

The tempering temperature after oil quenching had clear effect on the structure and then on the properties of steel (40X) as shown in Tables 3, 4 and in Figs. 2 and 3

such wide range of mechanical properties enable the choose of required heat treatment satisfied the application conditions.

So we recommend the use of oil quenching followed by tempering at 300 °C for high tensile load, while full annealed for soft machining of the steel (40X) .

The results obtained after tempering at different temperature could be represented in Fig. 2.

References

Brown JR (1986) Foseco Foundryman's handbook, 9th edn. Oxford, New York
Callister WD Jr (2003a) Materials science of engineer. Wiely, New York
Callister WD Jr (2003b) Materials science and engineering introduction. Wiley, New York
Flinn RA, Trojan PK (1994) Engineering materials and their applications, 4th edn. Wiely, New York
Rollanson EC (1970) Metallurgy for engineers. Edward Arnold, London
Totten GE (2009) Steel heat treatment handbook, 2nd edn. CRC Press, Boca Raton
Young JF (1998) and others—the science and technology of C.E.M

Investigation of Heat Treatment Effect on Mechanical Properties of High Strength Steel Bolt Material

U. Kınıt, M. Bozca, İ. M. Palabıyık, A. Sevinç and Ü. H. Büyükalgan

Abstract The objective of this study is to investigate heat treatment effect on mechanical properties of high strength steel bolt material. All sample bolts were M12 and bolts material were 30MnB4. During heat treatment, quenching and tempering processes were applied to high strength steel bolt material. Stress-strain curves were obtained for each sample steel bolt material for different heat treatment. Mechanical properties of steel bolt material such as yield strength, tensile strength and hardness were determined for different heat treatment. It was concluded that heat treatment is important process to change steel bolt material mechanical properties such as hardness, yield strength and tensile strength etc. By heat treating at different temperature levels it is possible obtain different quality of high strength bolt material.

Keywords Heat treatment · Mechanical properties · High strength · Steel bolt

U. Kınıt (✉) · M. Bozca
Yildiz Technical University, Istanbul, Turkey
e-mail: ukinit@yildiz.edu.tr

M. Bozca
e-mail: mbozca@yildiz.edu.tr

İ. M. Palabıyık
Istanbul Technical University, Istanbul, Turkey
e-mail: palabiyik3@itu.edu.tr

A. Sevinç · Ü. H. Büyükalgan
Çetin Cıvata Sanayi ve Ticaret A.Ş, Istanbul, Turkey
e-mail: atakan@cetin.com.tr

Ü. H. Büyükalgan
e-mail: hayri@cetin.com.tr

L. Ševčík et al. (eds.), *Modern Methods of Construction Design*,
Lecture Notes in Mechanical Engineering, DOI: 10.1007/978-3-319-05203-8_13,

1 Introduction

The objective of this study is to investigate heat treatment effect on mechanical properties of 30MnB4 high strength steel bolt material. The correlation between heat treatment and mechanical properties and microstructure was investigated.

High strength steel bolts are used widely to assembly machine parts under static or dynamic loading conditions in various industries. Therefore, mechanical properties of steel bolts are crucial for bolt manufacturer to meet required values such as yield strength, tensile strength and hardness etc. The mechanical strength of material can be improved by heat treatments. Experimental study includes bolt manufacturing, heat treatment and tensile test steps.

2 Material Selections

To investigate heat treatment effect on mechanical properties of high strength steel bolt material, 30MnB4 steel was selected. Chemical composition of 30MnB4 steel material is shown in Table 1.

3 Bolt Manufacturing

To investigate heat treatment effect on mechanical properties of high strength steel bolt material, 30MnB4 steel was selected. Bolts were manufactured by cutting, cold forming, heading and heat treated respectively.

The steel bolt material was manufactured by cold-forming to increase the strength of the steel bolt material, toughness and ductility.

Sample steel bolts were manufactured as a fully threaded hexagon cap bolts according to DIN 933 (2012). All sample bolts were M12. Sample steel bolts were prepared as 12 mm diameter and 40 mm height by cutting process. Then, cylindrical sample steel bolts were cold forged to obtain final diameter.

4 Heat Treatment

The objective of this study is to investigate heat treatment effect on mechanical properties of 30MnB4 high strength steel bolt material. The mechanical strength of material can be improved by heat treatments. Therefore, quenching and tempering processes were applied to high strength steel bolt material.

Table 1 Chemical composition of 30MnB4 steel material

C (%)	Si (%)	Mn (%)	Cr (%)	Ni (%)	A1 (%)	Cu (%)	Ti (%)	Cu (%)	B (%)
0.317	0.092	1.068	0.203	0.041	0.289	0.056	0.057	0.056	0.004

4.1 Quenching Effect

During the quenching of steel bolts, steel was heated to 890 °C. After quenching process, obtained martensite structure is too hard and brittle. Furthermore, transformation from austenite to martensite causes high residual stress in hardened parts. Therefore, tempering process is applied on hardened parts to reduce residual stress in hardened parts.

4.2 Tempering Effect

Aim of tempering process is reduce residual stress and hardness in hardened parts. Therefore, tempering process is applied to reduce residual stress and hardness after quenching process.

The steel bolt samples were heat treated in heat treatment furnace at the different temperature levels. Then, the steel bolt samples were cooled in boron oil. During the tempering of steel bolts, steel was heated to different levels of temperature.

5 Tensile Test

Standard tensile test was applied on sample steel bolt material. Tensile tests were applied using a 40 t ALŞA machine at room temperature. Stress-strain curves are obtained for each sample steel bolt material for different heat treatment. To investigate heat treatment effect on mechanical properties of 30MnB4 high strength steel bolt material, both without heat treatment and quenched and tempered sample steel bolts were tested. Standard tensile test was applied on sample steel bolt material according to EN-ISO 898-1. Test results are shown in Table 2.

Table 2 Mechanical properties of 30MnB4 steel bolt material

Mechanical properties	Tempering 380 °C	Tempering430 °C	Tempering 450 °C	Tempering 460 °C	Tempering 490 °C	Tempering 520 °C
Hardness (HRC)	40	38	36	34	33	30
Yield strength (N/mm^2)	1,220	1,019	1,005.9	989.2	974.7	895.6
Tensile strength (N/mm^2)	1,289	1,080.4	1,068.7	1,042.5	1,027	940
Bolt material quality grade	12.9	10.9	10.9	10.9	8.8	8.8

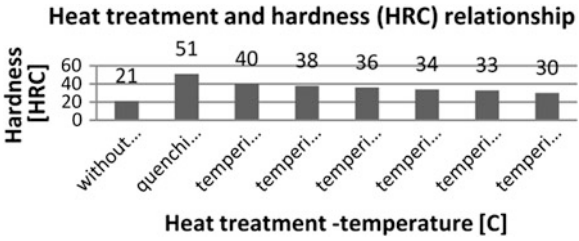

Fig. 1 Heat treatment and hardness (*HRC*) relationship

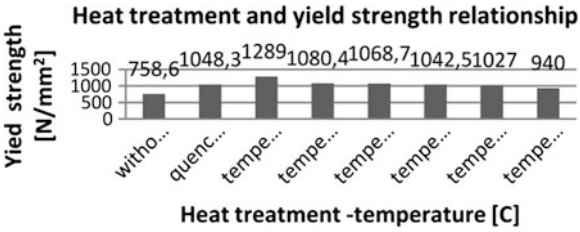

Fig. 2 Heat treatment and yield strength relationship

5.1 Heat Treatment and Hardness Relationship

Hardness of steel bolt material was measured for different heat treatment. Heat treatment and hardness relationship of 30MnB4 high strength steel bolt material is presented in Fig. 1.

Hardness of steel bolt material increases with reducing heat treatment temperature. While tempering process-temperature reduce from 520 to 380 °C, hardness (HRC) increases from 30 (HRC) to 40 (HRC).

5.2 Heat Treatment and Yield Strength Relationship

Yield strength was obtained by tensile test. Heat treatment and yield strength relationship of 30MnB4 high strength steel bolt material is presented in Fig. 2.

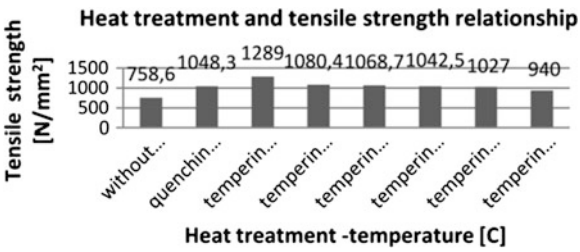

Fig. 3 Heat treatment and tensile strength relationship

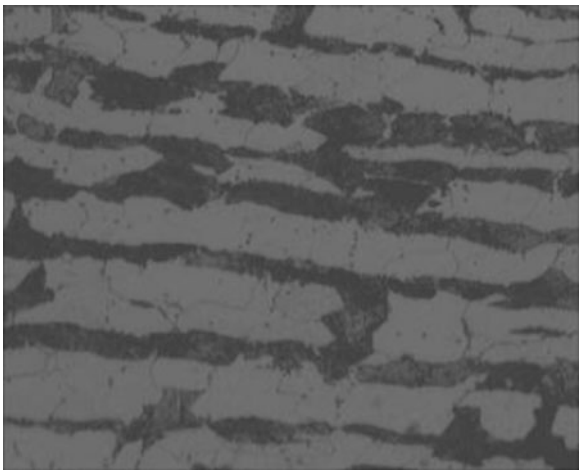

Fig. 4 Microstructure of high strength steel bolt material without heat treatment

Yield strength of steel bolt material increase with reducing of tempering process-temperature. While tempering process-temperature reduce from 520 to 380 °C, yield strength increases from 895.6 to 1,220 N/mm^2.

5.3 Heat Treatment and Tensile Strength Relationship

Tensile strength was obtained by tensile test. Heat treatment and tensile strength relationship of 30MnB4 high strength steel bolt material is presented in Fig. 3.

Tensile strength of steel bolt material increases with reducing of tempering process-temperature. While tempering process-temperature reduce from 520 to 380 °C, tensile strength increases from 940 to 1,289 N/mm^2.

6 Microstructures

Microstructure of high strength steel bolt material without heat treatment process is perlite structure and shown in Fig. 4.

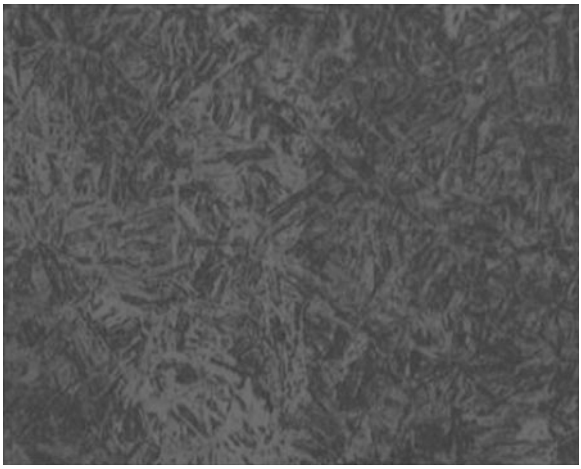

Fig. 5 Microstructure of high strength steel bolt material after quenching process

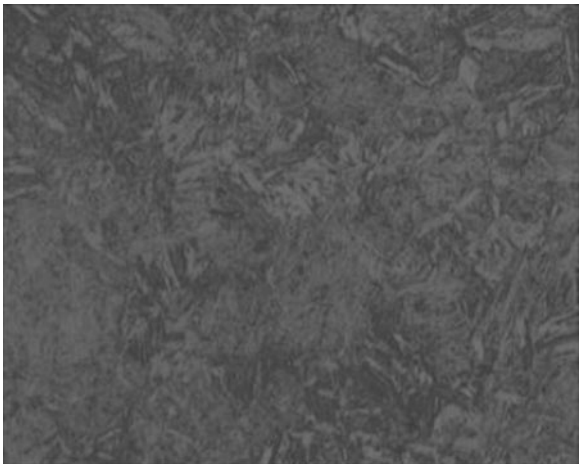

Fig. 6 Microstructure of high strength steel bolt material after tempering process

Microstructure of high strength steel bolt material after quenching process is martensite structure and shown in Fig. 5.

Microstructure of high strength steel bolt material after tempering process is tempered-martensite structure and shown in Fig. 6.

7 Conclusions

Heat treatment is important process to change steel bolt material mechanical properties such as hardness, yield strength and tensile strength etc. Following conclusions are drawn:

By quenching process, mechanical properties of 30MnB4 high strength material such as hardness, yield strength and tensile strength increases.

Hardness of steel bolt material increases with reducing tempering process temperature.

Yield strength of steel bolt material increase with reducing of tempering process temperature.

Tensile strength of steel bolt material increases with reducing of tempering process temperature.

By tempering processing at different temperature levels, it is possible obtain different quality of high strength bolt material such as 12.9, 10.9 and 8.8.

By tempering processing at 380 °C, it is possible to obtain the highest tensile strength and yield strength properties of steel material.

References

EN-ISO 898-1 Mechanical properties of fasteners made of carbon steel and alloy steel-part 1: bolts, screws, and studs with specified property classes-coarse thread and fine tread. http://www.Fastenal.com/content/Feds/pdf/Mechanical%20properties%20of%20Metric%20Fasteners.pdf

DIN 933 (2012) Hexagon cap screws fully threaded. http://www.Fastenal.com/content/Product_spcification/M.933.8.8.P.pdf

Power Flow Distribution of an Anti-backlash Designed Transmission

V. Klouček, J. Fábera, S. Prýl and V. Brozová

Abstract The contribution contains description of the anti-backlash designed planetary gearbox with Oldham couplings, integrated into chassis of an electric motor. The design is subject to a patent protection. The solution results of kinematics and dynamics of components, which held a general planar motion are presented. The following explains the power flow branching through transmission mechanism and the overall efficiency of mechanism is solved. The conditions for backlash elimination are discussed.

Keywords Backlash-free gears · Planetary gears · Efficiency of gearbox · Oldham coupling · Preload

1 Introduction

In engineering practice is very large and varied issue electric drives and motors. Because the standard electric motors (except for so called torque motors) operate at higher speeds and lower torques than often require their technical applications, it is usually necessary between the electric motor and driven mechanism insert the appropriate transmission mechanism.

V. Klouček (✉) · J. Fábera · S. Prýl · V. Brozová
VÚTS Liberec, a.s, Liberec, Czech Republic
e-mail: vojtech.kloucek@vuts.cz

J. Fábera
e-mail: jaroslav.fabera@vuts.cz

S. Prýl
e-mail: stanislav.pryl@vuts.cz

V. Brozová
e-mail: veronika.brozova@vuts.cz

L. Ševčík et al. (eds.), *Modern Methods of Construction Design*,
Lecture Notes in Mechanical Engineering, DOI: 10.1007/978-3-319-05203-8_14,

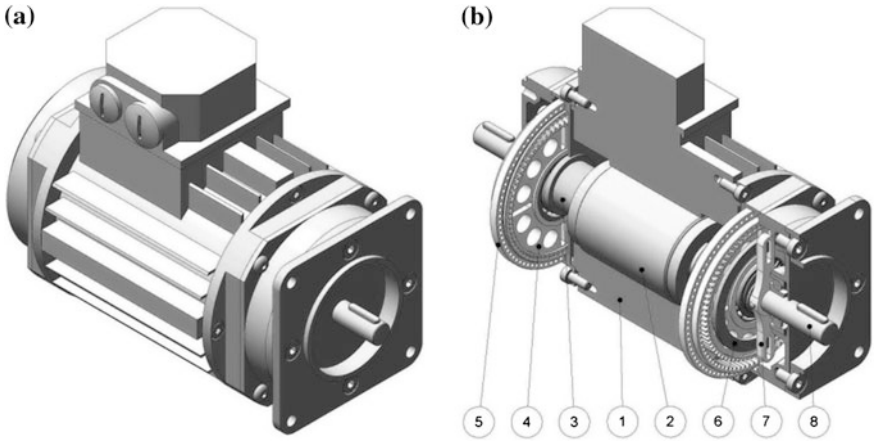

Fig. 1 **a** Electric motor with integrated gearbox. **b** Internal structure: 1—stator with stator winding. 2—Rotor. 3—Eccentric cam. 4—Planet wheel. 5—Central gear with internal teeth. 6—Oldham coupling. 7—Output shaft carrier. 8—Continuous output shaft

According to various aspects, there are diverse requirements on the transmission mechanisms. They are especially high efficiency, high loading capacity and durability, low noise emission, precise repeatability of the output shaft angular position, small space requirements, low cost, etc. The purpose of this paper is design of a special gear mechanism, which is integrated into chassis of the electric motor.

The gear mechanism is an anti-backlash designed, thus ensures a well defined dependence of the output shaft rotation angle to the input shaft. Another advantage of this concept is extremely compact design that makes the whole device can be called "low-speed motor" (Fig. 1).

The article aim is publication of principle and properties of new gear mechanism concept, which is patent protected. There is the design description in the article, outcomes of the transmission mechanism kinematics and dynamics and will be determine overall efficiency.

2 Design of Integrated Gearbox

2.1 Internal Structure

The design of the "low-speed motor" so arranged that to the three-phase asynchronous motor chassis with a squirrel cage is integrated gear mechanism with internal teeth (Fig. 1). In order to eliminate all the backlashes in the gearing and

bearings, is branched into two identical gears, between which is inserted the flexible component (Hale and Slocum 1994; Klouček 2011).

The paths of transmission are located symmetrically around the the plane of symmetry of the motor. The rotor is equipped at the ends of eccentric cams on which are stored by rolling bearings toothed wheels (satellites). These are in mesh with the central wheels with internal teeth, which are rigid supported in the chassis of the motor. From the satellites is converted rotary motion to output shaft through an annular Oldham couplings and carriers.

Output shaft rotation is opposite to the rotor rotation. Overall transmission ratio is given by Eq. (1), where z_k is number of teeth of central wheel with internal teeth and z_s is number of teeth of sattelite.

$$i = -\frac{z_k}{z_k - z_s} \tag{1}$$

2.2 The Backlash Elimination

The backlash elimination in the gear mechanism is achieved by turning the central wheels and fixation of their positions in the base frame. Because the exact location of the wheels, in which are all backlashes just eliminated, is not known before assemble, it is necessary connection between the central wheels and the frame to be solved that it is possible to fix the wheel in any angular position. This property have connections with force contact, such as compression joints. At the same time in the long-term use must not cause self rotation central wheels, which would result in loss of anti-backlash effect. This property have connections with shaped contact, such as grooved joints.

For correct function of the transmission mechanism described construction, it was necessary to resolve this contradiction. It was designed joint with shaped contact and continuous adjustment angular position as follows: Central wheel has number of teeth z_k and on it's circuit is drilled $(z_k + 1)$ holes for pin. The basic frame has drilled along the circuit $(z_k + 2)$ holes for pin, thus creating a vernier (Fig. 2).

The correct angular position is ensured by one pin that is inserted into a pair of holes, which lie against each other. Number n_p of mutual angular positions of central wheels are not infinite, but is very high. The number is given by (2).

$$n_p = z_k(z_k + 1)(z_k + 2) \tag{2}$$

For $z_k = 80$, as in the already made prototype, is $n_p = 531{,}360$, which corresponds to an angular accuracy of approximately $\pm 2.5''$. Such accuracy can be within tolerances of standard engineering practise considered as a continuous adjustment of angular position.

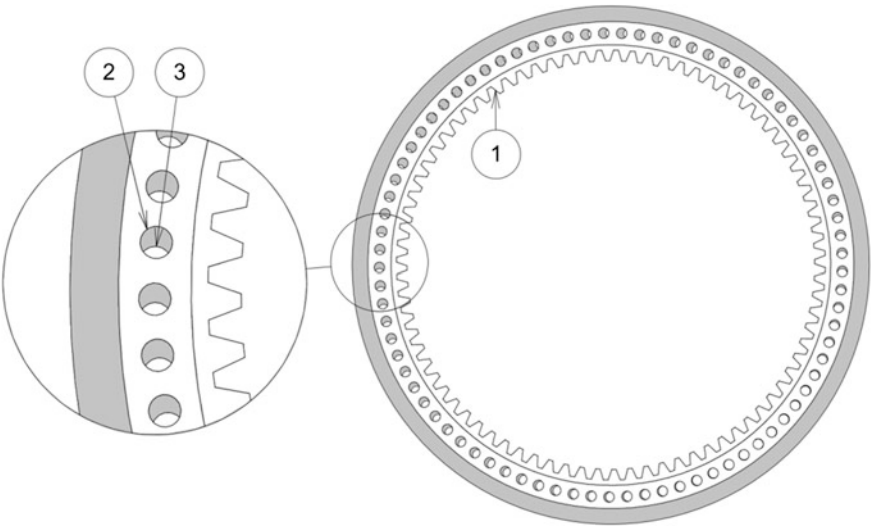

Fig. 2 Vernier for backlash elimination in gear mechanism: 1—number of teeth of central wheel z_k. 2—Number of holes for pin on central wheel ($z_k + 1$). 3—Number of holes for pin on basic frame ($z_k + 2$)

An important feature of this mechanism is its static indeterminacy. From the indeterminacy results output shaft torsional preload M_{Tk} in the area between carriers. It must be considered in assessing the load capacity and durability of individual components and in determining overall efficiency.

3 Kinematics and Dynamics

Figure 3a shows the kinematic diagram of the integrated gearbox. Figure 3b shows the equivalent planetary differential gear. By using Willis method is possible to determine the kinematics of mechanism and gear ratio (1). The integrated gearbox corresponds to the two differential gears (Fig. 3b), with joined output shafts and fixed central wheels.

Rotor with excentric cams and output shaft with carriers held rotary motion, satellites and Oldham couplings held general plane motion. In terms of dynamics is important motion of Oldham couplings.

Because some mechanism components held rotary motion, in which their centers of mass lies off the axis of rotation, it is necessary to solve dynamic balancing of mechanism. The subassembly consisting of rotor, excentric cams and satellites with bearings can be designed so that the resulting dynamic forces were zero. This subassembly is possible to balance on balancing machine.

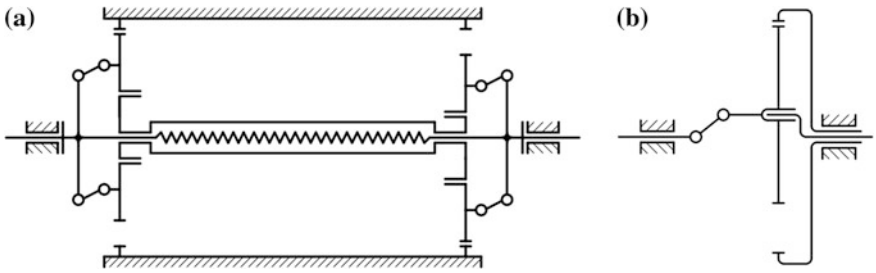

Fig. 3 **a** Kinematics scheme of integrated gearbox. **b** Kinematics scheme of equivalent planetary differential gear

The only mechanism components, the dynamic forces can not simply eliminate, are the Oldham couplings. They held the same general plane motion, which are mutually turned by 180°. During operation thus causes dynamic reaction moment that is transmitted through the bearings to the base frame, which is the main disadvantage of the described integrated gearbox design. Its time dependence is harmonic at constant rotor speed. Detailed solution of force conditions resulting to the outcome (3), where $M_{R,\max}$ is amplitude of the reaction moment, m_{oc} mass of Oldham coupling, e eccentricity of excentric cam, ω_1 rotor angular speed, i gear ratio, ζ_s distance of satellites and f_R the reaction moment frequency.

$$M_{R,\max} = m_{oc}\frac{e\omega_1^2}{i^2}\left[(1+i)^2+1\right]\zeta_s, \quad f_R = \frac{\omega_1(1+i)}{2\pi i} \tag{3}$$

4 Efficiency of Gear Mechanism

Because the integrated gearbox mechanism includes two parallel identical planetary gears, there will be branching of power flow. The output shaft power can be taken at both ends. Schematic of power flow through gear mechanism is on Fig. 4.

As mentioned above, the torque M_{Tk} is the output shaft torque preload, that arises due to the static indeterminate assembly. Due to this preload, occurs power circulation. Through each path of the mechanism flow powers P_A and P_B. Power which is applied to the rotor is given by $P_1 = M_1\omega_1$, power piped by output shaft is $P_2 = (M_{2A} + M_{2B})\omega_2$. Overall efficiency of mechanism η_v is given by (4).

$$\eta_v = \frac{M_{2A} + M_{2B}}{\frac{M_{Tk}+M_{2B}}{\eta} - \eta(M_{Tk} - M_{2A})} \tag{4}$$

From Eq. (4) implies that the overall efficiency depends on the gearbox load and torsional preload of output shaft.

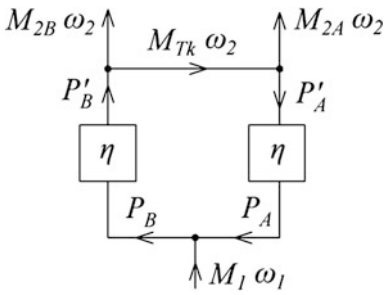

Fig. 4 The power flow scheme of integrated gearbox mechanism

The value η is the efficiency of the planetary gear, which includes each path of the transmission. The mechanism consists of a spur gear with internal teeth and annular Oldham coupling. For the efficiency applies (5), where η_g is efficiency of the spur gear and η_{oc} is efficiency of Oldham coupling.

$$\eta = \eta_g \, \eta_{oc} \tag{5}$$

There occurs a sliding friction on the Oldham coupling. The principle of the calculation of its efficiency is based on the determination of mechanical work of friction forces. The efficiency is given by (6), where f is the slide friction coefficient, e eccentricity of excentric cams, i gear ratio and d diameter of Oldham coupling.

$$\eta_{oc} = 1 - \frac{8f\,e\,(1+i)}{\pi d} \tag{6}$$

Spur gear efficiency depends on many parameters and its numerical determination is not simple. This efficiency is usually determined experimentally, e.g. (Petry-Johnson et al. 2007).

5 Conclusion

Aim of the article was publication of principle and properties of atypical designed gear mechanism.

Acknowledgements The research work was made possible by VÚTS Liberec, a.s. and research project TIP FR-TI1/594.

References

Hale LC, Slocum AH (1994) Design of anti-backlash transmissions for precision position control systems. Precis Eng 16(4):244–258

Klouček V (2011) Dynamics of the anti-backlash designed gearings with elastic elements. In: International conference on vibration problems, Praha

Petry-Johnson TT, Kahraman A, Anderson NE, Chase DR (2007) Experimental investigation of spur gear efficiency. In: Proceedings of the ASME

Computing and Design of Electric Vehicles

L. Kucera, I. Gajdac and P. Kamas

Abstract The article deals with design of electric vehicle as response of needs for the environmentally sustainable road transport system which reduces noise, emissions and minimize energy consumption.

Keywords Electric vehicle · EDISON project · Design

1 Introduction

Research and development of vehicles on the alternative drives with a vision of the environmentally sustainable road transport system for reducing noise, emissions and minimizing of energy consumption has several directions at this time. Electric vehicles (EV) powered by the electric batteries or hydrogen fuel cells are global trends at this time. We can characterize electric vehicles by zero in emissions, smooth and quiet running engine, high efficiency and the possibility of its recovery. EV main constraints are the limited electric driving range, the time needed for recharging of the batteries and the lack of infrastructure for recharging and battery replacement. The main challenges for manufacturers and suppliers of electric components are research and development of batteries with high capacity

L. Kucera (✉) · I. Gajdac · P. Kamas
University of Zilina, Zilina, Slovakia
e-mail: lubos.kucera@fstroj.uniza.sk

I. Gajdac
e-mail: igor.gajdac@fstroj.uniza.sk

P. Kamas
e-mail: peter.kamas@fstroj.uniza.sk

L. Ševčík et al. (eds.), *Modern Methods of Construction Design*,
Lecture Notes in Mechanical Engineering, DOI: 10.1007/978-3-319-05203-8_15,

Table 1 The efficiency of energy transfer used for vehicle drives

Engine of vehicle	Efficiency—from processing to battery or tank (%)	Efficiency—from battery or tank to wheels (%)	Total efficiency (%)
Diesel engine	88 (oil processing, transport)	18 (efficiency of engine and complete transmission)	16
Gasoline engine	82 (oil processing, transport)	15 (efficiency of engine and complete transmission)	12
Hybrid drive	82 (oil processing, transport)	30 (efficiency of engine and complete transmission)	25
Battery electric drive	43 (electricity and distribution)	67 (efficiency of engine and complete transmission with efficiency of charging)	29

and minimum weight optimization of charge and prolong battery life, battery recycling management systems, energy recuperation combined with other alternative energies.

2 Why to Develop Electric Drives

According to the analysis of experts in the field of automotive development, the efficiency of energy transfer used for vehicle drives with different drive systems is shown in Table 1.

Electric is the highest efficiency of energy uses for drive system of the EV. Without using recharge system for batteries, it is mean for example photovoltaic panels as a basic part of the vehicle or as a home source of electricity. When we will use these complete systems for household lightings and for recharging of vehicle batteries the initial financial cost represents about 18,000 EUR. With a light car can be drive up to 100 km daily. EV can be charged at the night from the stored energy and the remain energy can be used for night lighting, too.

3 Current State

Knowledge about EV drives and its structures is very low at present time. It is necessary to find ways how to operate EV the most effectively. It is important to create a concept vehicle for further research and development on electric drive and its components. Standard mass-producers of vehicles rebuild own serial vehicles to electric drive but the variability is missed. The design of these rebuild vehicles are very limited to car the body structure. It is therefore important to create a new concept with the high potential variability of the internal arrangement of the drive. Final design of the development phase must including a comprehensive study of

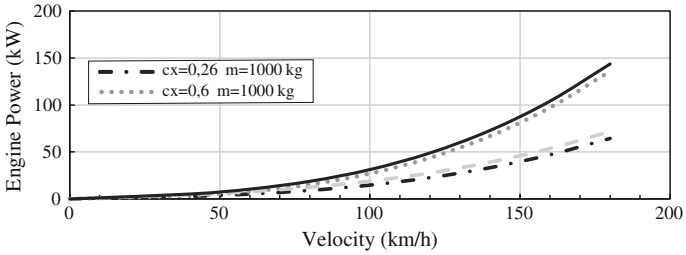

Fig. 1 Engine power depending on speed, weight and Cx

current electric motors, control systems, batteries, clutches, tires and other legislation. According to the design calculations made so far are decisive criteria for specific expected use of the vehicle weight, drag coefficient, and other passive resistance with an alternative battery charging system recovery in the right range by brake applications. The proposal of integrated photovoltaic system for autonomous recharging is suitable alternative.

4 Preview of Utilization and Storage of Energy for EV

The equivalent of an EV is vehicle with gasoline engine with the average fuel consumption of 6 L per 100 km according to the evaluation of electric vehicles in the U.S. and Japan. In 6 L of gasoline is energy E = 55 kW h. For maximum efficiency of internal combustion engine is 30 % to 100 km used energy E_C = 17 kW h. Figure 1 shows that vehicle with given engine power can move at a steady speed from 65 to 100 km/h. It is depend on the weight of the vehicle and Cx—coefficient of drag. It is therefore necessary to express the amount of energy needed to ride of a particular distance, depending on vehicle type, traffic type and the maximum speed. Operating range of each vehicle is the stored energy in the tank respectively batteries. Standard vehicles with internal combustion engines have a drive range up to 1,000 km without refueling. EV and its energy storage in batteries are depended on their weight and dimensions.

The basic criteria for mass of LiIOn battery or LiFePOY4 battery depending on the accumulated energy represents Fig. 2. The diagram shows the current state of batteries mass from 17 to 55 kW h of accumulated energy. (Leitman)

Used parameters of EV for computing are total weight of EV, weight and battery capacity, coefficient of drag, required acceleration, passive losses, type of traffic, the costs for operation and maintenance. We can use the energy in batteries up to 70 % from total stored energy. For the simulation software MATLAB or SIM-DriveLine determine use combined traffic. For the combined traffic 50 % in the city and 50 % outside the city created a test circuit has a characteristic route:

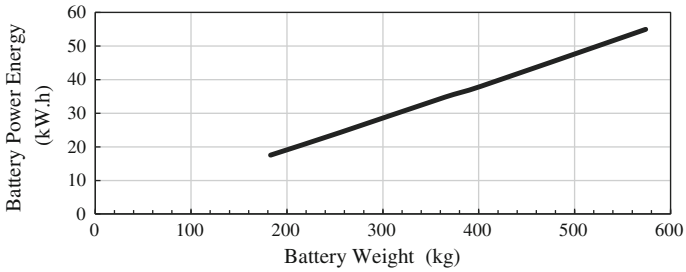

Fig. 2 Battery power depending on battery weight

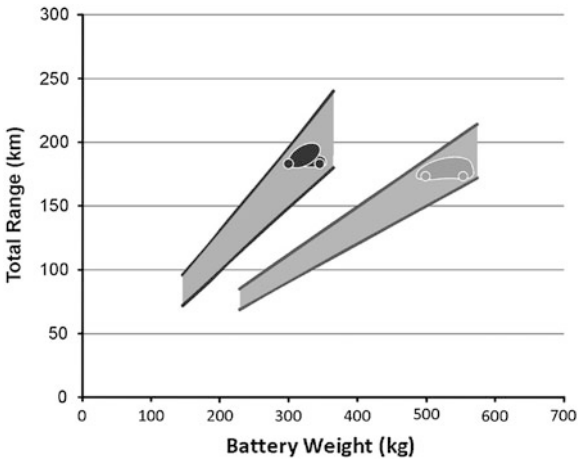

Fig. 3 Spectrum of the ride range

- 15 km horizontal road (economy—80 km h^{-1} or fast 100 km h^{-1})
- 5 km uphill road (60 km h^{-1})
- 5 km downhill road with recovering (60 km h^{-1})
- 10 km urban traffic (20 times acceleration from 0 to 50 km h^{-1} where acceleration a = 1.5 m s^{-2}, 20 times deceleration from 50 km h^{-1} to 50 stop with recovering where deceleration a = 1.5 m s^{-2}, other urban route will soluted by simulation program with 50 km h^{-1} constant velocity).

Computer simulation program calculate expected ride range of the EV depending on batteries weight. It is shown on the Fig. 3, where are expressed areas for vehicles of different mass at the chart (pink—weight up to 900 kg, green weight up to 1,900 kg), traffic type 50/50 (city, outside the city), with an average speed in the city 50 km h^{-1}, outside the city, 80 km h^{-1} which represents an economic and an average driving speed of 50 km h^{-1} in the city, outside city 100 km h^{-1} which is a fast ride.

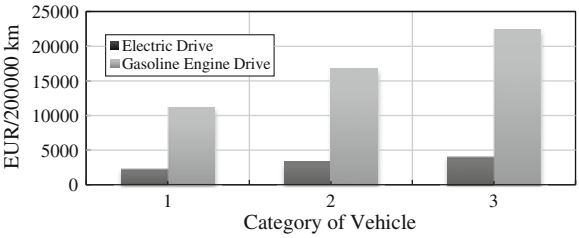

Fig. 4 Comparison of cost for EV and gasoline engine drive

Fig. 5 EDISON—functional integration drive-line, design, final design

Computer analysis show that the costs of operating EV and vehicle with combustion engine with 200,000 km of ride and various types of vehicles for the current price of electricity (0.09 Euros /kW h) and gasoline (1 L = € 1.4) are made in diagram on Fig. 5. Categories of vehicle by the Fig. 4 represent 1—small car, weight up to 900 kg or fuel consumption about 4 L per 100 km, 2—weight up to 1,500 kg or fuel consumption about 6 L/100 km, weight up to 1,900 kg or about fuel consumption 8 L/100 km (Kohar and Hrcek 2010).

5 Alternative Design of the Light Experimental EV

One of the key objectives of nonconventional drive for EV creating is a sufficient volume of quality knowledge for developing a new alternative vehicle concept, including truss frame design. Gained knowledge in the field decides the direction of EV development. The team of teachers and students from the University of Žilina are developing a small, lightweight electric vehicle EDISON. The design of EDISON EV is not based on standard technologies. The basic idea is lightweight tubular frame of EDISON EV. On this frame will possible modified exterior components created from laminates, but also carbon steel compositions.

The design of EDISON EV is oriented on alternative transport system for urban and suburban traffic. EDISON represents a non-standard truss frame created from light steel tube and composite body parts. The main items of the common stage for experimental EV development were oriented on:

- design of drive transmission: model of drive-line system in three drive modes (charging, drive and recovery), computing of parameters for required engine power, battery capacity, control system specification, computer simulation for EV oriented on dynamic of drive,
- design of functional integration drive-line system according to frame (3D measurement of elements for creating experimental EV)
- design of frame: ergonomic and geometrical analysis, 3D model, static and dynamic FEM analysis
- design of styling and exterior and interior surfaces design (alternatives for steel and composite materials, PMMA, CGSA,)
- animation and visualization of vehicle.

The actual stage of project solution is oriented on manufacturing of frame, body parts and components, assembly chassis, driveline system and interior component. Figure 5 represents view of progress EDISON experimental EV.

6 Conclusions

To create possibilities and to participate on research and development of alternative energy drive cars without similar experiments will one of the key conditions for increasing the level of education. For more information about the project EDISON visit website www.edison.uniza.sk.

Acknowledgments This work was supported by the Slovak Research and Development Agency under the contract No. SUSPP-0014-09 and project VEGA 1/0721/13 Energetická bilancia elektromobilov a hybridných vozidiel.

References

Leitman S, Brant B Built your own electric vehicle, 2nd edn. No. 0-07-164351-6
Kohar R, Hrcek S (2010) 5 examples of genetic algorithms and their use in optimization of technological systems. Mach Des 2010, ISSN 1821-1259

The Vibrodiagnostics of Gears

Ľ. Kučera and T. Gajdošík

Abstract The Article is about diagnosing and evaluating of faults at gear contact transmissions by vibrodiagnostics. It describes a diagnostic unit for testing planetary gearboxes by the vibrodiagnostics, designed at the Department of Design and Mechanical Elements. The Article interprets faults occurring at sun gear on the first planetary gearing of a tested transmission and its manifestation in a whole transmission vibration frequency spectrum, being compared with an undamaged frequency spectrum.

Keywords Vibrodiagnostics · Frequency · Spectrum · Damage

1 Laboratory Equipment

Laboratory research is aimed to identifying artificially provoked faults at individual gear wheels of planetary gearings in the whole transmission vibrations frequency spectrum. In the laboratory, there are installed the measuring system IMx-S—SKF and three acceleration transducers 100 mV/g—SKF (Fig. 1) there, situated so as it would read vibrations within all three basic axes (x, y, z). It is possible to manage, browse, export and evaluate data, collected by the unit IMx-S, after being connected to a PC by the software *SKF @ptitude Analyst*.

The testing unit (Fig. 1) includes a two-pole asynchronous electric motor with the power of 15 kW, controlled by a phase inverter, followed by a tested transmission A2000 and by another one A2000, but—in a reverse position, i.e., gear

Ľ. Kučera (✉) · T. Gajdošík
Žilinská univerzita v Žiline, Žilina, Slovakia
e-mail: kuceral@fstroj.utc.sk

T. Gajdošík
e-mail: tomas.gajdosik@fstroj.uniza.sk

L. Ševčík et al. (eds.), *Modern Methods of Construction Design*,
Lecture Notes in Mechanical Engineering, DOI: 10.1007/978-3-319-05203-8_16,

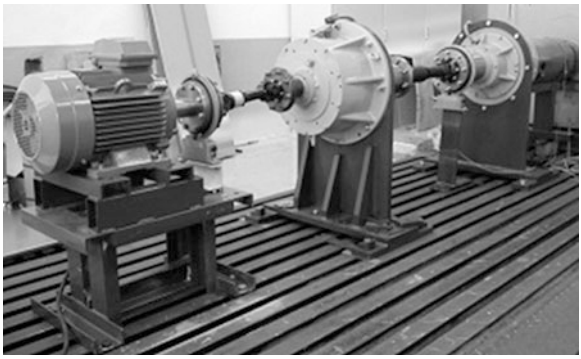

Fig. 1 Testing unit KKaČS for gears tests

ratio of the both transmissions' serial configuration equals 1. The whole system is complemented by a dynamometer. Components of the testing unit are interconnected by cardan shafts. The tested transmission A2000 (valid for reducing transmission, too) is a double-row planetary gearbox with a straight involute gear (Gajdošík et al. 2013).

2 Preliminary Tests

Both transmissions were, before beginning the measuring, completely taken to pieces, cleaned and, there was scanned its technical condition. There were substituted sealings and further necessary parts.

The research is carried out gradually, within several stages. Primarily, there was measured frequency spectrum of an undamaged transmission; first—being unloaded, and then, under load. The no load test served for becoming familiar with the testing unit and, in particular, for collecting primary data applicable for identifying the transmission's individual nodal points within the vibrations frequency spectrum. After having identified the individual nodal points, they were measured under the load. The vibrations velocity frequency spectrum of the loaded transmission is shown at Fig. 2. When comparing further spectra of already damaged transmission, just the frequency spectra collected by measuring under the load, served as a standard.

The primary measurings included testing at a varied lubricating oil level, too. At first, the oil amount was increased from the prescribed operational amount of 5 to 7 L and then, having the transmission in motion, gradually reducing the oil amount down to 4 L. The frequency spectra analysis has shown that the parameter does not markedly affect the vibration spectrum but, it affects overall transmission efficiency. If comparing the spectra relative to both oil limit values, there was not noticed any difference; it comes to this, that it is not possible to expressly identify any partial loss of the lubricating oil by the applied methods.

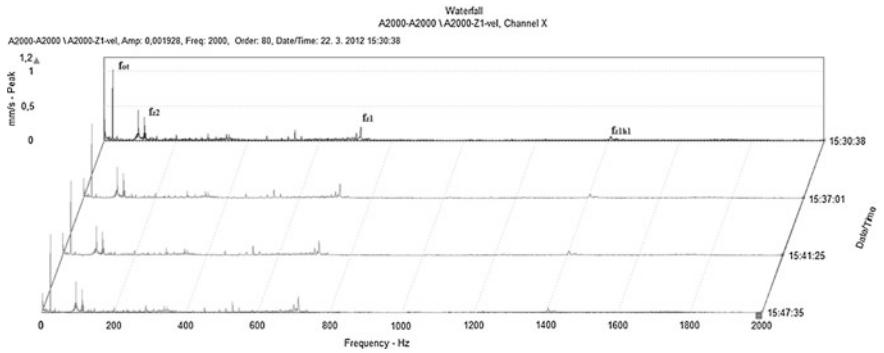

Fig. 2 Loaded transmission A2000 vibrations velocity frequency spectrum

The Fig. 2 clearly shows rotational frequency of input shaft ($f_{ot} = 25$ Hz), as well as gear contact frequency of the second planetary gearing ($f_{z2} = 116$ Hz) with a sideband and contact frequency of the first planetary gearing ($f_{z1} = 730$ Hz) with side band and its first harmonic ($f_{z1h1} = 1{,}460$ Hz) (Prodaj 2012).

3 Damage Tests

After being collected, analyzed and evaluated the primary data, there begun further stage of the testing, namely an intentional damaging of the tested transmission. At the very beginning, there was damaged sun gear of the first planetary gearing.

Accordingly, a full width cut made onto a sprocket was the first measured damage (Fig. 3).

The damage on the sprocket has manifested as a shape strain of the lateral gear contact of the first planetary row within the vibrations velocity frequency. As seen on the Fig. 4, amplitude of the lateral band first peak is much higher than the amplitude itself of the gear contact frequency, which suggests damage on the gearing.

In the enveloped accelerations frequency spectrum (Fig. 5), the damage was manifested as a tooth frequency amplitude increase of the damaged central wheel f_{zC1} and as an intensification of its harmonics, in particular (f_{zC1h2}, f_{zC1h3}, f_{zC1h4}).

An intentional pitting on one side of a first gearing sun gear sprocket was another measured damage. The measured values are similar to the values observed with the cut, however, amplitude values are low order ones as in the vibrations velocities spectrum, so in the enveloped accelerations spectrum. However, there is amplified the contrary peak at the first planetary gearing lateral band, which implies that the peak varies in dependence on direction of rotation, as with the cut on the sprocket, the direction of the rotation was left and the amplified peak right and, with the pitting, the direction of the rotation was right and the amplified peak left.

Fig. 3 Damaged sprocket of the first planetary row central wheel on the transmission A2000

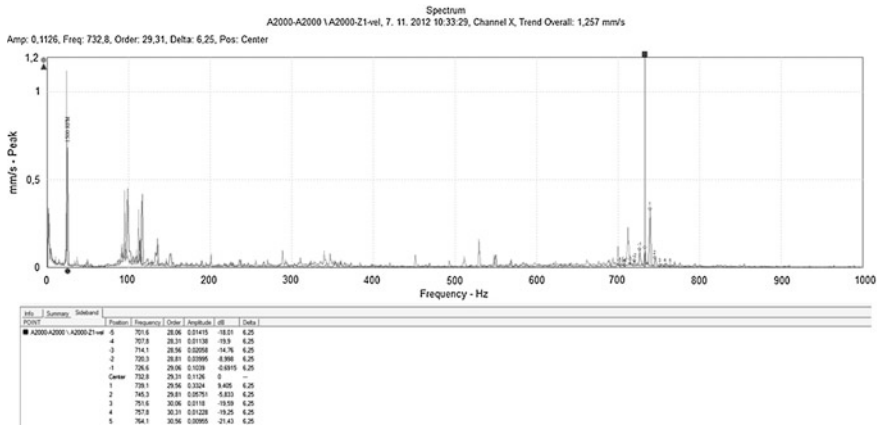

Fig. 4 Comparison of vibration velocity frequency spectrum of the undamaged (*blue*) and the damaged one (*violet*) transmission with marked lateral band of the first planetary row gear contact

The intentional pitting on one side of each sprocket of the central planetary gearing was the ultimate one of the measured damages (Fig. 6).

The detailed view of the vibrations velocity spectrum (Fig. 7) shows that the lateral band shape was radically changed against the undamaged condition; the

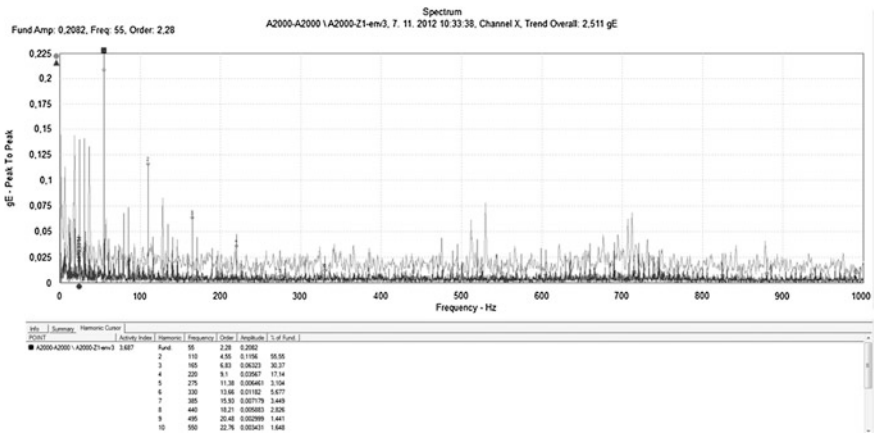

Fig. 5 Enveloped accelerations frequency spectrum; filter 3 of the undamaged (*blue*) and the damaged (*violet*) transmissions with highlighted sprocket frequency of the central wheel of the first gearing and its harmonics

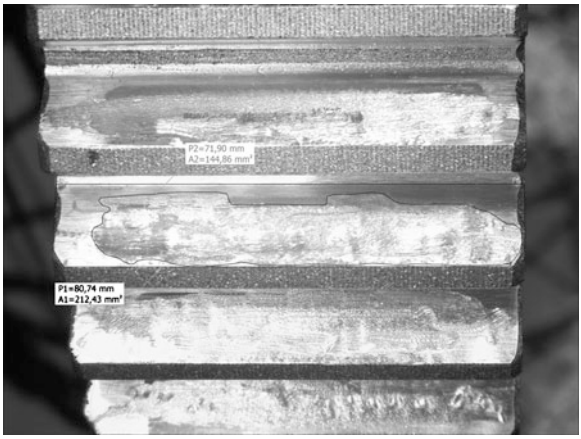

Fig. 6 Pitting on each sprocket lateral band of the central planetary gearing wheel

band is visibly asymmetrical and the amplitudes of its peaks are by its size above the amplitude of the first gearing contact. As seen on the Fig. 7, the first gearing contact frequency seems to include even another wider lateral band, the delta of which is equal to the first gearing central frequency ($\sim$55 Hz). Peaks of the amplitudes are amplified again contrary to the direction of the transmission rotation.

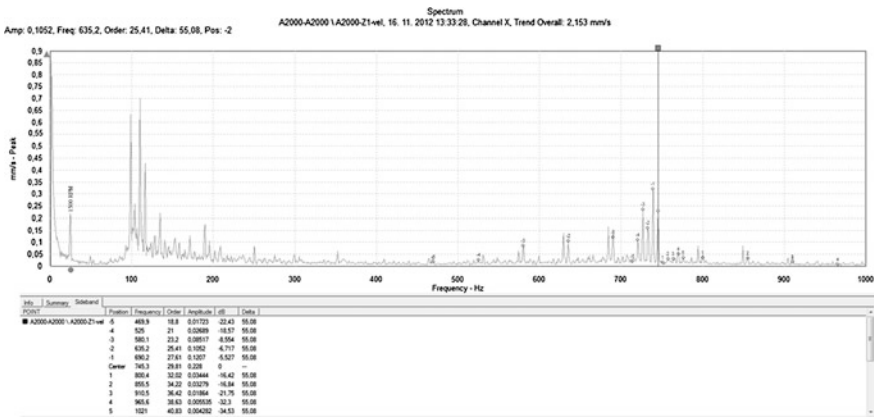

Fig. 7 Frequency spectrum of the transmission vibrations velocity with each sprocket pitting of the central wheel of the first planetary gearing with marked lateral bands of the first planetary gearing contact

4 Conclusions

The measuring done by now show that it is possible to diagnose damages of its individual parts within the frequency spectra of a measured transmission but it is necessary to choose an appropriate frequency spectrum of diagnostics and evaluation method. We know also which frequency response is related to individual damages pursuant to the measured data and, the frequency response may be then compared with practically collected values—there can be determined the transmission condition. The laboratories measuring still continue.

Acknowledgments The article was created with support of Slovak Research and Development Agency (SRDA), Project No. APVV 087-10: "Inteligentné diagnostické systémy prevodoviek a ich komponentov".

References

Gajdošík T, Bucala J, Kovalíček M (2013) Vibrodiagnostic of gearboxes, transcom 2013, Žilina

Prodaj J (2012) Aplikácia a diagnostika vybraných uzlov stacionárnych a mobilných prevodových systémov. Dissertation, Žilina

New Way in Steel Bead Design

R. Madaj

Abstract The article deals with solving problems occurring in the bead wire production as a stage of a complex process of tire manufacturing. It highlights the process of producing the semi-product with the options of solving the problems in the design process and then transferring the problem to the realm of the virtual reality by application of computer software.

Keywords Bead wire · Tire production · Single purpose machine · Design

1 Introduction

The success of the product in the current period is based not only on the fulfillment of customer requirement, the required quality, reasonable prices, but often success of the product is based on the introduction in the required time. In the product development to fulfill the imposed requirements, we integrate optimization or innovation, whether in the form of new technical means or methods, which to some extent are able to remove negative influence arising from the sale of the product. Into the stages of design and development were introduces computing and computational software to simplify and accelerate activities of process. Designers and engineers are applying the program means for creating the mathematical models of processes or machinery for the purpose of finding a solution to the problems in realm of virtual reality. A significant advantage of simulation processes and machines in virtual reality is the economic factor and the speed of the method against experimental procedure. Therefore, for solving the problems from

R. Madaj (✉)
University of Žilina, Žilina, Slovak Republic
e-mail: rudolf.madaj@fstroj.uniza.sk

L. Ševčík et al. (eds.), *Modern Methods of Construction Design*,
Lecture Notes in Mechanical Engineering, DOI: 10.1007/978-3-319-05203-8_17,

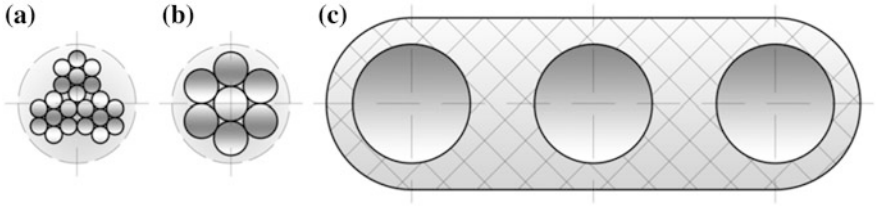

Fig. 1 The steel cord (**a**), tire wire (**b**) and strip (**c**) (Kohár and Hrček 2010)

the field of production of semi-finished bead wire as a function part of tire, we applied 3D software, to create an new variant of steel bead.

1.1 Traditional Design of Tire Bead

Tire manufacturing we consider as a complex process involving several stages, such as tire preparation, production of tire casing, vulcanization and finalization. In each stage, we can meet with wide range of tasks, for which it is necessary to propose solutions to minimize or suppress the negative effects in the other processes. One of the problematic sections is also the production of semi-finished bead wires, where a steel cord or tire wire is rubberized. The steel cord (Fig. 1a) consists of a thin high tensile wires twisted into the shape of rope and tire wire (Fig. 1b) is a wire with circular cross section.

Reinforcing material of required properties wounded on a coil is placed in a bobbin case and then is drawn with a regulation and continuous smooth braking. The free end of steel cord then passes through the extruder, wire drawing machine and then into a wire winder. As the temperature of the rubberizing in extruder increases around the value, it is necessary to cool the rubberized bead wire or tire wire after the extruder stage to the required temperature to avoid deformation and bonding of rubberized steel cord (hereinafter referred to strip, Fig. 1c) while winding it in the last stage of the line. To solve the problem described above, there are several solutions such as implementation of the strap gravitational storage with cooling by the air flow or the implementation of the cooling cylinders with flowing liquid inside. From the requirements arise the need to solve the cooling of a strip by the air flow in gravitational storage, the other points are dealt exactly with this problem and it will be considered to be structurally simpler and more economical.

1.2 New Design of Bead Wire

The new design of bead wire is based on bypassing rubber coating technological operation that serves as reinforcement steel wire rope after winding and ensure its

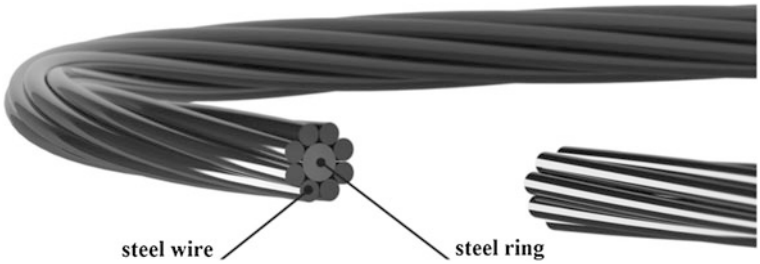

Fig. 2 The spiral bead wire (steel ring—core and wire)

connection with other components in the tire. Bead wire consists of two parts. One is welded steel ring and second is steel wire. The wire is coiled around the ring to the helix and therefore its name is the spiral bead wire (Fig. 2).

1.3 Variants of Production Method

- Option A

Core (Fig. 3), Position (1) is attached to the shift structure (2) with six driven pulleys (3), which rotate in its core axis. The sliding construction mounting of the core consists of two identical parts because of the high speed operation, This construction with the pin in the center (4) around which it rotates. In the lower position sliding design, the core wire attached on the roller (3), sliding construction is turned In its imposition of 180° and ejected the necessary distance to work area of spool. After completion of the work process, i.e., winding wire for packing the core of the sliding of the core construction delays from workspace coil (arrow) and the whole structure is rotated by a further 180°, while on the opposite side of the package during winding on the core is selected from pulleys finished the wire and inserted a new core. This process saves the time required for one wire.

When loading the core into the workspace, spool must be in the starting position (Fig. 3-2) because the core must be placed at the middle of the imposition ring (5) which is cuted. The ring is stored in four pairs of pulleys (6), which provide the position and rotation about its own axis. Start wrapping wire is gripped to the core (1). The ring starts to turn and spool starts to unravel the wrapping wire (7). Brake is placed on the coil, because of wire tension must be stable. Coil is led by a pulleys to ensure the wire hoops. Turning the ring gear is provided by the outer part (the drive can be performed also, for example. Friction pulleys) pair of gears because of the hoop is cut so as to rotate each tire at least one sprocket. After winding wire wrapping wire is cut off and the working process is completed. Slide spool structure shall be moved, rotated and placed onto the a new core ready for wrapping new wire. Coil can withstand for 10 cores. After the unloading of spool is this removed and placed a new.

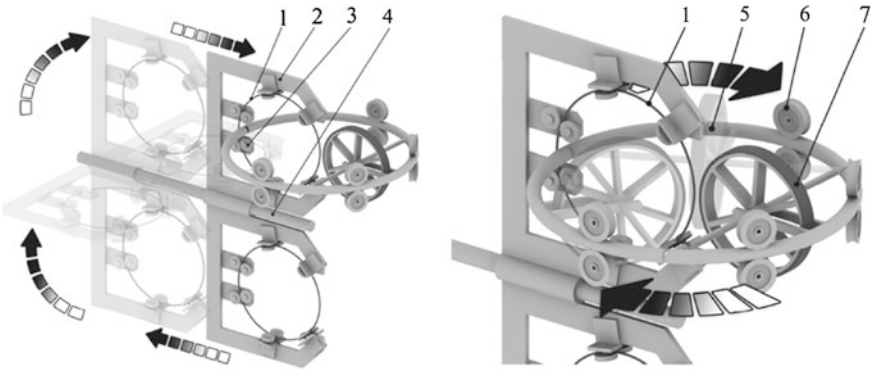

Fig. 3 The spiral bead wire production method Option A

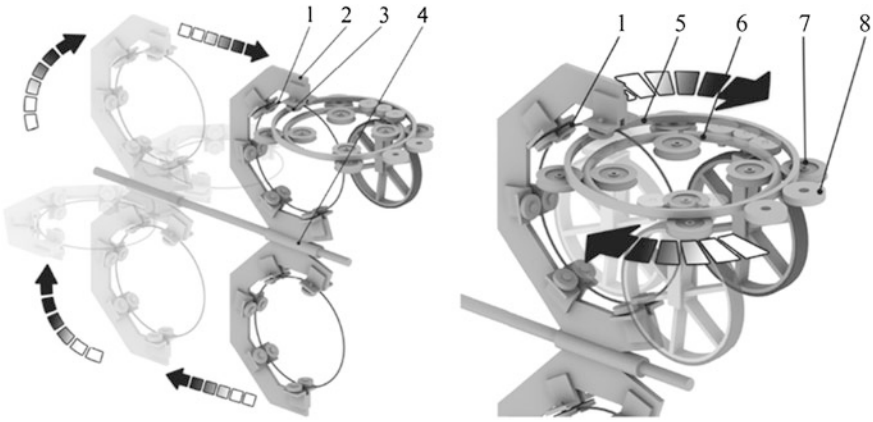

Fig. 4 The spiral bead wire production method Option B

- Option B

The core (Fig. 4-1, position 1) in the second variant is also fixed on the shift structure (2) using five driven rollers (3) to rotate the core in its axis. Sliding design consists of two identical parts because of the high speed operation, the construction of a central storage (4) around which it rotates. In the lower position slider design, the core wire attached on rollers, sliding design turns in his deposition about 180° and ejected the necessary distance to the workspace. After completion of the work process, i.e., winding wire wrapping the core of the movable core construction delays from workspace spool and the entire structure rotates up to 180°, while on the opposite side of the package during winding on the core is selected from the finished wire pulleys and adds a new kernel. This process saves the time required for one wire.

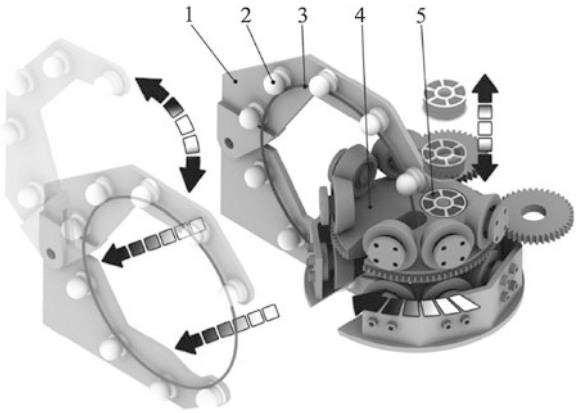

Fig. 5 The spiral bead wire production method Option C

When loading the core (1) the work area must be spool and ring gear (5) providing the initial position of spool position, viz. (Fig. 4-2) reason that the core may be placed at the middle of the ring (6) imposition of spool and sprocket rotation spool that are cut. The ring is stored in four pairs of pulleys (7), which provide the position and rotation about its own axis. Start wrapping wire is held in place on core induction welding. The ring starts to turn down turns and starts to unravel the spool wire wrapping. On the brake coil is placed because of and stretching nenadmerného must not fit wire. Difference between the first and the second variant in the sense of rotation of the spool, in the first variant, the spool is rotated around the core spool, the angle of the cutting plane relative to the plane of the core is always changing. This is the second variant, removed, or cut spool plane is always parallel to the plane of the core and the packaging does not occur in the torsion wire. Position parallel to the plane of the core provides top (cut) ozubenýveniec that turns down speed so as to ensure the reel is still the same location. Coil is made with the feed pulleys which ensure its wire fixed position. Turning the ring gear is provided by the outside of the pair of gears (8) because of the hoop is cut so as to rotate each tire at least one sprocket. After winding wire wrapping wire is cut off and the working process is completed. Slide spool structure shall be moved, rotated and placed onto the a new core ready for wrapping wrapped around wire. Endurance spool is 10 pips (or the number may be larger). After the unloading of the spool removed and placed new spool with wire wrapping.

- Option C

Tongs (Fig. 5-1, position 1) take hold the core (3) into the pulleys (2). The core is placed in the working position of the middle C-rotor (4) by slider. In the C-rotor is located a small coil (5), in which the wrapped wire around one core. In the first step, start wrapping wire attached to the core (spot welding, or Holding the grasping device first half-revolution). Follow starts reverse rotation of the core and C-rotor in the desired ratio, in which a small spool depends sheathing wire and is

wound on the core. After taking up all of the small spool wire, C-rotor stops in its starting position to the hoop wound ticks postponed and prepared the new core for the next cycle. At the same time replace the empty spool for a full cycle repeats.

2 Conclusions

When the new design of bead wire will be applied to the tire production lines, the costs will be reduced. New bead wire is more stronger than old version and it is more comfortable for manipulating and storing. It is necessary to design a new production high capacity production lines for mass produce. If it will be possible to secure sufficient production, new tires get better performance and become safer.

Acknowledgments This work was created by the implementation of the "Reengineering of the product portfolio of VIPO a.s.", "ITMS: 26220220091" to support the Operational Programme Research and Development financed by the European Fund for Regional Development.

References

Kohár R, Hrček S (2010) Examples of genetic algorithms and their use in optimization of technological systems. In: Machine design. ISSN 1821-1259, pp 241–246

Brumerčík F, Bašťovanský R, Lukáč M (2010) Aplikácia expertných metód, analýz a simulácií pri inovácii technických systémov, ISBN 978-80-554-0267-3, Žilina

Moaveni S (2003) Finite element analysis: theory and application with ANSYS. s.l.: Pearson Education. s. 822. ISBN 8131760642/ ISSN 9788131760642

Málik L, Medvecký Š, Chrzová J, Hrček S, Lukáč M (2009) Konštruovanie 2. Žilina: EDIS. ISBN 978-80-8070-971-1

Development of Dependable Controllers in the Context of Machines Design

J. Machado and J. C. Campos

Abstract In the domain of machines' design, one of the most important issues to solve is related with the controller's design, mainly, guaranteeing that the machine will behave as expected. In order to achieve a dependable controller, some steps can be considered, such as the formalization of its specification—before being translated to the program that will be inserted in the controller device—and the respective analysis and verification. Nowadays, some formal analysis techniques, such as formal verification, are used to achieve this purpose. The dependability of a controller, however, is impacted by its execution context. This paper proposes an approach for the formal verification of the specification of mechatronic system's controllers, which considers, on the formal verification tasks, the behavior of the plant and the behavior of the Human Machine Interface of the Mechatronic system. Some conclusions are extrapolated for other systems of the same kind.

Keywords Dependable controllers · Machines' design · Formal verification · Human machine interface · Partial plant models

1 Introduction

The development of controllers' software for mechatronic systems, when performing all machines' design tasks, is a very complex and exigent process.

A mechatronic system is composed, mainly, by three parts: Controller, Plant and Human Machine Interface (HMI) (see Fig. 1). These parts interact and behave

J. Machado (✉)
Mechanical Engineering Department, CT2M, Minho University, Guimarães, Portugal
e-mail: jmachado@dem.uminho.pt

J. C. Campos
Informatics Department and HASLab, INESC TEC, Minho University, Guimarães, Portugal
e-mail: jose.campos@di.uminho.pt

L. Ševčík et al. (eds.), *Modern Methods of Construction Design*,
Lecture Notes in Mechanical Engineering, DOI: 10.1007/978-3-319-05203-8_18,

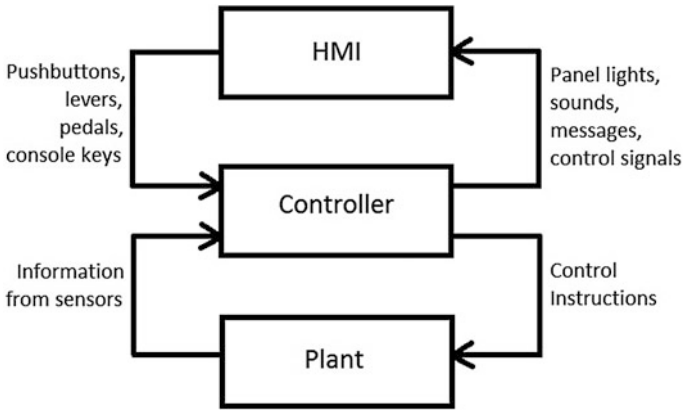

Fig. 1 General configuration of a mechatronic system

together, and the development of the software to be introduced in the controller, must take into account the behavior of those parts and the interrelation between them.

Several steps can be performed in order to obtain a dependable controller: first, the use of methodologies for obtaining the structure of the controller's specification (Machado and Seabra 2009); second, the use of a formalism to describe, formally, the intended behavior for the controller (David 1995); third, the use of analysis techniques, in order to guarantee the dependability of the specification (Johnson 2007); and, fourth, the translation of the specification into a controller program and respective implementation on a physical controller (Machado et al. 2006).

The first two steps are very well studied and there are formalisms and tools that can be used to perform them. For the structure of the controller specification it is possible to use GEMMA (ADEPA 1992) or Multi-Agent formalisms (Sohier 1996), for example. For the specification formalisms such as Petri Nets (Murata 1989), SFC (IEC 2002) or Statecharts (Harel 1987) can be used. For the implementation, PLCs (Moon 1994) and Microprocessors (Brusamolino et al. 1984), among others.

If we consider step 4, as being systematic, the most important step remains step 3, where the specification must be tested, simulated and verified.

This paper proposes a methodology to obtaining a dependable specification, which is focused on the analysis of the specification by using formal verification techniques. The paper discusses the relevance of considering aspects related with the behavior of the plant, and the behavior of the HMI, when developing the specification for the controller of a mechatronic system.

The paper is organized as follows: Sect. 2 provides an overview of the main steps considered in the design of a mechatronic system; Sect. 3 proposes a case study to be used in the ensuing discussion; Sect. 4 discusses aspects related to

considering plant behavior in the development of a specification; further, Sect. 5 discusses aspects related to considering the HMI behavior in the development of a specification; and finally, Sect. 6 presents some conclusions and future work.

2 Steps for Designing a Mechatronic System

The development of controllers' software for mechatronic systems, raises a number of challenges. From the desired behavior specifications, until the implementation of a controller program for a mechatronic system, the controller designer needs to use some different and complementary formalisms and tools that help him in all the necessary steps. Taking into account aspects related to systems' dependability, the designer must be able to use together these formalisms and tools in order to achieve the desired behavior for the system.

From the analysis of needs, passing by the conception, realization into the implementation and exploitation of a mechatronic system, there are several steps that must be realized (Fig. 2). During each step of the controller's design, a corresponding step exists that relates to the development of the plant (physical part of the system: motors, cylinders, sensors, …). For instance, step 3 corresponds to the specification of the controller and the step 3' corresponds to the specification of the plant.

The approach presented in this paper is focused on the steps 3, 4 and 5 of the Fig. 2.

3 Case Study

The chosen system for this case study lies in the well-known category of "pick-and-place" systems (Fig. 3).

Its function is to take parts, fed by gravity into three feed chutes, for placement in a single unloading chute. Sensors pp1, pp2 and pp3 indicate the presence of a part in one of the feed chutes, while sensor pp0 signals the presence of a part in the unloading chute. The device that enables picking and placing a part is composed of a group of three pneumatic cylinders plus a vacuum suction cup system. The vertical cylinder (VC) places the suction cup in contact with a part. Longitudinal cylinders L1C and L2C are arranged in series to allow positioning the vertical cylinder VC in front of the four chutes (L2C stroke is twice as long than L1C stroke). The four reached positions are thereby detected by position sensors s0, s1, s2 and s3. The depression in the suction cup is obtained by virtue of a venturi and detected by a vacuum sensor.

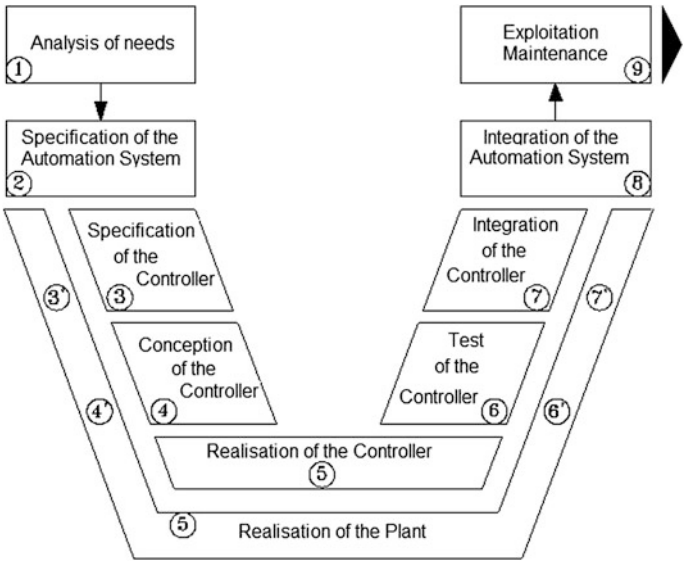

Fig. 2 Steps considered on the design of a mechatronic system

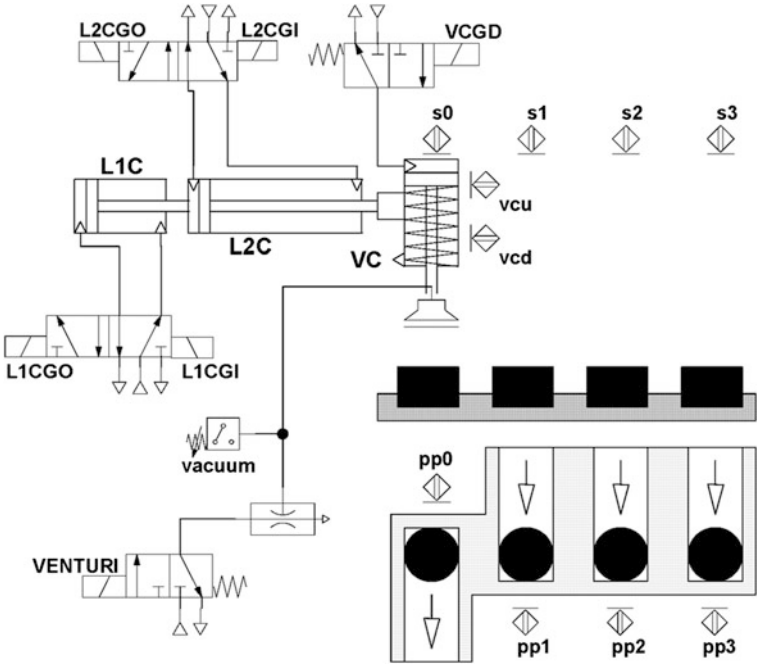

Fig. 3 Pick and place system

4 Specification Analysis Considering Plant Behavior

As part of a dependable controller design approach, the system being targeted for verification can thus be (Frey and Litz 2000) either the controller on its own, presumed to be operating within an open loop on the plant (a non "model-based" verification), or the {controller + plant} assembly set interacting within a closed loop ("model-based" verification).

One problem with model-checking is related to the state explosion problem. The state of the model may become too big for verification to be feasible with reasonable resources. In this paper we report on results of work on mode-based verification resorting to partial models of the Plant. This enables the use of smaller models, thus making it possible to verify larger systems.

This solution allows us, also, a stronger proof of safety properties, which will become stronger as much as the plant model is reduced (Machado et al. 2006).

Considering the approach proposed in (Machado et al. 2006), formal verification tasks can be performed with the assumption of a closed loop behavior of the controller model and the plant model. Also, in the same work, it is proposed that a possible solution for obtaining the plant model for this system is considering a set of plant modules, and the solution proposed is the combination of twelve plant modules in order to obtain a modular solution for the entire system plant model.

In (Machado et al. 2006) a set of behavior properties for the exposed system is considered, to be proven using verification by model-checking. This set of properties is composed by *safety properties* and *liveness properties*. The same work proposes a systematic approach to prove the set of properties using, or not, the plant model of the system, depending on the specific type of property under consideration. It was observed that some safety properties were not proved without a plant model, but were proved when the entire plant model was used.

Hence, in this paper, we analyze what happens if only a part of the plant model is used. For instance, consider the following behavior property: "*While the vertical cylinder is moving down, all the other cylinders stay in deployed or retracted position*". This property cannot be proved without a model of the plant. With the full model of the plant, the property took 109 min to prove (Machado et al. 2006), using the NuSMV model-checker, and a machine with a Pentium III processor at 1 GHz and 1 GB of RAM.

When we intend to prove the property, the use of the entire plant model is not a good solution, for two reasons: first, because the proof of safety properties will become stronger as the plant model is reduced (Machado et al. 2006) and, second, because the global model becomes bigger and more difficult to analyze by the model-checker.

Considering this property, which deals only with the three cylinders of the system, it seems enough to use only the models of these three cylinders. Using the same machine for calculations, the same Model-checker NuSMV and, now, considering a partial plant model—composed by the models of the three cylinders of

the system—the property can be proved only in 12 min (about 10 % of the time needed if the entire plant model is considered).

Indeed, this smaller plant module is enough to prove the property. However, this cannot be adopted as a systematic rule. Ongoing work is showing us that, for some properties, this rule cannot be applied.

5 Specification Analysis Considering HMI Behavior

Above, the role of a plant model in the verification of a controller's specification was discussed. The plant, however, is not the only factor affecting the behavior of the controller. When a human operator is present, the operator's actions at the HMI are also relevant. See for example the discussion in (Leveson 1995).

Consider the example discussed in the previous sections. If a HMI control panel is present that allows the operator to start/stop the system at any time, then verification of a property like: "*a picked part will always be placed in the unloading chute*" will always fail because the operator might stop the system [see the discussion in (Campos and Harrison 2001)]. In order to avoid this, a model of the operator needs to be included. If a strict operations procedure is assumed, this model is easy to express. It describes the sequences of operations as prescribed by the operations procedure. This type of model, however, is usually too restrictive.

Typically problems will arise when the operator deviates from the prescribed procedure. In the more general context of interactive computing systems this is addressed by describing the possible operator responses to the different output of the system (Doherty et al. 2008). Hence it could be expressed that the operator will only stop the system if no part is currently picked up. Under that assumption, the proof becomes feasible. In this approach, proving the safety of the system implies deriving and making explicit assumptions about how the operator must behave. In doing so, we identify potential points of failure and areas where the controller might need to be improved to account for user error. Hence, we could improve the controller to only act on a stop signal from the operator after the currently held part is placed in the unloading chute.

6 Conclusions

This paper illustrated how consideration of partial plant models (instead of a global plant model) and of operator models can be useful for the formal verification of Industrial Mechatronic Systems' Controllers.

Even if it is possible to see the importance of this approach, we have not developed, yet, a systematic approach to finding out, quickly, which models must be considered in order to verify a specific behavior property of the system. This will be the next step of this project.

References

ADEPA (1992) GEMMA—ADEPA. France

Brusamolino M, Reina L, Spalla MF (1984) An example of microprocessor's application in minicomputer systems: a copy volume design and implementation. Microprocessing Microprogramming 13(5):331–339

Campos JC, Harrison MD (2001) Model checking interactor specifications. Autom Softw Eng 8(3):275–310

David R (1995) Grafcet: a powerful tool for specification of logic controllers. IEEE Trans Control Syst Technol 3:253–268

Doherty GJ, Campos JC, Harrison MD (2008) Resources for situated action. Lecture notes in computer science, vol 5136. Springer, pp 194–207

Frey G, Litz L (2000) Formal methods in PLC programming. In: Proceedings of the IEEE conference on systems, man and cybernetics (SMC 2000)

Harel D (1987) Statecharts: a visual formalism for complex systems. Sci Comput Program North Holland 8:231–274

IEC (2002) IEC 60848—GRAFCET specification language for sequential function charts. Edition 2.0 b

Johnson TL (2007) Improving automation software dependability: a role for formal methods? Control Eng Pract 15(11):1403–1415

Leveson NG (1995) Safeware: system safety and computers. Addison-Wesley, Reading

Machado JM, Seabra E (2009) A systematized approach to obtain dependable controllers specifications. In: Proceedings of 20th international congress of mechanical engineering

Machado J, Denis B, Lesage J-J, Faure J-M, Silva JFD (2006) Logic controllers dependability verification using a plant model. In: Proceedings of 3rd IFAC workshop on discrete-event system design (DESDes), pp 37–42

Machado J, Denis B, Lesage J-J (2006) A generic approach to build plant models for DES verification purposes. In: Proceedings of the 8th international workshop on discrete event systems (WODES'06), pp 407–412

Moon I (1994) Moddeling programmable logic controllers for logic verification. IEEE Control Syst Mag 53–59

Murata T (1989) Petri nets: properties, analysis and applications. Proc IEEE 77(4):541–580

Sohier C (1996) Pilotages des cellules adaptatives de production: apport des systemes multi-agents. PhD thesis, École Normale Supérieure de Cachan, Paris, France

Hexapod: The Platform with 6DOF

R. Martonka and V. Fliegel

Abstract Hexapod is a platform with 6 degrees of freedom. This device can thus in a certain range to generate a general movement. Typically, we meet him at various simulators such as cabin aircraft, submarines, spacecraft, etc. (Fig. 1) (Létání and Letecké Zážitky 2013). Construction hexapod consists of six linear units, which mechanically connects the base and the platform. The general movement of the platform is defined by a combined expansion and plugging of linear units. For the correct simulation of the real movement of the cab is necessary to know the transformation required general motion of the linear motion units. This article deals with the mathematical description of the general transformation of the real motion into linear motion units hexapod and demonstration of use in the laboratory to laboratory hexapod.

Keywords Hexapod · Platform with 6 DOF · Linear motor · Transformation movement

1 Introduction

In engineering practice is used by a large number of designs that simulate motion platforms. The design of such mechanisms is dependent on its mobility. The mobility, or the amount of simultaneous movements performed mechanism, is characterized by the number of degrees of freedom. For example, the actual linear motor has a maximum of two degrees of freedom, namely a linear movement and

R. Martonka (✉)
Department of Design of Machine Elements and Mechanism, Faculty of Mechanical Engineering, Technical University of Liberec, Liberec, Czech Republic
e-mail: rudolf.martonka@tul.cz

V. Fliegel
Technical University of Liberec, Liberec, Czech Republic
e-mail: vitezslav.fliegel@tul.cz

L. Ševčík et al. (eds.), *Modern Methods of Construction Design*,
Lecture Notes in Mechanical Engineering, DOI: 10.1007/978-3-319-05203-8_19,

Fig. 1 Simulators—cabin of aircraft

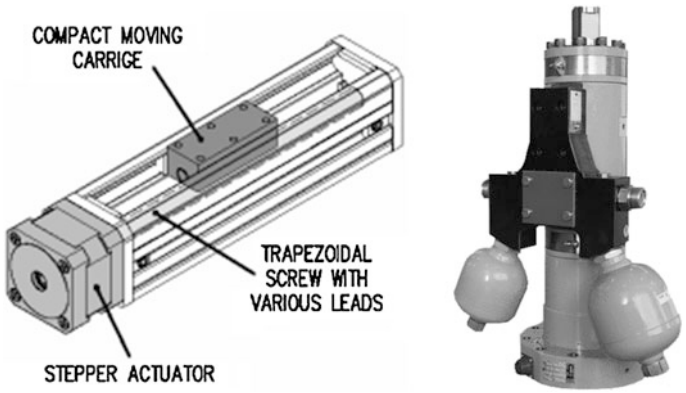

Fig. 2 Linear motors with 1 degree of freedom—linear movement

rotation about the direction of linear motion. Construction of the linear motor often prevents rotational movement (Fig. 2). If you use a large number of these engines, it would be possible to create a mechanism with high mobility or a high number of degrees of freedom but this physically impossible. Anybody can have a maximum of 6 degrees of freedom, i.e. three linear orthogonal directions and three rotations around these directions. Therefore it is used for simulating a generic movement the mechanism with the six motors. The combination of linear and rotary motors is free, it is only limited by the total number of the motor. In our case it was used six linear motors performing linear motion (Figs. 1, 3).

2 Transformation of Movement

We use the platform with 6 DOF for laboratory tests used parts or prototypes. Real movement of the test piece is most commonly defined and obtained by measuring the time course of acceleration in selected locations and directions on the test piece. Example of the measured signal in one direction is at Fig. 4.

Fig. 3 Laboratory platform with 6 degrees of freedom (6 DOF)

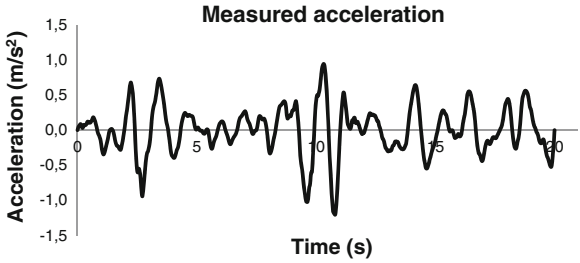

Fig. 4 Measured signal on a test piece—acceleration

To reproduce these signals under laboratory conditions we need to convert the waveforms of the acceleration on waveforms position (stroke) of selected points on the test piece (Fig. 5).

Placing the test piece on laboratory platform is defined by the relative position of the measured points on the test piece and platforms. At this point it is necessary to transform the real movement of the test piece into a linear movement of the linear motor. This transformation is given by the vector equation of the general movement (1), which is converted to a displacement of the entire body and the rotation body around the selected point. This transfer is necessary to know the relative position of at least two points with known motion vectors. The entire transformation is of course made in three orthogonal directions−coordinate vectors (2).

$$\overrightarrow{B(t)} = \overrightarrow{A(t)} + \overrightarrow{AB(t)} \tag{1}$$

$$\overrightarrow{\begin{pmatrix} X_B \\ Y_B \\ Z_B \end{pmatrix}(t)} = \overrightarrow{\begin{pmatrix} X_A \\ Y_A \\ Z_A \end{pmatrix}(t)} + \overrightarrow{\begin{pmatrix} X_{AB} \\ Y_{AB} \\ Z_{AB} \end{pmatrix}(t)} \tag{2}$$

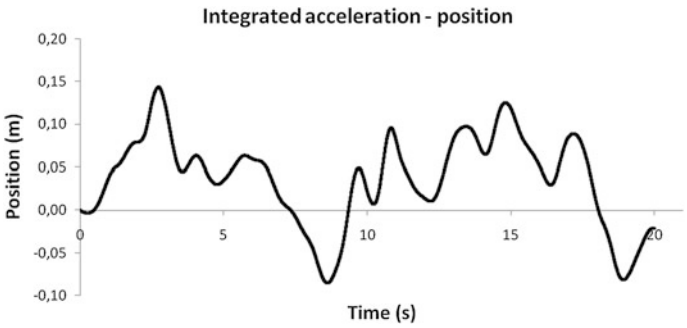

Fig. 5 Double integrated acceleration signal—position

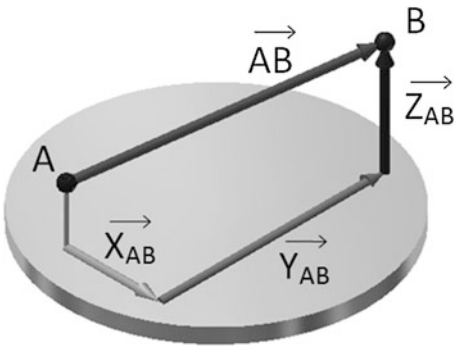

Fig. 6 Transformations vector and components of vector

After making the necessary adjustments we obtain three waveforms strokes for different orthogonal directions (for coordinate of point A) and from Eq. (3) we obtain three coordinates of vector rotation ω around these directions (Fig. 6).

$$\overrightarrow{\begin{pmatrix} X_{AB} \\ Y_{AB} \\ Z_{AB} \end{pmatrix}}(t) = \begin{pmatrix} X_{AB} \\ Y_{AB} \\ Z_{AB} \end{pmatrix} \cdot \overrightarrow{\begin{pmatrix} \omega x_{AB} \\ \omega y_{AB} \\ \omega z_{AB} \end{pmatrix}}(t) \tag{3}$$

The six time histories are then used in a simulation model of a platform (Fig. 7) (AUTODESK) which is generated for each time history of the stroke of linear motors.

Sample time history of one stroke of the linear motor is shown in Fig. 8.

In the same way, we obtain a set of strokes for all six linear motors (Fig. 9) which is exported to a data file applicable to the control software test of the hexapod platform.

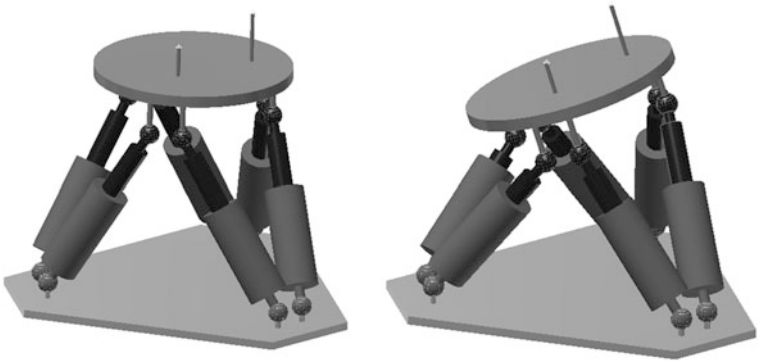

Fig. 7 Virtual model of platform

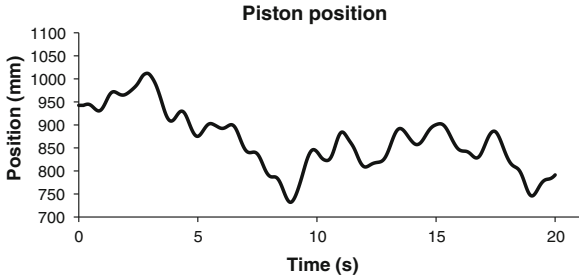

Fig. 8 Signal of piston position of linear motor

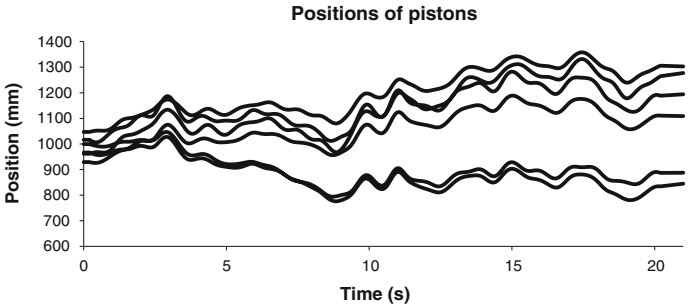

Fig. 9 Signals of all 6 linear motors

3 Conclusions

In conclusion, we can state that the chosen method of obtaining input signals to move the piston rod is divided into several simple steps. This is well-controlled, or is easily exposed and thus correctable error in the inspection of the experiment.

References

Létání and Letecké Zážitky (2013) Létání na simulátorech. Létání na simulátoru AIRBUS A320 [2013] [cit. 10-06-2013]. Available from http://www.letani-zazitky.cz/product/letani-na-simulatorech/letani-na-simulatoru-airbus-a320/43

Linear Stepper Motor Axis: Linear Motors [online] [cit. 10-06-2013]. Available from http://www.servo-drive.com/stepper_motor_linear_axis_linear_stepper_motor.php

Servo Drive Products: Linear Motors [online] [cit. 10-06-2013]. Available from http://www.servo-drive.com/stepper_motor_linear_axis_linear_stepper_motor.php

INOVA Testing Systems: Hydrostatic Bearing Linear Actuators [online] [cit. 10-06-2013]. Available from http://www.inovatesting.net/en/products/actuators/

AUTODESK INC. *Autodesk Inventor 2013—software*

Stand for Measuring Temperatures of the Main Gears of Automobile Differential

M. Mazac

Abstract This paper deals with the design of a universal stand for measuring of the temperature of the main gear of automobile differential and other operation parameters of light automobile gearboxes. The stand is designed for loading of gearboxes in almost real operating conditions. The stand can be used for measurements of main operating parameters of a gearbox but the temperature and thermal parameters of gearbox parts are most important. Emphasis is placed on the measurement of temperature near surfaces of gear teeth. During the measurements on this stand, it is possible to have realistic operating conditions as during real performance of automobile gearbox: the main operation parameters are real mounting of gearbox (real mounting rigidity) and real drive by combustion engine (irregularity of rotation). The goal of this paper is a short conceptual study of an easy stand for measuring temperatures of gears and other operation parameters of automobile gearbox operating in almost realistic conditions.

Keywords Temperature · Measuring · Gear · Gearbox

1 Introduction

Global consumption of oil is very important topic in present, but a lot of new automobiles powered by gasoline or diesel engines are produced every year in the world. Only a small part of energy content in fuel is used for the actual propulsion of cars. Total balance of the utilization of the energy contained in the fuel is presented in Fig. 1.

M. Mazac (✉)
Technical University of Liberec, Liberec, Czech Republic
e-mail: martin.mazac@tul.cz

L. Ševčík et al. (eds.), *Modern Methods of Construction Design*,
Lecture Notes in Mechanical Engineering, DOI: 10.1007/978-3-319-05203-8_20,

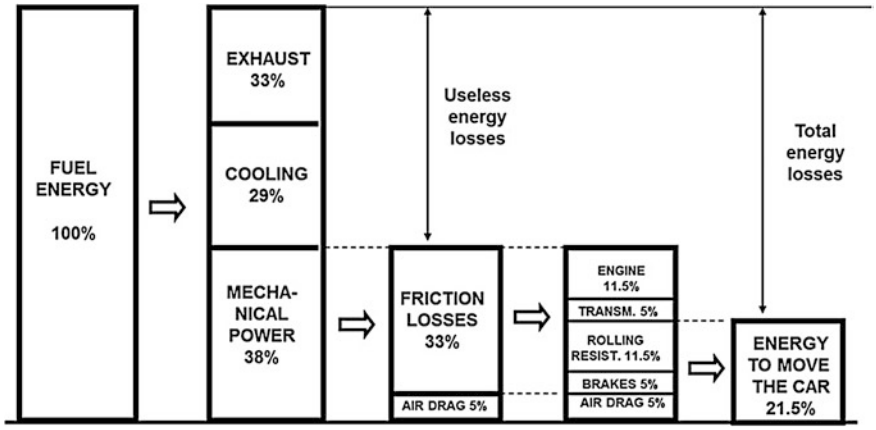

Fig. 1 Utilization of fuel energy (Holmberg et al. 2011)

Most of the producers of automobiles want to improve (decrease) a consumption of energy of their products. Producers want to increase efficiency of their internal combustion engines and decrease power losses of powertrains of their cars. Gearbox is usually a main part of the powertrain of an automobile. Mechanical gearboxes are used in many types of cars and there is no other chance for a car to run without them. The main function of gearboxes is the transformation of energy produced by engine. A part of this energy is changed to heat and it sure can't be used for effective drive of the car later on. This energy symbolizes energy losses in the gearbox.

During operation of gearbox, the energy is changed to heat as stated above. Friction is a main process which causes these changes. During operation of gears, friction is an inseparable process. Gear heating is one of the characteristic parameters which represent the quality of energy transfer. Measuring of gear temperatures is possible (Rao and McPherson 2009) by modern measuring methods. Temperature measurements were performed on experimental gear usually. This thesis deals with design of stand for experimental measuring of temperatures of gears in a real gearbox. The tested gearbox should be operated under conditions similar to its real operation.

2 Test Stand

The test stand is designed as an equipment for measuring temperatures on the main gears of the differential in a real automobile gearbox. Place for measurement of temperatures was chosen as a critical point of heat generation. During the real operation conditions, the tested gearbox is powered by a real internal combustion engine. The tested gearbox is attached to a real engine block, which has a rigidity

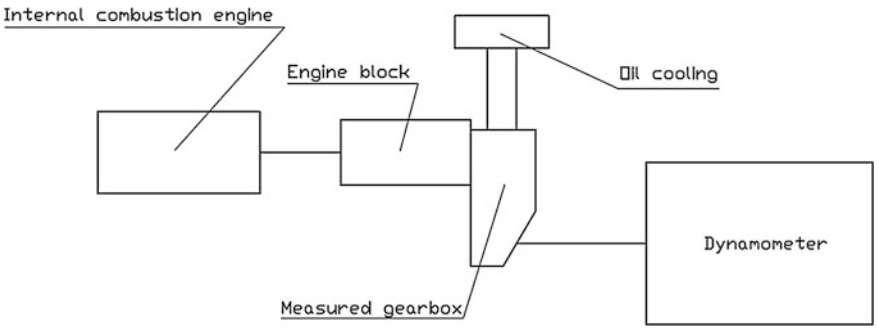

Fig. 2 Block scheme of the stand

identical to the engine used in a car. The function of differential is limited, only one wheel output is functional. An asynchronous electrical dynamometer is used as a load on the differential output. A simple block scheme of the stand is in Fig. 2.

2.1 Tested Gearbox

This stand is designed for measuring of a production Škoda Auto gearbox MQ100. This gearbox is mounted to a Škoda Citigo car. It is relatively new type of gearbox. MQ100 is a twin-shaft, 5-speed, manual gearbox with helical gears with HCR teeth. Place where temperature should be measured is near of the teeth of the main differential gear (final drive). The final drive works continuously during usual operation of gearbox. This place is poorly cooled and oil can be damaged here. Scheme of the MQ100 gearbox and a place of temperature measurement is in Fig. 3a. Cutaway view of the gearbox MQ100 is in Fig. 3b.

2.2 Drive of the Stand

For drive of the testing stand, a combustion engine is used. Standard gearbox MQ100 is mounted to a 1,0/44 kW internal combustion engine in a common car. This engine is a three-cylinder naturally aspirated spark ignition engine. Similar engine as the 1,0/44 kW is an older 1,2/44 kW. For this stand is better to use the older 1,2/44 kW engine. Torque is a little bit higher for the 1,2/44 kW then for the 1,0/44 kW in lower RPM. Higher torque is useful for operating in regimes on the upper level of the maximum gearbox load but at around 3,000 rpm. The characteristics of 1,2/44 kW engine are given in Fig. 4.

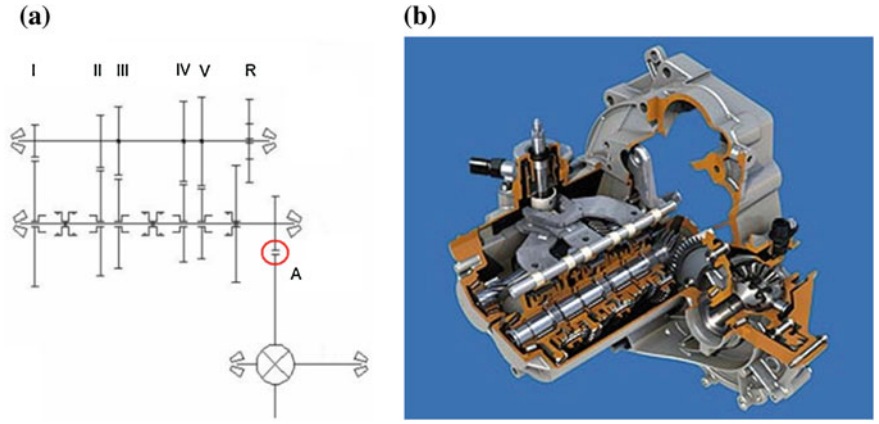

Fig. 3 **a** MQ100 scheme (Škoda Auto a.s. sources), place of temperature measuring. **b** MQ100 cut (www.atzonline.com)

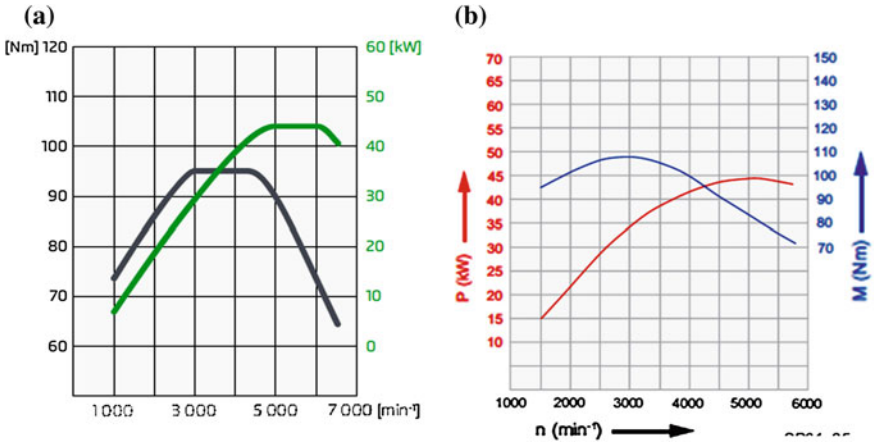

Fig. 4 **a** 1,0/44 kW characteristics (Škoda Auto a.s. sources). **b** 1,2/44 kW characteristics (Škoda Auto a.s. sources)

2.3 Dynamometer

For a good choice of dynamometer it sure is necessary to know the torque characteristic of the output from the gearbox. Torque on the output from gearbox is shown in Fig. 5. For the calculation of output torque, the transfer ratio was used. The output torque was calculated considering 4,300 rpm and 59 ft-lb (95 Nm) torque on the input.

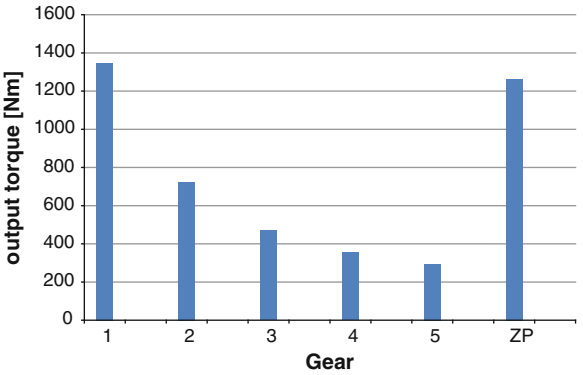

Fig. 5 Output torque

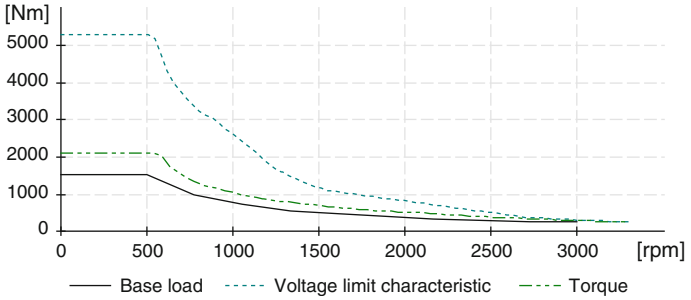

Fig. 6 Characteristic of dynamometer (Siemens s.r.o)

The maximum torque on output of gearbox is about 840 ft-lb (1,350 Nm) and that is why is necessary to choose a dynamometer with higher possible braking torque. For final braking of the measured gearbox, a Siemens asynchronous electric dynamometer with a maximum torque of 1,320 ft-lb (2,120 Nm) was chosen. Dynamometer is installed in laboratories of TUL. Parameters of the dynamometer are in Fig. 6.

2.4 System for Temperature Measurements

Transfer of the information about temperature from the rotating shaft is somewhat complicated. The principle of equipment for measuring of temperatures is based on resistance thermal sensors. Transfer of the data is realized by infrared telemetry. Such a system is not common commercially available but it is under development at the university, and will be described in detail in another publication.

3 Conclusions

This short paper describes a conceptual study of the stand for testing of an automobile gearbox. Stand is especially designed for MQ100 gearbox produced by Škoda Auto a.s.. The rigidity of the gearbox mounting is similar as in a real car. The tested gearbox is powered by a real internal combustion engine. Measurement of temperatures on drive gear of differential is the main aim of the stand. The system for temperature measurements will be described in another thesis. With some easy modifications, it is possible to measure many operating parameters of gearboxes on the stand. This equipment for testing of gearboxes will be located in TUL laboratories.

Acknowledgments The paper reported here was made possible by SGS project of Technical University of Liberec.

References

Holmberg K, Andersson P, Erdemir A (2011) Global energy consumption due to friction in passenger cars. Tribol Int. doi:10.1016/j.triboint.2011.11.022

Rao SB, McPherson DR (2009) Gear tooth temperature measurements, Gear Solutions

Materials Selection in Mechanical Design

I. Mazínová and P. Florian

Abstract The contribution deals with material selection strategy in mechanical design. Material selection is tackled in four steps. The first step is *translation*—reinterpreting the design requirements in terms of function, constraints, objectives, and free variables. The second step is *screening*—deriving attribute limits from the constraints and applying these to isolate a subset of viable materials. The third step is *ranking*—ordering the viable candidates by the value of a material index, the criterion of excellence that maximizes or minimizes some measure of performance. The last step is *documentation*—seeking documentation for the top-ranked candidates.

Keywords Material selection strategy · Material property charts · Material indices

1 Introduction

There is no need to emphasize that materials play the key role during product life cycle. Material selection often determines success or failure of a product on the market. Therefore it should be taken into account in the early stages of the design process. However, having over 100,000 engineering materials to choose from makes this task significantly demanding. Fortunately, this process might be facilitated by using computer-aided-materials-selection software (CAMS) and materials charts.

I. Mazínová (✉) · P. Florian
University of West Bohemia, Pilsen, Czech Republic
e-mail: mazini@kks.zcu.cz

P. Florian
e-mail: pflorian@kks.zcu.cz

L. Ševčík et al. (eds.), *Modern Methods of Construction Design*,
Lecture Notes in Mechanical Engineering, DOI: 10.1007/978-3-319-05203-8_21,

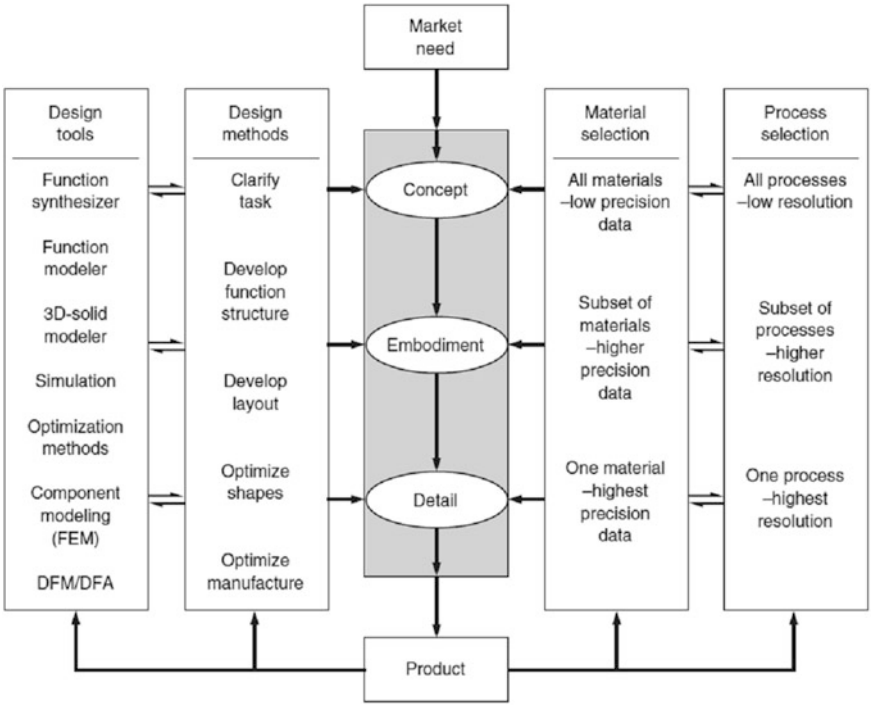

Fig. 1 Materials selection and design process (Dieter 2009)

Figure 1 present ideal relation between materials selection and design process. The earlier material selection is applied the more time can be saved in the later stages of the design process. It also shows that each following step in the design process needs more precise data. Manufacturing process selection is often overlooked but should be taken into account as well.

2 The Selection Strategy

2.1 Translation

Every component has to meet certain requirements. These requirements can be expressed by *functions*: carrying load, transmitting heat, damping vibration, etc. And the functions are satisfied with respect to *constraints* concerning dimensions, mass, cost, environment and so on. It is also vital to determine *objectives*; to make the component as cheap as possible, as light as possible, as stiff as possible, etc. There are also *free variables* which are not limited by any constraint but may influence overall performance. Summing functions, constraints, objectives and free

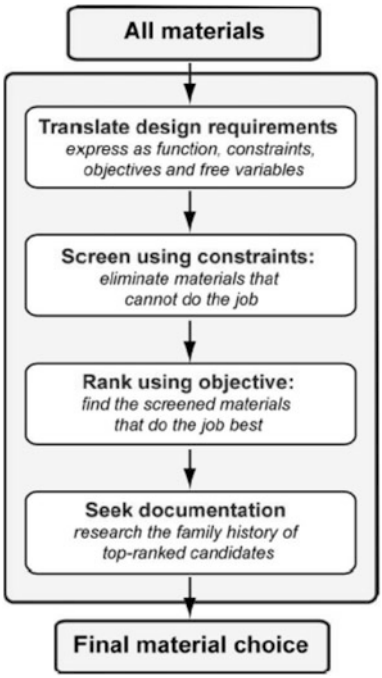

Fig. 2 The strategy for materials selection (Ashby 2011)

Table 1 Function, constraints, objective, and free variables

Function	• What does the component do?
Constraints	• What non-negotiable conditions must be met?
Objective	• What is to be maximized or minimized?
Free variables	• What parameters of the problem is the designer free to change?

variables together results in boundary conditions for material selection. The process of relating the boundary conditions to material properties is called *translation*. During translation designer's requirements are expressed by material attributes such as tensile strength, thermal conductivity, fracture toughness and so on. Ranges of values of each material attribute are also clarified in this step in order to implement them into computer-aided-material selection software (Fig. 2; Table 1).

2.2 Screening

Until this stage all materials were considered as potential candidates. But in this step the materials which do not comply with boundary conditions stated in translation phase are screened out. This process narrows down the list of potential

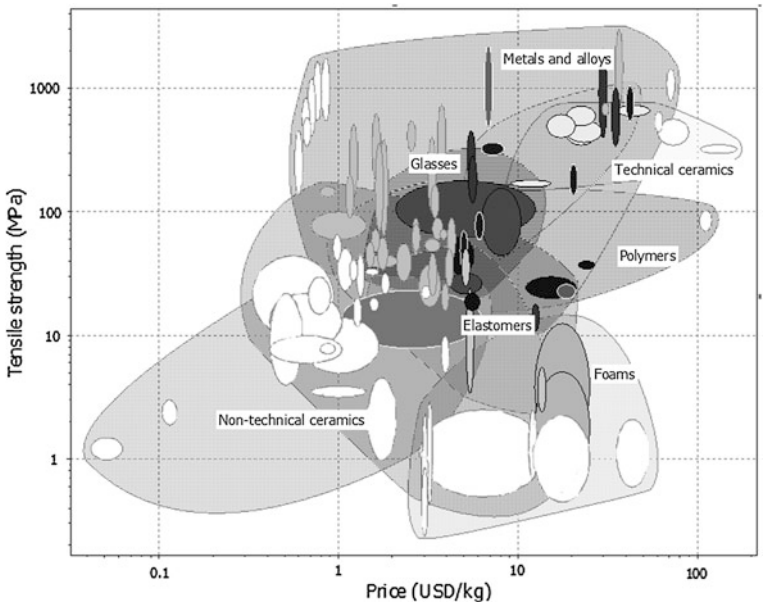

Fig. 3 Materials chart with applied constraints

candidates. Using CES EduPack (2012) in this step is convenient. Figure 3 contains white bubbles which represent unsuitable materials that do not meet attribute limits.

2.3 Ranking

Despite having smaller subset of materials after screening phase the list of potential candidates might be still too long to allow choosing a suitable material. The aim of the ranking stage is to put the remaining materials in order according to their performance. To do this material indices can be applied.

The performance of a structural element is determined by three things: the functional requirements, the geometry, and the properties of the material of which it is made. The performance P of the element is described by an equation of the form

$$\boldsymbol{P} = \left[\begin{pmatrix} \textbf{\textit{Functional}} \\ \textbf{\textit{requirements}}, \boldsymbol{F} \end{pmatrix}, \begin{pmatrix} \textbf{\textit{Geometric}} \\ \textbf{\textit{parameters}}, \boldsymbol{G} \end{pmatrix}, \begin{pmatrix} \textbf{\textit{Material}} \\ \textbf{\textit{properties}}, \boldsymbol{M} \end{pmatrix} \right]. \quad (1)$$

Performance of a material is given by one or more attributes e.g. the best materials for heat sinks are the ones with high value of heat conductivity λ, but

Table 2 Examples of material indices (Ashby 2011)

Function, objective, and constraints	Index
Tie, minimum weight, stiffness prescribed	$\frac{E}{\rho}$
Beam, minimum weight, stiffness prescribed	$\frac{E^{1/2}}{\rho}$
Beam, minimum weight, strength prescribed	$\frac{\sigma_y^{2/3}}{\rho}$
Beam, minimum cost, stiffness prescribed	$\frac{E^{1/2}}{C_m\rho}$
Beam, minimum cost, strength prescribed	$\frac{\sigma_y^{2/3}}{C_m\rho}$
Column, minimum cost, buckling load prescribed	$\frac{E^{1/2}}{C_m\rho}$
Spring, minimum weight for given energy storage	$\frac{\sigma_y^2}{E\rho}$
Thermal insulation, minimum cost, heat flux prescribed	$\frac{1}{\lambda C_p\rho}$
Electromagnet, maximum field, temperature rise prescribed	$\frac{C_p\rho}{\rho_e}$

ρ density; E Young's modulus; σ_y elastic limit; C_m cost/kg; λ thermal conductivity; ρ_e electrical resistivity; C_p specific heat

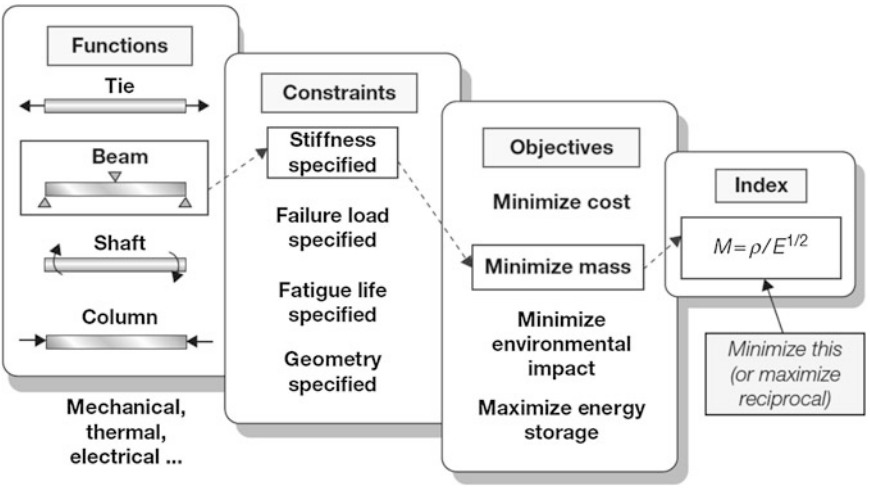

Fig. 4 Translation procedure and appropriate material index (Ashby 2011)

light, stiff ties need materials with high value of Young's modulus E and low values of density ρ as well. This means that materials with high ratio E/ρ would be very suitable for stiff ties. The ratio E/ρ is an example of *material index*. Material indices might be expressed by a single property (e.g. λ) or more properties (e.g. E/ρ). The key procedure of the ranking stage is searching maximum or minimum values of appropriate material indices in order to find the most suitable material for given application; however, the particular index should be derived already during translation (Table 2).

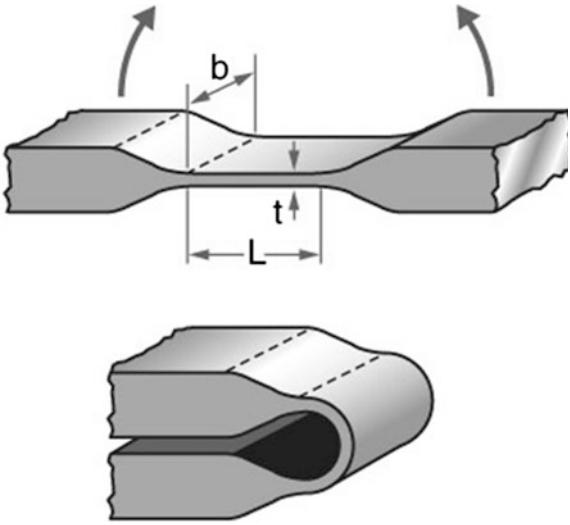

Fig. 5 Elastic hinges (Ashby 2011)

Figure 4 presents translation procedure and selection of an appropriate material index.

2.4 Documentation

In this final step only a few candidate materials should be on the list. It is important to gather precise data from materials suppliers to be able to conduct analyses and calculations since the data in the material database are not precise enough.

3 Case Study: Elastic Hinges and Couplings

Ligaments of elastic hinges must bend repeatedly without failing. A cap of a shampoo bottle is an example; elastic hinges are used in high-performance applications too, and are found widely in nature. Which materials make good hinges?

Translation: We consider the hinge (Fig. 5) for the lid of a box. The box, lid, and hinge are to be molded as a single unit. The hinge is a thin ligament that flexes elastically as the box is closed, as shown in the figure, but it carries no significant axial loads. Then the best material is the one that (for given ligament dimensions) bends to the smallest radius without yielding or failing (Table 3).

Table 3 Examples of material indices (Ashby 2011)

Function	Elastic hinge
Constraint	No failure, meaning $\sigma < \sigma_f$ throughout the hinge
Objective	Maximize elastic flexure
Free variable	Choice of material

Screening: However in this case, there is no need to screen prospective materials.

Ranking: So now we need to develop an index by which we can rank materials for their elastic flexure. When a ligament of thickness t is bent elastically to a radius R, the surface strain is

$$\varepsilon = \frac{t}{2R} \tag{2}$$

and—since the hinge is elastic—the maximum stress is

$$\sigma = E\frac{t}{2R}. \tag{3}$$

This must not exceed the yield or failure strength σ_f. Thus the minimum radius to which the ligament can be bent without damage is

$$R \geq \frac{t}{2}\left[\frac{E}{\sigma_f}\right]. \tag{4}$$

The best material is the one that can be bent to the smallest radius, that is, the one with the greatest value of the index

$$M = \frac{\sigma_f}{E}. \tag{5}$$

We can now apply performance index to set of prospective materials. We need the $\sigma_f - E$ chart again (Fig. 6). Candidates are identified by using the guide line of slope 1; a line is shown at the position $M = \sigma_f / E = 2 \times 10^{-2}$. The best choices for the hinge lie to the right of this line: They are all polymeric materials. The shortlist (Table 4) includes polyethylene, polypropylene, nylon, and, best of all, elastomers, though these may be too flexible for the body of the box itself. Cheap products with this sort of elastic hinge are generally molded from polyethylene, polypropylene, or nylon. Spring steel and other metallic spring materials (like phosphor bronze) are possibilities: They combine usable σ_f / E with high E, giving flexibility with good positional stability (as in the suspensions of relays).

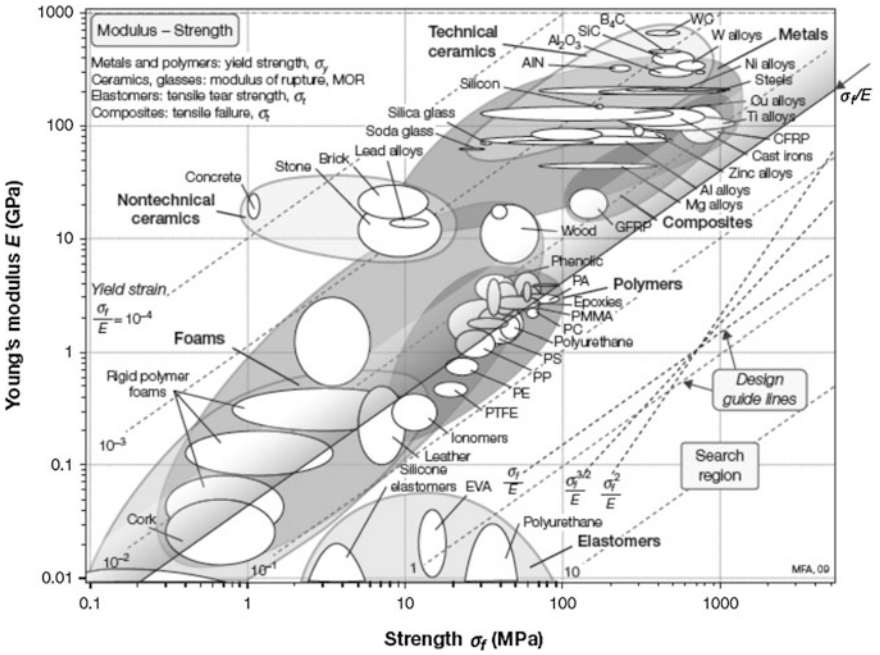

Fig. 6 Translation procedure and appropriate material index (Ashby 2011)

Table 4 Material for elastic hinges (Ashby 2011)

Material	M ($\times 10^{-3}$)	Comment
Polyethylene	32	Widely used for cheap hinged bottle caps, etc.
Polypropylene	30	Stiffer than Polyethylene; easily molded
Nylon	30	Stiffer than Polyethylene; easily molded
PTFE	35	Very durable; more expensive than PE, PP, etc.
Elastomers	100–1,000	Outstanding, but low modulus
High strength copper alloys	4	M less good than polymers; use when high tensile stiffness is required
Spring steel	6	

4 Conclusions

Material properties limit performance. We need a way of surveying them to get a feel for the values that design-limiting properties can have.

Acknowledgments The presented paper has been undertaken within framework of the Project No. CZ.1.07/2.2.00/28.0206 "Innovation of design training in the fields of interdisciplinary knowledge, computer, educational and linguistic support with increasing of modularization and knowledge consistency, eliminating duplications and involving specialists from industry." financed by European Social Fund and a state budget of the Czech Republic.

References

Ashby MF (2011) Materials selection in mechanical design. Elsevier, Butterworth-Heinemann, UK

CES EduPack software (2012) Granta design limiting. Cambridge, UK. Available at (www.grantadesign.com)

Dieter GE, Schmidt LC (2009) Engineering design. McGraw-Hill, New York, pp 459

Tip Rounding of a Spur-Gear Pinion-Type Cutter

M. Němček

Abstract A tool for gears manufacturing—pinion-type cutter is defined by standards ČSN 222505-06, ČSN 222570,76,80-82. Only a sharp edge of tip ends is under consideration in these standards and in the literature too (Šalamoun and Suchý in Čelní a šroubová soukolí s evolventním ozubením. SNTL–Nak-ladatelství technické literatury, Praha, 1990). So it is easy to get all related geometrical parameters of machined gears. If some tool tip rounding is required, certain problems with calculating of some their geometrical parameters occur. This contribution deals with these problems for a spur-gear pinion-type cutter. Three tasks are solved concretely. Input is a demanded tool tip rounding radius, a demanded height of the rounded part of a tip or a full rounded tip is demanded (both parameters are finding).

Keywords Pinion-type cutter · Tip rounding · Shifting coefficient

1 Introduction

They usually deal with a pinion-type cutter with sharp edge of tip ends ($\rho_{a0} = 0$) in related publications concern about gear manufacturing, or they speak about this radius only marginally or neither. When nonzero tip radius is used there is necessary to know all geometrical parameters of the tooth tip for quality calculation of geometric and mesh parameters of manufactured gears. This contribution tries to show a methodology for three basic types related with an assessment of tool tip parameters with rounded tip edge of a pinion-type cutter:

- calculation of h_ρ for exist ρ_{a0}
- calculation of ρ_{a0} for exist h_ρ
- calculation of ρ_{a0} a h_ρ for a fully rounded tip.

M. Němček (✉)
VŠB-Technical University of Ostrava, Ostrava, Czech Republic
e-mail: milos.nemcek@vsb.cz

L. Ševčík et al. (eds.), *Modern Methods of Construction Design*,
Lecture Notes in Mechanical Engineering, DOI: 10.1007/978-3-319-05203-8_22,

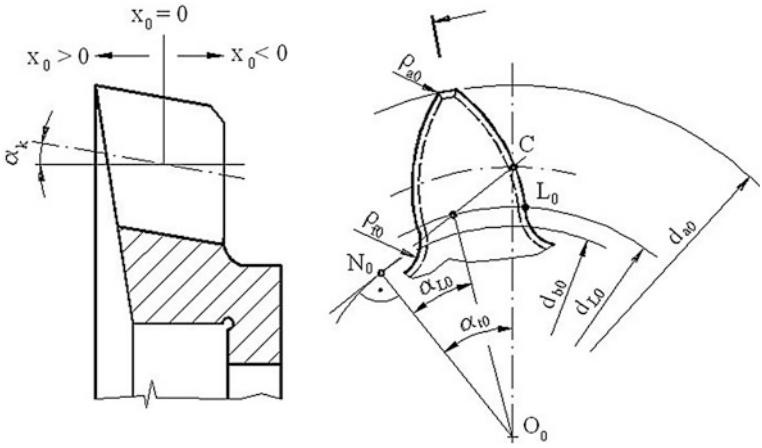

Fig. 1 One tooth of a pinion-type cutter (Němček 2003)

2 Pinion-type Cutter

A shape of the tool is on the Fig. 1. An awkward feature of it is that after each regrinding of a tool face the shape of a tooth will change—an addendum shifting coefficient x_0 is changing from its maximal positive value (a new tool) up to the smallest acceptable negative value. Within this change all of related diameters are changing too, especially its tip diameter d_{a0}. It is necessary to know a size of an angle α_k (clearance angle) for determination of an addendum shifting coefficient x_0.

3 Calculation of a Pinion-type Cutter Tip Rounding

As mentioned above, a tool tip is not always ends by a sharp edge. Mainly when external gearing is manufactured, a certain tip rounding is demanded (car industry). This radius runs from minimal values (several hundredths of a module) to a fully rounded tip. Contrary to a rack cutter or a hob a current value of an addendum shifting coefficient x_0 affects the size of a tip radius. The calculations are simple ones. Only for some calculations it is necessary to use numerical solving of a transcendental equation.

3.1 Calculation of h_ρ for Exist ρ_{a0}

This task is the simplest one of the three mentioned above. Equations for solving result from basis of an involute geometry and from the Figs. 2 and 3. For next

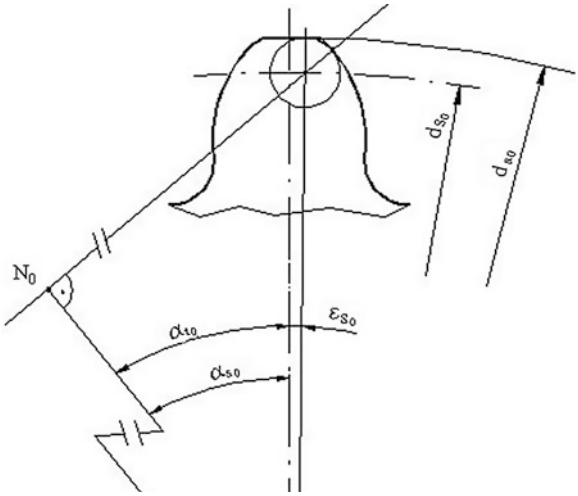

Fig. 2 Angles for a tip rounding of a pinion-type cutter

steps it is important to realize the difference between a height of a tool clearance addendum c_{a0} (given by a basic profile) and a searched parameter h_{ρ}. This parameter could equal to the height c_{a0} (in special cases).

It starts from a fact that an involute and tip rounding radius must have common tangent and normal lines in the point Y_0. So this normal line must go through the center of a circle S_0 and it is simultaneously the tangent line to the basic circle at the point N_0. Its angle is α_{S0}. The diameter on which the point S_0 is laying is easy to determine $d_{S0} = d_{a0} - 2 \cdot \rho_{a0}$

$$\alpha_{S0} = \arccos \frac{d_{b0}}{d_{S0}} \tag{1}$$

The circle diameter d_{Y0}, on which the last point of an involute face of tool Y_0 is laying, can be directly figured out from the right triangle O_0, N_0, Y_0.

$$d_{Y0} = 2 \cdot \sqrt{(0.5 \cdot d_{b0} \cdot \tan \alpha_{S0} + \rho_{a0})^2 + (0.5 \cdot d_{b0})^2} \tag{2}$$

For exact assessment of a position of the centre S_0 on the circle d_{S0} it is just to calculate the angle ε_{S0} (to the tooth axis) by the Fig. 3.

$$\varepsilon_{S0} = \frac{\Delta s_{S0}}{0.5 \cdot d_{S0}} \tag{3}$$

For tooth thicknesses on the circle d_{S0} it applies

$$\Delta s_{S0} = \frac{s_{S0}}{2} - \frac{\rho_{a0}}{\cos \alpha_{S0}} \tag{4}$$

An unknown parameter h_ρ is finally setting

$$h_\rho = \frac{d_{a0} - d_{Y0}}{2} \tag{5}$$

3.2 Calculation of ρ_{a0} for Exist h_ρ

The second task is in principle an inverse task of the first one. The Figs. 2 and 3 are also valid for it. Inasmuch as an unknown parameter now is ρ_{a0}, it is impossible to set the diameter d_{S0}. On the contrary the diameter d_{Y0}, on which the last point of an involute face of tool Y_0 is laying, is given by equation $d_{Y0} = d_{a0} - 2 \cdot h_\rho$. This diameter is substituting into Eq. 2, and into the same equation is substituting $d_{S0} = d_{a0} - 2 \cdot \rho_{a0}$. Then a homogenous transcendental equation with one unknown (searched radius ρ_{a0}) is created.

$$\left(\frac{d_{Y0}}{2}\right)^2 - \left(\frac{d_{b0}}{2}\right)^2 - \left(\frac{d_{b0}}{2} \cdot \tan\left(\arccos\frac{d_{b0}}{d_{a0} - 2 \cdot \rho_{a0}}\right) + \rho_{a0}\right)^2 = 0 \tag{6}$$

A numerical solution of this equation is easy. After getting the radius ρ_{a0} the diameter d_{S0} is $d_{S0} = d_{a0} - 2 \cdot \rho_{a0}$ and a position of its center S_0 is given by Eqs. (3) and (4).

3.3 Calculation of ρ_{a0} and h_ρ for a Fully Rounded Tip

It pays that (Fig. 3) the center of the rounded tip must lay on the tooth axis. The begin is an equality in the Eq. (7) which results from an involute geometry (Fig. 4).

$$\frac{s_{S0}}{2} = \frac{\rho_{a0}}{\cos \alpha_{S0}} \tag{7}$$

For $\cos \alpha_{S0}$ is substituting into Eq. (7)

$$\cos \alpha_{S0} = \frac{d_{b0}}{d_{a0} - 2 \cdot \rho_{a0}} \tag{8}$$

And for s_{S0}

$$s_{s0} = d_{S0} \cdot \left(\frac{s_0}{d_0} + \text{inv}\, \alpha_t - \text{inv}\, \alpha_{S0}\right) \tag{9}$$

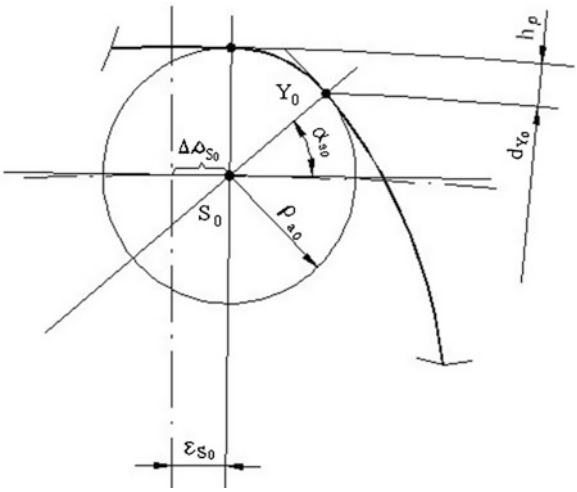

Fig. 3 Detail of a tip rounding of a pinion-type cutter

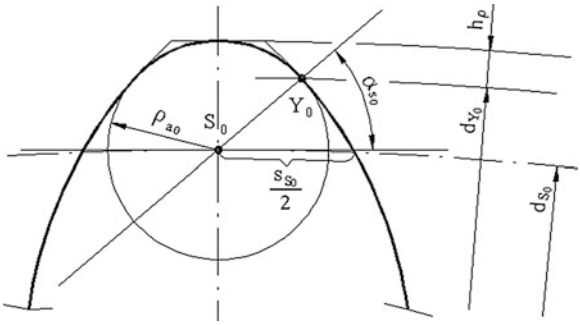

Fig. 4 Geometry of fully rounded tip of a pinion-type cutter

The resultant transcendental equation with one unknown ρ_{a0} is then

$$(d_{a0} - 2 \cdot \rho_{a0}) \cdot \left(0.5 \cdot \left(\frac{s_0}{d_0} + \text{inv}\,\alpha_t - \text{inv}\,\alpha_{S0}\right) - \frac{\rho_{a0}}{d_{b0}}\right) = 0 \qquad (10)$$

A numerical solution of this equation is again easy. But the unknown ρ_{a0} is more contained in the angle α_{S0}. And this angle is substituting with Eq. (8). The calculation continues in determining of the diameter $d_{S0} = d_{a0} - 2 \cdot \rho_{a0}$, and in a calculation of the diameter d_{Y0} [by Eq. (2)]. At the conclusion h_ρ is enumerated by the Eq. (5).

4 Conclusions

By contrast to a rack cutter which is always without a shifting coefficient (it is basically a gear with infinite number of teeth) there is a big influence of a shifting coefficient x_0 for pinion-type cutter. The value of its shifting coefficient is changing during its lifetime from a maximal positive value to the smallest negative value, see

Fig. 1. This changing produces a related change of the tip diameter d_{a0} and of a tool tooth thickness s_{S0}. This finding is very important for designing of a pinion-type cutter with rounded tips. One of four options of a design should be chosen

(a) the same rounding ρ_{a0} along the whole facewidth (if tip dimensions allow it)—h_ρ is changing continuously
(b) the same height h_ρ along the whole facewidth (if tip dimensions allow it)—ρ_{a0} is changing continuously
(c) both values are changing linearly with a decreasing shifting coefficient x_0
(d) it is evident that for fully rounded tip the radius ρ_{a0} must change continuously along the facewidth of a pinion-type cutter.

If a designer wants to use such a tip rounding radius in order that the tip rounding connects to an involute tooth edge directly at the start of a tool clearance addendum ($d_{Y0} = d_{a0} - 2 \cdot c_{a0}$), he must use calculation of ρ_{a0} for given h_ρ. But it is necessary to substitute h_ρ by c_{a0}. For this task they do not least forget to check if the rated radius is not greater then maximum permissible one. This maximal permissible radius matches the value for fully rounded tool tip. The rated radius for common values of c_{a0} is usually smaller one.

This paper brings a description of calculation methods for finding parameters of a pinion-type cutter tip rounding. This tool is mostly used with a sharp edge on teeth tips but they use versions with rounded tips as well. A very design hides specific difficulties. Very important fact is that after each regrinding toll parameter are changing. Therefore it is necessary to take into account this fact. The optimal way is to enter into a design of a tool in a pre-production stage and within this process to define rounding parameters by the part 3.

Acknowledgments This research has been realized using the support of Technological Agency, Czech Republic, programme Centres of Competence, project #TE01020020 Josef Božek Competence Centre for Automotive Industry. This support is gratefully acknowledged.

Contribution has been done in connection with project Increasing of Professional Skills by Practical Acquirements and Knowledge, reg. no. CZ.1.07/2.4.00/17.0082

References

Němček M (2003) Vybrané problémy geometrie čelních ozubených kol. MONTANEX a.s. Ostrava. ISBN 80-7225-111-23

Šalamoun Č, Suchý M (1990) Čelní a šroubová soukolí s evolventním ozubením. SNTL – Nakladatelství technické literatury, Praha. ISBN 80-03-00532-9

Experimental Hydrostatic Stand to Energy Recovery Research for Vehicles

J. Nevrlý

Abstract The hydrostatic stand to energy recovery research has been designed and used to carry out necessary experiments before preparing a design of a hydrostatic module on a real commercial vehicle. The main project is oriented on research and development of a new product—a hydrostatic module to energy recovery during breaking and acceleration of commercial vehicles using control to energy transfer optimization based on mathematical modeling of the system function. The predecessors of the experimental stand: designs of stationary experimental stands and moving equipment—the hydromobil are mentioned. The scheme of the hydraulic circuit of the stand, the photo of the stand and the diagram of the hydrostatic drive control are introduced. The measuring results are shown.

Keywords Energy · Recovery · Stand · Experiment · Vehicle

1 Introduction

In the last decades and years, the price of crude oil and petrol has increased considerably. Consumption of energy has become one of basic issues. The effort to lower the consumption is a trend worldwide.

The basic idea of this energy recovery system is to use the kinetic energy of the braked vehicle which is commonly lost by braking and useless changed in warm. The energy will be recovered by the change of kinetic energy to hydraulic energy (Pourmovahed et al. 1992a, b; Nevrlý 2011), which will be used during the following start of the vehicle. In this way, the load of the combustion engine can be reduced; the saving of fuel can reach more than 25 % together with increase of

J. Nevrlý (✉)
Brno Technical University, Brno, Czech Republic
e-mail: nevrly@fme.vutbr.cz

L. Ševčík et al. (eds.), *Modern Methods of Construction Design*,
Lecture Notes in Mechanical Engineering, DOI: 10.1007/978-3-319-05203-8_23,

economic effectiveness, reliability, reduction of brake wear and ecologic improvement of operation. This system is especially suitable in vehicles working in frequent cycle braking-start (Nevrlý and Nykodým 2011) as e. g. garbage trucks, forklift trucks, city busses, rollers etc.

An important area worthy for further research is an investigation by means of experimental stands in the field of large vehicles supported by computer simulation. Such a project could result in a controller that would be directly downloadable into a vehicle. The laboratory experimental stand is a necessary instrument in such a research.

2 Design of the Stand

2.1 The Predecessors of the Experimental Stand

The experimental stands described in this section have been designed within the framework of master's or bachelor's theses in the Institute of Machine and Industrial Design, Faculty of Mechanical Engineering, Brno University of Technology in co-operation with the firm Bosch-Rexroth during the last four years, the author of this article has been supervising them. The master's thesis of Indruch (Nevrlý 2012a) deals with design of an experimental test bench (Fig. 1) for recovery energy simulation in the machines equipped with hydrostatic energy transmission.

The thesis of Ranuša (Nevrlý 2012a) deals with the design of an experimental device—stand (Fig. 2) for simulation and recovery energy for utility vehicles. The thesis of Mikula and Stodolák (Nevrlý 2012a) deals with the design and construction of the radio-controlled hydromobil which is driven by means of compressed gas and fluid. The drive system uses kinetic energy saved by braking of the vehicle during mechanical—hydraulic recovery (Fig. 3).

2.2 Design of the New Stand

The task for the new experimental equipment was testing of operation states and measuring of the most important operation quantities for further analysis, mathematical modeling and computer simulation leading to size optimization of substantial elements and to optimization of valves control.

The scheme of the hydraulic circuit of the stand, which has been produced in Bosch Rexroth in Brno, is depicted in Fig. 4. The stand has been connected to dynamometer as a load in the laboratory of the Faculty of Mechanical Engineering BUT. The valve block is also connected between the pump and the motor in hydraulic circuit at serial connection version. The high pressure bladder hydraulic accumulator is connected to the valve block. The low pressure hydraulic

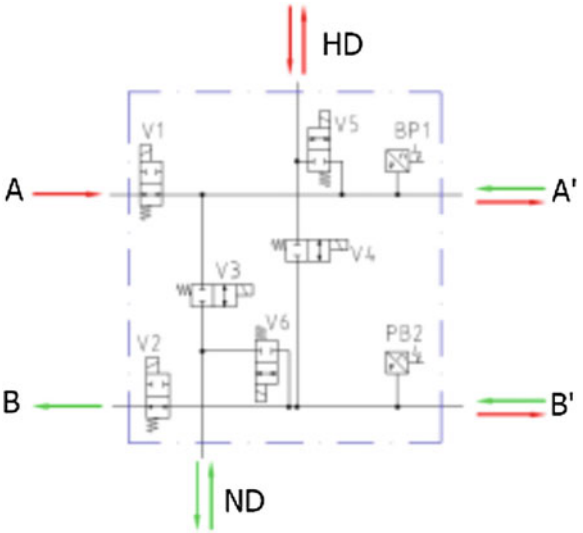

Fig. 1 The experimental test bench design for energy recovery (Nevrlý 2012a)

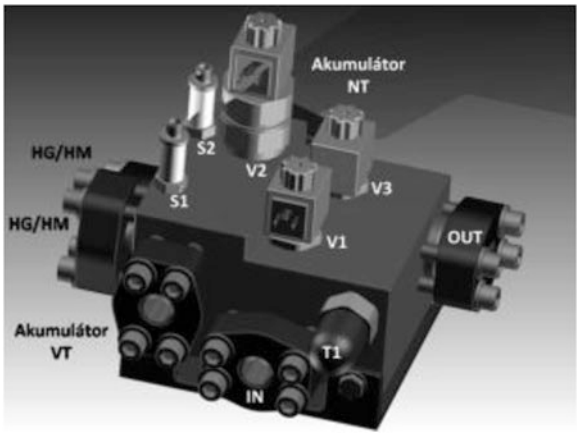

Fig. 2 The stand design for simulation (Nevrlý 2012a)

accumulator is connected to the hydraulic circuit and the exchange of oil between these accumulators takes place during braking or acceleration of the load.

3 Control System of the Stand

A closed control system has been developed to use the stand and to choose test operation parameters. The control system contains program routines starting individual operation regimes of the stand. Basic functionality of the system is secured by the following operation regimes: STOP, Set RPM, Decel, Accel, Fill aku ND and the regime Automat (Figs. 5 and 6).

Fig. 3 The hydromobil, the Brno International Trade Fair

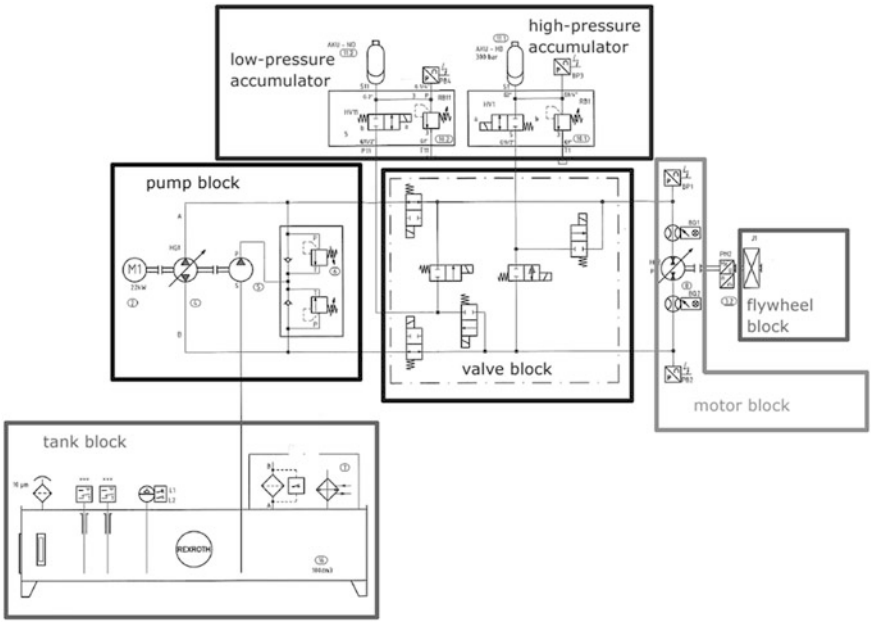

Fig. 4 The scheme of the hydraulic circuit of the stand (Nevrlý 2012b)

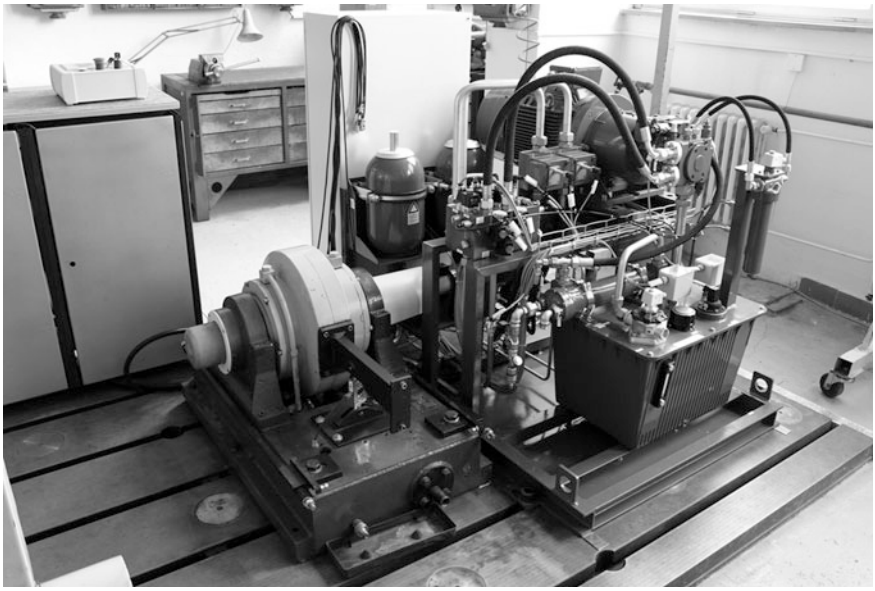

Fig. 5 The stand for research of energy recovery

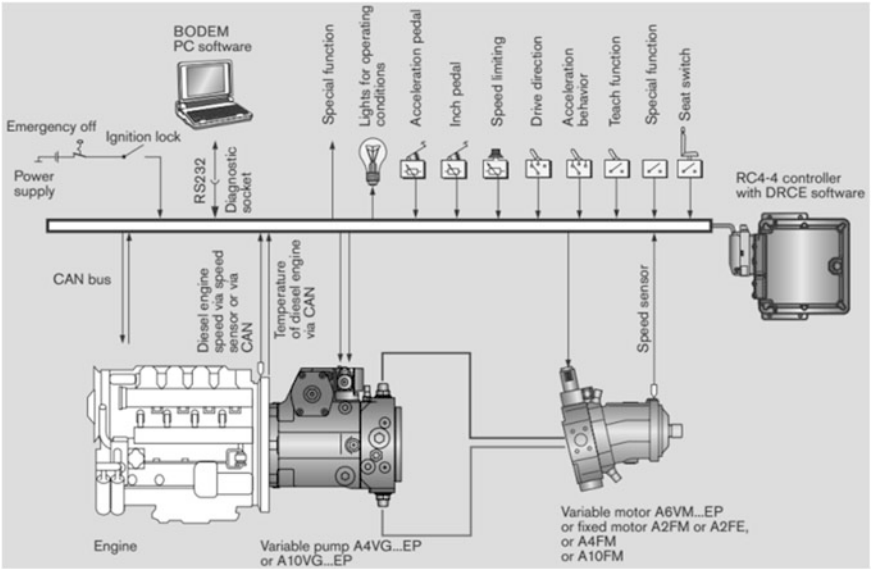

Fig. 6 The diagram of the hydrostatic drive control (Nevrlý 2012b)

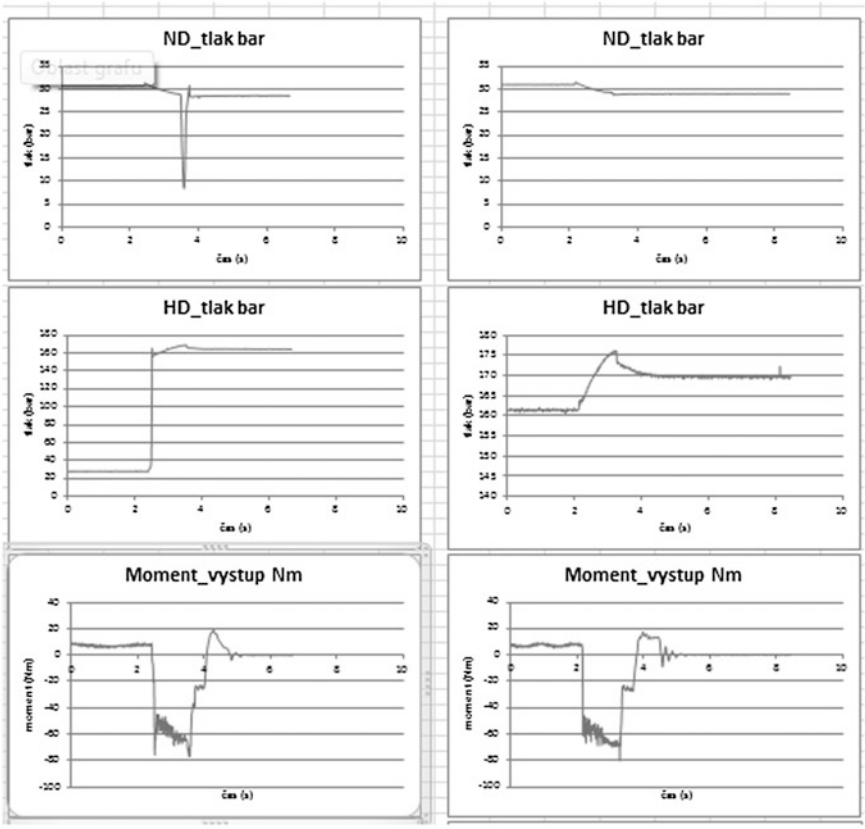

Fig. 7 An example of measured quantities courses

4 Measuring Results

Measuring has been carried out by means of the stand under different operation regimes. The data have been gained using appropriate sensors of pressure, oil flow, torque, revolutions etc. in places depicted in the hydraulic scheme mentioned above. Some courses of measured quantities can be seen in Fig. 7. Such and numerous similar results are being used as data for mathematical modeling and optimization of the energy recovery system for a pneumatic road cylinder. The courses of the torque going under the zero level in the Fig. 7 correspond to the recovered energy.

5 Conclusions

This paper presents some aspects of the development of the hydraulic hybrid drive experimental stands for heavy cycle-rate operating commercial motor vehicles. The new stand represents a necessary and useful instrument in effort to create an effective energy recovery system for a pneumatic road cylinder.

The time courses of pressure, flow in different parts of the hydraulic circle have been received along with velocity and torque of the hydraulic motor in various regimes of the stand operation. These courses represent important data for optimization of hydraulic circuit activity and for the research of energy recovery within the extent of such experimental equipment. At the same time, the measured courses, data and various operation parameters serve as comparative material for mathematical models during computer simulation of the stand function. Building and use of the described experimental hydrostatic stand to energy recovery research for vehicles represents useful or even an inevitable step before design and application of a hydrostatic module for hydraulic energy recovery applied on a real commercial vehicle.

Acknowledgments The present work has been supported by the Ministry of Education, Youth and Sports of the Czech Republic in the framework of the research project Eureka—LF12029 and by European Regional Development Fund in the framework of the research project NETME Centre under the Operational Programme Research and Development for Innovation—NETME Centre, ED0002/01/01, CZ. 1.05/2.1.00/01.0002.

References

Nevrlý J (2011) Kinetic energy recovery at heavy cycle-rate operating commercial motor vehicles. Research report (in Czech), Institute of Machine and Industrial Design, Faculty of Mechanical Engineering, Brno University of Technology

Nevrlý J (2012a) Hydraulic energy recovery stands for vehicles. In: Proceedings of 53rd international conference of Machine Design Departments, Brno University of Technology, Faculty of Mechanical Engineering, Institute of Machine and Industrial Design, Mikulov, pp 199–206. ISBN 978-80-214-4533-8

Nevrlý J (2012b) Recovery hydrostatic module for utility vehicles (in Czech). Periodical report 2012 of the project LF12029, Institute of Machine and Industrial Design, Faculty of Mechanical Engineering, Brno University of Technology, Brno

Nevrlý J (2012c) Hydromobil into the second round (in Czech). Události, vol 22, no 10. Brno University of Technology, Brno, pp 18–19

Nevrlý J, Nykodým L (2011) Modeling of hydraulic energy recovery for large vehicles. In: Proceedings of the 21st international conference on hydraulics and pneumatics, VŠB-TU (Ostrava University of Technology) Ostrava, pp 71–78. ISBN 978-80-248-2430-7

Pourmovahed A, Beachley NH, Fronczak FJ (1992a) Modeling of hydraulic energy regeneration system—part I: analytical treatment. J Dyn Sys Meas Control 114:155–159

Pourmovahed A, Beachley NH, Fronczak FJ (1992b) Modeling of hydraulic energy regeneration system—part II: experimental program. J Dyn Sys Meas Control 114:160–165

Test Rig for Gearboxes of Rail Vehicles

K. Petr, V. Dynybyl and J. Chmelař

Abstract This report summarizes development of test rig for gearboxes of rail vehicles. Tested gearbox will be simultaneously dynamically loaded in two modes. First is impact load in 3 main directions that simulates shocks transferred from wheels into gearbox. The other one is standard torque load. Structure for impact load is hexapod compounded of 6 hydraulic cylinders connected to a frame that holds tested gearbox. Part of development was also design of frames for electric motors.

Keywords Parallel structure · Spherical joint · Test rig · Gearbox · Rail vehicles

1 Introduction

Proving quality of products by experiments and tests gives company in consumer's eye certain advantage over the other companies in same field of industry.

Among companies that produce gearboxes for rail vehicles there is a lot of competition too. To be a leader, company must produce reliable gearboxes with minimal cost and must guarantee its operating life. To ensure top quality product, they use sophisticated tools during development. In first phase of design they make tests on virtual prototypes where single parts or whole assemblies are analyzed.

K. Petr (✉) · V. Dynybyl · J. Chmelař
Czech Technical University in Prague, Prague, Czech Republic
e-mail: karel.petr@fs.cvut.cz

V. Dynybyl
e-mail: vojtech.dynybyl@fs.cvut.cz

J. Chmelař
e-mail: jakub.chmelar@fs.cvut.cz

L. Ševčík et al. (eds.), *Modern Methods of Construction Design*,
Lecture Notes in Mechanical Engineering, DOI: 10.1007/978-3-319-05203-8_24,

In further phases of development, real prototypes are tested to check and confirm results obtained from virtual ones. Tests are also performed to get some new know-how about behavior of gearbox in run.

1.1 Main Function

Testing gearbox by putting it into rail vehicle would be quite complicated and expensive. Besides real operating condition it does not brings any additional value. Measuring and visual control would be very difficult to accomplish and probably there will be a limited time for testing given by owner of test rail circuit. Solution of mentioned problems is building a special test device in area of producer of gearboxes, which could be customized for testing various types of gearboxes and could simulate wide spectrum of load cases.

Test rig described it this paper will be used for dynamical testing of gearboxes for rail vehicles. Measured data will be used by department of Research and Development to:

- study the behavior of gearbox in operating conditions,
- fatigue prediction of parts,
- analysis of vibrations and impacts transferred to gearbox from wheels,
- Acoustical (noise) analysis.

2 Description of Test Rig

Main concept is shown in Fig. 1. In the middle of picture is placed tested gearbox which is held by system for impact testing (hexapod structure). On the left, there is a driving asynchronous electrical motor that through an acceleration gearbox drives input shaft of tested gearbox. Output shaft of tested gearbox is connected to another asynchronous electro motor, which runs in generator mode and simulates load from traction (Dynybyl 2009).

Test rig is also equipped by safety brakes and safety clutch that are located on output shaft from driving motor.

Tested gearbox is dynamically loaded in 3 directions during tests therefore it is connected to both motors by CV joints. They guarantee fluent run even if the gearbox makes slight movements. The gearbox is to the mentioned system connected same way as it is actually placed in rail vehicle (Fig. 2). There are two bearing houses that simulates wheels and are connected to an output shaft from gearbox. On side of input shaft, the gearbox is connected to case of vehicle by a carrier bar. On each end of bar, there are silent-blocks that allow gearbox to make slight movements and damp impacts and vibrations transferred farther to case of vehicle.

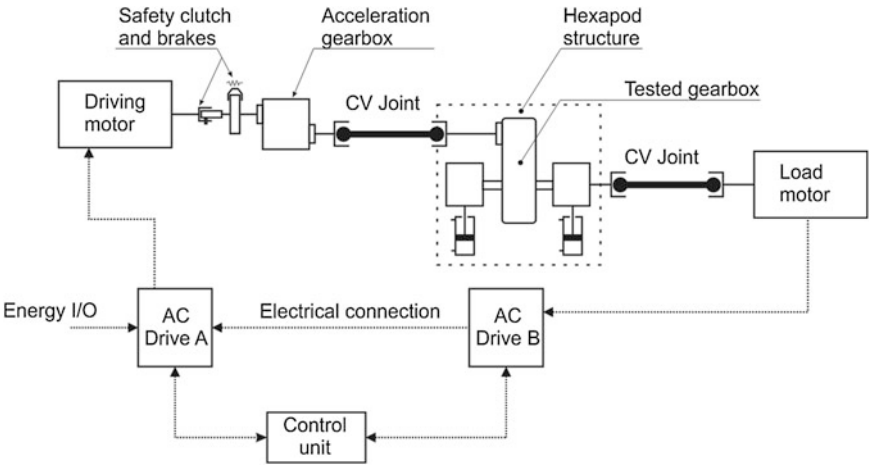

Fig. 1 Main concept of test rig

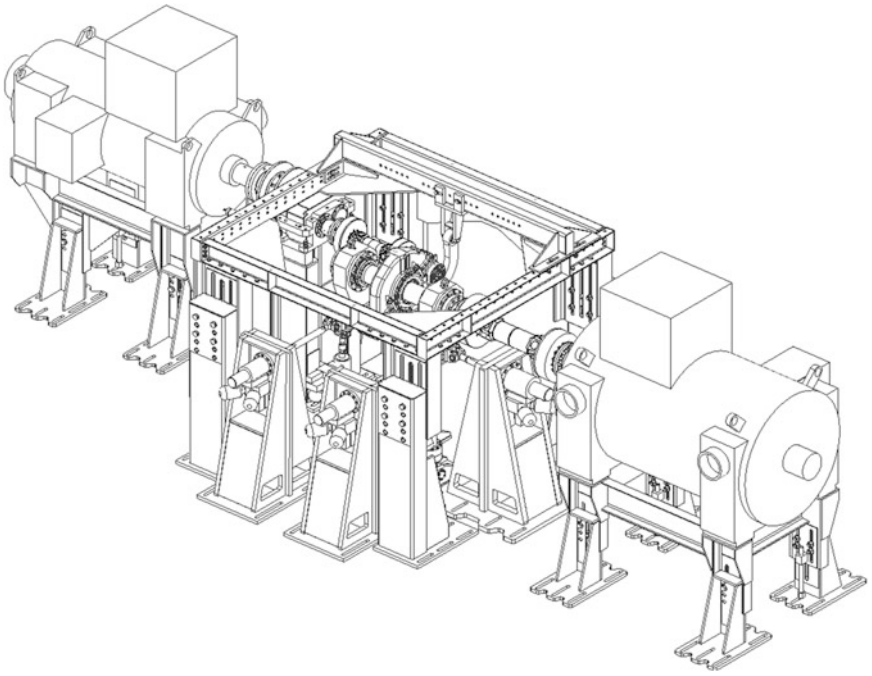

Fig. 2 Full assembly of test rig

3 System for Impact Loading

Gearbox will be tested in two modes. One is impact load in three directions. The other one is torque load that simulates load from traction. This paper is focused on the first mode—impact load.

In duty, the gearbox faces many vibrations and impacts transferring via output shaft from wheels. Those impacts are caused e.g. by imperfect connections between rails or by rough surface of rails. These loads can rapidly decrease operating life of gearboxes therefore it is worth to study behavior of gearboxes under this type of load.

Main parameters of system are maximal acceleration and amplitude of impacts that could be reached by the cylinders. For each axis defined in Fig. 3, is acceleration 10 g and amplitudes are $[x, y, z] = [\pm 6, \pm 6, \pm 25]$ mm, maximal reachable frequency of impacts is for all axes 2 Hz.

System for impact load is hexapod structure that compounds of six hydraulic cylinders that are connected to a frame that holds tested gearbox. Cylinders are to the frame connected by spherical joints. Supporting structures for cylinders are designed to hold out the reactions force during test cycle.

This layout allows us to simulate many modes of loading. It is not just limited to impact load, but we can simulate e.g. inclination of gearbox during a ride in arc and other.

3.1 Hydraulic Cylinders

Cylinders used in structure are hydraulic servo-cylinders CGS280 from Bosch Rexroth AG that are intended to be used in test rigs like this.

For axes defined in Fig. 3, there are used following cylinders with basic force:

- X—two 40 kN cylinders,
- Y—one 100 kN cylinder,
- Z—three 40 kN cylinders.

For safety the hydraulic system is equipped with backup unit that holds system alive for at least 1 min in case of electricity blackout. One minute is time period in which all systems of test rig are shut down and rotating parts are yet stopped by mechanical-hydraulic safety brakes.

3.2 Frame for Holding Tested Gearbox

Frame that holds the housing simulating wheels is welded structure. It compounds of standard rectangular profiles that are in certain places stiffen with steel sheets.

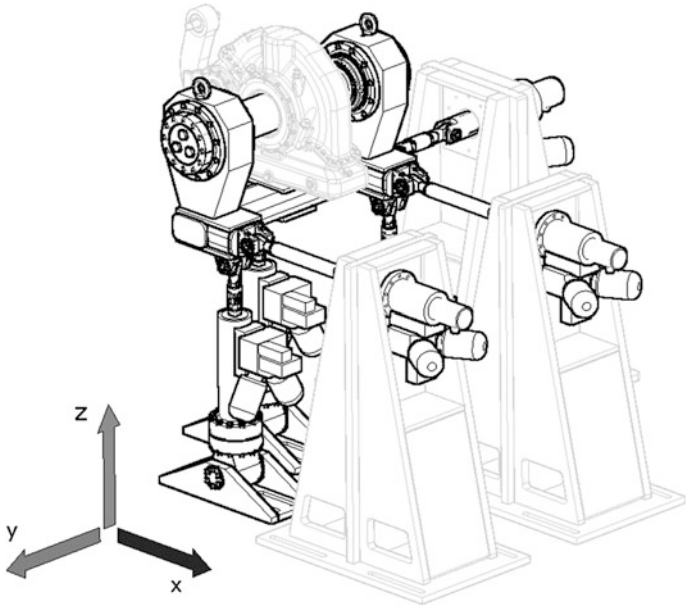

Fig. 3 System for impact loading with defined axis system

Fig. 4 Frame with clamped gearbox

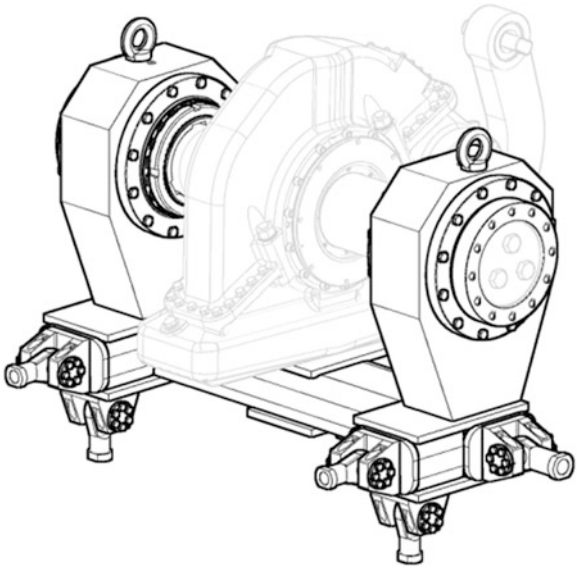

As could be seen on Fig. 4, to the frame are also attached houses for spherical joints. These joints are bought from company Rota Precision Ltd and are specially designed for dynamic loads.

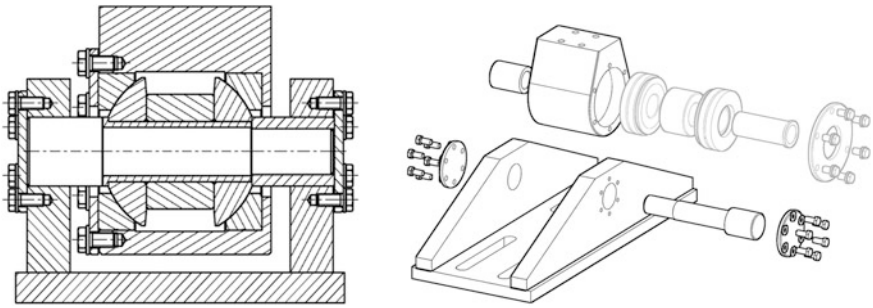

Fig. 5 Spherical joint (*left figure*) and spherical joint assembly (*right figure*)

3.3 Spherical Joints

Spherical joints are essential part of hexapod structure. It was decided to design joints that crates base for Z axis (Fig. 3).

The part that allows spherical motion are two against each other preloaded axial spherical plain bearings. They are placed in housing and preloaded with clamping sheet and bolts from side of housing. Both bearings are on the hinge that is locked in base housing that is clamped to the base table with T-grooves. This layout allows spherical motion in 5° to all sides. That is more than is needed (Fig. 5).

4 Frames for Motors

One of the requests given at the beginning of development of test rig was modularity. The rig is intended to be used for more types of gearboxes, so even the frames that holds motors should be vertically adjustable.

The construction of frames are designed to transfer the load from motor right into the ground. They were also optimized using modal analysis in FEM for first Eigen-frequency to be as high as at least 50 Hz because of exciting frequencies from motors.

Frames compounds of 4 adjustable legs that are together connected with standard U profiles. All parts are designed from sheets and are welded together since it is very cheap and productive technology.

The frame for driving engine (Fig. 6) was customized upon changed size of base desk during cost-reduction revision of stand during development.

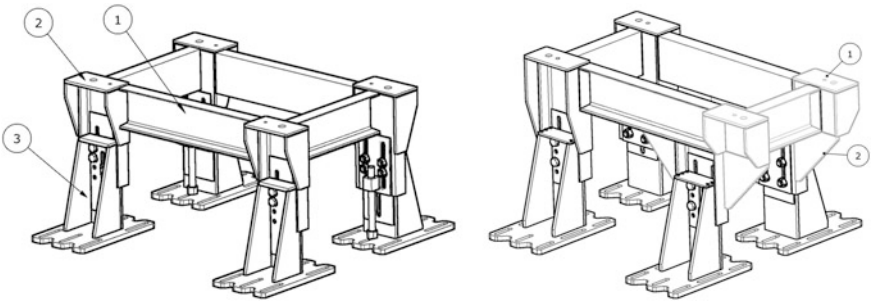

Fig. 6 Frame for load and driving motor

5 Conclusions

In this paper summarized circa one year long development of test rig for gearboxes of rail vehicles. Limited size of paper does not allow to describe each particular design phase, so here is presented the state of project in the end of January 2013. Currently this test rig is being built in Wikov MGI.

Acknowledgments The research work reported here was made possible by Ministry of Industry and Trade of the Czech Republic grant No. FR-TI3/261.

Reference

Dynybyl V (2009) Výkonová metrologie: experimentální podpora vývoje a inovací mechanismů ve strojírenství, Vyd. 1. České vysoké učení technické v Praze, Praha, 152s. ISBN 978-80-01-04325-7

The Elimination of Gear Noise in a Six Speed Gearbox for Passenger Cars

J. Prokop

Abstract The article deals with analysis of the noisiness sixth gear and determination of correction of cogs, which could remove negative cogs noisiness.

Keywords Gearbox · Helical front gears · Noisy gears · Modification of gears

1 The Initial Situation

At the start of production in Mlada Boleslav of the new 6-speed gearbox type for passenger cars, there was an identifiable noise in load mode from the engine when the sixth gear was engaged in the 2,100 RPM to the 2,900 RPM range (see Fig. 1). The limitation of top rotations are based on the speed limit on the roads in the Czech Republic.

1.1 Analysis: Quality of Gears

The first step in the analysis was the measuring of the gears. No anomalies were identified (errors during the production of parts—Fig. 2) which could have led to increased noise from the gears.

Following on from the above, the next step in the analysis of produced noise was the testing of changes under load in the gearbox.

J. Prokop (✉)
Škoda Auto, Mladá Boleslav, Czech Republic
e-mail: Jaroslav.prokop2@skoda-auto.cz

L. Ševčík et al. (eds.), *Modern Methods of Construction Design*,
Lecture Notes in Mechanical Engineering, DOI: 10.1007/978-3-319-05203-8_25,

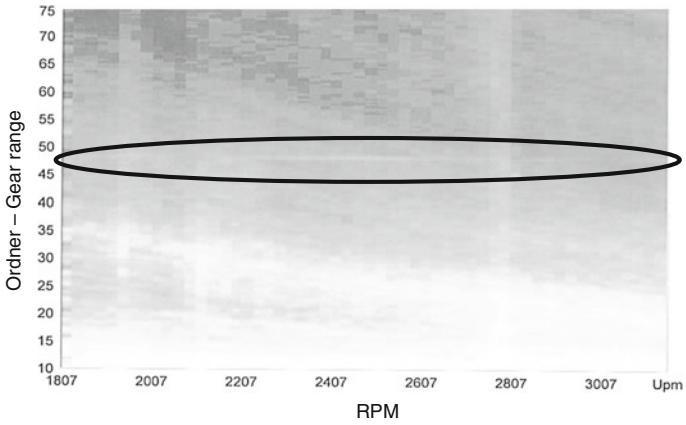

Fig. 1 The recorded sound from a microphone in the vehicle whilst in sixth gear—the area marked in blue reflects the increased noise from the gears

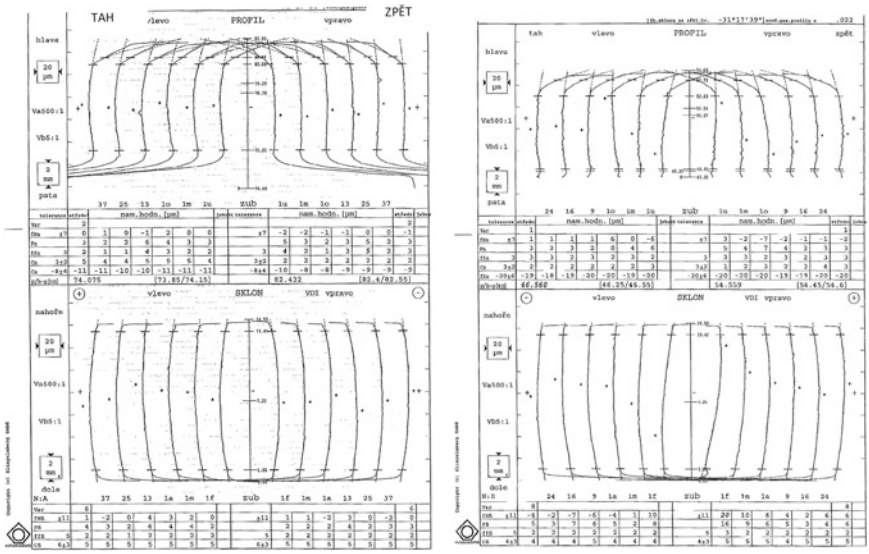

Fig. 2 Gear drive deviations

1.2 Analysis: Track Frame

The entire gearbox was placed on a text bench simulation an installed on in a car under a gear torque load as required. In our case it was a load of 1, 41 and 100 % of the maximum load transmitted torque (Fig. 3).

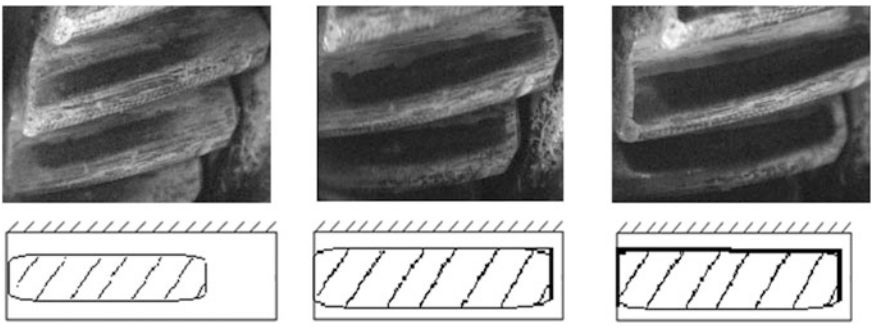

Fig. 3 Track frame of 1, 41 and 100 % of the load torque—the strong line shows the *sharp edge* of the gear frame

From this track i tis obvious that at a low load there is no contact with the sharp edge, whilst edge contact becomes visible during a larger load. It is therefore apparent that as a result of deformation of the entire system gear tracks need to be adjusted from the left to the right gear. This could compensate for deviation of the helix angle.

2 Optimization

The adjustment described above could compensate for deviation of the helix angle under a load (Linke 2010).

2.1 Optimization: The Examination of Optimized Gearing

On the basis of these observations the gears were made with the corrected cog helix angle to compensate for the displacement of the track under load (see Fig. 4).

2.2 Optimization: Track Frame

Newly corrected gears were tested again on the track frame under the same load levels.

In Fig. 5 it can be seen that the correction of angle deviations of the helical bolt at about 10 μm, eliminated the sharp edges of the frame at a load of 41 %.

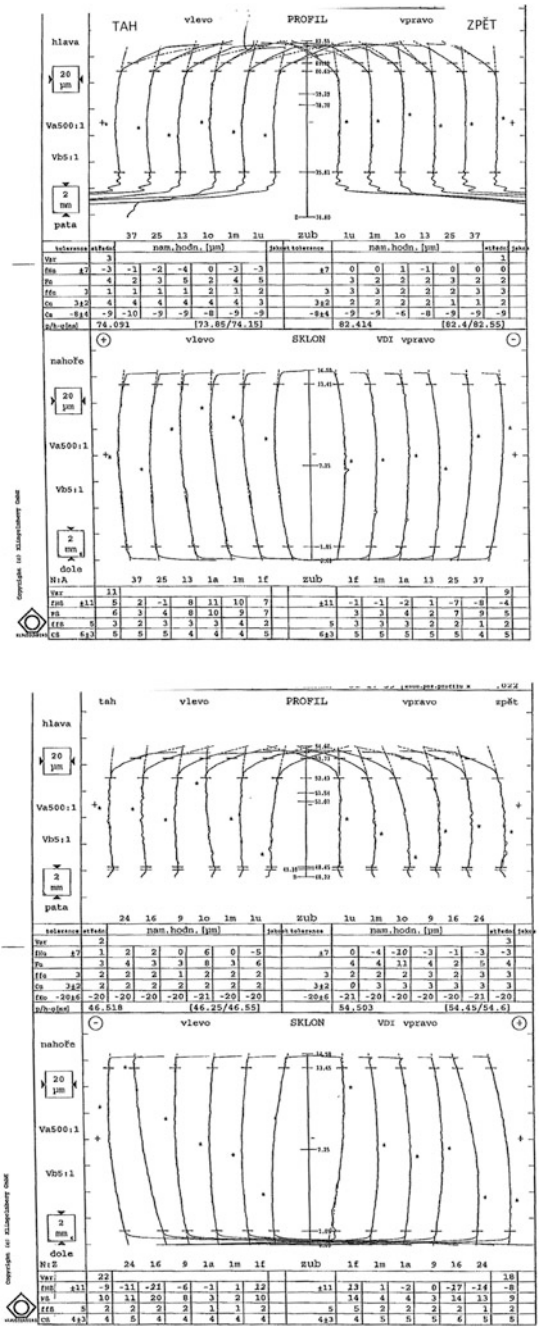

Fig. 4 Optimized gear drive deviations

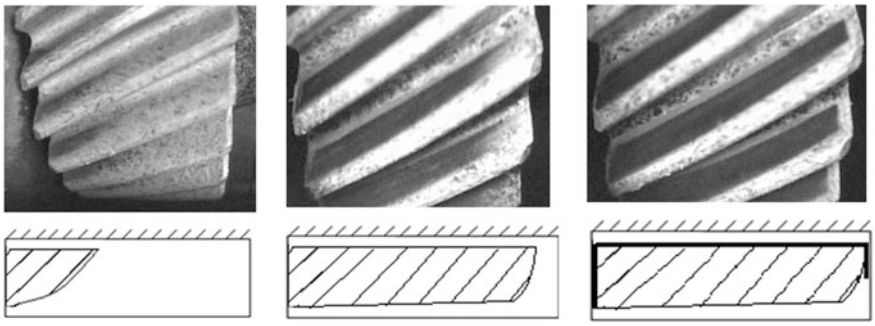

Fig. 5 Track frame of 1 %, 41 % and 100 % of the load torque—the strong line shows the *sharp edge* of the gear frame

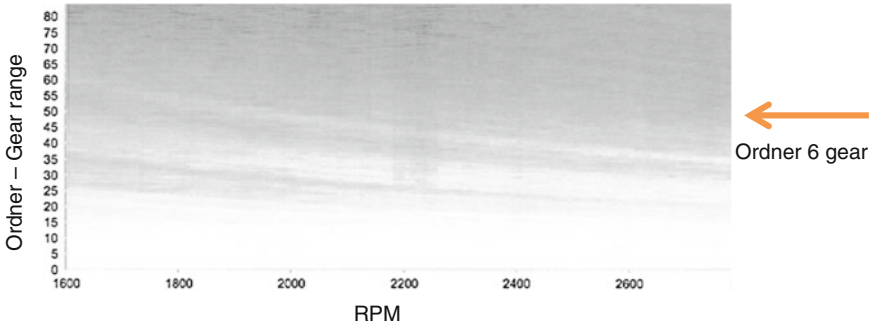

Fig. 6 The recorded sound from a microphone in the vehicle whilst in sixth gear—the area indicated by the *arrow points* to the activity of the sixth gear

2.3 Optimization: Verification of Noise in the Car

The optimized gears that were made based on the results of the stop were tested in the car (Moravec 2009).

No noise from the sixth gear in the car was recorded in the car throughout the test speed range (Fig. 6).

3 Conclusion

The tests in the car revealed that a change of 10 μm of the helix angles removed the noise from the 6th gear. This modification was successfully implemented into gear production.

References

Linke H (2010) Stirnadverzahnung, Berechnung—Werkstoffe—Fertigung, Hanser, 2010
Moravec V, Dejl Z, Němček M, Folta Z, Havlík J (2009) Čelní ozubená kola v převodovkách automobilů. VŠB-TU Ostrava

Design of the Masks Civil Protection

L. Ševčík

Abstract The contribution describes the design of the masks for use in civil protection. The aim of the research was the development of a new type provided that the production of the filter will be large series. The filter contains a special layer of nanofibres for filtering very small particles. Advantage of the design is easy to manufacture and assemble filter. For the optimization design was used DFX methods. In conclusion is a comparison of measurements of each variant.

Keywords Masks · Filters · Layer of nanofibers · Design · Assembly

1 Introduction

This paper describes the design of the masks for use in civil protection. The aim of the research was the development of a new type provided that the production of the filter will be large series. The filter contains a special layer of nanofibres for filtering very small particles. Advantage of the design is easy to manufacture and assembly filter. For the optimization design was used DFX methods. In conclusion is a comparison of measurements of each variant. The goal is to design a new type of anti-particulate filter mask in the project "Applied research on a new generation of protective masks with nano to increase the protection of the design, technological and material aspects." The paper deals with design easily replaceable filters containing nanowires and nano/microparticles of different parameters based on nanofibers intended for detection of microorganisms and mount system nano filters. For this task will be solved only with particle filters. These do not contain

L. Ševčík (✉)
Department of Design of Machine Elements and Mechanism, Faculty of Mechanical Engineering, Technical University of Liberec, Liberec, Czech Republic
e-mail: ladislav.sevcik@tul.cz

L. Ševčík et al. (eds.), *Modern Methods of Construction Design*,
Lecture Notes in Mechanical Engineering, DOI: 10.1007/978-3-319-05203-8_26,

absorbent material—sorbent. They work on the principle of mechanical sorting, not run them in any chemical reaction.

The particles can be captured on the filter surface—surface filtration and they are deposited on the surface of the screen. These filters can be cleaned mechanically. The second types of filters are the filters in which the particles are settled in the volume of the filter. These filters are not easy to clean, since the particles are within a volume of the filter material. There are often used pre-filters in the filters to increasing operational time of filter, the filter membrane protects from adverse dimensionally larger particles. Filter is superficial and pre-volume.

2 Particle Filtering

Filtration is the method of separating insoluble solids, liquids and gases from other solids, liquids or gases under different particle size of fractions or dissolving. The active fraction in the filter compared to a carrying medium, which is not bound. To understand the purpose and work of breathing filters are home to some basic knowledge (Kimmer 2012).

Filters for protective masks are constructed from several points of view. According to their sorption capacity, purpose and versatility they can be divided into:

- Civilian industrial protective filters they are usually dedicated to a particular pollutant, which bind with high efficiency even after a long time, but other contaminants bind weakly or not at all (Reischel and Knivsland 1997).
- Normal protective filters are designed for use in medium containing 1 % to a maximum of 2 % by volume (10,000–20,000 ppm) emissions. Higher concentrations of pollutants the small filter breaks through very quickly, and its use is inappropriate. The only reliable means are the self-contained breathing apparatus with own air supply, independent of the ambient atmosphere.
- Breathing apparatus should be used when the minimum amount of oxygen in the air is 17 %, because the decrease in the amount of oxygen below this level (normal value is 20.9 %) would have been choking the bearer of the mask due to a lack of oxygen, but that filter would be otherwise functional. With this is to be expected in the case that the site (enclosed spaces are especially dangerous) there was a burning or outburst of large quantities of gas is heavier than air.

There are two basic ways to capture and disposal of toxic substances using a filter—it is filtration and absorption:

Filtration—it uses the physical, chemical or physico-chemical binding contaminants on the substrate filter without changing its molecule.

Absorption—toxic substances are stored inside the structure of the absorbent media/dissolve therein. The slurry (solid fraction in the liquid), the spillway through the filter, wherein fluid flows through a solid fraction having a particle

size ≥ pores in the filter will remain captured on the filter or in the structure of the filter. On the basis of filtration works against smoke liner protective filters or automotive air filter. Pure liquid filters are not used in protective masks.

The other ways are Adsorption and Reaction. These will not be used in this design of filter. Filtering ability (effectiveness) is given by the number of beta, where beta is the ratio defined by the relationship:

$$\beta x = Nu/Nd, \tag{1}$$

where

x specifies the size of particles, which are derived from particle counts listed in a relationship,

Nu the number of particles larger than the dimension x at the input to the filter in the unit volume of the filtered medium,

Nd the number of particles larger than the dimension x at the output of the filter unit volume the filtered medium.

When the filter element declares capture for particles with dimensions x = 25 μm and $\beta 25 = 200$, this means that if the filter is 10,000 particles per unit volume at the output of the filter (the filtrate) may be 50 particles larger than 25 micron in the unit volume of the filtered liquid.

Filtration efficiency E is then given by:

$$E = (1 - \frac{1}{\beta}) \cdot 100 = (1 - \frac{1}{200}) \cdot 100 = 99.55\,\%. \tag{2}$$

All filters have the dynamic adsorption capacity and breakthrough time. Dynamic sorption capacity determines how many grams of a given pollutant filter is able to capture or destroy before its phagocytic capacity will be exhausted and the penetration through the filter pollutants. This means hitting the person wearing the mask of the pollutants and the loss of the protective properties of the mask until you replace the filter. Here it should be noted the fact that the filling of the sorbent in the filter does not take place smoothly, but the air (and with it the pollutants) is drawn path of least resistance. That can lead to a situation where a pollutant filter pierce scored quickly through a relatively small volume of the filter, while the majority of pollutant sorbent is not still filling up. This is necessary for the real-treated with caution. Manufactures of filters measures set sorption filter capacity under optimal laboratory conditions, which in reality does not usually occur, and the filter capacity is smaller.

Breakthrough time is the time in minutes after which the filter is capable of capturing the pollutant in its known concentration in the air, known dynamic sorption capacity of the filter and known volume of air passing through the filter. Generally, a high concentration of pollutants in the air or high flow air filter can shorten the period during which the filter is capable of protecting its wearer.

Fig. 1 Designed filter

3 The Proposed Structure of the Particle Filter

Connection with the filter masks was implemented through the surface masks—flat surface with seal (Lenfeld 2013)—seating area filter in the face of the mask must be sealed in the area, namely in front of the filter. The filter should have a greater rigidity than the abutment face masks that could be molded. Thrust mechanisms must be spaced around the circumference.

The advantage is its simplicity of shape of filter—no need to screw surfaces.

The disadvantage of this connection is the size of the area and a small contact pressure, the possibility of penetration filtered pollutants.

A common feature for composing the filter material is to get as much surface pleated fabric into the smallest possible volume. The offered design uses supporting form with open ends.

Design of the particle filter is based on the mechanical properties of textile filter material and the possible design dimensions in the mask, Fig. 1. The goal was to filter area should be 1.5 dm^2, material "Spanbond" in two layers of polypropylene and between them is a layer of nanofibers. This textile sandwich structure has a relatively low flexural rigidity and low buckling and so it was decided to positively support the filter fabric layer parts cover. The following image is composed of outdoor filter cover and support work, which fits into the inner support part, in which there is pre-stacked filter fabric. These parts fit together and cover both sides of the filter layer. Parts can be glued. Fabrics in inner comprise a pair of interlocking fingers alternately, so that one finger holds the previous tooth of inner part of the filter the filter material and the second finger stubs to the next tooth.

Filter is composed of two plastic parts. In one of them is stacked filter fabric with nanofibers. At the bottom of this section there are the cover ribs preventing damage to the filter layer. The second plastic part comes from the upper side and protects the filter layer from the outside. On the upper part the glue is applied. Both these parts including the filter layer are compressed and combined with glue,

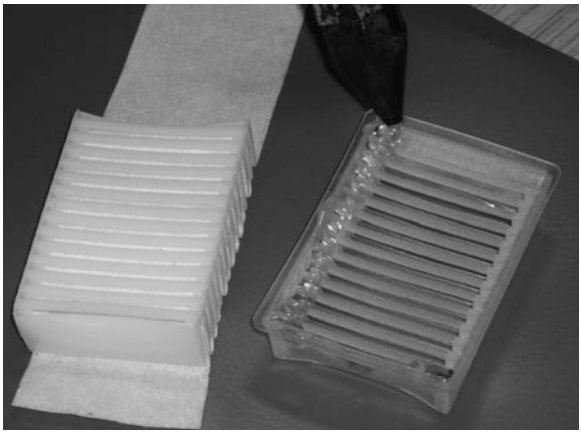

Fig. 2 Assembly of filter glued with hot glue

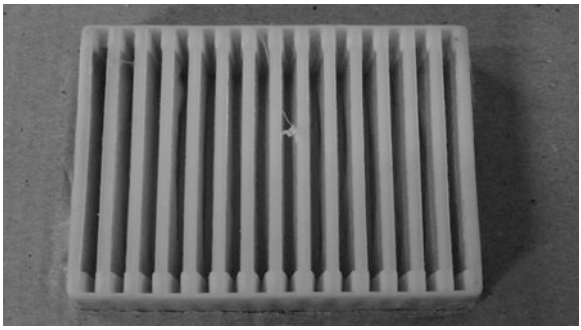

Fig. 3 Real filter glued to paper pads

Fig. 2. The filter element is supported by ribs and sealing facets around the circumference of the filter.

Several parts of filter were produced by rapid prototyping. The filter was glued into the opening paper pads, Fig. 3, and tested on a special machine. We measured passes particles of varying size and pressure drop across the filter. Pressure drop is an important variable in the comfort of using the filter.

For the tests were prepared several filters without gluing or with various adhesives. The measurement results of different variants show that adhesion does not affect the passage of particles. However, it is very likely that in spite of these results the filters will be glued for safety reasons, Fig. 4.

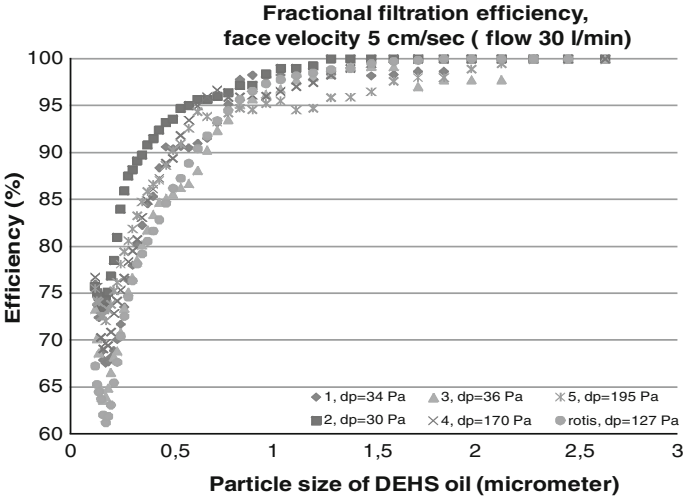

Fig. 4 The measurement results

4 Conclusions

We managed to design a simple filter made from filtration textile and two plastic parts. Two moldings support the filter fabrics maintain its shape, fix textile at the perimeter seal against the ingress of particles and provide protection against mechanical damage. Advantage is the ease of automated assembly equipment filters based on pneumatic actuators. Installation is carried out including the application of the adhesive to reduce the probability of penetration of bacteria and viruses. The measurement results of different variants show that adhesion does not affect the passage of particles. However, it is very likely that in spite of these results the filters will be glued for safety reasons.

Acknowledgments Thank you to the project of Ministry of the Interior of the Czech Republic. This paper was supported by the project VG20122014078.

References

Kimmer D (2012) Research and development of filter materials based on nanowires and their application to filter protective face masks. MPO

Lenfeld P (2013) Applied research on a new generation of protective masks with nano to increase the protection of the design, technological and material aspects. MV

Reischel J, Knivsland D (1997) US patent Des. 378,610, Full face respirator

Vibration Device for Long-Term Testing of Car Seats

P. Srb and V. Fliegel

Abstract Testing of automobiles is important for increasing safety and passengers' comfort. The device is designed to simulate the load of a seat during a car ride under different conditions. The device can work continuously for several days unattended. Long-term testing is useful to obtain knowledge about wear-out particularly of the comfort layer and other parts of the seat. Electric step motor and cam mechanism were used to create the vibrations.

Keywords Automobile seats · Vibrations · Long-term testing · Cam mechanism

1 Introduction

The design for the vibration testing device was commenced due to the need for long-term testing of car seats in proseat company. There were following initial requirements.

On the seat there should be placed an indentor and relevantly substantial weight oscillated by required frequency. For example, an electric motor with eccentric flywheel is used for the oscillating; it is also used as a part of the weight. The device must allow the seat to clamp with a backrest; the backrest shall not touch the indentor or other device components during the test.

Since there are interferences of various oscillations during the test, it is desirable that the frame of the device should be relatively robust. The test consists of

P. Srb (✉) · V. Fliegel
Technical University of Liberec, Liberec, Czech Republic
e-mail: pavel.srb@tul.cz

V. Fliegel
e-mail: vitezslav.fliegel@tul.cz

L. Ševčík et al. (eds.), *Modern Methods of Construction Design*,
Lecture Notes in Mechanical Engineering, DOI: 10.1007/978-3-319-05203-8_27,

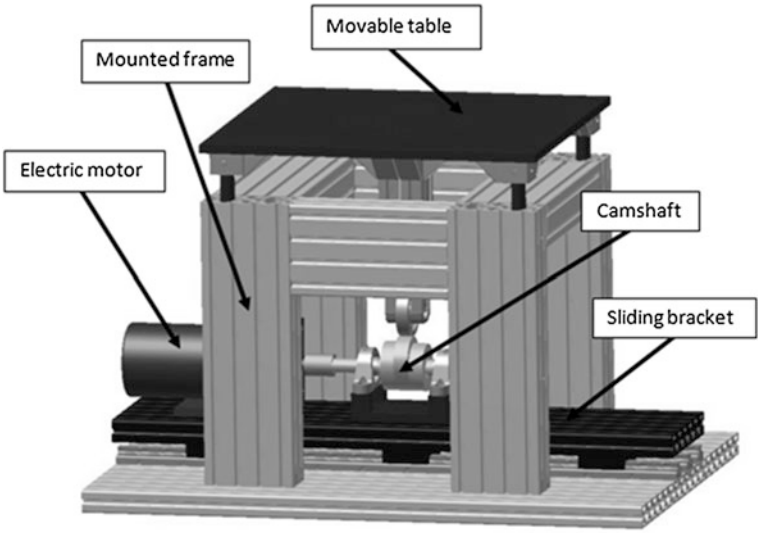

Fig. 1 First concept of vibration device

sections with different frequencies e.g. 5,000 × 0.5 Hz + 20,000 × 2 Hz + 40,000 × 5 Hz, pulse frequency does not have to be kept accurately (±20 %), it is desirable that the device can work continuously for several days, frequency rearrangement does not have to be automatic, but it would be an advantage. The device should not make impossible later equipment of scanning the current position of the indentor, that would extend the use of the device for different types of tests.

2 Description of the First Concept

The first concept of the vibration device is shown in Fig. 1. Main part is a mounted frame made of aluminium profiles (Item 2007). On a base plate is placed a sliding bracket. On the sliding bracket is fastened an electric step motor which is connected to a camshaft module by flexible coupling. The camshaft module contains three changeable cams. Into the frame is inserted a movable table which is secured in four points. In the middle of the table is placed a support with a roller cam follower which transfers rotation of the camshaft to reciprocating move of the table.

Table 1 Revolutions and acceleration for each cam

	Frequency (Hz)	Revolutions (rpm)	Maximal acceleration (ms^{-2})
Cam 1	1	30	0, 6
	2	60	2, 2
	3	90	5
Cam 2	4	120	3, 3
	5	150	5, 2
	6	180	7, 5
	7	210	10
	8	240	7, 1
Cam 3	9	270	9
	10	300	11
	11	330	13, 4
	12	360	16
	13	390	18, 8
	14	420	21, 8
	15	450	25

3 Camshaft Design

Later, the design requirements on the process of vibrations were defined more precisely: achieving pulses of acceleration 25 ms^{-2} with frequency of repetition 1–15 Hz. After considering several possibilities it was determined that for acceleration 25 ms^{-2} at the frequency 1 Hz it would require a cam with diameter of hundreds of mm and the whole device would be too hard on engine power. For these reasons the requirements were revised and a compromise solution was proposed when there would be used three cams for three frequency bands which can be seen in Table 1. In this solution there is achieved the initially required acceleration 25 ms^{-2} only at the frequency 15 Hz, but the requirements on the size of the device and engine power are acceptable.

The detailed design of the cam mechanism was made using a design accelerator which is integrated in the software Autodesk Inventor Professional 2012.

The course of acceleration was chosen so that there will be two pulses of positive acceleration during one rotation of the cam symmetrically distributed after 180° rotation of the cam as shown in Fig. 2.

There were designed three cams for nominal values of acceleration 5, 10 and 25 ms^{-2}, with diameter of the base circle 80 mm and for diameter of the roller follower 90 mm. For a strength check it was calculated with accelerating weight 80 kg. The cams and the camshaft shown in Fig. 3 were designed so that they could be changed easily e.g. due to changes in the required characteristics of acceleration.

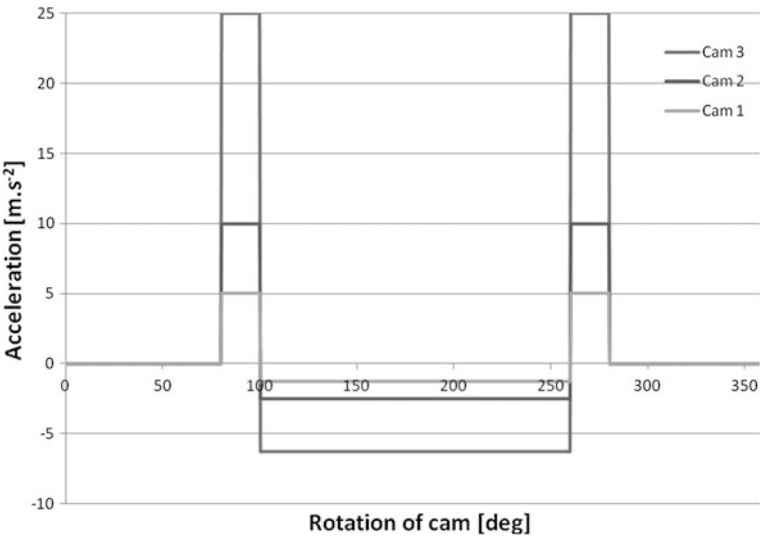

Fig. 2 Course of acceleration of each cam

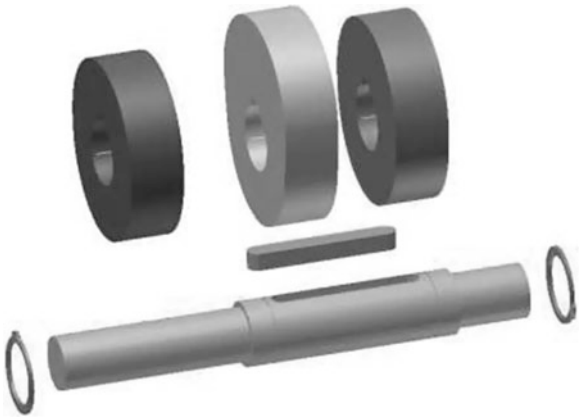

Fig. 3 Shaft with changeable cams

4 Electric Equipment

The vibration device is powered by a pair of three-phase stepper electric motors YK31328A (Fig. 4) with maximal torque 50 Nm. Motors are connected in tandem mode and controlled by YKB3722MA stepping driver with microstep (Fig. 4). The stepping driver is operated by computer by RS323 protocol.

The vibration device is equipped by two position sensors and two accelerometers. Data capturing of measured quantifies supports an external multifunction data acquisition device connected to the computer by USB protocol (Petřík 2011).

Fig. 4 Stepping electric motor (*left*), microstep stepping driver (*right*)

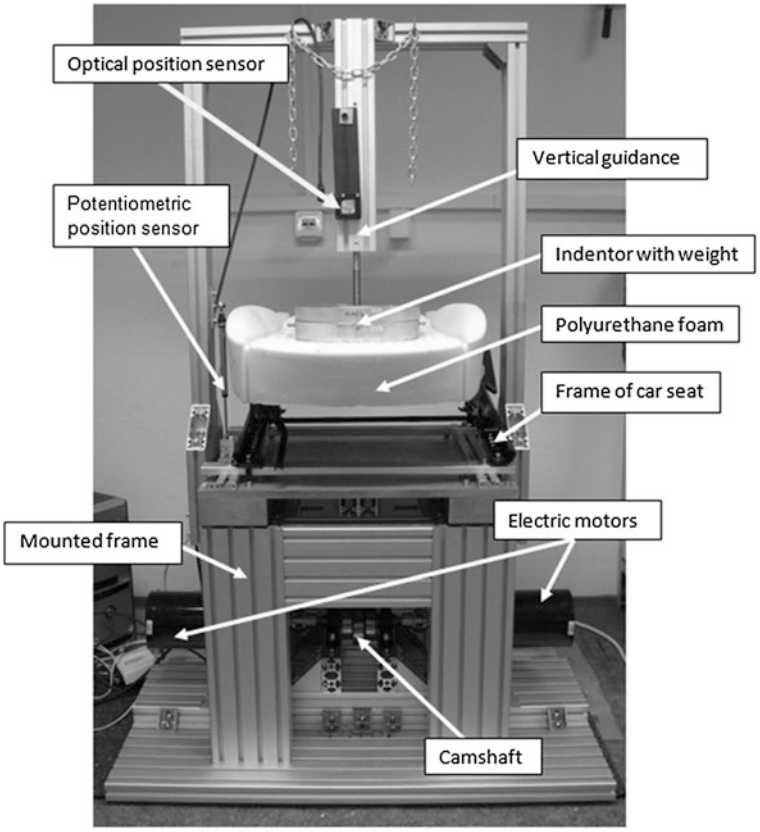

Fig. 5 Final design of the vibration device

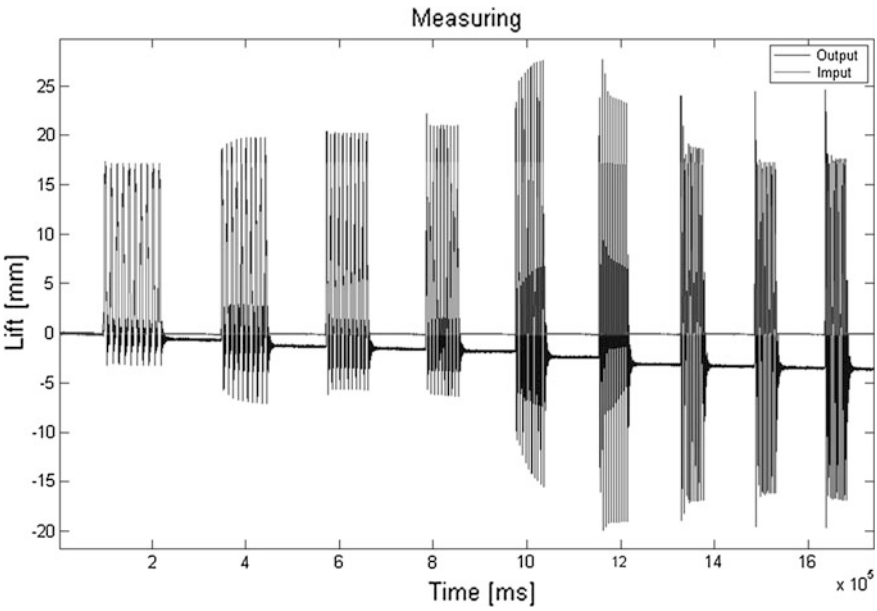

Fig. 6 Example of measurement cycle

5 Final Design

The final design is shown in Fig. 5. Unlike the first design there were used two step motors connected into tandem for greater power. An upper frame allowing vertical guidance of load was added to the construction and another frame was added to the table easy mounting of the seat.

Replacement of the cams is possible manually. After locking the table in the upper position it is possible to move the console with motors and cams to the position for running concrete cam.

6 Conclusion

The device allows performing dynamic tests of foam parts as well as whole seats in the frequency range 1–15 Hz, lifting range 3–17 mm (Fig. 6 shows an example of measurement cycle). The excitation signal generated on the cam is determined by its profile and rotation. While respecting permanent contact of the cam with the table (there is no bounce), the excitation signal is very stable even in long-term interval. This device is particularly suitable for the performing of long-term durability tests of car seats that are relatively expensive in real traffic (approx 80,000 km).

Acknowledgments This device was made with support of company proseat Mladá Boleslav s.r.o.

References

Item MB Building Kit System Catalogue (2007) Item Industietechnik und Maschinenbau GmbH, Solingen

Petřík J, Martonka R (2011) Measuring platform for seat testing. Sborník referátů: 52. konference kateder částí a mechanismů strojů s mezinárodní účastí : 6.-9.9.2011, Ostravice, horský hotel Sepetná. 1. vyd. Ostrava: Vysoká škola báňská—Technická univerzita Ostrava, pp 185–187. ISBN 9788024824505

Design of Suspension Roller Working Units Used in Agricultural Machines

P. Syrovátka, V. Dynybyl and J. Andruš

Abstract This article deals about the design of suspension roller working units for agricultural machines. The design should be not so complicated, and not very expensive. Also must be robust, with respect of the working conditions on field. There was carried out experimental measurement in real conditions, then analysis of measured data was made. Also conceptual design and MKP analysis are included in this article.

Keywords Suspension · Rubber · Experimental measuring · MKP analysis · Silentblock

1 Introduction

The goal of this work is to design part of an agricultural machine, which eliminate load impact from ground to the machine. These impacts reduce life of the frame and elements like bearings, screw connections and other joints. Principally roller bearings are the most defective elements on the agricultural machine.

Position of the critical point of the agricultural machine is shown in the Fig. 1. Detail of the used bearing unit is in the Fig. 2.

Knowledge of an operational load is needed to design the dimension of a suspension element, which will eliminate load impact to the machine. Equipment

P. Syrovátka (✉) · V. Dynybyl · J. Andruš
Czech Technical University in Prague, Prague, Czech Republic
e-mail: pavel.syrovatka@fs.cvut.cz

V. Dynybyl
e-mail: vojtech.dynybyl@fs.cvut.cz

J. Andruš
e-mail: jan.andrus@fs.cvut.cz

L. Ševčík et al. (eds.), *Modern Methods of Construction Design*,
Lecture Notes in Mechanical Engineering, DOI: 10.1007/978-3-319-05203-8_28,

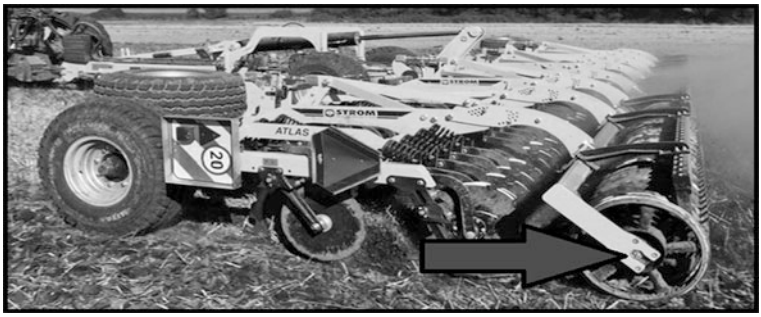

Fig. 1 Position of the critical point

Fig. 2 Detail of bearing units

for the measurement of the operational load was prepared, calibrated in laboratory, than installed on the machine and loads were measured in the real conditions on the field (Harris 2002).

Also mechanical parameters of rubber materials are needed to be determined. Rubber material is preferred by authority to the design of suspensions. Rubber sample for tension test was prepared and tested (Horný 2012).

Then the suspension element was designed and verified using MKP analysis.

2 Experimental Measuring

2.1 Preparation of the Measurement

Measuring of the operational loads was made on the machine in the real conditions. The position of the measuring point must be close to the critical point. Four critical points were chosen on the machine, see Fig. 3. For this reason four special supports (equipment for measurement) were designed and manufactured. Then strain gauges were installed on the special supports.

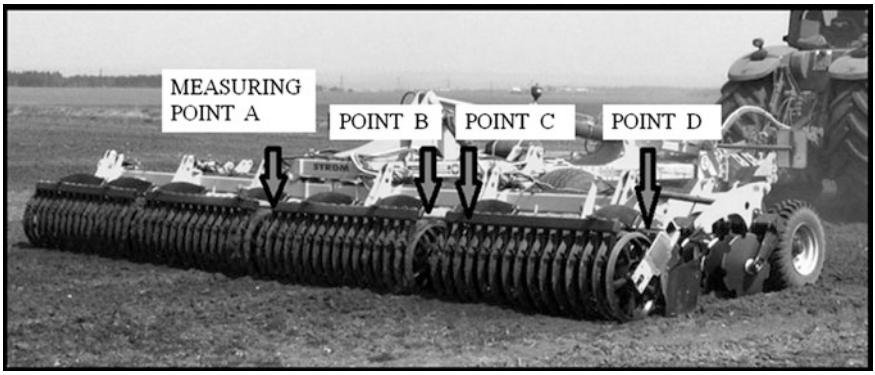

Fig. 3 Measuring points on machine Swifterdisc

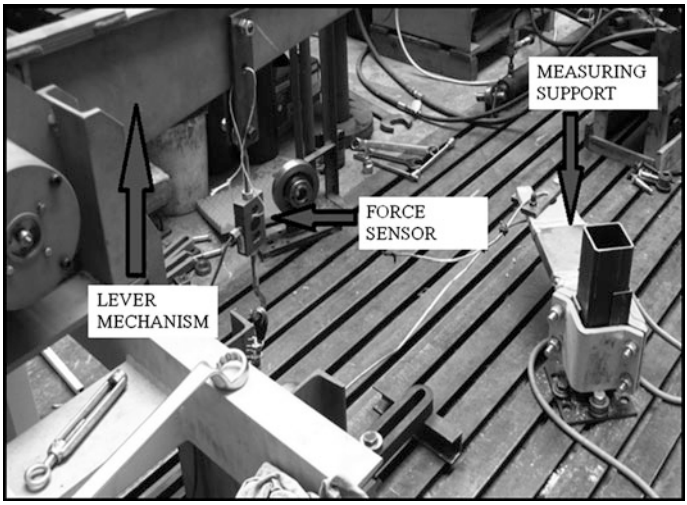

Fig. 4 Calibration of support for measuring operational load in laboratory

2.2 Calibration of the Measuring Support

After installing of the strain gauges each support was calibrated in the laboratory in Faculty of Mechanical Engineering, CTU, see Fig. 4. Force sensor was used, signals from force sensor and from support were recorded and then evaluated. Reasons Reason of the calibration was to get the measuring constant of the measuring supports.

Fig. 5 Measuring in real conditions

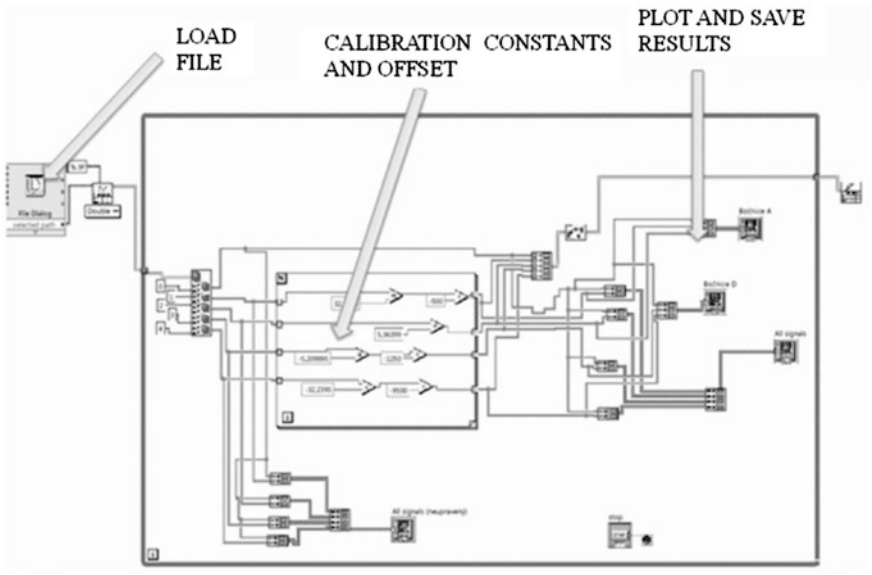

Fig. 6 Software transforming record data to force

2.3 Measuring in the Real Conditions

Calibrated measuring supports were installed on the machine, cables, measuring equipment and PC were prepared on the machine and in a tractor cabin. Installation and the measuring equipment are required not to limit operation of the machine and also have to be protected against dust, water and other mechanical effects like stones (Fig. 5).

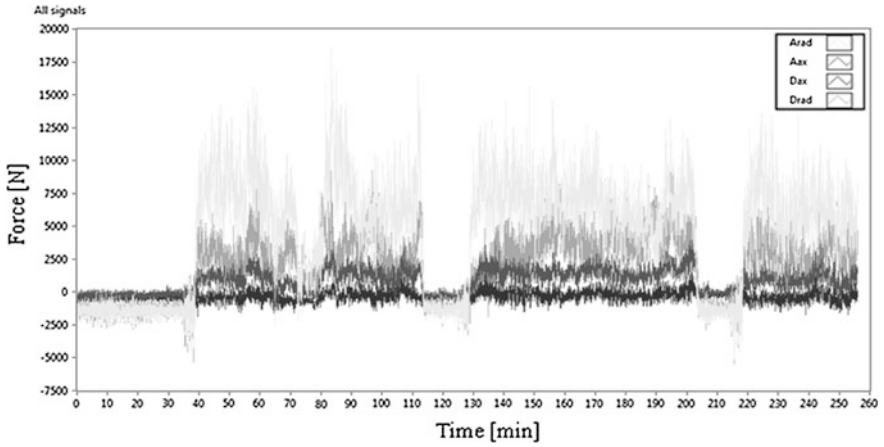

Fig. 7 Plot data from measuring in real conditions

3 Analysis of Measured Data

Four signals were recorded and then transformed in LabView to forces using calibration constants. Scheme of the used program is in the Fig. 6. Two signals represent vertical loads and other two signals represent horizontal loads. Vertical loads press on the bearing in radial direction and horizontal loads press on the bearing in axial direction.

Results are plot in the graph, example of the graph is in the Fig. 7. It is possible to distinguish phases, when machine is working and phases, when machine make turn at the end of the field. During the working phase vertical loads were higher than the horizontal loads. In the working phase all the weight of the machine is carried by a tractor and roller. In the turning phase radial loads were negative because machine goes on axle and measuring support hold roller.

4 Design of Suspension

4.1 Conceptual Design

Some conceptual designs of the suspension were created. One of the designs is in the Fig. 8. It contains a ring of technical rubber vulcanized between two steel rings. Outer ring is supposed to be installed in the housing and a rolling bearing is in the inner ring. Rolling bearing resists high speed of roller better than a sliding bearing. Rubber ring absorbs load impacts and life of the bearing is increased.

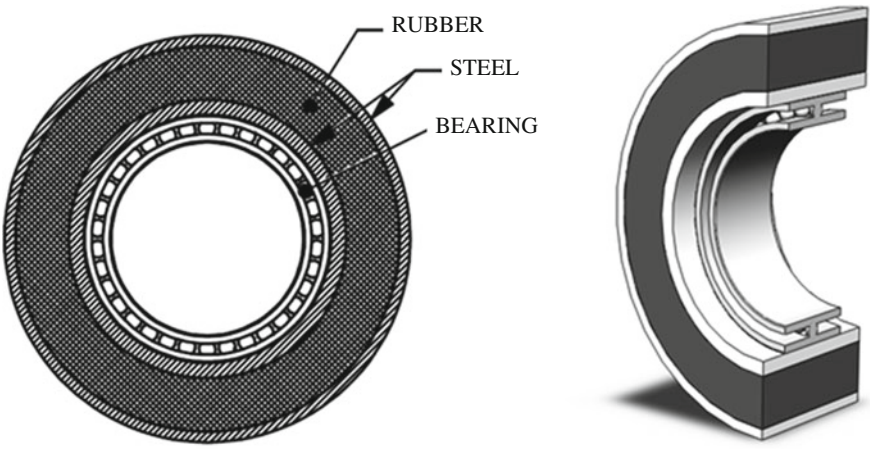

Fig. 8 Conceptual design of suspension

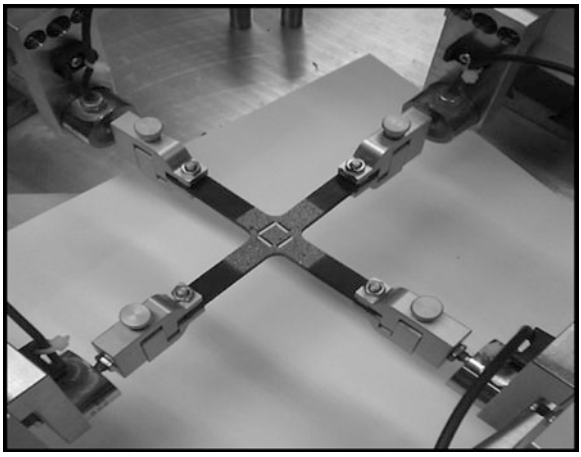

Fig. 9 Biaxial tense test of rubber

4.2 MKP Analysis

MKP analysis needs many of mechanical parameter of rubber material for simulating hyper-elastic model. Samples for linear and biaxial tense test were prepared and manufactured in two materials which were recommended by producer of technical rubber and silentblocks. These tests were realized in laboratory of Faculty of Mechanical Engineering, CTU, Fig. 9.

MKP model uses mechanical parameters of rubber obtained from tension tests and loads on the model were obtained from experimental measuring. Load simulation of a rubber suspension is shown in the Fig. 10.

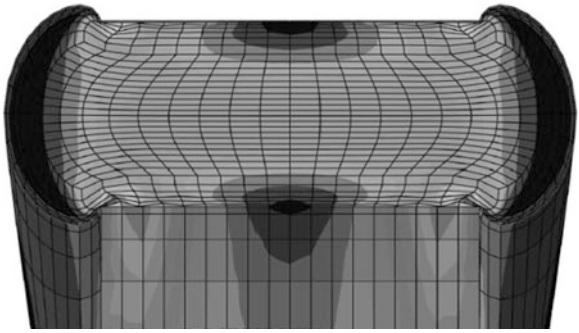

Fig. 10 MKP analysis

5 Conclusions

This article is brief cross-section of a comprehensive work which contains data from measuring, many designs of suspensions and MKP analyses of these designs. One example of the suspension design is shown in this article. There are other designs of the suspension but they are property of the company Strom-Bednar and cannot be presented. The design with best parameters will be realized in prototype and tested in real conditions. Results of these tests determine final type of the suspension.

Acknowledgments The research work reported here was made possible by company Strom-Bednar and supported by TAČR.

References

Harris CM (2002) Shock and vibration handbook. Charles Batchelor Professor Emeritus of Electrical Engineering, Columbia University, New York

Horný L (2012) Experimenty pro určení konstitutivního modelu pryže při velkých deformacích. Výzkumná zpráva, FS ČVUT v Praze, Ústav mechaniky, biomechaniky a mechatroniky, Praha, (15 str.)

Identify the Sources of Vibration and Noise on Cars Gearbox by Spectral Analysis

E. Tomeh

Abstract This report allows outlining the advantages of using technical diagnostics methods on the gearbox of personal cars. These methods are an instrument in the modern way of controlling assembly and production quality of gearbox parts. The measured vibration spectra also serve for predictive maintenance of a personal car gearbox, for excluding needless maintenance activities and for planning the performance of maintenance in the most efficient way.

Keywords Gearbox · Maintenance · Technical diagnostics · Vibration

1 Introduction

The necessity of examination the technical condition of personal car gearboxes results from a need to make decisions connected to quality. It might be a decision regarding either the maintenance of the gearbox or changes to be made in the construction and technology. Nowadays conditions and high consumer demands require of the producer to look for ways to increase productivity of manufactured machinery in order to stabilize the quality of noise and vibrations (Fig. 1).

Technical diagnostics of the gearbox is based initially on measurement and analysis of vibrations of the main joints in the gearbox. The measurement is made in predefined conditions of maintenance when a new gearbox is installed. Incorrect assembly of parts or deterioration of technical condition are expressed by a change of vibration level or spectra which allows to find out the cause for vibration and noise, to evaluate the length of further maintenance, to identify the damaged gearbox joint and to plan correction of the gearbox. The ability to identify and

E. Tomeh (✉)
Technical University of Liberec, Liberec, Czech Republic
e-mail: elias.tomeh@tul.cz

L. Ševčík et al. (eds.), *Modern Methods of Construction Design*,
Lecture Notes in Mechanical Engineering, DOI: 10.1007/978-3-319-05203-8_29,

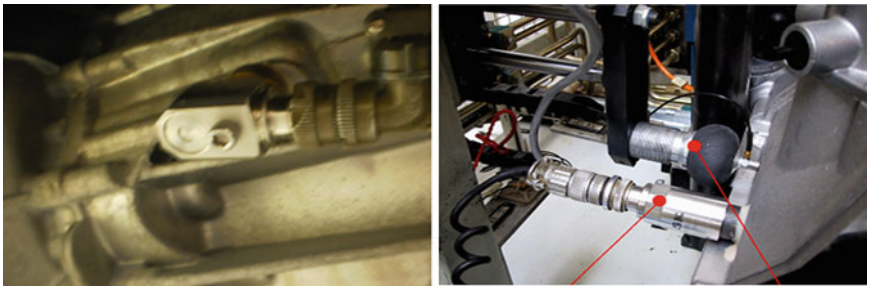

Fig. 1 The sensors of measurement on the gearbox (Tomeh 2003b, 2007)

remove the cause of deterioration of the technical condition is an appreciable advantage. The results can be directly applied in car factories. There are two main factors which play a part in the application of the results:

1. Every needless de-assembly of the gearbox parts deteriorates its technical condition and causes vibration and noise increase.
2. There is no need of only replacing the damaged part as far as the causes of the damage are not eliminated.

2 Reasons for Gearbox Vibration Measurement

The noise produced by car has a negative influence on the closest surrounding as well as on who is in the car, especially the driver. Disturbing influences effecting driver's attention during driving can endanger the security of all participants of the traffic.

The biggest source of car noise and vibration lies in the antifriction bearing, the cog wheelwork, the used and damaged edges of cogs and the incorrect assembly of cog wheelwork. The main aim is:

1. **Detection**—recognition of changes of the vibration intensity and of the number of specific parts of vibration spectra. Vibration should be measured as close as possible to the bearings or other important gear joints in three directions: axial, horizontal–radial and vertical-radial.
2. **Pointing out the causes of vibrations**—finding out the cause and the place of origin of gearbox overload. For spectra analysis and time course, an exact calculation of vibration excitation frequency is needed. Therefore, it is necessary to draw kinetic scheme of the gear with the following data: number of cogs of the cogwheels, rotations of the motor and types of antifriction bearings.
3. **Solutions**—to make necessary steps and after their realization to affirm them by measuring the influence on gear's dynamic behaviour and on the endurance and reliability of the parts. The determination of causes of noise and damages of the gear parts derives from the comparison of the measured spectra with the spectra of a new and correctly constructed gearbox and with the spectra of further

development. This method captures other types of vibration causes as well, such as unbalance of rotating parts, Misalignment, mechanical loosening, cogs and bearing damage, etc.

Already in initial stage, defect arousal can be detected by a change of amplitude of one or more elements of vibration spectra. Deterioration of the defect is followed by gradual increase of vibration amplitudes. The trend of analysis, of examination and determination of the defect and its causes includes all the measured values of a specific place of measurement with dependency on time. By using this trend, we can calculate the optimal maintenance period or repair term.

There is a big difference between determining the sources of gearbox vibration and noise and the analysis of the cause of their origin. Replacing only the bearing which shows signs of damage caused by strong vibrations is not the solution of the problem. Usually, there is other reasons for excessive level of dynamic power which causes damage of the bearing. We must then find out the origin of the causes (unbalance, Misalignment, loosening, etc.) As long as we don't do so, we cannot say we realize a program of identification of the causes of vibrations and noise, but only a program of exchanging the bearings.

3 The Results of the Measurement

In new personal car gearboxes, it's possible to evaluate the quality of manufacture and assembly of their constituents:

- In case shafts are not Misalignment and the cogwheels are eccentric, the result is amplitude modulation with frequency f_R around f_Z with amplitude growth of higher harmonic constituents $2f_Z$, $3f_Z$.
- Misalignment of the gear shafts in gear entry and exit results in an increase of intensity of side-zones about f_Z.
- Damage of cog edges (usage, plastic deformation, pits) is manifested in the spectrum in a relatively bigger increase of higher harmonic constituents' amplitudes $2f_Z$ and $3f_Z$ in comparison with the increase of the basic constituent f_Z simultaneously with side amplitudes.
- It is possible to identify the damage condition of the bearing from vibrations spectra.

The results of frequency calculation show frequency 49.27 Hz for inner ring of pinion in the bearing placed in "glasses" (it is derived from calculated rotations 970 min^{-1}, which respond to the deducted entry rotations 3,350 min^{-1}. The deduction is made with certain mistake. This fact leads to a small deviation of frequency measurement calculation).

From the envelop analysis, vibration increase at frequency 48.75 Hz, amplitude 0.09 gE was found out. At another measured frequency of 97.5 Hz, there is a

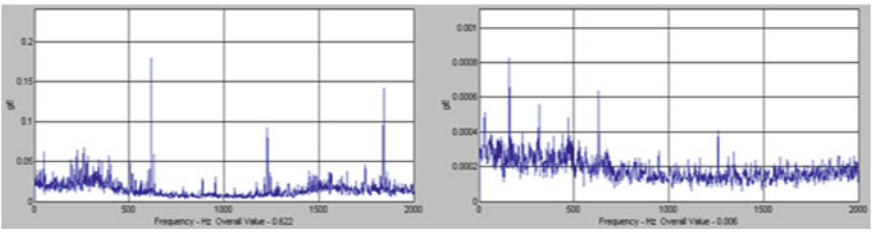

Fig. 2 Acceleration in the first gear, before and after replacement of the bearing (Tomeh 2007)

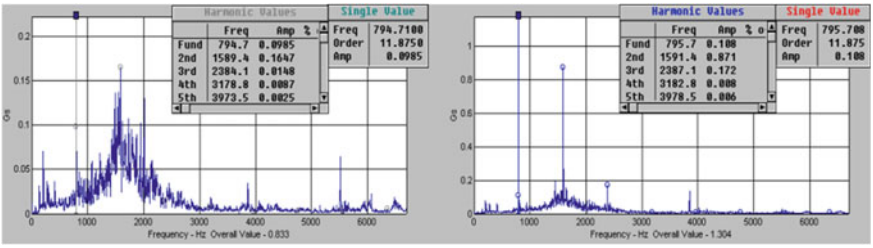

Fig. 3 Third gear level spectrum of vibration, measured by order analysis (Tomeh 2007)

second harmonic damage of the inner ring with amplitude 0.05 gE. Around it, there are modulations in a range of $f_R = 16$ Hz. 112.5 Hz with amplitude 0.04 gE and 81.25 Hz with amplitude 0.06 gE.

The amplitude values and occurrence of modulation signalise the damage of the pinion—bearing placed in "glasses". After its replacement the total effective acceleration of vibrations decreased from 0.62 to 0.006 gE, which means approx. 99 % (Fig. 2).

There was also a decrease of the damage frequency amplitude of the pinion-bearing inner ring from 0.09 to 0.0003 gE, which means approx. 99.6 %. The amplitude of the second harmonic constituent of the damaged inner ring that was 0.05 gE, decreased to 0.0002 and the modulation in the range of $f_R = 16$ Hz disappeared (Fig. 3).

Vibrations spectra are a very useful way of elaboration of signals and it enables the analysis of special gearbox types and the determination of reasons for vibration.

The evaluation of the technical condition of gearboxes based on the analysis of vibration measuring with the use of the chosen diagnostic method:

– allows an early identification of worsening of gearbox condition,
– if the increased level of vibration is recognized on time, then it is possible to take proper and cost effective steps which will prevent bigger damage of the gearbox constituents.

To ensure the quality of the production, regular vibration measurements are carried out on machine tools for the manufacture of gearbox parts in cars. These

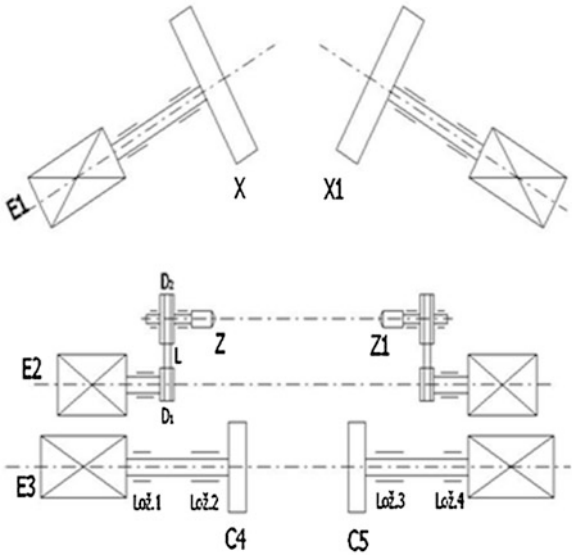

Fig. 4 Kinematic scheme of SAIMP grinders (Tomeh 2003a)

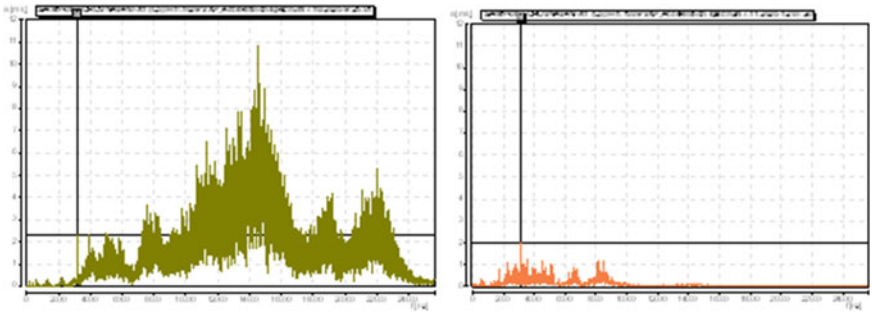

Fig. 5 The spectrum of the vibration acceleration before and after replacing the bearings in the position defined as Bearing 3 (Tomeh 2003a)

measurements of vibration spectra are taken for SAIMP machine that is an automatically controlled cylindrical grinding machine, which performs grinding of bearing diameter on pinion for cars gearbox.

In this article, there is an example in the location is identified as C5, namely on the right side of the machine—see Fig. 4 labelled Bearing 3 and Bearing 4.

The analysis of the measured spectra (Fig. 5) in the mentioned locations shows damage of the inner ring of the rolling bearing FAG 71909 HC CTP4S.UL (Bearing 3). In the spectrum, one of the main components of the acceleration vibration frequency is 3,236 Hz. It is the second harmonic frequency of the bearing inner ring.

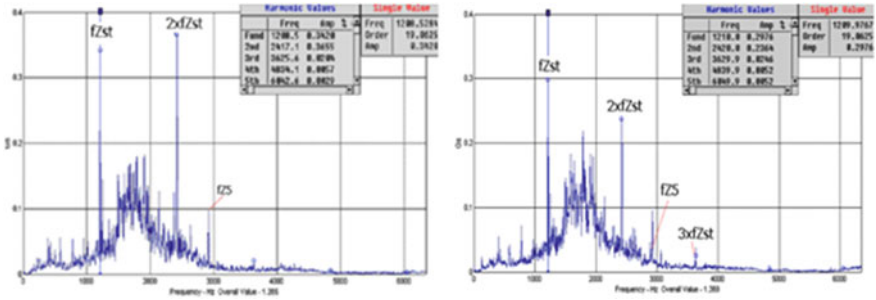

Fig. 6 The spectrum of vibration acceleration (order analysis)—engine braking- Fifth speed Gear- before and after replacing rolling bearings FAG 71909 HC CTP4S.UL at Bearing 3 on the SAIMP machine (Tomeh 2007)

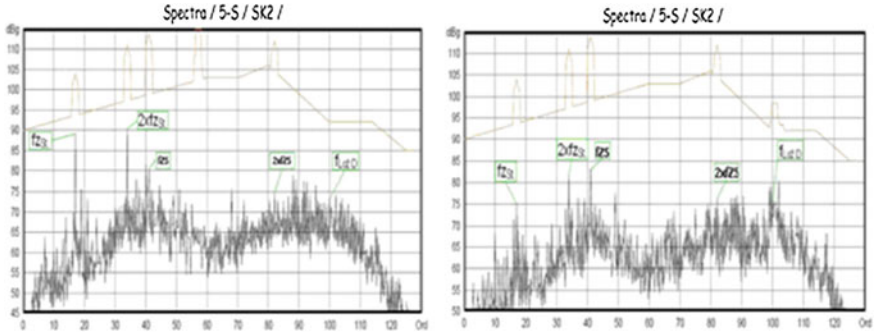

Fig. 7 Spectrum of vibration—fifth speed gear of shaft SK2—in acceleration- before and after replacing rolling bearings FAG 71909 HC CTP4S.UL at Bearing 3 on the SAIMP machine (Tomeh 2007)

The frequency of the inner ring of the bearing is 1,618 Hz, the amplitude at this frequency is 2.306 m s^{-2} and the effective value of acceleration is 105.7 m s^{-2}.

After replacement of rolling bearings FAG 71909 HC CTP4S.UL the vibration measurements were repeated with the same conditions. Only the speed of motor slightly differed. It decreased from 8,658 min^{-1} (before replacing) to 8,622 min^{-1} (after replacing). The amplitude is reduced from the original 2.306 m s^{-2} to 2.02 m s^{-2}. But the effective value of the acceleration decreased significantly from 105.7 m s^{-2} (before replacing the bearings) to 8.1 m s^{-2} (after replacing the bearings).

For this purpose, there was a total of two measurements. The first was the measurement of the gearbox with a pinion, which was made on the SAIMP machine before replacing the rolling bearings FAG 71909 HC CTP4S.UL at the location defined as Bearing 3. The second was the measurement of the gearbox with a pinion, which was made on the SAIMP machine after replacing the rolling Bearing in the same location. In each of these measurements, the gearbox was loaded on the acceleration and engine braking. See Figs. 6 and 7.

4 Conclusions

The damage condition of the inner ring of a pinion, placed in "glasses", was identified from the vibration spectra. The gearbox vibration measurement is not only limited to the diagnostic described. There are other methods derived from vibration measurement which can be used when looking for and determining Causes of damage in time of adjustment, construction, placement or changes of technical parameters.

The paper briefly outlined the advantages of using spectral analysis method on machine tools for the production of gearbox parts for a personal car. The paper shows the effect of manufacturing precision of pinion gearbox, machined by a grinder SAIMP, on the gearbox noise.

References

Tomeh E (2003a) Identifying motor vehicles mechanical defects by vibrodiagnostics methods. In J Middle Eur Constr Design Cars 1:1214–0821

Tomeh E (2003b) Hodnocení hlučnosti automobilových převodovek měřením vibrací. In: DIAGO 2003, ISBN 80-248-0210-4

Tomeh E (2007) Diagnostic methodology of rolling element and journal bearings. Script Liberec 2007, TU in Liberec, p 66

Optimization Methods for Minimizing Vibrations and Noise Radiation of Gearboxes

V. Vanek

Abstract The paper will present our successful results of the effective implementation of the engineering Design Science (DS) knowledge into the process of the engineering design of optimized gear systems (GS) from the point of view of their dynamic behaviour. The new strategies and approaches to the effective implementation of some methods, improved by use of the Theory of Technical Systems, allow the mathematical modeling of the elementary shaft assembly with transmission gear wheels and their definitions on the completely new base of designing of the GS. The new philosophy supports very effectively an optional combination of intuitive, methodical-empirical and flexible systematic strategy of thinking. We have focused especially on the third highest hierarchical level (LIII) of use of engineering design knowledge i.e. on "Flexible systematic strategy based significantly on system of structured knowledge" which optimally supports the creativity of engineering designers. Any technical product is required to fulfill many properties; therefore pursuit of multicriterial optimization is the non-trivial issue. In this case the use of the LIII is very helpful, providing better support for keeping requested "direction" to "goal" states of properties and simultaneously keeping "balance" of their "goal" states when are designing the new technical products (in this case gearboxes).

Keywords Technical system · Machine element · Dynamics · Vibration · Gearing

V. Vanek (✉)
University of West Bohemia, Pilsen, Czech Republic
e-mail: vanekv@gmail.com

L. Ševčík et al. (eds.), *Modern Methods of Construction Design*,
Lecture Notes in Mechanical Engineering, DOI: 10.1007/978-3-319-05203-8_30,

1 Introduction

In the area of systematic access in design a significant role is played by tools, which decrease the time of the design, make possible design of optimal technical systems and procedure of creating a fully new design variant. Vibration and noise radiation are often secondary outputs from a transformation process during the development of technical systems, where rotation is transformed from n_1 to n_2 and transmission is by turning moment M_t.

2 Process of Optimization of Gear Systems

The process of optimization of GS was allocated into three basic steps from aspect of dynamical properties: (Hosnedl 2001)

- Detection of the motion instability of GS
- Analysis of the vibration of the shaft type assembly system
- The evaluation of the dynamic behaviour of STA and the design of the improved variants of GS.

For the support of the running solutions in every individual phase, the subsidiary modules in MATLAB language were built up, enabling the simulation of the dynamic behavior of gear systems. Every module can be used individually and independently on the previous use of other modules (Fig. 1) (Vanek 2000).

3 Mathematical Model of STA

Shaft type assembly system (STA) was broken down into shaft assembly groups (STG). STG were modeled by FME as 1-D continua and were coupled by linear and time invariable tooth couplings (Slavik et al. 1997). The model STA, thus created, was attached to the frame by bearing couplings with radial clearances. Each STA is composed of machine elements and its organ structure is shown in Fig. 2.

4 Trial Model

Computational modules were tested on the model of the simple three-stage gear system with gear wheels (Fig. 3).

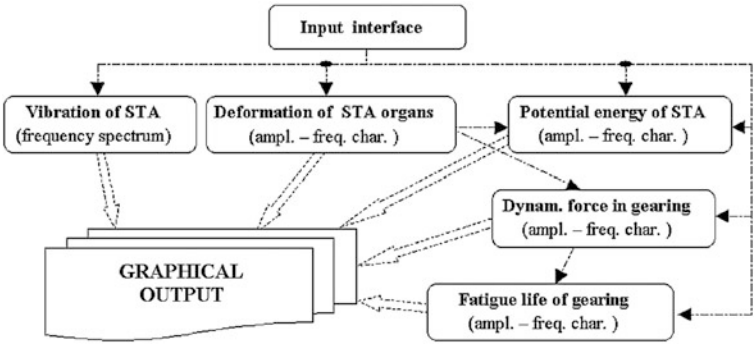

Fig. 1 Structure of the computation module created in MATLAB

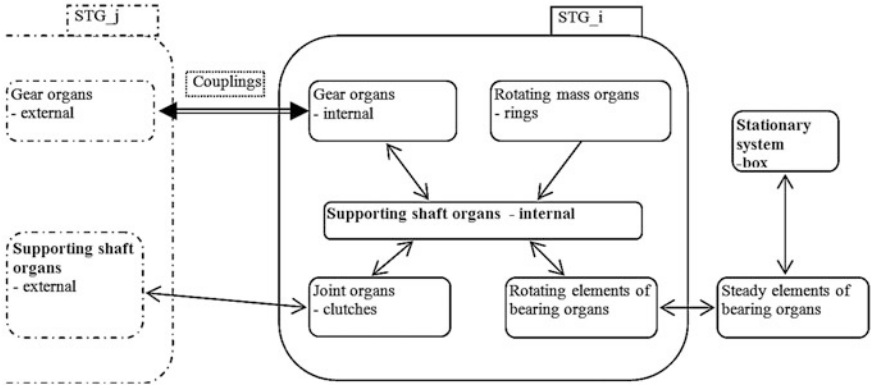

Fig. 2 Organ structure of STA

5 Analysis of Results

From the analysis of amplitude characteristics follows, that the vibration of GS are seen in the tooth-frequency $\omega_{z_{STG1\_0}} = 2{,}424$ rad s^{-1} of high-speed gear, which corresponds to speed of the high-speed driving STG1_0 $n_{STG1\_0} = 643$ rev min^{-1}. The resonant state $\omega_{z_{STG1\_0}} = \Omega_{10}$ is most significant in the frequency range of excitation $\omega_{z_{STG1\_0}} \in \langle 1{,}885 \div 18{,}850 \rangle$ rad s^{-1}, which corresponds to the revolution range of STG1_0 $n_{STG1\_0} \in \langle 500 \div 5{,}000 \rangle$ rev min^{-1}. This follows also from the amplitude characteristic of the upper estimate of the state of stress energy (Fig. 4). This resonant state is caused by the first harmonic component of deviations in tooth-mesh high-speed gear GO1_0_1/2_0_1 at speeds STG1_0 $n_{STG1\_0} = 814$ rev min^{-1}.

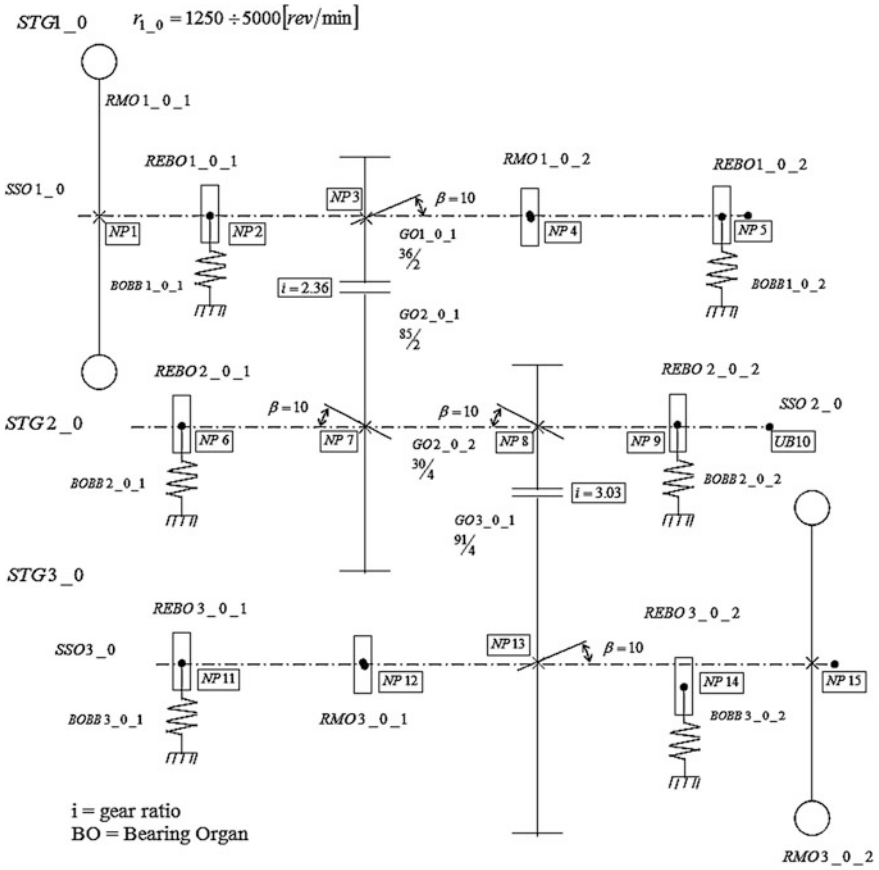

Fig. 3 Organ structure of gear system in the form of kinematic pattern

From the analysis of amplitude characteristics of the upper estimate of the generalized coordinates (Fig. 5) and dynamic forces (Fig. 6) in the gearing follows, that at these speeds show strong resonant states of transverse deformation (and hence the radial component of the reaction) in REBO1_0_1 − REBO 3_0_2.

From Fig. 7 is further seen, that the fatigue life $T_{1\_0\_1/2\_0\_1}$ of a high-speed gear is substantially lower than the fatigue life $T_{2\_0\_2/3\_0\_1}$. The largest decrease the life of teeth occurs at the speed STG1_0 $n_{STG1\_0} = 4,536$ rev min^{-1}, when $T_{1\_0\_1/2\_0\_1} = 175 \times 10^4$ h. We can therefore conclude that the observed lowest lifetime of the toothing in high-speed gear exceeds the durability requirements of the GS $L_h = 20{,}000$ h.

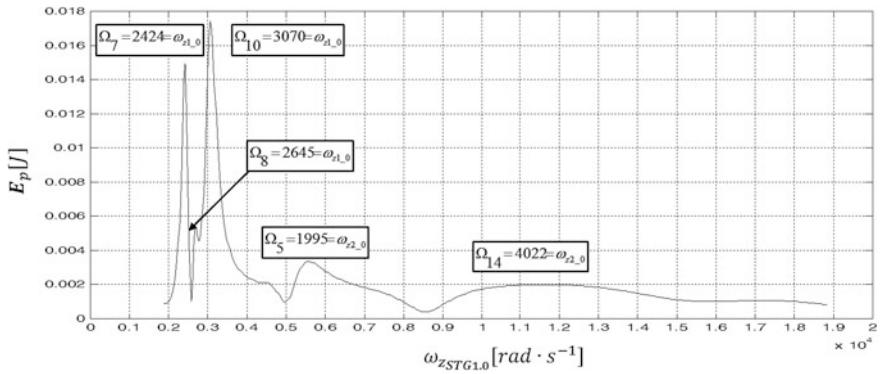

Fig. 4 Amplitude characteristic of the state of stress energy

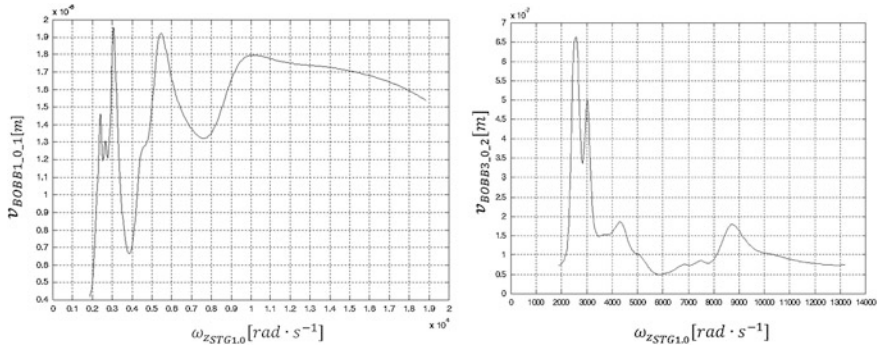

Fig. 5 Nodal points generalized displacements in the direction $\vec{\mathbf{v}}$ under BO

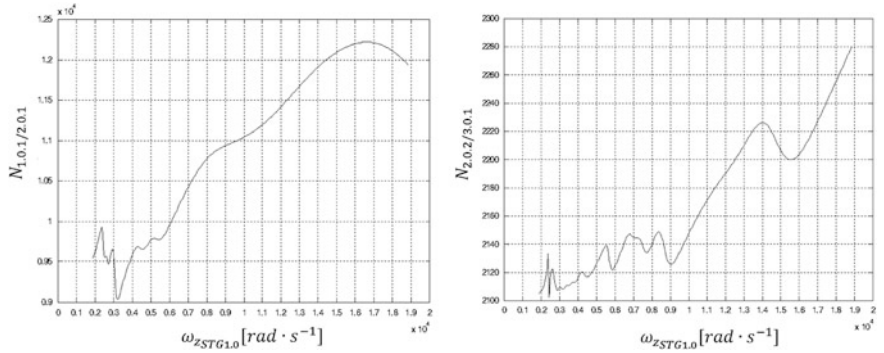

Fig. 6 Dynamic forces transmitted through the teeth

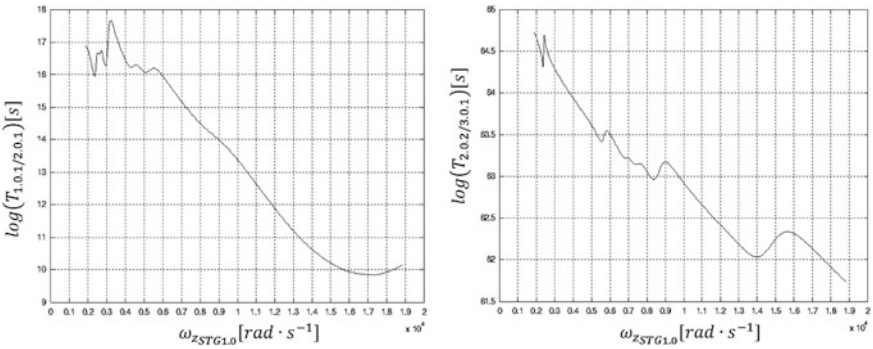

Fig. 7 Fatigue life of toothing

6 Conclusions

Mentioned computational system allows solving and designing the optimal gearing systems on the basis of the simulation of the dynamic behavior, which is the basic demand on the quick evaluation of the suitability of suggested solutions with respect to the demanded criteria. The use of the mathematical simulation of the dynamic behavior of gearing systems by searching of the optimal solution allows to designing and to comparing the individual proposed variants of GS from the point of view of some followed parameters and is then the large benefit in the practice. Though the mathematical simulation has evidently its own problems due to simplifications and omissions some facts, it is possible in any cases to deduce at the design of certain variant (under use of the same method) whether the improvement of the followed properties of the new variant of GS was achieved on the original variant of the solution.

Acknowledgments The work presented in this article has been undertaken within framework of the Project No. CZ.1.07/2.2.00/28.0206 'Innovation of design training in the fields of interdisciplinary knowledge, computer, educational and linguistic support with increasing of modularization and knowledge consistency, eliminating duplications and involving specialists from industry.' co financed by the European Social Fund and a the state budget of the Czech Republic.

References

Hosnedl S, Vanek V, Borusikova I (2001) Design science for engineering practice. In: Culley S, Duffy A, McMahon C, Wallace K (eds) Design applications in industry and education. ICED 01, Glasgow (GB), pp 363–370

Slavik J, Stejskal V, Zeman V (1997) Zaklady dynamiky stroju (The bases of machine dynamics). CVUT, Prague (CZ)

Vanek V (2000) Metody pro navrhovani optimalizovanych prevodovych systemu (The methods for designing of the optimized gearing systems). UWB, Pilsen (CZ)

Design Frame for Car eTUL

R. Voženílek and P. Brabec

Abstract This paper deals with the design frame electric car eTUL. The vehicle is designed for two people sitting in a row. Presented frame construction is designed as a weldment of profiles. In its proposal was based on the proposed design of the study. Design of the frame run parallel with the verification of its properties in the finite element method and the results of this analysis were optimized. The frame was gradually analyzed at loads simulating the following conditions: static mode of the vehicle, vehicle acceleration, deceleration of the vehicle cornering, dynamic mode. The main objective was to provide sufficient stiffness at low vehicle weight. It was also determined torsional stiffness, which is an important parameter in the design of vehicle bodies.

Keywords Vehicle · Frame · FEM · Torsion stiffness

1 Introduction

Most concurrent cars using self-supporting body, which is produced from a large variety of materials. Their choice depends on the given properties. The whole frame may consist of different shaped sheets which are welded together. The most widespread and most commonly used material for the production of steel. The main reasons for its use include high strength, good ductility and weld ability,

R. Voženílek (✉) · P. Brabec
Technical University of Liberec, Liberec, Czech Republic
e-mail: robert.vozenilek@tul.cz

P. Brabec
e-mail: pavel.brabec@tul.cz

L. Ševčík et al. (eds.), *Modern Methods of Construction Design*,
Lecture Notes in Mechanical Engineering, DOI: 10.1007/978-3-319-05203-8_31,

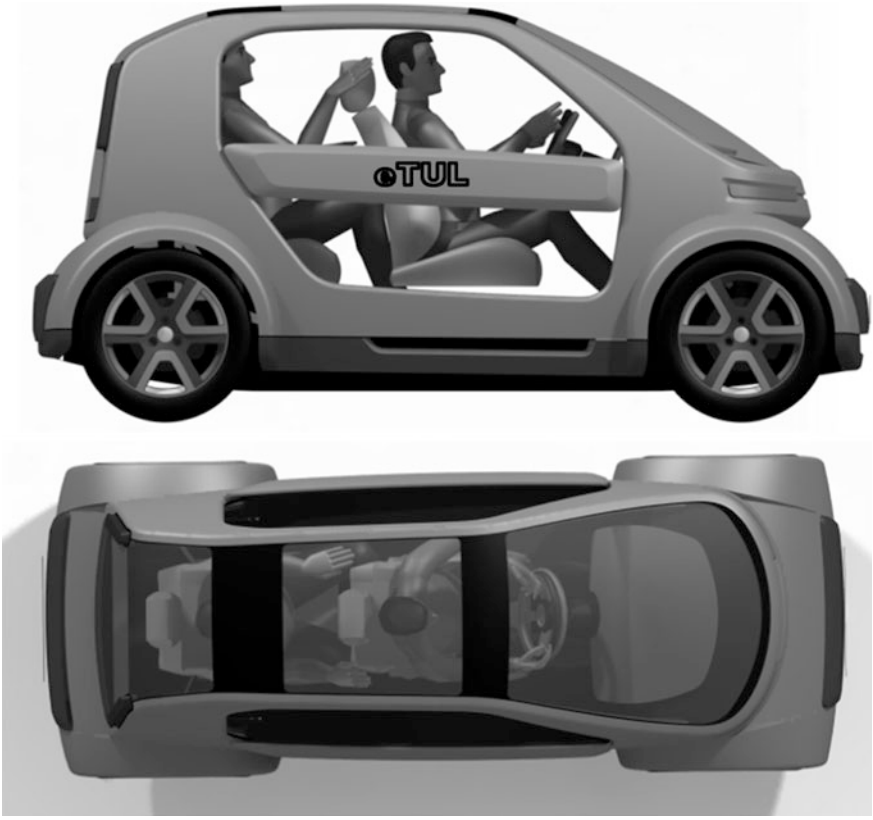

Fig. 1 Design of car (Pilvousek 2012)

good price and at an appropriate surface treatment also long life. Another material that is used is aluminum. They are used especially in doors and other parts. The advantage over steel of lower weight and greater resistance to corrosion. The disadvantage is its high cost and complex welding technology.

ETUL vehicle frame was designed as a two-seater. The vehicle is designed for the urban was therefore placed great focus on its overall dimensions. The vehicle's driver and passenger sitting behind.

The drive unit is an electric motor which is coupled with a gearbox located at the front of the car. The drive is only the front axle, which is also steered. The electric motor is powered by batteries. You are in the middle of the car, directly under the vehicle crew. On either side of the door, allowing comfortable entry and exit driver and passenger to the right or left side as needed (Fig. 1).

2 Design of Frame

When designing a frame electric went from an already created design model, which formed the cover for the frame design. Used the software Catia V5, where, thanks to a module for creating surfaces (Shape) ran their design of curves and always in two planes. Using other tools of this program, each of the frame electric gradually constructed. She was chosen lattice structure, which was formed by tubes of circular cross section and profiles of square or rectangular cross section. The connection is secured by welds.

When creating was considered with the set ups of components, which include the attachment of axles, shock absorbers, springs, front and rear lights, electric motors, gear boxes, batteries and other parts of a car. Therefore it is necessary to perform the design so as to guarantee the installation of these components directly to the frame, which is able to drive without a body.

When driving on electric frame are several forces that arise from the weight of the vehicle, crew, or cargo that is transported. Furthermore, the excitation of road irregularity, rolling resistance, inertia effects of mass during acceleration or deceleration, centrifugal force during cornering and others. Calculation of reaction forces on the frame was made using some simplifying assumptions for the individual driving conditions. Including: static mode of the vehicle, vehicle acceleration, deceleration of the vehicle cornering, dynamic mode.

When driving a car on a rough road may be situations where the frame will be loaded by in torsion and that when both rear wheels move on inequality. For example, the left will pass over some bumps and potholes in the second. Therefore, another important parameter is the torsion rigidity of the vehicle frame about a longitudinal axis. Here we find also using FEM analysis. We consider here the ideal rigid front axle and bearing points of the bridge to the frame electric car will avoid all displacements and rotations. Load frame we use the known forces which will operate in the area where the springs rear axle. The first will be a positive force vector in the direction of the axis for the second negative. Both of size F1, 2 = 1,000 N. arm (distance between saves rear springs) on which forces are x = 0.838 m Afterwards, using known relationship calculate the torsion stiffness electro mobile.

Of the known maximum displacement axis for arm length between the imposition of springs, calculate the angle of rotation of frame structure around the longitudinal axis x.

Using a right triangle express angle α:

$$\alpha = \text{arctg } z/(x/2) \quad [^\circ] \tag{1}$$

From the known relation calculate torsion stiffness:

$$k = M/\alpha = (F\_1, 2 \cdot x)/\alpha \quad [(N \cdot m)/^\circ] \tag{2}$$

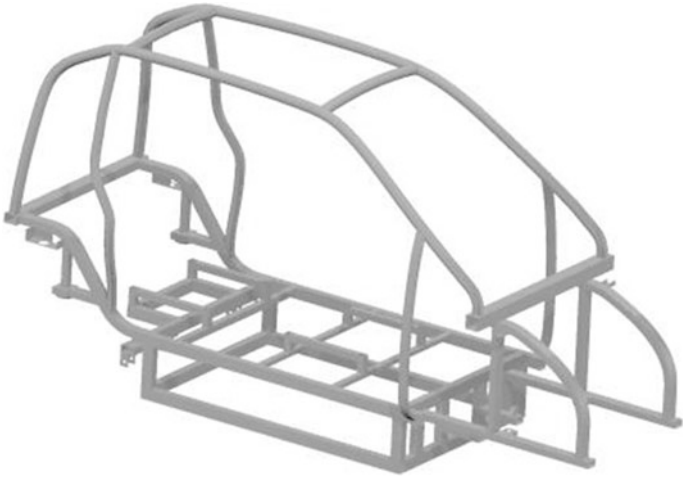

Fig. 2 Design of frame—the first variant (Patocka 2013)

3 Results

The resulting torsion stiffness electro mobile shown in Fig. 2 is 1,643 Nm/°. In comparison with a four-seat vehicle Mitsubishi i-MiEV, where the value of torsion stiffness the frame is 8,337 Nm/° (Eckstein et al. 2011) appeared to be low, so the frame was optimized to increase stiffness values. The values of stiffness vehicles Mitsubishi i-MiEV has been found experimentally on the test.

To the rear of the frame, in place of the storing spring was added to a square of 30 × 30 × 2 mm across and diagonally. It was also stiffened storage space for the battery on the circumference identical profiles. Also diagonally this section was stiffened using a profile of rectangular cross section 40 × 20 × 2 mm. This optimized design can be seen in Fig. 3.

Torsion rigidity is increased to 1,949 Nm/°. However, this value is still low, therefore the increased thickness profiles of 2–3 mm.

Maximum stress optimized design to increase the wall thickness decreased to 153.7 MPa, which operate on the storage front springs and dampers. The total displacement was reduced to 0.572 mm. Torsion rigidity is increased to 3,223 Nm/°.

This optimized structure is not appropriate to add additional profiles. There is enough space available and, after adding other bearers would grew especially the total weight of the frame, but the torsion stiffness should be increased only by a small value. With such a proposed frame structure electro mobile would increase torsion rigidity of adding sections to the top of the car frame. It is not possible for reasons of space for side doors and glass design of the vehicle (roof) (Table 1).

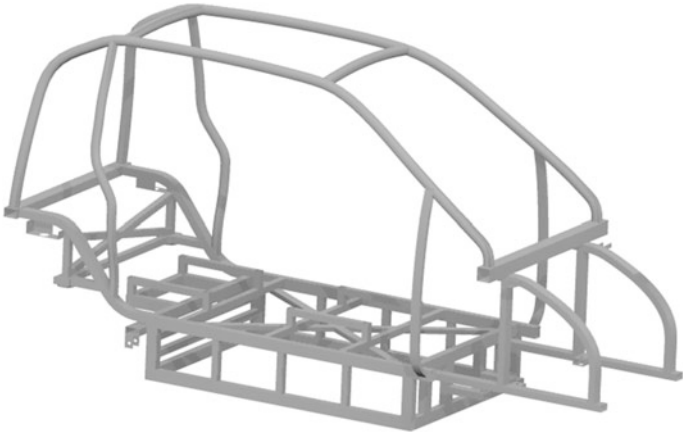

Fig. 3 Design of frame—the second variant (Patocka 2013)

Table 1 Comparison of alternatives proposed vehicle frame

Type of construction	The maximum displacement (mm)	Torsion stiffness (Nm/°)	Weight (kg)
The first variant (Fig. 2)	1.093	1,643	93.3
The second variant (Fig. 3)	0.681	1,949	107.8
The second variant (Fig. 3) with stronger profiles	0.572	3,223	142.9

4 Conclusions

Torsion stiffness electro mobile after optimization increased by 96 % (the weight of the vehicle frame is increased by 53 %), its value is not entirely comparable with some electric vehicles. This is also a different concept vehicle, where two crew members sitting behind a vehicle width is only 75 % of current vehicles. To increase body rigidity can significantly contribute battery box design. Box with batteries will be located under the crew, and thereby increase the stiffness of the vehicle. For example, a vehicle Mitsubishi i-MiEV is body stiffness by adding a box with batteries increased to 9,394 Nm/° (Eckstein et al. 2011).

References

Eckstein L, Göbbels R, Wohlecker R (2011) Benchmarking of the electric vehicle Mitsubishi i-MiEV. ATZ Autotechnol 11:26

Patocka L (2013) Navrh ramu elektromobilu, Technical University of Liberec, Diploma work

Pilvousek L (2012) Elektromobil pro dve osoby, Technical University of Liberec, Diploma work

Part II
Engineering Analyses

D. Herak, A. Kabutey, K. Kaláb, R. Slanina, P. Maršálek, R. Kohár, S. Hrček, J. Křička, E. Kronerova, J. Kratky, V. Kubec, I. Mašín, Z. Matuszak, G. Nicewicz, K. Petr, V. Dynybyl, M. Dub, S. Poljak, R. Bašťovanský, R. Slanina and P. Sniehotta

Currently, the practice calls for fast and accurate solution, which is important for the study and understanding of design problems to create corresponding analysis. It is always based on physical laws and mathematical theory described by empirical relationships approaching the mechanical behavior of the problem. In the case where use of analytical solutions are not convenient or even possible (e.g., geometrically segmented and difficult equipment, contact problems, modal analysis, and transmission analysis of whole machines or other special tasks), an approximate solution using numerical methods can be used. With the help of CAD software (Computer Aided Design) in connection with the Finite Elements Method (FEM) appropriate analysis can be achieved for solving design problems and significant time savings not only in the prototype phase. In Part II—Engineering Analysis authors in 13 articles present study, analysis, and procedures for solving of various design problems.

Tangent Curve Model for Describing Mechanical Behavior of Oil Bearing Crops Under Compression Loading

D. Herak and A. Kabutey

Abstract This article is focused on the utilization of tangent curve for description of mechanical behavior of pressed mixture under compression loading. The integral part of this article is also derivation of the general tangent curve and its boundary conditions.

Keywords Compression loading · Tangent curve function · Pressed mixtures

1 Introduction

For more detailed understanding of the linear pressing process it is necessary to understand the mechanical behavior of pressed mixture under compression loading (Blahovec and Reznicek 1980; Fomin 1978; Herak et al. 2010). The pressed mixture during pressing is compressed in direction of the pressing and deformations in other directions are limited figure. This type of pressing can be called linear pressing. The course of the deformation characteristic, dependency between compressive force and deformation, is in most cases determined by experiments and it can be described by general equation

$$F(x) = f(x) \tag{1}$$

where F is compressive force and x is deformation of pressed mixture. Detailed knowledge describing the shape of the deformation characteristic is necessary for precisely determining the magnitude of the compressive force, strain energy and modulus of elasticity in compression. The shape of these curves and its distribution

D. Herak (✉) · A. Kabutey
Department of Mechanical Engineering, Faculty of Engineering, Czech University of Life Sciences Prague, Kamycka 129, Prague, Czech Republic
e-mail: herak@tf.czu.cz

L. Ševčík et al. (eds.), *Modern Methods of Construction Design*,
Lecture Notes in Mechanical Engineering, DOI: 10.1007/978-3-319-05203-8_32,

in deformation diagram are the most important factors needed for accurate determination of pressing energy performance. Also, determined ranges of the pressing force magnitude depending on the deformation may help to design more appropriate and propose a complete technological process. Specified dependency between volume energy and deformation can be used as one of the input amounts which need for complete energetic audit.

2 Materials and Methods

Tangent curve, which was originally used to describe the mechanical behaviour of the jatropha seeds under compression loading (Herak et al. 2010), was modified as a general curve suitable to describe the deformation characteristics. This curve can be described by the following equation

$$F(x) = A \cdot [\tan(B \cdot x)]^n \tag{2}$$

where F(N) is compressive force, A(kN) is force coefficient of the mechanical behavior, B (1/mm) is deformation coefficients of the mechanical behavior, x (mm) is deformation and n (–) is exponent of the function. This function has a simple derivation and integration, which can be used to determine the strain energy and modulus of elasticity in compression. With aid of derivations of this function it can be used to find an appropriate method for regression using the Marquardt Levenberg algorithm (Marquardt 1963), which provides numerical solutions to the problem of minimizing deviations in general nonlinear functions over space of function parameters. The Marquardt Levenberg algorithm is an iterative technique that locates the minimum of a function that is expressed as the sum of squares of nonlinear functions. It has become a standard technique for nonlinear least-squares problems (Lourakis 2005). Marquardt Levenberg algorithm utilizes derivation of function by searched coefficients for determining these coefficients of the function using for fitting measured data. These derivations can be generally described by the following equations

$$\frac{dF(x)}{dA} = [\tan(B \cdot x)]^n \tag{3}$$

$$\frac{dF(x)}{dB} = A \cdot n \cdot x \cdot [\tan(B \cdot x)]^{n-1} \cdot \left[(\tan(B \cdot x))^2 + 1\right] \tag{4}$$

These equations [Eqs. (3), (4)] can be mathematically adjusted to the shape Eqs. (5) and (6) in which contains compressive force function [Eq. (2)].

$$\frac{dF(x)}{dA} = \frac{F(x)}{A} \tag{5}$$

$$\frac{dF(x)}{dB} = n \cdot x \cdot \left[\frac{F(x)^{\frac{n+1}{n}}}{A^{\frac{1}{n}}} + \frac{F(x)^{\frac{n-1}{n}}}{A^{\frac{-1}{n}}} \right] \tag{6}$$

Such modified equations allow finding the coefficients without calculating trigonometric functions; this expression of Eqs. (3) and (4) is essentially a polynomial function. These equations in this way modified for fitting of measured data can be optimal used for Marquardt Levenberg process which is utilized in mathematical software MathCAD 14.

The dependency between compressive force and deformation (Eq. 7) can be expressed from Eq. (2).

$$x = \frac{1}{B} \arctan \sqrt{[n]} \left(\frac{F(x)}{A} \right) \tag{7}$$

Solving Eq. (7) for compressive force approaching to the infinity it is possible to obtain Eq. (8) for limit deformation δ (mm) expressed by deformation coefficient of mechanical behaviour.

$$\delta = \lim_{F(x) \to \infty} x = \frac{\pi}{2 \cdot \mathrm{B}} \tag{8}$$

Using Eqs. (2) in (8) it can be also obtained Eq. (9) describing limit deformation expressed by compressive coefficient and initial pressing height.

$$\delta = \frac{\pi \cdot H}{2 \cdot \mathrm{G}} \tag{9}$$

The pressed volume is determined by Eq. (10) and it belongs to the limit deformation.

$$\Delta V = \frac{\pi \cdot D^2}{4} \cdot \frac{\pi}{2 \cdot B} \tag{10}$$

Limit volume compression K (–) is given by Eq. (11) and it is ratio between pressed volume Eq. (10) and initial volume of pressing Eq. (3).

$$K = \frac{\Delta V}{V} = \frac{H - \delta}{H} \tag{11}$$

Simplifying Eqs. (11) and (9) it can be derived Eq. (12) describing limit volume compression expressed by the compressive coefficient.

$$K = 1 - \frac{\pi}{2 \cdot G} \tag{12}$$

Putting Eq. (2) in Eq. (12) it can be derived Eq. (13) for the limit volume compression expressed by deformation coefficient of mechanical behaviour and initial pressing height.

$$K = 1 - \frac{\pi}{2 \cdot B \cdot H} \tag{13}$$

Equation (13) can be also formulated by Eq. (15) with aid of limit strain ε (–) Eq. (14) which is derived as ratio between limit deformation Eq. (9) and initial height of pressing.

$$\varepsilon = \frac{\delta}{H} = \frac{\pi}{2 \cdot G} \tag{14}$$

Tangent curve equation (Herak et al. 2011a), which was originally used to describe the mechanical behaviour of the jatropha seed under compression loading, was modified as a general curve which is suitable to describe the deformation characteristics (Herak et al. 2011b) and was verified by the finite element method (Petru et al. 2012). This curve can be described by Eq. (15) which is derived by modifying the basic equation of tangent curve Eq. (2) in which element in the brackets is multiplied by ratio of initial pressing heights, H.

$$F_D(x) = A \cdot \left[\tan\left(B \cdot H \cdot \frac{x}{H}\right)\right]^n \tag{15}$$

Product of coefficients of mechanical deformation behaviour B and initial heights H can be called G, the compression coefficient, and it is described by Eq. (16).

$$G = B \cdot H \tag{16}$$

Substituting Eq. (16) into Eq. (15), the following can be obtained considering the initial height of pressing:

$$F_D(x) = A \cdot \left[\tan\left(G \cdot \frac{x}{H}\right)\right]^n \tag{17}$$

The compression stress $\sigma_D(x)$ (MPa) inside the pressing vessel with the bulk seeds (Eq. 6) can be determined by dividing Eq. (17) by pressing plunger area S_D (mm^2) Eq. (19), where D (mm) is inside diameter of pressing vessel.

$$\sigma_D(x) = \frac{F_D(x)}{S_D} \tag{18}$$

$$G_D = B \cdot H \tag{19}$$

Considering the assumption which is very well known from the mechanics of heterogeneous materials (Budynas and Nisbett 2008) that the compression stress inside the bulk seeds is not dependent on diameter of pressing vessel and it is based on the assumption that the porosity of the material is constant. From these assumptions, it follows that the pressing process of the various pressing vessel diameters could be similar. This hypothesis of the properties of the bulk seeds can be described by Eq. (20), where subscripts I and II indicate two different diameters of pressing vessels.

$$\sigma(x) = \sigma_{D_I}(x) = \frac{F_{D_I}(x)}{S_{D_I}} = \sigma_{D_{II}}(x) = \frac{F_{D_{II}}(x)}{S_{D_{II}}} \tag{20}$$

Dependency between individual courses of compression force Eq. (21) can be given by adjusting the previous equation.

$$F_{DI}(x) = F_{DII}(x) \cdot \frac{S_{DI}}{S_{DII}} \tag{21}$$

Substituting Eq. (21) into Eq. (17) an equation describing how the compressive force also depends on the diameter of the pressing vessel can be derived.

$$F_{DI}(x) = A_{D_{II}} \cdot \left[\tan\left(G \cdot \frac{x}{H}\right)\right]^n \cdot \frac{{D_I}^2}{{D_{II}}^2} \tag{22}$$

The ratio of the force coefficient of mechanical behaviour and the corresponding square of pressing vessel diameter can be denoted as C (N mm^{-2}) this being the stress coefficient of mechanical behaviour Eq. (23).

$$C = \frac{A_{D_{II}}}{{D_{II}}^2} \tag{23}$$

By simply adjusting the compressive force equation [Eq. (22)] and using Eq. (23), the general tangential curve which describes the dependency between compressive force and deformation of bulk seeds, the inner diameter of pressing vessel and initial height of pressing can be derived.

$$F(x, D, H) = C \cdot D^2 \cdot \left[\tan\left(G \cdot \frac{x}{H}\right)\right]^n \tag{24}$$

Based on Eq. (24) can be seen that the dependency between force coefficient of mechanical behaviour A and diameter of pressing vessel D can be described by:

$$A(D) = C \cdot D^2 \tag{25}$$

3 Results and Discussion

It is evident that results of the present study are similar to the results of the previous studies focused on the mechanical behavior of oil bearing crops seeds under compression loading at uniform diameter of pressing vessel (Herak et al. 2011a, b, 2013).

However for description of mechanical behavior of bulk seeds, different solution methods generally based on the Darcy's Law (Fomin 1978) and fluid flow through porous media (Singh and Kulshreshtha 1996) have been used. Darcy's law and rheological properties of deformable solid matrix of bulk seeds are

fundamental for developing mathematical models to mechanical behavior of oilseeds (Petru et al. 2012; Raji and Favier 2004; Herak et al. 2012). The mechanical behavior of bulk oilseeds can be described also by methods based on the Terzagi's model (Shirato et al. 1986) or similar models. However, these models cannot be used to resolve individual particles and their properties, as well as relationships between particles, unlike the tangent curve equation which considers the bulk seeds as a unit, the constrains between the pressing vessel and the bulk seeds, and also the pressing process. Obviously, the tangent curve method can be used for the description of mechanical behavior of different types of bulk oilseeds and other materials such as wood or paper chips under compression loading where the rigidity of pressing vessel is much greater than the rigidity of the bulk samples (Herak et al. 2010, 2011a, b, 2012, 2013). Notwithstanding this fact, the development of mathematical models based on tangent curve equations for the description of deformation characteristics and mechanical behavior of oilseeds could also be influenced by moisture content, temperature and pressing velocity. Thus, mathematical models could predict the change of the tangent curve coefficients based on the compression factors.

4 Conclusion

It was found that tangent curve function can be used for describing the mechanical behavior of the mixtures of the plant seeds, oil bearing crops, wood chips and waste paper chips under compression loading. Tangent curves can be used for fitting measured amounts since relationships between measured amounts and tangent curve amounts were statistically significant. Generally, this tangent curve function could be appropriate for use in pressing any pressed mixtures during linear compression.

References

Blahovec J, Reznicek R (1980) Frakcionace píce (Fractionation of the forage). VŠZ v Praze, Prague, p 370

Budynas R, Nisbett K (2008) Shigley's mechanical engineering design, 8th edition. The McGraw-Hill Companies, New York

Fomin VI (1978) Vlažnoje frakcionirovanije zeljonych kormov (Wet fractionation of green forage). Rostov on Don, Izdatelstvo Rostovskovo universiteta, p 160

Herak D, Gurdil G, Sedlacek A, Dajbych O, Simanjuntak S (2010) Energy demands for pressing *Jatropha curcas* L. seeds. Biosyst Eng 106:527–534

Herak D, Kabutey A, Sedlacek A (2011a) Mathematical description of rape seeds' (*Brassica napus* L.) mixture mechanical behavior under compression loading. Scientia Agriculturae Bohemica 42:31–36

Herak D, Kabutey A, Sedlacek A, Gurdil G (2011b) Tangent curve utilization for description of mechanical behaviour of pressed mixture. Res Agric Eng 57:13–18

Herak D, Kabutey A, Divisova M, Svatonova T (2012) Comparison of the mechanical behaviour of selected oilseeds under compression loading. Notulae Botanicae Horti Agrobotanici Cluj-Napoca 40:227–232

Herak D, Kabutey A, Divisova M, Simanjuntak S (2013) Mathematical model of mechanical behaviour of *Jatropha curcas* L. seeds under compression loading. Biosyst Eng 114:279–288

Lourakis MIA (2005) A brief description of the Levenberg-Marquardt algorithm implemented by Levmar, ICS FORTH, Heraklion

Marquardt DW (1963) An algorithm for the least-squares estimation of nonlinear parameters. SIAM J Appl Math 11:431–441

Petru M, Novak O, Herak D, Simanjuntak S (2012) Finite element method model of the mechanical behaviour of *Jatropha curcas* L. seed under compression loading. Biosyst Eng 111:412–421

Raji AO, Favier JF (2004) Model for the deformation in agricultural and food particulate materials under bulk compressive loading using discrete element method II: theory, compression of oilseeds. J Food Eng 64:373–380

Shirato M, Murase T, Iwata M, Nakatsuka S (1986) The Terzaghi-Voight combined model for constant-pressure consolidation of filter cakes and homogeneous semi-solid materials. Chem Eng Sci 41:3213–3218

Singh S, Kulshreshtha M (1996) Mathematical modelling of juice expression from carrots under uniaxial compression. J Food Eng 27:323–336

Identification of the Shaft Failure Causes Based on the Description of Fracture Surfaces

K. Kaláb

Abstract It is well known that the fracture face can provide a lot of information about the failure causes (Sachs in J Fail Anal Prev, ASM Int 5(2):11–15, 2005). The article deals with the appearance of shaft fatigue fracture surface analysis to detect the causes of this damage. Based on the recent failure of the mechanical eccentric press KAISER KSTU 630 t and many images of this even it shows how important it is to understand the surface features of fatigue fracture.

Keywords Fracture face · Surface analysis · Fatigue zone · Shaft eccentric pins

1 Introduction

Mechanical eccentric press KAISER KSTU 630 t was operated 10 years, i.e. About 68,000 h. Shaft material was moderately alloyed stainless chromium–nickel–molybdenum steel for quenching and tempering 30CrNiMo8 according to EN 10083-3:2007 (DIN 17200). After finishing the $Re_{Min} = 700$ MPa and Rm = (900 ÷ 1,100) MPa. The shaft has a high fatigue limit under alternative stress and the combined method. It is suitable for heavy-duty and large parts.

After removing the connecting rod heads and eccentric housings it was observed 3 places of shaft damage situated on the eccentric pins (Figs. 1, 2).

K. Kaláb (✉)
VŠB-Technical University of Ostrava, Ostrava, Czech Republic
e-mail: kvetoslav.kalab@vsb.cz

L. Ševčík et al. (eds.), *Modern Methods of Construction Design*,
Lecture Notes in Mechanical Engineering, DOI: 10.1007/978-3-319-05203-8_33,

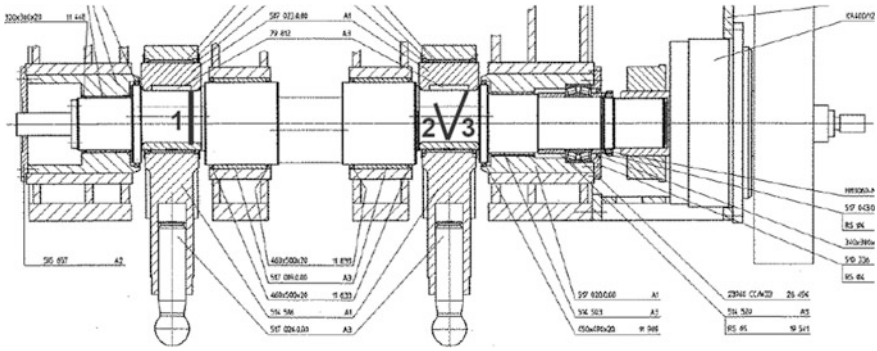

Fig. 1 Eccentric shaft and its 3 damages

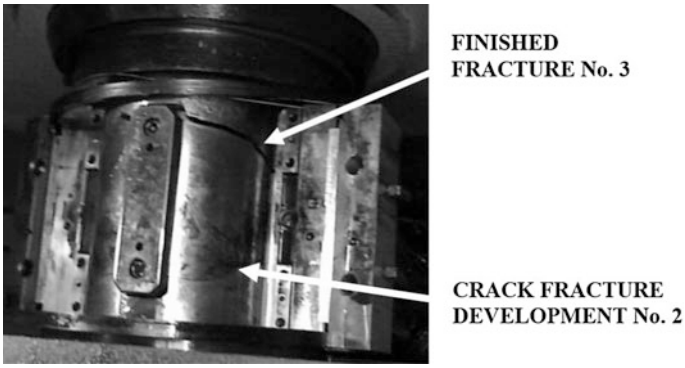

Fig. 2 Eccentric pin and its damages

2 Analysis of the Causes of the Shaft Failure

Fracture surface No. 1 with the major surface features of fatigue face is shown in Fig. 3. The origin is where the crack actually started. The crack then grew slowly across the fatigue zone. Eventually, the crack reached the point where the remaining material was overstressed, and the overload zone resulted. The plane of fatigue zone is very important, because it develops perpendicular to the plane of maximum stress in the part, thus helping to understand the source of the stress.

The bisector of the overload zone doesn't point directly at the origin (A). This shows there was some rotating bending involved, but other forces plane bending have combined with it to cause the failure. The fact that the origin is so close to the bisector shows the plane bending was greater of the two forces when the crack began. The breach was material from the center of fracture initiation origin (A) on the surface of the pin opposite the keyway excessive, unilateral bending pin

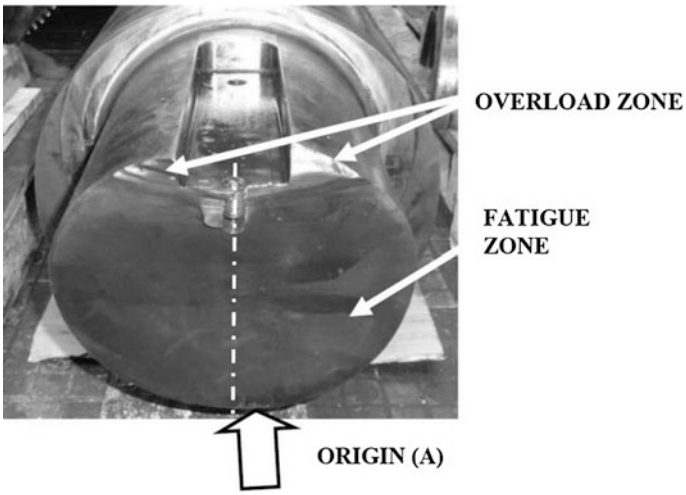

Fig. 3 Fracture surface No. 1

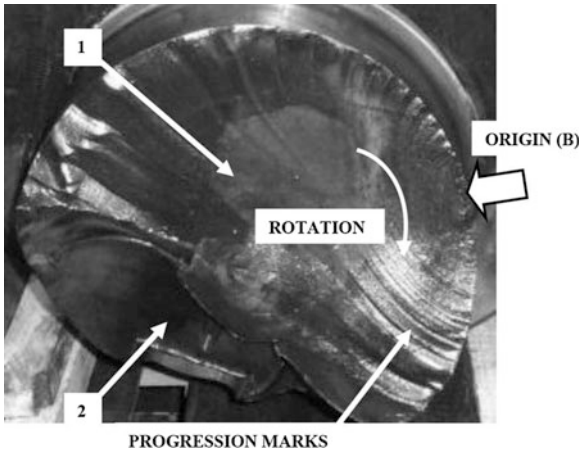

Fig. 4 Fracture surface No. 3

shaping resistors with a maximum forming force at the bottom dead center, i.e. plane bending. It is a place with the largest bending tensile stress on the pin.

The important feature is the shape of the fracture as viewed from the side. Because the fracture face essentially is a flat plane, it is possible to exclude the presence of stress concentrators on the surface. The appearance of smooth, planar fracture surface perpendicular to the axis of rotation, showing the slow progress of fracture and final fracture at low stress (the small area of final fracture). The presence of the single origin (A) also indicates the failure with low overstress.

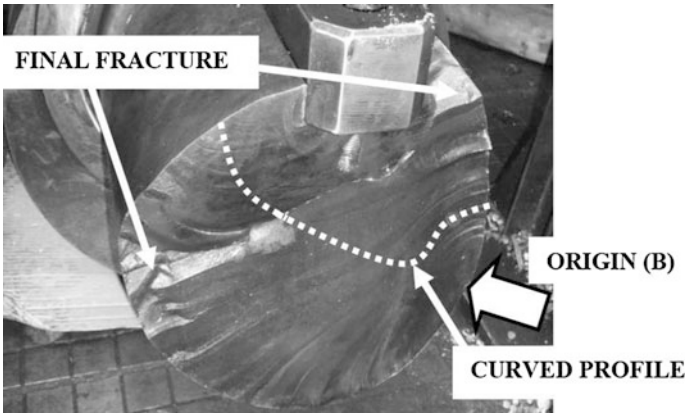

Fig. 5 Fracture surface No. 3 of the second part

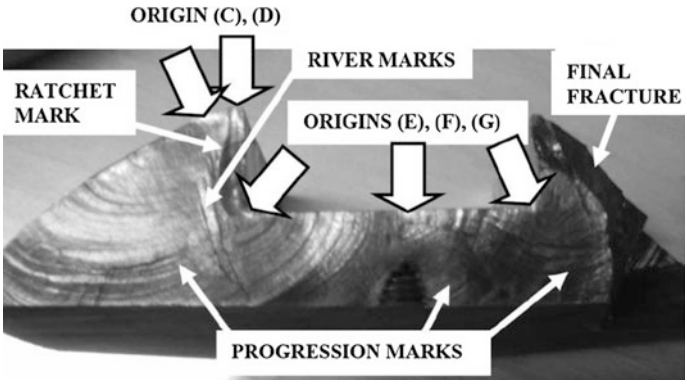

Fig. 6 Virtual model of platform

Fracture surface No. 3 is shown in Figs. 4, 5, 6, 7. The fracture was created during cyclic loading combined rotating bending and torsion, and was initiated at several levels and locations. The fracture surface shows two areas of own fatigue failures (1) and (2) with the characteristics surface features of high-cycle fatigue face with very good drawing of process for developing fatigue cracks.

The area (1) is shell-macroscopically smooth with large number of striking, distorted progression marks. Progression marks show how the crack has grown and are only present in fractures where there have been substantial variations in the component stress as the crack grew across the piece. They show gross changes in load and occurrence overload cycles during the development of the crack section. The breach was material from the center of fracture initiation origin (B) on the surface of the pin. The line process fracture cross-section shows the combined stress.

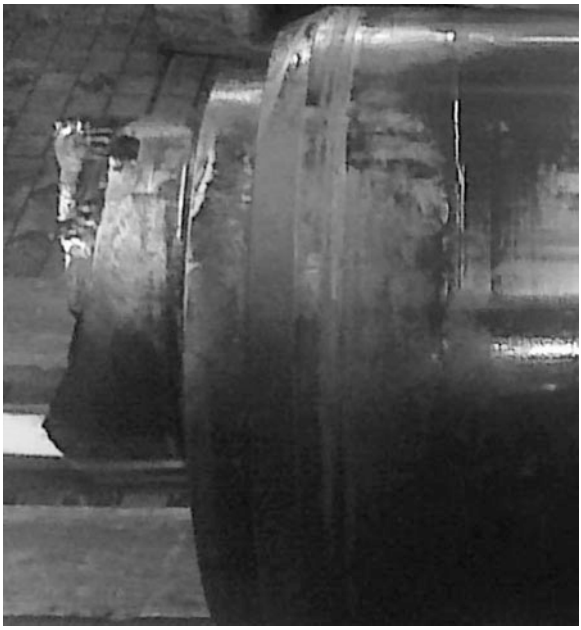

Fig. 7 Side view of the pin fracture on the drive side

The area (2) is analyzed in Fig. 6. There are several crack origins.

The presence of multiple origins may be the result of either high stress or high stress concentrations. In our case it was high stress concentrations. Most of them are origins (C) and (D) between which is typical ratchet mark which indicates the boundary two adjacent failure planes.

The presence of ratchet mark indicates multiple origins and relatively high total stresses. Ratchet mark was resulted from high stress concentrations. By looking at the edges of the ratchet marks, one can tell that the primary load causing the failure was torsional, the sides is tapered. (If plane bending or tension has caused the failure, the sides of the ratchet marks would be essentially perpendicular to the fracture face). River marks show the direction of progression of the fatigue crack.

Side view of the pin fracture on the drive side shows the combined torsional and bending.

3 Conclusions

The story of the breach of the shaft based on the description of the fracture surface and the failure analysis: Fractures No. 1 and No. 3 had a completely different formation and progress. As the first shaft fracture was the fracture No. 1 and primary major cause of breach of the shaft was the radial forming force of plane bending.

The consequence and the continued operation were created high stress of the shaft and the torsion failure No. 2 and No. 3.

Acknowledgments Contribution has been done in connection with project Increasing of Professional Skills by Practical Acquirements and Knowledge, reg. no. CZ.1.07/2.4.00/17.0082.

Reference

Sachs NW (2005) Understanding the surface features of fatigue fractures: how they describe the failure cause and the failure history. J Fail Anal Prev, ASM Int 5(2):11–15

Reliability Analysis of Telescopic Universal Joints Shaft

K. Kaláb, R. Slanina and P. Maršálek

Abstract This article shows the use combination of simulation methods Simulation Based Reliability Assessment (SBRA), Failure Mode and Effect Analysis (FMEA) and Fault Tree Analysis (FTA) on telescopic universal joints shaft. We obtain a considerable improvement and refinement of system reliabilities by incorporating method SRBA to the methods FMEA and FTA. This is very important, especially if done early enough in the development cycle.

Keywords Failure probability · Risk assessment · Analysis

1 Introduction

Telescopic shaft with two joints is important mechanical part which used in vehicles driveline and wide range of industrial applications to transmit torque from the actuator aggregate to driven aggregate by changes in the current distance and angle axes of both units. This mechanical part is subjected to reliability analysis, FMEA, FTA and SBRA methods. Telescopic universal joints shaft is used in vehicles to connection sprung aggregate with rigid aggregate whose reciprocal position changes due to suspension of the vehicle. This one also services connection aggregates, which both belong to sprung matter, when joint shaft enables changes in the relative positions of shafts, which occurs due to elastic storage in a

K. Kaláb (✉) · R. Slanina · P. Maršálek
VŠB-Technical University of Ostrava, Ostrava, Czech Republic
e-mail: kvetoslav.kalab@vsb.cz

R. Slanina
e-mail: radim.slanina@vsb.cz

P. Maršálek
e-mail: petr.marsalek@vsb.cz

L. Ševčík et al. (eds.), *Modern Methods of Construction Design*,
Lecture Notes in Mechanical Engineering, DOI: 10.1007/978-3-319-05203-8_34,

Fig. 1 Telescopic universal joints shaft with plain bearing 4GA05 according DIN 808

frame, compensates frame deformation and manufacturing or assembly inaccuracies. Fox examples joint shafts with two joints are used in vehicles wheel drive vehicles with quadrangular swinging half axles, when a transfer gearbox is part of the sprung matter of vehicle. These shafts are used in automobile drives with front-wheel drive as homokinetic ball joints. Joints shafts are often used also to drive special-purpose equipment such as a winch, farm equipment for tractor etc. In present time market offers a wide range of standard, universal, driving, sliding two joints shafts, which are suitable for a wide range of commercial vehicles and industrial equipment.

2 Failure Modes Description of Universal Telescopic Joints Shaft

Standard telescopic shaft with two shafts type 4GA05 according DIN 808 is shown in Fig. 1. The cardan-joint, which is spherical mechanism, is shown in Figs. 2 and 3. The work of this part is shown in Fig. 4.

Telescopic universal joints shaft is shown in Fig. 5. This joints is given by nominal power $P_{KH} = 3$ kW, nominal revolutions $n_{KH} = 700$ rpm, random chance angle of deviation shaft position $\alpha = (0 \div 20)°$ with dimensions—$d_{KH} = 22$ mm, $D_{KH} = 45$ mm, $L_{2KH} = 95$ mm, $C_{KH} = 22$ mm, $L_{minKH} = 250$ mm, $L_{maxKH} = 280$ mm, $X_{KH} = 30$ mm, $D_{1KH} = 47$ mm, $B_{KH} = 50$ mm, $m_{KH} = 2.35$ kg and splined shaft $6 \times 23 \times 28$ with parameters $z_{DKH} = 6$, $D_{DKH} = 28$ mm, $d_{DKH} = 23$ mm a $R_{DKH} = 0.3$ mm.

Fault reasons: (ČSN EN 60812 2007)

1. clevis damage in extreme fiber of first joint,
2. overload tire pressure between coupling pin and a clevis of first joint,
3. damage of coupling pin by shear from first joint,
4. deformation of the teeth grooves and hip gouging,
5. clevis damage in extreme fiber of second joint,
6. overload tire pressure between coupling pin and a clevis of second joint,

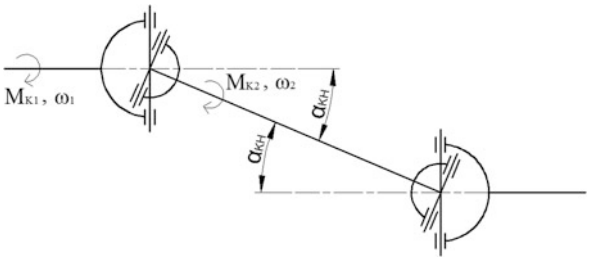

Fig. 2 Principle of cardan-joints or telescopic joints shaft

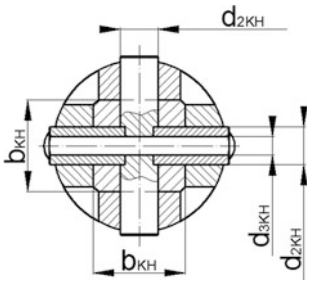

Fig. 3 Performance of cardan-joint

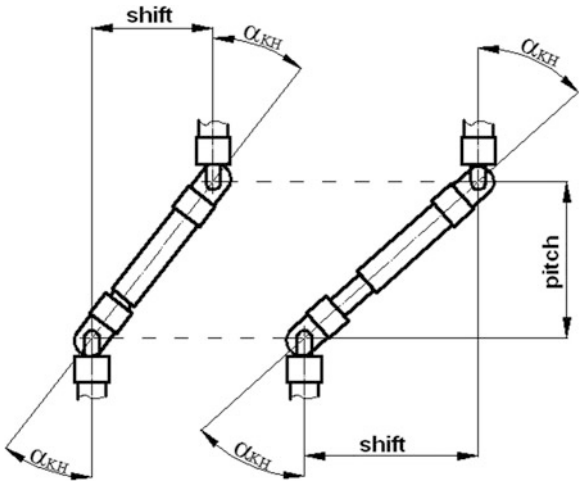

Fig. 4 Work of telescopic joints shaft

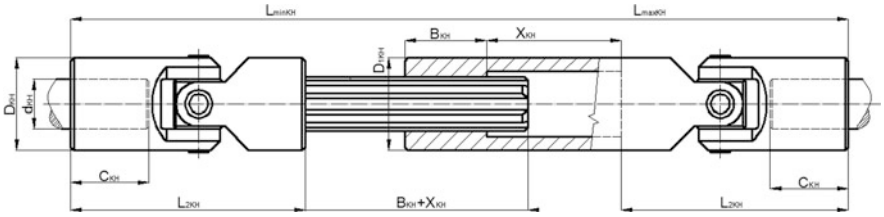

Fig. 5 Telescopic universal joints shaft 4GA05 according DIN 808

Design scheme subsystem propshaft paper machine FMECA											
Nr. Node	Name of node	QTY	Nr. Node	Name of node	QTY	Nr. Node	Name of node	QTY	Nr. Node	Name of node	QTY
10	Mechnaical part	1	100	Propshaft	2	1000	1. node propshaft	1	10000	Fork	2
									10001	Pin	2
						1001	Moving shaft	1			
						1002	2. node propshaft	1	10020	Fork	2
									10021	Pin	2
						1003	Cover	1			
						1004	Lubrication	1			
						1005	Others	1			

Fig. 6 Design schemes

7. damage of coupling pin by shear from second joint,
8. failure of rubber cuff,
9. fault of telescopic shaft,
10. lubrication failure.

3 Reliability Evaluation

From analytical methods for reliability analysis of system was selected combinations inductive methods FMEA and deductive method FTA with calculation using method SBRA. The solution starts from the simplest elements to the lowest level towards the superior systems. Method FMECA is extension of method FMEA consists in the fact that they are included in the means for classification the severity of failure modes in order to prioritize measures. This classification is done by combining the severity and frequency, which creates a relative measure called the criticism. This is a very effective means to show a sufficient level of reliability and security of the system analyzed by the supplier to the customer. Information about the structure and defining the boundaries of the serial was made in Fig. 6.

Occurrence probability classification F_i	1	2	3	4
(a)				High risk
(b)	Number of nodes: 1003 a 1004			
(c)			Number of nodes: 1005	
(d)		Number of nodes: 10000, 10001, 10020 a 10021		
(e)	Low risk	Number of nodes: 10001 a 10021	Number of nodes: 1001	Number of nodes: 10000 a 10020

Seriousness classification S

Fig. 7 Criticality matrix of telescopic universal joints shaft 4GA05 according DIN 808

Table 1 Risk acceptability assessment

Frequency occurrence of fault consequence	Relevance classification of fault consequence			
	1 Inconsequential	2 Marginal	3 Critical	4 Catastrophic
(A)—Very frequent occurrence	Undesirable	Undesirable	Incompetent	Incompetent
(B)—Frequent occurrence	Acceptable	Undesirable	Undesirable	Incompetent
(C)—Sometimes occurrence	Acceptable	Acceptable	Undesirable	Undesirable
(D)—Very weak occurrence	Insignificant	Acceptable	Acceptable	Undesirable
(E)—Unlikely occurrence	Insignificant	Insignificant	Acceptable	Acceptable

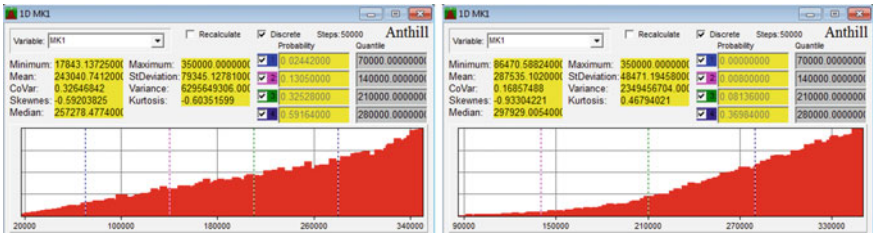

Fig. 8 Load spectrum Nr. 3—type (**a**) and Nr. 6—type (**b**) according ČSN 01 4686

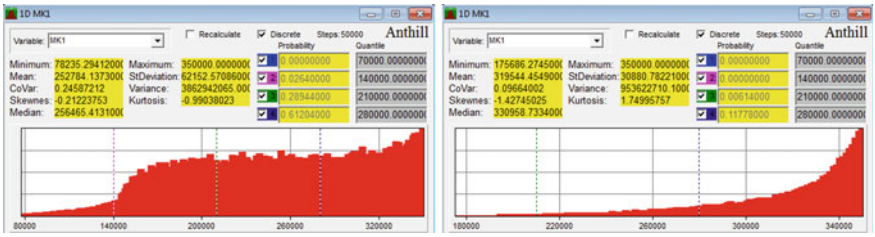

Fig. 9 Load spectrum Nr. 10—type (**a**) and Nr. 13—type (**b**) according ČSN 01 4686

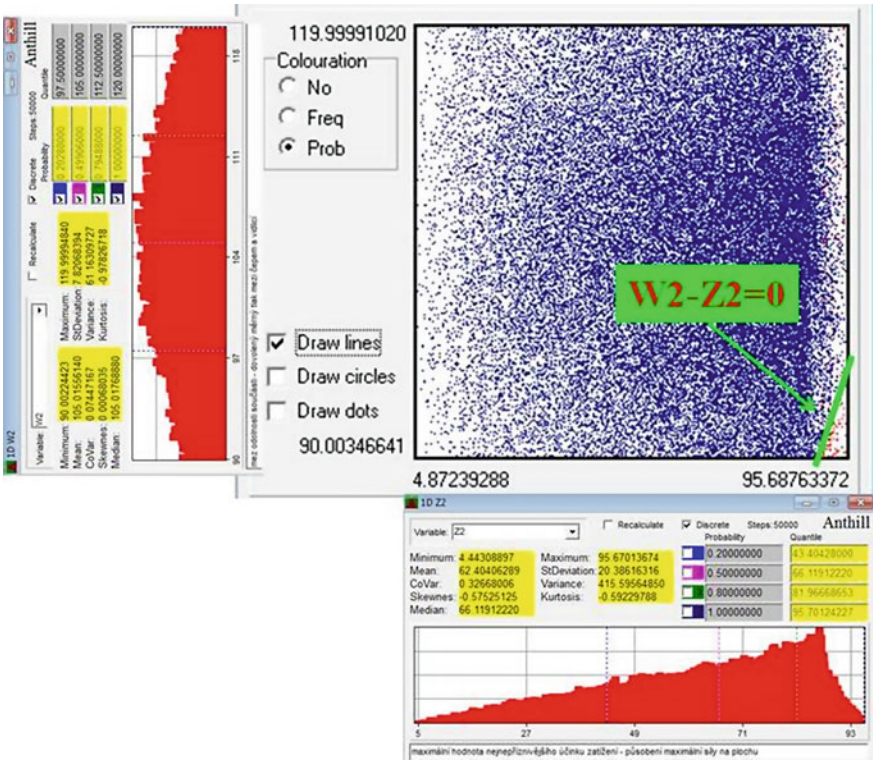

Fig. 10 Example of simulation evaluation of the reliability function of overload tire pressure between coupling pin and a clevis of first joint by method SBRA

For telescopic universal joints shaft was prepared a worksheet and structural diagram method FMECA. Criticality matrix is shown in Fig. 7. Risk acceptability assessment is defined in Table 1. Shaft is loaded by 4 types spectrum illustrated in

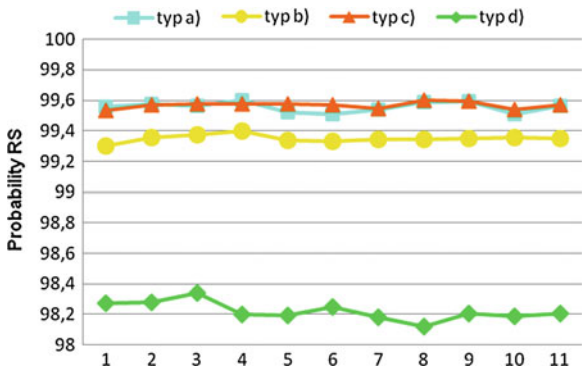

Fig. 11 Chart of 11 simulation estimates non failure shafts for 4 load types

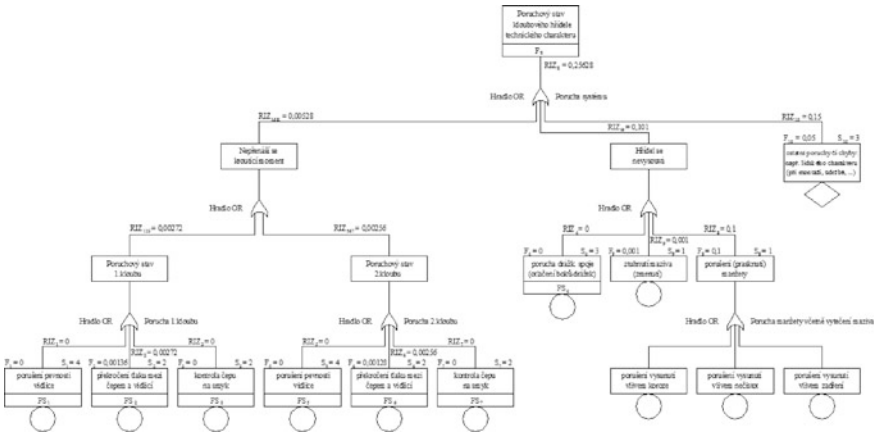

Fig. 12 Fault tree analysis for telescopic universal joints shaft and her risk classification according SRBA method

Figs. 8 and 9. Example of simulation evaluation by method SBRA is shown in Fig. 10. Simulation estimates of reliability for the 4 types of shaft load are illustrated in Fig. 11. In Fig. 12 is shown FTA evaluation by method SBRA.

Acknowledgments This work was supported by Ministry for Education, Youth and Sports, Czech Republic, project—specific university research Nr. SP2013/4.

References

ČSN EN 60812 (2007) Techniky analýzy bezporuchovosti systémů—Postup analýzy způsobů a dů-sledků poruch (FMEA). Úřad pro technickou normalizaci, metrologii a státní zkušebnictví, Praha, 43 p

Dynamic Analysis of Rolling Bearings with Elastic Cage

R. Kohár and S. Hrček

Abstract The aim of this paper is to detail the creation of a large tapered roller bearing model with flexible body cages in the Adams program suite for subsequent dynamic analysis and to obtain information about kinematic and dynamic relationships of steel and plastic cages under various operating conditions. The bearing model was made to closely resemble its real-life counterpart, which allows us to estimate load conditions, dynamic conditions of individual bearing parts and interactions between them.

Keywords Tapered roller bearing · Flexible body · Cage · Adams · Dynamic analysis

1 Introduction

This article details the creation of a virtual bearing model allowing the analysis of individual bearing components under dynamic behavior. Although inner and outer bearing rings and rollers are defined as solid materials, the bearing cage models also take into account elastic properties thereof. Chapter 2 details the creation of the said models. Two models of tapered roller bearings will be considered: one with steel cage and the other with plastic cage.

R. Kohár (✉) · S. Hrček
University of Zilina, Zilina, Slovakia
e-mail: robert.kohar@fstroj.uniza.sk

S. Hrček
e-mail: slavomir.hrcek@fstroj.uniza.sk

L. Ševčík et al. (eds.), *Modern Methods of Construction Design*,
Lecture Notes in Mechanical Engineering, DOI: 10.1007/978-3-319-05203-8_35,

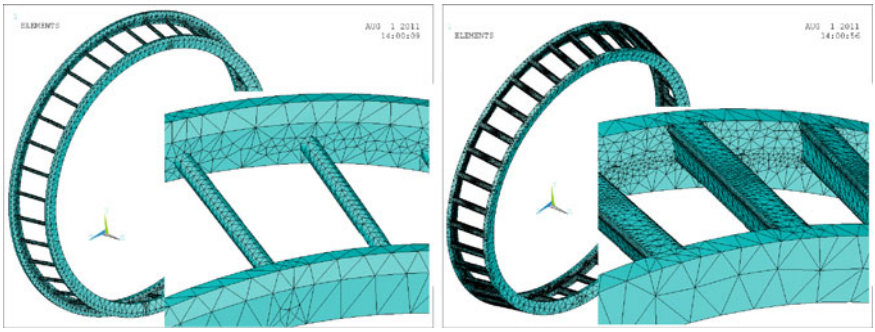

Fig. 1 Finite-element mesh of steel (*left*) and plastic (*right*) cage in Ansys program

2 Creation of "Flexible Body" Cage Models

Dynamic simulations of the tapered roller bearing were performed in the MSC.Adams system. Model creation along with definition of material properties, contact parameters, geometric and kinematic boundary conditions is detailed in Kohár et al. (2012). A Modal Neutral File (MNF) file was necessary to take into account flexible properties. The said file contains important information pertaining to inertial and flexible model properties, including information necessary to integrate the flexible model within the virtual prototype in MSC.Adams program. The actual MNF file can be created in various FE programs such as Nastran, Ansys or Abaqus.

The flexible cage model was created in FE software Ansys which contains a built-in macro for this purpose. The first step consisted of finite-element mesh creation along with the definition of material properties (Fig. 1, Table 1).

After generation of the finite-element mesh and material definition a macro is executed, creating the MNF file which requires the following user input: System of Model Units, Eigenmodes, Element Results, Shell Element Result Output Control, Filename, Solve and create export file to ADAMS.

MNF file analysis and further modification thereof is possible using the MD Adams/Flex Toolkit. The "MNF–MNF Optimizer" was used to analyze and reduce the complexity of the cage models by removing Internal Solid Element Geometry. An alternative approach is to apply the Mesh Coarsening Algorithm, resulting in reduced element counts and increased calculation speed. However, the mentioned approach also modifies node coordinates, which would invalidate load simulations obtained by dynamic simulations for further analysis in FE programs and was thus not used (Adams 2011).

The next step after applying the above process consists of integration of "flex body" within MSC.Adams/View modeler. Figure 2 shows the flexible model integration algorithm within the dynamic simulation.

Table 1 Material properties of steel and plastic cage

	Density [kg/m^3]	Young's modulus [Pa]	Poisson constant [−]	Element type	Number of elements
Steel cage	7,850	2.02×10^{11}	0.29	Solid 187	39,105
Plastic cage	1,100	3×10^{9}	0.42	Solid 187	259,694

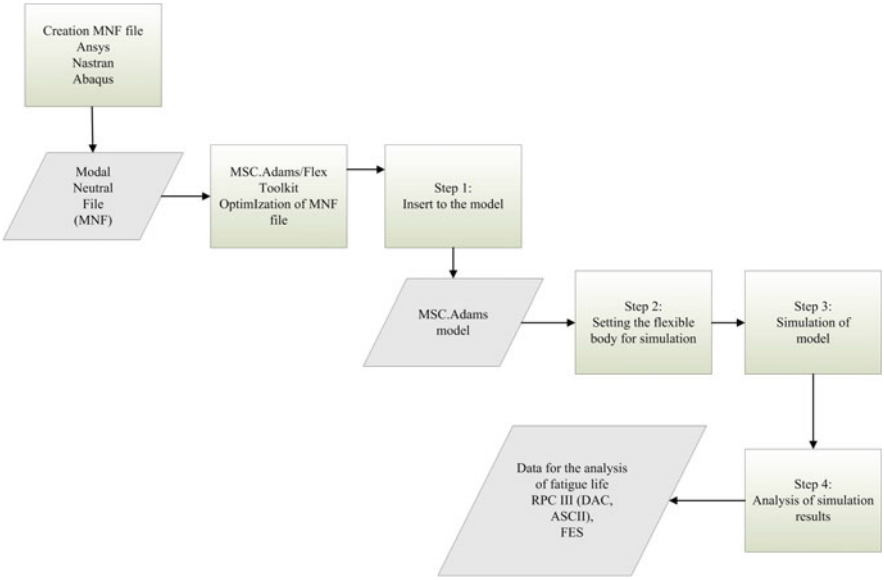

Fig. 2 "Flexible body" integration algorithm within the dynamic simulation

3 Dynamic Simulation Results: Axial Load Force Fa = 518 kN with Rotational Speed n = 15.5 rpm

Dynamic simulation results with axial load force and rotational speed n = 15.5 rpm represent force interactions between individual bearing parts, movement of bearing cage center of gravity and angular velocity thereof.

Figure 3 shows a comparison of load distribution of individual rollers with theoretical calculations based on Frohlich (1980), wherein element load Q_{max} = 56,568 N. Results of the dynamic simulation have been obtained in time t = 10 s.

Figure 4 shows forces between roller and cage, roller and inner ring and angular velocity of this roller. Maximum force between steel cage and rollers was observed during interaction of the cage with roller n. 22 and is equal to 686 N (Fig. 4 up, green line). Also shown is the force between inner ring and roller n. 22 (red line),

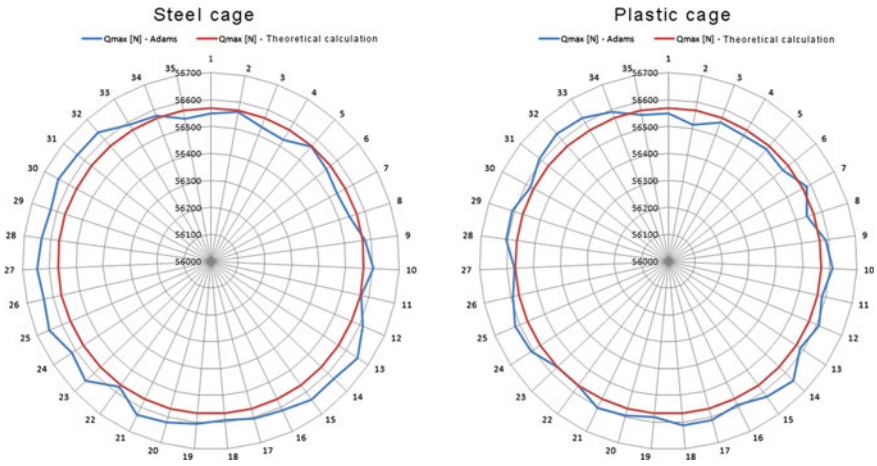

Fig. 3 Load distribution of individual elements compared with theoretical calculations

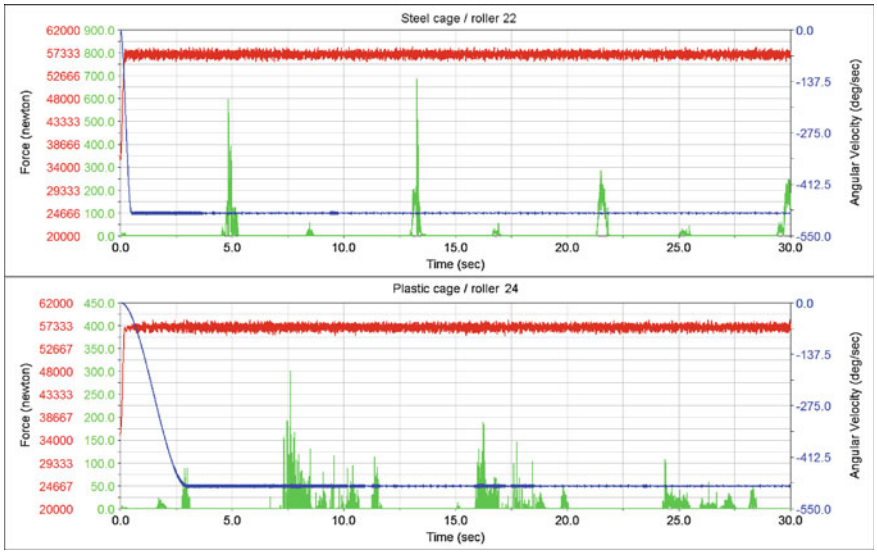

Fig. 4 Force interaction between inner ring and rollers (*red lines*), force interaction between cage and rollers (*green lines*) and angular velocity of rollers

which varied between 54,023 and 58,593 N. The blue line displays angular velocity of roller n. 22 and varies between 484 and 495°/s.

Maximum force between plastic cage and rollers was observed during interaction of the cage with roller n. 24 and is equal to 301 N (Fig. 4 down, green line). Also shown is the force between inner ring and roller n. 24 (red line), which varied between 54,273 and 58,571 N. The blue line displays angular velocity of roller

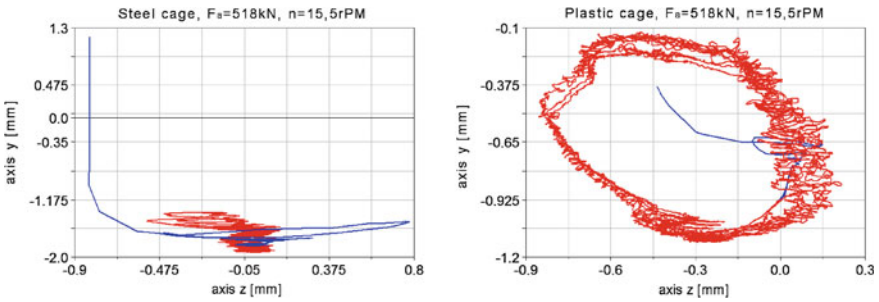

Fig. 5 Movement of center of gravity of steel cage (*left side*) and plastic cage (*right side*) in the y–z plane under axial load

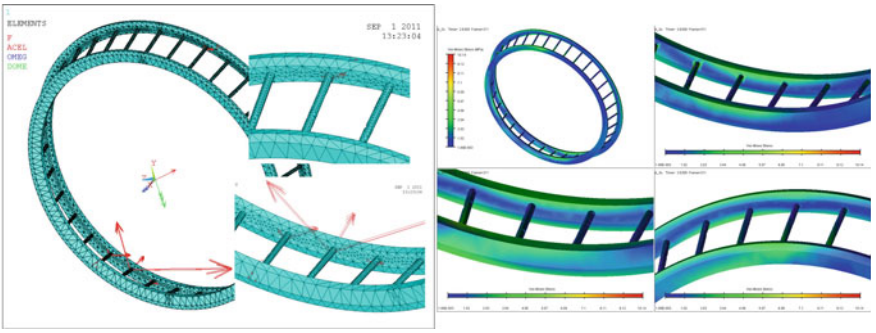

Fig. 6 Force interaction between steel cage and rollers (*left side*) and maximum von Mises stress of steel cage

n. 24 and varies between 485 and 494°/s, similar to the velocity observed for the steel cage.

Figure 5 shows the center of gravity location in the y–z plane of steel and plastic cage, Fig. 6 shows force interaction between inner ring and rollers and the von Mises stress of steel cage and Fig. 7 shows force interaction between inner ring and rollers and the von Mises stress of plastic cage.

Analysis of dynamic simulation results has shown the steel cage is in contact with rollers in lower and upper parts of the bearing, with forces in the upper bearing parts reaching up to 700 N at cage guides and 100 N at lower parts, also at cage guides. Maximum von Mises stress of 10 MPa has been recorded in time t = 2.63 s (Fig. 6).

Dynamic simulation of plastic cage bearing has shown similar results to those presented above. The plastic cage is in contact with rollers in lower and upper parts of the bearing. Forces in the lower part of the bearing reach up to 300 N at cage guides and up to 50 N at upper parts of the bearing cage guide surfaces. Maximum von Mises stress of 0.6 MPa has been recorded in time t = 16.8 s (Fig. 7).

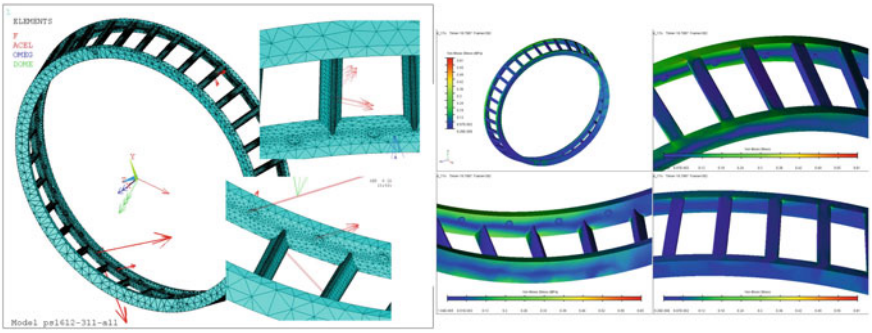

Fig. 7 Force interaction between plastic cage and rollers (*left side*) and maximum von Mises stress of plastic cage

4 Conclusion

The aim of this article was to detail the creation of a tapered roller bearing model in the Adams software suite to be used for further dynamic analysis and to obtain information about individual parts during the simulation process taking into account the properties of the plastic bearing cage.

Dynamic analysis results have shown increased load variation of individual elements in steel cage when compared to the plastic cage, with a difference of 0.5 % for minimum load. Minimal differences were observed under maximum loading conditions. Angular velocities of both analyzed cages shared similar waveforms. Analysis has also shown that forces generated by interaction of rollers and plastic cage were 56 % lower when compared to the steel cage. Likewise, the overall plastic cage stress was an order of magnitude lower compared to the steel cage. The center of gravity of the plastic cage varied by 0.4–0.5 mm in all three axes when compared to the steel cage.

Acknowledgments The research work reported here was made possible by the Slovak Research and Development Agency under the contract no. VEGA 1/0844/13.

References

Adams MD (2011) Reference guide

Frohlich J (1980) Technika uložení s valivými ložiskami. Nakladatelství technické literatury, n.p, Praha

Kohár R, Medvecký Š, Hrček S (2012) Usage of dynamic analysis to determine force interactions between components of rolling bearings with different rotation speed. Mach Des 4(3):145–150. ISSN 1821-1259

Static Analysis of Crawler Excavator Chassis

J. Křička

Abstract Modern and high-power machines for surface mining of energy-producing raw materials require mechanisms of thoroughly perfect design and dimensioning. The theory of structure of mechanisms and methods of mechanics provide an indispensable theoretical foundation. The presented research work deals with the static analysis of crawler excavator chassis.

Keywords Statics · Analysis · Crawler · Chassis · Excavator

1 Introduction

The crawler chassis are used in various types of machines, for example agricultural machinery, earth moving machines and machines for surface mining including large-sized excavators (Hojdar et al. 1991).

The chassis are manufactured in different variants of crawler design. Chassis serves several important functions:

1. the transmission of weight and external forces to terrain,
2. safeguarding the working stability while moving forward, backward and turning around,
3. safeguarding that the allowed load of terrain in not exceeded,
4. the transfer to new locality of mining.

The connection of chassis to terrain is a complex issue. Thus, the research of chassis connection to its surroundings is planned for the next part of the project.

J. Křička (✉)
Czech Technical University, Prague, Czech Republic
e-mail: Jaroslav.Kricka@fs.cvut.cz

L. Ševčík et al. (eds.), *Modern Methods of Construction Design*,
Lecture Notes in Mechanical Engineering, DOI: 10.1007/978-3-319-05203-8_36,

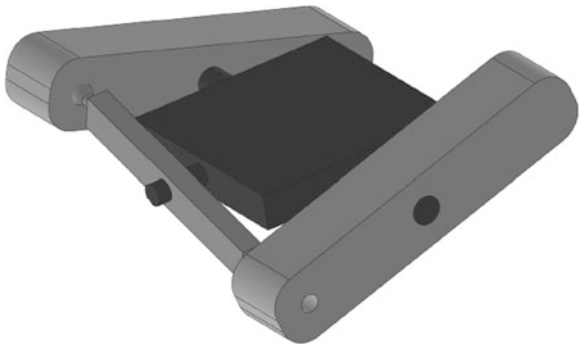

Fig. 1 Crawler excavator chassis, 3D model

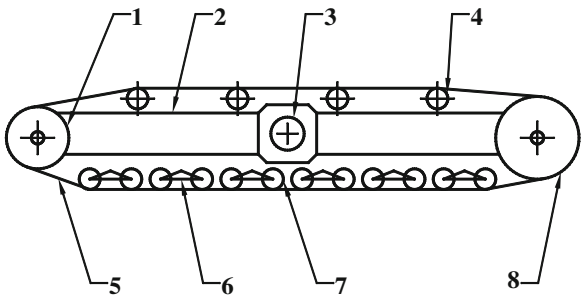

Fig. 2 Detail of crawler

2 New Mechanism of Crawler Chassis and his Solution

Figure 1 shows very simplified 3D model of chassis we analyse.

This type of chassis is of a new construction. According to the manner of excavator to its own chassis there are four-point supports. The movement of pair of crawlers is dependent by means of transverse beam. Each chain belt has its individual and reversible controlled driving device which enables the machine to move in random bend or turn on the spot. Real chassis consists of the following main parts: (1) chain driving wheel, (2) longitudinal girder, (3) king journal, (4) supporting roller, (5) chain driving wheel, (6) undercarriage balance beam, (7) travelling roller, (8) idler sprocket, Fig. 2.

Figure 3 shows the kinematic diagram of simplified chassis and type of connections compiled in accordance with Fig. 1.

The illustrated spatial mechanism is assembled from five rigid bodies including frame. Each body has six degrees of freedom in space. To find a solution it necessary to describe every body by the system of six linear algebraic equations (Stejskal et al. 1998). The system of equations is driven by the extent of

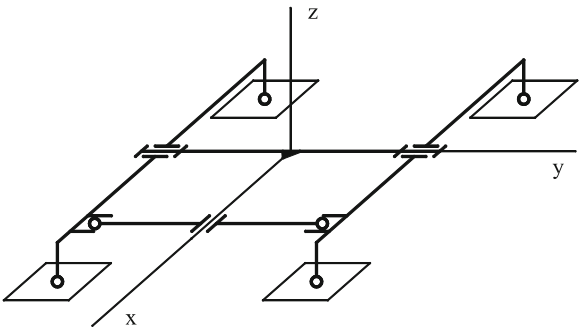

Fig. 3 Kinematic schema of chassis

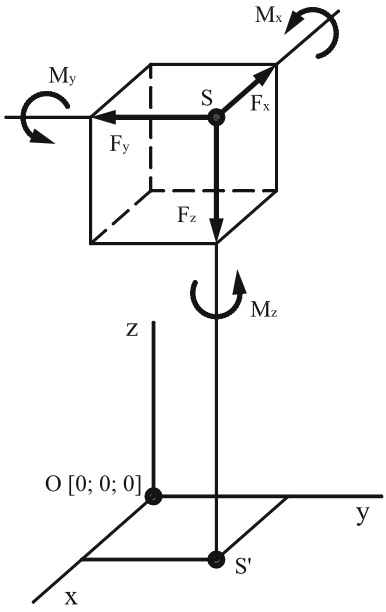

Fig. 4 Workload of chassis

simplification of the real machine which might by performed on various levels (Brát 1981).

The load of chassis is based on the assumption that the workload is situated in the level of ball trajectory by space system forces and moments, Fig. 4.

The load of chassis is caused by its own weight, wind, breakout forces, forces of inertia and resistance to movement (Hojdar et al. 1991).

During manoeuvring the machine can move on the smooth plane surface or overcome different obstructions, Fig. 5.

It influences the stability and load of all components of chassis. In extreme cases one undercarriage balance beam can transfer a half of total weight of machine.

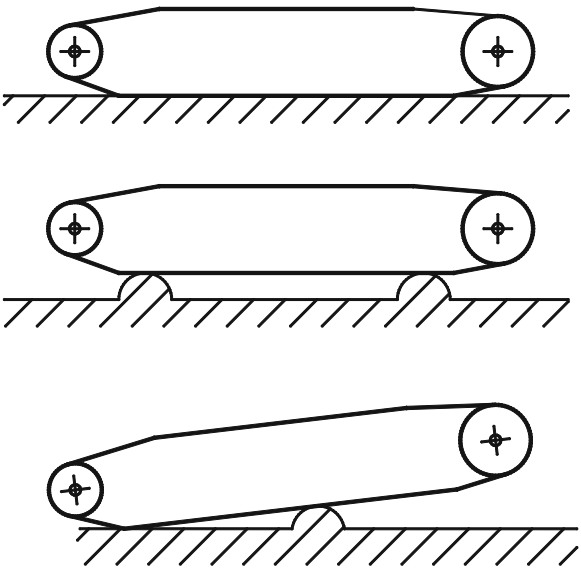

Fig. 5 The contact of chassis with the surrounding muddy or rocky terrain

The knowledge of forces and their size is important for dimensioning all parts of chassis which have a direct impact on reliability and lifespan of chassis. Numerical computation of unknown forces and moments has to executed for a great number of different operational situations. Acquired results will be used for designing and dimensioning of all chassis parts and for power determination of driving motors.

3 Conclusions

The contact of chassis with the surrounding muddy or rocky terrain presents an interesting issue. This will be the subject of further research.

References

Brát V (1981) Maticové metody v analýze a syntéze prostorových vázaných mechanických systémů. Academia, Praha

Hojdar J, Helebrant F, Gondek H (1991) Povrchové dobývací stroje. VŠB v Ostravě, Ostrava

Stejskal V, Březina J, Knězů J (1998) Mechanika I. ČVUT v Praze, Prague

Press-on Joint of Rotating Discs

E. Kronerova, J. Kratky and V. Kubec

Abstract This paper deals with the connection of shaft and gear wheel (disc) in high-speed gearboxes with a low-speed shaft. This type of connection and the conditions under which it operates may lead to separation of the disc from the shaft and thus to overall defect of the gearbox.

Keywords High-speed gearbox · Press-on joint · Rotation

1 Introduction

When evaluating a press-on joint using statistical methods, the fact that the disc rotates is disregarded. During rotation of an unloaded disc with an opening, the disc deforms in the direction of the centrifugal force. The disc is thus on its inner and outer dimensions shifted away from the centre. If we consider the shaft to be a disc without an opening, its external diameter shifts away from the centre of the shaft. This means that in conditions of zero pressure in the contact surfaces the disc and shaft move in the same direction and separation should not occur.

However, if there is non-zero pressure on the disc and shaft contact surfaces, then under the influence of rotation the internal diameter shifts away from the axis and at the shaft the internal diameter is forced towards the shaft axis.

E. Kronerova (✉) · J. Kratky · V. Kubec
University of Bohemia, Bohemia, Czech Republic
e-mail: kronero@kks.zcu.cz

J. Kratky
e-mail: kratkyj@kks.zcu.cz

V. Kubec
e-mail: vkubec@kks.zcu.cz

L. Ševčík et al. (eds.), *Modern Methods of Construction Design*,
Lecture Notes in Mechanical Engineering, DOI: 10.1007/978-3-319-05203-8_37,

2 Calculating Press-on During Rotation

When calculating the press-on of the disc under rotation under loaded torque for the same materials we must first determine the required pressure (Eq. 1) and overlap (Eq. 2) from the static analysis of the press-on (Bolek 1989).

$$p_p = \frac{2 \cdot M_t \cdot s_f}{\pi \cdot d_1^2 \cdot l \cdot f} \tag{1}$$

$$\Delta d_{p1} = \left|\Delta d_{p1}^h\right| + \left|\Delta d_{p1}^k\right| = \frac{d_1}{E} \cdot p \cdot (1 + C_2) \tag{2}$$

Next, maximum and minimum overlap required to transfer the load can be determined. From these values it is possible to determine the minimum and maximum pressure that arises in the contact area during rotation (Eq. 3) (Fig. 1).

$$p_{\min/\max} = \frac{\Delta d_{p1_{\min/\max}}}{d_1} \cdot \frac{E}{(1 + C_2)} \tag{3}$$

This pressure is then the loaded pressure for calculating the press-on of a rotating disc. For this calculation it is necessary to determine the radial and tangential stress in the disc and shaft according to Eqs. 4 and 5 for the inner diameter of the hub and the outer diameter of the shaft.

$$\sigma_r(r) = K_1 - \frac{K_2}{r^2} - (3 + \mu) \cdot K_\omega \cdot r^2 \tag{4}$$

$$\sigma_t(r) = K_1 + \frac{K_2}{r^2} - (1 + 3\mu) \cdot K_\omega \cdot r^2 \tag{5}$$

K_1 a K_2 are integration constants and K_ω is the constant including the rotating disc.

After determining the stress at boundary point r1 the required overlap can be determined, which is necessary to maintain the disc and shaft in connection during rotation (Eq. 6) (Fig 2).

$$\Delta d_{\omega 1} = \left|\Delta d_{\omega 1}^h\right| + \left|\Delta d_{\omega 1}^k\right| = \frac{d_1}{E} \cdot \left[\left|\sigma_{t1}^h - \mu\sigma_{r1}^h\right| + \left|\sigma_{t1}^k - \mu\sigma_{r1}^k\right|\right] \tag{6}$$

By analysis of the values of the overlap created by pressing on and overlap which is needed for rotation it can be determined whether the connection transfers the load applied at certain speeds. If the difference between overlap during rotation and the press-on is less than the required overlap, then separation occurs at the press-on joint (Kříž 1994).

Figure 3 shows a particular case and stress changes are shown in Fig. 4.

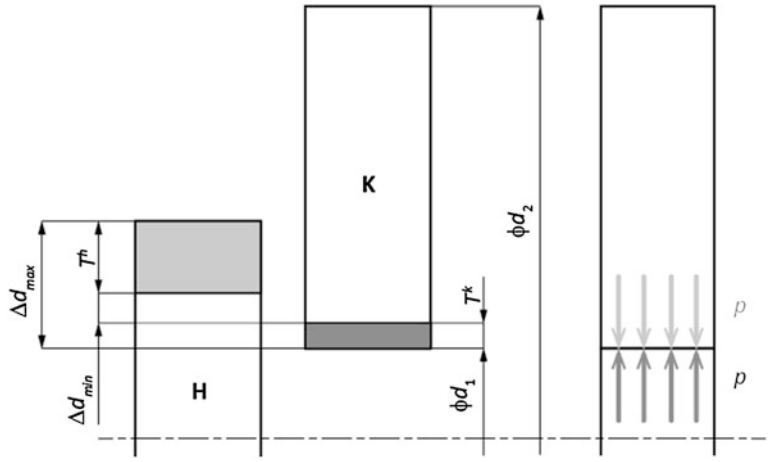

Fig. 1 Press-on joint

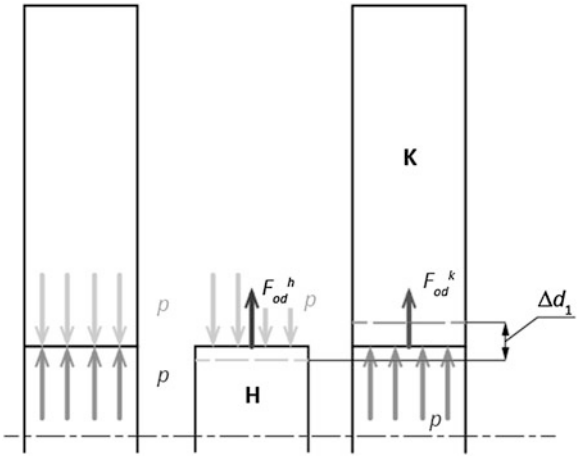

Fig. 2 Force analysis of rotation

Calculation of pressure-on rotating disk of constant cross-section				
zadání				
power	P	kW	8 500,00	
speed	n	min^{-1}	1 500,00	
inner diameter of the hub	d_1	mm	250,00	
outer diameter of the hub	d_2	mm	1 680,00	
hub length	l	mm	130,00	
coefficient of friction	f		0,12	
safety	s		2,00	
materiál kotouče				
tensile modulus hub	E_k	Mpa	206 940,00	
poison number	μ_k		0,29	
density	ρ_k	kg/m^3	7 829,00	
materiál hřídele				
tensile modulus shaft	E_h	Mpa	206 940,00	
poison number	μ_h		0,29	
density	ρ_h	kg/m^3	7 829,00	
výsledky				
required pressure	p_p	Mpa	70,70	
required overlap	Δd_p	µm	174,69	
tolerance on the diameter of the hole wheels			H7	
upper tolerance			46,00	
lower tolerance			0,00	
minimum value of the lower shaft tolerance			220,69	
shaft tolerances on diameter			u6	
upper tolerance			313,00	
lower tolerance			284,00	
			min	max
overlap to press-on			238,00	313,00
pressure in pressure-on	p	Mpa	96,30	126,70
displacement of the shaft	$\Delta d_{w1}{}^k$	µm	-82	-108
displacement of the wheel	$\Delta d_{w2}{}^k$	µm	291	330
resulting overlap for rotation	Δd_w	µm	373	438
extreme values overlap	Δd_1	µm	135	125
			not	not
release speed min	n_u	min^{-1}	1 511	1 451
the resulting pressure in the joint	p_s	Mpa	54,76	50,52

Fig. 3 Calculating press-on joint under rotation (Hosnedl and Krátký 1999)

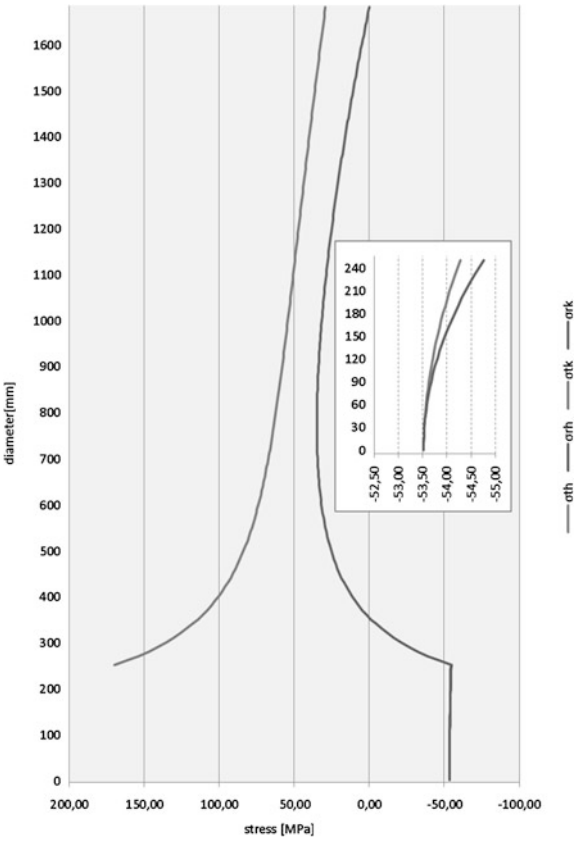

Fig. 4 Stress changes for shaft and disc

3 Conclusions

If we lower the required pressure in the contact area of shaft, we thus also reduce the required overlap. By reducing the required overlap, we also reduce the overlap necessary for rotation and the resulting overlap and then the press-on joint holds. Reduction of the required pressure can be achieved by changing the length of the disc.

The next step in analysing the press-on joint will be the influence of rotation on the width of the disc and then solving different widths of disc hubs and rims.

Acknowledgments This contribution was created within of the project SGS-2013-050.

References

Bolek A, Kochman J (1989) Části strojů. Sv. 1. 5., přeprac. vyd. (v SNTL 1. vyd.). SNTL, 775 p. Technický průvodce; Sv. 6. Česká matice technická; Čís. 349, Praha. ISBN 80-03-00046-7

Hosnedl S, Krátký J (1999) Příručka strojního inženýra: obecné strojní části. 1, Spoje, otočná uložení, hřídelové spojky, akumulátory mechanické energie, Vyd 1. Computer Press, Praha, 313 s. Edice strojaře. ISBN 80-7226-055-3

Kříž R (1994) Strojírenská příručka, Sv. 5. 1. vyd. Scientia, Praha, 241 p. ISBN 80-85827-59-X

A Comparison of DFA Methods for Manual Assembly

Ivan Mašín

Abstract DFA methods are essential tools in providing feedback to designers about design′s efficiency from the assembly viewpoint. Several DFA methods are available for the determination of product complexity and easy of assembly. Three DFA-methods considered in this study are the Boothroyd–Dewhurst method, the Modified Westinghouse Method and the DFA Lucas method. These methods were applied to existing product and evaluated in the comparison table. Methods and results were also compared with the BasicMOST work measurement system.

Keywords Design efficiency · Assembly · DFA

1 Introduction

Design for Assembly (DFA) is a methodology for evaluating part and product designs and the overall design of an assembly. It is a quantifiable way to identify unnecessary parts in an assembly and to determine assembly times and costs.

The nature of assembly difficulty has been measured and a defined by many techniques (Boothroyd–Dewhurst method, Modified Westinghouse Method, DFA Lucas method, Hitachi—Assembly Evaluation Method, Hinckley Assembly Complexity Factor, Sony Standard Time Assembly method e.g.).

All of DFA methods breakdown the assembly operations into discrete tasks by which the handling, feeding, insertion and processing activities are evaluated according to shape, orientation, alignment, insertion direction, fastening processes and other conditions.

I. Mašín (✉)
Department of Design of Machine Elements and Mechanism, Faculty of Mechanical Engineering, Technical University of Liberec, Liberec, Czech Republic
e-mail: ipi.masin@iol.cz

L. Ševčík et al. (eds.), *Modern Methods of Construction Design*,
Lecture Notes in Mechanical Engineering, DOI: 10.1007/978-3-319-05203-8_38,

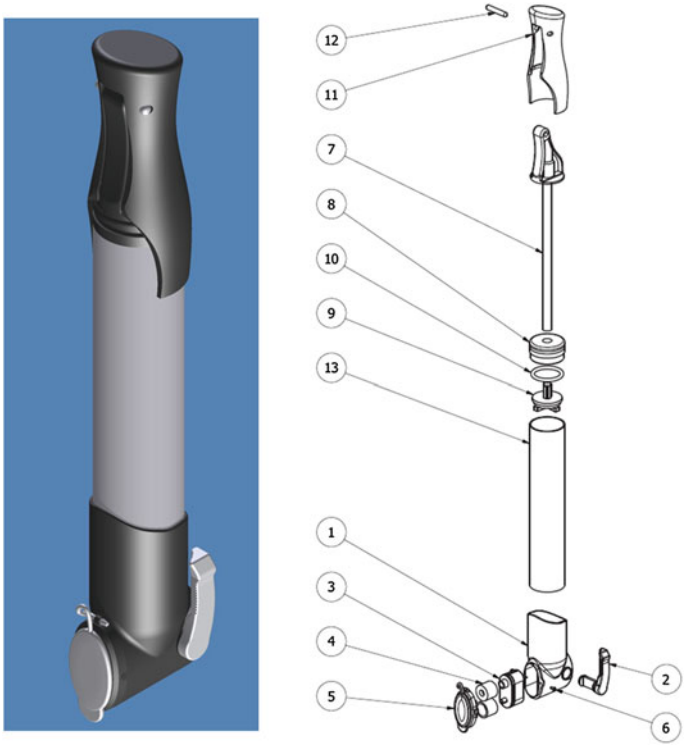

Fig. 1 Assembled product

DFA methods generally support understanding how the part characteristics affect its assembly and what properties of an assembly task determine assembly productivity. This understanding is used for an early feedback to the design process to decrease assembly cost (Whitney 2004).

The term assembly difficulty refers to some metrics and indicators that were developed to quantify ease of manual, automatic or robotic assembly. In the literature we can find indicators like total assembly time, assembly cost ratio, assemblability evaluation score, design efficiency, handling ratio, fitting ratio e.g.

2 Scope and Condition of the Study

The scope of the study refers to the parameters in with the study was operating in. As a product with adequate complexity was chosen the bicycle pump (Fig. 1) with 15 parts. For manual assembly operations was considered a standard workbench (Fig. 2).

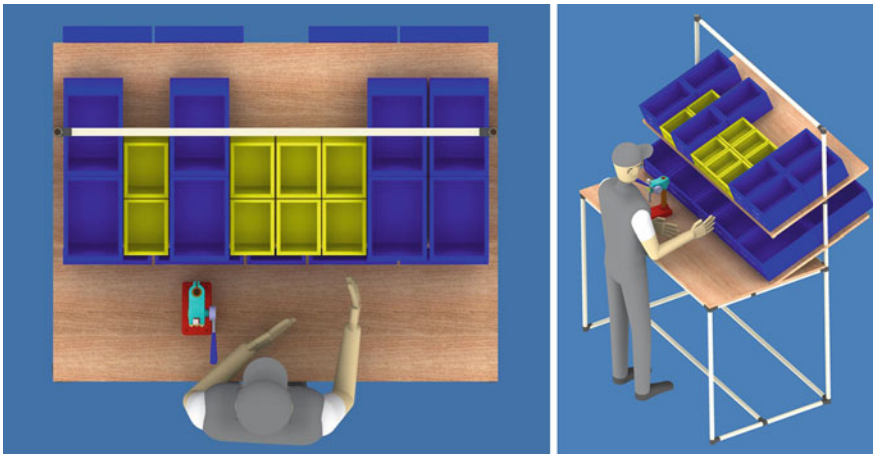

Fig. 2 Workplace for manual assembly

Design efficiency of chosen product was analyzed by representative DFA methods:

- Modified Westinghouse Method
- Boothroyd–Dewhurst DFA Method
- Lucas DFA Method.

These methods have their origins in the industrial engineering measurement systems/techniques like MTM (Methods-Time Measurement) and MOST (Maynard Operation Sequence Technique). Methods are based on measuring the ease or difficulty with which parts can be handled and assembled together into a given product.

3 Assembly Time and Design Efficiency Analysis

Factors such as part size, thickness, alignment, insertion conditions, fastening process are assessed and added up when analyzing design by the Modified Westinghouse Method. Extract from the analysis is illustrated at the Fig. 3.

The Boothroyd–Dewhurst DFA Method was developed in the late 1970s by G. Boothroyd, at the University of Massachusetts. The analysis cannot be employed to create a design from nothing but rather is used to evaluate and refine an existing design. The total assembly time for each component part is obtained by adding the handling time of that part to its insertion time—partial times are obtained from synthetic data (tables). The opportunity for reducing time and cost is found by examining each part in turn and identifying whether each exists as a separate part

Part Nr.	Component Working element	Handling condition	Size	Thickness	Orientation about insertion axis	End to end alignmnet	Insertion direction	insertion conditions	Insertion clearence	Fastener time	Fastening proces time	Time per part	Frequency	Total time	Insertion	Elimination
1	body				1,00	1,00						2,00	1	2,00		
2	lever	1,50			1,00	1,00	1,40		0,90			5,80	1	5,80	1	
3	valve				1,50	1,50	1,40		0,90			5,30	1	5,30	1	
4	rubber				1,00	1,00	1,40		0,90			4,30	2	8,60	1	
5	cap	1,50			1,00	1,00	1,40		0,90			5,80	1	5,80	1	
6	screw		0,40	0,20	0,25	1,00	0,60			4,00		6,45	2	12,90	1	
7	piston rod				1,00	1,00						2,00	1	2,00	1	
8	plug				1,50	1,00	1,40		0,90			4,80	1	4,80	1	

Fig. 3 Extract from modified westinghouse method analysis

for fundamental reasons. Analysis based on Boothroyd–Dewhurst DFA Method is presented in Table 1.

The Lucas DFA Method is a result of the collaboration between Lucas and the University of Hull. The method involves the assigning and summing of penalty factors associated with potential design problems with the inclusion of feeding as well as insertion. Three scores, design efficiency, feeding ratio and fitting ratio, are generated. These scores can then be compared to thresholds or to values established for previous designs. Extract from the analysis is illustrated at the Fig. 4.

To properly evaluate DFA methods, we need a standard to which they can be compared. For comparison with DFA methods the pre-determined motion time system BasicMOST was applied. The objective of BasicMOST is to quantify work content by evaluating it in terms of what all work involves—the movement of objects. BasicMOST was designed to be much faster than other work quantification techniques because of its simpler structure. It groups together into predefined sequences the basic motions that frequently occur (Fig 5) (Beiter 2000).

4 DFA Methods Comparison

The purpose of this study was to compare results obtained using different DFA methods. For the subjective comparison following criteria were used:

- Speed of analysis
- Accuracy of assembly time (time estimates)
- Work elements reflection
- Workplace reflection
- Definition and reproducibility

Table 1 Boothroyd–Dewhurst DFA method analysis (Boothroyd 2002)

Nr.	Component	Freq.	Manual handling code	Manual handling time (s)	Manual insertion code	Manual insertion time (s)	Total time (TM)	Theoretical minimum parts (NM)
1	Body	1	00	1.13			1.13	0
2	Lever	1	10	1.50	00	1.50	3.00	0
3	Valve	1	10	1.50	01	2.50	4.00	1
4	Rubber	2	01	1.43	00	1.50	5.86	0
5	Cap	1	10	1.50	01	1.50	3.00	0
6	Screw	2	04	2.18	38	6.00	16.36	0
7	Piston rod	1	00	1.13			1.13	0
8	Plug	1	00	1.13	00	1.50	2.63	0
9	Piston	1	01	1.13	34	6.00	7.13	1
10	Sealing	1	00	1.13	30	2.00	3.13	0
11	Handle	1	00	1.13	00	1.50	2.63	0
12	Pin	1	00	1.13	31	5.00	6.13	0
13	Tube	2	00	1.13	38	6.00	14.26	1
Design efficiency (3 × NM/ TM) × 100			12.8 %			Total	70.39	3

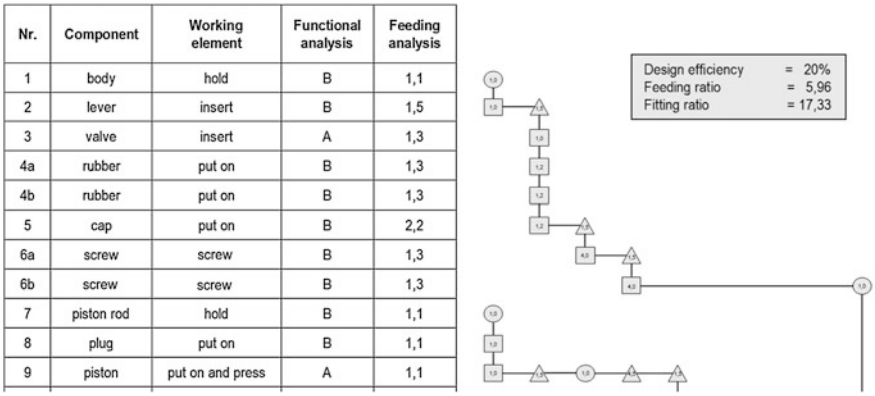

Nr.	Component	Working element	Functional analysis	Feeding analysis
1	body	hold	B	1,1
2	lever	insert	B	1,5
3	valve	insert	A	1,3
4a	rubber	put on	B	1,3
4b	rubber	put on	B	1,3
5	cap	put on	B	2,2
6a	screw	screw	B	1,3
6b	screw	screw	B	1,3
7	piston rod	hold	B	1,1
8	plug	put on	B	1,1
9	piston	put on and press	A	1,1

Fig. 4 Extract from Lucas DFA method analysis

- Designer effort
- Training
- Design efficiency metrics
- Waste identification
- New design support (simplification) (Table 2)

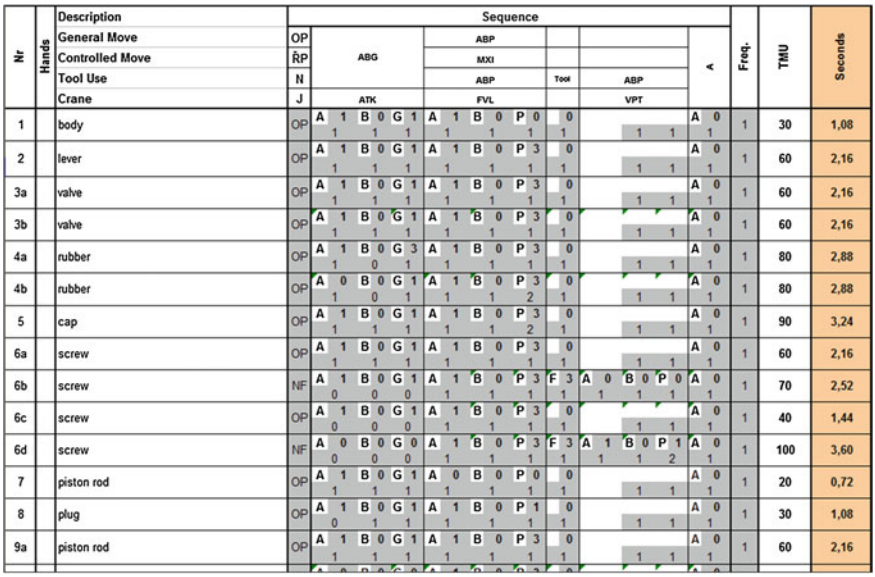

Nr	Hands	Description	Sequence							Freq.	TMU	Seconds
		General Move	OP	ABG		ABP						
		Controlled Move	RP			MXI						
		Tool Use	N			ABP	Tool	ABP	A			
		Crane	J	ATK		FVL		VPT				
1		body	OP	A 1 B 0 G 1		A 1 B 0 P 0	0 1		A 0 1	1	30	1,08
2		lever	OP	A 1 B 0 G 1		A 1 B 0 P 3	0 1		A 0 1	1	60	2,16
3a		valve	OP	A 1 B 0 G 1		A 1 B 0 P 3	0 1		A 0 1	1	60	2,16
3b		valve	OP	A 1 B 0 G 1		A 1 B 0 P 3	0 1		A 0 1	1	60	2,16
4a		rubber	OP	A 1 B 0 G 3		A 1 B 0 P 3	0 1		A 0 1	1	80	2,88
4b		rubber	OP	A 0 B 0 G 1		A 1 B 0 P 3	0 1		A 0 1	1	80	2,88
5		cap	OP	A 1 B 0 G 1		A 1 B 0 P 3	0 1		A 0 1	1	90	3,24
6a		screw	OP	A 1 B 0 G 1		A 1 B 0 P 3	0 1		A 0 1	1	60	2,16
6b		screw	NF	A 1 B 0 G 1		A 1 B 0 P 3	F 3 1	A 0 B 0 P 0	A 0 1	1	70	2,52
6c		screw	OP	A 1 B 0 G 1		A 1 B 0 P 3	0 1		A 0 1	1	40	1,44
6d		screw	NF	A 0 B 0 G 0		A 1 B 0 P 3	F 3 1	A 1 B 0 P 1	A 0 1	1	100	3,60
7		piston rod	OP	A 1 B 0 G 1		A 0 B 0 P 0	0 1		A 0 1	1	20	0,72
8		plug	OP	A 1 B 0 G 1		A 1 B 0 P 1	0 1		A 0 1	1	30	1,08
9a		piston rod	OP	A 1 B 0 G 1		A 1 B 0 P 3	0 1		A 0 1	1	60	2,16

Fig. 5 Extract from basicMOST analysis

Table 2 Comparison table

Criteria	Modified westinghouse method	Boothroyd–Dewhurst DFA method	Lucas DFA method	Basic MOST
Speed of analysis	0	+	+	0
Accuracy of assembly time	−	0	0	+
Work elements reflection	0	0	0	+
Workplace reflection	0	0	0	+
Definition and reproducibility	−	−	0	+
Designer effort	0	0	0	−
Training	0	0	0	−
Design efficiency metrics	0	+	+	−
Waste identification	0	−	0	+
New design support (simplification)	0	+	+	−
Score	−2	1	3	1

5 Conclusions

A rational design for easy and low-cost manual assembly is the selection of the most appropriate method for manual assembling products. For design efficiency and assembly difficulty evaluation several DFA methodologies were developed. DFA methods are based on measuring the ease with which parts can be handled and assembled together into a given product.

Presented study compared selected DFA methods from the point of view of 10 criterions. Study shows among others that wide-spread DFA techniques are problematic from the definition and reproducibility viewpoint. In some cases utilization of BasicMOST technique during product design phase can provide similar benefits to individual designers or innovation teams.

References

Beiter KA, Cheldelin B, Ishii K (2000) Assembly quality method: a tool in aid of product strategy, design, and process improvements. In: Proceedings of DETC 2000, ASME

Boothroyd G, Dewhurst P, Knight W (2002) Product design for manufacture and assembly. Marcel Dekker, New York

Whitney D (2004) Mechanical assemblies: their design, manufacture, and role in product development. Oxford University Press, Oxford

Analysis of Marine Electric Power Plants Loads

Z. Matuszak and G. Nicewicz

Abstract Some aspects of marine electric power plants load registration and identification have been presented. Methods of operating data collecting about marine electric power plant loads based on an example of three vessels—a chemical tanker, a container ship and a tanker—have been shown. Power plants of these vessels have been described. Examples of collected operating data are given. The paper presents part the of carried out marine electric power plant load identification research.

Keywords Marine electric power system · Load registration · Load identification

1 Introduction

It is not possible to build ship power plant (different types and size) in land conditions as well as to conduct an appropriate research on them in order to determine a demand for the electric energy, and simultaneously identify loads, reconstructing real operating conditions (Balcerski 1991, 1992; Balcerski and Bocheński 1991). Hence it is necessary to conduct research on the actual objects in operating conditions. Special measuring team's occurrence during long-term voyages of sea ships in different operating conditions is hampered and connected both with costs and organizational problems of these type undertakings. In these conditions a collection of appropriate operating data and information about object parameters presents a big problem in research conduction concerning identification

Z. Matuszak (✉) · G. Nicewicz
Maritime University of Szczecin, Szczecin, Poland
e-mail: z.matuszak@am.szczecin.pl

G. Nicewicz
e-mail: g.nicewicz@am.szczecin.pl

L. Ševčík et al. (eds.), *Modern Methods of Construction Design*,
Lecture Notes in Mechanical Engineering, DOI: 10.1007/978-3-319-05203-8_39,

of real machinery and marine devices operation as well as layouts of energetic systems. The presented material contains an attempt to describe such a type of research.

From the point of view of the functions fulfilled, it is possible to divide energy receivers on board into four groups (Śmierzchalski 2004; Wojnowski 1992): main propulsion devices, main propulsion auxiliaries, general-ship's devices, hotel devices and economic equipment.

In most merchant ships the main propulsion is carried out with the use of low or medium speed piston internal-combustion engines, which directly provide the mechanical energy to the propeller.

In the presented material research results of marine power station loads in three different ships were characterized: *m/v COSCO Long Beach* container ship; *m/v Skagica* chemical tanker and *m/v Navion Clipper* oil tanker in different so-called operating states.

The determination of electric energy demand for ship is carried out at the unit design stage. The following factors decide above all about the value of electric energy demand (Śmierzchalski 2004; Wojnowski 1992): ship's type and size as well as type of transported cargo; type and power of main engine as well as type of applied fuel; considered, given unit characteristic of the load condition (ship's operating state); electrification and automation ship degree; swimming area; crew and passengers amount.

Assuming that all pumps operating the main engine are electrically powered, and the ship has been equipped with air-conditioning installation, an average daily electric load during sea travel at the maximum continuous output of the main engine can be calculated from a model (Wojnowski 1992):

$$W = 0.020\, N_w + 1.6\, Z + 9\sqrt{Z} + 80 \tag{1}$$

where:

W average daily electric load [kW]
N_w maximum continuous output on the shaft [kW]
Z number of people on board

Observation of energy systems load in three ships was conducted during their work for the following period of time: 86 days for *m/v COSCO Long Beach* container ship; 85 days for *m/v Skagica* chemical tanker; 87 days for *m/v Navion Clipper* oil tanker.

At that time the accepted following operating ships states were recorded: free swimming (sea voyage), travel by the channel, stop in the port (cargo operation), maneuvers (arrival into the port, departure from the port or dock), stop on the anchorage, storming, drifting. The mentioned states refer to all units. For *m/v Navion Clipper* ship the concept of the operating state—DP load was implemented.

Free swimming (sea voyage)—it is a state (Wojnowski 1992) in which the unit swims through open sea or ocean. This state is characteristic by constancy power load. Most often one generating set is used then.

Travel by the channel—it is the unit travel through limited water region, river or channel. Increased power plant readiness, and additionally generating set is started is required then.

Stop in the port—it is an operating state, during which the ship stays in the port and cargo operation is conducted. Power load and its changeability depends mainly on the unit type as well as period of its stop in the port. The pumps operating the main engine are turned off in container ship at longer stop, relative load is rather small, and one generating set works. Load value in the oil tanker is greater at unload, then energy is needed to drive cargo pumps; two generating sets usually work. At load one is enough.

Stop at the dock—during the research one of the ships stayed in the shipyard; arrival and departure maneuvers from the dock due to cargo character were categorized on graphs to arrival/departure from the port. Stop of ship at the dock is an operating state characterized by low power load, which uses the energy from shipbuilding power lines or its own generating sets.

Maneuvers—it is a state during arrival or departure from the port or dock, characterized by large electric power loads and their changeability caused above all by a use of bow thrusters. A work of few generating sets is necessary.

Storming—a state in which the unit swims through opened sea at not-supporting weather conditions (strong wind, rough sea). During storming, the power station is usually maintained on alert by attaching an additional generating set.

Stop at the anchorage—it is a unit operating condition with a use of an anchor during the stop. Electric power load is usually constant, except of raising or lowering the anchor.

Drifting—a state in which the unit is on an opened sea, and the main engine is turned off or adjustable screw propeller is on zero position. Loads and their character depend on whether the unit use bow thrusters and whether the readiness to start the main engine is maintained.

DP load—a state which refers to the unit working in the dynamic positioning system (DP). Cargo operation on a sea area by the unit storing petroleum is conducted. During cargo operation the main engine (control pitch propeller is on zero position) and three thrusters work. Loads height and their changeable character requires a use of four generating sets (the fifth remains in reserve).

As it is seen from the operating states analysis, electric power loads largely depend on conditions in which the unit works and on the task performed. In some states a demand for electric energy requires independent work of one generating set, in others a parallel work of two or more sets is necessary.

2 Studied Characteristics of the Ships Power Plants

The power plant of *m/v Skagica* chemical tanker built in 1977 in Germany by shipyard *O&K Orenstein & Koppel AG* in Luebeck was the first analyzed object. The ship apart from liquid chemicals can transport petroleum products. The unit has 26 cargo tanks with the total capacity of 7,546 m^3. During the research the ship transported ethanol on the route Brazil–Cuba–Guatemala–Spain in summer period.

The power plant of *m/v Skagica* consisted of medium speed four-stroke engine *MaK 6MU551AK* about power 2,942 kW driving by elastic clutch and reduction gear four-bladed solid propeller. At the main engine speed 425 rpm, the propeller speed amounts 160 rpm. Ship power station has four generating sets consisting of diesel engines *Volvo Penta* driving by elastic clutches synchronous generators. Two sets consisted of engines about power 207 kW and generators about power 205 kVA; remained two engines about power 247 kW and generators power 279 kVA. In the system an emergency generating set was not installed. In case of black-out, the generating set no 4 is started automatically with an electric starter from the battery (remained sets are started by means of compressed air starters).

The power plant of the *m/v COSCO Long Beach* container ship, built in 2004 in South Korea by shipyard *Hyundai Heavy Industries* in Ulsan was a next analyzed object. The ship has eight cargo holds and can transport 7,455 containers, out of which 500 containers can be reefer containers. During marine electric power system load observations the unit swam on the route China–United States in summer period.

The power plant of the container ship created a low speed main engine—*Sulzer 12RTA96C* about power 68,640 kW directly driving six-bladed solid propeller and power station consisting of four generating sets.

Container ship *m/v COSCO Long Beach* was adapted to transport 500 reefer containers. By such load state, these containers would constitute the biggest receiver of electric energy about load 3,500 kW. However, such state did not appear, because their number during the research period did not exceed 100.

The second receiver about large electric energy consumption was a bow thruster, placed in the cylindrical tunnel perpendicular to ship's pivot, about maximum power consumption of 2,500 kW (it required the use of three generating sets). Due to the effectiveness of the bow thruster at small ship speeds, it was used only during unit maneuvers.

Relatively high power of the electric energy was absorbed by electric motors of the following pumps: the main engine lubricating oil pumps—2 × 400 kW; fresh water cooling system pumps—2 × 200 kW; ballast pumps—2 × 110 kW; sea water pumps—2 × 100 kW; steering gear pumps—2 × 160 kW. Two main engine blowers required 370 kW.

The third research object was power plant of *m/v Navion Clipper* oil tanker, built in 1993 in Japan by shipyard *Mitsui Engineering & Shipbuilding* in Tamano. Its task is to transport petroleum from drilling rigs and other units storing oil to

port terminals. Cargo can be transported in 12 tanks about the total capacity of 82,015 m^3. During the research the unit navigation area included North Sea, Atlantic Ocean and Gulf of Mexico in the summer period.

The power plant of the *m/v Navion Clipper* oil tanker creates a low speed main engine *MAN B&W 6S60MC* about power 10,590 kW directly driving four-bladed control pitch propeller and power station consisting of five generating sets with four-stroke diesel engines *Bergen KRG 8* type about power 1,325 kW each and five synchronous generators about power 1,550 kVA each. Emergency source of electric energy constitutes a set compound of the engine *Yanmar 6 HAL-HTH* type about power 225 kW and generator about power 250 kVA.

The structure of the marine power plant results from its work character. During ship's cargo operation at drilling rig, the most important task is to keep it at a specific position, and responsible for that is dynamic positioning (*DP2*). Three thrusters (two bow thrusters and one stern thruster) are the main elements of DP system. During cargo operation the work of the main engine as well as thrusters is necessary.

The biggest receivers of electric energy are three identical thrusters placed in cylindrical channels, two in bow part, one in aft part of the vessel. Each of thrusters is powered by an electric motor about power 1,100 kW. To other electric energy receivers with considerable power consumption must rank electric motors of the following pumps: ballast pumps—2 × 150 kW; main engine lubricating oil pumps—2 × 75 kW; fire and general service pumps—2 × 75 kW; sea water pumps—3 × 37 kW; LT cooling water pumps—2 × 37 kW.

3 Electric Power Loads Comparison of the Examined Units

The basis for analysis of the marine electric power systems loads in the examined units was its loads registration in all sorts of operating states. Exceptionally laborious work in case of computer loads register lack was used to conduct collation of collective loads for individual configurations of attached electric energy sources (Kijewska and Nicewicz 2004a, b; Kijewska et al. 2006; Matuszak and Nicewicz 2007; Nicewicz 2003). Collations were carried out for all appearing operating states and in the presented material only a collective collation was described for medium loads of the researched ships power station (Fig. 1) and average value of relative loads of the researched ships power stations (Fig. 2).

From the collation on Fig. 1 follows the obvious information that the ship with the greatest tonnage has a large power plant and its demand for the electric energy is the greatest in each of the appearing operating states.

Collation presented on Fig. 2 is more meaningful. It says that the biggest loads appeared for *m/v Navion Clipper* oil tanker during maneuvers; and for *m/v Skagica* chemical tanker a maneuvers period is a time of the smallest loads (it is possible to

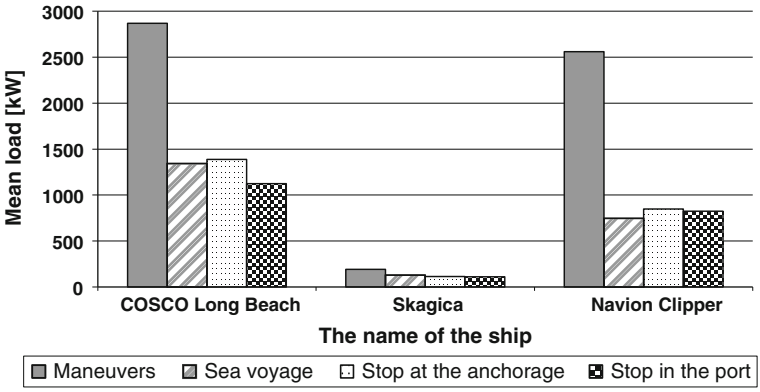

Fig. 1 Setting-up of examined marine electric power plants mean loads

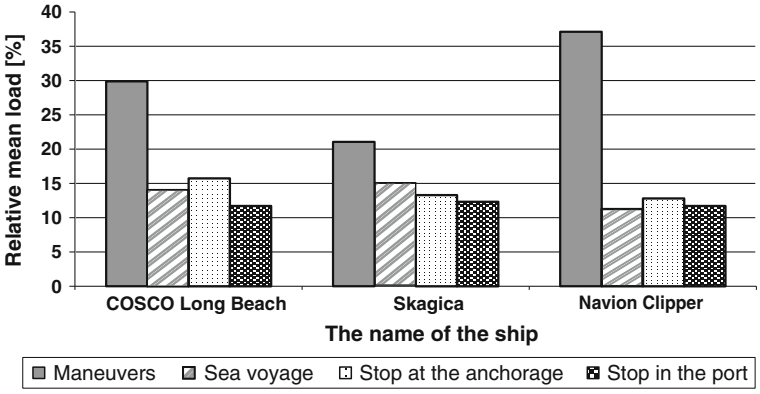

Fig. 2 Setting-up of examined marine electric power plants relative mean loads

explain it by the fact that central hydraulic system deals with the drive of the biggest energy receivers).

4 Final Remarks

The presented research, called identification of marine electric power systems loads was conducted on different unit types with transport function in the process of their operation by foreign and national shipping enterprises. Above very modest and trimmed results of the research were quoted. The research was carried out in the years 2002–2007 registering loads of the marine electric power systems in ever typical for the given unit, so-called in shipbuilding, operation states as well as in

different climatic-weather conditions. The ships were built in the years 1977–2005. Units were built in shipyards in Bulgaria, China, France, Germany, Japan, Norway, Poland, South Korea, Taiwan and Yugoslavia. A detailed analysis was provided on ships the age of which did not exceed 30 years. 14 ships types include six different size of container ships (7500 TEU–1100 TEU), two types of semi-container ships, 3 types of bulk carriers and one type of general cargo ship, DP2 oil tanker and chemical tanker/tanker.

A detailed database concerning loads of marine electric power systems, which rose as a result of identification research, is used for different purposes. One of them is to estimate emissions by ships in ports, which was carried out in the Mechanical Department of Maritime University in Szczecin as part of the international project realization: *BSR InnoShip: Baltic Sea cooperation for reducing ship and port emissions through knowledge and innovation.* Knowledge of the actual operational ship's power station loads, including individual generating sets, in all operating states has a great importance at estimating the exhaust emission by ships. The results of the research were used among others at works (Borkowski et al. 2012; Nicewicz and Tarnapowicz 2012), providing a new view for methodology to determine emissions.

References

Balcerski A (1991) Studium projektowania układów energetycznych trawlerów łowczo—przetwórczych. Zeszyty naukowe Politechniki Gdańskiej nr 474, Budownictwo Okrętowe LVIII, Gdańsk

Balcerski A (1992) Problemy tworzenia i wykorzystania banku informacji o parametrach i warunkach eksploatacji okrętowych układów energetycznych. Eksploatacja Silników Spalinowych o Zapłonie Samoczynnym Część 2—EXPLO-SIL'92. Akademia Marynarki Wojennej, Gdynia 1992, pp 5–11

Balcerski A, Bocheński D (1991) Układy technologiczne i energetyczne jednostek oceanicznych. Wydawnictwo Politechniki Gdańskiej, Gdańsk

Borkowski T, Tarnapowicz D, Nicewicz G (2012) Ships mooring in the port as a threat to our natural environment. Manage Syst Prod Eng 2(6):22–77 (ISSN 2299-0461)

Kijewska M, Nicewicz G (2004) Analiza rozkładu obciążeń zespołów prądotwórczych elektrowni okrętowej statku transportowego dla wybranego stanu eksploatacyjnego. Надежность и Эффективность Технических Систем. Международный Сборник Научных Трудов, KGTU, Kaliningrad 2004, pp 64–72

Kijewska M, Nicewicz G (2004) Estymacja gęstości rozkładu obciążeń zespołów prądotwórczych elektrowni okrętowej w wybranym stanie eksploatacji. Zeszyty Naukowe Politechniki Gdańskiej nr 598 (seria: Budownictwo Okrętowe Nr LXV), Gdańsk 2004, pp 79–87

Kijewska M, Matuszak Z, Nicewicz G (2006) Identyfikacja obciążeń systemu elektroenergetycznego siłowni okrętowych w rzeczywistych warunkach eksploatacyjnych. SYST J Transdisciplinary Syst Sci 11:334–340

Matuszak Z, Nicewicz G (2007) Possibilities of diagnosing a marine electrical power system. In: DIAGO 2007, pp 233–238

Nicewicz G (2003) Charakterystyka obciążeń układu energetycznego siłowni statku transportowego z napędem spalinowo–elektrycznym. Zeszyty Naukowe nr 68 Wyższej Szkoły Morskiej, Szczecin 2003, pp 345–350

Nicewicz G, Tarnapowicz D (2012) Assessment of marine auxiliary engines load factor in ports. Manage Syst Prod Eng 3(7):12–17

Śmierzchalski R (2004) Automatyzacja systemu elektroenergetycznego statku. Centrum Graficzne GRYF, Gdańsk

Wojnowski W (1992) Okrętowe siłownie spalinowe. Wydawnictwo Politechniki Gdańskiej, Gdańsk

The Estimation of the Marine Main Diesel Engine Energy Balance

Z. Matuszak and G. Nicewicz

Abstract The basis of impact of energy device (marine main diesel engine) on its environment in terms of energy and exergy is characterized. Types of energy and exergy characterizing the marine main diesel engine are presented. The description of energy and exergy components for the estimation of exergy balance of the main diesel engine is made. A discussion on the compilation of diesel engine exergy balance is presented. Exergy balance is drawn up for two temperatures, corresponding to temperatures in the engine room of the ship in the arctic (25 °C) and tropical (45 °C) conditions.

Keywords Energy balance · Exergy balance · Diesel engine

1 Introduction

A thermal machine or a thermal device is a device that performs at least one of the energetic processes: transforming one form of energy to another or changing the energy of an energy carrier. These implementations take place in a diesel engine as a result of ongoing thermodynamic changes.

The diesel engine as a complex element is thus a system in which the role of each part and the energy carrier (energy factor) depends on the place in the whole. Energy carrier is a real factor, which in cooperation with the device enables the realization of one of the previously mentioned energy processes. Power factor, and especially its flow, is a source of substantial and energetic losses (Shukuya 2013;

Z. Matuszak (✉) · G. Nicewicz
Maritime University of Szczecin, Szczecin, Poland
e-mail: z.matuszak@am.szczecin.pl

G. Nicewicz
e-mail: g.nicewicz@am.szczecin.pl

L. Ševčík et al. (eds.), *Modern Methods of Construction Design*,
Lecture Notes in Mechanical Engineering, DOI: 10.1007/978-3-319-05203-8_40,

Matuszak 2005; Matuszak and Nicewicz 2010; Querol et al. 2013). These losses are due to such tribologic friction as well as other unconventional (e.g., erosion) and caused by suppression. In this way the diesel engine in addition to its energy function performs the function of a complex loss node (Matuszak 2008; Wichrowski 1986).

The energy medium (energy carrier) is a simple component, isolated from the environment, which is in the mutual relationship with the machine. It is also characterized by physical and chemical enthalpy. The impact of environment on the system (input) results in changes in interactions within the system and changes in physical, chemical and dynamic properties of the system components (Shukuya 2013; Querol et al. 2013; Matuszak 2008).

In the diesel engine the environment impact on the system (input) can take the following forms (Matuszak 2008):

- propulsion energy, accompanied by the interaction within the system of a mechanical (kinetic and dynamic), thermal and chemical nature;
- thermal and environmental impacts not causing losses directly, but intensifying them (e.g., pollution, bad cooling);
- effects of additives (coolant, lubricants, etc.) necessary to operate a device (diesel engine) with a carrier of energy and substances.

The system (diesel engine) output may have the following types of impact on the surroundings (Matuszak 2008):

- useful effect of energetic character;
- material losses of the examined technical objects;
- external energy losses;
- substances, released to the surroundings, that are products of performed physical-chemical processes and additionally used substances.

The work characteristic of heat machines and devices consists in the determination of the so called loss nodes (Wichrowski 1986), based on the analysis of the interaction of components in system models of heat machine and heat device losses. The loss node is understood as a physical or chemical process that is a source of exergy or energy and material losses of heat device components. This study focuses on exergy nodes and losses (Matuszak 2008).

The stream exergy for an examined part of a thermodynamic system, such as a marine main diesel engine or its part, can be defined from this relation (Wichrowski 1986; Szargut and Petela 1965; Szargut 2000):

$$B_z = B - V(p - p_{ot}) \tag{1}$$

where:

B total exergy,
V volume in the analyzed part of the system,
P pressure in the analyzed part of the system,

p_{ot} ambient pressure.

The value of potential exergy B_p can be determined in reference to the level of surroundings.

The kinetic exergy B_k is determined by the absolute velocity w relative to the surface of the Earth.

The value of thermal exergy B_t results from incompatibilities between thermal parameters and chemical composition of the analyzed substances and the values defining the components of the thermodynamic system surroundings.

The remaining components of exergy are its other forms, e.g. the exergy of surface tension, or of electric charge.

Generally in the examination of working processes of energy machines and devices it is enough to take into account thermal, kinetic and potential exergy. It should be noted that the physical exergy B_f equals zero if the examined substance has the temperature and pressure equal to those of the environment. The substance, in turn, has a positive chemical exergy if its composition is different from the composition of the environment; however, it should be taken into consideration while examining the process of exchange of substances with the environment.

The above described processes are of particular importance for marine energy facilities since the vessels perform their transportation duties in both the Arctic climatic zones and in areas with tropical climates.

2 Balance Sheet Components for the Assessment of Marine Main Diesel Engine Exergy Balance

The increase of energy of energetic plant is independent of the way of transition between the states, but presents the contrast between the initial and the terminal energy (Matuszak 2008; Szargut and Petela 1965):

$$\Delta E_u = E_{uk} - E_{up} \tag{2}$$

where:

E_{uk} the terminal energy of the system;

E_{up} the initial energy of the system.

After separation from the energy of the kinetic and potential energy, the remaining energy can be considered as internal energy (Matuszak 2008; Szargut and Petela 1965):

$$E_u = E_k + E_p + U \tag{3}$$

where:
E_k macroscopic kinetic energy of the system,
E_p macroscopic potential energy of the system,
U internal energy of the system

So the main components of the internal energy of the diesel engine are the kinetic energy of forward movement (translational) and rotational of molecules, the energy of vibratory motion (oscillation) of atoms in a speck, the potential energy of mutual attraction between particles, the chemical energy, associated with remodeling particles, the energy of electronic states. In the material an attempt to define the components that affect the estimation of the exergetic balance of the marine main diesel engine.

Generally the exergetic analysis may be presented in the form of in the form of balance of a closed internal exergy loss (Matuszak 2005; Wichrowski 1986; Balcerski 1990; Szargut 2007):

$$B_d = \Delta B_u + B_{wu\dot{z}} + L + \sum \Delta B_{zr} + \delta B_w + \delta B_z \tag{4}$$

where:
B_d exergy of fluids put into the system,
ΔB_u increase in the system exergy,
$B_{wu\dot{z}}$ useful exergy of fluids put out of the system,
L mechanical or electric work performed by the system,
ΔB_{zr} increase in the exergy of external heat source being in contact with the system,
δB_w, δB_z internal and external loss of exergy.

The temperature of the heat source is higher than the environmental temperature and the directions of the heat flow and exergy flow are compatible. Nevertheless, if the temperature of the heat source were lower than the cooled space ($T < T_0$), exergy would be increased.

Below dependences necessary to estimate exergy balance of the main engine are given. They were received after taking into account the energy and the exergy of the working mediums (energy carriers) of the main engine. Thus the following forms of energy were included: the chemical energy (fuel), energy of charging air, energy of lubricating oil, energy of cylinder cooling water (high temperature cooling system) and charging air cooling water (low temperature cooling system) and energy of exhaust gases.

Heat corresponding to the maximum continuous output (Matuszak and Nicewicz 2010; Szargut 2000):

$$Q_e = 3{,}600 \cdot N_e \ [\mathrm{kJ/h}] \tag{5}$$

where:
3,600 equivalent of the heat energy [kJ/kWh],
N_e maximum continuous output [kW].

Exergy, corresponding to the maximum continuous output:

$$\Delta B_e = Q_e \frac{T - T_0}{T} \text{ [kJ/h]} \tag{6}$$

where:
T temperature of the medium,
T_0 temperature of the environment.

Exergy put into with fuel:

$$\Delta B_{pal} = G_e \cdot W_d \frac{T - T_0}{T} \text{ [kJ/h]} \tag{7}$$

where:
G_e mass stream of consumed fuel,
W_d fuel calorific value.

Exergy delivered with charging air:

$$\Delta B_{pow} = \dot{G}_p \cdot c_p \cdot T_p \frac{T - T_0}{T} \text{ [kJ/h]} \tag{8}$$

where:
$\dot{G}_p$ mass stream of charging air,
c_p mean specific heat of charging air,
T_p temperature of environmental air.

Exergy of exhaust gases losses:

$$\Delta B_s = \dot{G}_s \cdot c_s \cdot \Delta T \frac{T - T_0}{T} \text{ [kJ/h]} \tag{9}$$

where:
$\dot{G}_s$ mass stream of exhaust gases,
c_s mean specific heat of exhaust gases,
ΔT difference between exhaust gasses temperature after turbine and temperature of the environment.

Exergy received by the lubricating oil:

$$\Delta B_{cho} = \dot{G}_o \cdot c_o \cdot \Delta T \frac{T - T_0}{T} \text{ [kJ/h]} \tag{10}$$

where:
$\dot{G}_o$ mass stream of lubricating oil,
c_o mean specific heat of lubricating oil,
ΔT difference between main engine lubricating oil inlet and outlet temperatures.

Exergy of cylinder water cooling losses:

$$\Delta B_{chcyl} = \dot{G}_w \cdot c_w \cdot \Delta T \frac{T - T_0}{T} \text{ [kJ/h]} \tag{11}$$

where:
$\dot{G}_w$ mass stream of cylinder cooling water,
c_w mean specific heat of water,
ΔT difference between main engine cylinder cooling water inlet and outlet temperatures.

Exergy of charging air c water cooling losses:

$$\Delta B_{chp} = \dot{G}_{chp} \cdot c_{chp} \cdot \Delta T \frac{T - T_0}{T} \text{ [kJ/h]} \tag{12}$$

where:
$\dot{G}_{chp}$ mass stream of cooling water,
c_{chp} mean specific heat of water,
ΔT difference between charging air cooling water inlet and outlet temperatures.

The law of exergy conservation, similar to that of energy conservation, is not applied to the exergy analysis. With some assumptions that will be set forth further herein, the exergy balance can be used. The equation of exergy balance has the form given below (Szargut and Petela 1965; Szargut 2000):

$$B_d = \Delta B_u + B_w + L + \sum \Delta B_{\acute{Z}r} + \delta B_{d-w}, \tag{13}$$

where:
B_d exergy of fluids put into the system,
B_w exergy of fluids put out of the system,
ΔB_u increase in the system exergy,
L work performed by the system,
$\Delta B_{źr}$ increase in the exergy of external heat source being in contact with the system,
$\delta B_{d\text{-}w}$ internal loss of exergy of irreversible changes of the system.

Calculating the increase in the exergy of external heat source, we assume that the source temperature is that of the so called control surroundings of the

thermodynamic system at the place of heat flow (Szargut and Petela 1965; Szargut 2000):

$$\Delta B_{\acute{Z}r} = -Q_{\acute{Z}r}\frac{T - T_{ot}}{T}, \tag{14}$$

where:

$Q_{\acute{z}r}$ heat released by the source to the system,
T absolute temperature of the heat source measured on the control surroundings where there is heat flow,
T_{ot} absolute environ-mental temperature.

For the preset conditions of the thermodynamic system work, the increase in system exergy ΔB_u equals zero.

The exergy balance may constitute a basis for the determination of exergetic efficiency (Szargut and Petela 1965; Szargut 2000):

$$\eta_B = \frac{B_{u\dot{z}} - B_{sn} + L_{u\dot{z}} + E_{elu\dot{z}} + \Delta B_{\acute{Z}ru\dot{z}} + \Delta B_{uu\dot{z}}}{B_N + L_N + E_{elN} - \Delta B_{\acute{Z}rN}}, \tag{15}$$

where:

$B_{u\dot{z}}$ useful exergy of the process products,
B_{sn} exergy of raw non-energy materials,
$L_{u\dot{z}}$ useful work of the process,
$E_{elu\dot{z}}$ electric energy of the process,
$\Delta B_{\acute{z}ru\dot{z}}$ increase in the exergy of external heat sources participating in the thermodynamic process,
$\Delta B_{uu\dot{z}}$ useful increase in the system exergy,
B_N exergy of propulsion substances, e.g. fuels,
L_N propulsion work,
E_{elN} propulsion electric energy,
$\Delta B_{\acute{z}rN}$ decrease in the exergy of external propulsion heat source.

The useful exergy $B_{u\dot{z}}$ only takes into account components of product exergy that are necessary for further thermodynamic processes. One may assume that exergetic efficiency defines the so called degree of imperfectness or quality of the process in comparison with the ideal reversible thermodynamic process. Obviously, in actual thermodynamic processes the efficiency is always less than one. This is not however applied in the analysis of the described marine main diesel engine.

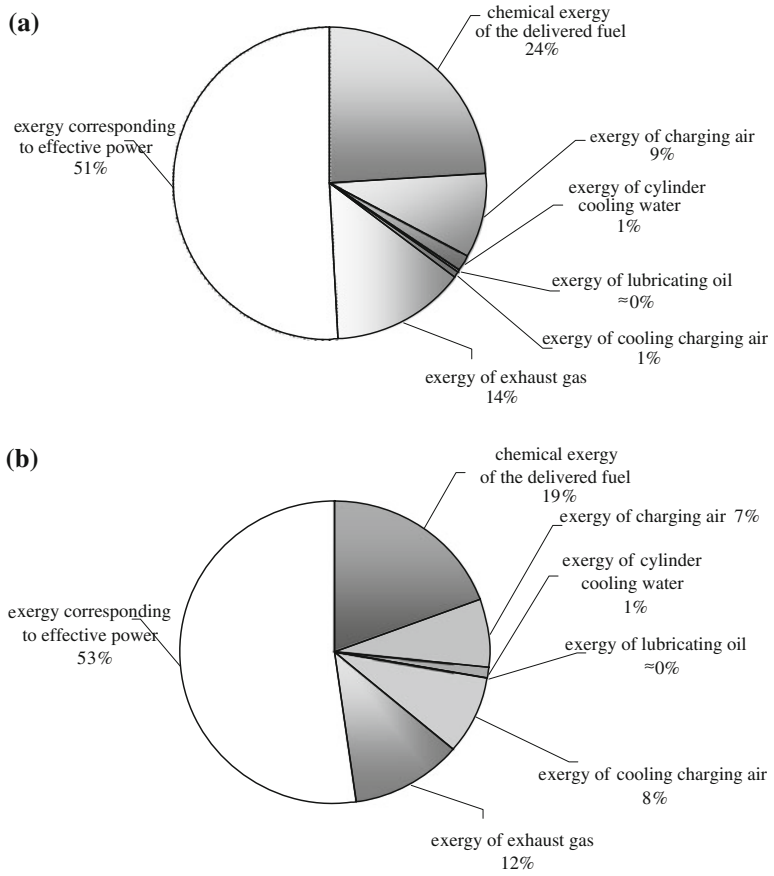

Fig. 1 Engine MAN B&W exergetic balance for ambient temperatures 25 °C (**a**) and 45 °C (**b**) (figures simplified and rounded)

3 Final Remarks

According to the methodology used by designers and operators of the engine room (Balcerski 1990) the heat loss in power devices, including the diesel engine, comprises: incomplete combustion loss (up to 1 % for liquid marine fuels); waste of imperfect combustion (up to 1.5 % for fuel marine liquid); outlet loss, which depends mainly on the temperature of exhaust gases and the devices heating mediums supplied to the engine (loss from 6 to 20 %); loss to the environment (6 %). As shown above, the characteristics of the engine loss is very general.

Figure 1 presents the results of attempts to estimate the exergy balance of the main diesel engine. Energy (exergy) components characterizing the work of the engine are limited to the basic ones. The balance sheet was drawn up for two

temperatures, corresponding to temperatures in the engine room of the vessel in the arctic (25 °C) and tropical (45 °C) conditions.

Characteristics of the balance components estimated on the basis of actual measurements significantly different from the data obtained from literature, was also presented in Balcerski (1990), Matuszak (2005). Influence on it may rely on engine operating parameters recorded under real engine operating conditions on the ship, which took into account the losses characterized below.

The so-called internal exergy nodes losses that occur in the diesel engine according to Wichrowski (1986) are: irreversible combustion process; irreversible process of heating energy carrier, tribological and erosion processes of friction; irreversible substrate heating processes; irreversible processes of compressing air (if there is air feeding device), an irreversible exhaust heat transfer to circulating factor, various types of throttling processes.

The external exergy nodes losses are: the heat flow to the environment; physical and chemical exergy outlet loss, physical and chemical exergy loss in combustion products (especially in the solid products), loss of physical and chemical exergy in the process of transportation fuel from ambient to the device, heat replacement between the carrier of chemical energy and the environment, the outflow of energy carrier to the environment due to leakage (rare).

Losses arising within the marine diesel engine are: exergy losses due to friction between the elements of the thermal unit; the loss of exergy due to irreversible heat flow of exhaust gas to the circulating medium, the loss of exergy due to irreversible process of blast (compression) of air (turbo-recharge).

References

Balcerski A (1990) Marine power plants. Wyd. Politechniki Gdańskiej, Gdańsk (in Polish)

Matuszak Z (2005) Exergy as a measure of energy device quality. Mieżdunarodnyj sbornik naucznych trudow "Nadiożnost i effektiwnost techniczeskich sistem", Kaliningradskij gosudarstwiennyj techniczeskij uniwersytet, Izdatelstwo KGTU, Kaliningrad 2005, pp 162–167

Matuszak Z (2005) Exergy losses in energy devices of a marine power plant. Mieżdunarodnyj sbornik naucznych trudow "Nadiożnost i effektiwnost techniczeskich sistem", Kaliningradskij gosudarstwiennyj techniczeskij uniwersytet, Izdatelstwo KGTU, Kaliningrad 2005, pp 168–173

Matuszak Z (2008) Losses of energy in a marine oil-fired boiler. Arch Thermodyn 29(4):97–107

Matuszak Z, Nicewicz G (2010) Attempt to estimate exergy balance of a ship's main diesel engine. J Energy Sc 1(1):93–101

Querol E, Gonzalez-Regueral B, Luis Perez-Benedito JL (2013) Practical approach to exergy and thermoeconomic analyses of industrial processes. Springer, Berlin

Shukuya M (2013) Exergy. Theory and applications in the built environment. Springer, Berlin

Szargut J (2000) Thermodynamics. Wydawnictwo Naukowe PWN, Warszawa (in Polish)

Szargut J (2007) Exergy. Guide for calculations and applications. Wyd. Pol. Śląskiej, Gliwice (in Polish)

Szargut J, Petela R (1965) Exergy. WNT, Warszawa (in Polish)

Wichrowski W (1986) Physical ageing of heat machines. WNT, Warszawa (in Polish)

FEM Simulation of Flank Breakage on Tooth of Gears and Experimental Photos

K. Petr, V. Dynybyl and M. Dub

Abstract This article deals with the reasons for gear failure—Flank breakage on tooth of spur gears with helical and straight involute gears. Gear flank breakage can be observed on edge zone-hardened gears. The creation of flank and tooth breakage are described in this article. In the article are also described FEM simulation of this gear failure and short photo documentation from real load tests on mechanically closed stand for testing of gearing with helical gears.

Keywords Gear-Mesh · Elastic-plastic deformation · FEM · Tooth breakage · Flank breakage

1 Introduction

Failure of teeth of gears can be divided into several basic cases, but only three of them cause a tooth (gear) failure. The first case is a tooth breakage, the second case is a flank breakage and the third case is a pitting (see Fig. 1).

The other cases of failure of teeth are associated with failure of the tooth flank, which contributes to higher vibration and noise. These cases are the wear (abrasive) at low peripheral speeds and high loads, scuffing and in the last case it is a micro-pitting.

K. Petr (✉) · V. Dynybyl · M. Dub
Czech Technical University in Prague, Prague, Czech Republic
e-mail: karel.petr@fs.cvut.cz

V. Dynybyl
e-mail: vojtech.dynybyl@fs.cvut.cz

M. Dub
e-mail: martin.dub@fs.cvut.cz

L. Ševčík et al. (eds.), *Modern Methods of Construction Design*,
Lecture Notes in Mechanical Engineering, DOI: 10.1007/978-3-319-05203-8_41,

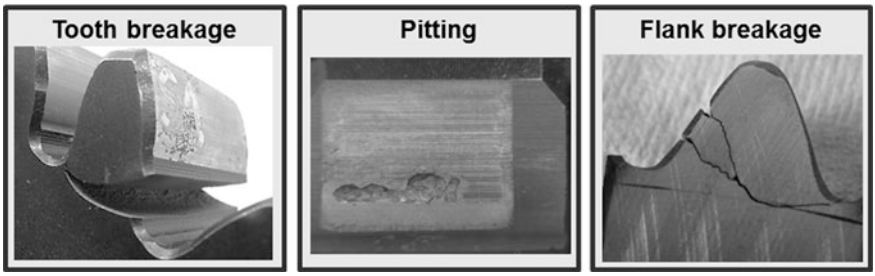

Fig. 1 Three important cases of tooth (gear) failure

1.1 Tooth Breakage on Tooth of Gears

The tooth breakage of gear starts at the surface, but how will be write in next paragraph, the flank breakage of gear had the primary crack starter (PR) in the volume of the tooth.

The bending fatigue failure (tooth breakage) occurs over a long period of time. The initiation of crack takes place at the weakest point, normally at the root of the tooth or at the fillet, where high stress concentration exists together with highest tensile stress from bending or from the surface defects as shown in Fig. 1 or 2. The crack slowly propagates over 80–90 % of the life.

1.2 Flank Breakage on Tooth of Gears

Flank breakage is a complex problem of stress in the tooth which is caused by shear stress from the rolling friction, distribution of the internal residual stress, shear stress from the tangential force, bending stress and additional internal stress caused by non-quality material (see Fig. 3).

In the Fig. 4 is shown a model explaining the path of a fatigue crack. The primary crack starter (PR) is located in the region of the pitch diameter and can be found underneath the case-hardening depth ($x_{PR} = 1.5 \cdot$ Chd), where the stress is significantly lower than within the case-hardening depth (Chd) (Bauer and Bohl 2010).

Only these micro-cracks which are in line with the direction of the main shear stress (in the direction of normal line) can propagate towards the load tooth flank and towards the core (Fig. 4). It cannot be excluded that the micro-cracks are generated during or shortly after the last heat treatment process.

In the location of the PR (Fig. 4) starts to grow tensile residual stress after heat treatment and there is a relatively high value of main shear stress as well (Fig. 3). This combination is ideal for the creation of the fatigue cracks (flank breakage). During the optimization of the Chd it's necessary that this dangerous zone is with

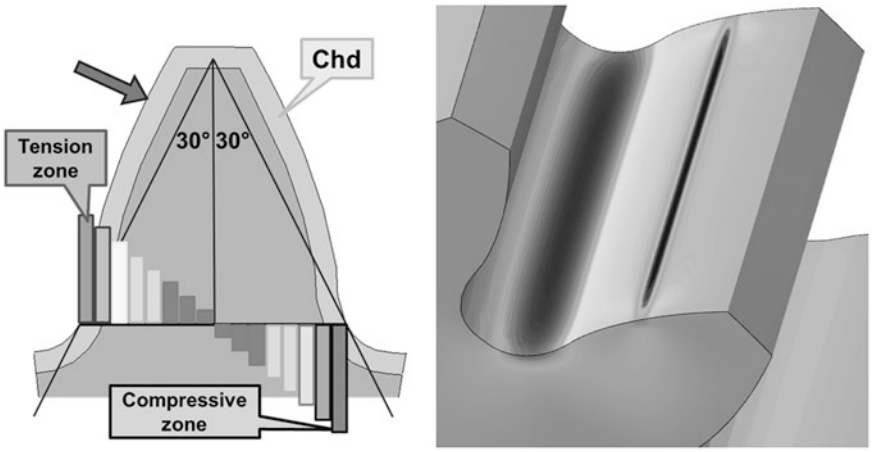

Fig. 2 Tooth breakage on tooth of gears. Scheme for analytical calculation and FEM simulation

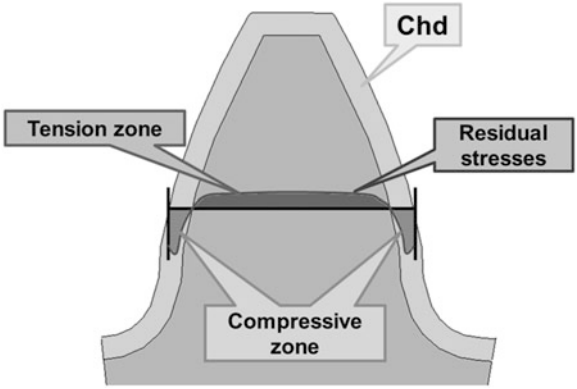

Fig. 3 The shape of residual stress and identification of tension and compressive zones (Petr et al. 2012)

the least possible main shear stress. The main shear stress doesn't depend on the Chd. For this reason, larger Chd moves the problematic zone (PR zone in the Fig. 4) to lower values of main shear stress.

The tensile residual stress always starts at the interface of the case-hardening depth and core of tooth.

2 FEM Modelling of Flank and Tooth Breakages on Tooth of Gears

For the modelling was used program Abaqus 6.12 at FME, CTU in Prague.

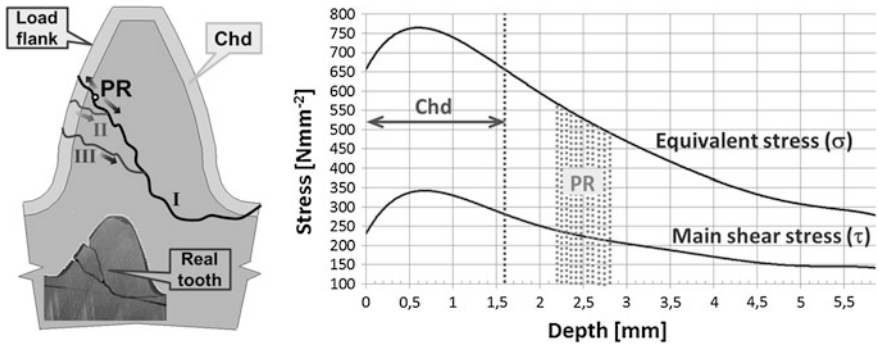

Fig. 4 Path of the fatigue crack (*left figure*). Distribution of equivalent stress and main shear stress (*right figure*) over the depth (path of depth is in the direction of *normal line*) (Petr et al. 2012)

2.1 FEM Modelling of Tooth Breakages on Tooth of Gears

For calculation is possible used static simulation, one tooth and desk (pulsation principe—see Fig. 5) or principe, which is write in next paragraph.

2.2 FEM Modelling of Flank Breakages on Tooth of Gears

The solution of the contact problem is created in the gearing (3D model—gear and pinion), which are bonded in the coordinates of intersections axis of the shaft and the front planes of the gearing on the deformed shaft in the given plane, to define the gear mesh, and are loaded by the load moments. The contact bond between the tooth face of the gears is added to the model and meshed. The gears are connected with the center point of rotation with help of interaction type COUPLING. The subsequent rolling of the gears and the implementation of all moments are applied through these points. In the Fig. 6 is shown the complete FEM model.

Simulation of gear mesh is performed quasi-statically. The material model of core is elastic. The material model of case-hardening area is elastically-plastic (until yield value is elastic, then plastic). Parameters of material model are according experimental measurement of hardness gradient.

In the Fig. 7 are see differences of distribution of main shear stress inside of tooth for different pressure angle (20° and 25°) and Chd = 1.6 mm. Direction of main shear stress (blue colour in Fig. 6) is towards opposite tooth root, which means that has same distribution as the path of the fatigue crack (Fig. 4).

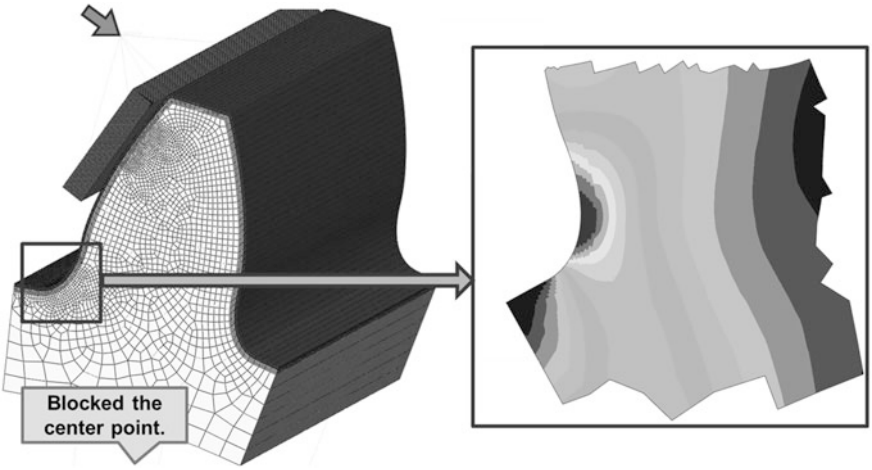

Fig. 5 The complete FEM model of gearing for calculation of tooth breakage (Petr et al. 2009, 2010)

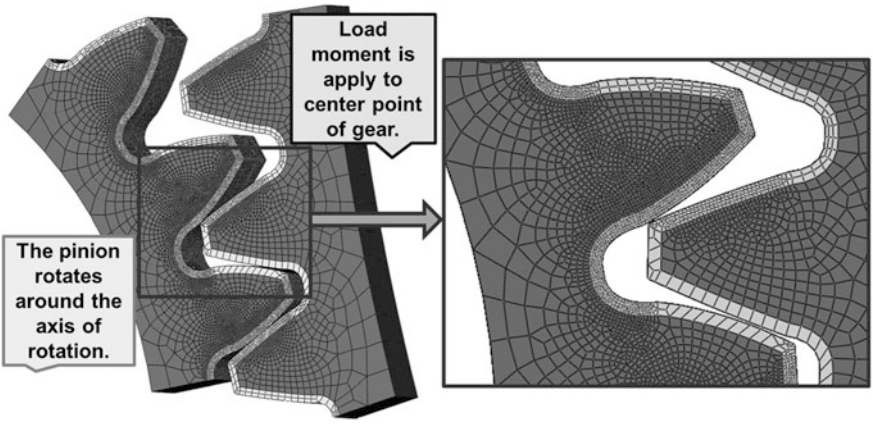

Fig. 6 The complete FEM model of gearing for calculation flank breakage (Petr et al. 2009, 2010, 2012)

3 Experimental Verification (Photos)

Experimental tests of gearing carried out on the pulsator (tooth breakage) or on mechanically closed test stand (flank breakage). In Figs. 1 and 9 as shown example of tooth breakage and in Fig. 8 are shown examples of flank breakage.

At the edge is seen saturated layer by carbon after case-hardening. Carbon toward to the core decreases (Fig. 10).

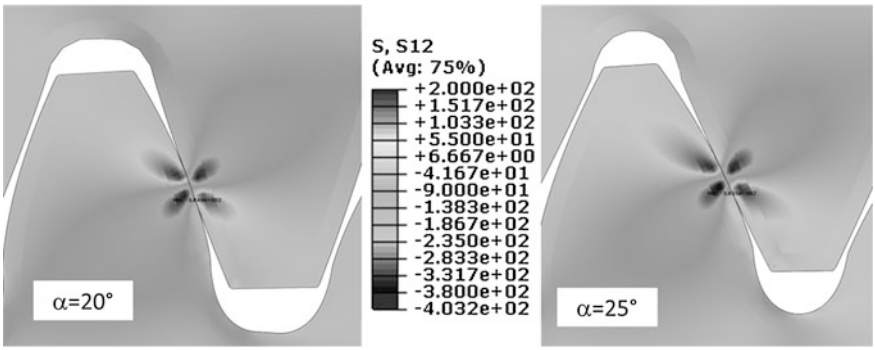

Fig. 7 The main shear stress for different pressure angles and case-hardening depth 1.6 mm

Fig. 8 Examples of flank breakage in the region of pitch diameter (Wikov MGI, a.s.)

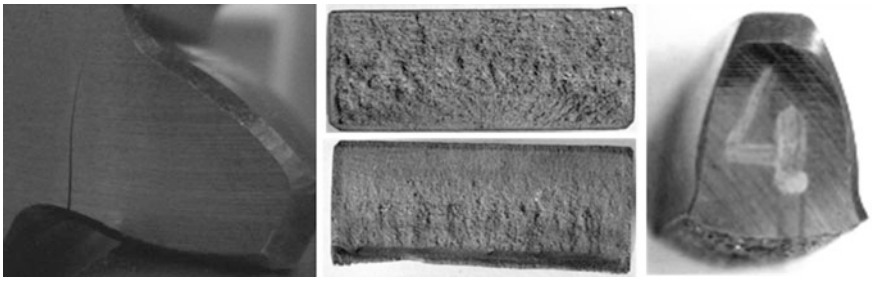

Fig. 9 Examples of tooth breakage—initializations of damage (FME, CTU in Prague)

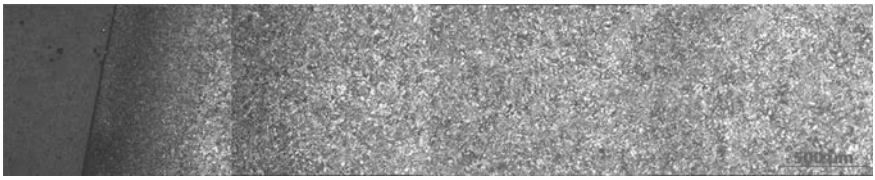

Fig. 10 Gradient of structure from the surface (tooth flank) to the core (FME, TUL of Liberec)

4 Conclusions

From this analysis suggests that when using a greater pressure angle than is angle 20° is necessary to calculate with the fact that is moved position of the maximum main shear stress towards from flank tooth to core. A positive aspect of a greater pressure angle then is 20° is a greater resistance to bending stress.

This method of calculating the stress inside the tooth is very time-consuming, but very precisely monitoring of potential problems with the exceeding of the individual limit states of the material.

Acknowledgments The research work reported here was made possible by Ministry of Industry and Trade of the Czech Republic grant No. FR-TI4/054.

References

Bauer E, Bohl A (2010) Flank breakage on gears for energy systems. In: Höhn RB (ed) Proceedings of international conference on gears, VDI-society for product and process design and TUM, Munich, Germany, Oct 2010. VDI Verlad GmbH, Düsseldorf, pp 1039–1052. ISBN 978-3-18-092108-2

Petr K, Žák P, Dynybyl V, Kanaval J (2009) FEM optimization of gear flanks shape modifications. In: Mihailidis A (ed) Proceedings of the 3rd international conference power transmissions, Kallithea, Greece, Oct 2009. Sofia Publications, Thessaloniki, pp 93–100. ISBN 978-960-243-662-2

Petr K, Kanaval J, Dynybyl V (2010) Modification and non-standard methods of increasing tooth flank resistance of gears. In: Höhn RB (ed) Proceedings of international conference on gears, VDI-society for product and process design and TUM, Munich, Germany, Oct 2010. VDI Verlad GmbH, Düsseldorf, pp 1439–1142. ISBN 978-3-18-092108-2

Petr K, Dynybyl V, Křepela J (2012) FEM modeling of the loading capacity of teeth with a respect of the case hardening depth and pressure angle. In: 53rd international conference of machine design departments, Mikulov, Czech Republic, 12–14 Sept 2012. Brno University of Technology, Faculty of Mechanical Engineering, Institute of Machine and Industrial Design, 2012, pp 227–234. ISBN 978-80-214-4533-8

Vibration Resistance of High Speed Assembly Secured Bolted Joint with Nut DIN 985

S. Poljak and R. Bašťovanský

Abstract In various mechanical devices are the bolted joints most used demountable joints. In the cause loss of coherence structures, in addition to downsizing, improper installation, and lack of protection against corrosion and inadequate safeguard against loosening joint, which occurs at variable load structure. The behavior of screw connection for vibration load must be verified using different types of tests.

Keywords Bolted joint · Vibration · Nylon insert lock nut

1 Introduction

Connection using bolts and nuts are used in various industries such as automotive, railway, etc. Is known that the most glands become detached when applied to components associated transverse re-load after they have been tightened to a desired preload force F_M.

For testing the reliability of dynamically loaded bolted joints were developed vibration test, which is governed by DIN 65151. In implementing this test uses a device named after its creator—Junker testing device (Wiegand et al. 2006). Nut is screwed together two boards. The device is designed so that the developing eccentric micro movement upper plate relative to the lower plate. The preload in this formed joint sensed strain gauge sensor and written to the diagram pretension - time

S. Poljak (✉) · R. Bašťovanský
Faculty of Mechanical Engineering, Department of Mechanical Parts, University of Žilina, Žilina, Slovakia
e-mail: silvester.poljak@fstroj.uniza.sk

R. Bašťovanský
e-mail: ronald.bastovansky@fstroj.uniza.sk

L. Ševčík et al. (eds.), *Modern Methods of Construction Design*,
Lecture Notes in Mechanical Engineering, DOI: 10.1007/978-3-319-05203-8_42,

(number of cycles). This way of testing is to determine the possible relation between residual preload in bolted connections and external forces as a function of time, where external forces are derived Junker vibration test equipment (http://www.nord-lock.com/default.asp?url=6.28.37). In this study, is reported behavior of bolted connections exposed to vibration insured with nuts. DIN 934 and nuts DIN 985 In the experiments, a decrease in preload screw connections are testing on Junker vibration device type (Fig. 1). The principle of Junker test is on the Fig. 2. The nuts DIN 985 were tightened by tightening electronic device at different speeds. The different speed was 400, 830, 1,845 and 4,040 rpm.

2 Experiment

For verifying of security methods dynamically loaded bolted joints by tightening the nuts DIN 985 at different speeds, we used the test device type Junker. As measured samples we used screws with inner hexagon socket M10 × 1.5 × 45 DIN4762-8.8 with nut M10 DIN 985 strength class 8, zinc—coated. We applied the nut DIN 934 for visual comparison. In the measurements we chose the assembly preload force 26 kN, which corresponds to 70 % of the nominal yield strength $Rp_{0,2}$. At the first, the specimens were tightened to 15 % $Rp_{0,2}$, which is corresponding to a force 5 kN and then released the preload force equal 0 kN 5 times in order to eliminate subsidence material between the surfaces threaded bolts and nuts and a bearing surface between the nut and washer. The specimens were tightened together at different speeds to us the required preload with applied nut DIN 985. Frequency of cycles of sliding plates was chosen 20 Hz. The test was lateral displacement of plates ±0.5 mm at idle and maximum number of repeated cycles are 200, it corresponding to a time of about 10 s duration of the test. Nuts and bolts were lubricated with oil SAE 10W30 viscosity class ISO VG 46 Sampling frequency was 10 Hz. Length of movable clamping plates was approximately 20 mm. During tightening, the temperature was measured after tightening the nuts with touch thermometer. Measured temperature values of nut are shown in Table 1.

3 Experimental Results

Graph 1 shows the result of Junker vibration test. The bolt preload was adjusted to approximately 26,500 N, which corresponded to 70 % $R_{P0,2}$ (nominal yield strength). For each test where were used different speeds bolted joint assembly there was a decrease in preload screw with increasing time duration of the test (number of cycles). The initial decrease is attributable to preload of microplastic subsidence and deformation of the material. Residual stresses in bolted connections that the test falls below 5 % $R_{P0,2}$ (nominal yield strength), can be regarded as insufficient, there was a total breakdown screw connection.

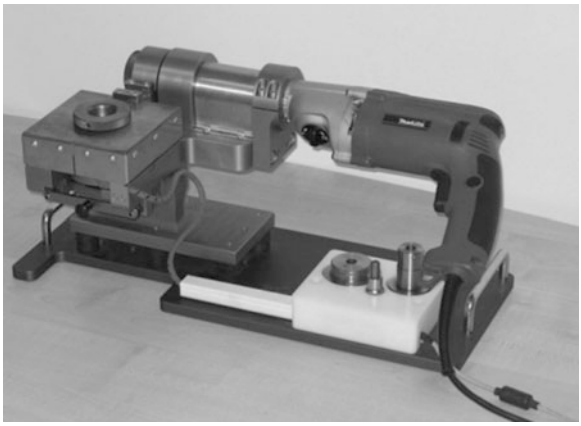

Fig. 1 Junker testing rig

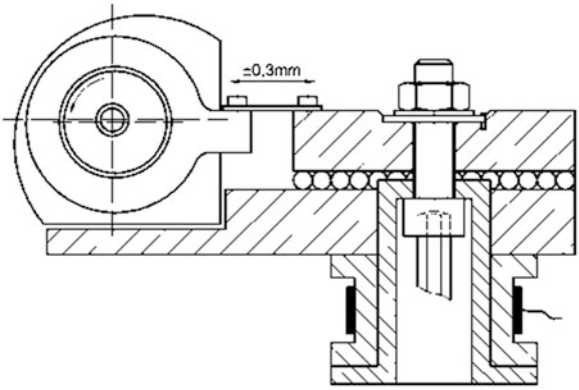

Fig. 2 Principle of junker testing rig

Table 1 Temperatures of assembled nuts

Speed of tightening	Temperature (°C)
Manual assembly	43.2
400 rpm	63.8
830 rpm	41.6
1,845 rpm	35.4
4,040 rpm	31.1

For easier understanding and quality assessment tests were residual preload bolt reflected in Table 2 (Evaluation of Junker test)after the time duration of the test 10 s (after about 200 cycles). In the graph we can see as affects the speed of installation of the decrease preload screw connections vibrations effects.

Deformation of nylon inserts at different speeds tightening is shown in Figs. 3, 4, 5, 6, 7 and 8. The images can be observed that the speed of tightening has a very significant effect on the deformation of the nylon insert. High speed of tightening

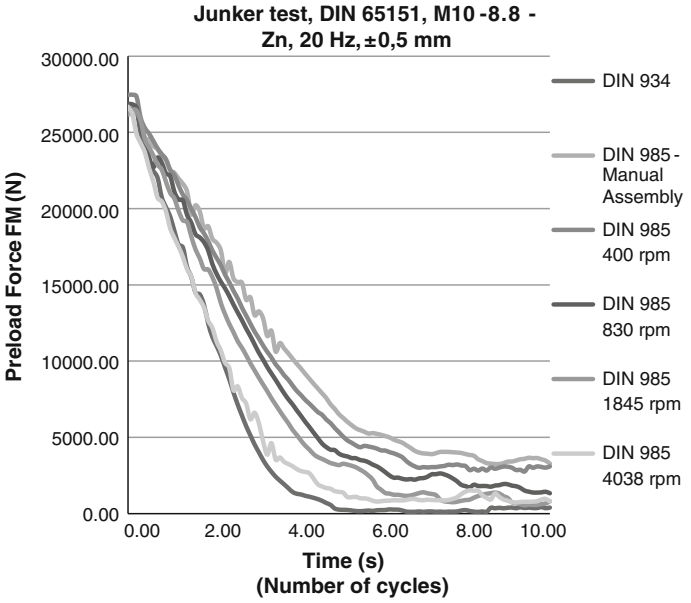

Graph 1 Junker test

Table 2 Evaluation of Junker test

Assembly, method	$F_M = 70\ \%\ R_{P0,2}$ (N)	% F_M after 10 s (200 cycles)
DIN 934 manual assembly	26,564	1.02
DIN 985 manual assembly	26,795	8.62
DIN 985 400 rpm	26,803	8.17
DIN 985 830 rpm	26,324	3.50
DIN 985 1,845 rpm	26,192	2.13
DIN 985 4,040 rpm	26,692	2.07

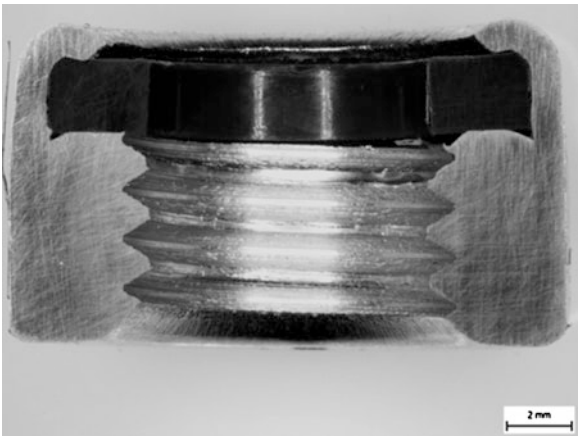

Fig. 3 DIN 985, nylon insert nut

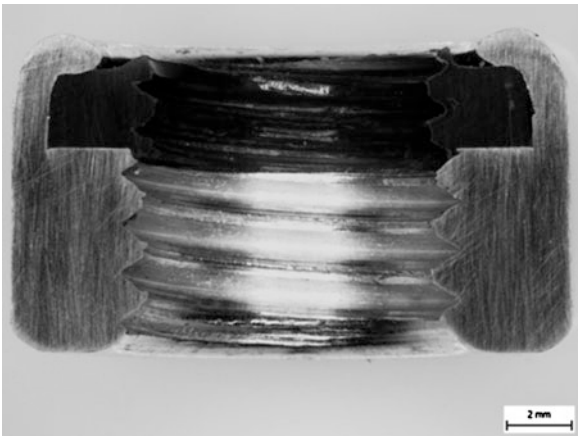

Fig. 4 DIN 985, deformation nylon insert nut after manual assembled

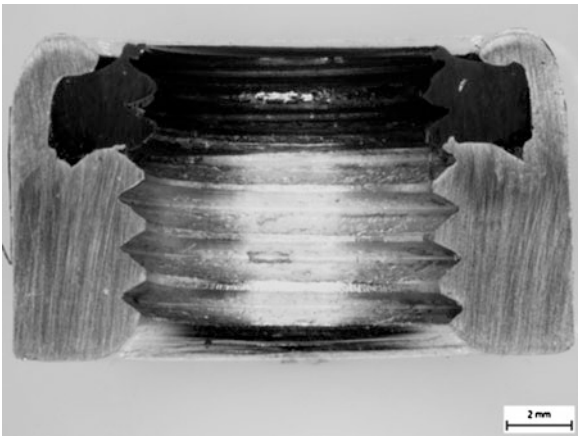

Fig. 5 DIN 985, deformation nylon insert nut after assembled at 400 rpm

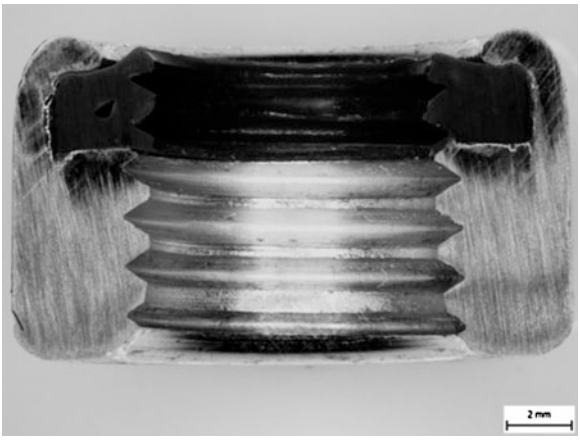

Fig. 6 DIN 985, deformation nylon insert nut after assembled at 830 rpm

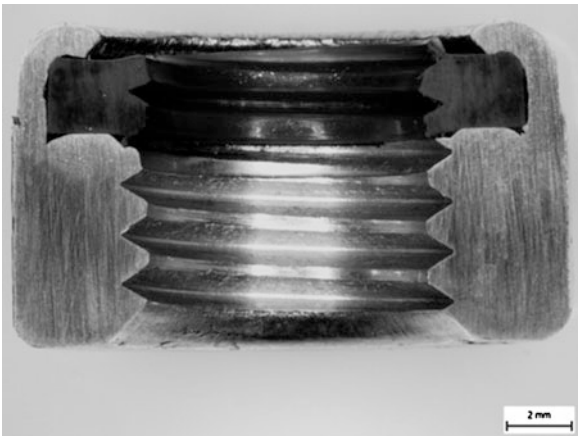

Fig. 7 DIN 985, deformation nylon insert nut after assembled at 1,845 rpm

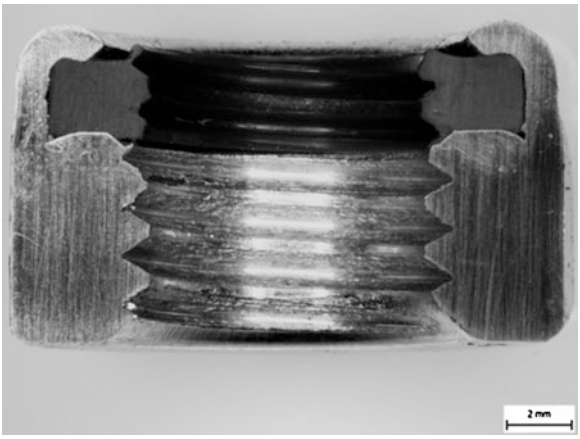

Fig. 8 DIN 985, deformation nylon insert nut after assembled at 4,040 rpm

has resulted in forming of nylon inserts into such a shape that does not fulfill function at all of safety feature in screw connection.

Measured temperature values are shown in Table 1. High speed tightening did not result in an increase in temperature whole nut but probably only been plastification contact surface nylon ring and screw thread which resulted in his subsequent shaping.

Of residual stresses in bolted connections can evaluate the screw joint secured with nut DIN 985 mounted manually or with electronically tightening mechanism with a speed of 400 per minute can be considered as a safe screw connection in as meaning that the there is not to a total breakdown bolted joint. From the Graph 1 (Junker test) and the Table 2 (Residual tension in bolted connections) can be evaluated that the screw connection where they were used nut DIN 985 and were

mounted at speed 830, 1,845, and 4,040 rpm are unsuitable for use dynamically loaded bolted joints. Thus, the secured bolted connections risk total breakdown and the subsequent collapse of the whole structure. After this manner mounted screw connection with locking nut DIN 985 is fully comparable to the unsecured screw connection with nut DIN 934. Nut DIN 985 in no way a substitute for permanent secured bolted joints against vibration by increasing the friction on the contact surface, or form fit.

4 Conclusions

In the engineering industry, but also in a number of other disciplines (electrical engineering, construction, furniture industry, etc.) include screws, screw and threaded joints among the most advanced demountable joints.

The most common cause of loss of cohesion structure in addition to down-sizing, improper installation and insufficient corrosion protection is insufficient safeguard against loosening bolted joint, which occurs at variable load structure.

Currently there is no exact mathematical model, able to describe the real behavior of bolted connections for vibration load, so it is necessary to determine resistance to from loosening the bolted joint exposed to vibration empirically using different types of tests. Experiments have shown that a high speed tightening the locking nut DIN 985 has an effect on behavior of the following secured bolted joint. Bolted joint secured with nuts DIN 985 and mounted with high speeds does not fulfill its base role, namely to prevent a total collapse bolted joint. Speed of tightening the nut DIN 985 does not increase temperature. High speed of tightening was shaping to nylon inserts and reduces friction between the nylon ring and threaded screw (there was polished contact surface of nylon ring).

Acknowledgements This work was created by the implementation of the project support Agency for Research and Development APVV—SUSPP-0014-09 Center components of transport equipment and APVV 0087-10—Intelligent diagnostic systems and their transfer components.

References

Wiegand H, Kloos KH, Thomala W (2006) Schraubenverbindungen. In: Merlet JP (ed) Parallel robots. Series: solid mechanics and its applications. Springer, Berlin

http://www.nord-lock.com/default.asp?url=6.28.37

Improving the Performance of Profiles Straightener SIMAC RD750 on Rolling Mill HCC at ArcellorMittal

R. Slanina and P. Sniehotta

Abstract In the process of manufacturing rolled steel profiles is straightening of cooled profiles a very important part of the production. In order to increase production efficiency, on heavy rolling mill at ArcelorMittal Ostrava, a study was created which aimed to determine if of the straightener it is possible to straight bigger profiles than for which was the straightener originally designed. The study included the current status detection, analysis of straightening principle, analysis of forces acting on straightener and proposed measures to increase the straightening efficiency. This article describes the conduct and results of this study.

Keywords Straightener · Analysis of forces · Rolling mill · Steel profiles

1 Introduction

Profiles straightener on rolling mill is a device that ensures that the manufactured profiles achieve the required straightness according to customer requirements. At ArcelorMittal it is the straightener Simac RD750.

Profiles intended for straightening, come from rolling mill on the cooling bed, where they wait for straightening. After turning the profile to straightening position, the profile is introduced into the straightener. Then the profile is cut to the desired length and tied for transport.

At ArcelorMittal was the requirement to research the process of straightening. The result of this research should be an analysis of straightening of existing

R. Slanina (✉) · P. Sniehotta
VŠB—Technical University of Ostrava, Ostrava, Czech Republic
e-mail: radim.slanina@vsb.cz

P. Sniehotta
e-mail: patrik.sniehotta@vsb.cz

L. Ševčík et al. (eds.), *Modern Methods of Construction Design*,
Lecture Notes in Mechanical Engineering, DOI: 10.1007/978-3-319-05203-8_43,

profiles and theoretical design for straightening of larger profiles. The study had three main parts:

- Determine current calculation methods for straightener design
- Determine current technical state of the straightener
- Straightening the existing profiles TH 36 a theoretical proposal for straightening larger profiles

2 The Finding of the Current Calculation Methods for Straightener Design

2.1 Measured Signals

From the perspective of the principle straightening, during this process occurs in the profile to two types of deformation—elastic and plastic. From a theoretical point of view (see [Pokorný et al. 1990]), the most affected are the first 4 cylinders of the straightener.

On these cylinders is both flexible as well as plastic deformation. On the remaining cylinders is then only elastic deformation. Then the cumulative total force acting on all the straightening rolls can be expressed as follows:

$$F_{rov} = Re \cdot W_y \cdot [3 \cdot k + (n - 5)] \frac{8}{t} \tag{1}$$

where

F_{rov}	total cumulative straightening force (N)
Re	yield strength of the material (MPa)
Wy	section modulus profile in case of elastic bending (mm^4)
k	ratio of the elastic and plastic section modulus in bending axis (−)
n	total number of straightened cylinders (−)
t	pitch of cylinders (mm)

The biggest problem is to express from this cumulative force maximum force acting on one cylinder. This problem was solved by making measurements on the straightener and then comparing the results of measurements and calculations.

From the previous formula can be expressed the necessary power for straightening

$$P_{rov} = \frac{Re^2 \cdot v \cdot S \cdot k_{def}}{2 \cdot E} \cdot \eta_c \tag{2}$$

where

v	straightening speed (ms^{-1})
S	profile cross-section (mm^2)
k_{def}	resulting coefficient of plastic deformation penetration by straightening (−)
E	modulus of elasticity of the material (MPa)
η_c	overall efficiency of the straightener (mm)

Effect of temperature on the output power by straightening, is already included in the coefficient k_{def}.

$$k_{def} = \sum_{i=2}^{i=n-1} \left(\frac{k_i^2}{1 - k_i} \right) = k_2^2 . \left[\frac{1}{1 - k_2} + k_2 . (n - 3) \right] \quad (3)$$

where k_2—coefficient of plastic deformation penetration under the second straightening roller (0.8–0.6) (−)

3 Determining the Current Technical State of the Straightener

The straightener is powered by two electric motors, each rated at 132 kW. Powered is the upper row of cylinders. Power transmission is handled by four-speed gearbox. Gears of the fourth stage evenly distribute power to all driven rollers (Fig. 1).

Shafts 1–3 and the input shaft of the 4 stage are loaded from the drive power. The results show that the only critical point is gearing resistance against contact stress. There can be already seen the influence of small hardness of the surface layer of gearing (Fig. 2).

Output shafts the fourth stage (shafts of the upper cylinders) are loaded not only by forces from the power drive, but also by straightening forces from straightened profile. The result is increased wear of bearings and straightener housing on these shafts. Similarly are loaded lower straightening rollers shaft. By the straightening rollers (see figure), it is evident that there is an uneven wear (Fig. 3).

If we get into relation this condition and the measurement results (see next section), it is very likely that this condition was caused by a big shaft deflection (Fig. 4).

In that case there is a diversion from vertical axis of the cylinder (both upper and lower). As a consequence, the “wedging” of straightening rolls in the profile. Between the roller sides and the profile creates an additional force, thanks to which are the demands increasing on the overall performance for profile straightening. Along with other factors, it comes to a straightener stop.

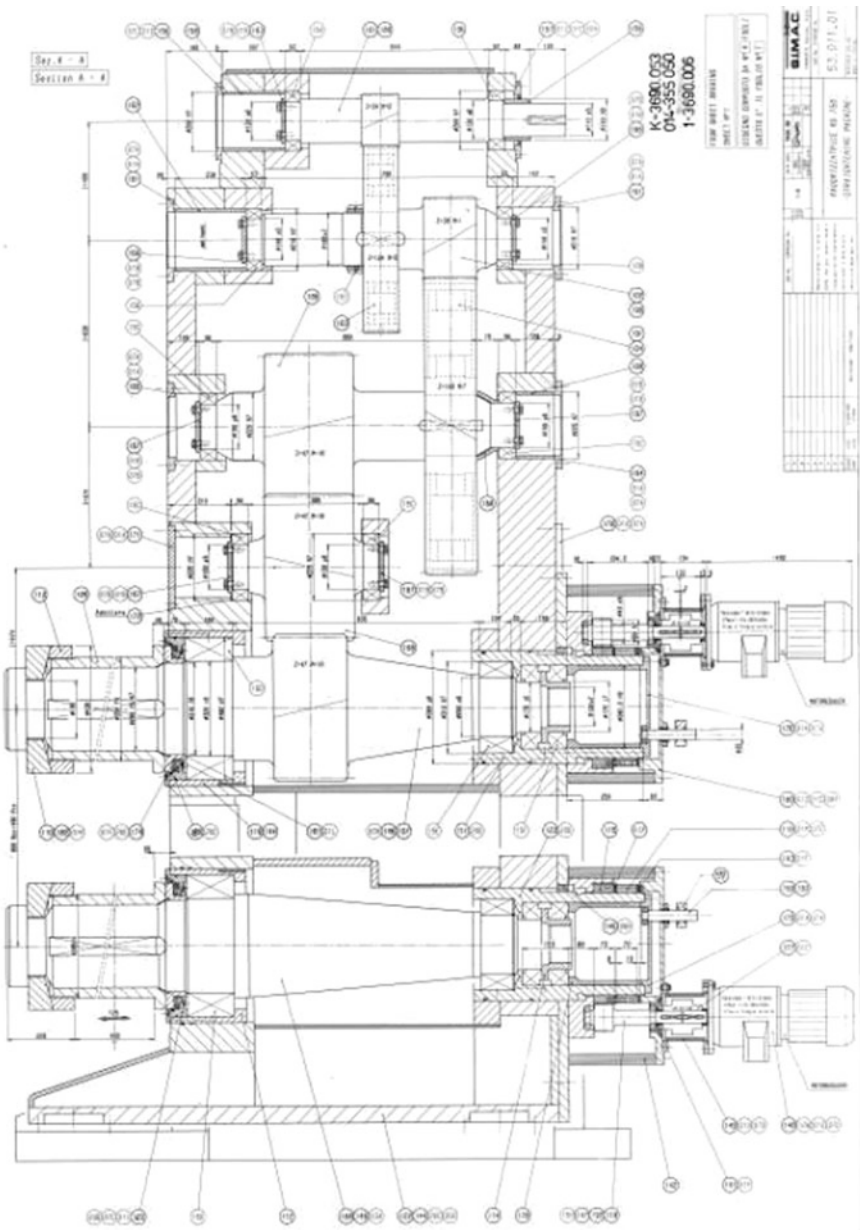

Fig. 1 Straightener schematic

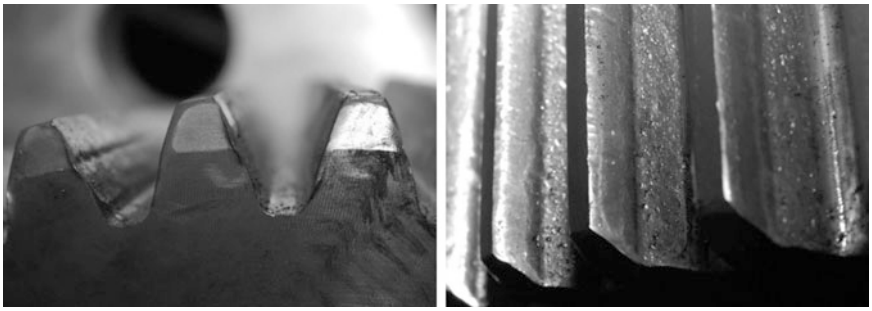

Fig. 2 Sample the gearing condition

Fig. 3 Wear of straightener straightening rolls

Fig. 4 Theoretical and real position of straightening rolls against straighten profile

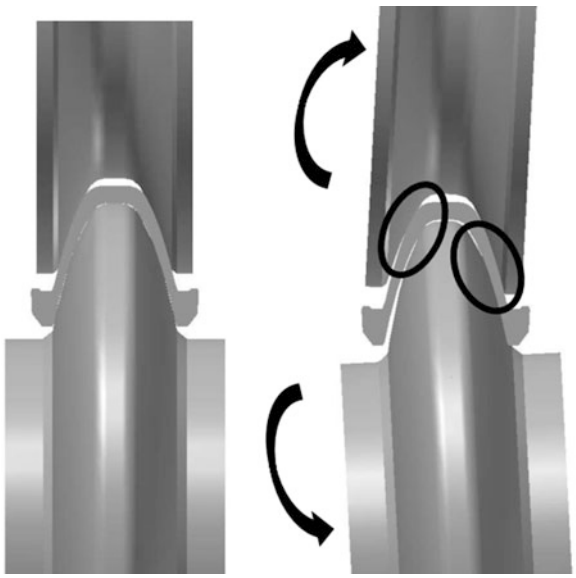

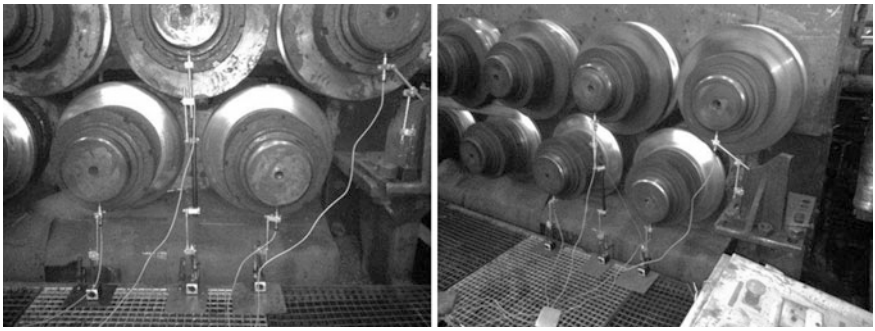

Fig. 5 Demonstration of measurement

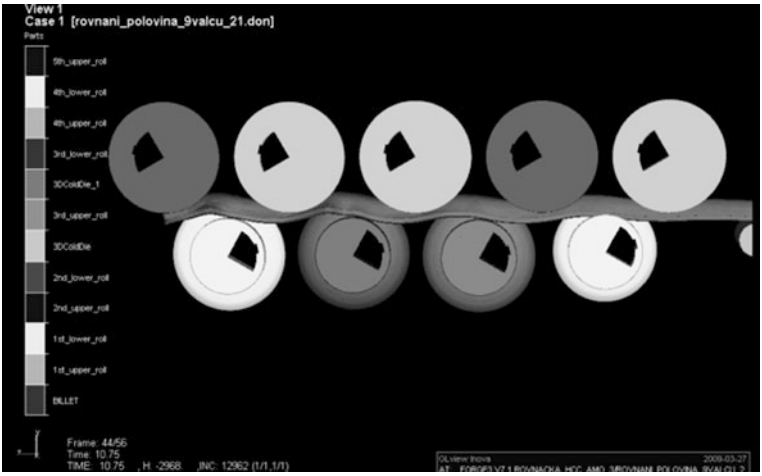

Fig. 6 Passage of the profile through the straightener in the model

4 Straightening Existing Profiles TH 36 and Theoretical Design for Straightening Larger Profiles

In order to determine the correct force ratios, we performed the measurement directly on the straightener. The aim of the measurement was to measure the deflection of the first four shafts (first and second upper and first and second lower). From these values was then determined by a calculation the size of forces that cause the deflection (Fig. 5).

The measurement shows that the most affected are the second upper and second lower shaft from the input side.

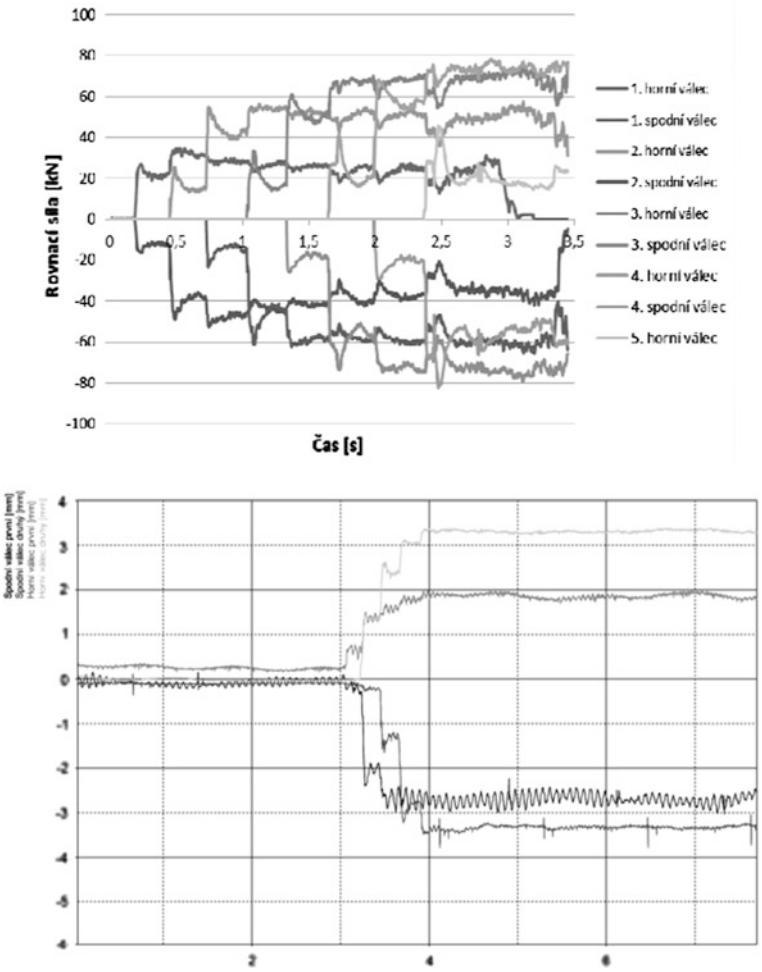

Fig. 7 Computer calculation created in transvalor forge and the results of shaft deflection measurement (0–8 s)

To compare the results of measurement, a computer model of straightening was created in Transvalor Forge. The model has been simplified so that the wheels are stiff, deforming is only the straighten profile and the task is symmetric (Fig. 6).

The result is size of the straightening forces acting on the roller in vertical axis (Fig. 7).

5 Conclusions

The main recommendation is in this case, to change the rollers offset when setting the straightener. While passing through the third lower roller, it came to a large bending of the profile. This resulted in a big stress and stopped straightener. Another recommendation was to calculate during the production of straightening rollers with the expected deformation shaft and rollers "tilting" from the vertical plane to avoid unnecessary friction between the profile and straightening rollers.

Acknowledgments This work was supported by Ministry for Education, Youth and Sports, Czech Republic, project—specific university research Nr. SP2013/4

Reference

Pokorný A (1990) Tvářecí stroje. VŠB v Ostravě, p 243. ISBN 80-7078-068-1

Part III
Experimental Methods and Measuring

Abdulkareem A. Wahab Albehigi, Rasha H. Hashim, O. Dajbych, M. Hrudičková, Z. Folta, O. Kohl, B. Kopiláková, M. Bošanský, J. Zápotočný, R. Kovář, R. Martonka, P. Maršálek, M. Burián, M. Trochta, J. Mrázek, F. Starý, O. Kult, P. Němeček, J. Popelka, P. Brabec, P. Srb, Z. Folta, R. Uhlíř, P. Mossóczy, P. Malý, D. Vejrych, A. Zatočilová, D. Koutný, D. Paloušek and J. Brandejs

Engineering work usually consists of an experimental and a theoretical part. Based on their results, engineers make a suitable solution to the problem. In recent years, the so-called "virtual experiment" has appeared. This type of experiment can significantly reduce the cost of repeated optimization tests and is applied when the experiment is impossible due to size of construction (extremely large or very small), high price, and absence of measuring instruments. However, it is clear that the experiment despite its price and time requirements still has an irreplaceable role in the design and optimization of construction and not only because of formation of new, mostly composite materials, but also due to new methods of surface treatment, which give them new properties. Part III—*Experimental methods and measurement* includes 15 contributions dealing with new experimental methods, measurement methods, and apparatuses necessary for their implementation.

Experimental and Theoretical Analysis of the Surge in a Centrifugal Compressor

Abdulkareem A. Wahab Albehigi and Rasha Hyder Hashim

Abstract Surge is an unstable operating mode of compression systems which occurs at low mass flow where the pressure delivered by the compressor is less than the plenum pressure. This instability is global, one-dimensional and nonlinear. It is characterized by a limit-cycle oscillation in mass flow and pressure rise. This paper presents the application of active control of surge in centrifugal compressor, with the measurement and evaluation of the thermodynamic operational parameters of the compressor system. A closed coupled valve with plenum in the Moore-Greitzer compression system model and controller for surge. A model for centrifugal compression system with time varying compressor speed is derived. The variable speed compressor characteristic is derived based on energy losses in a compressor components. Active control of surge in connection with varying speed is studied.

Keywords Compressor · Surge · Plenum · Losses · Pressure rise · Mass flow

1 Introduction

Compressors are machines that compress air or gas. The Compressors are widely used for the pressurization of fluids. Applications involve air compression for use in air craft engines, in industrial gas turbines and in turbocharged combustion engines. The centrifugal compressor consists of mainly three parts: Impeller, diffuser and volute (collector). The impeller, which can be recognized as the blade

A. A. W. Albehigi (✉) · R. H. Hashim
Engineering College, Babylon University, Babylon, Iraq
e-mail: drkareem959@yahoo.com

L. Ševčík et al. (eds.), *Modern Methods of Construction Design*,
Lecture Notes in Mechanical Engineering, DOI: 10.1007/978-3-319-05203-8_44,

wheel, increases the fluid velocity by spinning at a relatively high speed. Note that fluid enters the impeller axially with respect to the shaft driving it, and leaves radially.

Fluid enters the compressor through the inducer, also called impeller eye. The inducer is a region restricted by the compressor inlet radius and hub radius, for which the entering fluid is exposed to the impeller blades. The hub is simply a region of the impeller wheel dedicated to the shaft driving it. When leaving the impeller, the fluid enters the diffuser. The task of this component is to reduce the fluid velocity in order to gain pressure.

2 Centrifugal Compressor Stage

Every centrifugal compressor stage consists of several basic parts. Schematic sketch of common used compressor stage of multistage centrifugal compressor is given on Fig. 1a. Sucked gas flows through suction part of compressor (0, −0–1) to impeller, where its velocity is due to centrifugal forces increase, at the same time pressure of gas is also increased. Then the gas flows into diffuser where part of its kinetic energy is changed to pressure energy. To get into next stage the direction of flow must be changed in return channel. Changes of energy in particular parts of compressor stage are shown in Fig. 1b, we can see that highest increase of pressure occurs in the impeller.

A centrifugal compressor consists essentially of a rotating impeller followed by diffuser and the collector (volute). Figure 1c Shows diagrammatically the various elements of a centrifugal compressor. Both the static pressure and the velocity are increased within the impeller. Impeller can be single or double—entry type, depending on the pressure rise and flow rate needed. The fluid will then enter a diffuser, where the velocity is decreased. The purpose of the diffuser is to convert the kinetic energy of the fluid leaving the impeller into pressure energy. The hub is the curved surface of revolution of the impeller a–b, the shroud is curved surface c–d (Gravdahal et al. 2001). Figure 1c represent also the velocity triangle at impeller entry and exit where C represents the absolute velocity of air, U represent impeller tip speed and W represent relative velocity of air. Absolute velocity of air C has two components, tangential component Cθ and radial component Cr. The flow entering a centrifugal compressor in axial direction, this is due to no tangential component velocity at entry of compressor, due to absence of inlet guide vanes, that is mean (α1 is 900) and (Cθ1 is zero). In general the mechanical and thermodynamic processes in a centrifugal compressor are described by the continuity equation, momentum equation, the first and second law of thermodynamics. Applying these general principles to the real flow in centrifugal compressors.

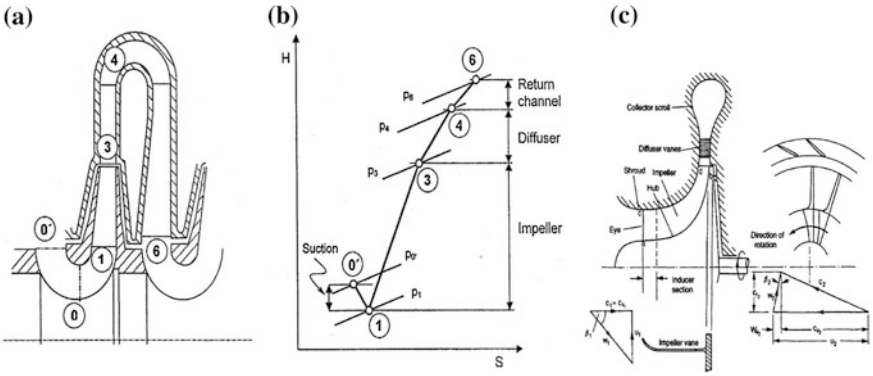

Fig. 1 **a** Compressor stage (Gysling 2013). **b** Changes of energy for compressor. **c** Centrifugal compressor stage and velocity diagrams

3 Basic Surge Concepts

Surge is unstable operation mode of centrifugal compressors, which occurs when the operating point of the compressor is located to left of the surge line, which is the stability limit in the compressor map. The phenomenon is manifested as oscillations of the mass flow, pressure rise and rotational speed of the compressor. Surge is highly undesired and can cause severe damage to the machine. Traditionally, surge has been avoided using a surge avoidance scheme. Such schemes use various measures to keep the operating point of the compressor away from the surge line. Typically, a surge control line is drawn at distance from the surge line, and the surge avoidance scheme ensures that the operating point does not cross this line. This method restricts the operating range of the machine and efficiency is limited. Active surge control is fundamentally different to surge avoidance in that the unstable phenomenon is sought to be stabilized instead of avoided (Grong 2009). Surge appears to be more important instability in centrifugal systems and can affect the whole system and should be avoided. It is characterized by large amplitude limit—cycle oscillation in mass flow rate and pressure ratio. Surge start to occur in a region of the compressor map, where the pressure—mass flow characterized for a constant speed have a positive slop. Surge can be further defined according to the amplitude of the oscillations. Mild surge refers to small amplitude oscillation with a frequency near the Helmholtz resonator frequency. Classic surge is nonlinear phenomenon with larger oscillations and a lower frequency than mild surge but the mass flow fluctuations remain positive. Deep surge is most severe of these types, as reversed mass flow can occur in the compressor. This type of oscillation can cause reduced performance and efficiency of the compressor and even in some cases failure due to large unsteady aerodynamic force on blades (Gravdahal et al. 2001).

3.1 Surge Control

It is seen that the surge can lead to failure of the system due to large mechanical loads in the blading. Furthermore, these instabilities restrict the machines performance and efficiency. There are several methods for surge avoidance exists and active surge control and examples include recycle, bleed and throttle valves, gas injection, variable guide vanes and a number of others. The most widely used method in industrial compressor systems today is to use a recycle valve to divert gas from the compressor outlet and back to the inlet. This is to keep the flow through the compressor above the critical limit. The major drawback of the recycle valve is that the gas is run through the same compressor several times. This increases the energy consumption of the compressor. This solution has proved reliable, but is somewhat inefficient. Active surge control is a popular research field. The purpose of active surge control is to stabilize the compressor when operating within the unstable region of the compressor map. This is achieved by extending the stable operating envelope of the compressor (Shehata et al. 2009). Surge control techniques have been extensively explored. The main advantages of these techniques are their applicability to a wide range of machines and their considerable performance improvement compared to other techniques. Moreover, these techniques can be easily added to existing machines. Traditionally, using surge avoidance technique However, these techniques limit the operational range and reduce the efficiency of the compression system. Therefore, active surge control has been introduced as an alternative approach to suppressing surge rather than avoiding it.

3.2 Experimental Work

The main purpose of the experimental work detection the surge by measuring mass flow and pressure and noted when occurs positive curve between them the surge is begin. Secondly control the surge by move the surge line towards the left side. In Sect. 1 of this works the mass flow rate was measured from water manometer and the pressure were measured from (1) mercury manometer (2) sensors, and plotted them (mass flow rate and delivery pressure) in four rotational speeds (21,000, 23,000, 25,000 and 27,000) rpm. From the experimental curves noted that the peak pressure represent initial of the surge. Also calculated and plotted isentropic efficiencies in each speed by measuring temperatures at inlet and outlet and then plotted the efficiency with delivery pressure. Section 2 represented design plenum and connected to the system by piping and valves to move the surge point towards the left side. Figure 2 shows the schematic diagram of the experimental test rig with plenum. The compressor used in this study is a single—stage centrifugal compressor. This compressor test rig production from PLINT &PARTNERS LTD and it type VS—57, from Paxton product. The compressor consists of: (1)

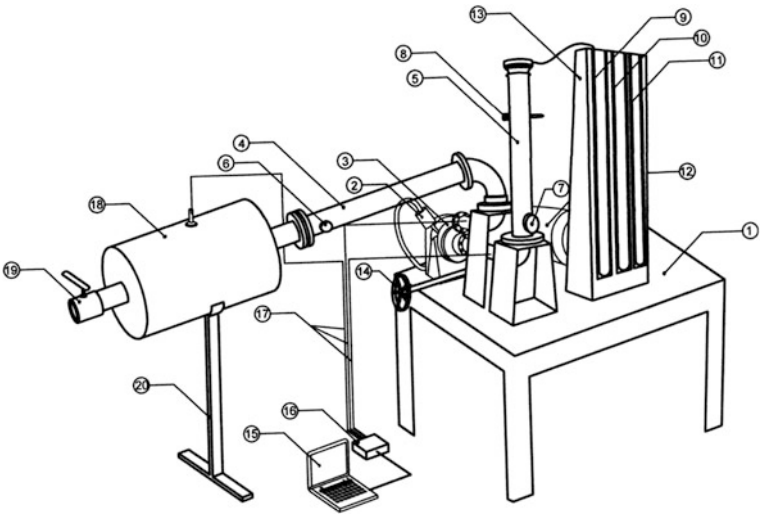

Fig. 2 Schematic diagram of the experimental rig with plenum

Impeller: The impeller has 10 blades and rotates in high speed between (21,000–29,000). The outlet tip diameter is 145 mm and inlet tip diameter is 65 mm. (2) Volute: The volute surrounding the impeller and use to convert the kinetic energy into static pressure by gradual expansion. Figure 3 shows the volute with impeller. In this study used the sensors to calibrate with U—tube manometer, these monometers contain mercury as a liquid manometer and then used sensors as a part of the system instead of the mercury manometers. Theoretical analysis: Study of mathematical analysis of the compressor characteristic for a variable speed compressor. The dynamic model used based on the thermo—and fluid mechanics processes taking place in a centrifugal compressor. The energy losses in the compressor are derived the characteristic, fluid friction and incidence losses, as well as other losses, in the compressor components are modeled, and a variable speed compressor characteristic is developed based on this analysis. The physical model considered in this study is shown in Fig. 4 which represent compression system with close coupled valve.

A compression system consisting of a centrifugal compressor closed coupled valve (CCV), compressor duct, plenum volume and a throttle. The calculation of the compressor pressure rise will be based on energy transfer and energy losses in the various parts of the compressor. Governing equation:

$$\text{isoentropic efficiency} = \frac{\Delta h_{\text{ideal}}}{\Delta h_{\text{actual}}} = \frac{h_{2s} - h_{01}}{h_{02} - h_{01}} \tag{1}$$

$$\text{isoentropic efficiency} = \frac{C_p\ T_{01}\left(\frac{T_{2s}}{T_{01}} - 1\right)}{C_p\ (T_{02} - T_{01})} \tag{2}$$

Fig. 3 Impeller and volute of centrifugal compressor

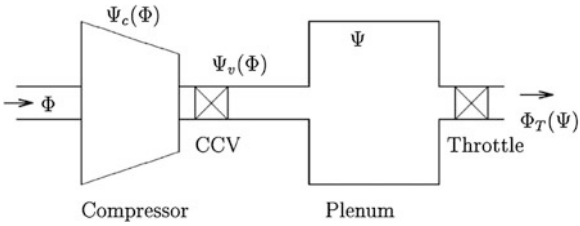

Fig. 4 Centrifugal compression system with CCV

$$\text{isoentropic efficiency} = \frac{C_p\ T_{01}\left[\left(\frac{P_2}{P_{01}}\right)^{\frac{\gamma-1}{\gamma}}-1\right]}{C_p\ [T_{02}-T_{01}]} \tag{3}$$

$$\text{isoentropic efficiency} = \frac{C_p\ T_{01}\left[\left(\frac{P_2}{P_{01}}\right)^{\frac{\gamma-1}{\gamma}}-1\right]}{\Delta h_{0c,\,ideal}} \tag{4}$$

$$P_2 = \left[1+\frac{\eta_{is}\times\Delta h_{0c,\,ideal}}{C_p\ T_{01}}\right]^{\frac{\gamma-1}{\gamma}}\times P_{01} \tag{5}$$

$$\Delta h_{0c,\,ideal} = U_2\ C_{e2} \tag{6}$$

$$\text{slip factor } (\sigma) = \frac{C_{\theta 2}}{U_2} \Rightarrow C_{\theta 2} = \sigma U_2 \tag{7}$$

$$\Delta h_{0c,\,ideal} = \sigma U_2^2 \tag{8}$$

$$\text{The slip factor is define as } \sigma \cong 1-\frac{2}{i} \tag{9}$$

The approximation is known as Stanitz formula, where is the number of impeller blades, the slip factor varies between 0 and 1. To calculate the isoentropic efficiency of the compressor, applies the equation of Cumpsty definition:

$$\eta_{\mathrm{i}}\ (\mathrm{m}, \mathrm{U\_1}\ ) = \frac{\Delta \mathrm{h}_{0\mathrm{c,ideal}}}{\Delta \mathrm{h}_{0\mathrm{c,ideal}} + \Delta \mathrm{h}_{\mathrm{loss}}} - \Delta n \tag{10}$$

$\Delta \mathrm{h}_{\mathrm{loss}}$ term is the summation of the friction losses and incidence losses in impeller and diffuser respectively and $\Delta \mathrm{h}$ is term to the summation of another losses that low effect.

$$(\Delta \mathrm{h}_{\mathrm{loss}} = \Delta \mathrm{h}_{\mathrm{if}} + \Delta \mathrm{h}_{\mathrm{ii}} + \Delta \mathrm{h}_{\mathrm{df}} + \Delta \mathrm{h}_{\mathrm{di}}) \tag{11}$$

$$\Delta \mathrm{h}_{\mathrm{if}} = \mathrm{C}_{\mathrm{h}} \frac{1}{\mathrm{D}} \frac{\mathrm{w}_{1\mathrm{b}}^2}{2} \tag{12}$$

$$\Delta \mathrm{h}_{\mathrm{if}} = \frac{\mathrm{C}_{\mathrm{h}} l}{2\mathrm{D}\rho_{01}^2\ \mathrm{A}_1^2 \sin^2 \beta_{1\mathrm{b}}}\ \mathrm{m}^2 \tag{13}$$

$$\Delta \mathrm{h}_{\mathrm{ii}} = \frac{\mathrm{w}_{\theta 1}^2}{2} \tag{14}$$

$$\Delta \mathrm{h}_{\mathrm{ii}} = \frac{1}{2} \left(\mathrm{U}_1 - \frac{\cot \beta_{1\mathrm{b}}\ \mathrm{m}}{\rho_{01}\ \mathrm{A}_1} \right)^2 \tag{15}$$

$\Delta \mathrm{h}_{\mathrm{if}}$, $\Delta \mathrm{h}_{\mathrm{ii}}$ are friction losses in impeller, and incidence losses in the impeller respectively. In the present model and equations, it is required to calculate the outlet pressure from different rotational speeds and in different percentage open throttle valve. To calculate the outlet pressure used the incidence losses $\Delta \mathrm{h}_{\mathrm{ii}}$ instead of total losses to show the surge area. These values of the total pressure measuring in four different rotational speeds (21,000, 23,000, 25,000, 27,000) rpm and in seven percentage open throttle valve (10, 20, 30,40, 50, 60, 80 and 100 %).

4 Results and Discussion

Figure 5 represents the compressor map with surge line without plenum, these curves obtain them at four rotational speeds. Figure 6 represents the compressor map with surge line with plenum, these curves obtain them in four different rotational speeds. Figure 7 represents the compressor map theoretically between the mass flow rate and pressure at four rotational speeds without plenum. Figure 8 represents the pressures and mass flow rates experimental and theoretically without plenum at speed 21,000 rpm. Figure 9 represent the pressures and mass flow rates experimental and theoretically without plenum at speed 27,000 rpm.

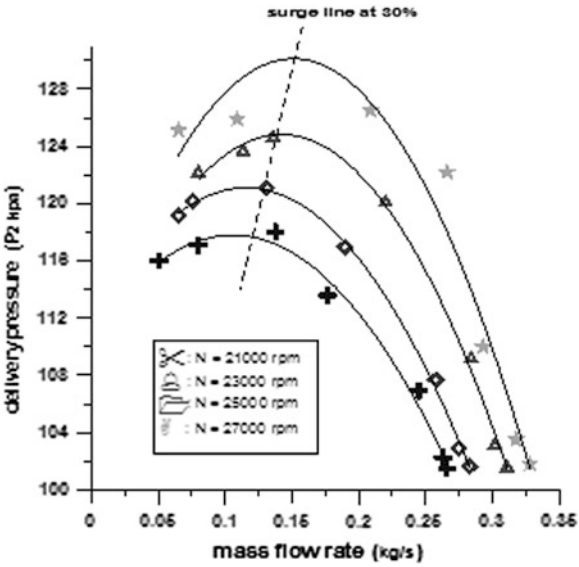

Fig. 5 Mass flow rate and delivery pressure without plenum at four speeds with *surge line*

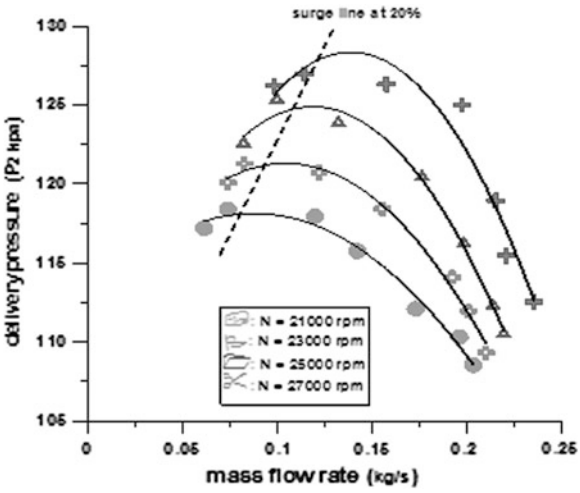

Fig. 6 Mass flow rate and delivery pressure with plenum at four rotational speeds with *surge line*

Figure 10 represent the relationship between the mass flow rates and pressures experimental and theoretically in three speeds rotational. Figure 11 represents the mass flow rate and pressure theoretically with plenum and without plenum. Figure 12 represents the relationship between the mass flow rate, delivery pressure and isentropic efficiency experimental at speed rotation 21,000 rpm.

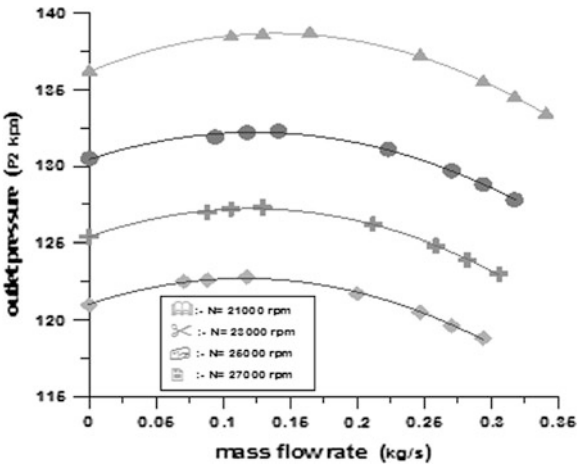

Fig. 7 Mass flow rate and outlet pressure from calculating with out Plenum in four rotational speeds

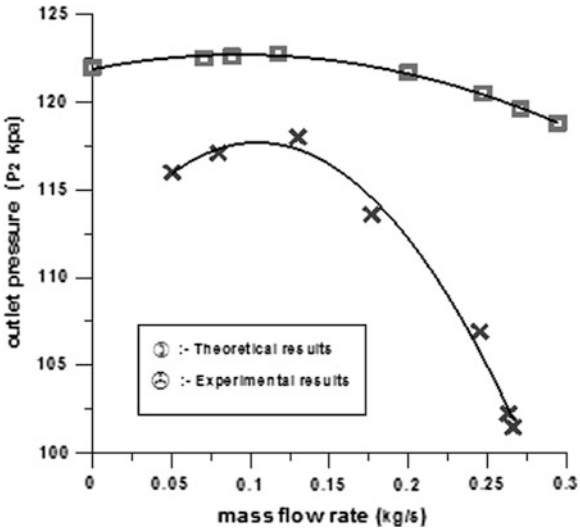

Fig. 8 Mass flow rate and outlet pressure from experimental and theoretical

5 Conclusions

1. It has been found after connected the plenum the surge area decrease and the surge line moved towards the lift side of the compressor map. 2. It has been found that the advantage using the plenum is delay occurrence the surge phenomenon, where the surge start occur at 20 % open throttle valve after connect the plenum. 3. The experimental results indicated that the surge could be suppressed at the initial stages of its inception. 4. The energy transfer equations and energy losses

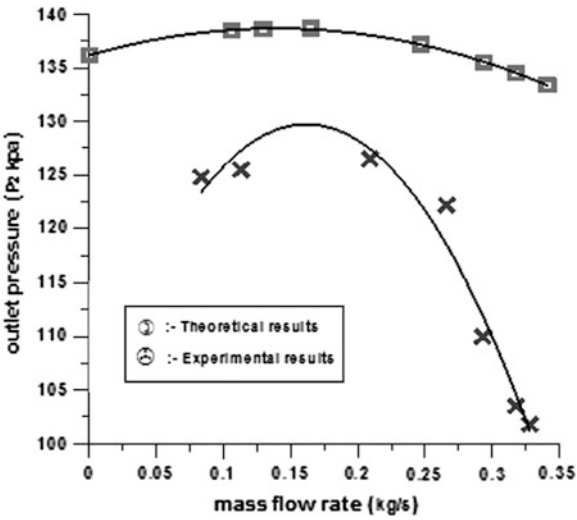

Fig. 9 Mass flow rate and outlet pressure theoretic from experimental and theoretical work without plenum at 27,000 rpm

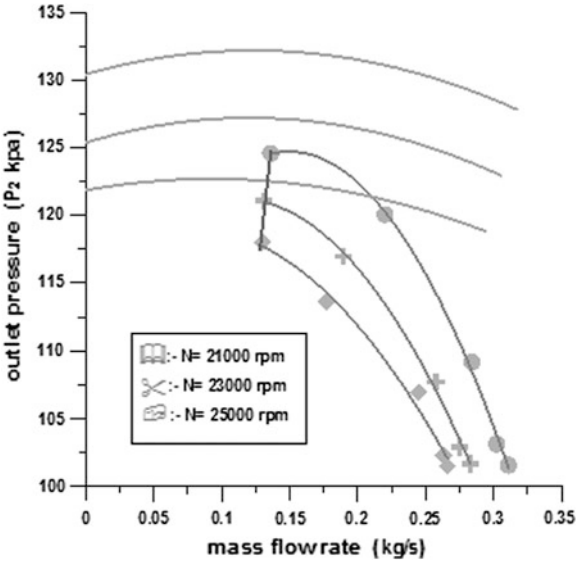

Fig. 10 Mass flow rate and pressure cally and experimentally

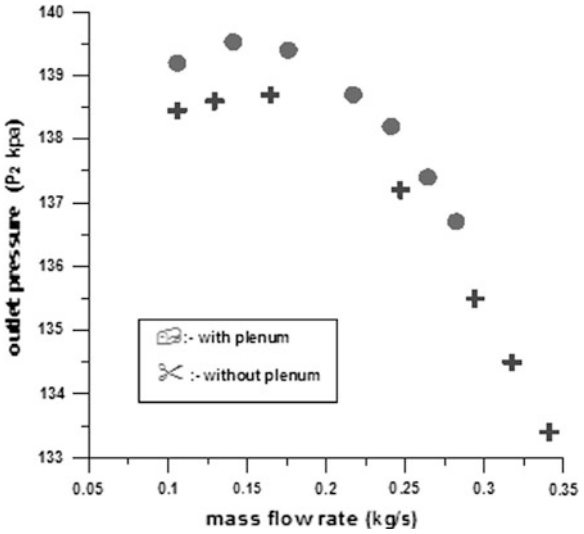

Fig. 11 Mass flow rate and pressure and theoretical with and without plenum

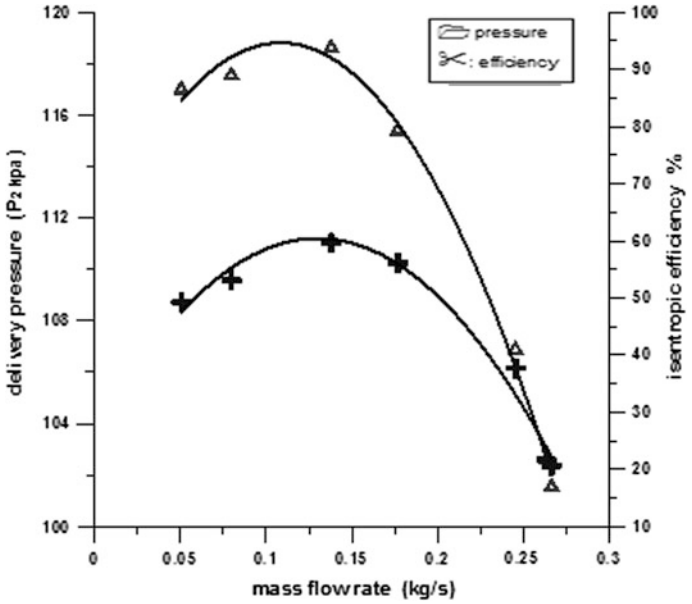

Fig. 12 Mass flow rate, delivery pressure isoentropic efficiency at 21,000 rpm

equations, it has been adopted in this research showed that fluctuation in outlet pressure calculated from different type of losses. 5. The positive curve of the compressor occur because the incidence losses.

References

Gravdahal JT, Egeland O, Vatland SO (2001) Active surge control of centrifugal compressor using drive torque. In: Proceedings of the 40th IEEE conference, vol 2, Department of Engineering Cybernetics, Norway

Grong TS (2009) Modeling of compressor characteristics and active surge control. M.Sc. thesis, Norwegian University of Science and Technology, June 2009

Gysling DL (2013) Dynamic control of centrifugal compressor surge using tailored structure, M. Sc thesis, Pennsylvanian State University

Shehata RS, Abdullah HA, Areed FFG (2009) Variable structure surge control for constant speed centrifugal compressors. Control Eng Pract 17:815–833

Coefficient of Thermal Expansion of Electric Guitar String Material Determination

O. Dajbych

Abstract The coefficient of thermal expansion of electric guitar string material was obtained by its fundamental frequency measurement. The method of using a guitar tuner is very simple and has better advantage compared to other possible methods of determining the coefficient of thermal expansion. The obtained results and experiment could be useful as educational illustration material in subjects such as Strength and Elasticity or Technical Mechanics.

Keywords Coefficient of thermal expansion · Electric guitar string · Fundamental frequency · Tuner

1 Introduction

Methods for obtaining coefficient of thermal expansion bring several problems which could significantly decrease accuracy, make the measurement very difficult or require special equipment. Such as push-rod dilatometer, laser interferometric dilatometer, capacitive dilatometer and other special laboratory devices and conditions (Kanagaraj and Pattanayak 2003).

Therefore an experiment simple enough so it could be done in simple laboratory conditions even at home was prepared. Similarly as in Dajbych (2012) the method was primarily meant as educational example thus the method, number of measurements and statistical significance was not considered.

O. Dajbych (✉)
Czech University of Life Sciences Prague, Prague, Czech Republic
e-mail: dajbych@tf.czu.cz

L. Ševčík et al. (eds.), *Modern Methods of Construction Design*,
Lecture Notes in Mechanical Engineering, DOI: 10.1007/978-3-319-05203-8_45,

2 Materials and Methods

2.1 Strings

Strings used for the experiment were Ernie Ball Top Heavy Bottom Electric Strings. Wound strings were made from nickel plated steel wire wrapped around a hex shaped steel core wire. The plain strings were made of specially tempered tin plated high carbon steel (Fig. 1).

Because wound strings' outer layer would distort results and complicate calculation only plain strings (*e*, *b*, *g*) were used in the experiment. Manufacturer's claims that their diameters should be 0.010 in., 0.013 in. and 0.017 in., thus 0.254, 0.330 and 0.432 mm.

Mechanical and physical properties of the strings material (Table 1) needed for calculation were taken from previous experiment (Dajbych 2012).

2.2 Calculation

Several basic formulas were used for the calculation. These include the following: object elongation caused by temperature difference (1), elongation caused by tensile stress based on Hoocke's law (2) and fundamental frequency of string (3).

$$\Delta l = \alpha \cdot \Delta t \cdot l_0 \tag{1}$$

$$\Delta l = \sigma \cdot \frac{l_0}{E} \tag{2}$$

where Δl is elongation in (m), α is coefficient of thermal expansion in (K^{-1}), Δt is temperature difference in (K), l_0 is initial length in (m), σ is tensile stress in (Pa) and E is Young's modulus of elasticity in (Pa).

$$f = \frac{1}{2l}\sqrt{\frac{F}{m_1}} \tag{3}$$

where f is fundamental frequency of string in (Hz), l is length of string in (m), F is force applied to string in (N) and m_1 is weight of 1 m of string in (kg m^{-1}). This can be modified with basic geometrical and physical principles into (4).

$$f = \frac{1}{2l}\sqrt{\frac{\sigma}{\rho}} \tag{4}$$

where f is fundamental frequency of string in (Hz), l is length of string in (m), σ is tensile stress in (Pa) and ρ is density of string material in (kg m^{-3}).

Fig. 1 Ernie Ball Top Heavy Bottom Electric Strings. Originally in dark orange

Table 1 Mechanical properties of strings material (Dajbych 2012)

Property	Value	Units
Modulus of elasticity E	200	GPa
Density ρ	7,600	kg m^{-3}

Combining (1) (2) and (4) we obtain final formula for coefficient of thermal expansion (5).

$$\alpha = \frac{4 \cdot \rho \cdot l^2}{E} \cdot \frac{f_1^2 - f_2^2}{t_2 - t_1} \tag{5}$$

where α is coefficient of thermal expansion in (K^{-1}), t_1 and t_2 are temperatures in (K), l is length in (m), E is Young's modulus of elasticity in (Pa), ρ is density of string material in (kg m^{-3}), f_1 and f_2 are fundamental frequencies in (Hz) of string for corresponding temperatures.

2.3 Measuring Method

The string was tightened on a measuring device as shown to Figs. 2 and 3 consisting of a block from ash wood with dimensions 400 × 20 × 15 mm, 2 *GROVER* guitar tuning knobs and 2 string locks used on guitar for better tuning stability with vibrato tremolo. It was left in thermally stable environment of room temperature. Then the string was tuned to initial frequency which was chosen by ear

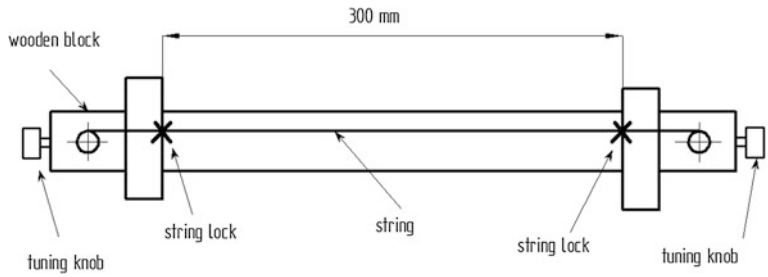

Fig. 2 Measuring device scheme

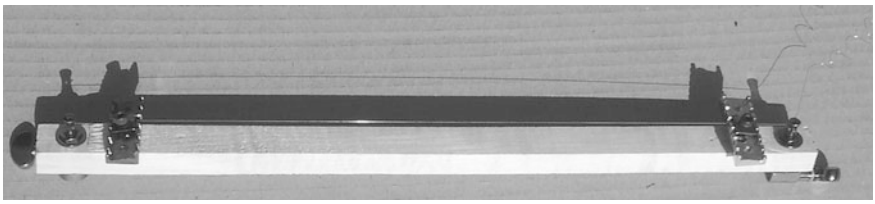

Fig. 3 Measuring device

for good sound of given string and the device was exposed into another environment with different stable temperature. After 30 min what is long enough for such small amount of steel mass to exchange thermal energy with environment so the temperature of the string settled the frequency was measured and the environment was subsequently changed again. For test of overall device stability was the last measurement was done again by room temperature.

Multifunctional measuring device *UNI-T UT39C* with temperature probe was used for temperature measurement.

Mobile phone Samsung Galaxy S2 i9100 with Android application *Tuner—gStrings Free* was also used. The string was hit with guitar pick and the sound was transferred though phone microphone to analyzing software.

For lower temperature environments the fridge *Calex R220* and its freezer were used. For higher temperature *EKZ KB-8 Standart G* oven was used.

3 Results and Discussion

30 measurements were carried-out where each string was repeated twice. An example of one cycle of tests of one string is given in (Table 2). Where α_1 is calculated for difference between first and current measurement and α_2 is calculated for current and previous measurement.

Table 2 Different test of string e measurement

t (°C)	f (Hz)	α_1 (K^{-1})	α_2 (K^{-1})
25	423.8	–	–
9	438.2	1.06×10^{-5}	1.06×10^{-5}
−12	454.3	0.99×10^{-5}	0.94×10^{-5}
40	411.0	0.98×10^{-5}	0.99×10^{-5}
25	420.1	–	0.69×10^{-5}

Table 3 Coefficient of thermal expansion

String	α (K^{-1})
e	0.98×10^{-5}
b	0.97×10^{-5}
g	0.94×10^{-5}
Total	0.96×10^{-5}

From the table, it is obvious that the measuring device was not fully stable and the string lost initial tense during test cycle which is most evident from difference between first and last measurement at the same temperature. Other cycles showed similar results.

Table 3 shows final results with all 2×7 values were averaged as mean for each string separately and then total mean was calculated.

It was shown that Eq. (5) could be suitable for determination of coefficient of thermal expansion. It was found that there was a gradual release of string during test cycle, bending compliance of wooden base of the measuring device and own thermal expansion (contraction) of wooden base which was not included into calculation. With the assumption that wooden base also balanced the temperature with environment we could add about $0.3–0.4 \times 10^{-5}$ K^{-1} generally stated for wood.

For the exact measurement of coefficient of thermal expansion would be necessary to use more rigid base for string tightening and material with high modulus of elasticity and low coefficient of thermal expansion. Bigger should be used so the force provided by the string would have insignificant influence on bending. It is also important to set the tempering interval correctly so that the string temperature settles with little effect on the base.

The advantage of the suggested method is requirement for quite available equipment and immediate possibility to measure the frequency in the tempering environment without moving the sample to measuring device stationed in different temperature conditions or leaving the measuring instrument in the environment. The tuner was put into the fridge or oven right after opening the door and the measurement was completed in several seconds before the temperature change could affect the string.

4 Conclusions

A simple experiment was performed which shows possibility to measure the coefficient of thermal expansion of vibrating object by measuring its fundamental frequency in statically indeterminate case. As example guitar string and its pitch change was introduced.

It also appeared that rigidity and thermal stability of the fixing device which represents the frame is critical for accuracy.

References

Dajbych O (2012) Physical and mechanical properties of electric guitar string material. In: Proceedings of 53rd international conference of machine design departments, pp 63

Kanagaraj S, Pattanayak S (2003) Measurement of the thermal expansion of metal and FRPs. Cryogenics 43(7):399–424

Processing of Automobile Gearbox Load Spectra

M. Hrudičková and Z. Folta

Abstract The paper deals with acquisition and processing of automobile gearbox load spectrum in usual traffic operations. Spectrum was obtained on the basis of extensive measurement and results are used for life-time tests under research and development of automotive gearboxes.

Keywords Gearbox · Load spectra · Torque measurement · Enumeration

1 Introduction

Overall objective of extensive measurement was acquisition of comprehensive automobile gearbox load spectra during different drive mode. This process was possible to do on the basis of time behaviour torque measured on both of the axle-driving shafts, immediate vehicle speed, engaged gear and position of gas pedal. The results are used in life-time tests of gearboxes on test stand made under Josef Bozek Research Centre of Engine and Automotive Engineering II.

2 Acquisition of Operating Data

Measured value: during drive was synchronically scanned:

- the torque from right and left axle-driving shaft,

M. Hrudičková (✉) · Z. Folta
VŠB-Technical University of Ostrava, Ostrava, Czech republic
e-mail: Milena.Hrudickova@vsb.cz

Z. Folta
e-mail: Zdenek.Folta@vsb.cz

L. Ševčík et al. (eds.), *Modern Methods of Construction Design*,
Lecture Notes in Mechanical Engineering, DOI: 10.1007/978-3-319-05203-8_46,

- present engaged gear,
- immediate vehicle speed,
- immediate position of gas pedal.

Further, from vehicle control system was subtracted:

- average fuel consumption in measured section,
- made distance.

Value of made distance was compared with GPS data and together with grade line and map of every made route was recorded to PC.

Applied measuring device: For torque measuring on both half-axis was applied telemetric contactless sensing signal from rotate parts from ESA Messtechnik GmbH (Germany). Engaged gear was recorded with the assistance of tactile micro switches located at gear shift. Immediate vehicle speed was recorded by magnetic axle speed sensor.

Torque measurement: half-axis are stressed during acceleration by torque from drive and during motor braking are stressed by torque with negative sign. Further, half-axis are stressed during wheel braking. During different drive mode, the gearbox is loaded by torque, which proves on half-axis. Knowledge of moment curvature in half-axis enables to obtain statistic of individual gear load and to determine load spectrum during vehicle different drive mode. For relatively simple and accurate acquisition of load parameter between gearbox and wheel half-axis are predestine because of theirs elementary shape and accessibility, between engine and gearbox after recalculation too.

After complete installation of both half-axis in laboratory conditions (Fig. 1) was tested functionality of signal transmission between rotary and stationary antenna.

Operational range of both half-axis distance fluctuated till 15 mm, ergo markedly less than state telemetry producer (purportedly commonly right to 40 mm). Final antenna positioning on right half-axis is in Fig. 2.

Testing drive routes: Testing drive routes was selected in the city of Ostrava and environs with respect to proportional representation of different drive mode during usual vehicle traffic, for example municipal, interurban and highway mode. Load spectrum during special drive mode with elimination surrounding traffic (for reason safety and traffic rules) was picked chosen stages on test circuit of joint-stock company Tatra Kopřivnice. Example of ready to enumerate recording is in Fig. 3.

3 Enumeration

Enumeration for each study parameter was pursued into 40 well-proportioned levels. According to evaluated curves was determined level range for enumeration from maximum ranges of torque, engage gears and speeds, namely as follows:

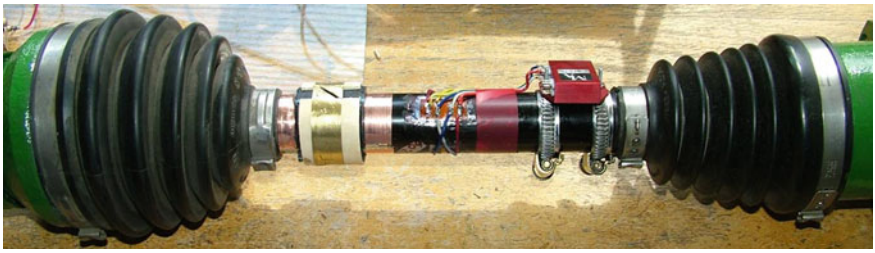

Fig. 1 Left half-axis after sensors and transmitting antenna installation

Fig. 2 Antenna positioning on right half-axis

Level_speed_engine	0 … + 8,000 RPM (41 levels per 200 RPM)
Level_speed_output	0 … + 1,600 RPM (circa 160 km/h) (41 levels per 30 RPM)
Level_torque_engine	− 150 … + 300 N·m (41 levels per 12 N·m)
Level_torque_output	− 1,200 … + 1,800 N·m (41 levels per 75 N·m)
Level_speed	0… + 200 km/h (41 levels per 5 km/h)

For actual enumeration was used two-level method. The aim of enumeration is to find number of load cycles applied to the gearwheel‘s tooth:

- at actual engaged gears,
- at the appropriate level of torque during the test drive.

Input parameters were:

- engine speed and torque of separate gear for input torque enumeration,
- output speed and torque from gearbox for output torque enumeration.

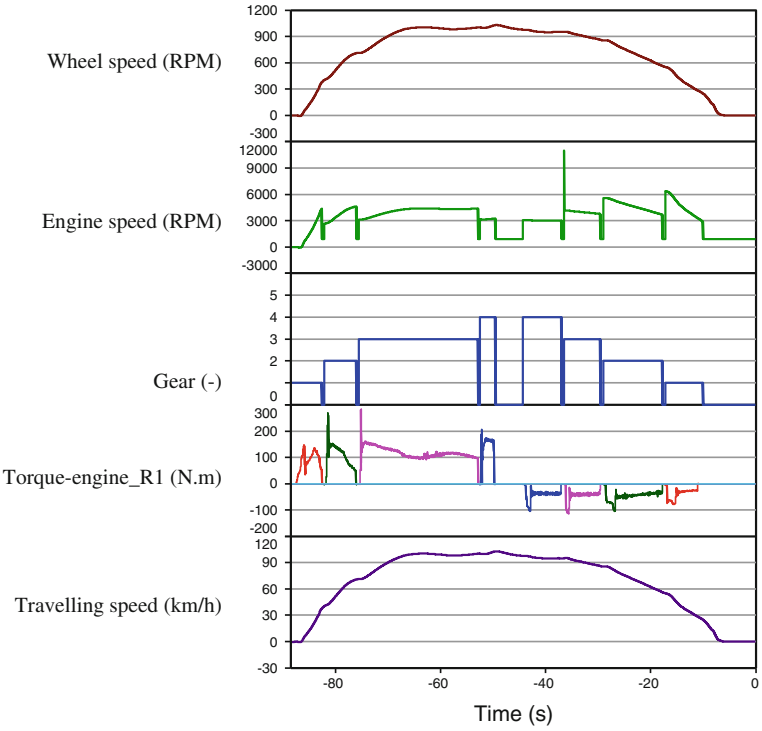

Fig. 3 Input curves for enumeration

Result of each enumeration is matrix, when are itemized torque levels in rows and speed levels in columns. Value in matrix corresponds to relative time abundance of set torque level in set speed level (complete travelling speed time is 100 %). Graphic representation of example of gear R1 is in Fig. 4.

For each level, then was calculated its relative frequency

$$t_{i,rel} = \frac{t_i}{\sum t_i} \tag{1}$$

and relative cumulative frequency for first level:

$$t_{1,rel,cum} = t_{1,rel}$$

for remaining levels:

$$t_{i,rel,cum} = t_{i,rel} + t_{i-1,rel}$$

Frequency in torque level 0 $N{\cdot}m$ wasn't included to calculation.

Stated enumeration informs about exposure time of separate torque levels (1). For gear and bearings calculation is important to know time, but turn number in set level.

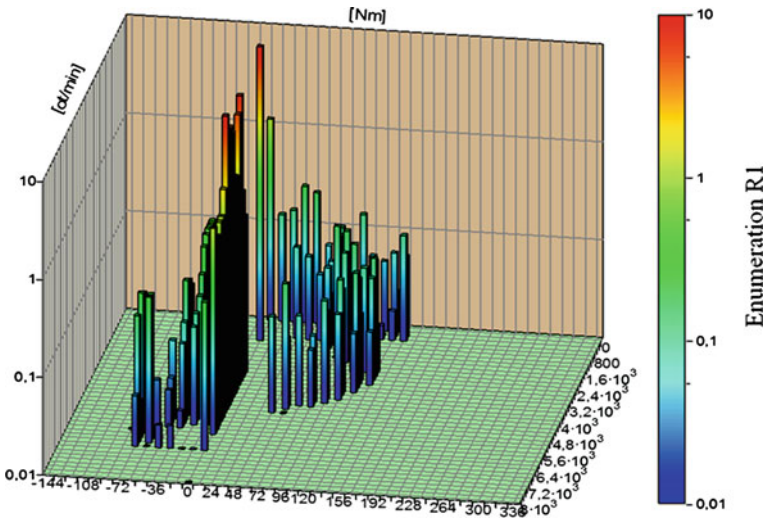

Fig. 4 Relative time frequency of torque in level, engaged the first gear—R1

Because enumeration was executed in dependence on immediate running speed n_i, it was possible to carry out recalculation of time abundance t_i to number of shaft turn Ni according to theorem

$$N_i = t_i \cdot n_i$$

For each level, then was calculated its relative frequency too

$$N_{i,rel} = \frac{N_i}{\sum N_i} \tag{2}$$

and relative cumulative frequency

$$\begin{aligned} &\text{for first level:} && N_{1,rel,cum} = N_{1,rel}, \\ &\text{for remaining levels:} && N_{i,rel,cum} = N_{i,rel} + N_{i-1,rel} \end{aligned} \tag{3}$$

Stated running speed frequencies are described in graphs (for example in Fig. 5). Frequency in torque level 0 $N{\cdot}m$ wasn't included to calculation too.

Stated enumerations were executed

- torque during engage 1st, 2st, 3st, 4st and 5st gear,
- input torque into gearbox,
- output torque from gearbox.

Torque level mean	Relative frequency	Cumulative frequency
Nm	-	-
189	0,000E+00	0,000E+00
182	0,000E+00	0,000E+00
175	0,000E+00	0,000E+00
168	0,000E+00	0,000E+00
161	0,000E+00	0,000E+00
154	0,000E+00	0,000E+00
147	0,000E+00	0,000E+00
140	0,000E+00	0,000E+00
133	0,000E+00	0,000E+00
126	0,000E+00	0,000E+00
119	0,000E+00	0,000E+00
112	0,000E+00	0,000E+00
105	0,000E+00	0,000E+00
98	0,000E+00	0,000E+00
91	0,000E+00	0,000E+00
84	2,942E-03	2,942E-03
77	1,113E-03	4,055E-03
70	2,937E-02	3,342E-02
63	4,530E-02	7,872E-02
56	5,027E-02	1,290E-01
49	3,411E-02	1,631E-01
42	2,105E-02	1,841E-01
35	1,790E-02	2,020E-01
28	3,072E-02	2,328E-01
21	2,526E-03	2,353E-01
14	0,000E+00	2,353E-01
7	0,000E+00	2,353E-01
0	0,000E+00	2,353E-01
-7	1,665E-02	2,519E-01
-14	4,168E-01	6,687E-01
-21	6,502E-02	7,338E-01
-28	6,138E-03	7,399E-01
-35	1,643E-01	9,042E-01
-42	9,584E-02	1,000E+00
-49	0,000E+00	1,000E+00
-56	0,000E+00	1,000E+00
-63	0,000E+00	1,000E+00
-70	0,000E+00	1,000E+00
-77	0,000E+00	1,000E+00
-84	0,000E+00	1,000E+00
-91	0,000E+00	1,000E+00

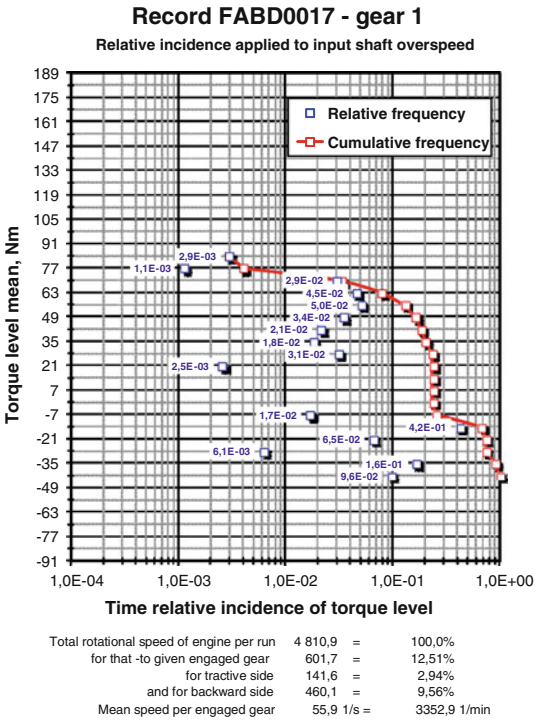

Fig. 5 Running speed frequencies of torque levels

Following statistic information was part of each enumeration

(a) for time enumeration:

- drive time in measure segment altogether,
- from this by set gear,
- from this for each tractive side,
- and for backward side,

(b) for speed enumeration:

- complete number of engine turn per measure segment drive,
- from this for set gear,
- from this for tractive side,
- and for backward side,
- average speed during engage gear.

4 Conclusions

Load spectrum acquired from real traffic on different roads and during different drive modes is optimal test instrument for arrangement of desired composition of load cycles for time-life testing. Above mentioned way of load spectrum evaluation enables by change of torque and speed to complete gearbox load spectrum according with demand.

Acknowledgments This research has been realized using the support of Technological Agency, Czech Republic, programme Centres of Competence, project # TE01020020 Josef Božek Competence Centre for Automotive Industry. This support is gratefully acknowledged. Contribution has been done in connection with project Increasing of Professional Skills by Practical Acquirements and Knowledge, reg. no. CZ.1.07/2.4.00/17.0082.

References

Folta Z (2004) *Příspěvek k navrhování strojních součástí na základě vyhodnocení provozního zatížení.* Conferment work. 1st edn. Ostrava: VŠB-TUO, 136 pp

Folta Z, Hrudičková M (2008) *Zpracování zátěžných spekter převodovky osobního automobilu za různých jízdních podmínek* [online]. [cit. 2013-09-04], Ostrava: Department of Machine Parts and Mechanisms, VŠB-TUO, 32 pp. Document in PDF format. Accessible in: http://www3.fs.cvut.cz/web/fileadmin/documents/12241-BOZEK/publikace/2008/2008_004_01.pdf

Multi Room Throttle Valve

O. Kohl

Abstract This text discusses how to use multi room throttle valves in pneumatics circuits. There are presented two valves. One of which is common—with one hole and the other with more holes. Both valves are subjected to an experiment using CFD, which should verify the effectiveness of throttling by multi room throttle valve compared to common throttle valve with calculating followed by comparing the values of the coefficient of local losses.

Keywords Throttle valve · Compressed air · CFD · Local losses

1 Introduction

In pneumatics circuits are used for reducing the flow of compressed air throttle valves. Energy of compressed air is converted by throttle valve through friction of air particles to heat. In case of intensive throttling leads to a significant overheating of the body of valve.

The aim of the research is to develop a valve, whose own throttling element will be based on the aperture with a higher quantity of holes. It will have a high coefficient of local losses and at the same time will the body provide the sufficient heat dissipation.

The throttle valve is compared with a valve in which is only one hole, where the total nominal pipe size of both valves is the same.

Due to the advanced development of computer technology will all experiments conduct with mathematical models and are solved by finite element method (FEM), with CFD.

O. Kohl (✉)
Technical University of Liberec, Liberec, Czech Republic
e-mail: ondrej.kohl@tul.cz

L. Ševčík et al. (eds.), *Modern Methods of Construction Design*,
Lecture Notes in Mechanical Engineering, DOI: 10.1007/978-3-319-05203-8_47,

2 Structural Designs

Construction of multi room throttle valve for this case is that in the pipeline of diameter 50 mm is inserted an aperture with length of 50 mm. It is a rod in which are drilled 25 holes with a diameter of 4 mm (see Fig. 1) (Kunc 2009).

This construction is compared with the local narrowing of 50–20 mm for the same length of 50 mm (see Fig. 2).

3 Experiments

Holes in the first sample have the same total nominal pipe size as the hole of the second sample (1) and (2).

$$DN_{25\times 4\,\mathrm{mm}} = 25 \cdot \frac{\pi \cdot d_1^2}{4} = 25 \cdot \frac{\pi \cdot 4^2}{4} \tag{1}$$

$$DN_{1\times 20\,\mathrm{mm}} = \frac{\pi \cdot d_2^2}{4} = \frac{\pi \cdot 20^2}{4} \tag{2}$$

The efficiency of construction designs of throttle valves will compare with values of coefficient of local losses, which will be calculated from the simulation results.

The total pressure loss of piping section in compliance with experimental scheme in Fig. 3 is equal to the difference between the total pressure at the inlet and the outlet and is equal to the sum of the pressure loss of friction and pressure loss of local resistance.

$$\Delta p = p_{in} - p_{out} = \Delta p_t + \Delta p_m \tag{3}$$

Measure of pressure loss can be obtained by subtracting the loss of 1 m long straight section of the inlet pipe.

$$F = p_1 - p_2 \tag{4}$$

Pressure loss of friction will be determinate by the total length of straight pipe section.

$$\Delta p_t = F \cdot (L_1 + L_2) \tag{5}$$

Local pressure loss can be expressed as the product of the coefficient ξ and the dynamic pressure.

$$\Delta p_m = \xi \cdot \frac{w^2}{2} \cdot \rho \tag{6}$$

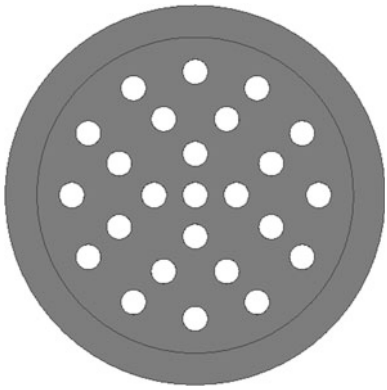

Fig. 1 View into the pipeline with a multi room throttle valve

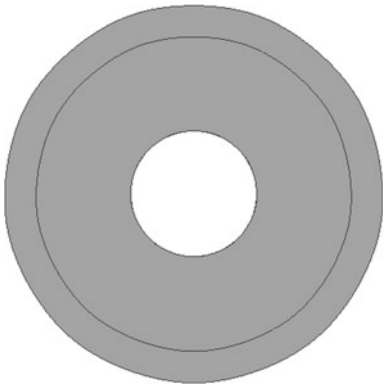

Fig. 2 View into the pipeline with aperture with diameter of 20 mm

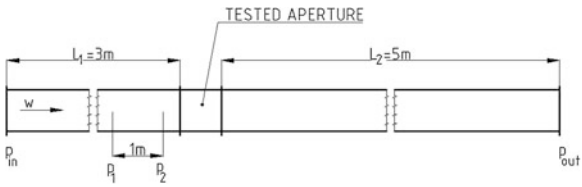

Fig. 3 Experiment scheme

When we substitute Eqs. (3)–(6) then we set the coefficient of local losses (Recknagel 1995; Schwarzer 2010; Zmrhal 2009).

$$\xi = \frac{2 \cdot (\Delta p - \Delta p_t)}{w^2 \cdot \rho} \tag{7}$$

The coefficient of local losses is the sum of local and frictional losses in its own fitting (Idelchik 1993).

$$\xi = \xi_t + \xi_m \tag{8}$$

Table 1 Boundary conditions

Value name	Marking	Value	Unit
Material of pipeline and aperture	Aluminum, ρ_{Alu}	2,700	kg/m^3
Fluid	Air, ρ_{Air}	1.29	kg/m^3
Ambient temperature	t_A	20	°C
Fluid temperature	t_F	20	°C
Starting velocity	W	5	m/s
Pressure at outlet	P	0	Pa

Table 2 The results of experiment and the subsequent calculation

Aperture (mm)	p_{in} (kPa)	p_{out} (kPa)	P_1 (kPa)	P_2 (kPa)	ξ_m
25 × 4	103.65	101.35	103.34	103.26	0.10294
1 × 20	101.99	101.34	101.97	101.93	0.02047

3.1 Boundary Conditions

For both compared constructions were chosen identical boundary conditions. Flow velocity was chosen constant 5 m/s. For solution was applied a turbulence model k-ε RNG and standard wall function (Table 1).

3.2 Simulations and Results

For calculation was used a simulation program based on principle CFD—Software Autodesk Simulation CFD 2013 in which was made meshing too. It was made a simulation model of multi room throttle valve and throttle valve with one hole, for both of them is calculated the coefficient of local losses.

In the pipeline with a total length of 8 m is placed measured element. The element occupied in the pipeline with nominal pipe size of 50 mm a length of 50 mm. Before the aperture is a pipe with a length of 3 and 5 m behind the aperture (see Fig. 3) (ASHRAE 2001; Brooks 1993).

The simulation result is further processed; it is a source of data (Table 2), which is used to calculate the coefficient of local losses (8).

Although are in both design the friction surfaces, in which flow the air, identical, are values of the local losses different. In case of multi room throttle valve is the coefficient of local losses 5 times bigger. Figure 4 shows a section of pipe with a velocity field of multi room throttle valve.

Velocity in holes of multi room throttle valve reaches values up to 46 m/s. Velocity field of simple throttle valve (see Fig. 5) shows the maximum value of 38 m/s.

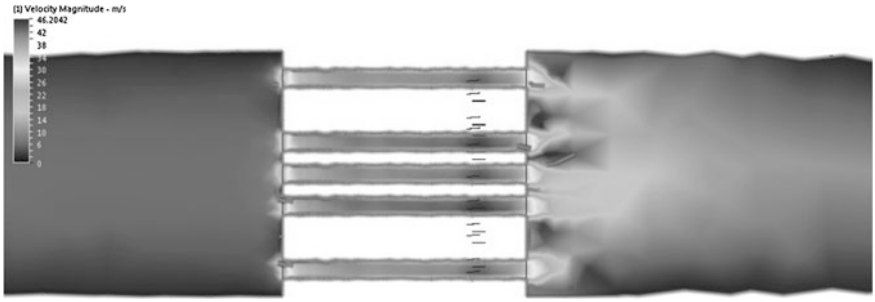

Fig. 4 Velocity field of multi room throttle valve

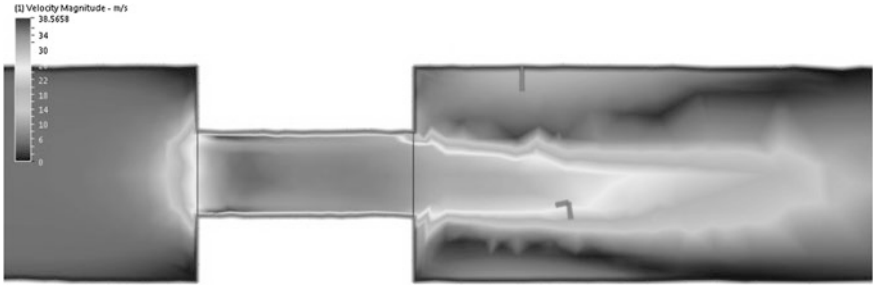

Fig. 5 Velocity field of simple throttle valve

4 Conclusion

Computer Simulation CFD method can be advantageously used to determine the coefficient of local losses (resistance) of pipe fittings for any application. In comparison with the measurement of the real part of waste with computer simulations, is the necessity of producing complex and expensive measuring lines. Simulations are, with regard to the minimum time of calculation, demanding primarily on hardware. The advantage of simulation calculation is the possibility to evaluate the coefficient of local losses based on the difference of the total pressures, which is by the real experiment laboured and very difficult. The measured values of the coefficient of local losses are often evaluated on the basis of the difference of static pressures (Chytrý 1993; Ferstl 2006).

The above described experiment represents an effective use of multi room throttle valves compared to normal throttle valves. While maintaining the same nominal value sizes in two compared valves shows effective throttling the valve with more smaller holes than the valve with one big hole. Another advantage is better cooling of the valve body, which should be made of thermally conductive material. In the area around the holes can be integrate cooling loop. Estimated field of use the multi room throttle valves is in pneumatic circuits, where there are rapid

changes in the direction of fluid flow, for example by seats suspension of trucks and building machines.

Acknowledgments I want to thank the head of my dissertation Prof. Lubomír Pešík, CSc. for valuable advice during the work on the job.

References

ASHRAE Handbook (2001) Fundamentals 2001. ASHRAE, Atlanta

Brooks PJ (1993) New ASHRAE local loss coefficients for HVAC fittings. ASHRAE Trans 99(2):169–193, paper number 3709 (RP-551)

Chytrý J, Hemzal K. a kol (1993) Větrání a klimatizace. Technický průvodce č. 31. Bolit Brno, Praha

Ferstl K (2006) Větrání a klimatizace. Jaga group, Bratislava

Idelchik IE (1993) Handbook of hydraulic resistance—3. Betelu House Inc., vydání

Kunc T (2009) Místní tlakové ztráty vzduchotechnikcé potrubní sítě. Diplomová práce. ČVUT v Praze, Fakulta strojní, Praha

Recknagel H, Sprenger E, Schramek E (1995) Taschenbuch fur Heizung + Klimatechnik 94/95

Schwarzer J, Zmrhal V (2010) Stanovení součinitelů místních ztrát pomocí CFD, 19. In: Konference Klimatizace a větrání 2010, OS 01 Klimatizace a větrání

Zmrhal V, Schwarzer J (2009) Numerical simulation of local loss coefficients of ventilation duct fittings. In: Proceedings of building simulation, IBPSA, Glasgow

Influence of the Type of Gearing to Pitting Damage

B. Kopiláková, M. Bošanský and J. Zápotočný

Abstract The most common damage of operating tooth face is fatigue of material, caused by creation of pitting. At the beginning of the paper is briefly characterized the emerging pitting and what is the decisive factor in its creation. The main gear parameters are explained, which affect the damages caused by pitting with focus on C–C gearing. Testing methodology is presented on Niemann's stand at three different layers of working load. Attention is focused mainly on the influence of pitting damage in regard to the type of the gear, since the creation of pitting at the same working load and other operating conditions occur within a different number of cycles. Results of the experiment are compared with the results already obtained in involute gearing.

Keywords Pitting · Tooth face · Fatigue wear · C–C gearing · Involute gearing

1 Introduction

During the operation of a gear there occurs under the influence of surface and subsurface stress the contact fatigue. This damage is manifested by removing metal caused by pitting on the surface of the working parts of the tooth. Areas of point defects on the surface or at the boundary between the core and the hardened layer

B. Kopiláková (✉) · J. Zápotočný
Trenčín University A. Dubček in Trenčín, Trenčín, Slovakia
e-mail: beata.kopilakova@tnuni.sk

J. Zápotočný
e-mail: jan.zapotocny@tnuni.sk

M. Bošanský
Slovak University of Technology in Bratislava, Bratislava, Slovakia
e-mail: miroslav.bosansky@stuba.sk

L. Ševčík et al. (eds.), *Modern Methods of Construction Design*,
Lecture Notes in Mechanical Engineering, DOI: 10.1007/978-3-319-05203-8_48,

are gradually spreading and shear tracks arise. Forms of contact fatigue are a surface fatigue pitting, micro pitting, shelling, peeling and deep fatigue pitting (Černý et al. 2010).

The first cracks occur due to a pulsating load and action of rolling—sliding friction. Usually this is done on the surface or in a thin surface micro-exposure. Cracks are inclined at an acute angle to the surface in the direction of frictional forces and the hydrostatic forces, the oil gets into them. When contact occurs then the particle surface is splintering and allows for the formation of pits, thus the formation of pitting.

2 Material and Methodology

Pitting as a type of contact fatigue wear in gear drives is manifested by creation of small and larger holes on the surface working parts of tooth. It depends on the type of materials, the conditions of lubrication and friction. On the formation of pitting also affect factors such as: geometrical gearing parameters, traction conditions determining load of teeth by external forces, resolved shear ratios on the teeth flank, frictional forces, surface finish tooth flanks, choice of material and hardness of working tooth flanks and pinion gear, lubricating oil properties and operating conditions. Distinguishes the initial (running-in) and ongoing (progressive) pitting. When putting gear in operation, initial pitting arises. The pits have a dimension of a few tenths of millimeter and are formed on the heads and heels of teeth (Fig. 1a). With the number of operating cycles pitting continues across desktop and creates so called progressive pitting (Fig. 1b), resulting in an increased noise.

In the area of contact of two tooth flanks causes normal force F_{bn} touch stress in accordance with the Hertz theory of contact stresses. Elastohydrodynamic ratios are taken into account by specific coefficients. For the limiting state touch stress tooth flanks are considered when in unhardened surfaces of the tooth flanks will pitting damage at 2 % of the total surface of all teeth (for hardened to 0.5 %) or 4 % of the surface of one tooth. Size of the load in interaction point depends on its current position to the interaction abscissa AE (Bošanský et al. 2009).

In the single-pair interaction is load of tooth flanks at maximum. From end-points of single-pair interaction B, D towards the initial interaction point A it is considered a linear decline of a loading force. In accordance with the Hertz theory comes to a straight contact of two solids and the calculation is based on the contact of two cylinders whose diameter is equal to the diameter of curvature of touch curves at the computing point X. For maximum normal stress at some touch point X applies:

$$\sigma_{H(X)} = \sqrt{\frac{F_{bn(x)} \cdot \sum k_{(X)}}{\pi \cdot b} \cdot \frac{1}{\left(\frac{1-\mu_1^2}{E_1} + \frac{1-\mu_2^2}{E_2}\right)}} \tag{1}$$

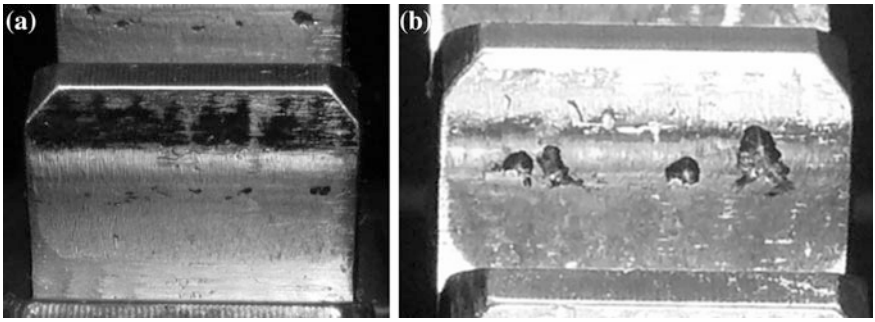

Fig. 1 Pitting: **a** initial, **b** progressive

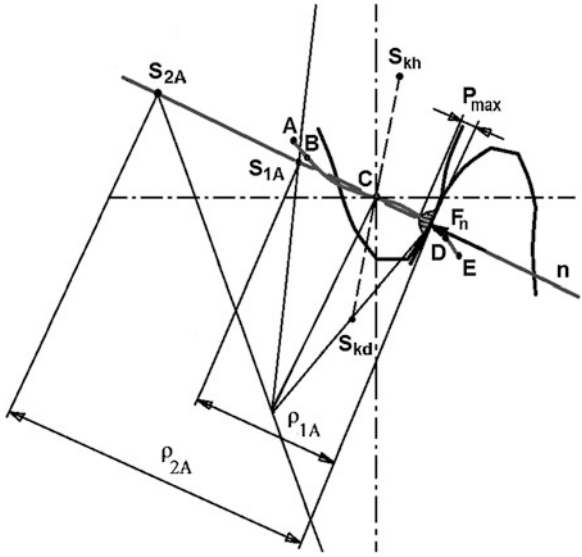

Fig. 2 Interaction of two convex–concave gearing (Bošanský et al. 2012)

where size

$$\sum k_{(X)} = \frac{1}{\rho_{1X}} + \frac{1}{\rho_{2X}}$$

also depends on the nature of the engaging movement and represents the sum of curvature affecting tooth flanks of meshing gears at point X. The greater the value of the sum or the smaller the radius of curvature ρ_{1X}, ρ_{2X} will be meshing involute in considering point X, the greater the contact load stress on teeth. Size $\sigma_{H(X)}$ is also function of $F_{bn(x)}$ and depend on how load is divided between the teeth in the engagement. Unlike involute gearing (interaction of convex part of the tooth with convex part of the opposite tooth) is in the case of convex—concave gearing—

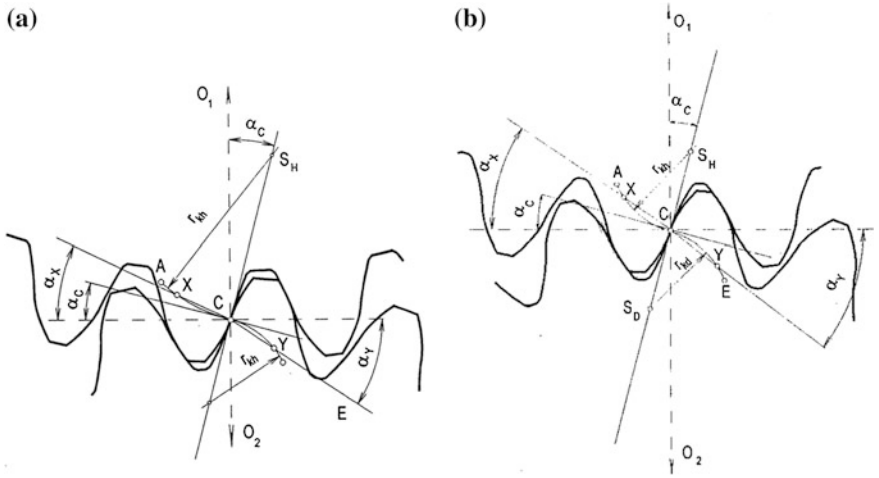

Fig. 3 K–K gearing (Bošanský et al. 2006): **a** symmetrical, **b** asymmetrical

Fig. 2 (interaction of convex part of the tooth with a concave part of the opposite tooth), thus in the K–K gearing in contact with teeth in terms of relations (1) there is smaller touch tension.

2.1 C–C Gearing and Pitting

Heel of the teeth in the case of gears are vulnerable to creation of pitting as the head of the tooth. At first, pitting is created on the heels just below the rolling circle. Here are smaller reduced radiuses of curvature and tension. Later they expand to the heel and at higher loads occur at the heads of gears. For involute pitting it occurs under a rolling circle. Convex–concave gear can be generally understood as any gearing, whose tooth flank forms a curve or curve with a convex and concave part (Fig. 2). These gearing occur when the engaging line has an "S" shape.

Thus, under C–C gearing will be further considered the spur plane gearing, whose is the shape of the tooth is given by engaging line consisting of two, in accordance with point C asymmetrical (Fig. 3a) or symmetrical curves (Fig. 3b) with the inflexion point at point C, at which centers of curves S_{kh} and S_{kd} are not located at the centers of the intersection of rotation of gears (Bošanský et al. 2006a). Modifying some of the parameters α_C, r_{kh}, r_{kd}, z or their combination can be achieved a change of shape of the profile curve of tooth flank K–K gearing (Bošanský et al. 2006a). Their change cannot be arbitrary, but only in boundaries, to ensure the creation of such shape of the tooth gearings that will occur into engagement of the convex part of the tooth with a concave part of opposite tooth and vice versa, thus arises convex–concave engagement. In this type of interaction pitting arises right in the roller circle area.

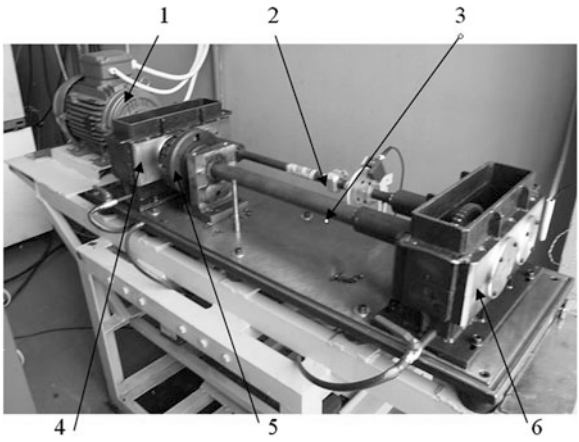

Fig. 4 Test equipment with a closed flow performance: *1* driving electric motor, *2* torsion shaft, *3* connecting torsion shaft, *4* operating gear box, *5* double plate stretching clutch, *6* test gear box

2.2 Methodologies of Tests

K–K gearing interaction conditions are different as in the case of external involute gears. Therefore, it is necessary to experimentally verify the theoretical considerations of the contact strength of K–K gearing obtained by FEM and to see if it is possible usual practices for involute gearing to apply for KK gearing. It is assumed that when checking in touch or bend some experimentally discovered material constants for common involute gearing will not be used in the calculations for K–K gearing. One of such parameters is the fatigue strength $\sigma_{H\,\mathrm{lim}}$ under stress in touch. For the experimental detection fatigue strength values for K–K gearing has been used standard test equipment with a closed stream output called Niemann's gear box, also referred to as Niemann's test bench, in accordance with DIN 51354 according to the methodology FZG, as well as for standard gearing according to DIN 3990 T5. It is the most frequently used device for testing the tooth flak damage in terms of pitting. Specific test equipment selected for the experiment in Fig. 4.

To ensure the test gears it is necessary to provide accurate and consistent measurement methodology to minimize inaccuracies caused by systematic and random errors during the experiments. The basic principle of test is based on standards for testing gears on load machines DIN 51354. The principle consists in the gradual loading the gears and the survey of the number of cycles to failure of the test sample.

Tests were made on both sides of each tooth flank test gear wheels with K–K profile. Together there were 8 experiments. Test wheels were loaded in three levels—level A, B and C (Fig. 5), with a gradual decrease in load. On the first and second level there were three experiments. At the third level near the high-cycle fatigues were performed two experiments. The loads on the individual levels were set with lever mechanism. During each experiment the working oil temperature was regularly monitored with a digital thermometer. After a certain number of

Level mark	Torque load Mk on the test pinion [Nm]	Combination of components at the rotation of flanges of stretching clutch P - lever, Z1 ÷ Z6 - weights T - rod	Serial number of the position of the (notch) rod to the lever	The distance R of the load from the clutch center 300+n.50=R [mm]	Mk_1 from the lever [Nm]
A	265	P+T+Z1+Z2	9	325+8.50=725	25,9
B	185	P+T+Z1+Z4	9	325+8.50=725	25,9
C	125	P+T+Z1+Z6	5	325+4.50=525	25,9

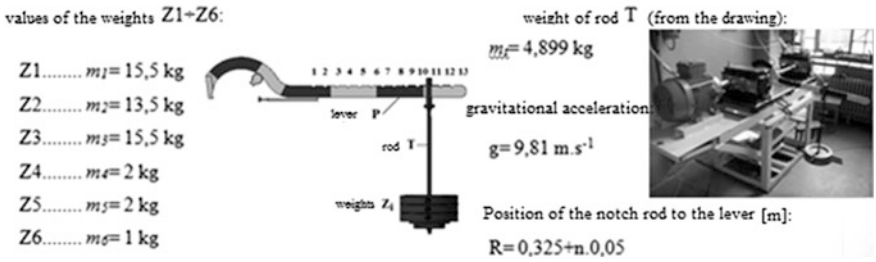

Fig. 5 Necessary data for determine the value of Mk for each level

cycles the experiment was interrupted to evaluate the pitting damaged area. With digital microscope attached via USB interface to a personal computer was created a digital image of the tooth flanks of the gears.

To evaluate the percentage of damaged tooth flanks by pitting was developed software Pitting-Check, which lets you process the digital image. The program contains utilities that to a simple system enable a sampling system to mark areas damaged by pitting. It also takes into account the geometric parameters like the chamfered teeth and alike. The method streamlines the procedure for evaluating the state of damage during the experiment (Bošanský et al. 2006b).

Calculation of percentage of damage to the tooth flanks by pitting determines the ratio of the marked area on the total active surface of the tooth, respectively total area of all tooth flanks. Based on the extent of damage has been determined further action of the experiment, or its completion.

2.3 Results of the Experiment and Their Comparison with Involute Gearing

The experiment was carried at SjF STU in Bratislava on Niemann's stand for HCR gearing and subsequently under the same conditions and load for K–K gearing. Description of creation of pitting shows that in K–K gearing was this type of fatigue damage much less aggressive than in non-standard involute HCR profiles, where initialization of cracks occur at greater depth. At the first loading stage

(level A) at K–K gearing, where $M_k = 265$ Nm, limit state of touch stress occurred at 19×10^6 cycles. Percentage of damage to the tooth flank was evaluated using software Pitting-Check and was 4.04 %. On the lower level of loading on level B, where $M_k = 185$ Nm it occurs at 50×10^6 cycles with damage 3.83 % on the one tooth flank. In the third lowest loading level at $M_k = 125$ Nm damage was 0.4 % at 64×10^6 cycles, when the experiment was terminated.

3 Conclusion

In this paper has been tested convex–concave gearing in terms of creation of pitting. From existing results follows that when it is compared with the HCR gearing the damage in terms of creation of pitting on various levels appeared at much larger number of loading cycles and even at level C ($M_k = 125$ Nm) did not appear, although the gear carried out more than 60 mil. cycles at a given load.

Acknowledgments The research work reported here was made possible by grant projects VEGA 1/0277/12, 1/1035/12.

References

Bošanský M, Vereš M, Gaduš J (2006a) Theory of convex–concave and plane cylindrical gearing. STU Bratislava 180 p. ISBN 80-227-2451-3

Bošanský M, Koša R, Vereš M, Medzihradský A, Nemčeková M (2006b) The possibilities evaluation of damage tooth form to pitting. *Nové trendy v konštruovaní a v tvorbe technickej dokumentácie 2006*. SPU Nitra, Nitra. ISBN 978-80-552-0585-4, s.84-91

Bošanský M, Vereš M, Rusnák J, Tököly P (2009) Design II. STU Bratislava 325 s. ISBN 978-80-227-3510-0

Bošanský M, Vereš M, Tököly P, Vanya A (2012) Non-standard gearing. STU Bratislava 159 s. ISBN 978-80-227-3713-5

Černý M, Filipek J, Mazal P (2010) Pitting damage of gears. Acta Univ. Agric. et Silvic. Mendel. Brun LVIII(2):51–60

Tensile Test of the Car Parts Materials in a Climatic Chamber

R. Kovář and R. Martonka

Abstract Mechanical testing plays an important role in evaluating fundamental properties of engineering materials as well as in developing new materials and in controlling the quality of materials used in design and construction. If a material is to be used as part of an engineering structure that will be subjected to a load, it is important to know that the material is strong enough and rigid enough to withstand the loads that it will experience in service. Three different materials were used for testing. Each one of them was cut from a bumper of another type of vehicle. The test was carried out in climatic chamber. By using the tensile test the properties of these materials were determined at different temperatures.

Keywords Tensile test · Plastics · Car parts

1 Introduction

If a material is to be used as part of an engineering structure that will be subjected to a load, it is important to know that the material is strong enough and rigid enough to withstand the loads that it will experience in service. As a result, engineers have developed a number of experimental techniques for mechanical testing of engineering materials subjected to tension, compression, bending or torsion loading. The most common type of test used to measure the mechanical

R. Kovář (✉)
Technical University of Liberec, Liberec, Czech Republic
e-mail: radovan.kovar@tul.cz

R. Martonka
Department of Design of Machine Elements and Mechanism, Faculty of Mechanical Engineering, Technical University of Liberec, Liberec, Czech Republic
e-mail: rudolf.martonka@tul.cz

L. Ševčík et al. (eds.), *Modern Methods of Construction Design*,
Lecture Notes in Mechanical Engineering, DOI: 10.1007/978-3-319-05203-8_49,

properties of a material is the Tension test. The tension test is widely used to provide basic design information on the strength of materials and is an acceptance test for the specification of materials. The major parameter that describes the stress-strain curve obtained during the tension test is the tensile strength.

2 The Tensile Test

In the test, a specimen suitable for gripping into the jaws of the testing machine type that will be used is prepared. The specimen used is approximately uniform over a gage length (the length within which elongation measurements are done) (Fig. 1).

Tensile specimens are machined from the material to be tested in the desired orientation and according to the standards. The cross section of the specimen is usually round, square or rectangular. For metals, a piece of sufficient thickness can be obtained so that it can be easily machined; a round specimen is commonly used. For sheet and plate stock, a flat specimen is usually employed. The change in the gage length of the sample as pulling proceeds is measured from either the change in actuator position (stroke or overall change in length) or a sensor attached to the sample (called an extensometer). According to the loading type, there are two kinds of tensile testing machines. Firstly, we know screw driven testing machine. Using this machine during the experiment, elongation rate is kept constant. Secondly, there is device called hydraulic testing machine. This machine keeps the loading rate constant. The loading rate can be set depending on the desired time to fracture. A tensile load is applied to the specimen until it fractures. During the test, the load required to make a certain elongation on the material is recorded. Engineering Stress is obtained by dividing the load by the original area of the cross section of the specimen.

$$Stress \rightarrow \sigma = \frac{F}{S} \tag{1}$$

$$Strain \rightarrow e = \frac{\Delta l}{l_0} \tag{2}$$

Elastic Region is placed on the part of the stress-strain curve up to the yielding point. Elastic deformation is recoverable. In the elastic region, stress and strain are related to each other linearly. That is described by Hooke's Law (3):

$$\sigma = E \tag{3}$$

The linearity constant E is called the elastic modulus which is specific for each type of material. Plastic region is placed on the part of the stress-strain diagram after the yielding point. At the yielding point, the plastic deformation starts. Plastic deformation is permanent. At the maximum point of the stress-strain diagram (4), necking starts. Tensile Strength is the maximum stress that the material can support.

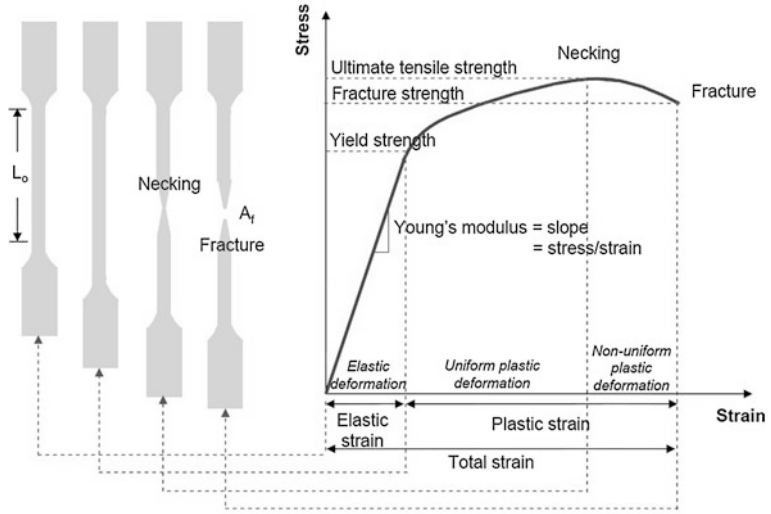

Fig. 1 Process of the tensile test

$$\sigma_{UTS} = \frac{F_{\max}}{S_0} \tag{4}$$

Because the tensile strength is easy to determine and is a quite reproducible property, it is useful for the purposes of specifications and for quality control of a product. Extensive empirical correlations between tensile strength and properties such as hardness and fatigue strength are often quite useful. For brittle materials, the tensile strength is a valid criterion for design. Yield Strength is the stress level at which plastic deformation starts. The beginning of first plastic deformation is called yielding. It is an important parameter in design (CSN EN ISO 527-1,2 (640604) 1997).

3 The Experiment

For the experiment three kinds of material were used. Each material comes from some part of a vehicle. Specifically, it comes from a front bumper. Specimens were not obtained by injection. They were cut from a functional part, so their dimensions were not according the norm. Width of each specimen is 10 mm, but thickness depends on the thickness of the product. Each material is based on polypropylene and contains some specific components. Masterbatch is added to the base plastic to improve its quality. Masterbatch can contain UV stabilizers and anti-burning elements. Additional ingredient to the plastic is talc which increases the dimensional stability of the product. Four tests under different climatic

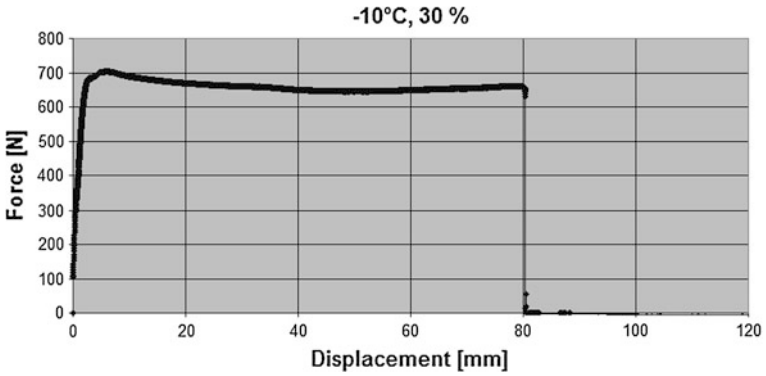

Fig. 2 Sumika D320G02, −10 °C, 30 %

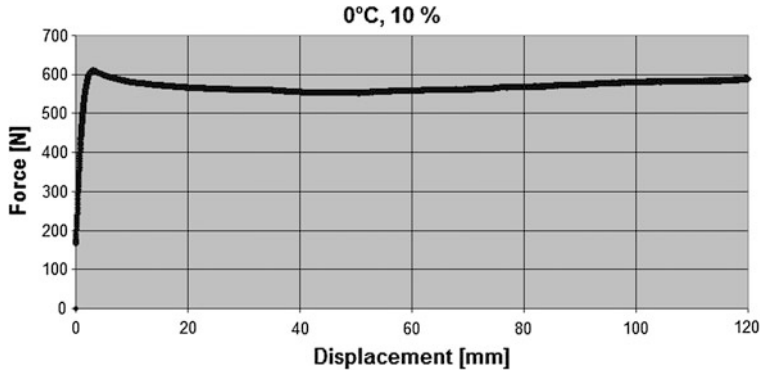

Fig. 3 Sumika D320G02, 0 °C, 10 %

conditions were carried out for each material. Each specimen stays ten minutes in the chamber before the test starts, to have a temperature of his vicinity. The goal was to compare the yield strength in relation to different temperatures. For correct results should deduct the value of 15 N. This value is caused by the passive resistances of moving parts testing machine. In the charts has been computed with this error (Karger-Kocsis 1999).

First tested material is labeled Sumika D320G02. It is made from basic Sumika and 15 % of talc. Initial cross section the test sticks has value 0.000028 m^2. Progress of the tests is shown in the Figs. 2, 3, 4 and 5.

Second material is labeled 20MBTF. The plastic is composed of 87 % of natural Sabic and 13 % of masterbatch. Half of masterbatch consists of talc. So there is 6.5 % of talc in the entire volume. Initial cross section the test sticks has value 0.00003 m^2. Progress of the tests is shown in the Figs. 6, 7, 8, and 9.

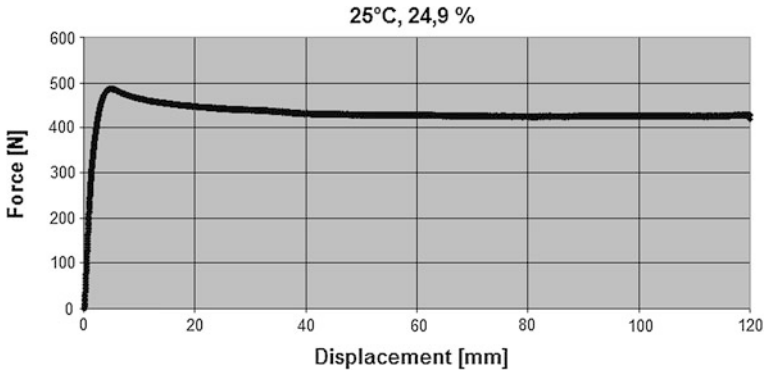

Fig. 4 Sumika D320G02, 25 °C, 24.9 %

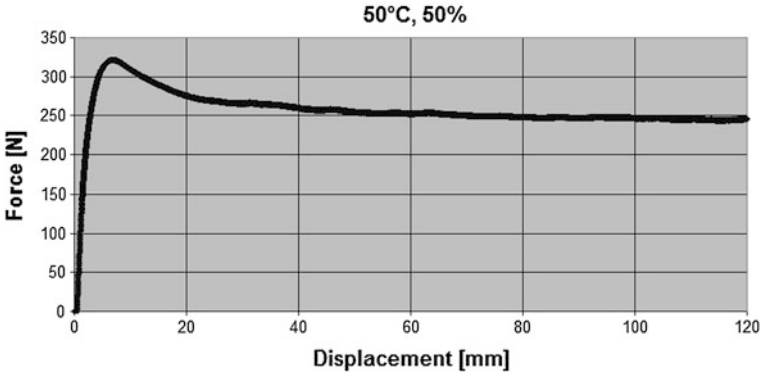

Fig. 5 Sumika D320G02, 50 °C, 50 %

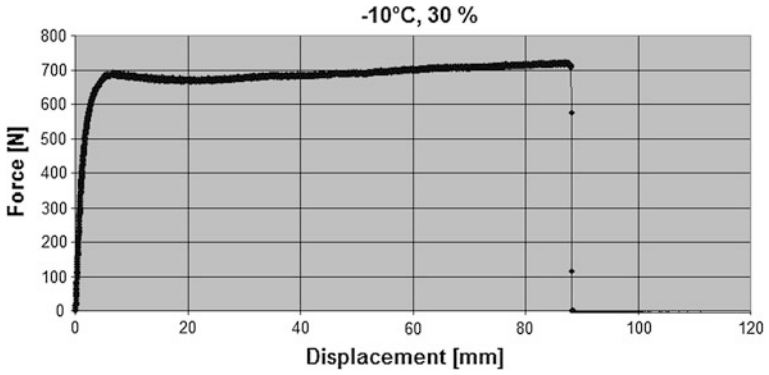

Fig. 6 20MBTF, −10 °C, 30 %

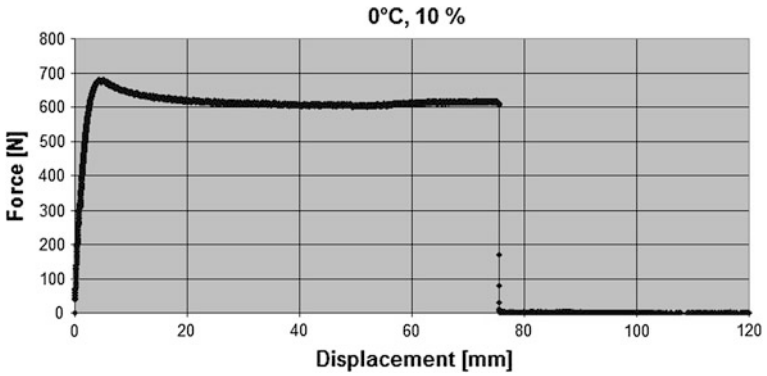

Fig. 7 20MBTF, 0 °C, 10 %

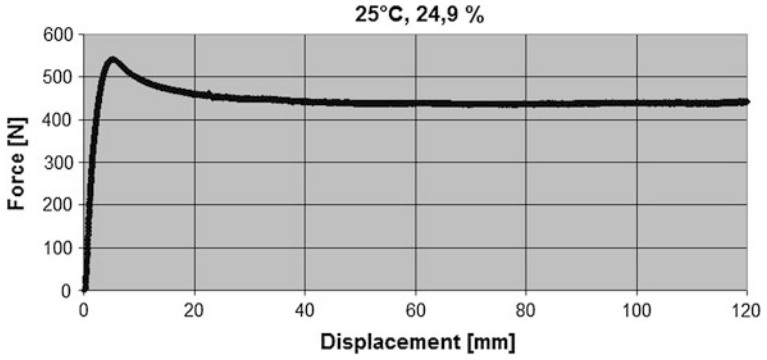

Fig. 8 20MBTF, 25 °C, 24.9 %

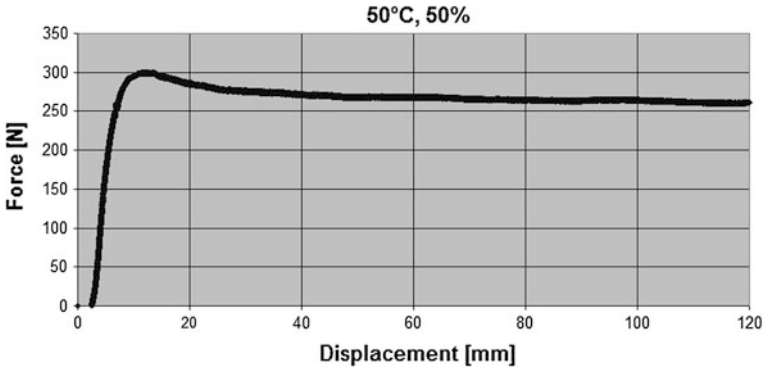

Fig. 9 20MBTF, 50 °C, 50 %

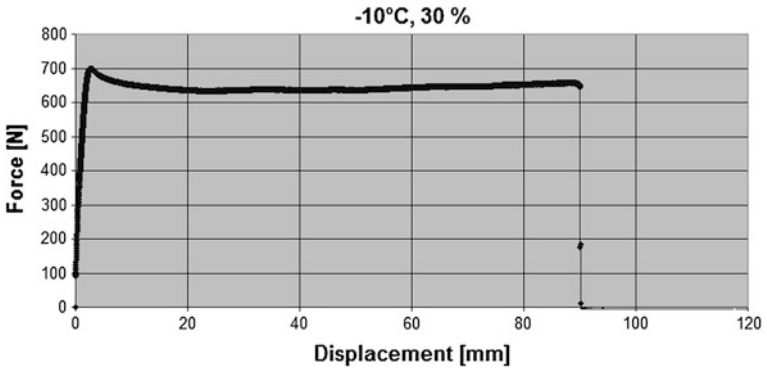

Fig. 10 108MF10, −10 °C, 30 %

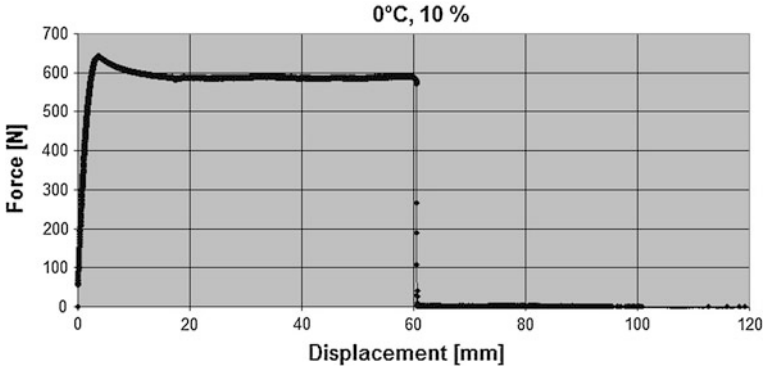

Fig. 11 108MF10, 0 °C, 10 %

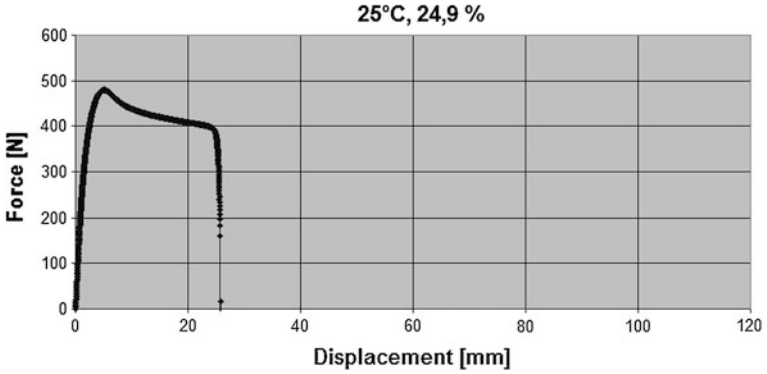

Fig. 12 108MF10, 25 °C, 24.9 %

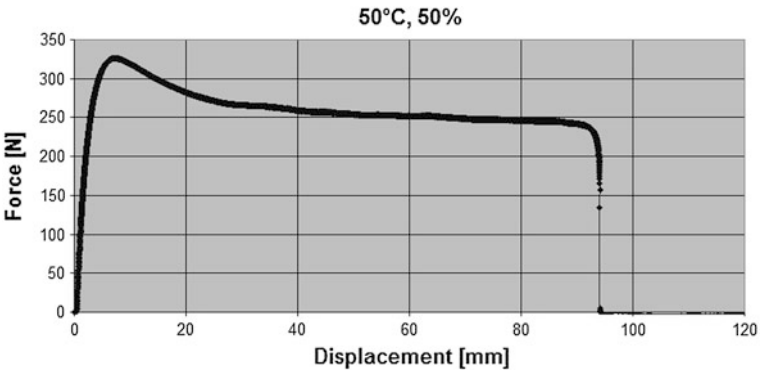

Fig. 13 108MF10, 50 °C, 50 %

Table 1 Values of yield points of tested materials

Values of yield stress (MPa)					Masterbatch	Talc (%)
Temperature (°C)	−10	0	25	50		
Humidity (%)	30	10	24.9	50		
Sumika D320G02	25.11	21.79	17.36	11.46	Yes	15
SABIC-20MBTF	25.80	22.63	18.03	9.97	Yes	6.5
SABIC-108MF10	23.30	21.37	16.00	10.87	No	0

Last material is labeled 108MF10. That is the only natural Sabic plastic without any masterbatch or talc. Initial cross section the test sticks has value 0.00003 m^2. Progress of the tests is shown in the Figs. 10, 11, 12, and 13.

4 Conclusion

During the tests were found progressions tensile tests of different materials at different temperatures. Each material was tested at different temperatures and humidities. An investigation of effect of temperature on the material was conducted and yield point was chosen as a measure. The value of yield point was calculated from position values of jaws and measured power which was developed at the tear specimen. From the graphs we can read that the temperature has an effect on value of yield point. The higher is the temperature, the more elastic the material becomes. We need lower force and greater distance to tear the specimen. At lower temperatures the value of yield point is the highest. Effect of ingredients is apparent. The material without any ingredients has the lowest value of yield point. Moreover, there was a break during each test independently of the ambient temperature. Therefore, masterbatch and talc improve properties of the basic plastic material and make him more elastic. All values of yield point for all tests are shown in Table 1.

Acknowledgments This work was supported by the Ministry of Education of the Czech Republic within the SGS project no. 28011 on the Technical University of Liberec.

References

ČSN EN ISO 527-1,2 (640604) (1997) Plasty—Stanovení tahových vlastností. CNI Praha, Praha, 25 s

Karger-Kocsis J (1999) Polypropylene: an A–Z reference. Kluwer, Dordrecht. ISBN 04-128-0200-7

Experimental Research of Gear Contact Fatigue Strength

P. Maršálek, M. Burián and M. Trochta

Abstract This paper deals with experimental research of gear contact fatigue strength. This research is realized on the universal experimental machine with gear samples from non-alloy stainless steel for through hardened C45. In particular it deals with testing methodology and evaluation method of allowable number in contact (fatigue limit). The results will be compared with equivalent materials presented in the standards dealing with calculation of load capacity of gears.

Keywords Pitting · Failure · Contact fatigue strength · Experiment · Methodology

1 Introduction

The end of technical life gears may be due to many causes, which in itself reflects the kinematic complexity of this type of mechanism. One of the primary failure forms is fatigue failed by pitting. This type of failure is, together with a fatigue fracture of the tooth an integral part of the calculation of load capacity of gears. While the pitting is not as dangerous as fatigue fracture of the tooth, significantly reduces the quality of the gear transmission. The cause fatigue failure of the tooth flank surfaces are mainly sliding friction and contact pressure between the pairs of

P. Maršálek (✉) · M. Burián · M. Trochta
VŠB-Technical University of Ostrava, Ostrava, Czech Republic
e-mail: petr.marsalek@vsb.cz

M. Burián
e-mail: miroslav.burian@vsb.cz

M. Trochta
e-mail: miroslav.trochta@vsb.cz

L. Ševčík et al. (eds.), *Modern Methods of Construction Design*,
Lecture Notes in Mechanical Engineering, DOI: 10.1007/978-3-319-05203-8_50,

meshing teeth. More information about contact fatigue provides such as Glaeser and Shaffer (1996).

For correct control calculation is necessary to know the allowable bending stress number σ_{FE} (MPa) and allowable contact stress number σ_{Hlim} (MPa), which are given in the standards ISO (ČSN EN ISO 6336-5 2005) and ČSN (ČSN 01 4686-5 1988). These values correspond to the reference operating conditions and dimensions of the reference test gears. If operating conditions and dimensions of gears are significantly different from the reference values, can be used the correlation coefficients for the calculation of load capacity. The best solution for getting allowable stress number is experiment. This is necessary especially when it is used for example: small normal module, modification of tooth shape, special heat treatment or unconventional material etc.

2 Test Samples, Testing Machine and Their Conditions

2.1 Test Samples

The specification and processing method of the test samples are described in Table 1. These gear wheels are intended to measure transmission errors and subsequently to the realization fatigue tests. The steel grade is non-alloy stainless for through hardened C45, which corresponds with steel 12 050 according to ČSN standard. All wheels are made only by milling. Quality of the samples was demonstrated by measuring the manufacturing deviations.

2.2 Testing Machine

The universal experimental machine (see Fig. 1) enables testing of the gears either in conformable sense of loading and rotating or in unconformable sense. The testing gear is placed in the testing gearbox on the left branch of the testing circuit. On this gear are carried out fatigue tests. The technology gear is placed in the technology gearbox on the right branch of the testing circuit. This gear is oversized, which ensures its longer service life compared to the testing gear. After the test are exchanged only a samples in the testing gearbox. Dimensions of gearboxes are adjusted for the exchange of transmission ratio in the range: pinion diameter 40–70 mm and wheel diameter up to 100 mm. This universal experimental machine enables testing gear with working centre distance 65 mm. The maximum setting torque is 200 Nm. Maximum revolutions are 3,000 RPM with the possibility of switching to 1,500 RPM. More information about construction of this testing machine published Havlík and Wágner (2007).

Table 1 Specification of the test specimens

Specification	Drive pinion	Driven gear
Basic rank according	DIN 867	
Normal module (mm)	1.25	
Normal pressure angle (deg)	20	
Helix angle (deg)	16	
Number of teeth	35	66
Working centre distance (mm)	65	
Material	C45	
Material quality grade	MQ	
Heat treatment	Through hardened	

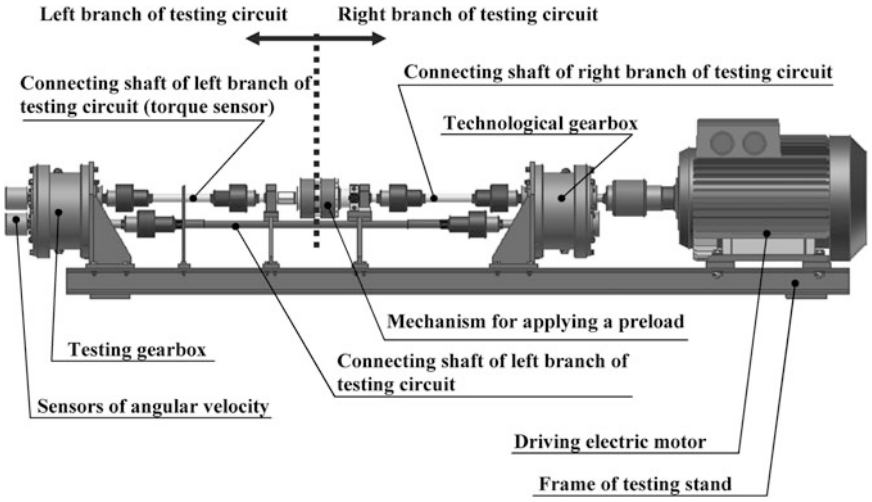

Fig. 1 Universal experimental machine for testing of gear fatigue properties

3 Experiment Methods

For realization of running gear test is in first part necessary to determine a relationship between tangential load F_t and nominal contact stress σ_{H0}, which is defined by the standard ISO (2006) using the equation:

$$\sigma_{H0} = Z_\beta \cdot Z_\varepsilon \cdot Z_E \cdot Z_H \cdot \sqrt{\frac{F_t}{b_w \cdot d_1} \cdot \frac{u+1}{1}}. \quad (1)$$

For the purposes of the experiment the nominal contact stress σ_{H0} corresponds to the pitting stress limit σ_{HG} (result of experiment), because the minimum required safety factor for surface durability s_{Hmin} equals one. If it is needed obtained results compared with the allowable contact stress number σ_{Hlim} must be used Equation:

Table 2 Reference values of limit failed in contact

Description	Equation	Source of reference values	Non-hardened gears (%)	Hardened gears (%)
Total working flank area of gears D_{p+g}	(4)	(ČSN EN ISO 6336-5 2005)	2	0.5
		(CSN 01 1988)		
Working flank area of a single tooth pinion D_{pi} or gear D_{gi}	(5)	(ČSN EN ISO 6336-5 2005)	4	4
		(ČSN 01 4686-5 1988)	8	

$$\sigma_{Hlim} = \frac{\sigma_{HG}}{Z_{NT} \cdot Z_L \cdot Z_V \cdot Z_R \cdot Z_W}. \tag{2}$$

It is necessary to emphasize that the values σ_{Hlim} are chosen for 1 % probability of damage, but the test results usually have 50 % probabilities of damage. The comparison of these values of probability of damage allows the statistical analysis, for example (Rettig and Weiß 1981).

Using the Eqs. (1) and (2) can be obtained a constant of testing gear:

$$\sigma_{Hlim} = \sqrt{F_t} \cdot K_0 \rightarrow K_0 = \frac{Z_\beta \cdot Z_\varepsilon \cdot Z_E \cdot Z_H \cdot \sqrt{\frac{u+1}{b_{wH} \cdot d_1}}}{Z_{NT} \cdot Z_L \cdot Z_V \cdot Z_R \cdot Z_W}, \tag{3}$$

The allowable contact stress number σ_{Hlim} (MPa) is derived from contact pressure that may be sustained for 5 millions stress cycle without the occurrence of progressive pitting. Test gears are deemed to have failed by pitting when the following conditions defined in Table 2. These values can be obtained by approximation of the intermediate results of the test, as shown in Fig. 2.

$$D_{p+g} = \sum_{i=1}^{k=z_1} D_{pi} + \sum_{i=1}^{k=z_2} D_{gi}, \tag{4}$$

$$D_{pi,gi} = \frac{\sum D_{p,g}}{S_{p,g}}, \tag{5}$$

where

$D_{p,\,g}$ is total working flank area of pinion or gear damaged by pitting

$S_{p,\,g}$ is total working flank area of pinion or gear.

Result of Eq. (4) allows correctly choose the number and distribution of load levels for the realization of fatigue tests. For a good approximation, it is appropriate to realize at least seven fatigue tests. From the perspective of saving time and money should start testing at higher loads of timed strength. The resulting curve should correspond to the Fig. 3.

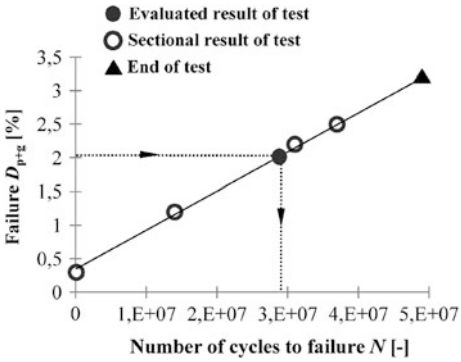

Fig. 2 Approximation of the gear running test result

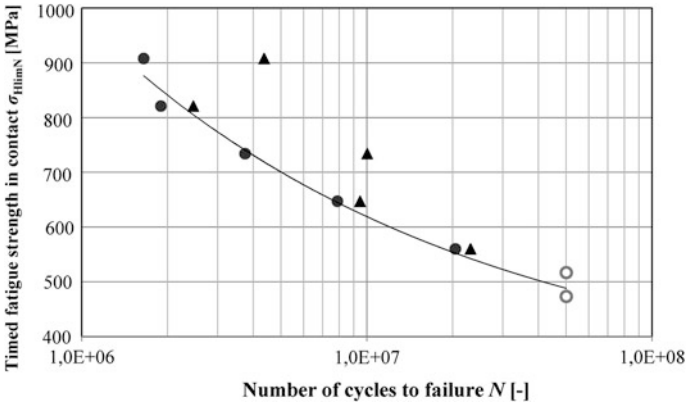

Fig. 3 Theoretical shape of S–N curve from running test for material C45

Each test should be preceded by a run-in gearing in the quarter load. This phase can be terminated when the run-in gear reaches at least 70 % of the working flank area of the teeth. Tests should be carried out under constant load until damage that must be periodically monitored.

4 Conclusions

This paper has briefly presents a way to realize gear running test on the universal experimental machine. The aim of the project is to create a methodology for evaluating gear fatigue behavior of structural materials in contact. Test samples have significantly lower normal module size ($m_n = 1.25$ mm) and also a considerable facewidth ratio $\psi_m \approx 25$. It will therefore be necessary to adjust the

methodology for detection of damage on working flank area of gears (Koša et al. 2007). Obtained results of experiment will be compared to reference values of test samples according to standards ISO (ČSN EN ISO 6336-5 2005) and ČSN (ČSN 01 4686-5 1988).

Acknowledgments This work was supported by Ministry for Education, Youth and Sports, Czech Republic, project—specific university research Nr. SP2013/4 Gear fatigue tests on the universal experimental machines.

References

ČSN 01 4686-5 (1988) Pevnostní výpočet čelních a kuželových ozubených kol—Část 5: Me-ze únavy a údaje o materiálech. Úřad pro normalizaci a měření, Praha, 54 s

ČSN EN ISO 6336-5 (2005) Výpočet únosnosti čelních ozubených kol s přímými a šikmými zuby—Část 5: Údaje o pevnosti a kvalitě materiálů. Úřad pro technickou normalizaci, metrologii a státní zkušebnictví, Praha, 63 s

Glaeser WA, Shaffer SJ (1996) Contact fatigue. In: ASM handbook, vol 19. ASM International, pp. 331-336

Havlík J, Vágner T (2007) Zkušební zařízení automobilových převodů. 48. Medzinárodná konferencia katedier častí strojov a mechanizmov. Zborník príspevkov. Bratislava, s 386–391

ISO 6336-2 (2006) Calculation of load capacity of spur and helical gears. Calculation of surface durability (pitting). International Organization for Standardization, Switzerland, 33 p

Koša R et al (2007) Vyhodnocovanie pittingu na Niemannovom stande modernou digitálnou metódou. 48. Medzinárodná konferencia katedier častí strojov a mechanizmov. Zborník príspevkov. Bratislava. s 441–446

Rettig H, Weiß T (1981) Statistisch belegte Wöhlerlinien der Zahnfußfestigkeit für gebräuchliche Zahnradstähle. Stahl und Eisen, Nr. 6, s 413–416

Test Rig for Packaging Films

J. Mrázek, F. Starý and O. Kult

Abstract The article deals with the measurement of mechanical properties of stretch films. Stretch films are used for packing of goods for transport to transport pallets. The end wrap of film is after the completion of packaging process usually welded or tied. Mechanical properties of films and film endings affect the quality of the whole wrap and ensure transportation safety. When developing new ways of joining film endings it is necessary experimentally verify these new methods. For this reason experimental test rig was developed for measuring mechanical properties of foils and their joints.

Keywords Stretch film · Stretch film welded joint · Stretch film tied joint · Mechanical properties of stretch film · Test rig

1 Introduction

Mechanical properties of the wrapping foil and especially the mechanical properties of foil ending (ending of the last film layer) directly indicate the quality of the packaging process. Poor packing leads to the film release and vibrations during transport are releasing the wrap. When the wrap releases, then layers of goods fall apart and there is possibility of damage. Badly packaged goods cannot be manipulated by handling devices and must be manually transshipment. Such

J. Mrázek (✉) · F. Starý · O. Kult
Faculty of Mechanical Engineering, CTU in Prague, Prague, Czech Republic
e-mail: jiri.mrazek@fs.cvut.cz

F. Starý
e-mail: frantisek.stary@fs.cvut.cz

O. Kult
e-mail: ondrej.kult@fs.cvut.cz

L. Ševčík et al. (eds.), *Modern Methods of Construction Design*,
Lecture Notes in Mechanical Engineering, DOI: 10.1007/978-3-319-05203-8_51,

events afterwards delays and with this makes transportation of goods more expensive.

In the market with packaging material (films) is a wide range of types and materials of films. Ending weld or knot has all packaging equipment essentially unique and may vary by device manufacturers. In assessing the mechanical properties of packaging films is necessary always access to film with its joint. It is their joint of thin film, which is the crack initiator.

There was designed and manufacture an experimental device for measuring of mechanical properties of stretch films in CVUT (Starý and Mrázek 2012).

2 Methodology of Measurement

Methods of stretch foil measuring differ according to demanded results. Basic is test of ductility, further shear test between layers of film. Separate method is ductile test of joint, where are used principles of both mentioned methods (Fig. 1) (Kult 2013).

3 Ductile Measurement

Preparation of stand for ductile test consists of reeling of film on fixed cylinder with prestretch to achieve normal force between the layer of a film and fixed aluminum cylinder. With increased normal force and the coefficient of friction between the film and the aluminum surface of the cylinder increases the frictional force that prevents film slippage on cylinder. Thus, the cylinder is wrapped 3–5 times depending on the width of the film. Last 2 film layers wrapped around the cylinder are not pre-stretched and it is only controlled the direction of film flow on cylinder. Helical wrap direction would result in unbalanced loading of film and faster destruction of the sample at lower load and thus inaccurate results. The roll of film is unwound to another, driven, cylinder of stand. From the total length of the distance between the cylinders (1,500 mm) is necessary to unwind approximately additional 1–1.5 m of film to repeat the wrapping of film as on fixed cylinder. The sample preparation must be done with disconnected electromotor. Firstly, from the viewpoint of safety during handling on test rig to avoid winding of clothing or body parts in the belt transmission and secondly because of the positioning of cylinder. If the servomotor is under voltage and has set zero speed, it keeps driven cylinder at same position despite external power influences, so it is not possible to rotate with the cylinder and wind the free end of the film up. After wrapping driven cylinder the film is only tighten to the initial position, which means zero slack, however, it does not bring any other preload into the film. Stand with stretch film is now ready for measurement (Fig. 2) (Kamenický 2013; Kříbala 2013).

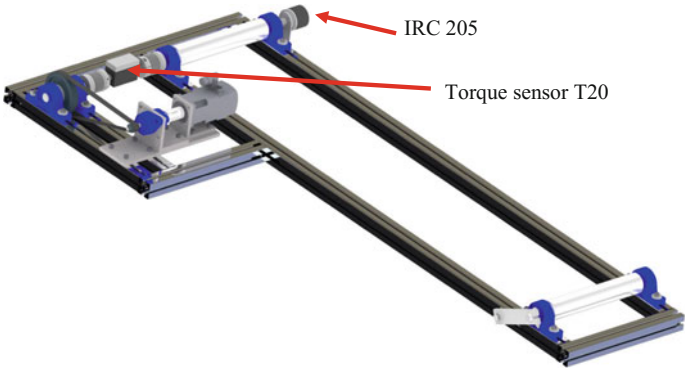

Fig. 1 Test rig

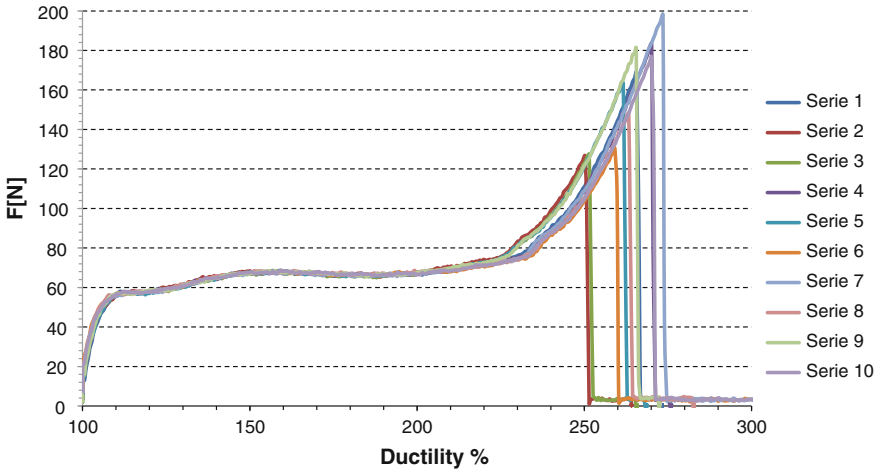

Fig. 2 Recording from ductile measurement

4 Shear Measurement

Shear measurement is prepared almost like ductile measurement, with the difference that the film prepared on a pair of cylinders is disconnected. The fixed cylinder is necessary to wrap the same way as in the case of the ductile measurement to prevent slippage of film and disruption of measured values and the same way has to be wrapped on a second layer of film on the driven cylinder. Film overlap for shear measuring has to be performed at maximal distance of 100 mm away from fixed cylinder. In case that the distance is greater, it is possible that the film overlap is wound on a driven cylinder, and thus values of film contact interruption are not documented. Suitable overlap is 0.5–1 times the width of film

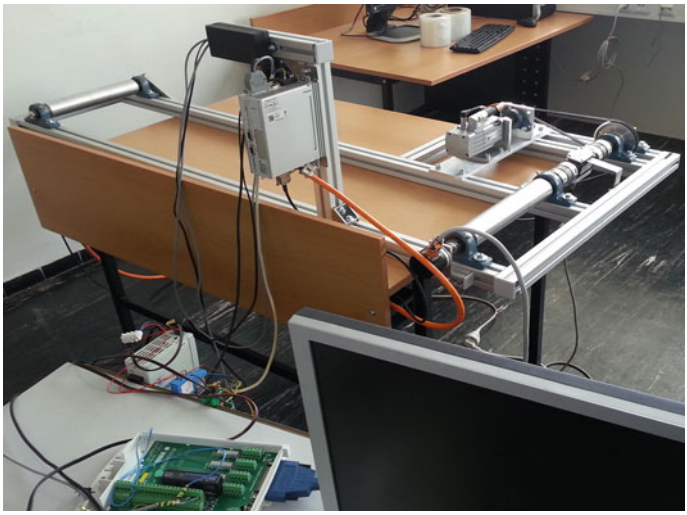

Fig. 3 Test rig

to ensure the "debonding" of contact layers. The film has to be tighten to zero slack without further prestretching and start the measurement.

5 Measurement

The measurements takes place in the case of ductile and shear measurement identically. The control interface of the stand is done in Labview, when after loading the program is necessary to fill the name under which the measurements are interpreted text files with the measured values. After turning on the servo controller is necessary to set the required working speed and switch motor into ready mode. The program stores readings from its start. The servomotor switched on by the starter button. After switching the motor on, it is running at the set speed and the film sample is wound on a driven cylinder. It is sensed torque and angular position of the driven cylinder. Experiment ends with the destruction of the film sample, switching off the motor and shutting down the program (Fig. 3).

6 Results of Joint Measurement

Optimal joint of film ending is that the mechanical properties are very close to the mechanical properties of film itself. Figures 4 and 5 shows that, it is possible to find such joint, which has the very similar behavior of ductility as film itself. Detail about joint and precise technical description is protected and therefore at this point

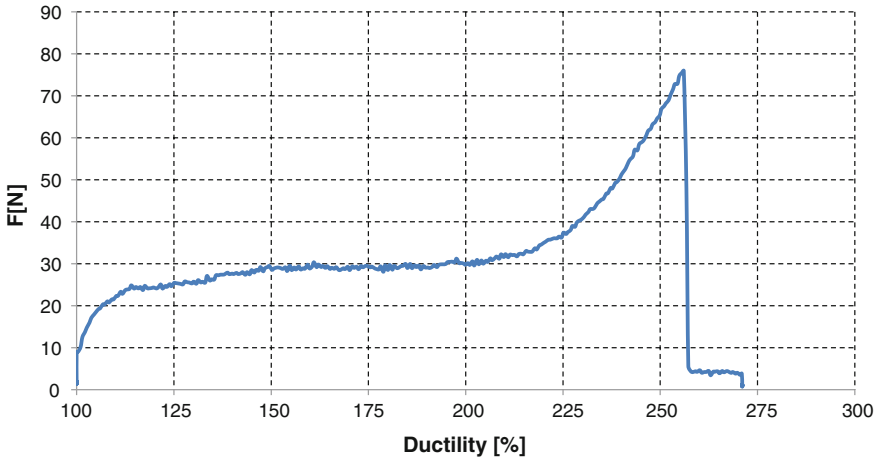

Fig. 4 Film ductility measurement

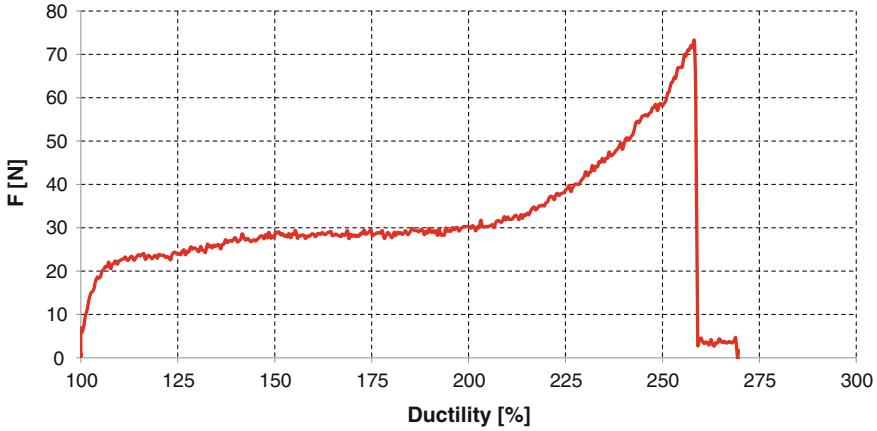

Fig. 5 Joint measurement

it cannot be published. From Figs. 4 and 5 is also visible that film itself as well as film joint can reach required ductility of 200 % and with almost linear constant progress and behavior bellow this value of both charts is almost identical.

7 Conclusions

Test rig for measuring of the mechanical properties of packaging films has been build. On the test rig were tested mechanical properties of commonly used films. On the stand has been tested variety of types and variants film ending joints. Film

joint suitable for commercial use was selected. This selected joint behaves mechanically almost identical to the film without joint. Detail about joint and precise technical description is industrially protected by company Pragometal and has not yet been released to the public until its protection is resolved.

Acknowledgments The research work reported here was made possible by Ministry of Industry and Trade of the Czech Republic grant No. FR-TI3/281. This project runs in cooperation with company Pragometal, s.r.o.

References

Kamenický J (2013) Mathematical and experimental stress analysis of the rotating ring of wrapping machine. In: Student's conference STC 2013. ISBN-978-80-01-05232-7. Available via STC. http://stc.fs.cvut.cz/pdf13/2592.pdf

Kříbala P (2013) FEM analysis of construction parts of wrapping machine. In: Student's conference STC 2013. ISBN-978-80-01-05232-7. Available via STC. http://stc.fs.cvut.cz/pdf13/2591.pdf

Kult O (2013) Virtual prototype welding of stretch foil. In: Student's conference STC 2013. ISBN-978-80-01-05232-7. Available via STC. http://stc.fs.cvut.cz/pdf13/2594.pdf

Starý F, Mrázek J (2012) Design of the wrapping machine with integrated manipulator. In: Proceedings of 53rd international conference of machine design departments, pp 275–280. ISBN 978-80-214-4533-8

Sound Absorption Measurement in Alpha Cabin

P. Němeček

Abstract Sound absorption is a fundamental characteristic of insulating materials which are used to reduce noise in enclosed spaces.

Keywords Acoustic absorption · Alpha cabin

1 Introduction

The issue of reducing noise in enclosed spaces is widely used in construction, industry and construction of motor vehicles. Reduce noise in places where a person must be in contact with the source and problem can't be solved only with soundproof panels, can be especially done with absorbing coating. Absorbent material has the task to transform acoustic energy into another form—especially in the heat. The objective is to minimize energy reflection from walls and other surfaces.

2 Sound Absorption

The basic characteristic of absorbing materials is sound absorption α, takes values from 0 to 1 and is depending on frequency. Absorption equal to one indicates a situation in which all acoustic energy is absorbed. Typical frequency response of sound absorption is shown in Fig. 1. In principle, the course has two parts, the low-frequency, starting at values close to zero and then conduct rises to the maximum

P. Němeček (✉)
Technical University of Liberec, Liberec, Czech Republic
e-mail: pavel.nemecek@tul.cz

L. Ševčík et al. (eds.), *Modern Methods of Construction Design*,
Lecture Notes in Mechanical Engineering, DOI: 10.1007/978-3-319-05203-8_52,

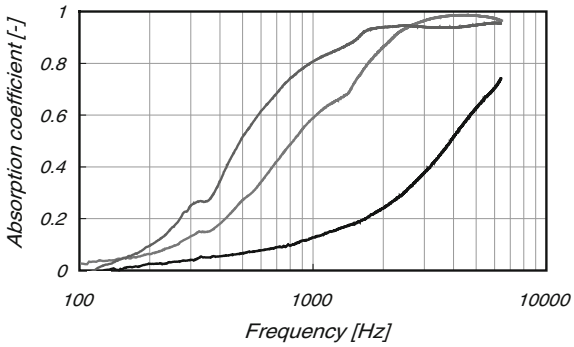

Fig. 1 Typical spectrum of sound absorption

Table 1 The frequency and wavelength of sound waves

f (Hz)	λ (m)	$\lambda/4$ (m)	f (Hz)	λ (m)	$\lambda/4$ (m)
20	17.20	4.30	800	0.4300	0.1075
25	13.76	3.44	1k	0.3440	0.0860
31.5	10.92	2.73	1.25k	0.2752	0.0688
40	8.60	2.15	1.6k	0.2150	0.0538
50	6.88	1.72	2k	0.1720	0.0430
63	5.46	1.37	2.5k	0.1376	0.0344
80	4.30	1.08	3.15k	0.1092	0.0273
100	3.44	0.86	4k	0.0860	0.0215
125	2.75	0.69	5k	0.0688	0.0172
160	2.15	0.54	6.3k	0.0546	0.0137
200	1.72	0.43	8k	0.0430	0.0108
250	1.38	0.34	10k	0.0344	0.0086
315	1.09	0.27	12.5k	0.0275	0.0069
400	0.86	0.22	16k	0.0215	0.0054
500	0.69	0.17	20k	0.0172	0.0043
630	0.55	0.14			

value, which reaches a frequency whose quarter wavelength is equal to the thickness of absorption material. For each third octave within the audible band, width of this material is given in Table 1. Since this frequency, acoustic absorption has been used with maximum efficiency, so it covers the range of sound absorption. In Fig. 1 is obvious that in order to take maximum advantage of the insulating material for absorbing acoustic energy at low frequencies, is required thickness in meters, for high frequencies in centimeters and millimeters. Therefore, it is difficult, often impossible, to absorb sound at frequencies up to 100 Hz (ČSN ISO 10534-1 Akustika; ČSN ISO 10534-2 Akustika).

The maximum absorption is, in addition to thickness of the material, given to the internal structure. If we take into account the most common structure—the fiber and porous materials, the maximum α primarily due to the size of the area

Fig. 2 α-cabin

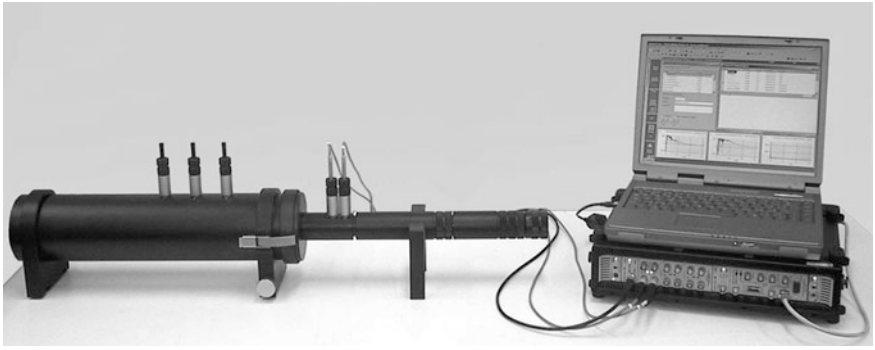

Fig. 3 Impedance tube

which leads to energy conversion, which is given is given by bulk density of fibers and presence or pores. Also important is the presence of air in structure of the material. The air carries the sound energy (kinetic energy of air molecules), which is primarily transformed into heat by the surface friction of fibers and pores.

Designer, which deals with noise reduction, must have available data of the spectrum of operating noise and optimize the supply of suitable absorptive material. The disadvantage is the contradiction between the requirement (noise at low frequencies) and material options (the laws of physics). If these data exist, it is necessary to determine which method was α determined. The problem isn't that the measurement methods works with error or have been radically different. The problem is if the absorption is investigated at vertical or directional impact of

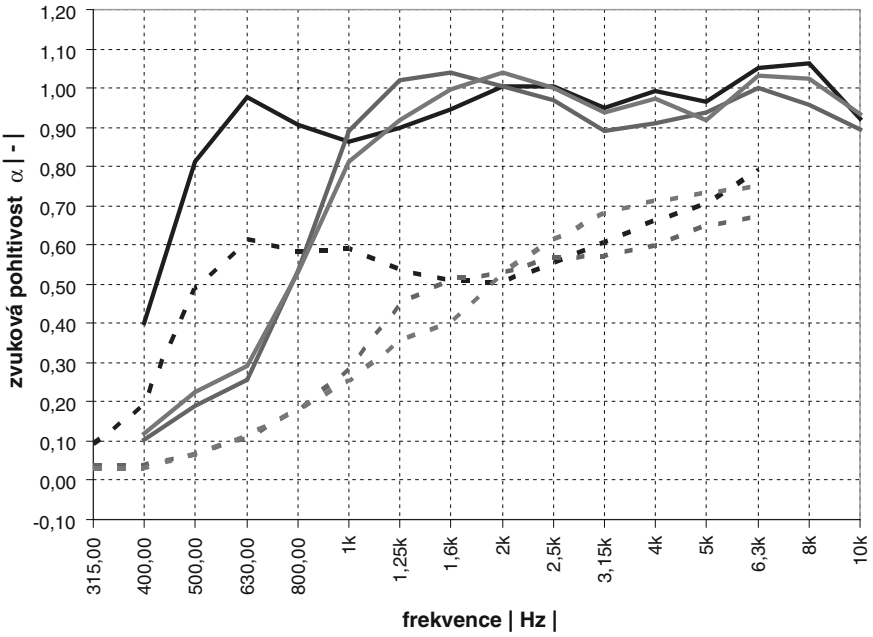

Fig. 4 Results of sound absorption measurement in α-cabin and in impedance tube

sound waves. Perpendicular impact indicates that the maximum acoustic energy is reflected at a distance of $\lambda/4$ from the area in which the absorptive material is applied. The directional impact is statistically probable occurring of maxima of acoustic energy at smaller distances. Perpendicular incidence shows a minimum ability to absorb sound; all-directional impact in this case describes the real situation and is close to practical conditions. It is therefore recommended to monitor results of all-directional impact, but the information from the perpendicular impact is important from the perspective of the minimum possible to provide material and which are therefore always guaranteed.

3 Sound Absorption Measurement

Sound absorption can be measured by these three types of measurement:

- In diffusion field according to standards
- In α-cabin
- In impedance tube.

Measurements in diffuse field are carried out according to ISO 354. It is an international standard when measurements are carried out in a room with a

minimum capacity of 150 m^3 per sample of area from 10 to 12 m^2. The results are valid for the band 100 Hz to 5 kHz at the all- directional impact of sound waves in the sample. It should be noted that this measurement is a fundamental way.

Measurements in α-cabin is almost identical with the measurements according to a standard, the cabin is reduction of normative conditions and is designed for all-directional impact. It is used mainly for measuring the materials for the automotive industry because it requires a sample size of 1.2 m^2. The main advantage in addition to sample size is recognized platform of α-cabin, and also the opportunity to describe components and products (seats, hoods, doors, panels) by absorbent properties. The cabin is shown in Fig. 2.

Impedance tube (Fig. 3) is designed for samples ∅100 mm (7.85×10^{-3} m^2), guarantees a frequency range up to 6.3 kHz, but operates at normal incidence of sound waves. The sample size provides substantial benefit to the creators of absorbing materials.

Figure 4 shows the results of the same absorptive material measurements in α-cabin (solid lines) and the impedance tube (dashed lines). It is obvious that differences in the omnidirectional and normal incidence are substantial and may lead to misinterpretation of erroneous conclusions.

4 Conclusion

When selecting a suitable material for sound absorption, there are 2 options:

1. Select from options and ensure the correct information or
2. Create your own absorptive material and determine its properties by measurements.

If the designer progresses through the development of own material and often use material that is currently available and which is not necessary described, he must either cope intuitively (apply the material and wait for the result), or obtain information by measurement. The sample should represent the real image (with finishes, waterproofing, anchoring elements, etc.). If the designer developing his own material, it is better to use the impedance tube measurements, optimizing the composition and structure of the sample and then measure the resulting solution to all directions (e.g. in α-cabin). Designers must also address the issue of sound proof materials, whose structure is different from the absorbing material. The main feature is the homogeneity, plasticity, high density and lack of air in the material properties thus fundamentally different from absorbing recycled materials. Absorption and sound insulation are properties which are related, but physically unrelated. Composite materials (and sound-absorbing materials) are usually a sandwich structure with separate layers with separate functions.

References

ČSN ISO 10534-1 Akustika—určování činitele zvukové pohltivosti a akustické impedance v impedančních trubicích—část 1: Metoda poměru stojaté vlny
ČSN ISO 10534-2 Akustika—určování činitele zvukové pohltivosti a akustické impedance v impedančních trubicích—část 2: Metoda přenosové funkce
ČSN EN ISO 354 Akustika—měření zvukové pohltivosti v dozvukové místnosti
ČSN ISO 13472-1 Akustika—Měření in situ zvukové pohltivosti povrchu vozovky—část 1: Metoda zvětšené plochy
ČSN EN 1793-1 Zařízení pro snížení hluku silničního provozu—zkušební metody stanovení akustických vlastností—část 1: Určení zvukové pohltivosti laboratorní metodou
ČSN EN 12354-6 Stavební akustika—Výpočet akustických vlastností budov z vlastností stavebních prvků—část 6: Zvuková pohltivost v uzavřených prostorech
ČSN EN ISO 11654 Akustika—absorbéry zvuku používané v budovách—hodnocení zvukové pohltivosti
Smetana C et al (1998) Hluk a vibrace. Sdělovací technika, Praha
http://www.rieter.com/en/general/acoustics-thermal/measurement-systems/alpha-cabin/

Emission Pollutants Measuring with the Help of Two Independent Methods

J. Popelka and P. Brabec

Abstract This paper describes problems of emission pollutants and at the same time comparison of two, on each other independent measuring technologies, is done. The data are obtained with the help of common analyzers and modern analyzers which uses infrared radiation. The author describes the line for a sample taking and the measuring equipment, which can substantially influence the measuring results due to its construction. The great importance is concentrated on evaluation of suitability of the particular methods for measuring fast changes in concentration of exhaust gases parts.

Keywords Gas pollutants · FTIR · Chassis dyno

1 Introduction

Nowadays the society is developing very fast and great emphasis is put on means of transport, especially their environmental burden. It is important to focused on so called active, but also passive production of dangerous pollutants. The passive production means production of pollutants during particular half-finished products. They aren't only products used for mounting on a car, but also by production materials, which are used for other production. The active production means particular pollutants production by the means of transport in operation.

The producer efforts in the automotive industry branch to decrease the pollutants production in both active and passive sphere. For this reason it is highly important to deal with measuring of emission or imission pollutants. No evaluation

J. Popelka (✉) · P. Brabec
Technical University of Liberec, Liberec, Czech Republic
e-mail: josef.popelka@tul.cz

P. Brabec
e-mail: pavel.brabec@tul.cz

L. Ševčík et al. (eds.), *Modern Methods of Construction Design*,
Lecture Notes in Mechanical Engineering, DOI: 10.1007/978-3-319-05203-8_53,

of changes, designed to lower concentration of pollutants decisive without measuring. For pollutants measuring it is necessary to know the problems of particular methods and to state, which ones are suitable for the particular measuring.

2 Description of the Test Bed

For experimental work the test bed equipment with the emission chassis dynamometer Freude Consine, was used. The brake is considered as 4 × 2, which means, it is for vehicles with one driving axle. Its capable 100 kW power is transported over wheels on two cylinders with diameter 1,219 mm. The chassis dyno is equipped to be able to simulate the real car operation. It can be done either in stationery regimes- it is driving with constant speed on the plain by on ordered speed level-or nonstationary, which simulate driving inside a town, outside a town and along the highway.

In this case the cyclus Euro Test NEDC 2000 was chosen. It consists of 4 town- and one motorway cycles. In this test controlling the car by the driver is necessary. The test is prepared in this way. The driver has to follow a display and choose speed levels and vehicle speed according to information. The speed has to be ranged in stated tolerance, otherwise the test isn't valid. Driving resistance and fan power which simulates air flowing according to driving speed is changed by brake manipulating (Figs. 1, 2, 3).

A personal car Škoda Yeti 4 × 4, equipped with an inflammable engine with volume 2,000 cm^3, power 103 kW, torque 320 Nm, was used for measuring. The car has a mechanic gear with 6 speed levels and technique for all-wheel drive. In this case the rear axle was deactivated by switching off the Haldex clutch. Whale base is 2,578 mm and air resistance coefficient Cx is 0.37.

3 Description of Measuring Device

3.1 Infrared Spectroscope FTIR

Infrared spectroscopy belongs to the group of non-destructive methods, which don't influence the exanimate sample while it is analyzed. However, this method provides rather exact information about composition of the particular sample. The method is based on measuring vibrations of individual elements, which are directly dependent on strength of chemical coupling and molecular geometry. For this reason infrared spectroscopy thought to be an excellent experimental technique. During research of chemical qualities a very important role has qualitative and quantitative analysis of investigated samples (Popelka 2013).

This device is equipped with a source of polychromatic radiation. From there the light ray enters the modified Michelson interferometer. Together with this radiation

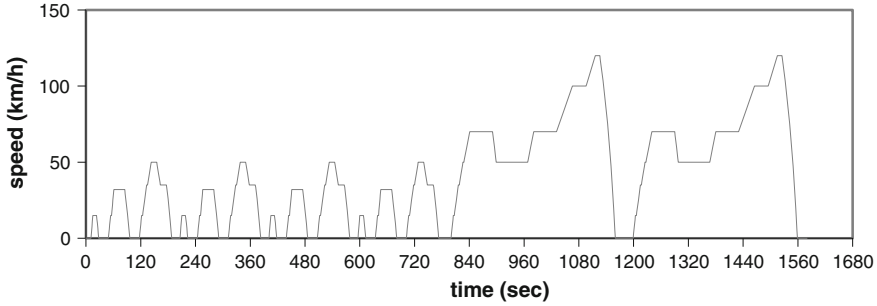

Fig. 1 Speed dependence on the time for the European test NEDC

Fig. 2 View of a vehicle installed on the chassis dyno

Fig. 3 Mobile infrared spectrometer Antaris IGS

a laser beam comes to the interferometer. Its task is to find out the exact position of the moving mirror. Interfering radiation goes though the mirror set in a cell, where is a sample of investigated gas and afterwards it descends on the radiation detector. Signal from the detector is recorded, based on the radiation path difference, in the interferogram. The path difference of the mirror is exactly defined by the He- Ne laser. Interferogram is consequently after adjustment transferred by the computer to the spectrum which we can work in a software way with.

The main task of the infrared spectrometer is to detect infrared spectrum of the sample, its dependence of infrared radiation intensity on the wave length. At present there isn't any infrared spectrometer which would detect wave lengths in the particular range and at the same time also the intensity of the radiation for individual wave lengths are detected gradually. However, this method is very exacting and disadvantageous from time, energy and technical point of view. FTIR spectrometer solves this problem just in more spheres. FTIR modulates wave lengths from infrared sphere to the sound frequency sphere. In this sphere detectors are able to record wave length and intensity at the same time.

3.2 The Set of Emission Pollutants Common Analyzers

The set of analyzers is completed in the way, which allows to evaluate particular components from the taken sample. The parts of the measuring tower are analyzers, which are designed for each component separately. In the other words, the taken sample must go through each of the analyzers.

For unburned carbohydrates measuring the flame—ionizing FIDE 2,000—Amluk is used. For nitride oxides (NO_x) the chemo luminescence analyzers CLA—Horiba is used. For CO part the analyzers VIA 510—Horiba and for CO_2 part the analyzer URAS—Horiba are used. The function of each of these analyzers is generally known, that's why I'm going to mention it here in details.

The measuring line is designed for a taken sample, which has to go both through the spectrometer and the Horiba analyzers. The sample is taken with a test probe from the car exhaust, it goes through a heated filter, then it is led into the spectroscope FTIR through a heated pipe and finally it enters into Horiba analyzers. For comparing of the results it was necessary to connect analyzers and the spectrometer in series. By parallel connection the objectivity of measuring can't be granted. The spectrometer FTIR has always to be place in the measuring route on the first position, because it is an undestructive method and for this reason it doesn't influence the exanimate sample. This fact can't be said about common analyzers (Fig. 4).

4 Results

See Figs. 5, 6, 7.

Fig. 4 The set of emission pollutants common analyzers

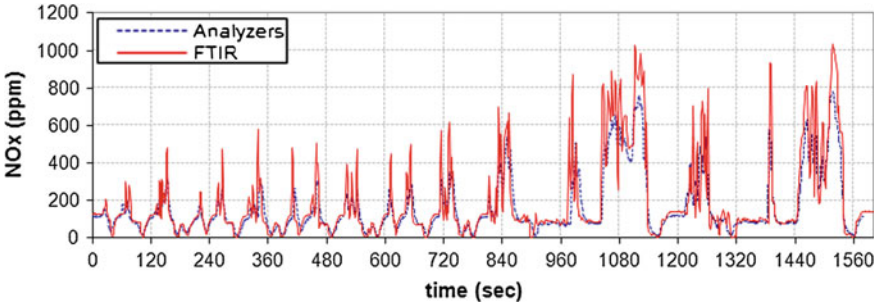

Fig. 5 Comparison of mixture nitrogen oxides courses

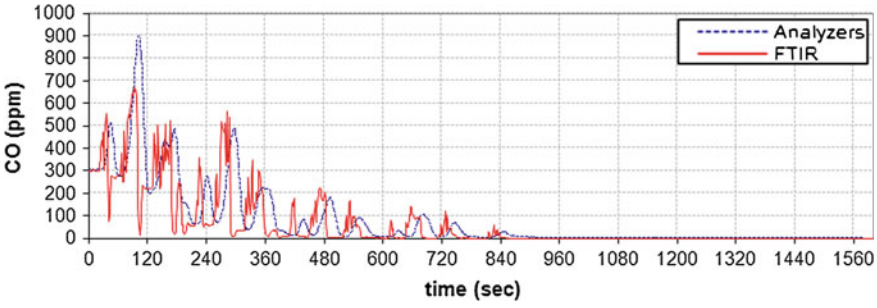

Fig. 6 Comparison of carbon oxide courses

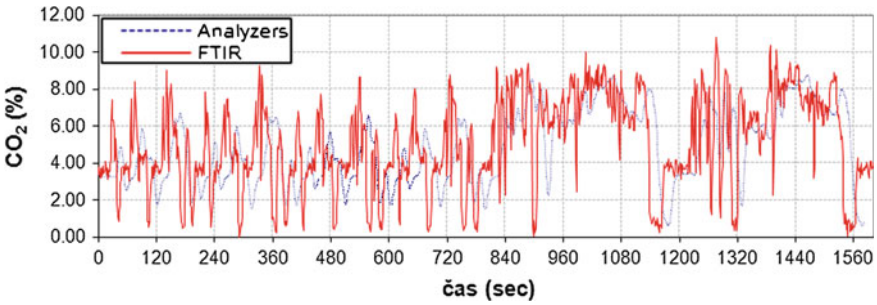

Fig. 7 Comparison of carbon dioxide course

5 Conclusions

The aim of measuring described in this article was to verify the suitability of particular methods for evaluation of concentration pollutants in exhaust gases. Based on the data received by measuring it is also possible to judge the measuring resolution ability by contact regimes of the engine.

The infrared analytic method (FTIR spectrometer) was developed to meet requirements, which are necessary for the most demanding applications for gas analysis. The device is able to evaluate up to hundred of components in an analyzed sample. In case of unburned carbohydrates and NO_x (nitrogen oxides) it detected concentration of particular components. For comparison with standard analyzers it is necessary to adjust the obtained data, because the standard analyzers provide information about components total, they provide the absolute concentration of both parts. In case of nitrogen oxides program environment creates the total sum which gives information about NO_x concentration. In case of unburned carbohydrates it isn't so easy, that's why only basic components CO, CO_2, NO_x are represented.

In both methods a sampling frequency approx 1 s was used. In spite of this fact, it was proved, that there is a considerable delay in registration of concentration changes. It is suitable to use these analyzers for evaluating fast changes without previous consolidating.

Regarding the placement, it is necessary to keep the placement and sequence of analyzers. When we want to be able to compare results received from both methods, the sample which goes through the spectrometer, must go through the analyzers, too. For this reason analyzers have to be in the end of the whole measuring line. The principle, in which they receive information about concentration, influence the consistence of the whole taken sample.

To sum ups, would like to say, that both analytic methods have their advantages and disadvantages. A substantial disadvantage of common analyzers is their slow reaction on concentration changes. The advantage is rather unlimited measuring time. In case of the spectrometer the measuring has to be divided into shorter

sections. The spectrometer evaluates a large amount of components in fast process. So, in case of a long measuring registration the computer technology is overload. The final data set is rather large and this fact causes that following work with the data is more difficult.

Acknowledgments The research reported in this paper was supported in part by the Project OP VaVpI Centre for Nanomaterials, Advanced Technologies and Innovation CZ.1.05/2.1.00/01.0005.

Reference

Popelka J (2013) Measuring of gas pollutants with the help of infrared spectroskopy, IDS 2013, Dubrovnik, Croatia

Mechanical Properties of Polyurethane Foam in Different Climate Conditions

P. Srb and R. Martonka

Abstract A study of mechanical properties of polyurethane foam is important for a comprehensive understanding of the deformation of its structure. It is important for comparison with other materials, because the current development trend of automobile seats tends to find new low-energy and low-density material. A comprehensive assessment of the polyurethane foam is particularly complicated, because polyurethane foam is a non-linear visco-elastic material. Therefore measurements were taken for two types of polyurethane foam in climate chamber in several different climate conditions.

Keywords Automobile seat · Polyurethane foam · Mechanical properties · Climate chamber

1 Introduction

The polyurethane foam is a cellular material with specific mechanical characteristics and with low density (generally around 55 kg/m^3 for seat cushions and mattresses). The polyurethane foam is possible to characterize as a nonlinear visco-elastic material (Petřík and Srb 2012). Assessment of its mechanical properties is very important for evaluating quality of seats and especially their safety. The importance is mainly in considering stress during deformation, which affects the pressure distribution in the contact zone and during interaction of the sample and the load (Petrů and Petřík 2009). This paper describes a static loading of the

P. Srb (✉)
Technical University of Liberec, Liberec, Czech Republic
e-mail: pavel.srb@tul.cz

R. Martonka
Department of Design of Machine Elements and Mechanism, Faculty of Mechanical Engineering, Technical University of Liberec, Liberec, Czech Republic
e-mail: rudolf.martonka@tul.cz

L. Ševčík et al. (eds.), *Modern Methods of Construction Design*,
Lecture Notes in Mechanical Engineering, DOI: 10.1007/978-3-319-05203-8_54,

polyurethane foam samples which was taken on the assembled experimental device inside the climate chamber. Testing was performed under different climate conditions occurring on the Earth where ordinary cars are used.

2 Static Characteristic of the Polyurethane Foam (ISO-2439 2008)

Static characteristics of elastic materials are determined by static tests when the tested sample is exposed to very low speed of deformation. The resulting course of power (stress) and deformation indicates static characteristic.

The graph shows that the polyurethane foam has a highly non-linear process of force on deformation. Loading and unloading curves form hysteresis loop. The area bounded by this hysteresis loop represents a range of damping in the material. While loading the polyurethane foam, the cells inside the material are deformed and they are not able to return in time to their original form before the deformation.

Compressive deflection coefficient, S_f, is given by the equation:

$$S_f = \frac{F_{65}}{F_{25}} \tag{1}$$

where

F_{25} is the force at 25 % indentation in compression, in newtons,
F_{65} is the force at 65 % indentation in compression, in newtons.

The hysteresis loss rate, A_f (%), is given by the equation:

$$A_f = \frac{Area\_0abcd0}{Area\_0abe0} \tag{2}$$

where

Area_0abcd0 is the area contained within the hysteresis curve 0abcd0
Area_0abe0 is the area under the curve 0ab (see Fig. 1).

3 Measurement Method

The measurements were taken in the external box of climate chamber; the size was approx. 1,000 × 1,000 × 500 mm, where various climate conditions could be achieved (temperatures approx. from −70 up to +130 °C, relative humidity approx. from 10 up to 90%). To the external box is connected a hydraulic cylinder

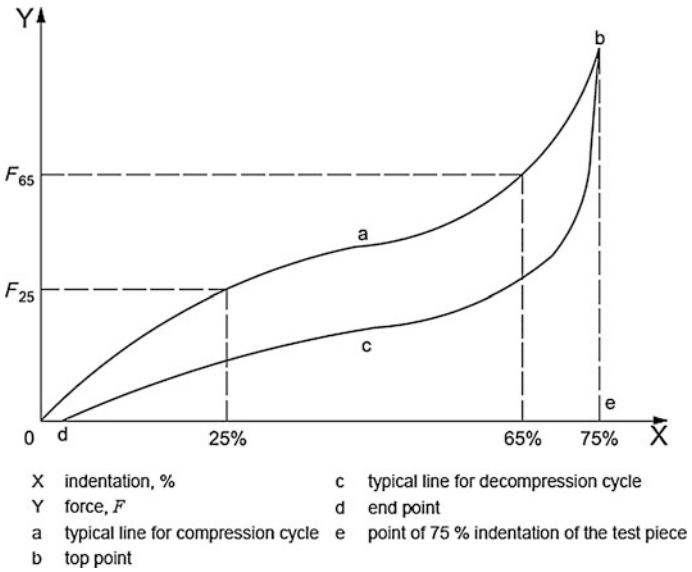

Fig. 1 Typical force-indentation curve (ISO-2439 2008)

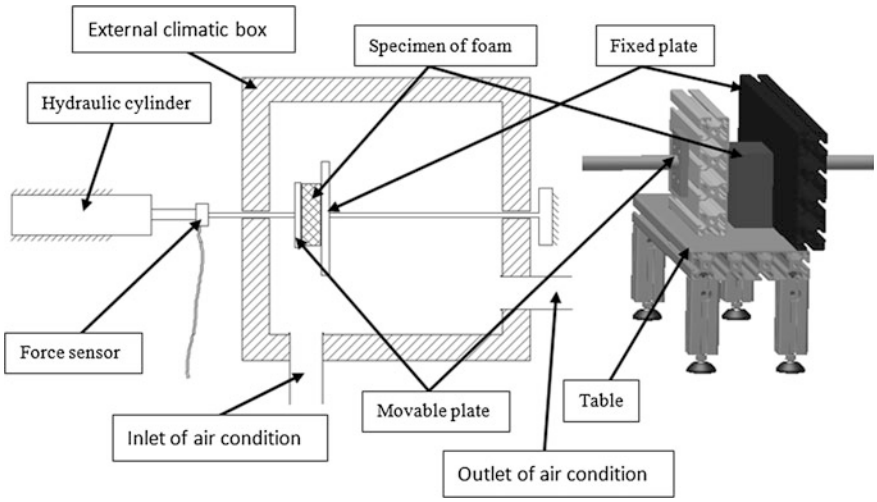

Fig. 2 Measuring device

that enables loading tested items by pressure or tension in the horizontal direction. For testing the foam it was necessary to set up a measuring device consisting of a table, fixed plate and movable pressure plate attached to the hydraulic cylinder see Fig. 2. The hydraulic cylinder is equipped with an integrated position sensor and a force sensor.

Fig. 3 Measured samples

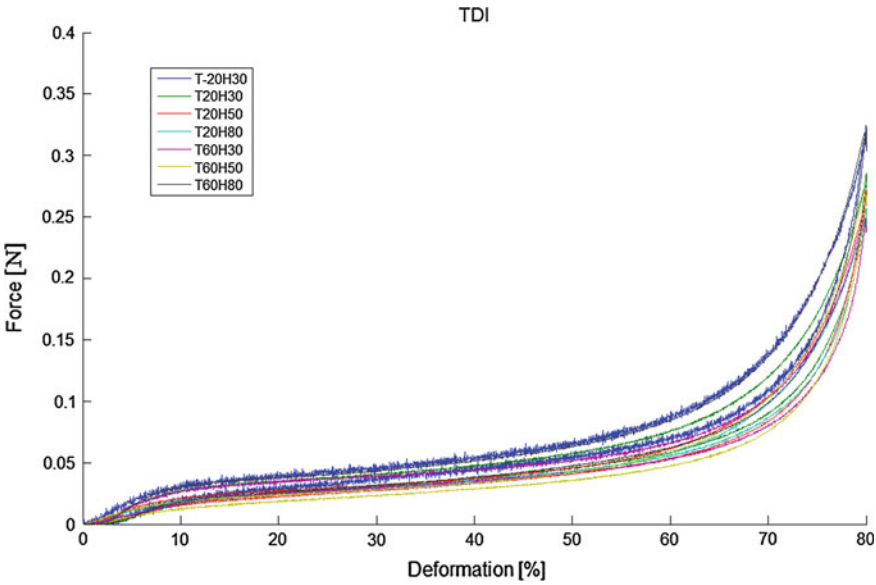

Fig. 4 Results of TDI foam

A sample of the measured foam was placed in the vertical position on the table between the fixed and movable plate. There was used a sample of the polyurethane foam of size 100 × 100 × 50 mm Fig. 2, the speed of pressure was chosen 100 mm/min up to 80 % deformation (40 mm). Four cycles of measuring were conducted, the last one was evaluated. The measurement was performed in seven types of climate conditions. Each sample stayed 15 min in the chamber before the measurement started to stabilise conditions. For the measurements were used two types of polyurethane foams (TDI, MDI). From each type of foam were taken five pieces, the resulting values are the average of five measurements (Fig. 3).

The measurement results are shown in Figs. 4, 5 and Tables 1, 2, where T means temperature and H means relative humidity, e.g. T20H30 means temperature 20 °C and relative humidity 30 %.

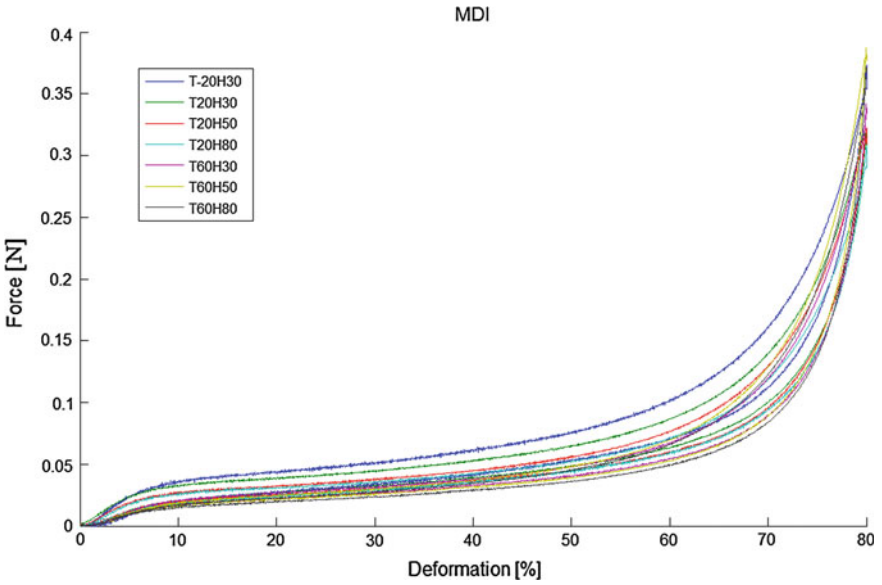

Fig. 5 Results of MDI foam

Table 1 Results of TDI foam

Climate conditions	Maximal force (N)	S_f (–)	A_f (–)
T-20H30	324	2.33	0.19
T20H30	285	2.45	0.23
T20H50	272	2.57	0.15
T20H80	257	2.61	0.06
T60H30	248	2.14	0.21
T60H50	270	2.88	0.21
T60H80	318	2.54	0.25

Table 2 Results of MDI foam

Climate conditions	Maximal force (N)	S_f (–)	A_f (–)
T-20H30	373	2.33	0.28
T20H30	318	2.45	0.26
T20H50	322	2.57	0.21
T20H80	307	2.61	0.17
T60H30	342	2.14	0.18
T60H50	387	2.88	0.21
T60H80	371	2.54	0.22

4 Conclusion

This article described an experimental measurement of the mechanical properties of polyurethane foam samples under different climate conditions. The values of maximum forces were evaluated which showed that at low temperatures the foam is stiffer, at 20 °C maximum force decreases with increasing humidity, at 60 °C maximum force increases with increasing humidity. Another evaluated parameter was compressive deflection coefficient, for optimal seats it should be between 2 and 4, which was achieved under all conditions. Last evaluated parameter was the hysteresis loss rate (damping) where is showed decreasing tendency with increasing humidity at 20 °C and slightly increasing tendency at 60 °C.

Acknowledgments This work was supported by the Ministry of Education of the Czech Republic within the SGS project no. 78001/115 on the Technical University of Liberec.

References

ISO-2439 (2008). Flexible cellular polymeric materials—Determination of hardness (indentation technique), 4. vyd. ISO copyright office, Geneva

Petřík J, Srb P (2012) Simulation of static loading of polyurethane foam. ACC J XVIII(1/2012/Issue A):85–91, Liberec. ISSN 1803-9752

Petrů M, Petřík J (2009) Systems to optimize comfort and developments of car seat. Acta Technica Corviniensis, Bulletin of Engineering, Annals of Faculty Engineering Hunedoara, fascicule 4:55–59. ISSN 1584-2665

Measuring of Torque on Testing Device for Measuring Transmission Error

M. Trochta, M. Burián, P. Maršálek and Z. Folta

Abstract This article is describing measuring of torque on a testing device for measuring transmission error. In introduction is description of device done, followed by a description of measuring device. Sensor is calibrated by two methods, and these methods are compared.

Keywords Torque · Measuring · Strain gauges · Calibration

1 Introduction

The test device for measuring transmission error Fig. 1 is design as close circle testing device. Testing circle is combined from testing gear box, technological gearbox, preload device, torsion shaft, connecting shaft and motor. Device enables testing of the gears either in conformable sense of loading and rotating or in unconformable sense. Maximum of the torque is 200 Nm. Maximum motor speed is 3,000 rpm with the option to switch to 1,500 rpm. Torque measuring device is installed on testing device for measuring torque during test on gears.

M. Trochta (✉) · M. Burián · P. Maršálek
VŠB—Technical University of Ostrava, Ostrava, Czech Republic
e-mail: miroslav.trochta@vsb.cz

M. Burián
e-mail: miroslav.burian@vsb.cz

P. Maršálek
e-mail: petr.marsalek@vsb.cz

Z. Folta
FS, VŠB—Technical University of Ostrava, Ostrava, Czech Republic
e-mail: zdenek.folta@vsb.cz

L. Ševčík et al. (eds.), *Modern Methods of Construction Design*,
Lecture Notes in Mechanical Engineering, DOI: 10.1007/978-3-319-05203-8_55,

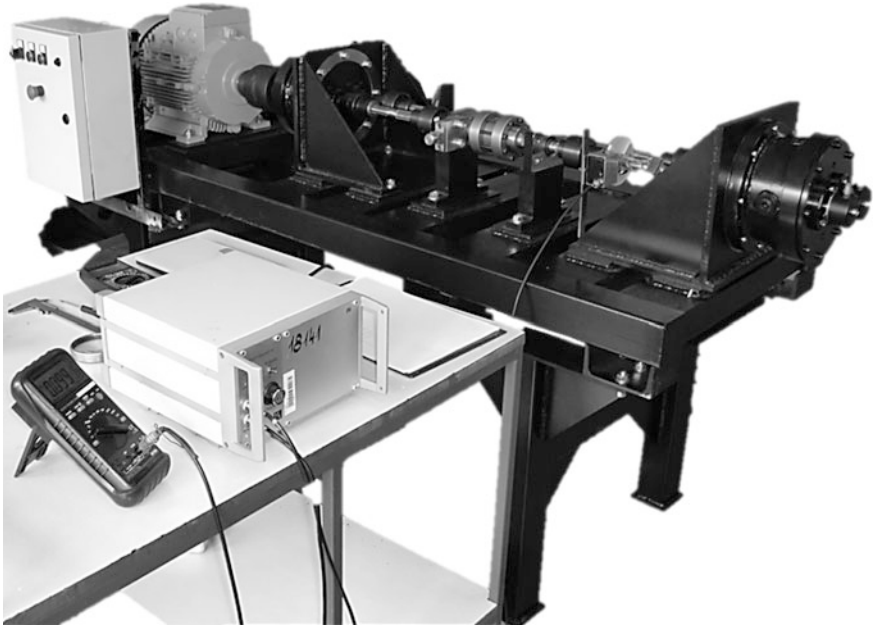

Fig. 1 Testing device for measuring transmission error

2 Torque Measuring Device

Torque is measured by strain gauges located on connecting shaft in the left part of testing close circle device. To measure torque on the opposite sides of shaft were glued two foil strain gauges Fig. 2.

Signal from strain gauges located on rotating shaft is not easy to transfer to measuring unit. To resolve this problem we use noncontact telemetric system from company ESA Messtechnik GmbH, Mnichov. The strain gauges are connected to the module containing the strain gauge amplifier, power supply and transmission block. System of fixed and rotating antennas is providing strain gauge module power and transferring signal from the module to measuring unit.

There are two ways how to calibrate strain gauges, the direct method performed by loading sensor with known load and the indirect method where we simulate the behavior of strain gauge bridge by changing the resistance of one strain gauge.

3 Direct Calibration

Testing device is design for maximum torque load 200 Nm. So calibration torque has to be lesser or equal. Calibration torque was deduced by the direct action of the weight of 9,755 or 5,201 g on the lever arm. Lever was located on the torsion shaft

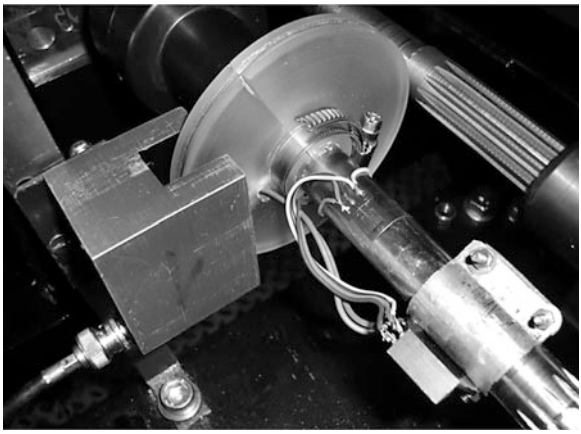

Fig. 2 Torque measuring device

Table 1 Calculated and measured data

Distance from the axis l (mm)	Measured voltage U_m (V)	Torque T (N mm)	Theoretical torque T_t (N mm)	Torque variance δ_T (%)	Theoretical voltage U_t (V)	Voltage variance δ_U (%)
428	2,026	40,958.1	40,408.6	−1.4	1,030	−7.0
435	2,096	41,628.0	41,804.7	0.4	1,120	−6.7
530	2,514	50,719.2	50,141.7	−1.2	2,194	−8.3
538	2,544	51,484.7	50,740.1	−1.5	2,230	−6.4
559	2,645	53,494.4	52,754.5	−1.4	1,213	−7.5
587	2,796	56,173.9	55,766.2	−0.7	1,276	−6.9
609	2,906	58,279.2	57,960.2	−0.6	2,717	−8.1
633	3,095	60,575.9	61,729.8	1.9	2,758	−8.4
…	…	…	…	…	…	…
602	1,534	30,715.1	30,595.6	−0.4	3,245	−4.8
611	1,56	31,174.3	31,114.2	−0.2	1,828	−4.2
669	1,754	34,133.6	34,983.5	2.4	3,526	−6.1

Slope of the regression line $S = 19{,}945$ N mm V^{-1}

on the left side of the test device. Shaft on the right side of the test device was fixed by the pin which is imbedded in the body of the tension device. Measured and calculated data can be seen in Table 1.

Theoretical torque can be calculated as (1):

$$T_t = S \cdot U_n \tag{1}$$

where

S slope of the regression line from calib. graph Fig. 3 $\left(\text{N mm V}^{-1}\right)$

U_n supply voltage bridge (V).

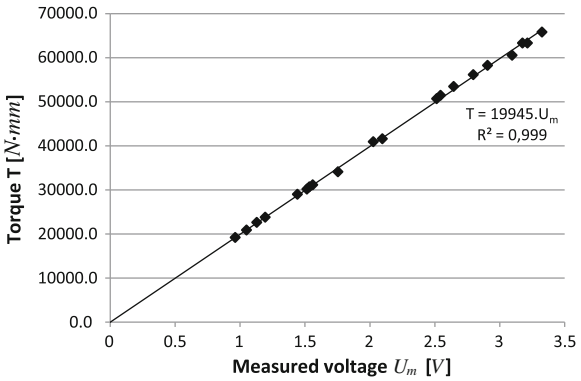

Fig. 3 Calibration graph

Torque variance (2):

$$\delta_T = \frac{T_t - T}{T_t} \cdot 100\,(\%) \tag{2}$$

where
T torque (N mm).

The result of direct calibration is the calibration constant with its variance $K = 19{,}945$ N mm $\mathrm{V}^{-1} \pm 2.4\,\%$.

4 Indirect Calibration

In indirect calibration we simulate the behavior of strain gauge bridge by changing the resistance of one strain gauge. To compare the direct and indirect method we need to recalculate torque to theoretical voltage. The equation describing the relation between torque and theoretical voltage is (Folta 2009) (3):

$$U_t = \frac{2{,}000 \cdot T \cdot k \cdot U_n \cdot n}{\pi \cdot D^3 \cdot G \cdot C}\,(\mathrm{V}) \tag{3}$$

where
U_t theoretical voltage (V)
k strain gauges constant (−)
n number of active strain gauges (−)
D shaft diameter (mm)
G modulus of elasticity in torsion (MPa)
C sensitivity (mV/V).

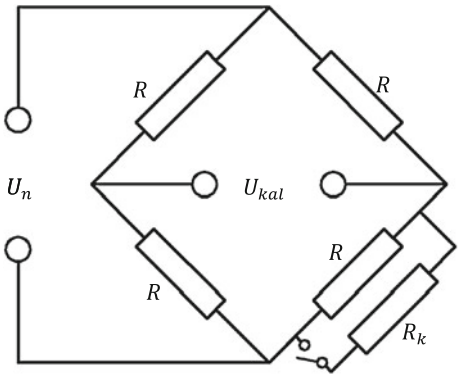

Fig. 4 Wheatstone bridge circle with calibration resistor

Sensitivity (4) can be calculated with use of calibration resistor connected to Wheatstone bridge (Fig. 4) with resistance 100,1 kΩ. Voltage measured when calibration resistor is connected to circuit is calibration voltage U_{kal}. Measuring is done when testing device is not preloaded with torque.

$$C = \frac{-1{,}000 \cdot U_n \cdot R}{4 \cdot U_{kal} \cdot (R + R_k)} = \frac{-1{,}000 \cdot 2,5 \cdot 120}{4 \cdot (-2) \cdot (120 + 100{,}100)} = 0{,}3742 \frac{\text{mV}}{\text{V}} \quad (4)$$

where
R resistance of strain gauges (Ω).

Voltage variance (5) is difference between measured voltage and theoretical voltage which corresponds to the voltage that corresponds to the theoretical deformation recalculated through indirect calibration. The resulting variations can be found in Table 1.

$$\delta_U = \frac{U_t - U}{U_t} \cdot 100\ (\%) \quad (5)$$

where
U measured voltage (N mm).

5 Conclusion

Designed torque sensor was calibrated using two methods direct and indirect method. Calibration constant $K = 19{,}945$ N mm $\text{V}^{-1} \pm 2.4$ % was calculated with use of linear regression by direct method. Between the two methods of calibration was calculated difference 8.4 %.

Acknowledgment This research has been realized using the support of Technological Agency, Czech Republic, program Centers of Competence, project # TE01020020 Josef Božek Competence Centre for Automotive Industry. This support is gratefully acknowledged.

Contribution has been done in connection with project Testing of gears on closed test circuits, reg. no. SP2013/13.

Reference

Folta Z (2009) Odporová tenzometrie. In: VŠB-TU Ostrava (online), (cit. 29 May 2013). Dostupné z: http://www.347.vsb.cz/staff/folta/Technicky_experiment/Tenzometrie_A.pdf

Experimental Testing of Agricultural Trailer

R. Uhlíř, P. Mossóczy and P. Malý

Abstract Article summarizes evaluation in option of operational testing of developed agricultural trailer. Measurement was made to determine operating load of trailer. Experiment was made in static and dynamic mode. Sensors were installed on front hitch and selected components of axle and frame of trailer. Furthermore, this report describes comparison of results of FEM analysis and experimental measurement.

Keywords Gauge · Frame · Towing attachment · Transport device · Hitch

1 Introduction

Developed agricultural trailer serve to transportation of selected agricultural products. It is designed as self-loading transporter and it is independent of the operator. Main mechanical parts of trailer are: steel welded frame, front trailer hitch, hydraulics lifting mechanism and transport holders of cargo (Fig. 1). Effective weight of the trailer is about 4,600 kg.

R. Uhlíř (✉) · P. Mossóczy · P. Malý
Department of Designing and Machine Components, Faculty of Mechanical Engineering, Czech Technical University in Prague, Prague, Czech Republic
e-mail: Roman.Uhlir@fs.cvut.cz

P. Mossóczy
e-mail: Pavel.Mossoczyr@fs.cvut.cz

P. Malý
e-mail: Pavel.Maly@fs.cvut.cz

L. Ševčík et al. (eds.), *Modern Methods of Construction Design*,
Lecture Notes in Mechanical Engineering, DOI: 10.1007/978-3-319-05203-8_56,

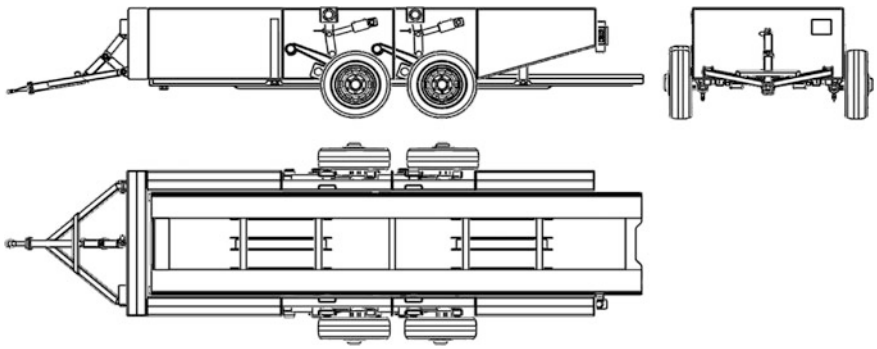

Fig. 1 Developed agricultural self-loading trailer

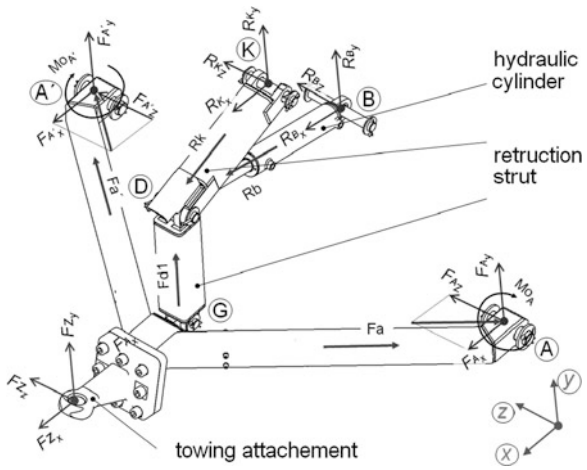

Fig. 2 Action forces and reactions on trailer hitch

2 FEM Analysis

During trailer development some experiments and FEM analyses were performed. The main objects of interests were trailer frame and selected mechanical parts of lifting mechanism. Input values for setting of boundary conditions were captured from experimental measurement. Each part of trailer was described and force acting has been identified. Acting forces and resulting reactions on front trailer hitch are shown in Fig. 2.

Other parts of trailer were described similarly (Fig. 3).

FEM calculations were solved for many settings and for many modes of operation conditions. Selected boundary conditions reflected real conditions which

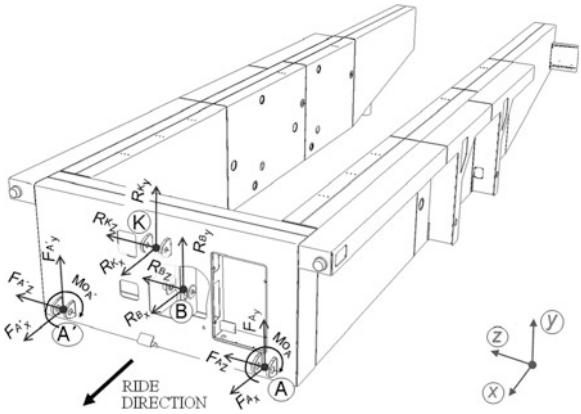

Fig. 3 Action forces and reactions on trailer hitch

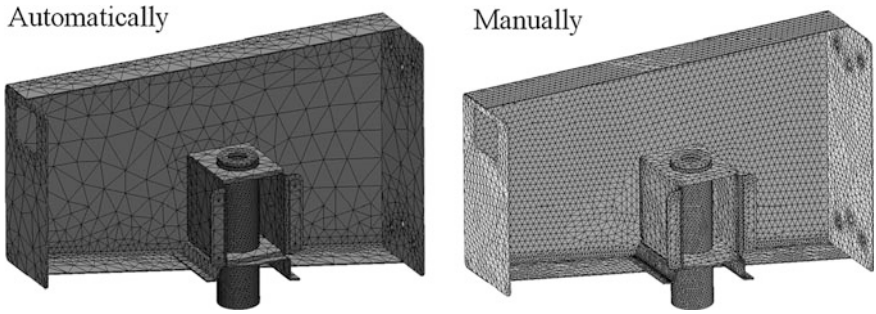

Fig. 4 Types of generated mesh

had been detected during experiment. To achieve relevant results of calculation the precision and quality of mesh has been thoroughly adjusted (Fig. 4).

Automatically generated mesh model consists of 33,804 elements and maximal dimension of elements is set up to 80 mm. Manually generated model structure consists of 94,597 elements with maximal element dimension of 15 mm.

3 The Experiment

Operational tests were planned as static and dynamic. Static tests serve mainly for estimation of first group of operation conditions and for trailer mechanisms behavior. Static tests were performed repeatedly, before and after the completion the dynamic tests. Dynamic tests which simulated specified operational conditions were executed on two different test polygons. The first test polygon contained routes like flat straight road, left and right turns, steep ascent, steep descent and

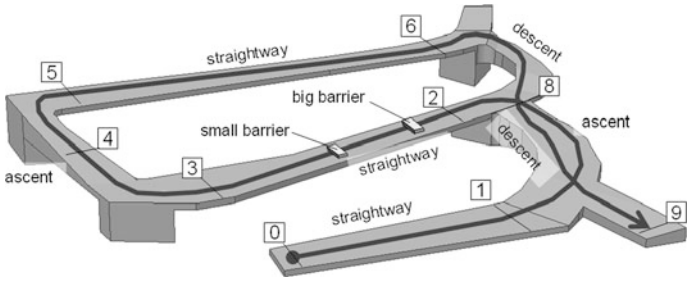

Fig. 5 Description of the first polygon

Fig. 6 Prepared barrier

their combination (Fig. 5). Moreover two different barriers were arranged on this polygon (Fig. 6).

Testing on the second polygon was characterized by more intensive load and by higher speed of trailer with smaller turn radius of polygon. The results of experiment were load characteristic for various types of operational conditions. Areas with maximal and minimal tension were found. The most unfavourable operation condition was identified (Dynybyl et al. 2009).

For overall design of tests and determination of boundary conditions on front hitch the special force sensor has been designed (Fig. 7). Sensor is able to measure in two axes and mounting of sensor is performed between towing attachment and its attachment flange (Uhlíř et al. 2011).

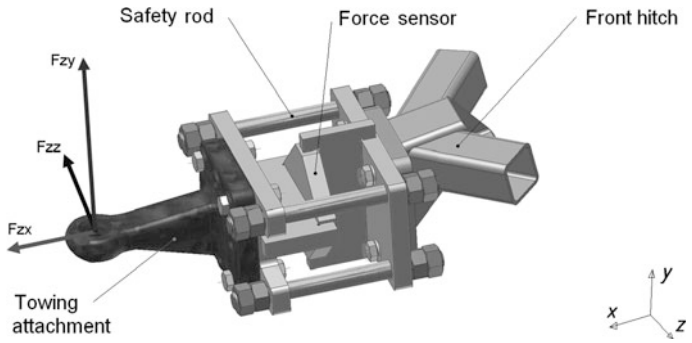

Fig. 7 Force sensor

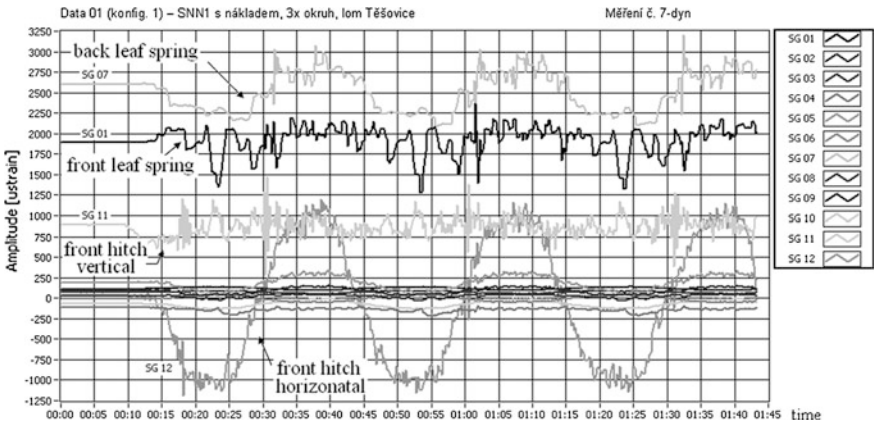

Fig. 8 Evaluation of the part of dynamic tests

Both types of operational tests were performed at the areal of company, which manufactured the trailer prototype. Some evaluation of the part of dynamic tests is shown in Fig. 8. Sinusoidal load of force sensor caused by turning is apparent (Uhlíř et al. 2011).

4 Final Comparison of FEM Analysis and Experimental Measurement

FEM analysis and experimental measurement of selected parts of construction have brought nearly similar results with deviation about 20 %. Comparison between two evaluation software is shown in Fig. 9 and results are shown in Table 1.

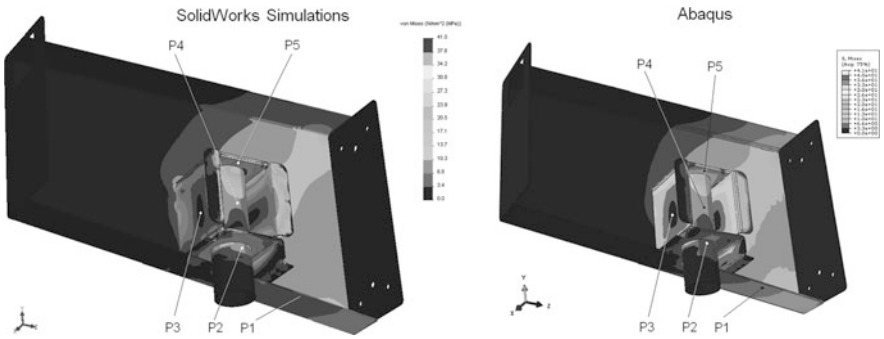

Fig. 9 FEM analysis results

Table 1 FEM analysis results

Software	Mesh quality	Range of tension at defined point (N mm^{-2})				
		P1	P2	P3	P4	P5
SW simulations	Standard	5 ÷ 10	5 ÷ 10	0 ÷ 5	5 ÷ 10	15 ÷ 20
SW simulations	Smooth	6.8 ÷ 10.3	6.8 ÷ 10.3	0 ÷ 3.4	6.8 ÷ 10.3	17.1 ÷ 20.5
Abaqus	Smooth	6.7 ÷ 10.0	3.3 ÷ 6.7	0 ÷ 3.3	6.7 ÷ 10.0	10.0 ÷ 13.3

5 Conclusions

Experimental measurement and FEM analysis have brought large amount of data. Data are described like operation load spectra for different forms of load, working speeds, terrain characteristics, etc. Many types of agricultural trailers and their operation conditions and their loadings are similar like developed type of trailer, and reached results may be applied here. The next goal is to designate the method of service life prediction of those similarly designed trailers.

Acknowledgments This work has been supported by project MPO: FR-TI1/119.

References

Dynybyl V, Češpíro Z, Kanaval J, Mossóczy P (2009) Výkonová metrologie—experimentální podpora vývoje a inovací mechanismů ve strojírenství. ČVUT, Praha. ISBN 978-80-01-04325-7

Uhlíř R, Mossóczy P, Petr K, Malý P (2011) Force sensor for front hitch of agricultural trailer. Int Mech Eng Forum, Prague, 2011, pp 173–178. ISBN 978-80-213-2156-4

Uhlíř R, Mossóczy P, Petr K, Malý P (2011) Provozní zkoušky silového snímače. Zborník 52. K K ČaMS, Ostrava, 2011, pp 291–294. ISBN 978-80-248-2450-5

Climate Chamber for Testing of Uniaxial Loading

D. Vejrych and R. Martonka

Abstract This paper examines the equipment for testing of materials under different climatic conditions with control of humidity environment. The described device allows testing samples for tension and pressure in uniaxial loading. For static testing, samples can be used in a separate climate chamber or in an external climate chamber with a possibility of fixing the samples and additional electronic elements for the transfer of accurate readings to an external computer with an assessing software. In the system, maximum and minimum values are recorded for measurements with a demonstration of the possible outcomes.

Keywords Temperature · Humidity chamber · Tension · Pressure

1 Introduction

In cases where it is necessary to optimize equipment or new material that works in the high temperature range the test equipment DY600C simulating the thermal conditions from the equator to the Arctic is used. Controlled thermal environment brings us new options for testing of materials in uniaxial and multiaxial loading by means of an external chamber. Loading is performed using precise hydraulic cylinders and combination of several tensiometers with computer visualization. The exact parameters and possibilities of the climate chamber and the external climate chamber for multiaxial stress measurements are described in the following section.

D. Vejrych (✉)
Technical University of Liberec, Liberec, Czech Republic
e-mail: David.Vejrych@tul.cz

R. Martonka
Department of Design of Machine Elements and Mechanism, Faculty of Mechanical Engineering, Technical University of Liberec, Liberec, Czech Republic
e-mail: Rudolf.Martonka@tul.cz

L. Ševčík et al. (eds.), *Modern Methods of Construction Design*,
Lecture Notes in Mechanical Engineering, DOI: 10.1007/978-3-319-05203-8_57,

2 Parameters

User capacity of the climate chamber is 559 l with internal dimensions of 850 × 740 × 890 mm and with the temperature range in the main chamber from −75 to +180 °C. This temperature can be hold with minimal temperature deviation of the values ranging from ±0.1 to ±0.3 °C. The process of heating up the chamber progresses in higher speed, 4.5 °C/min, than the process of cooling it which is 4 °C/min. Power consumption of this device is 8.6 kW. To achieve the performance of −70 °C the chamber is equipped with two compressors.

2.1 Parameters of an External Box

User capacity of an external box of the climate chamber is 4,000 l with internal dimensions of 1,168 × 1,797 × 2,021 mm and with the temperature range in the main chamber from −70 to +130 °C. This temperature can be maintained with minimal temperature deviation of the values ranging from ±0.1 to ±0.3 °C. The process of heating up the chamber progresses in higher speed, 3.5 °C/min than the process of cooling it which is 3 °C/min. The lower values at the external box are caused by small heat leakages in the pipes connected to the external box (Angelantoni industrie s.p.a).

3 Construction of Equipment

The test chamber is used as a functional unit consisting of several parts which can be divided into the static chamber that stores samples for testing of heat stress and other parts of the equipment such as a machinery space which is placed at the bottom of the climate chamber and serves as a mechanical space for refrigeration compressors, moistening and drying devices and other functional components for maintaining a desired climate within the test area of the chamber. The last element is the electronic control system for regulating the temperature and humidity based on the output values of an integrated microcomputer, together with a capacitive sensor and a platinum resistance sensor (PT 100), which provides long-term accuracy and durability. Values are regulated on the basis of the input values of defined temperature and humidity that are specified on the graphic display set up in the upper part of the device.

3.1 Static Chamber

The space inside is made of materials highly resistant to corrosion. The chamber is also provided with insulating material with high heat resistance that ensures the

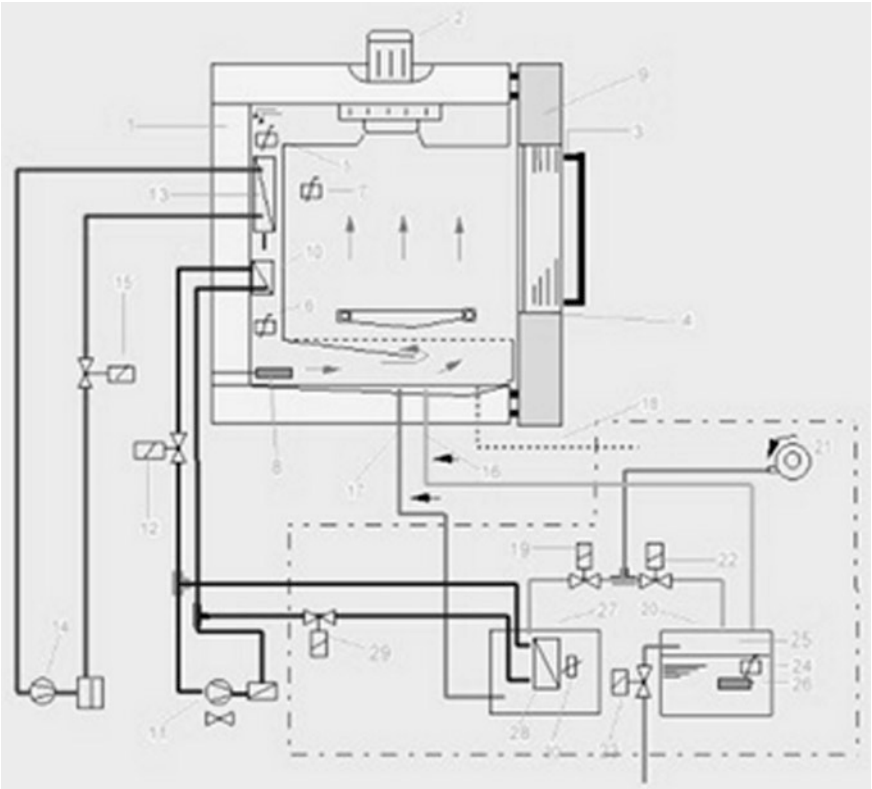

Fig. 1 Scheme of the climate chamber. *1* Isolated box, *2* fan test area, *3* lighting test area, *4* door contact switch for fun, *5* temperature sensor test area, *6* temperature sensor air duct, *7* capacitive sensor, *8* heating, *9* door of test area, *10* heat exchange for climate, *11* refrigerating compressor for climate, *12* magnetic vetil for climate, *13* heat exchanger for thermal regime, *14* refrigeration compressor, *15* magnetic valve circuit cold, *16* supply of moist air, *17* Supply of dry air, *18* offtake for condensate, *19* valve of drying, *20* humidification systém, *21* air turbine, *22* valve of moistening, *23* valve of water, *24* temperature sensor unit, *25* checking the water level, *26* heating unit, *27* dryer, *28* heat exchanger dryers, *29* the valve cold. Circuit for drying, *30* temperature sensor dryer

stability of temperature (1). Entrance door (9) is provided with a window providing an opportunity for observation of samples (in the range of temperature and humidity which allow observation of the sample). For better visibility, the chamber is equipped with a light source that is placed in front. For increasing the temperature, the device is equipped with a heating (8), after its activation the temperature is regulated by the fan (2) according to the output values from of the temperature sensor (5). Humidification unit (20) ensures changes in humidity and is regulated by the temperature sensor unit (24). Cooling system is taken care of by the compressor (14) which includes a dampening valve (22), the drying valve (19) with a necessary drain of accumulated condensate (Fig. 1).

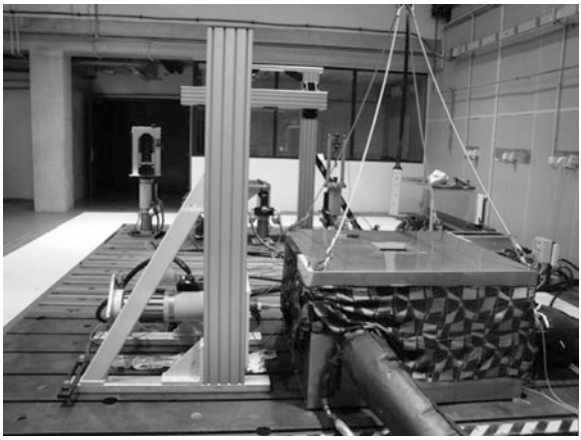

Fig. 2 High strength shoulder

Fig. 3 Hydraulic cylinder AH 25-250

At the thermal chamber it is possible to create a defined temperature and overall climate in the test area which means the defined temperature and the relative humidity range from 10 to 90 % with a highly stable moisture tolerance ±2–3 %. Microprocessor control is combined with a simple intuitive environment using the LCD touch screen. Other advantages include the capability of program controlling the flow of temperature and humidity in relation with time. The construction is provided with three grids in a static test area and lockable door for long-term testing without operator's presence.

3.2 Hydraulic Cylinder AH 25-250 (Inova Praha s.r.o)

The hydraulic cylinder AH 25 (nominal force in kN)–250 (stroke in mm) ensures sufficient force during uniaxial stress testing in an air-conditioned space. The

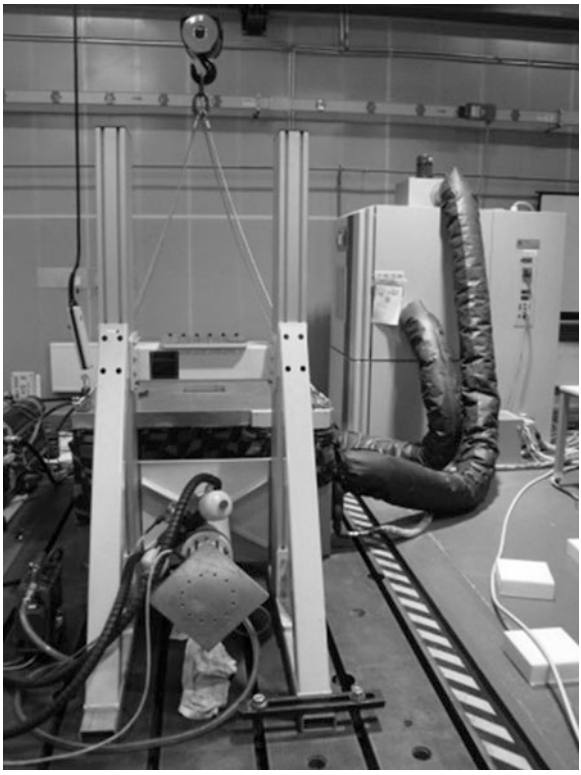

Fig. 4 External box with AH 25-250

maximum loading speed of the hydraulic cylinder is 1 m/s and the minimum movement is 0.05 m/s. The inductive position sensors LVDT (Linear Variable Differential Transformer) and a special sealing method for minimization of friction losses are parts of the piston rod. A modified gasket is provided to reduce friction, it despite create high pressure on the piston and the resultant defective tightness of the system is fixed with collecting groove for exhausting leaked oil by means of through the filter unit OF7 (Fig. 3).

4 External Box

The climate chamber is provided with an external box for testing of mechanical properties of materials. At present, the box is equipped with devices for uniaxial tension and pressure. For the accuracy of measurement it was necessary to put the box on spring panel ensuring a minimal transmission of the environmental influences. A high strength arm, which forms a static part of a support during testing of pressure and tension, is bolted down to the steel plate (Fig. 2). A stainless steel shaft of 20 mm diameter is mounted on the arm, it ends with a thread for clamping

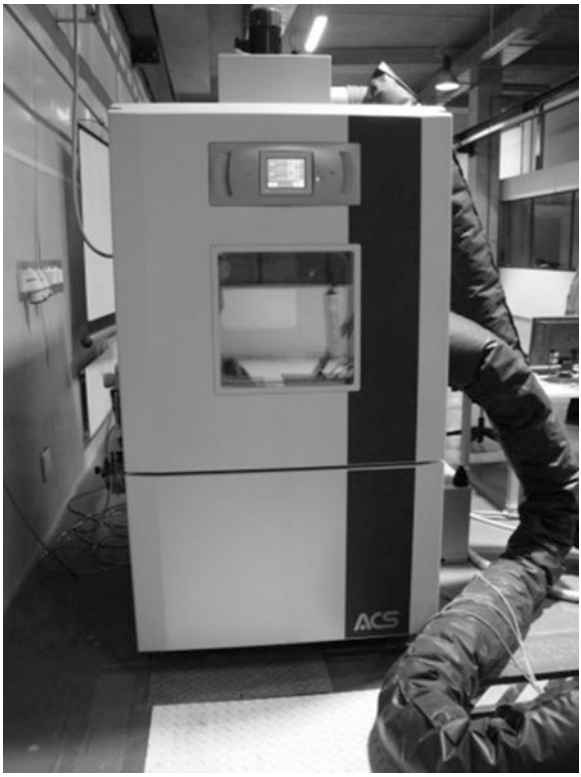

Fig. 5 Climate chamber

to the pressure plate or grab tongs for tensile testing of samples. The other side of the box is equipped with a powerful hydraulic cylinder AH 25-250 (Fig. 3). The hydraulic cylinder, placed in a custom made aluminium frame, is also provided with a threaded shaft with a diameter of 20 mm. The shaft is placed at the end of the hydraulic cylinder. Measurement is ensured by means of several traction potentiometers sending values of the hydraulic cylinders and the potentiometers to the control computer with assessing software (Figs. 4, 5, 6, 7).

4.1 Software Evaluation

The pneumatic cylinder is standardly supplied with evaluation software 1.5 TEST CONTROL enabling the measurement of 8 analogue channels for connection with tensiometer, accelerometer and for measuring position and strength. The laboratory KST is equipped with the most modern measuring devices with Dewetron System containing software for measuring values during pressure and tensile tests Devesat 7.05 allowing connection of up to 36 analogue channels in case of testing

Fig. 6 Evaluation software

Fig. 7 Display with humidity and temperature

of multiaxial loading. This software is used for its easy operating during one-off tests.

Dependence of the time of heating and cooling on time, together with a diagram of dependence of moisture on temperature is shown in Fig. 8 and 9.

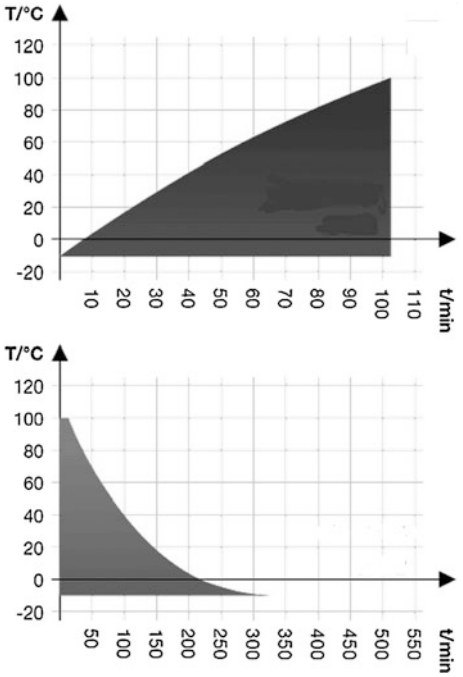

Fig. 8 Dependence of heating and cooling

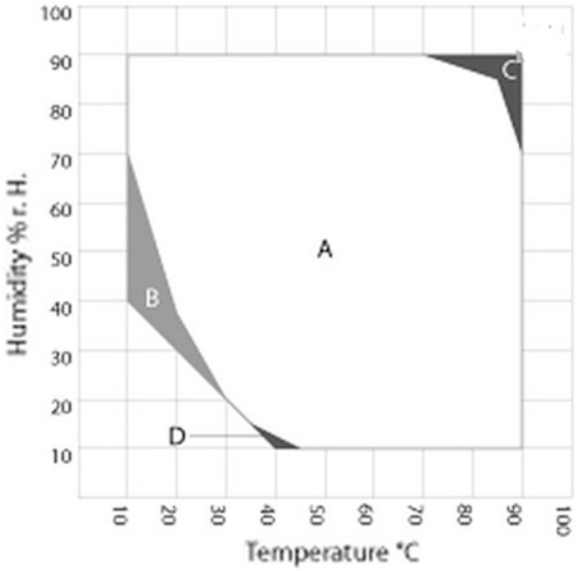

Fig. 9 Temperature diagram of humidity

5 Conclusion

The climate chamber with an external box allows testing of samples at different temperatures ranging from freezing to high temperature with humidity control. In conjunction with the multiaxial loading and series of potentiometers we obtain test equipment for simulation of all year round functioning in a variety of climates. It has wide application; many different items can be tested, from door handles and plastic car body parts to highly stressed interior components exposed to extreme temperatures during summer period. The device also allows long-term durability tests.

Acknowledgments This work was supported by the Ministry of Education of the Czech Republic within the SGS project no. 28011 on the Technical University of Liberec.

References

Inova Praha s.r.o (2013) http://www.inova.cz
Angelantoni industrie s.p.a http://www.angelantonitestechnologies.it

Experimental Verification of Deformation Behavior of Towing Hitch by Optical Measurement Method

A. Zatočilová, D. Koutný, D. Paloušek and J. Brandejs

Abstract The paper deals with verification of stress-strain results of finite element analysis (FEA) of the towing hitch for passenger's car by experimental measurement. For the purpose of experimental measurement a stand, which allows adjustment and monitoring of loading forces of the towing ball in two axes, has been designed. Monitoring of loading forces was performed by strain gauge force transducers and CatmanEasy software. Static deformations were measured by industrial photogrammetric system Tritop. 3D virtual model of towing hitch for FEA was created by reverse engineering using 3D scanner Atos III Triple Scan. The paper presents results of FEA in comparison with the results of photogrammetric measurements performed on an experimental stand.

Keywords Photogrammetry · 3D scanning · Mathematical modeling · Stress-strain analysis · Towing hitch

1 Introduction

Mathematical modeling using finite element method (FEM) is applied in many fields of product development, especially in mechanical engineering (e.g. aerospace, automotive, biomechanics, etc.). Based on FEM analysis it is possible to optimize the design of the proposed product, reduce production time and costs and increase the quality of the existing product (Roylance 2001). Results of these analyzes are always influenced by the degree of simplification of the model. Therefore, in some cases it is necessary to make comparative measurements on the real prototype. In practice, it is possible to measure the deformation behavior by a

A. Zatočilová (✉) · D. Koutný · D. Paloušek · J. Brandejs
Brno University of Technology, Brno, Czech Republic
e-mail: zatocilova.a@fme.vutbr.cz

L. Ševčík et al. (eds.), *Modern Methods of Construction Design*,
Lecture Notes in Mechanical Engineering, DOI: 10.1007/978-3-319-05203-8_58,

strain-gauge, however strain gauge measurements are limited to small local area and does not provide comprehensive information on stress distribution on the overall geometry. To verify the results of stress-strain analysis a measurement systems based on photogrammetry can be used with great benefits.

In the automotive industry a close-range photogrammetry is commonly used to measure the shape of the plastic and metal parts (Boesemann et al. 2000; GOM 2009), to control the geometry and dimensions of complete vehicles (González-Jorge et al. 2012), in cash tests (Xinguang et al. 2009) or to control the limit states of statically or dynamically loaded components. The results of the measurements are then used to modify the manufacturing tools or the processes (see case studies[1]). Photogrammetric off-line systems usually have accuracy of about 0.05 mm (Luhmann 2010).

This article describes the methodology of static deformation measurement of the towing hitch. The measurement was performed by using designed stand with strain gauge force transducers and photogrammetric system Tritop.

2 Approaches to the Analysis of Deformation of Towing Hitch

Two approaches to the analysis of static deformations are shown in the next diagram: (Fig. 1).

Stress-strain behavior was tested on towing hitch WESTFALIA (2007), which is used for towing of trailer or truck at passenger cars Skoda Octavia II or Skoda Superb. The towing hitch WESTFALIA is composed of two main parts—welded frame and hook. The frame is steel weldment consisting of a sheetmetal parts and tubes with rectangular cross-section. The frame is mounted to the car chassis using four screws M10x35. The towing hook is bolted to the two plates by through-bolts M12x80. During ordinary operation, the towing hitch is loaded dynamically. These dynamic effects are caused by braking and acceleration of the vehicle. The manufacturer states two constants determining the maximum load of the towing hitch: S = 100 kg and D = 10.2 kN (WESTFALIA 2007). The S value is the maximum allowed vertical loading of the hook. The D value is the theoretical reference force for the horizontal loading between towing vehicle and trailer. It was used as the basis for horizontal loading during the dynamic tests. In case of static analysis, this value was used as a maximum horizontal loading of the hook (The European Parliament and of the Council 1994) (Fig. 2).

[1] GOM MBH. Application Notes—TRITOP. Available at http://www.gom.com/industries/application-notes-tritop.html

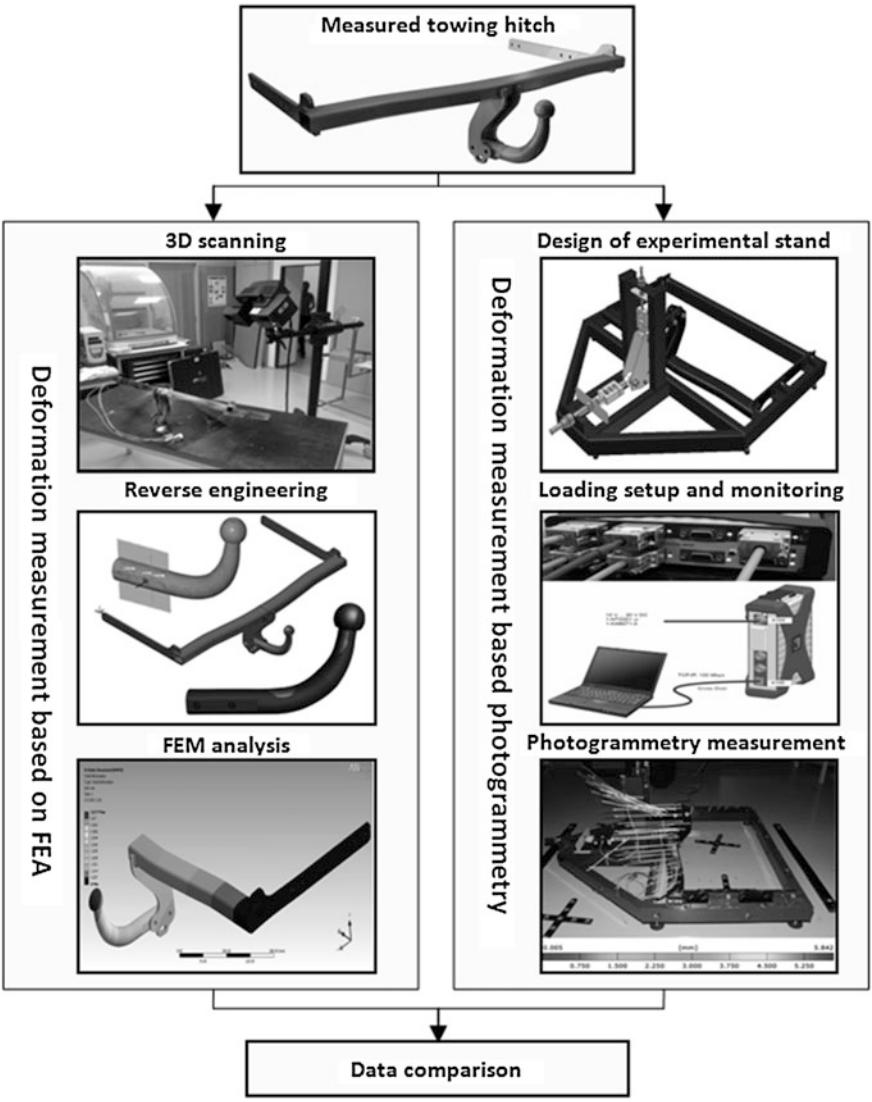

Fig. 1 Approaches to the analysis of deformation of towing hitch

3 Towing Hitch Deformation Analysis

3.1 Reverse Engineering of Towing Hitch

Finite element analysis was performed using module of Autodesk Inventor software. CAD model of the towing hitch for this analysis was firstly demanded from

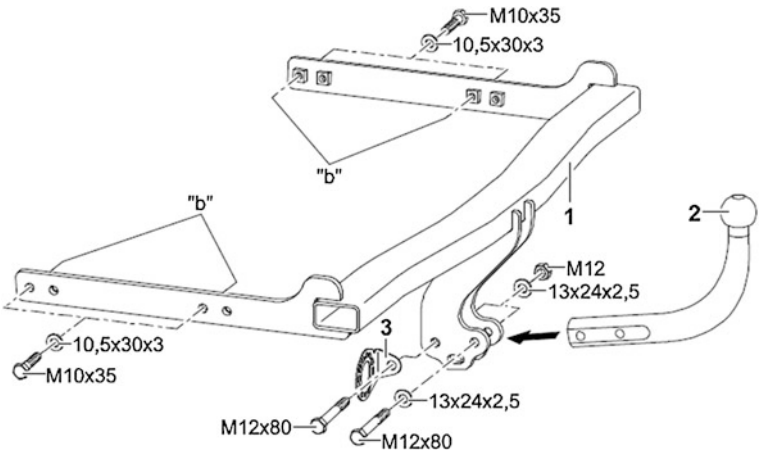

Fig. 2 Towing hitch WESTFALIA A 50-X

the Westfalia company, however the CAD data was not provided. Therefore, the exact copy of the towing hitch's geometry was created by reverse engineering method using 3D Scanner ATOS Triple Scan III.[2] The output is scanned 3D geometry in the form of polygonal mesh (STL format). The towing hitch was scanned using measuring volume 560 × 420 × 420 mm. Resolution over this measurement volume is 0.176 mm. For FE analysis was necessary to modify polygonal data to obtain smooth model without details and holes. The STL model was modified in the ATOS software and used to create geometrically accurate solid model using the Rapidform XOR3 software (Fig. 3).

3.2 FEA

The problem was solved as a contact; the contact was applied between the anchoring plates and the hook. Connection between frame and the hook was modeled as a fixed connection. Volume elements Solid 187 were used for the solution. Table 1 shows the material properties of normal structural steel S235. The solution was performed for the two loading stages—see Table 2 (Figs. 4 and 5).

In order to check the repeatability errors, the entire process of model creation including FEA analysis was repeated 3 times. Deviations of the model of frame from the original STL was in all cases less than ±1.2 mm. The following table shows the results of FEA (Table 3).

[2] ATOS Triple Scan: Revolutionary scanning technique. GOM MBH. GOM: Optical Measurement Techniques. Available at http://www.gom.com/metrology-systems/system-overview/atos-triple-scan.html

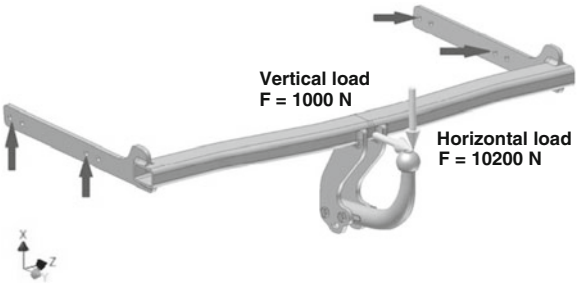

Fig. 3 CAD model with boundary conditions for FEA

Table 1 Material properties for steel S235

Material properties of used structural steel—S235	
Mass density (g/m^3)	7.85
Yield strength (MPa)	207
Tensile strength (MPa)	345
Young's modulus (GPa)	210
Poisson ratio (ul)	0.3

Table 2 Two loading stages of FEA

Used loading forces	Vertical (kN)	Horizontal (kN)
Loading 50 %	0.5	5
Loading 100 %	1	10.2

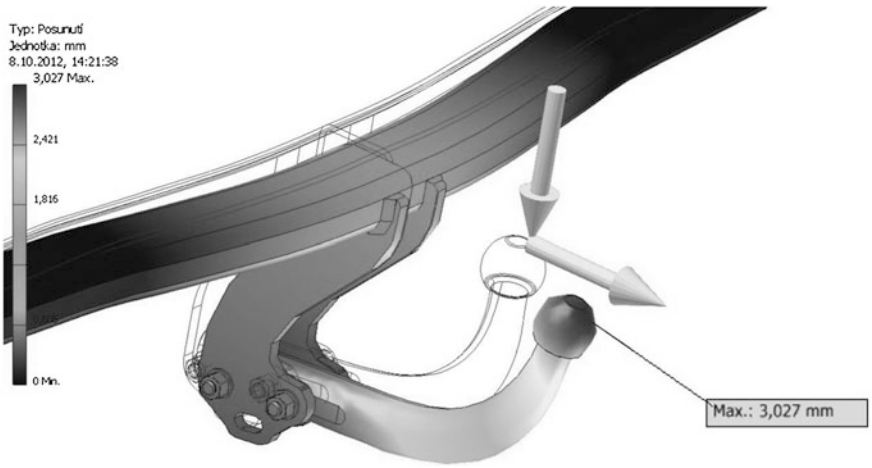

Fig. 4 FEA for 50 % loading force

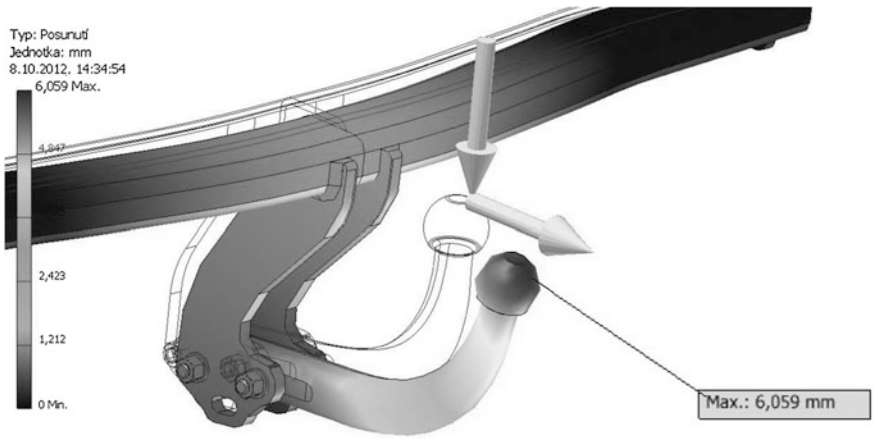

Fig. 5 FEA for 100 % loading force

Table 3 Results of FEA

Loading stage	Deformations (mm)			Max. difference (%)
	Analysis 1	Analysis 2	Analysis 3	
Loading 50 %	2.742	3.027	3.025	9.4
Loading 100 %	5.469	6.059	6.111	10.5

4 Towing Hitch Deformation Measurement

4.1 Design of Experimental Stand

Experimental stand (Fig. 6) consists of three main parts—the towing hitch, the supporting frame and the components used for transfer and measurement of the loading. The entire system is self-contained, and can be placed on any flat surface, any unevenness can be aligned by adjustable legs.

Anchor frame is weldment made from rectangular steel tubes 80 × 40 × 4 of structural steel S235. Brackets for assembly of towing hitch are welded on the frame. Towing ball is clamped between the plates with welded "cups". The cups have an internal conical recess and thus prevent the ball from slipping. The plates are connected around the ball by three bolts M8. To ensure a constant gap between the plates and to prevent their deflection during tightening a spacer tubes are used.

Loading of towing hitch is handled by horizontal and vertical threaded rods. Threaded rods are supported by bracket welded from steel profiles U80. The threaded rod goes through the U80 profile and on the other side is supported by axial ball bearing to reduce frictional torque when tightening the nut. By tightening of the nut the threaded rod is pre-stressed and required loading is induced.

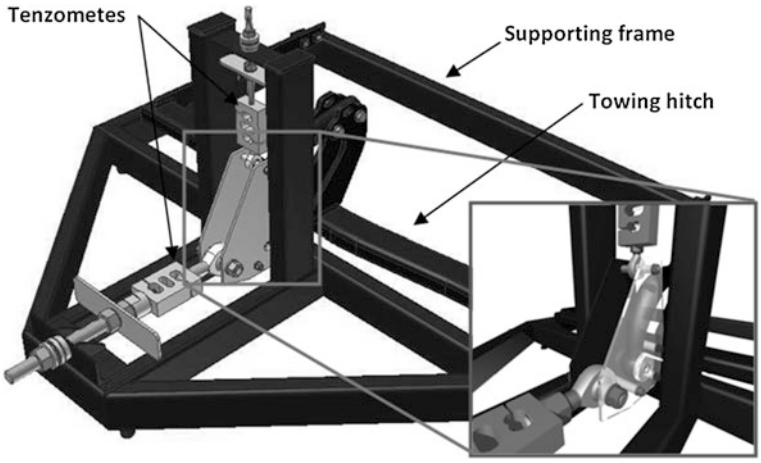

Fig. 6 Experimental stand for deformation measurement of towing hitch

The threaded rods are connected to strain gauge sensors of tensile and compressive force, which allows controlling the actual loading during tightening of the nut on the computer. The Hottinger Baldwin Messtechnik GmbH force sensors are used. For horizontal loading a S9 sensor with maximum allowable force of 20 kN is designed. For vertical loading it is RSCA C3 sensor with a maximum permissible force 2 kN. The signal from the strain gauge force sensors is transmitted through the measuring station QuantumX of HBM, type MX 840 A to a personal computer. Loading parameters are controlled by software CatmanEasy. Figure 7 shows the measurement chain [HBM].

4.2 Photogrammetry Measurement of Towing Hitch on Experimental Stand

Deformations of the towing hitch were measured using photogrammetric system Tritop.[3] Tritop system consists of a camera with flash and Wi-Fi device for immediate transfer of the captured images to a PC. Resolution of used camera (Nikon) was 21 mega pixels. Tritop system also includes special circular markers and two calibrated rods. In case of deformation measurement, a sufficient number of un-coded circular markers must be positioned on the measured object and to the surrounding area (e.g. on the floor), which will be static during the loading. To the

[3] TRITOP—Optical 3D Coordinate measuring machine. GOM MBH. GOM: optical measurement techniques. Available at http://www.gom.com/metrology-systems/large-scale-cmm.html

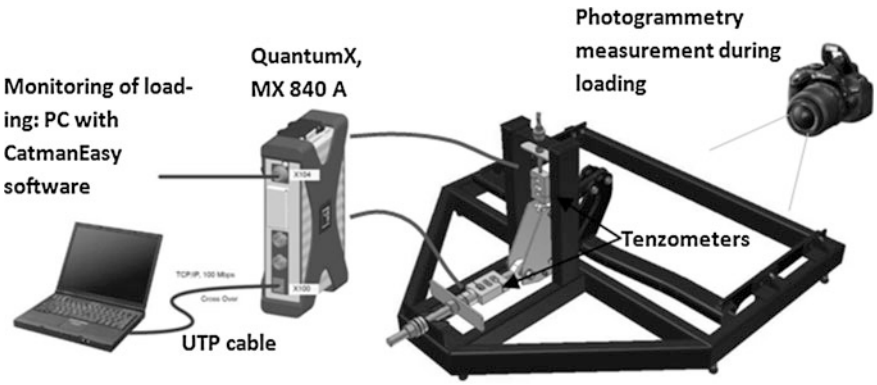

Fig. 7 Devices for deformation measurement

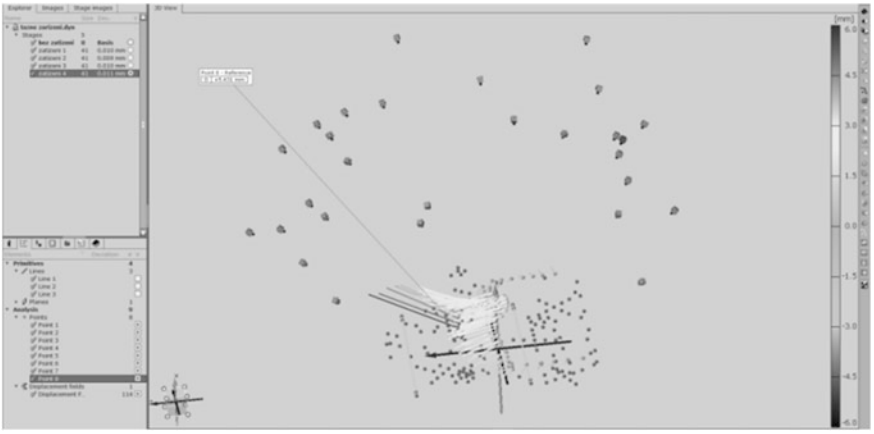

Fig. 8 Measurement evaluation in the Tritop software. Camera symbol represents one measurement position

vicinity of the towing hitch also coded markers and two calibrated bars should be placed.

Towing hitch, including frame was digitized from a distance of 2.5 m. Firstly without loading and sequentially with both loading stages. Images were taken from all sides of the frame along 45 at three height levels (Fig. 8). After evaluation in the Tritop software, results are displayed in the form of displacement vectors at the points where the un-coded markers were placed. Deformations of the towing hitch were always evaluated in comparison to the unloaded condition (Fig. 9).

Digitization of each loading state, including setup of loading forces took about 15 min; preparation of the measurement also took about 15 min. Table 4 shows the results of deformation analysis of the towing hitch.

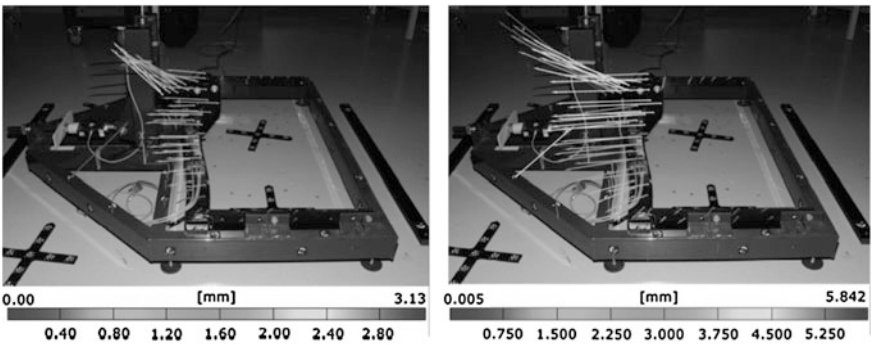

Fig. 9 Images with vectors of deformations. *Left* 50 % loading, *right* 100 % force

Table 4 Results of photogrammetry measurement

Loading stage	Deformations (mm)			Max. difference (%)
	Measurement 1	Measurement 2	Measurement 3	
Loading 50 %	3.130	2.995	3.025	4.3
Loading 100 %	5.842	5.664	5.791	3

Table 5 Results of methods comparison

	FEA (mm)	Max. dev. (%)	TRITOP (mm)	Max. dev. (%)	Max. dev. FEA versus TRITOP (%)
50 %	2.742	9.4	3.130		12.4
	3.027		2.995	4.3	
	3.025		3.025		
100 %	5.469	10.5	5.842		10.5
	6.059		5.664	3	
	6.111		6.111		

5 Results and Discussion

Table 5 shows the comparison of three FE analyses and three photogrammetric measurements of towing hitch deformations. The maximum difference of the FEA results is 10.5 % at loading stage 100 % and 9.4 % at loading stage 50 %. The maximum difference between the results of photogrammetric measurements is 4.3 % at loading stage 50 % and 3 % at loading stage 100 %. Table 5 shows that the variance of the measurement results using photogrammetry is smaller than in case of FEA. The results of photogrammetric measurements may be particularly affected by: the uniform distribution of coded and uncoded points on the object, the object position in the image (object should be approximately in the center of

the photo, if it's allowed by its dimensions); compliance of regular distribution of the images around the object and compliance of the measuring distance; size of the calibrated bars (should be approximately the size of the object). The difference of the FEA results is primarily caused by the shape variation of resulting CAD models after reverse engineering and by the density of elements in the finite element mesh.

6 Conclusion

This paper presents a methodology for deformation measurement of the towing hitch using an experimental stand and compares the results of repeated measurements with the results of finite element analysis. The towing hitch was loaded in horizontal and vertical direction, firstly with half force and secondly with the maximum allowable force. Monitoring of the loading was done by strain gauge force sensors via Catman Easy software. CAD model for the FEA analysis was created by reverse engineering using a 3D scanner Atos III Triple Scan. Measurements and finite element analysis was performed 3 times with the same input conditions. It was found, that the variance of the photogrammetric measurement is around 3 % and variance of the FEA results is about 10 %. In comparison of both methods, the identified strain differed by 0.39 mm at loading 50 % and 0.642 mm at loading 100 %.

Acknowledgement The work was supported by European Regional Development Fund in the framework of the research project NETME Centre under the Operational Programme Research and Development for Innovation. Reg. Nr. CZ.1.05/2.1.00/01.0002, id code: ED0002/01/01, project name: NETME Centre—New Technologies for Mechanical Engineering.

References

Boesemann W, Godding R, Huette H (2000) Photogrammetric measurement techniques for quality control in sheet metal forming. Int Arch Photogram Remote Sens 33(B5):48

DIRECTIVE 94/20/EC OF THE EUROPEAN PARLIAMENT AND OF THE COUNCIL of 30 May 1994 relating to the mechanical coupling devices of motor vehicles and their trailers and their attachment to those vehicles. No. L 195, 29. 7. 1994, vol 1. 2007, 1, pp 1–63. Available at http://eurlex.europa.eu/LexUriServ/LexUriServ.do?uri=CONSLEG:1994L0020:20070101:cs:PDF

GOM MBH (2009) Deformation analysis of car components. Available at http://www.gom.com/fileadmin/user_upload/industries/car_deformation_EN.pdf

González-Jorge H et al (2012) Photogrammetry and laser scanner technology applied to length measurements in car testing laboratories. Measurement 45:354–363

HBM—měřící technika—Snímače síly. Available at http://www.hbm.cz/

Luhmann T (2010) Close range photogrammetry for industrial applications. ISPRS J Photogram Remote Sens 65(6):558

Roylance D (2001) Finite element analysis. Department of Materials Science and Engineering Massachusetts Institute of Technology Cambridge, MA 02139, Feb 28, pp 16. Available at http://www.saylor.org/site/wp-content/uploads/2012/09/ME1023.2.3.pdf

WESTFALIA-Automotice GmbH (2007) Product details. Available at http://www.westfaliaautomotivede/index.php?id=54&L=1

Xinguang D et al (2009) Geometry features measurement of traffic accident for reconstruction based on close-range photogrammetry. Adv Eng Softw 40:497–505

Part IV
Products Innovation

J. Gavačová, M. Vereš, S. Hosnedl, J. Dvorak, M. Kopecky, L. Janik, P. Lepšík, M. Petrů, O. Novak and A. Lufinka

Responding to the demands of the market calls for permanent innovation. Part IV—*Products Innovation* is created by six contributions dealing with innovation of products, methods, and tools of systematical creativity. Two contributions deal with TRIZ methodology (theory of inventive problem solving) and its tools FOS (Function Oriented Search) and Altshuller's table of 40 inventive principles for technical contradictions solving.

Procedure for Developing Shaped Models Using the Generative Design Method

Jana Gavačová and Miroslav Vereš

Abstract Generative design, as a new method of product development and innovation, has become very important in the automotive industry. The reason for the introduction of this method into the process of development tasks solution is simple. This approach to car innovation leads to a reduction in the time spent developing prototypes. CAD software allows an approximate design to be used initially, with the ability to make subsequent changes. When the shape of a car is complete, styling is not closed, and can be modified until the time of confirmation of the final design. The underlying assumption for innovation in this field is simplicity, and especially time-saving, during the development of the prototype. Since the early days of intelligent design systems, opportunities for automotive design have expanded far beyond the boundaries of austere block shapes. These only made use of purely functional radiuses in the bending areas. By contrast, one of the most important goals of modern car design is the shape of its reflection lines. It is necessary to generate gentle and smooth curves in the car body, which, under lighting, will catch the eye.

Keywords Computer Aided Style · Generative design · Cloud of points · Shape analyses

J. Gavačová (✉) · M. Vereš
Institute of Transport Technology and Design, Faculty of Mechanical Engineering, Slovak University of Technology in Bratislava, Bratislava, Slovak Republic
e-mail: jana.gavacova@stuba.sk

M. Vereš
e-mail: miroslav.veres@stuba.sk

L. Ševčík et al. (eds.), *Modern Methods of Construction Design*,
Lecture Notes in Mechanical Engineering, DOI: 10.1007/978-3-319-05203-8_59,

1 Introduction

Even though they may appear similar, the fundamentals of generative design are in principle different to parametrical modelling. Parametric models are numerically controlled representations of design solutions which result in a new product with similar geometrical values (quantity indicators such as dimensions, weight etc.), but dissimilar in quality (e.g. aesthetic indicators, subjective user requirements, and needs). This means that generative design in new product development and innovation offers more than a geometric model. It offers the whole complex of information about a new product which has not only a deterministic nature, but also heuristic one. The practical use of generative design is part of the private policy of automotive companies. However, even though it is so beneficial, they do not use it much in practice. The important role of this method is based on its time saving opportunities. Until recently it took about 4–5 years to start a new model production. Today, if designers use generative design for developing a new prototype, it will cut the development time to 1–2 years.

2 Essentials of Generative Design

The basic scheme of the generative design process is shown on Fig. 1. It shows the cooperation during the prototype development.

At the first level of the development process there is just the designer who has to make the initial design. When the draft of the shape is complete, engineers start to invent/design/develop the functional elements. These are in contact with all the exterior surfaces. The clay model can be checked for its aerodynamic properties, passive safety, and so on. After that, the surface is scanned with a 3D scanning device. The output is a text file with coordinate points. A special algorithm selects, filters, and orders the points. The cloud of points is interpolated by a mesh which can be transformed into a surface. This surface is then controlled by the source code for the interface between inner and outer parts. The algorithms, rules, and source codes result in a generated model. In the case of the draft being changed, the CAD system automatically reprocesses the new data, and generates a new model.

3 From Clay Model to Universal Model

New CAD software simplifies transfer between draft and a CAD universal model. The designer works with the Computer Aided Style (CAS) which is integrated in the complete system together with CAD. The vision for the future is that there will be no conversions between these. In this new generation of CAD software

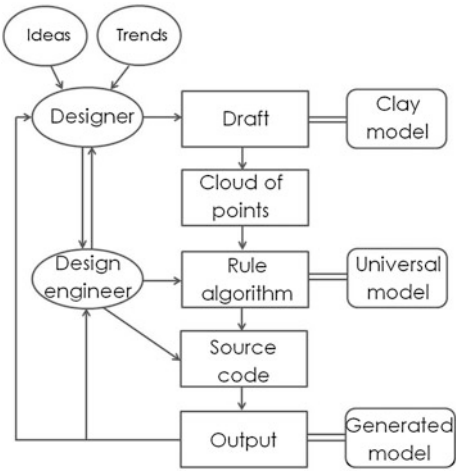

Fig. 1 Basic scheme of generative developing process of an automotive prototype

designers use graphic applications integrated into it. A model made using CAS software is a model in virtual reality. But there are some problems which can't be solved in virtual space alone. Aerodynamics must also be checked on a clay model. CAS from designer is transformed in Stl, Iges, Stp or other file formats. To make a real model (also called clay model) a 3D printer is used. Changes are applied directly onto the clay model in order to improve the shape. The complete shape, which is scaled, is then scanned.

Software generates points in ASCII files, Steinbichler files, Iges files etc. The cloud of points from a car's bonnet can be seen in Fig. 2a. The scanned surface had about 5 million points which were reduced to 300,000 using a filter. These points have no properties, they are just a cloud. So the visualisation is made by connections between points, shown in Fig. 2a. This is why the cloud of points has no proper shape and shows just an exploration envelope of the positions of the points.

An approximate shape is made by meshing (see Fig. 2a). This is when neighbouring points are connected and the area between them filled by a surface. This mesh is an intergrade between the cloud of points and the proper surface. The complete surface is shown in Fig. 2a.

4 Criterion for Shape Components

This paper focusses particularly on the generative design of automotive bodywork. Saleability is influenced by the smoothness of the shape. It is not just because of the nice curves of the body shell. Another criterion is the shape of objects reflected on the surface.

Fig. 2 Process of transforming cloud of points into surface using example of a car's bonnet

In software applications parametric equations from (Linkeová 2007) are used. If there is a closed interval I it is possible to describe a 3D curve by the parametric relation (1).

$$K(u) = [x(u), y(u), z(u)], \quad u \in I. \tag{1}$$

Firstly, the surface is as smooth as the derivation level of the curve at any point. The continuity between two curves or two segments of a curve is in (2). Here k represents the level of smoothness.

$$K^i(u) = N^i(v), \quad i = 0, 1, \ldots k \tag{2}$$

If there are curves with C^0 continuity this is called 'point continuity' and there is no smoothness. Using C^1 there is a 'tangent continuity'. A minimum of C^2 continuity is necessary in order to produce a smooth surface. This is called 'curvature continuity' and using it avoids any bad edges. For the aerodynamic properties and passive safety C^2 continuity of surface in every segment is best. Of course, curves can, in principle, also be described by n degree polynomial functions. Equation (3) shows polynomial function of third degree. In this case, it is very advantageous to change the shape of the profiles and change their aesthetic outcome by using higher derivative order (C^{n-1}) continuity. In this case Eq. (3) is accompanied by C^2 continuity.

$$y = A(x - x_0)^3 + B(x - x_0)^2 + C(x - x_0) + D. \tag{3}$$

Secondly, there must be a compromise between the engineer's model and the designer's draft. On bodywork particular aesthetic lines are used. In rule/algorithm there must be steps which recognize the required lines with a proper shape. After the categorization of the smoothness of the curves, comes a curve fitting algorithm. Splines describing the preliminary surface are used to represent the curves.

5 Surface Analyses

After generating the surface there must be a final check. Shape analyses are used in CAD software to control the aesthetics, inflection lines, reflection lines etc. The first check can be based on the curvature of the shape, which is mathematically described. The first curvature, also called flexion, is presented in Eq. (4).

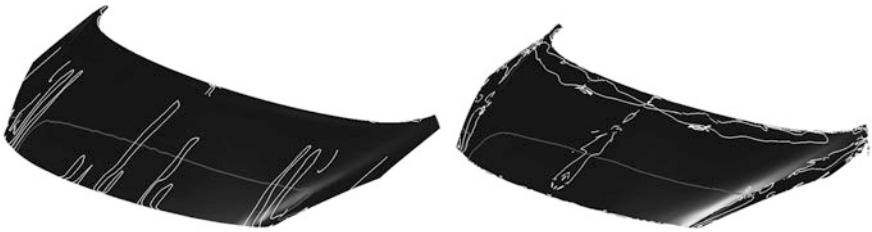

Fig. 3 Two models of a car's bonnet, made by using different algorithm, with analysis of reflection (*grey colour*) and *inflection lines* (*white colour*)

Based on Velichová (2003) for the same curvature of two connected curves, they have to have equal second derivation at the point of connection.

$$^{1}k = \frac{|K'(u) \times K''(u)|}{|K'(u)^3|} \tag{4}$$

If a second curvature, also called torsion, is required, there is an equation for it in (5). This means there is at least third equal derivation at the point of connection of the curves.

$$^{2}k = \frac{|K'(u)K''(u)K'''(u)|}{|K'(u) \times K''(u)|^2} \tag{5}$$

Other checks are visual and so they can't be replaced by mathematical formulas. An example of inflection lines and reflection lines can be seen in Fig. 3. To achieve the best shape of these they must be presented when the model is moved. Even though the shape of car model is aesthetic, it can look different when it is lit. One important visual check is environment mapping analysis. In this step the surface reflects real objects or surroundings. The shape of the reflected objects must also be smooth.

6 Connection Between a Class A Surface and a Class B Surface

For the assembly process it is necessary to fulfil certain functional relations. An A surface represents the shape, whilst a B surface represents proper position and function. Using the example of a bonnet, this means the need to fit braces, holes and other interior parts (in a broader sense to the whole car "body in white" structure). The scheme of connections in the CAD software can be seen in Fig. 4.

This is an example of how the source code can work to generate B surfaces. After updating the CAS, or A surface, by scanning this algorithm, B surfaces proceed to assimilate this change. This is the reason why an engineer has to prescribe the interfaces between an A surface and a B surface.

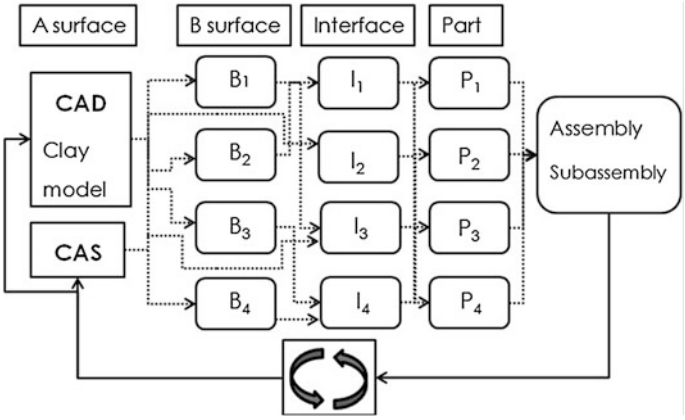

Fig. 4 Scheme of CAD relations for functional parts

7 Conclusions

In the past it was common for engineers to freeze the model after completing the design task. Consequently, no further changes were possible on A class surfaces after this point. In practice, generative design, based on the scheme in Fig. 1, could open new possibilities in the design process. Exterior shape is active during almost the entire time of developing the new prototype.

The generative design method can also be advantageously applied to the process of automotive mechanical parts development. Here it is useful to also incorporate into the whole process knowledge in the form of a special system. Using this method it is possible to solve problems connected with the assembled structure of complete mechanisms (changing and selecting the standardized or predevelopment parts stored in the design database), Additionally, the calculation and optimization tasks relating to the geometry and load capacity requirements can also be solved using this method. Such a task has been addressed in the design of automotive hybrid drives, where HCR gearing is used.

Finally, it is important to mention how working procedures are distributed in companies. The trend is to distribute work not just among workplaces in one firm, but also among workplaces all over the world in international concerns. Professional communication has changed from personal contact to internet connections across national boundaries. That is why generative design is gaining ground in the automotive industry (as the next element of Concurrent or Parallel Engineering). In conclusion, the future offers the possibility of working with simple adaptations of a model to produce changes without time-consuming procedures.

Acknowledgments This contribution has been elaborated partially as a result of the research project 1/0277/12, supported by the Slovak VEGA grant agency and at the same time presents the results of the project supported by the European Structural Funds No. 26240220076—"Industrial research into the methods and procedures in generative design and knowledge engineering in car development".

References

Linkeová I (2007) NURBS křivky. Praha: Nakladatelství ČVUT
Velichová D (2003) Konštrukčná geometria. STU, Bratislava

Interdisciplinary Engineering Design Projects in Cooperation with Industrial Partners

S. Hosnedl, J. Dvorak and M. Kopecky

Abstract Illustrative results of a number of student interdisciplinary team innovative design projects performed by engineering and industrial designers, and consulted by specialized experts are introduced in this paper. Projects have been managed and solved using the "Knowledge integrated design" (KID) comprehensive approach different from the 'Theory based approaches' like "Axiomatic Design" and/or "Theory of Technical Systems based Design", as well as from traditional "Instructive", "Intuitive", and/or "Trial and Error/Success" prevailing approaches used for design problem solving. The mentioned KID strategy stems from a systematic 'map' of descriptive and prescriptive "Engineering Design Science" (EDS) knowledge obtained both from theory and practice. Projects being solved by students and staff of University of West Bohemia were assigned, consulted and co-evaluated in cooperation with industrial partners from Czech Republic and abroad. Real design projects were analogously managed and solved for industrial and institutional partners like Linet s.r.o., MemBrain s.r.o., Autodesk ltd., etc.

Keywords Innovative design engineering · Knowledge Integrated Designing · Theory of technical products · Technical Systems · Design education

S. Hosnedl (✉) · J. Dvorak · M. Kopecky
University of West Bohemia, Pilsen, Czech Republic
e-mail: hosnedl@kks.zcu.cz

J. Dvorak
e-mail: dvorakj@kks.zcu.cz

M. Kopecky
e-mail: kopecky@kks.zcu.cz

L. Ševčík et al. (eds.), *Modern Methods of Construction Design*,
Lecture Notes in Mechanical Engineering, DOI: 10.1007/978-3-319-05203-8_60,

1 Introduction

Since 2004 the mentioned KID concept has been utilised and validated in its respective development stages in more than 120 student teams (from 6 to 8 students each) for solution of 25 quite different topics of the interdisciplinary engineering and industrial design innovative projects assigned, consulted and evaluated by 13 Czech and foreign industrial companies (Figs. 1, 2 and 3). Each year the projects were performed from scratch within 13 weeks of the winter term by engineering design and management students from our Faculty of Mechanical Engineering together with industrial design students from Institute of Art and Design, and consulted by physiotherapy and ergo therapy students from Faculty of Health Studies, and also selectively supported by students from our Faculty of Electrical Engineering, from University of Zielona Gora (PL) and University of Deggendorf (G) (Fig. 1) (Hosnedl et al. 2010; Hosnedl and Srp 2011). The projects are performed within the framework of the training part of the undergraduate master course "System design engineering of Technical products" (KKS/ZKM), which aims to provide students with foundation of the system of EDS knowledge about and for systematic and creative management and design engineering of technical products.

The concept of the projects is among others original in its continuous team cooperation of engineering and industrial designers as well as other specialised experts which knowledge is important, and of course, available. Within last years these experts have been mostly students of health studies as representatives of the key specialised views on the designed technical products of any kind—design for human safety (of all kinds), ergonomic, agreeability, design for environmental compatibility etc. Further students of electro-engineering, and students specialized on design for assembly, disassembly and recycling views from University of Zielona Gora (PL) have been also partially involved.

Most of students are so motivated by this concept that a number of project results have substantially over-exceeded the scheduled capacity of the subject and number of its credits. Closing competitive presentations of the interdisciplinary teams solving the same assigned topic also play the important motivation role. The project results are evaluated by committees consisted of representatives of all involved university faculties/institutes and industrial partners that assigned and consulted the respective topics (from 3 to 4 topics last years, as depicted in Fig. 3).

Evaluation criteria are predicted applicability of designed products in practise, quality of engineering and industrial design, and solution systematic. As a supporting criteria serve quality of the project documentation and presentation, and mostly also quality of physical industrial design models. Active members of all successful teams obtain diploma, as well as highly appreciated certificates about active participation in these projects signed by directors of the respective companies. In addition members of the winner team in each topic are awarded by financial price granted by the respective companies. The achieved results are greatly appreciated by participating industrial and research partners and our

Fig. 1 Minutes from excursions and consultancies with partners experts (*top*), and from competitive (*middle*) and workshop DESIGNERS^{2+} (*bottom*) student presentations

Fig. 2 Few samples of results of interdisciplinary team student engineering and industrial design projects assigned, consulted and co-evaluated in cooperation with industrial partners

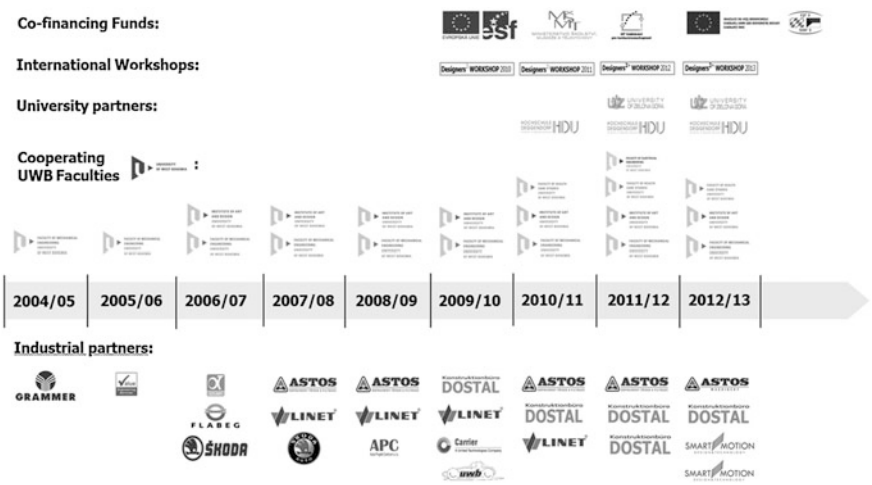

Fig. 3 Industrial, university and institutional partners involved in student interdisciplinary engineering and industrial design projects since 2004

university officials. Several students' outcomes also resulted in utility and industrial models.

The best teams together with the best teams from cooperating universities in Deggendorf (G) and Zielona Gora (PL) are invited to present their projects in the annual International workshops DESIGNERS 2+. Except of the top representatives of the involved universities incl. their faculties and of industrial partners, representatives of Pilsen and Pilsen region also participated in these workshops which usually have about 80 participants, mostly students from Czech Republic, Germany and Poland.

2 Systematic Knowledge Integrated Designing and Thinking

Usual approaches to design engineering of technical products/systems (TS) tend towards traditional, intuitive ways of using the knowledge, which have been acquired both from theory and (more and more in the course of time) from practice. Practising engineering designers in general 'do not like' the more systematic approaches, because of their 'rigidity', which they find to be incompatible with their own creativity. It is also obviously not effective and efficient to load the memory of practising engineering designers and engineering design students with acquiring engineering design knowledge exclusively in their specialised forms. They then need to use a great deal of their creativity for painstaking step by step

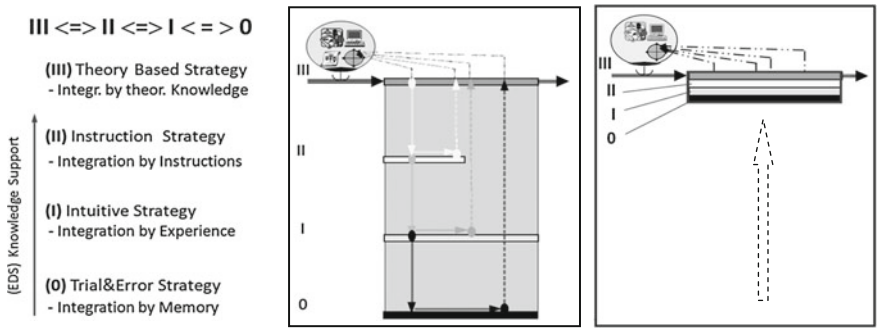

Fig. 4 Knowledge Integrated Designing (KID) (*left*) an Knowledge Integrated (systematic creative design) Thinking (KIT) (*right*) metaphorical schemes

discovery of analogies and applications of such specialised forms within the area of their work.

Usual instructive methodical approaches to engineering design procedures improve this situation. But if they are considered by themselves, they resemble more formal algorithms, rather than the needed 'handy workbench' of knowledge and tools for the creative work of engineering designers. We would like to introduce how this situation can be dealt with in order to obtain better results in engineering design research, education and practice.

Four levels of mutually bounded approaches/strategies for design problem solving can be recognised (Fig. 4).

(0) The '**Trial and Error (and success!)** based strategy' can be assumed to be a 'zero' level for problem solving. A series of trials (attempts) should find the solution by individual steps. Appraisal (evaluation) of the suitability of the solution for the situation is then necessary. Achieved quality of results and required cost and time are accidental so there is possibility exists that no result could be found in this way. Perhaps the only advantage is that 'almost no' previous knowledge and experience of the problem to be solved is required in a limit case. The repeated use of 'Trial and Error' methods results in some experience, i.e. practical knowledge which could serve as a basis for the higher levels of design problem solving. These levels could be structured roughly as follows:

I. The '**Intuitive** based strategy' which usually stems from previously acquired knowledge, and more and more on experience.
II. The '**Instruction** based strategy', mostly in a form of prescriptive or normative guidelines, which usually stems from summarised general knowledge, special theories and practical experience of their authors, arranged and presented differently (often mnemonically if possible to simplify their memorising).
III. The '**Theory** based strategy' which stems mainly from a framework of theoretically based structured knowledge—Engineering Design Science (EDS)—obtained by scientific 'mapping' both from theory and practice.

Of course each mentioned subsequent ‘higher’ hierarchical level includes the ‘lower’ level(s), and the real situation is in any case rather vague. When analysing the compatibility of these four strategies, i.e. possibility of flexible use of an optimal level appropriate to the solved problem, we can easily find great discrepancies among instruction level II and theoretically ‘lower’ levels I and 0. The reason is that principally quite ‘rigid’ instruction level II hardly provides designers with needed flexible support when returning from levels 0 and I back to level II (Fig. 4, middle).

It is obviously one of the main reasons for the above mentioned difficulties in the acceptance of the instruction approaches in practice. However, theory based level III, which provides designers with a transparent system/‘map’ of theoretically based knowledge on (and for) design engineering is very compatible with all lower levels, enabling the ‘correct’ location in this ‘map’ to be found easily after returning from the ‘lower’ levels (including instruction level II) (Fig. 4, midle top).

Our research, supported by industrial and academic experience and the feedback gained during cooperation with industry, proves that the generally used approaches to design engineering, which are ‘Trial and Error/Success approach’, ‘Intuitive approach’ and ‘Instruction approach’ are deficient in many aspects for current and future needs. We find that a theory [Theory of Technical Systems (Hubka and Eder 1988)] based integrated design problem solving approach, which we call multilevel Knowledge Integrated Designing (KID), is a very powerful vehicle for treating dialectic systematic and at the same time creative design engineering including its management.

It enables the most appropriate and consistent use of all the mentioned problem solving strategies, because the theory based engineering design ‘map’ of knowledge spans/covers the other ‘lower’ hierarchical levels (Fig. 4). Thus engineering and industrial designers, both ‘outside’ leaders and executive ‘inside’ ones, can manage, solve and monitor their projects on the theory based level. It enables them to ‘jump’ to other ‘lower’ levels at any time if appropriate, and ‘return’ back to the ‘map’ to follow the planned strategic design path.

However, TS Design Specification, Evaluation of alternatives of any output for objective Decisions, as well as Documentation including its archiving and transfer to other TS Life stages ought to be almost exclusively systematic (Hosnedl et al. 2011). We have also experienced that the ‘KID’ approach also helps to integrate the individual specialists within the interdisciplinary teams very effectively. (Hosnedl et al. 2008). We have experienced and validated that when any designer mastering the ‘KID’ concept it is naturally converted into a dialectic ‘systematic creative’ way of design thinking which can be metaphorically called ‘Knowledge Integrated (systematic creative design) Thinking’ (KIT) as metaphorically depicted in Fig. 4 (right).

3 Conclusions

We have applied and validated the outlined knowledge in a number of innovative projects including development of innovative professional CA software and relevant educational tutorials. We can prove that it can serve as a powerful foundation for research, education and industrial practice. In addition the introduced knowledge creates a powerful systematic management framework, which enables to adopt 'any' reasonable combination of the key problem solving strategies which are theory, instruction, intuition and trial and error/success based approaches.

The developed and already quite thoroughly validated concept of the KID theory and methodology of management and systematic creative solution of the interdisciplinary projects as well as its results are also positively acknowledged by international community (Eder and Hosnedl 2008, 2010) including USA and Japan (Hosnedl 2010; Hosnedl et al. 2011). In (Eder and Hosnedl 2010) is e.g. described on 20 pages one of the interdisciplinary student projects of the "Intensive hospital bed" solved for Linet Company in 2007. Also students are invited to present their successful projects abroad, e.g. at Autodesk University conference in Las Vegas (USA) in 2009, at WoodStEx conference in Barcelona in 2012, etc. The whole bulk of interdisciplinary student projects also evoked several educational, R&D and an educational business projects with industrial and institutional partners. We have submitted another paper describing one of them at the ICDM 2013, and hope and look forward to introduce it to the conference participants too.

Acknowledgement This paper includes partial results of Project SGS-2013-050 "Complex support of design engineering of technical products to improve their properties and competitiveness II".

References

Eder WE, Hosnedl S (2008) Design engineering—A manual for enhanced creativity. CRC Press Taylor & Francis Group, Boca Raton

Eder WE, Hosnedl S (2010) Introduction to design engineering: systematic creativity and management. CRC Press Taylor & Francis Group, Leiden

Hosnedl S (2010) Providing a digital prototyping industry center of expertise. In: Class Handouts of the Autodesk University 2010—AU 2010. ED223-1, ED322-2 V, 29 Nov–2 Dec 2010, Las Vegas, USA, 10 pp

Hosnedl S, Srp Z (2011) Sharing experience in design education based on research and industrial practice. In: Majer AM et al (eds) Proceedings of the 18th international conference on engineering design—ICED11, vol 8, TU Denmark, Copenhagen, pp 287–296

Hosnedl S, Srp Z, Dvorak J (2008) Cooperation of engineering and industrial designers on industrial projects. In: Proceedings of the 10th international design conference—DESIGN 2008. FMENA, Zagreb, pp 1227–1234

Hosnedl S, Dvorak J, Srp Z, Kopecky M (2010) Design specification and evaluation tool for design engineering and its management. In: Proceedings of the 11th international design

conference—DESIGN 2010. FMENA, Zagreb, 17–20 May 2010, Dubrovnik, Croatia, pp 799–810

Hosnedl et al (2011) Effective engineering design research, education and practice in context. In: Watanuki K, Kanada T (eds) Selected articles of the 2nd international design conference on design engineering and science—ICDES 2010. Tokyo, Japan, pp 31–36. ISBN 978-4-9905565-1-8

Hubka V, Eder WE (1988) Theory of technical systems. Springer, Berlin

Interdisciplinary Innovation of EDI Module Case Using 'Design for X' and 'Prediction of X' Knowledge and Methods System Based on TTS

M. Kopecky, S. Hosnedl, J. Dvorak and L. Janik

Abstract Practising engineering designers in general 'do not like' systematic approaches to designing, because of their 'rigidity', which they find to be incompatible with their own experience and creativity. On the other hand they need more and more specialized advanced knowledge and tools of external researchers who are however usually not familiar with the company specific products, knowledge and experience. We would like to outline how this situation can be enhanced with use of the "system map" of Engineering Design Science (EDS) knowledge and methods based on the Theory of Technical Systems (TTS). This paper is especially focused on use of 'Design for X' (DfX) and 'Prediction of X' (PoX) knowledge and methods where X usually means a TS property class, subclass, sub-subclass or a property respectively.

Keywords Design engineering · Theory of technical system · Design for X · Prediction of X · EDI module

M. Kopecky (✉) · S. Hosnedl · J. Dvorak
University of West Bohemia, Pilsen, Czech Republic
e-mail: kopecky@kks.zcu.cz

S. Hosnedl
e-mail: hosnedl@kks.zcu.cz

J. Dvorak
e-mail: dvorakj@kks.zcu.cz

L. Janik
MemBrain s.r.o, Stráž pod Ralskem, Czech Republic
e-mail: ludek.janik@membrain.cz

L. Ševčík et al. (eds.), *Modern Methods of Construction Design*,
Lecture Notes in Mechanical Engineering, DOI: 10.1007/978-3-319-05203-8_61,

1 Introduction

EDI module serves for production of ultra-clean water using elektrodeionisation membrane processes. The aim of the innovative project assigned by MEMBRAIN Ltd. Straz pod Ralskem, Czech Republic was to develop a highly competitive design of a mechanical case for EDI module having higher inner working volume (approximately 430 × 650 × 550 mm) as well as increased operation pressure resulted in testing pressure of 1, 2 MPa to increase its capacity and efficiency. Technological core of the EDI module consists of a sophisticated set of thin plastic frames and membranes protected by several Membrain Ltd. patents. To achieve optimal EDI operation of membrane processes it was stated that, based on former experience, maximum displacement of the internal plastic parts surfaces must not exceed 1 mm in any direction under the given testing pressure.

The locations were also stated and assembly dimensions of inputs and outputs from the EDI case to enable the necessary connections with other technological devices as well as capabilities to build both horizontal and vertical sets of EDI modules. The requirements for maximum mass, pleasant appearance and optimal low production and assembly cost were also roughly specified.

At that moment we could begin and thus started to search for principal alternatives of the conceptual organ structure and corresponding rough constructional structures of the EDI module case. It was not trivial task due to the necessity to support outer surfaces of the technological unit in all six coordinate directions, due to high forces about 20 tons affecting on each of all six evoked case walls, while keeping tight contact during both assembly and operation period among the technological unit surfaces and the six walls of the EDI case. Last but not least it was necessary not to over-exceed the limited strength and the limited displacement of any plate. We have found some promising conceptual alternatives and have selected one of them which was evaluated and selected as sub-optimal. These conceptual solutions cannot be introduced here because their IPR protection is negotiated and prepared to apply.

2 Design Specifications

At this step it was necessary to get to know and complete further requirements which the designed EDI module case should meet. These had to cover not only the above mentioned and additional stated “customer” ones focused mostly on operation and manufacturing processes but also other obligatory and even generally implied requirements (CSN EN ISO 2006) related together to all Life Cycle phases of the EDI module.

In general there are a lot of such requirements, having in addition different importance (weightings) from the only wished (voluntary) ones up to unconditional (compulsory) ones. Such a comprehensive specification of requirements has

thus key role on the final life cycle quality of any designed technical product. This task however emerged as the first serious difficulty for the heterogeneous "company-university" team which in addition could not meet and/or communicate at "anytime" due to the large mutual distance of their seats not speaking about that two external company expert advisers live and work in the Netherlands and Canada.

Thus the usual ways of design specification beginning from "Trial and Error" approach (i.e. without almost any design specification) through "Intuitive" one (usable however only by experienced experts) up to "Instructive" ones. These are however available only in a number of general instructions (e.g. in (CSN EN ISO 2006) and many others) based on knowledge and experience accumulated by their authors. Attempts to establish a concrete and comprehensive design specification of this kind by our company partners have been not effective due to uncertainties what are our needs as well as due to their very limited time capacities not speaking about probable quite nature subjectivity and un-completeness of the result.

Thus we decided to apply formally and only on key issues simplified well validated general structure of design specification on properties of technical products looked upon as technical systems (TS) which we have developed and already used in a number of interdisciplinary team design projects (Eder and Hosnedl 2010; Hosnedl et al. 2008). Its structure mirrors structure of the objective comprehensive general model of properties of technical products which stems from the above mentioned Theory of Technical Systems (Hubka and Eder 1988), and which is outlined in its latest version e.g. in Hosnedl et al. (2013).

This approach proved to be very effective, because we, academic researchers, quite simply listed our clearly arranged system of selected questions, and our company experts quite simply answered them. Of course this process proceeded continuously during the whole project including the evoked changes and supplements. These were recorded including the description of the reasons, date and authors. It significantly contributed to minimising of the evoked errors and corresponding loses of time because all about 10 team members had "anytime" at their disposal a complete systematically arranged list of the latest valid requirements.

3 Search for Alternatives of Solutions and Their Evaluation both with Use of DfX and PoX Knowledge and Methods

The following "embodiment design" steps (Eder and Hosnedl 2008, 2010) aiming at alternatives and finally at sub-optimal constructional structure including its sub-structures (called constructional organs) of the designed EDI module utilised all the above outlined solution approaches (Chap. 2) from the most simple "Trial and Error (and Success!)", through "Intuitive" and "Instructive" ones until the Theory

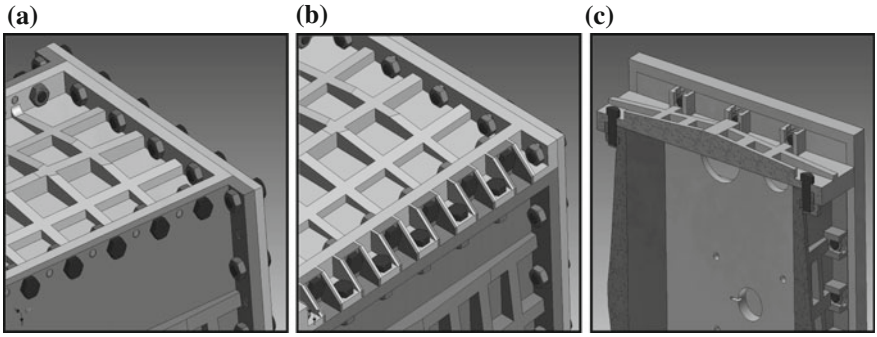

Alternative solutions of the connections of the EDI module case plates using:

Fig. 1 EDI module case constructional organ for the main function: case plates (their material, energy and information in general) connect together. **a** Bolt and pin connections. **b** Only bolt connections. **c** Bolt and shape lock connections

(EDS-TTS) based ones as e.g. outlined in (Hosnedl et al. 2008, 2013). The achievement of the respective requirements on EDI module properties was accompanied by available both recorded (explicit) and tacit (implicit) "Design for X" knowledge and methods.

The necessary evaluation of the designed alternatives and their variants of the EDI module constructional structure including its sub-structures was (had to be!) however performed again systematically according to the list of requirements to cover all the specified properties (Hosnedl et al. 2008, 2013). To perform it available both recorded (explicit) and tacit (implicit) "Prediction of X" knowledge and methods were utilized.

It is advantageous both for the designing and knowledge management that DfX and PoX knowledge and methods can be arranged according to the same structure like TS properties and thus also the mentioned list of requirements on properties of the designed product. Few examples illustrating the mentioned two steps search for solutions of alternatives of the EDI module main resp. evoked Constructional Organs (Eder and Hosnedl 2008), i.e. Function Carriers (Pahl et al. 2003), and their evaluation according to the criteria regarding the main required properties specified in the list of requirements followed by decision about the sub-optimal alternative is outlined in Figs. 1, 2 and 3.

Based on the outlined PoX knowledge and methods, and the multi-criteria evaluation which stemmed from the set of the specified properties the alternative c. of the connections in Fig. 1 was decided as a sub-optimal (including the not shown simple mutual galvanic connections of all plates).

Based on the outlined PoX knowledge and methods, and the multi-criteria evaluation which stemmed from the set of the specified properties the alternative c. in Fig. 2 was decided as a sub-optimal solution for side plates (including the shown appearance).

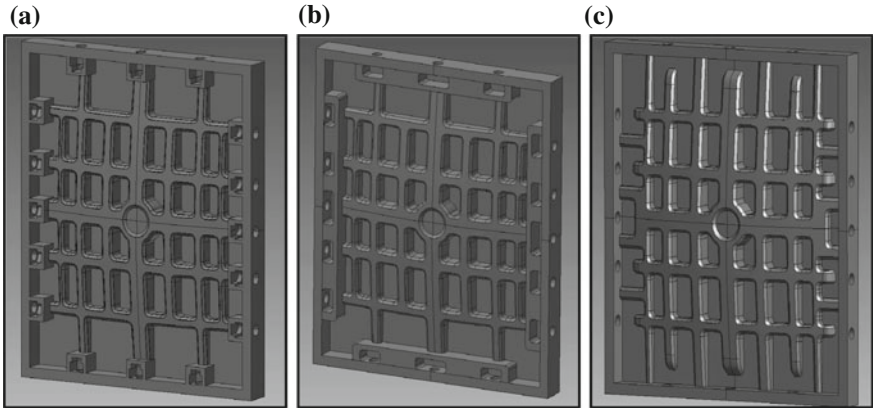

Fig. 2 EDI module constructional organ for the main function: create working space (an example for its side boundaries is shown)

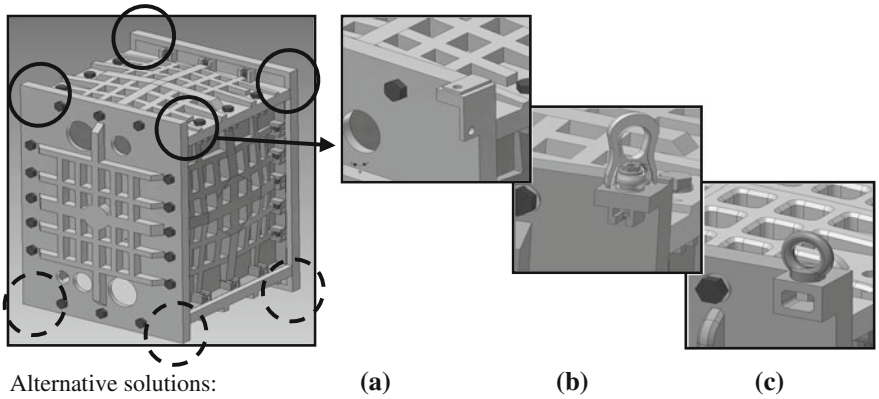

Fig. 3 EDI module aggregated constructional organs for the evoked functions: Enable EDI module(s) manipulate and transport, vertically and horizontally stack (not fully shown), and connect with a foundation (not shown)

Based on the outlined PoX knowledge and methods and the multi-criteria evaluation which stemmed from the set of the specified properties the alternative c. in Fig. 3 was decided as a sub-optimal solution for the depicted multi purpose constructional organ (Fig. 4).

Finally the whole EDI module Constructional Structure was analysed and sub-optimised regarding the strengths and displacements taking into account all the specified requirements on the required TS properties, especially manufacturability, assembly-ability, mass, industrial design and production cost in this case.

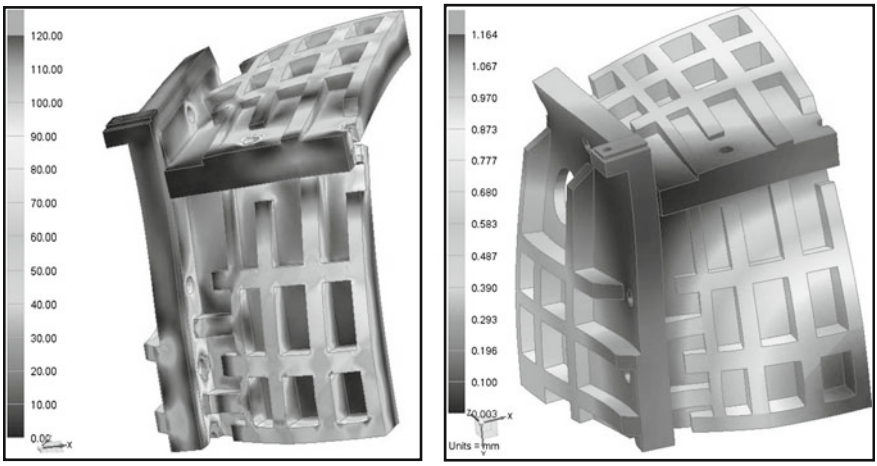

Fig. 4 FEM analyses of strengths (*left*) and displacements (*right*) for the EDI module case

4 Conclusions

We have already applied and validated the outlined large system of engineering design knowledge and methods in a number of projects in education and research including development of CA software in cooperation with industrial and institutional partners from Czech Republic and abroad. The knowledge and methods applied in these projects however had to be rather academic and a little heavy-handed to cover all areas necessary to teach, train and apply even if the respective project did not fully require it.

Thus we are happy that we have found a new challenging area of their rational and effective utilization, however keeping its systematic foundation without bothering all involved highly experienced partners with it. We very hope that the prototype of the designed EDI module which is just being manufactured meet and validate the presented assumptions within the reasonable tolerances and that we will be able to introduce its final solution in the ICMD conference on September.

Acknowledgements This paper includes partial results of the Project SGS-2013-050 'Complex support of design engineering of technical products to improve their properties and competitiveness II'. We also would like to greatly thank to company management of MEGA a.s., submitter of development of EDI modules, to its experts especially to Ing. Jiri Lipa and Ing. David Tvrznik and to its external experts Robert Gerard (NL) and David F. Tessier (CAN) for their excellent cooperation, ideas and recommendations, to the hired designers MgA. Daniel Pavlík and MgA. Jan Kopriva for their attractive industrial designs, and also to Ing. Karel Raz from the University of West Bohemia for its FEM calculations.

References

Birkhofer H (ed) (2011) The future of design methodology. Springer, London

CSN EN ISO 9000 (2006) Czech v. of the European Standard Quality management systems—Fundamentals and vocabulary (Czech Institute for Standardization, Prague)

Eder WE, Hosnedl S (2008) Design engineering—A manual for enhanced creativity. CRC Press, Taylor & Francis Group, Boca Raton

Eder WE, Hosnedl S (2010) Introduction to design engineering: systematic creativity and management. CRC Press, Taylor & Francis Group, Balkema, The Netherlands

Hosnedl S, Srp Z, Dvorak J (2008) Cooperation of engineering and industrial designers on industrial projects. In: Proceedings of the 10th international design conference—DESIGN 2008. FMENA, Zagreb, pp 1227–1234

Hosnedl S, Dvorak J, Kopecky M (2013) Integrated engineering design research and interdisciplinary education in cooperation with industrial partners. In: Proceedings of the 3rd international symposium on integrating research, education, and problem solving: summer IREPS 2013. Orlando, Florida, USA. Submitted paper accepted for presentation, 9–12 July 2013

Hubka V, Eder WE (1988) Theory of technical systems. Springer, Berlin

Pahl G, Beitz W, Feldhusen J, Grote KH (2003) Engineering design, a systematic approach, 3rd English edn. Springer, London (Transl. Wallace K, Blessing L from: Pahl G et al (2003) from Konstruktionslehre, Springer, Berlin)

Innovation of Car Seat Construction Using TRIZ-Based Tool: Function-Oriented Search

P. Lepšík, M. Petrů and O. Novak

Abstract The paper deals with the search and design of suitable security solution of an innovated construction of a car seat. The problem consists in the use of flexible reinforcements of the seats, which replaces an origin sheet metal. On this reinforcement the comfort seat cushion is placed on which a passenger sits. This reinforcement is pre-stressed with a certain force, but this force is inadequate during the crash. Consequently, the passenger can dip in the seat, which is very dangerous. Therefore it is necessary to use a suitable mechanism, for pre-stressing the reinforcement by a desired force in the case of crash. New TRIZ-based tool—Function-Oriented Search (FOS) method was utilized to find appropriate solutions. With its help several analogous solutions, which are applicable for this problem, were found. In the paper the advantages and disadvantages of these proposals are discussed, including the proposed optimal solution.

Keywords Car seat innovation · TRIZplus · Function-Oriented Search (FOS) · Flexible reinforcements · Crash

P. Lepšík (✉) · M. Petrů
Department of Design of Machine Elements and Mechanism, Faculty of Mechanical Engineering, Technical University of Liberec, Liberec, Czech Republic
e-mail: petr.lepsik@tul.cz

M. Petrů
e-mail: michal.petru@tul.cz

O. Novak
Technical University of Liberec, Liberec, Czech Republic
e-mail: novak.ondra1@seznam.cz

L. Ševčík et al. (eds.), *Modern Methods of Construction Design*,
Lecture Notes in Mechanical Engineering, DOI: 10.1007/978-3-319-05203-8_62,

1 Introduction

Nowadays the product innovations are more and more important for the companies. Trends and efforts of current car seat development are the reduction of the weight of individual parts, increase of the energy-efficient materials, which are ideally recyclable (Njeugna et al. 2010; Caudron 2003; Petrů 2012), content ratio. It is a complex optimization targeted on a weight reduction and energy performance of construction materials, because these parameters relate to the safety parameters and seating quality. Emphasis is on the replacement of the stuffing material of the comfortable seat, which is usually made of polyurethane foam—thus made from oil. Not only mass, energy and environmental savings can be achieved, but also some improvements in another required parameters (Petru et al. 2012; Hanel et al. 1997). These efforts are based on the concept of car manufacturers promoting the intensive weight reduction leading to a reduction of fuel consumption, lower emissions, increase of the car efficiency and environmental performance. The principle is to reduce the weight of all the components and parts of the car, which in the sum leads to a significant reduction of weight of the whole car. One of the possible reductions of the seat weight is the change of the cushion design by replacing the original sheet metal construction through the integration of the viscoelastic composite reinforcement (Petru et al. 2012b, c). But this proposed solution brings new problems especially during dynamic loading, arising from car crash. During the crash it is important to ensure a minimal submarine of the passenger into the seat in short time. In the opposite case the passenger body is moved beneath the safety belt, which stresses the pelvic bone. To explain this phenomenon, it can be stated that during a car crash at speed of 50 km/h the weight of a person increases up to 60 times (i.e. the person weighing 80 kg will be stressed by the instantaneous weight 4,800 kg, that is increase of 6,000 %). Kinetic energy is equal to the weight of a person in direct proportion to the square of the speed. Construction restraint system (seat belts) must be damped, as well as the air bag and re-transformed into the seat. Body weight causes a significant deformation during the interaction with the seat not only to comfortable stuffing, but also to the whole construction of the seat (reversible or irreversible). According to EuroNCAP displacement seat construction occurs up to 15 ± 3 cm in the horizontal direction during 0.260 ± 0.036 s depending on the kinetic energy of human body. Because of this reason it is necessary to use an appropriate mechanism allowing immediate prestressing of the viscoelastic reinforcement and preventing the submarine of the human body. TRIZ-based tool—Function-Oriented Search (FOS), which is a part of TRIZplus methodology, has been used for finding of suitable solution. The main idea of this approach is to find an existing technology (product or process) and transfer it to the initial problem, as a solution. Function-Oriented Search (FOS) offers a very effective action principle to solve the initial problem. We also do not need to spend a lot of time and effort proving the effectiveness of this new solution and putting it into practice, because the technology already exists (Litvin 2004). We

decided to use this method because we expected that a product from different branch should be able to do required functions.

2 Materials and Methods

2.1 TRIZplus Tool: Functional-Oriented Search (FOS)

Function-Oriented Search (FOS) is based on the following algorithm: (Litvin 2004).

1. Identify the key problem that restricts the product/process from solving the initial problem.
2. Formulate necessary function(s) for key problem solving.
3. Formulate required functional parameters.
4. Formulate a generalized function.
5. Identify a leading area(s) of industry where such types of functions are vitally important.
6. Find the best experts in the identified leading area.
7. Using professional databases and experts' knowledge, identify candidate technologies.
8. Select the technology(ies) closest to required functional parameters.
9. Formulate a secondary problem(s) that would potentially prevent the selected technology from being immediately implemented to solve the initial problem.
10. Solve that secondary problem(s).
11. Describe a slightly modified existing technology as the solution to the initial problem.
12. Submit necessary data to substantiate the effectiveness of the identified technology, and suggest a practical plan for its implementation.

Instead of the direct problem solving (even with all powerful TRIZ tools), this method states that almost all solutions necessary to solve problems do exist in a form of some specific technology implemented in some engineering area. We should find these best technologies and transfer them to the initial problem. There are two major creative steps in this process—how to:

- find the best technology,
- effectively transfer it to the initial engineering system (Litvin 2004).

One of the main steps of the introduced algorithm it is step 7, where we want to find an existing technology. The system which is focused on the problem/function-defined search in the patent databases is introduced in the patent (Horng and Huang 2010). This system as well as other system uses a semantic approach (Montecchi and Russo 2011).

We reduced FOS algorithm to the following seven steps and used them for solving our initial problem.

1. Identify the key problem that prevents the product from solving the initial problem.
2. Formulate necessary functions for key problem solving.
3. Formulate required functional parameters.
4. Formulate a generalized function.
5. Identify leading areas of industry where such types of functions are vitally important.
6. Using professional databases and experts' knowledge, identify candidate technologies and select one of them. (This step includes consideration of secondary problem(s)).
7. Describe a slightly modified existing technology as the solution to the initial problem and suggest a practical plan for its implementation.

3 Car Seat Innovation

3.1 Theory

The application of a incorporation of the visco-elastic composite reinforcement in the construction of car seat, which would ensure the loading function and possibility to place the comfortable cushion is not so problematic (Petrů 2012; Petru et al. 2012c), much more difficult is to find its control for the appropriate human load. For that purpose, three possible alternatives of the construction design of active adjustable visco-elastic reinforcement were suggested (Fig. 1).

In Fig.1a the scheme of mechanical model of the loaded visco-elastic reinforcement by the force F_{hum} corresponding to human body load is shown. The reinforcement is expressed by the serial connection of the spring—dashpot which corresponds to rheological Maxwell model. The control is performed mechanically or electromechanically by the stretching of the reinforcement. The reinforcement is on one side controlled on the initial stiffness by a rotary or sliding member, that preloaded spring about rotation angle φ and on the opposite side the spring is tensioned by a slide member about the value Δx. The required reaction control force F_R must be in equilibrium with the applied force F_{hum}, which compressed the reinforcement about the value Δy. This follows from the principle of virtual works (**1**).

$$\delta W = \sum_{i=1}^{n} \delta W_i = \sum_{i=1}^{n} F_i \cdot \Delta r_i = 0 \tag{1}$$

where δW is virtual work, F_i is component of the applied force, Δr_i is component of the resulting virtual displacement.

In the model 1b and 1c alternative solutions are given, which use to control the additional mechanisms. The pulley, which is operated by actuator 1b or actuator operated crank mechanism. These systems of active reinforcement allow setting the

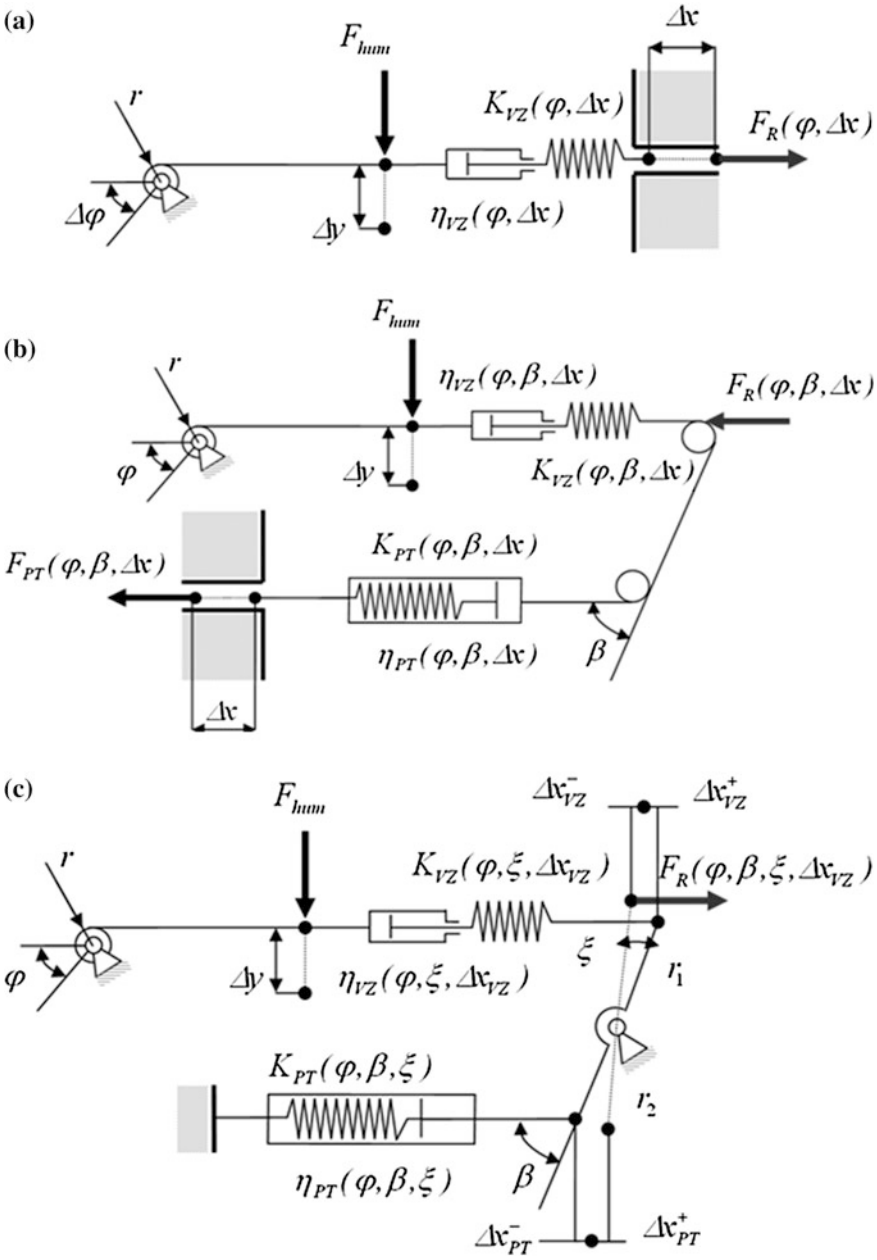

Fig. 1 Design of mechanical models of active adjustable regulation of seat reinforcing

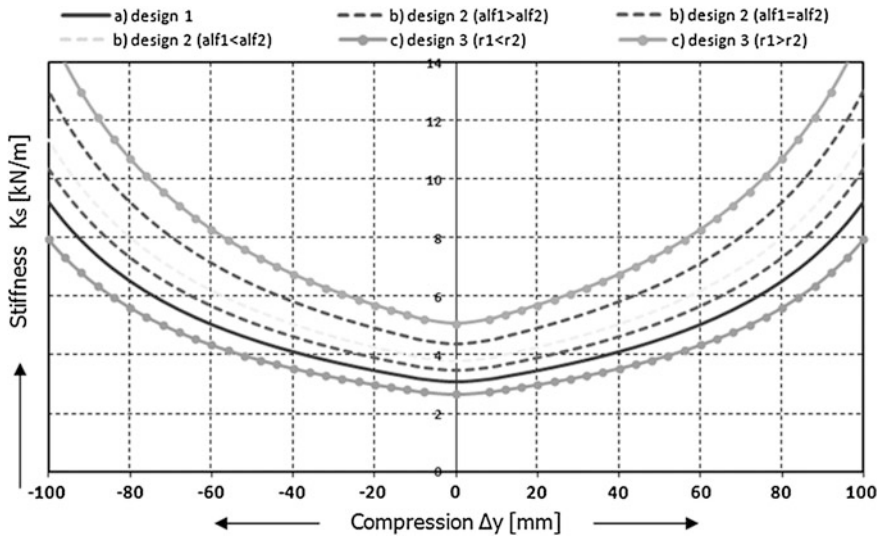

Fig. 2 Resulting courses of dependence of stiffness on compression

seat optimal stiffness in the low resonant frequencies. The results of proposed solutions affecting the total stiffness of the seat are shown in the graph (Fig. 2). Optimal active control of the seat should allow adjusting the stiffness characteristics. From the courses in Fig. 2 it is seen, that these requirements meet the design 3.

It is important, that the elasticity component of visco-elastic reinforcement is not significantly higher than dumping ability, because it can lead to vibrations similar to tensioned string as reported in Petrů (2012), which would be inappropriate for the final. Therefore it is necessary to include the elastic $\varepsilon_{Kvz}(t)$ and viscous component $\varepsilon_{\eta vz}(t)$ for the description of a variable strain rate of reinforcement ε_{KV}. By analogy, in the case of strain rate the situation can be described as (2).

$$\varepsilon_{VZ}(t) = \varepsilon_{Kvz}(t) + \varepsilon_{\eta vz}(t),\ \dot{\varepsilon}_{VZ}(t) = \dot{\varepsilon}_{Kvz}(t) + \dot{\varepsilon}_{\eta vz}(t) \tag{2}$$

Obviously, the elastic force of the reinforcement $F_{Kvz}(t,m) = K_{VZ} \cdot \Delta y(t)$, elastic stress in visco-elastic reinforcement $\sigma_{Kvz}(t,m) = E_{VZ} \cdot \varepsilon(t)$ and also damping force is $F_{\eta vz}(t,m) = \eta_{VZ} \cdot \Delta y(t)$ and therefore the damping stress in the visco-elastic reinforcement is $\sigma_{\eta vz}(t,m) = \eta_{VZ} \cdot \varepsilon(t)$, where E_{VZ} expresses the elasticity modulus. Then the rate of deformation of visco-elastic reinforcement $\dot{\varepsilon}_{VZ}(t)$ is expressed by the Eq. (3). If we introduce $\theta = 1$, $\theta_1 = 1/E_{VZ}$, $\theta_2 = 1/\eta_{VZ}$, then we can express the strain rate of the visco-elastic reinforcement by following parametric Eq. (3).

$$\theta \cdot \dot{\varepsilon}_{VZ}(t) = \theta_1 \cdot \dot{\sigma}_{VZ}(t) + \theta_2 \cdot \sigma_{VZ}(t) \tag{3}$$

where $\sigma_{VZ}(t)$ is total stress in visco-elastic reinforcement, $\dot{\sigma}_{VZ}(t)$ is a total stress rate in visco-elastic reinforcement.

In accordance with the established relations (2 and 3) the principle of virtual work for a contribution of external and internal forces of deformed body (4) can be extended

$$\delta W = \sum_{i=1}^{n} \delta W_{ext} + \sum_{i=1}^{n} \delta W_{\text{int}} = 0 \tag{4}$$

where δW_{ext} is the contribution of external forces, δW_{int} is the contribution of internal forces, while $sign(\delta W_{\text{int}}) = -sign(\delta W_{ext})$.

3.2 The Construction and Design: Identification of Key Problem that Prevents the Product from Solving the Initial Problem

The design of a car seat with improved damping is described below. The essence of the technical solution is the construction which comprises seat reinforcement which is formed by a knitted, woven fabric or another suitable elastic or visco-elastic planar rectangular material. Reinforcement is wound around the cylinder on one side and clamped in the lever mechanism on the other side, allowing the controlled setting of stiffness and damping for a given input frequency. This solution offers not only improved vibro-insulation characteristics of car seats, but also the deflection of elastic or visco-elastic reinforcement will help to reduce the geometric height of the seat. The control of characteristics of the system, such as stiffness and damping, serves adjustable spring with a damping member, by means of a lever mechanism, which pre-stresses the reinforcement to the desired stiffness and damping. Fixation of a Complete designed construction can be fixed directly to the solid parts of the car seat frame. The aim of solution is to allow active control of vibration isolating characteristics based on the weight of the occupant and the dynamic behavior of the vehicle. Another advantage is the possibility of reduction of the thickness of the polyurethane layer, or the possibility to use the cheaper non-polyurethane materials. The technical design is based on the kinematic design vibration isolation solution (Fig. 3), which is determined by the mutual arrangement of the springing and damping elements. They are connected with a lever mechanism to allow a controlled setting of the desired stiffness and damping of the seat, depending on the input impedance. Figure 1 shows kinematic scheme of construction design of the improved car seat damping.

From comparison of origin solution of currently used car seat design with designed solution (Fig. 2) it is evident that main difference consists in the parts on which passenger sits. In the case of original solution these parts is very stiff. If this part is loaded during common usage, the deformation is elastic only and its value is in the millimeters ranges. Even during the crash, the deformation is few millimeters only; of course in this case it is a plastic deformation. On contrary, new solution shows large deformation. The deflection is connected with correct

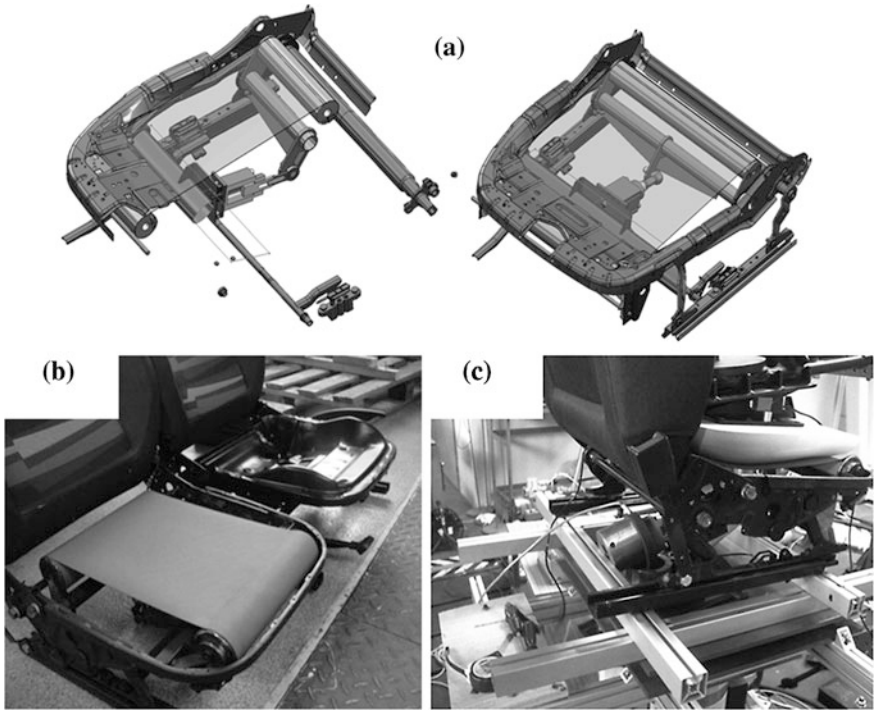

Fig. 3 **a** 3D model of seat construction with visco-elastic reinforcement, **b** real model of the seat with visco-elastic reinforcement without safety system, **c** preparation of experimental measurement with safety mechanism

function. But in the case of the crash the deformation magnitude can be in centimeters. This can lead to effect which is named as a submarine. The submarine effect is defined as tendency of passenger to slide beneath the seatbelt during crash. It can cause serious injury of the pelvic bone or internal organs in abdomen area, because safety belt during crash in improper position. Thus the key problem can be defined as follows: The key problem is the lack of security functions of the seat during impact, which leads to stretching of the reinforcement elastic layer and the submarine of passenger beneath the front seat crossbeam and the slide of safety belt.

3.3 Formulate Necessary Functions for Key Problem Solving

Necessary function: During common usage as standard driving, the reinforcement of the seat must be flexible, deformable and pre-tensioned with low force but during the crash it must be very stiff and pre-tensioned with large force.

3.4 Formulate Required Functional Parameters

The safety system must be added in the damping system of the system. It has to be able to create large momentum in very short time during crash. It preloads the elastic reinforcement to very high pre-stress. The system must be able to respond actively and in advance to a traffic situation with pre-stressing of reinforcement. Its activation must be done by supercritical overload—high deceleration caused by the crash and before the moment when the passenger begins loaded the reinforcement due to inertial force. It means that time of the activation and adaptation must be very short, approximately to 10 ms. The pre-stressing device must developed significantly high force, because it must overcomes the pre-stressing of fabric and load of passenger which is magnified by the acceleration. Also this force has to act until stopping of the car.

Required parameters can be defined as follows:

- activation and achieving of maximal force or momentum must be maximally 10 ms,
- acting force must be approximately 8, 2 kN,
- the force must acts until stopping of the car.

3.5 Formulate a Generalized Function

Generally the system, which can be used, has to meet requirement described in previous point. This system must create very high force on linear or curve trajectory, or very high momentum on the axis of rotating member. It is evident, that acceleration of this system has to operate with very high acceleration, but it must to be very safe during the usage for safety of all occupants in the cabin of the car. Previous characteristic must be met in very short time. The force cannot act for whole time (until the stopping of the car), but there must be system for fixation of the created deformation. The force must act against the direction of forces which acts during the crash.

3.6 Identify Leading Areas of Industry Where Such Types of Functions are Vitally Important

Known usable systems can be found in area of mechanical engineering, especially in the area of safety systems.

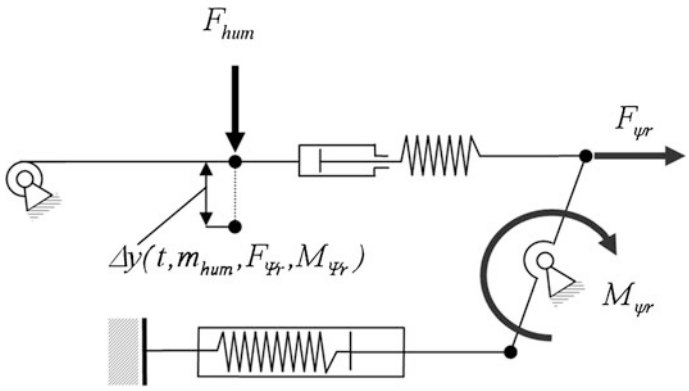

Fig. 4 Kinematic scheme of the actuating reaction forces of damping mechanism with new safety member (Wankel rotor) during the crash

3.7 Using Professional Databases and Experts' Knowledge, Identify Candidate Technologies and Select One of Them

For example lifts use brakes which are activated in the case of faster movement of the lift. In this case the jaws of brakes are pressed to rails which lead the lift. Similar systems are used for quick-brake of rail vehicles. These systems are used in dangerous situations, for example if some obstruction is on the rails. In this case the jaws located on the chassis of vehicles are pressed to rails. For both it is typical that it stops the movement of vehicle or device. But for the intended application the pure breaking system is not satisfactory. There must be some movement going against the forces arising during the crash. The system must act with a force that is in the opposite direction to the force resulting from the loading of reinforcement and its transformation by the damping mechanism of seat. For this purpose the device which overcomes arising action by its force is utilized. Such power can be created for example by the combustion engine with a crankshaft or Wankel rotary piston. It can be powered by fuel injection or compressed gas.

3.8 Describe a Slightly Modified Existing Technology as the Solution to the Initial Problem and Suggest a Practical Plan for its Implementation

Safety mechanism must during maximally 10 ms develop immediate force $F_{\Psi r}$ or moment $M_{\Psi r}$ acting on the lever mechanism. It causes a tensioning of the viscoelastic reinforcement. This prevents submersion of the human body, because the reinforcement deflection Δy is now dependent on the time t, the weight of the human body m_{hum} and the reaction force $F_{\Psi r}$ or moment $M_{\Psi r}$. It is schematically

shown in Fig. 4. Real model of the seat with elastic reinforcement is shown in Fig. 3. Figure 3b shows the experiment, where safety member is applied.

4 Discussion and Conclusion

In the various systems many problems can be found, which are solvable by the help of TRIZ-based tool—FOS method. This method use existing solution applied on problems from different areas. In this case the safety problem of car seat was solved. The solution was found in same area—mechanical engineering, but applied system uses known principle used for different application. As was shown, this method can lead to applicable solution of the problem. Currently the realization of experiment series in the laboratory of Applied Mechanics, Technical University of Liberec is prepared. The experiment will create the real functional sample of the seat with viscoelastic reinforcement including the new safety member for increasing of the safety during crash. The functionality and geometric arrangement of the seat will be subsequently evaluated from tests and measurements.

Acknowledgments The research reported in this paper was supported in part by the Project OP VaVpI Centre for Nanomaterials, Advanced Technologies and Innovation CZ.1.05/2.1.00/01.0005 which has been financed by The Ministry of Industry and Trade of the Czech Republic and Project Development of Research Teams of R&D Projects at the Technical university of Liberec CZ.1.07/2.3.00/30.0024 and the project of CREATex (CZ.1.07/2.2.00/28.0321), which has been financed by European Social Fund and The Ministry of Education, Youth and Sports of the Czech Republic.

References

Caudron JC (2003) Etude du marché du polyuréthane et Etat de l'art de ses techniques de recyclage. Rapport de l'ADEME (Agence de l'Environnement et de la Maîtrise del'Energie), French

Hanel SE, Dartman T, Shishoo R (1997) Measuring methods for comfort rating of seats and beds. Int J Ind Ergon 20:163–172

Horng A, Huang C (2010) Searching method based on a problem/function-defined interface for a patent database system, European patent application, No. 08001335.2

Litvin SS (2004) New TRIZ-based tool—Function-oriented search (FOS). In: ETRIA conference TRIZ future, pp 505–509

Montecchi T, Russo D (2011) FBOS: function/behaviour–oriented search. In: ETRIA conference TRIZ future, pp 165–176

Njeugna N, Schacher L, Adolphe DC, Schaffhauser J, Strehle P (2010) Development of a new 3D nonwoven for automotive trim applications. New trends and developments in automotive industry, Intech, pp 333–346

Petrů M (2012) Car seat with non-polyurethane material. Ph.D. thesis, Technical University of Liberec, pp 131

Petru M, Novak O, Lufinka A (2012) Study and analysis of transmissibility of car seat with non polyurethane material. In: Proceedings of 50th annual conference on experimental stress analysis, pp 321–326

Petru M, Novak O, Doubek M (2012) Seat, especially the driver's seat for cars or working machines. National patent (Czech Republic), No. 303075

Petru M, Novak O, Srb P (2012) Active adjustable system of car seat support for controlled reduction of vibrations. ACC J 18(A). Nat Sci Technol, 77–84

Reduce of Head Injuries During Whiplash Using TRIZ Methodology

P. Lepšík, M. Petrů and O. Novak

Abstract Currently, in the automotive industry great emphasis is put on reducing of the energy consumption of applied materials, weight reducing and performance optimizing. The reason is an environmental protection, sustainable development, reducing of fuel consumption and increasing of vehicle safety. One of the ways how to quickly find a suitable solution is the application of TRIZ method (theory of inventive problem solving). On existing solution is showed, how this method can help with an improvement of car headrest safety. With its help two solutions were designed and implemented. Their verification is done using FEM model. From the results of established models data for calculating the head injury criteria (HIC) factor have been obtained. From these data is clear that the proposed solutions improve the safety of headrest.

Keywords TRIZ · 40 Inventive principles · Technical contradictions · Car seat innovation · Crash · Safety

1 Introduction

Altshuller's matrix of 40 inventive principles for technical contradiction solving (see Fig. 1) is one of the most useful TRIZ tool which can help us to solve technical contradictions. The analysis of thousands of inventions by Altshuller

P. Lepšík (✉) · M. Petrů · O. Novak
Technical University of Liberec, Liberec, Czech Republic
e-mail: petr.lepsik@tul.cz

M. Petrů
e-mail: michal.petru@tul.cz

O. Novak
e-mail: novak.ondra1@seznam.cz

L. Ševčík et al. (eds.), *Modern Methods of Construction Design*,
Lecture Notes in Mechanical Engineering, DOI: 10.1007/978-3-319-05203-8_63,

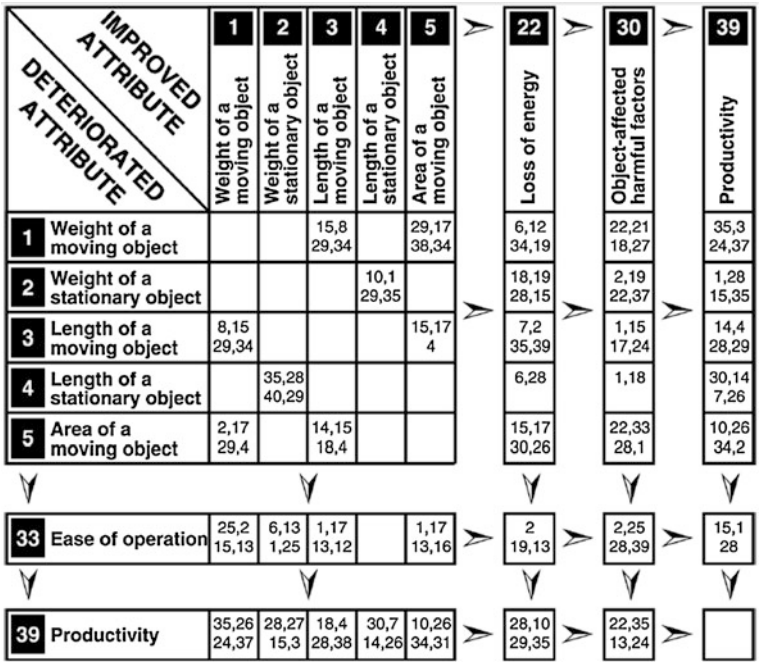

Fig. 1 Altshuller's matrix of 40 inventive principles for technical contradiction solving (Fey and Rivin 2011)

resulted in the formulation of typical system conflicts, such as productivity versus accuracy, reliability versus complexity, shape versus speed, etc. It was discovered that, despite the immense diversity of technological systems and the even greater diversity of inventive challenges, there are only about 1,250 typical system conflicts. Typical conflicts can be overcome by a relatively small number of inventive principles. There are 40 inventive principles for overcoming system conflicts, and each of them may contain a few sub-principles, totalling up to 100 (Fey and Rivin 2011). The inventive principles and typical system conflicts are combined in a system conflict matrix (or the Matrix, for short). The Matrix contains attributes that are the most common for all technological systems (e.g., weight, strength, length, surface area, power, ease of usage, etc.). These attributes are arranged in rows and columns. Suppose there is a need to improve some attribute of the system. If this improvement causes the worsening of another attribute (i.e., a system conflict develops), the intersection of the row and column corresponding to the conflicting attributes will show the potentially useful inventive principles (see Fig. 1) (Fey and Rivin 2011).

The parameter, that should be improved, is parameter 31 (Harmful side effect). If the parameter will be improved by the help of common, known solution, probably an increasing of applied materials occur. It will lead to a worsening of parameter 2 (weight of immobile object).

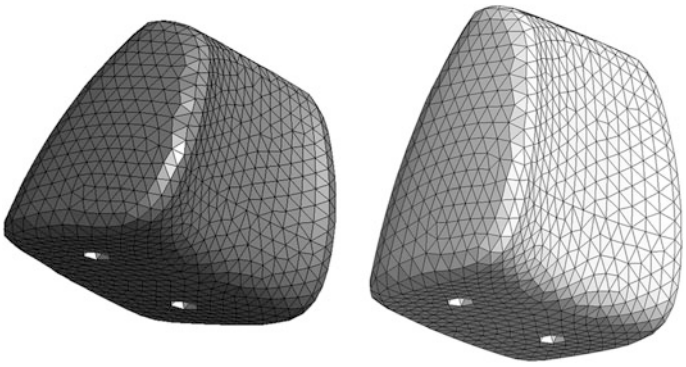

Fig. 2 Geometry of standard and optimized geometry

From the Altshuler′s matrix can be found, that the solution of technical conflict, when the parameter 32 is improved and parameter 2 is worsen, it is possible by invention principles 35, 22, 1, 39 (Cameron 2010; Terninko and Zusman 1998).

2 Materials and Methods

For the car seat innovation two different modifications were applied. Both ways of the modification can be found in the principle 35—"Change concentration or density". If the geometry of a backrest is appropriately changed, desired mechanical properties can be achieved. These changes consist in an increasing/decreasing of the material thickness, which is very important for the process of foam production. It is known that this process provides strongly exothermic reaction. The temperature of arising foam is depending on construction of moulding form and its cooling ability and amount of the foam in mould cavity. These are parameters, which allow changed properties of the foam—especially in the shape and diameter of foam cells. This is because the temperature of the arising foam has an influence on porosity and density of the foam. Thus it can be obtained from chemically same type of foams material with different properties. In the Fig. 2 are shown headrest with standard and optimized geometry.

Second applied principle was "Change degree of flexibility". The innovation of the headrest is based on a material replacement of currently used PU foam with material constructed from fibers which are bonded by elastic dispersion. Fibrous material has more open structure, which secures easy flowing of the air. It is very important, because during the impact the air can escape from the structure and does not create another member with certain stiffness. In the case of PU foam the air cannot escape from the structure immediately and during its compression a total stiffness of this material increases (Table 1).

Table 1 Properties of PU foam and fibrous material

Example 100 × 100 × 50 mm	Density (kg m^{-3})	Young's modulus (MPa)	θ = Vpol/V0 (−)
PU foam	50	31	0.130
Fibrous material	46	18	0.150

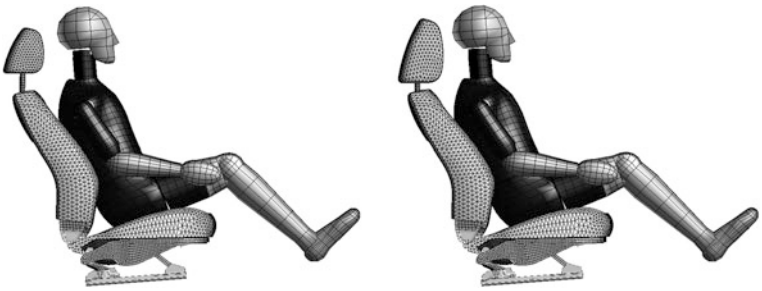

Fig. 3 FEM model of seat with dummy and headrest with standard and optimized geometry

2.1 FEM Model and Evaluation of Results

Results, which are presented, were created in simulation software PAM CRASH. Initial and boundary conditions are same as in real WHIPLASH crash. There are different testing methodologies—EURONCAP, NHTSA etc. and different testing dummies—Hybrid-III, BioRID-II etc. In the simulation was assumed boundary conditions (BC) according to (Safety Companion 2009; IIWPG 2005; Dongkyou 2006). The FEM model of the seat with standard and modified headrest geometry is shown in Fig. 3. These models include characteristics of PU foam headrests, PU foam of the seat, fibrous structure of the headrest and material properties of the dummy. Measure and simulation is described in detail in article (Petrik and Petru 2009; Petru and Petrik 2009; Petru et al. 2011).

An evaluation of headrest safety can be determined by the HIC factor (Head Injury Criteria). That is computed from acceleration of the head during crash to headrest in accordance with Eq. (1).

$$HIC = \left\{ \left[\frac{1}{t_2 - t_1} \int_{t_1}^{t_2} a dt \right]^{2.5} \cdot (t_2 - t_1) \right\}_{MAX} \tag{1}$$

where **t1** and **t2** is the initial and final time (ms) collision interval during which HIC peaks ($t2 - t1 = \Delta T < 36$ ms). These parameters are taken from FEM model results.

Table 2 Results of HIC factor

Simulation	Time t1 (ms)	Time t2 (ms)	A max (g)	HIC (−)
Headrest standard (accept)	50	65	14.21	504.781
Headrest Optimalization	45	60	11.67	429.567
Headrest with fibrous structure	45	60	13.54	498.136

3 Results and Discussion

In the Table 2 the HIC factor for standard and optimized headrest is showed. It is evident that different geometry, which brings different material properties, can affect the safety of the passenger. The value of HIC factor decreases about 15 %. In the case of comparison of PU foam with fibrous structure was applied denser and stiffer material that is why value of HIC factor is higher compare to previous case. The improvement of HIC was about 15 % too. Results showed that acceleration of head is influenced especially by a distance of the head from the headrest and stiffness of material. In the case of optimized geometry and fibrous material the acceleration can be reduced and resulting HIC factor will achieved values, which are acceptable.

4 Conclusions

This article deals with problem of car headrest safety. By the help of TRIZ method were found possible solutions. First solution changes geometry, which lead to a change of chemical reaction. It results in different material properties. Second solution use different material for a produce of headrest. For comparison of current solution with new one, the FEM model of complete car seat with dummy was established. All material properties and boundary conditions are taken from real experiments. The evaluation of proposed solutions is done by the help of HIC factor. From results is evident that suitable choose of geometrical and material properties can lead to improvement of HIC factor and safety of occupants. It can be concluded that TRIZ method is suitable tool for finding of appropriate solutions and can be applied for improving of headrest from point of view of occupant safety.

Acknowledgments The research reported in this paper was supported in part by the Project OP VaVpI Centre for Nanomaterials, Advanced Technologies and Innovation CZ.1.05/2.1.00/01.0005 which has been financed by The Ministry of Industry and Trade of the Czech Republic and Project Development of Research Teams of R&D Projects at the Technical university of Liberec CZ.1.07/2.3.00/30.0024 and the project of CREATex (CZ.1.07/2.2.00/28.0321), which has been financed by European Social Fund and The Ministry of Education, Youth and Sports of the Czech Republic.

References

Cameron G (2010) TRIZICS Teach yourself TRIZ, how to invent, innovate and solve impossible technical problems systematically. CreateSpace

Dongkyou P (2006) A study on the analysis technique for whiplash performance. KSAE paper KSAE06-S0184

Fey V, Rivin EI (2011) Innovation on demand new product development using TRIZ. Cambridge University Press, Cambridge

IIWPG Protocol for the Dynamic Testing of Motor Vehicle Seats for Neck Injury Prevention, Version 1.5, International Insurance Whiplash Prevention Group, January 4, 2005

Petrik J, Petru M (2009) Simulation of the transmissibility of the non-linear materials. In: Proceedings of the 8th international conference VIBROENGINEERING 2009, Klaipeda, Lietuva, ISSN 1822-1622

Petru M, Novak O, Prasil L (2011) Reduce of head Injuries during Whiplash by the help of materials with independent strain rate. In: Fifth international whiplash trauma congress, ISSN 1650-1969

Petru M, Petrik J (2009) Systems to optimize comfort and developments of car seats, acta technica corviniensis—Bulletin of engineering, ANNALS of faculty engineering Hunedoara Romania. Int J of Eng—fascicule 4 2009, ISSN 1584-2665

Safety Companion (2009) www.carhs.de

Terninko J, Zusman A, Zlotin B (1998) Systematic innovation an introduction to TRIZ. CRC Press, Boca Raton

Innovation of the Control System for Hydraulic Power Units

A. Lufinka

Abstract New hydraulic piping was built in the laboratory of applied mechanics. The arrangement of hydraulic circuits and new concept operator's station required a change of the control system for hydraulic power units. Ensuring of operational safety was the main criterion in the new design of the control system. Power units can not be started when their parameters are set incorrectly and they will be automatically stopped when limit values are exceeded. All status information is displayed on the operator's screen and from this station all power units can be controlled by software applications.

Keywords Hydraulic power unit · Control system · Safety system · Remote control

1 Introduction

New hydraulic circuit in the laboratory of applied mechanics supplies pressurized hydraulic oil to each testing machine. Its block diagram is shown in Fig. 1.

Testing machines are divided into two groups so the hydraulic circuit has two separated pressure hydraulic branches. Return pipe is common to both branches and the oil cooler is included in it. If the oil temperature reaches the maximum operating value, servo valve will be opened and returning oil will be cooled by the water flow. Two hydraulic power units for getting of pressure energy are connected to the central oil tank. Because each one has a different power each one can be connected by manually valves to both branches of the hydraulic circuit (Krátký 2012). If needed in the future, the hydraulic circuit can be extended by third hydraulic power unit.

A. Lufinka (✉)
Technical University of Liberec, Liberec, Czech Republic
e-mail: ales.lufinka@tul.cz

L. Ševčík et al. (eds.), *Modern Methods of Construction Design*,
Lecture Notes in Mechanical Engineering, DOI: 10.1007/978-3-319-05203-8_64,

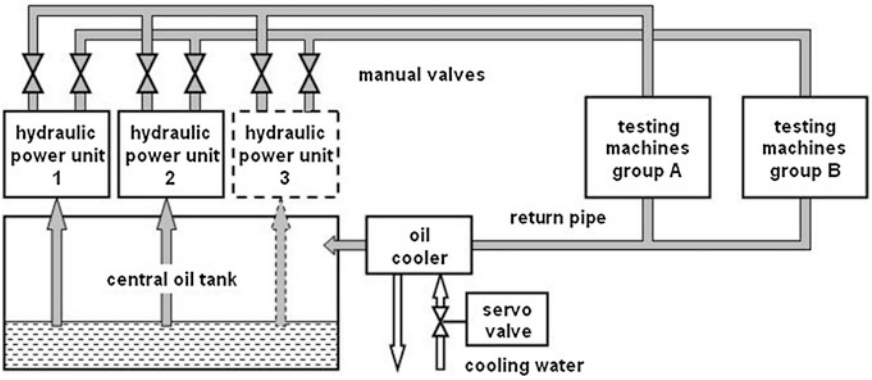

Fig. 1 Block diagram of the hydraulic circuit in the laboratory

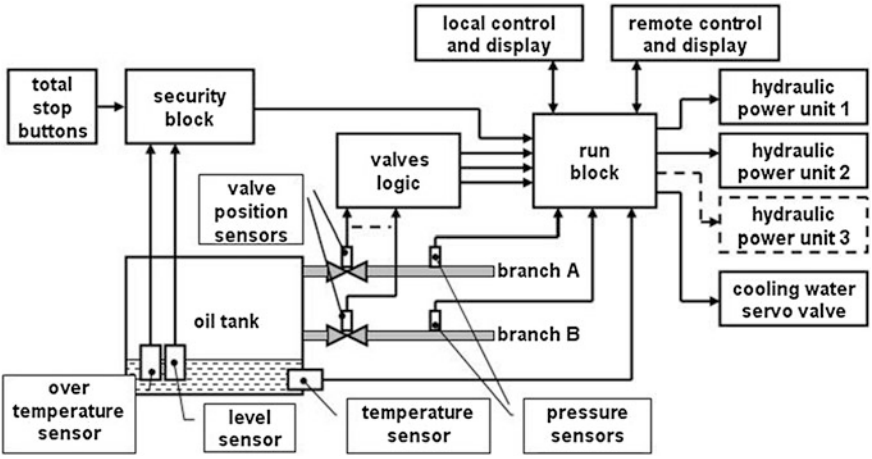

Fig. 2 Block diagram of the control system

Because the previous hydraulic system in the old laboratory had only one branch and the cooling system was also different this new solution required upgrade of the control system.

2 Control System

New control system processes three categories of requirements. Highest priority is given to the security. All hydraulic power units have to be immediately stopped automatically in case of any danger situation. The valves logic is the second part of the control system. It prevents starting of power units in poor opening combination

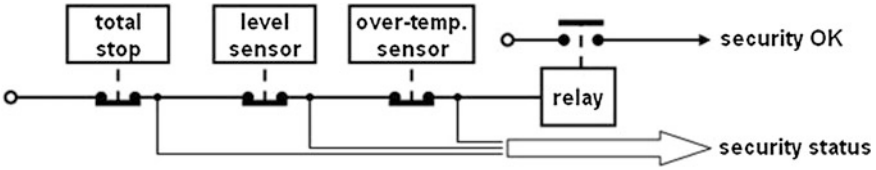

Fig. 3 Block diagram of the security block

of manual valves. The last part controls standard operations during running. It includes local or remote start of power units, local and remote operating status display and a control of cooling water servo valve according to oil temperature (Ďad'o and Kreidel 1996). Block diagram of the control system is shown in Fig. 2.

2.1 Security Block

The hydraulic system has three critical security conditions. They are low oil level in the central tank, over-temperature oil and activation of total stop buttons. Level and over-temperature sensors are placed in the central oil tank. Their outputs are simple contacts and because total-stop buttons also have contact output the security circuit is relatively simple. It consists of series of connected contacts of all security elements and a security relay (see Fig. 3). Signal from the relay contact is connected to the run block as a necessary condition for all running power units. Status of all security elements is connected to the run block for its displaying, too. If any element is activated, its contact is opened, the relay contact is switched off and all running units are stopped.

2.2 Valves Logic

Hydraulic power units are connected to the hydraulic system by manual valves. So the power units must not be started when these valves are in poor opening combination. Disabled combinations are: more units are connected to one branch and both valves by one unit are closed.

The valves logic is designed for three power units to suit the planned expansion of the hydraulic system. Each manual valve has a position sensor for its opening detection and signals from these sensors are evaluated by the valves logic (see Fig. 4).

Valves logic is built from standard CMOS chips OR, XOR and AND (Electronical Components Datasheets 2013), witch evaluate valves opening combination (function OR for "unit valves logic" and XOR for "branch logic". If start of some power unit is possible, the corresponding output signal "start enabled" is

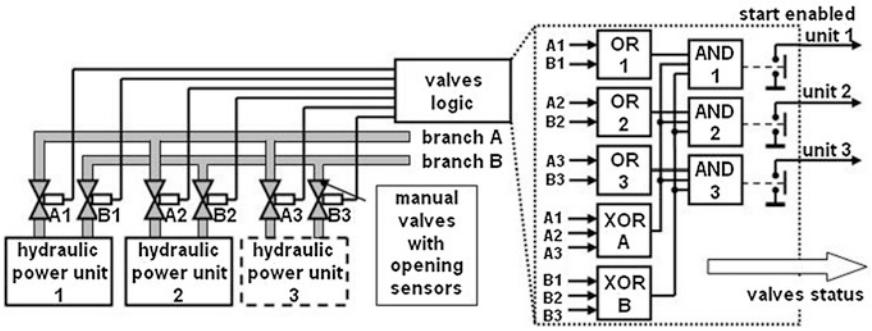

Fig. 4 Valves logic

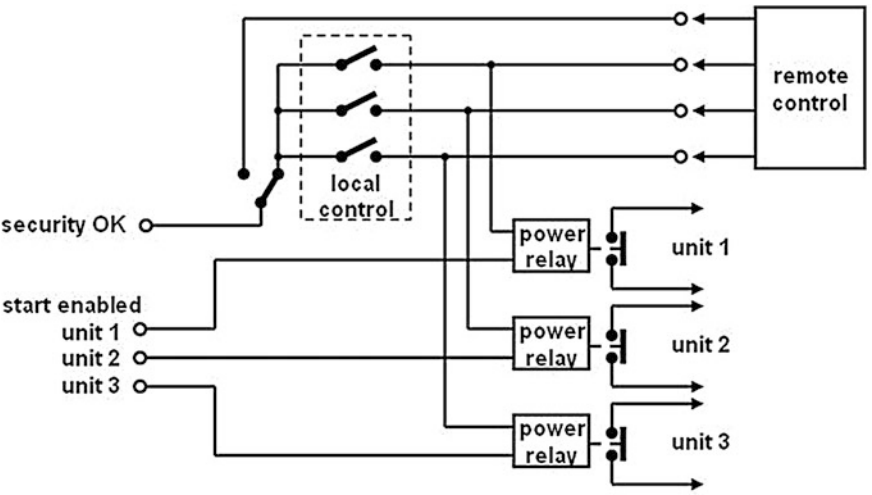

Fig. 5 Block diagram of the controlling power unit in the run block

grounded. This signal is connected to the next run block as a necessary condition for unit starting. Status of all valve positions is connected to the run block for its displaying, too.

2.3 Run Block

This block has three basic functions, local or remote start of power units, display all status information and cooling water servo valve control.

All power units can be started by manual switches in the electrical case on the central oil tank. If the first switch is set to "local control" and start conditions from

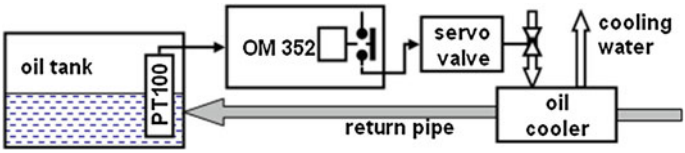

Fig. 6 Block diagram of the cooling water servo valve controlling in the run block

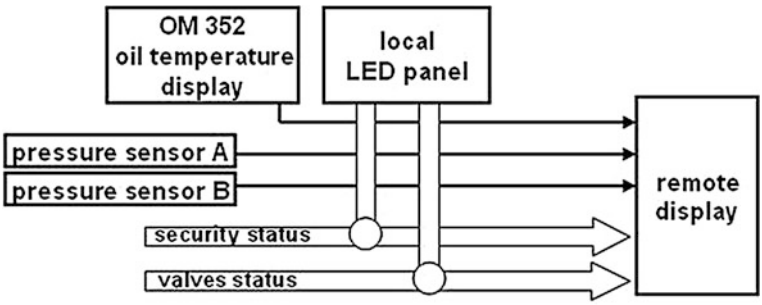

Fig. 7 Principle of the information display

security block and valves logic are complied, a hydraulic power unit can be started by corresponding switch and power relay (see Fig. 5).

If the first switch is set to "remote control", local switches are disabled and all power units are controlled by the remote control from an operator station. Remote control is realized as a software application on the operator's computer. Details are in the following chapter.

Oil temperature is measured by PT100 sensor in the central oil tank. The sensor is connected to the industrial controller OM352 that displays actual oil temperature and compares it with preset temperature value. If oil temperature reaches this value, output relay is switched on, servo valve of cooling water is opened and returning oil is cooled in the water cooler. It is shown in Fig. 6.

All status information is binary so it is displayed by two-colors LED on the local panel at the electrical case and it is connected to the remote status display, too. This display is realized similarly as the remote control by a software application on the operator's computer. Three analog signals (oil temperature and two pressures from branches A and B) are connected to the remote display (see Fig. 7).

3 Remote Control

All hydraulic power units are placed in a special soundproofed room. So their local control is very impractical for normal using during work in the laboratory. Thus a remote control system was created for their controlling from the operator station. The same applies to the display status information.

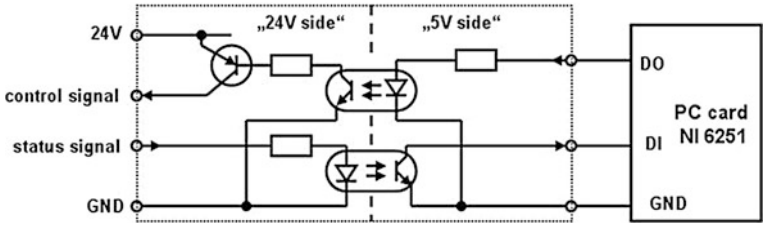

Fig. 8 Principle of the input and output level converter

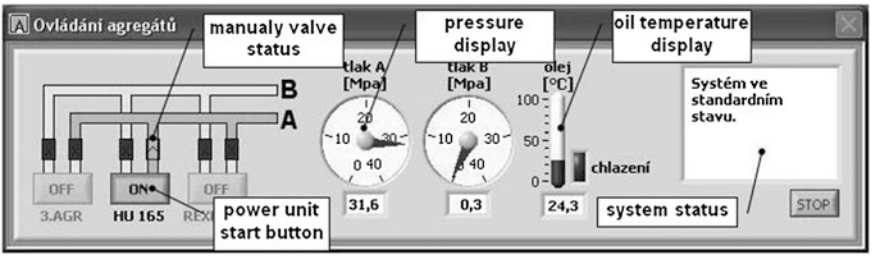

Fig. 9 Software for the remote control

Three control signals are needed for power units controlling, status information has sixteen signals, so remote control must have three logical outputs and sixteen logical inputs. Three analog inputs are needed for temperature and pressures signals. The IO card NI PCI 6251 from National Instruments was added to the computer. This card has 24 logical IO and 16 analog inputs and it is sufficient number for the remote control and display realization. Because all the logical statuses and control signals from electrical case have industrial 24 V level and computer card works with standard TTL level (5 V) a level converter had to be used for all these signals. This converter is designed from optocouplers (see Fig. 8) and it also serves as a galvanic separation of signals, which is very good for protection of the card inputs.

Analog temperature signal is galvanicly separated in OM352 device so it can be connected directly to the analog input of PC card. Signals from both pressure sensors are connected to analog inputs, too. Their galvanic separation is not necessary because these signals are connected only to this card.

3.1 Remote Control Software

Software application for the remote control is written in Labview (2003). It is produced by National Instruments as the used PC card so the card control is in Labview software very simple.

The application window is small, simple and neatly arranged. In the left side there are shown positions of all manually valves and start buttons. Button for power unit start is enabled only when its start is possible, it depends on results of valve logic. Running power unit and pressurized hydraulic branch are highlighted by green color and information about oil pressure and temperature are displayed in the middle of the window. Generally status information and warnings are displayed in the status box in the right side of the window. The application window is shown in Fig. 9.

4 Conclusion

Control and security of a new hydraulic system has been completely solved by building of the new control system. Power units cannot be run when valves opening combination is wrong and all units are automatically stopped after crossing the limits. Remote control and displaying of all the information on the operator's screen is very comfortable. The operator has always a complete overview of the hydraulic system status and this contributes to greater safety of work in the laboratory.

References

Ďad'o S, Kreidel M (1996) Senzory a měřicí obvody, ČVUT Praha
Electronical components datasheets (2013) http://www.alldatasheet.com/datasheet-pdf/pdf/8172/NSC/CD4001.html
LabVIEW 7 (2003) Express user manual, National Instruments Corporation
Krátký M (2012) Hydraulic systems technical documentation, Inova Praha s.r.o

Part V
Optimization and Design

L. Bartoň, P. Brabec, C. Scholz, R. Voženílek, Z. Folta, M. Hrudičková, R. Kovář, D. Vejrych, M. Petrů, L. Ševčík, I. Mašín, P. Lepšík, A. Lufinka, O. Novak, J. Popelka, F. Starý, J. Mrázek, P. Kříbala, J. Kamenický, M. Vereš, M. Kanović and M. Rackov

A problem of an individual part or assembly optimization, and complete construction is an integral part of developers, researchers, and engineers in the prototype and production phase of the product. It is a complex problem that is developed similarly as the final product. It uses mathematical and numerical analysis associated with the study of extreme minimizing (geometry, strength, flexibility, weight, fatigue), but there are also technological and economic limitations (manufacturability, total operating, and energy performance). The use of the modern software has led to the development of methods of supporting the search for optimal solutions based on optional criteria (cost, manufacturability). The parameters and criteria for optimization of the design must be always used and several times modified and verified, because during the development they are changed. Authors in Part V—*Optimization and Design* describe some possible solutions of selected problems of the optimization of components and their assemblies, where simulations are applied to assess the deformation and stress analysis, or other problems of machine mechanics.

A Mechanically Skimmed Screen

L. Bartoň

Abstract This paper deals with the renovation of a mechanically skimmed screen at the supply station on Hnevkovice dam. The paper resolves the combination of new parts and old renovated parts. A new chain gearing is designed. The new concept is dismountable and its placement of bearings is different.

Keywords Mechanically skimmed screen · Chain gearing

1 Introduction

A mechanically skimmed screen at the supply station on Hnevkovice dam cleans solid dirt from a grating at the beginning of the culvert to the supply station. The solid dirt is dragged up from the water to a waste container. The culvert is situated 13 meters underground. The whole mechanically skimmed screen, without engine or gearbox, is made from over 2,500 parts. It includes 13 meter-long girders and few millimeter-long bolts also.

The assembly is shown in Fig. 1. The screen is assembled from a fixed frame (1), which is fixed in the concrete on the ground. On the fixed frame is mounted a stretcher (2) and on the expender is mounted a guide frame (3) at one end and the rest of the body is supported loosely on the oblique wall of the culvert pit. The guide frame has two guide lines on each side. The guide lines are for guiding the pulley on the squeegee (4). Overall ten squeegees are connected by two 32.5 meter-long chains (5). In the bottom section of the guide frame is situated a chain gearing (6). On the fixed frame is placed the engine and gearbox (7), motive chain

L. Bartoň (✉)
University of West Bohemia, Pilsen, Czech Republic
e-mail: bartonlk@kks.zcu.cz

L. Ševčík et al. (eds.), *Modern Methods of Construction Design*,
Lecture Notes in Mechanical Engineering, DOI: 10.1007/978-3-319-05203-8_65,

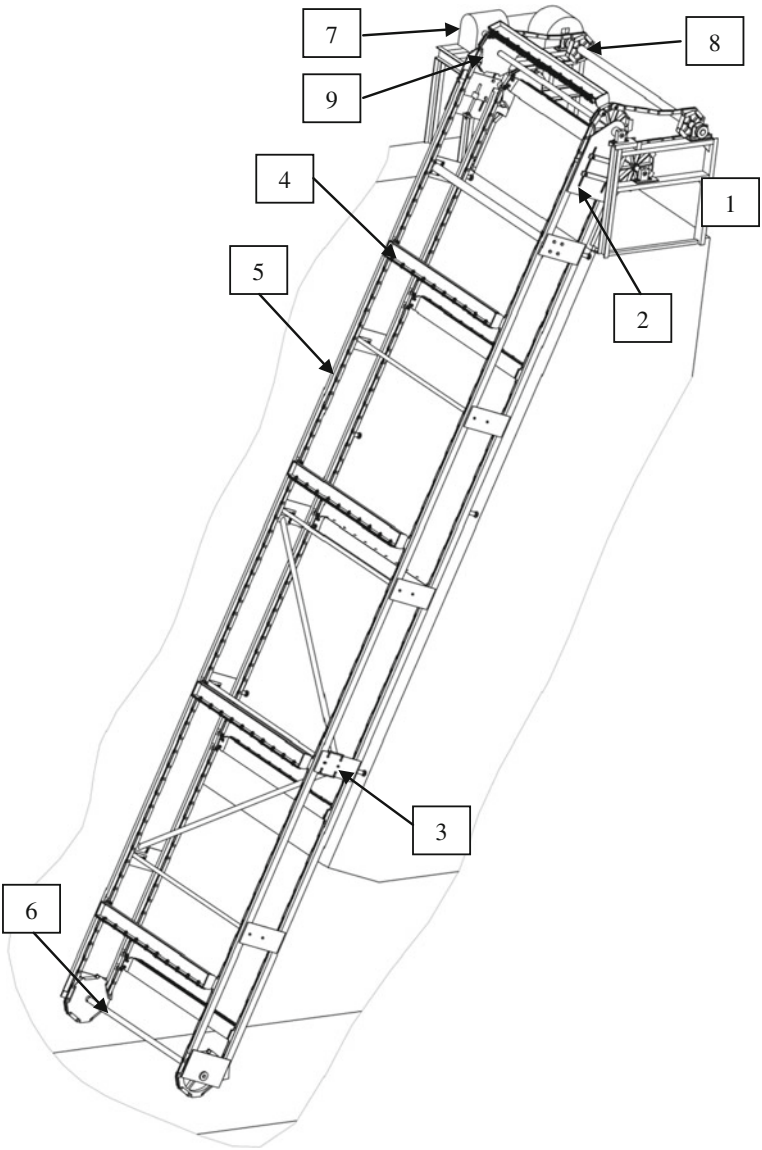

Fig. 1 The mechanically skimmed screen assembly

gearing (8) and four guide chain gears (9). The stretcher stretches the chain in case of slack. The tension in the chain is made by shifting the whole guide frame. This means by shifting the bottom chain gearing, which does not have a specific position but it moves within a certain range.

Fig. 2 The original condition

The mechanically skimmed screen was in operation until 2010. After that it was no longer used because it was defunct. Repair and renovation was necessary. The parts which were under water had to be replaced and the parts which were above water had to be repaired. It was also necessary to remove any operational defects.

2 The Operational Defect

The operational defect is the offset of the squeegee. Figure 2 shows the offset of the squeegee. It has a bad influence on the guiding pulleys in the guide lines. In case of bigger offset the pulley may become derailed and the whole device fail. It also has a negative influence on the efficiency of cleaning the water.

There were two causes for the offset of the squeegees. The first cause was asymmetrical extension of the chains. Some parts of the chain were several millimeters longer than others. The second and main cause was asynchronous rotation of the bottom chain gears. The chain gears were loosely mounted on the bottom shaft. The plain bearings worked in an aggressive environment under water in mud. During the years of operation the bearings were destroyed. The cogs of the shaft were asymmetrically worn and they were no longer cylindrical. There was dirt in the bearing which caused resistance against movement. Unfortunately the resistance was different for each bearing. When one gear had a bigger resistance than the other, it caused different rotation of gears. This had a bad effect on the offset of the squeegees.

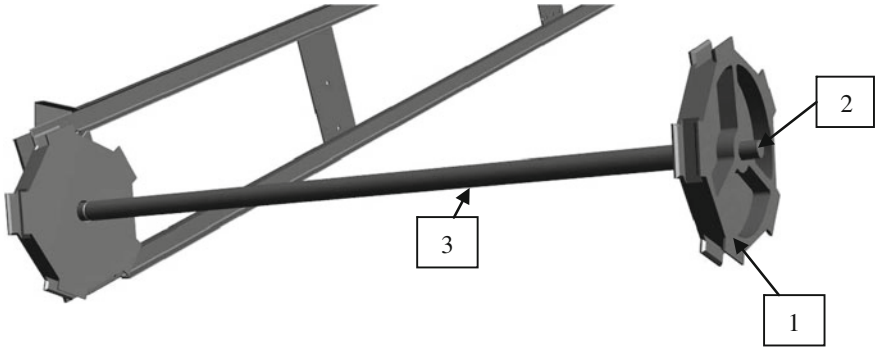

Fig. 3 The new chain gearing

3 New Concepts

It is necessary to design the gearing as one rigid unit. This eliminates the operating defect. The gears are synchronous and chains are also guided synchronously. The design is shown in Fig. 3.

The new chain gearing is made as a weldment. It is an assembly from three parts. The first part is the chain gear (1) which is welded to a through spine (2). The spine is welded to a spacing tube (3). The chain gear and spine are welded on the other side of the tube at the same angle. The plain bearing is no longer overmolded to the gear, it is part of the guide frame. The bearing is bronze with graphite nests, which should be suitable for application under water. The original gears were made as a cast. The new gears are made from sheet metal, making it possible to weld them on to the spine firmly.

4 Ease of Assembly

When assembling the whole machine, it is necessary to first take the guide lines and put the chain gearing between them. Next, the guide lines are connected by a brace which makes the guide frame one rigid unit. This guide frame is placed in the pit by a crane and mounted on the fixed frame. After that the chain is mounted. The prospective life cycle of the device is about ten years with proper maintenance. To change the bearing it is necessary to unmount the whole guide frame. This problem will be solved for the reconstruction of the second mechanically skimmed screen which should be renovated in 2013.

The first option is to make a removable bearing on one side of the guide frame. The bearing has to be removable towards the inside because the guide frame fills almost the whole width of the pit. There is no space between the frame and the wall. This solution is difficult for construction. It is expensive and difficult for

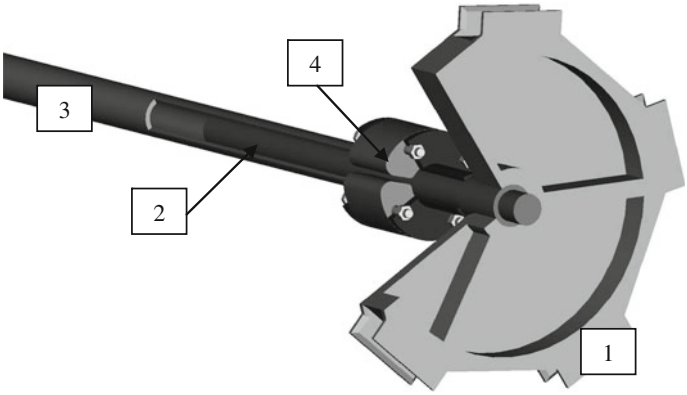

Fig. 4 The designed curtailment mechanism

manipulation. The better solution is to break the spacing tube and to add a shortening mechanism. Shortening the spacing tube makes the gearing removable. When the gearing is removed the bearing can be changed.

The shortening mechanism must guarantee:

- possibility of shortening the spacing tube by about 200 millimeters which makes it removable
- strength in bending and torsion
- rigidity which secures the alignment of the chain gears
- resistance to aggressive environment such as mud, dirt and garbage
- it must not block the movement of squeegees.

The shortening mechanism should guarantee:

- possibility to set up pitch of chain gears—thus making it possible to compensate pitch for any welding inaccuracy.
- easy design which reduces costs.

The designed shortening mechanism as a part of the gearing is shown in Fig. 4.

One spine (2) is inserted into the spacing tube (3), providing rigidity and alignment of gears (1). There are two flanges. One is welded on the spine and the other is welded on the spacing tube. Spacers are inserted (4) between the flanges. These spacers are cut lengthwise which enables their removal. The flanges are connected by four screws which go through the spacers. When the screws and the spacers are removed the spine can be inserted deeper into the spacing tube and the pitch between the chain gears is shorter. The whole gearing can be removed from the bearings. The length of the spacers defines the accurate pitch of the chain gears. Any welding inaccuracy can be compensated by these spacers.

5 Conclusions

The screen was renovated in autumn 2012. A new concept of chain gearing without a dismounting mechanism was used. The device has been operating with no problems for a half year now. The new concept with the dismounting mechanism is registered with utility model number 287 492.

Effect of the Piston Pin Stiffness on the Deformation of the Piston Skirt

P. Brabec, C. Scholz and R. Voženílek

Abstract The present contribution is concerned with the problems of the deformation of the piston skirt due to the power load caused by the pressure of gases, eventually, by the inertial masses. This deformation is influenced considerably by the choice of the dimensions of the piston pin. The deformation has been calculated by means of the finite elements method. The main purpose of the present article is to show the connections between the ovalisation of the piston pin and the specific deformation of the piston skirt. This deformation, which brings about a partial jamming of the piston as a rule, can be eliminated either in the manufacture (employing a negative oval at a certain point of the skirt) or by the design of the piston pin.

Keywords Ovalisation of the piston pin · Deformation of the piston skirt · Finite elements method (FEM)

1 Introduction

The piston pin is the connecting link transferring the forces between the piston and the connecting rod. These forces, generated by the action of the pressures in the cylinder and by the effects of the inertial masses of the piston, stress and deform it. The calculation of the strength of the piston pin is of a secondary

P. Brabec (✉) · C. Scholz · R. Voženílek
Technical University of Liberec, Liberec, Czech Republic
e-mail: pavel.brabec@tul.cz

C. Scholz
e-mail: celestyn.scholz@tul.cz

R. Voženílek
e-mail: robert.vozenilek@tul.cz

L. Ševčík et al. (eds.), *Modern Methods of Construction Design*,
Lecture Notes in Mechanical Engineering, DOI: 10.1007/978-3-319-05203-8_66,

importance usually, because with the dimensions chosen properly, high multiples of the safety limits are achieved as a rule. For the proper function, there is decisive the calculation of the deformations of the piston pin in dependence upon its seating in the piston. A poorly dimensioned piston pin can bring about cracks in the upper section of the boss for the piston pin, leading to a damage of the piston as a consequence; in particular, during the period after the start of the engine immediately, when the piston is not heated sufficiently yet, the peak pressures, combined with a small play of the piston pin in the boss, can bring about high loads upon the same. Once the piston has been heated, the play increases, and the effect of the ovalisation of the piston pin upon the stress in the boss decreases. Henceforth, the solution is a rigid piston pin seated in flexible bosses of the piston; however, this solution can be applied to a limited degree only, owing to the contradictory requirement of low masses to be displaced. The problems of the stress upon the strength of the piston due to the deformations of the piston pin (in the bending and in the ovalisation) have been given a wide publicity (Basshuysen and Schäfer 2002). Due to our experience of engine specialists, we are aware that a wrong choice of the dimensions of the piston pin, causing a high ovalisation, can bring about deformations of the piston skirt with subsequent partial jamming. This experience, known as the "squaring of the piston", is hardly mentioned in the publications, and therefore, it is the topic of our contribution.

For the comparison of the results obtained by us employing the finite elements method in the ovalisation of the piston pin, we have chosen the simplified method recommended by the firm Kolbenschmidt (Scholz 2003). The ovalisation of the piston pin Δd means the increase of its diameter in the direction vertical to the load F. Equations for the calculation of the ovalisation according to the Kolbenschmidt method: (Fig. 1)

Ovalisation of the piston pin:

$$\Delta d = \frac{1}{12} \cdot \frac{F \cdot r_m^3}{E \cdot J_0} \tag{1}$$

Mean radius of the pin:

$$r_m = \frac{d_a + d}{4} \tag{2}$$

Ovalisation moment of inertia:

$$J_0 = \frac{l}{96} \cdot (d_a - d)^3 \tag{3}$$

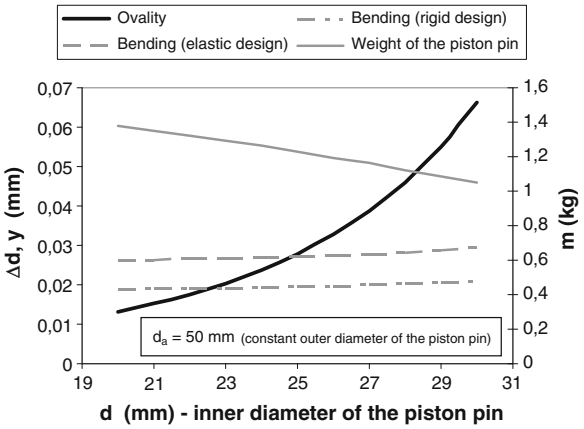

Fig. 1 Ovalisation of the piston pin at a constant outer diameter of the piston pin (the Kolbenschmidt method)

2 Creation of the Model

The calculation has been effected employing the finite elements method in the environment of the software ProMECHANICA. In the quality of the model, there has been chosen an assembly consisting of the piston, the piston pin and the connecting rod at the position of the upper dead centre of the engine. Because of the symmetry, one quarter of this assembly has been modelled only, employing marginal conditions of the symmetry, and averting displacements in the direction of the cylinder axis in the bottom section of the connecting rod.

Both for the piston pin and the connecting rod, material characteristics of the steel have been given, and the piston has been of aluminium alloy. Moreover, this assembly has been loaded with the combustion pressure of 14 MPa, acting upon the head of the piston (Table. 1).

Two influencing factors have been considered, namely the effect of the play between the piston pin and the piston (immediately after the start of the engine, and when the piston has been heated to the operating temperature), and the effect of the size of the inner diameter of the piston pin. There have been calculated three variants of the piston pin, with the inner diameters d = 21, 25, 29 mm. For these variants, there has been chosen the play between the piston and the piston pin after heating of 0.04 mm. Moreover, there has been calculated a variant with the inner diameter of the piston pin d = 25 mm, employing a play between the piston and the piston pin of 0.01 mm, simulating the condition immediately after the start of the engine.

Table 1 Material characteristics of the model and its dimensions

Component	Material	Young module (MPa)	Poisson number (−)	Spec. weight ρ (kg/m^3)	Dimension	Size (mm)
Piston	Al-alloy	68,940	0.3	2,710	d_a	50
Piston pin	Steel	199,900	0.27	7,830	d	21, 25, 29
Connecting rod	Steel	199,900	0.27	7,830	D	130
					l	107
					B	48

d_a outer diameter of the piston pin
d inner diameter of the piston pin
D bore
l length of the piston pin
B width of the connecting rod

3 Comparison of the Calculated Values

In the following table, we see the values of the ovalisation of the piston pin calculated by the Kolbenschmidt method and the finite elements method. The resulting deformation of the piston skirt is characterised in an analogous way, by the form of ovalisation in three planes.

The table shows well the conformity of the maximum values of the ovalisation of the piston pin obtained by different calculating methods. The finite elements method allows to follow the courses of the deformations in different planes and points. Moreover, it is possible to compare the effect of the size of the inner diameter of the piston pin upon the magnitude of the ovalisation, and in order to have a complex idea, upon its bending deflection as well.

The effect of the play between the piston pin and the piston, which changes depending upon the heating (the operating condition) of the engine, is patent, too. With the diminishing play, the ovalisation of the piston pin is smaller, however, the deformation of the piston skirt increases, which is evident from the comparison of the variants (b) and (d) in the Fig. 2.

The Fig. 2 shows the courses of the deformations, showing well the considerable influence of the not yet heated piston upon the increase of the ovalisation in the plane under the angle 45°. This influence is more important than the increase of the inner diameter of the piston pin by 4 mm (Hrubín 2013).

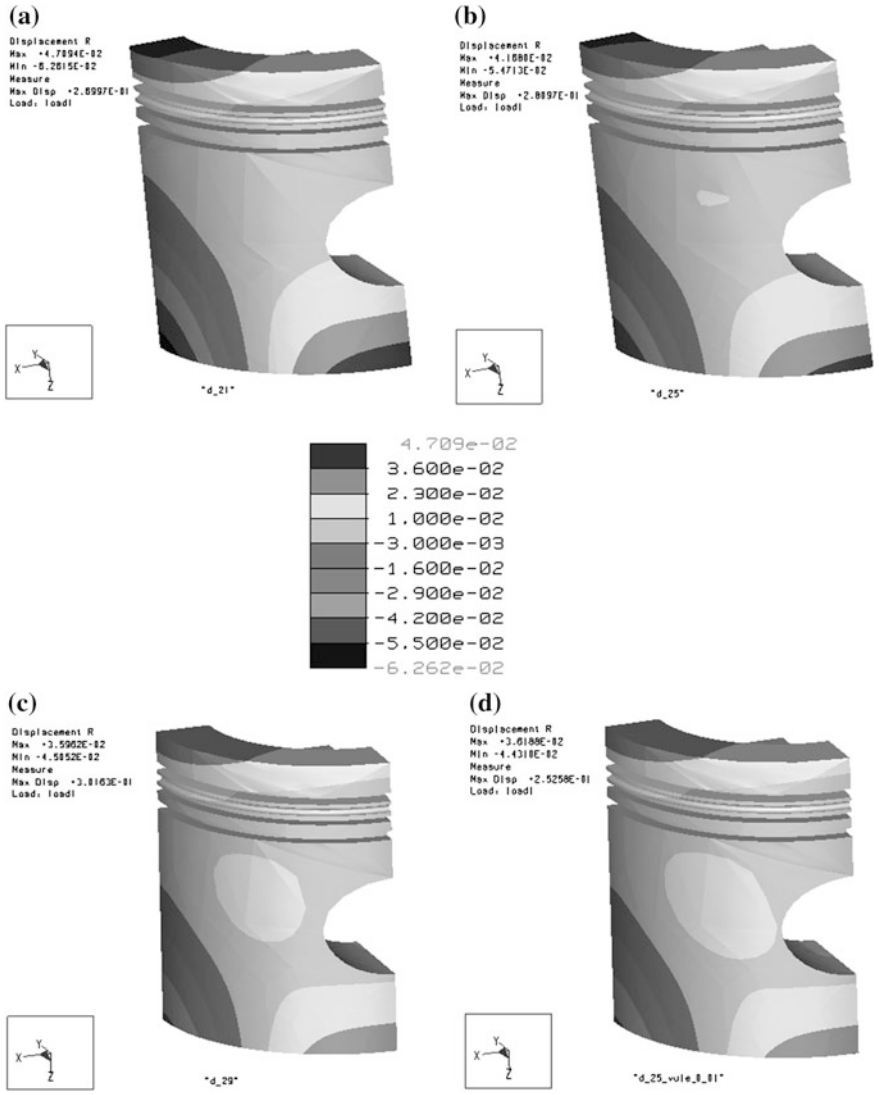

Fig. 2 Deformation of the piston skirt (change of the radius R) (**a**) d = 21 mm, (**b**) d = 25 mm, (**c**) d = 29 mm, (**d**) d = 25 mm after the start (play between the piston pin and the piston 0.01 mm)

Table 2 Calculated values

Kolbenschmidt method			Finite elements method				
Ovalisation of piston pin Δd (mm)			Max. ovalisation of piston pin Δd (mm)		Max. ovalisation of piston skirt ΔD (mm)		
			Outer diameter	Inner diameter	A	B	C
Play 0.04 mm	$d = 21$ mm	0.016	0.017	0.018	0.094	−0.125	0.012
	$d = 25$ mm	0.029	0.026	0.028	0.083	−0.109	0.016
	$d = 29$ mm	0.058	0.043	0.044	0.072	−0.090	0.022
Play 0.01 mm	$d = 25$ mm		0.020	0.022	0.072	−0.089	0.026

A in the plane of the piston pin
B vertically to the piston pin
C in the plane under the angle 45°

4 Conclusions

The contribution describes the procedure employed to create the model, the choice of the marginal conditions and the loading. The purpose has been to ascertain the magnitude and the position of the maximum deformation of the piston skirt, depending upon the choice of the inner diameter (alleviation) of the piston pin, and depending upon the play between the piston pin and the piston. This deformation can bring about even a partial jamming; henceforth, its investigation is very important for the proper function of the engine. From the Table 2, we can see that the magnitude of the ovalisation of the piston pin calculated by the Kolbenschmidt method draws near to the values calculated by means of the finite elements method. A more significant difference has been ascertained with the piston pin with a maximum alleviation (inner diameter d = 29 mm).

The maximum positive ovalisation of the piston skirt has been found in the point I, namely $\Delta D = 0.072 \div 0.094$ mm. With the real piston, this area is corrected by means of a manufacturing oval, or with the modern pistons, it does

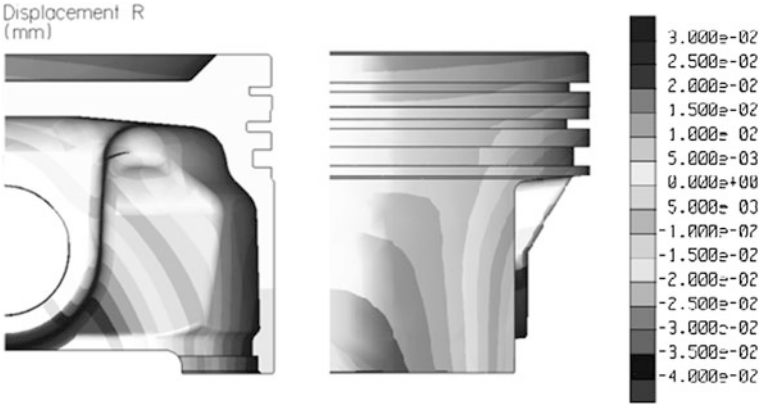

Fig. 3 Sample calculated displacement piston in the direction of R in cylindrical coordinate system (identical to the cylinder axis) for piston suitable for cars

not take place at all. Another perilous area with a high value of the ovalisation of the piston skirt is the point II. The magnitude of the ovalisation of the piston skirt here depends very much both upon the size of the play between the piston pin and the piston and upon the choice of the size of the inner diameter of the piston pin. The ovality at this point increases very much with the decreasing play between the piston pin and the piston and with the increasing inner diameter of the piston pin. In the manufacture of the piston, this area can be corrected partially by the so-called double (positive or negative) oval, however, providing a stationary regime of the engine.

From the previous analysis, we can see that the choice of the sizes of the piston pin and of the play in its seating are very important, in particular with the engines with frequent changes of the temperature regime. As a general principle, it can be said that the ovalisation deformations of the piston pin can be lowered by reducing its inner diameter. On the other hand, the bending deflection of the piston pin can be reduced by increasing its outer diameter (Fig. 3).

References

Basshuysen R, and Schäfer F (2002) Internal combustion engine handbook—basic, components, systems, and perspectives. Vieweg Verlag, Germany, ISBN 0-7680-1139-6

Hrubín J (2013) Optimalizace pístu a ojnice motoru Jawa 837. Technical University of Liberec, diploma work

Scholz C (2003) Constructional project of the piston combustion engine. Technical University of Liberec, ISBN 80-7083-693-8, pp 10

Design Assistance System (DASY)

Z. Folta and M. Hrudičková

Abstract The article describes the knowledge and database program DASY that was developed through the work of a Josef Božek Competence Centre for Automotive Industry. It is designed to accelerate of the development of machine parts and structures. Article shows exemplarily optimization and design using system DASY and utilization of the external programs for this activity.

Keywords Design · CAE · DASY · Optimization · Knowledge database

1 Introduction

The DASY program is developed in a research center Josef Božek Competence Centre for Automotive Industry. His main task is to simplify and accelerate the process of designing machine parts and mechanisms. It may contain a number of knowledge and experience acquired in previous years by other workers.

2 What is DASY

DASY is knowledge and communication software for interactive work between a designer, calculation programs, knowledge databases and CAD systems (Bogomolov 2013).

Z. Folta (✉) · M. Hrudičková
VŠB-Technical University of Ostrava, Ostrava, Czech Republic
e-mail: zdenek.folta@vsb.cz

M. Hrudičková
e-mail: milena.hrudickova@vsb.cz

L. Ševčík et al. (eds.), *Modern Methods of Construction Design*,
Lecture Notes in Mechanical Engineering, DOI: 10.1007/978-3-319-05203-8_67,

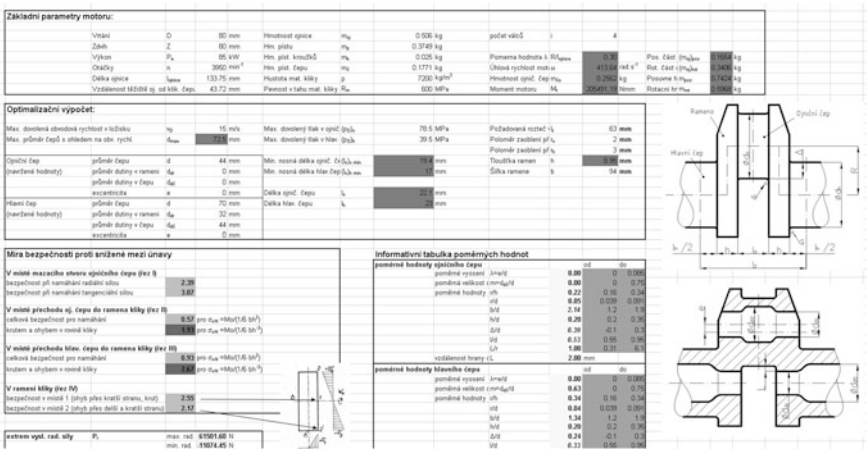

Fig. 1 Calculation prepared in MS excel

The system DASY allows:

- store experience from previous activities,
- programing some computational procedures,
- create components and assemblies,
- store, group and reuse created components,
- store, group and reuse created models,
- use some external software that can assist in design process,
- perform multi-objective optimization using software which haven't this functionality built-in,
- automatically can change the parametric CAD model according to the results of calculations.

The main goal is minimize of time, required for an engineer to make specific improvements in the model and then analyze it. DASY feature is illustrated by the following examples.

3 Crankshaft Optimization

The following example describes a method for optimizing a crankshaft dimensions using the calculation prepared in MS Excel. We use a calculation prepared in the previous period, including both dimensional and strength calculations (Fig. 1).

Next we prepare a scheme of the optimized shaft and define (in the DASY) variables that assign dimensions and other values such as volume or weight, etc. (Fig. 2).

At the same time we define in the DASY methods of calculation creating equations (Fig. 3) or external links to excel file (Fig. 4).

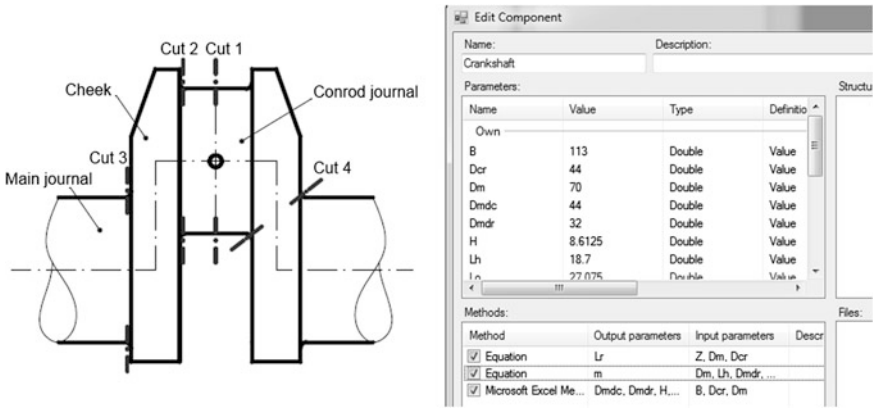

Fig. 2 Define the variables and parameters

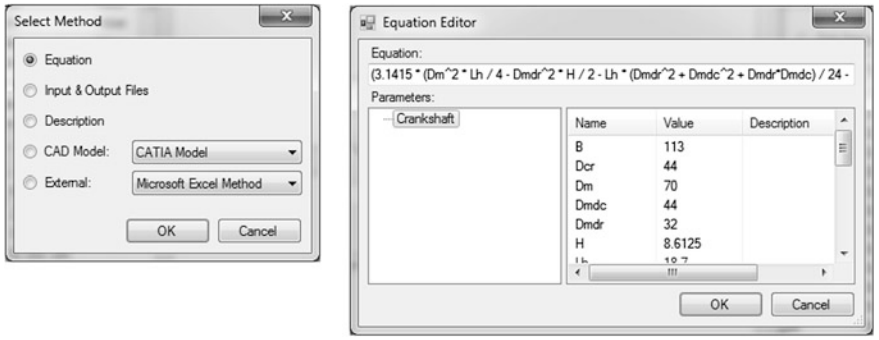

Fig. 3 Equation for shaft mass calculation

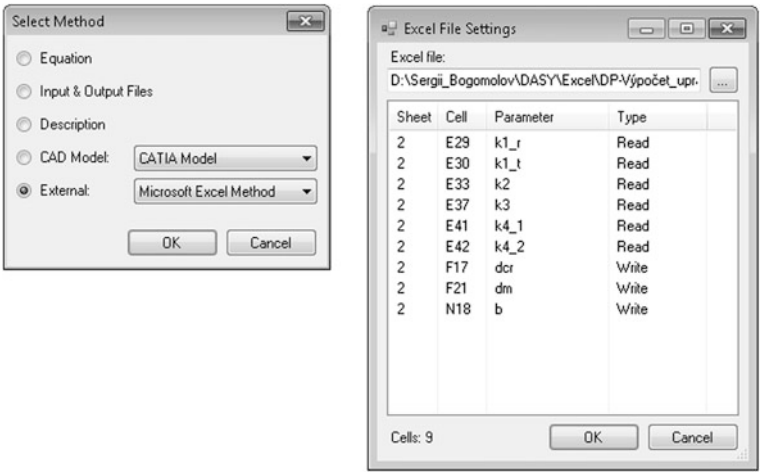

Fig. 4 Parametric external link for MS excel plugin

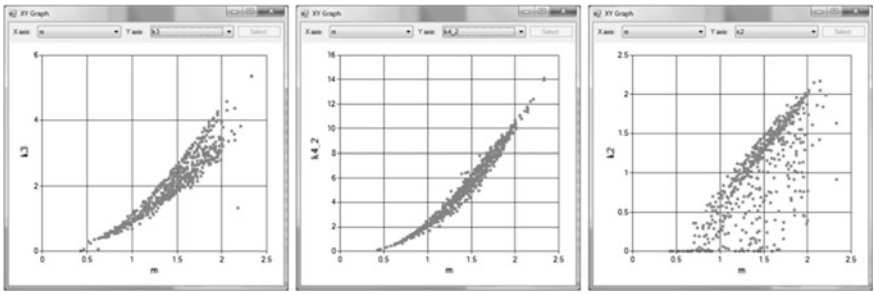

Fig. 5 Some results of optimization

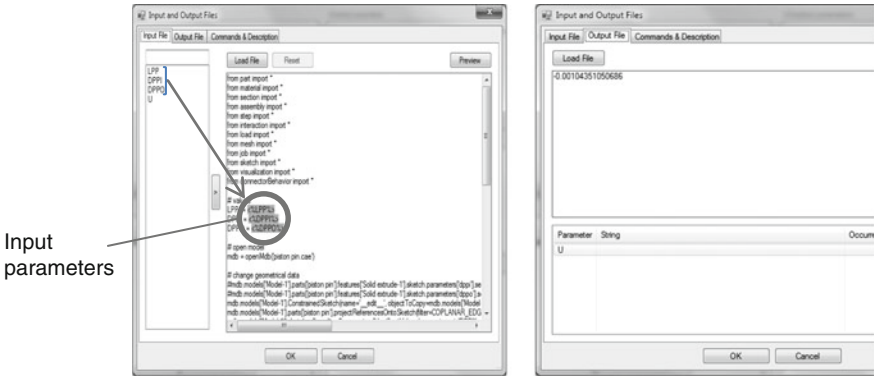

Fig. 6 Input text file in Abaqus formatting (*on the left*) and a value coming from the Abaqus calculation (*on the right*)

Finally, we determine the parameters optimization and activate the optimization. DASY repeatedly calling both excel (via plugins) and equations. On the end DASY draw graphs of the results (Fig. 5).

4 Communication Via Text Files

If external software cannot communicate via the plugin, it is possible use communication via text files. This communication is shown in the following example of piston pin optimization. DASY write input data into input text file in suitable format.

Next DASY call external software (in example Abaqus) with reference to this file. External software carry-out a calculations and stores the resulting data to the output file. DASY loads the resulting data and decide about next action of optimization (Figs. 6, 7).

Fig. 7 Command line for execute of Abaqus

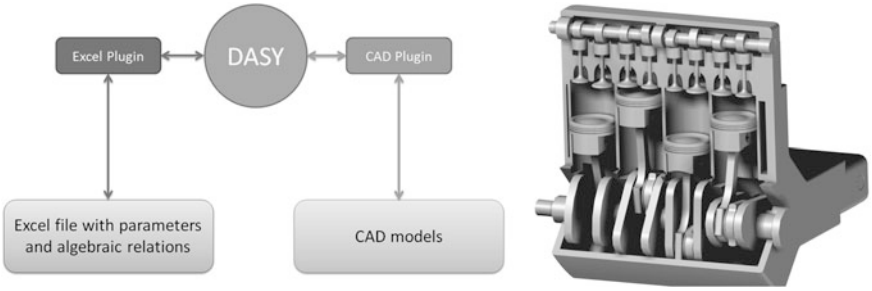

Fig. 8 Diagram of engine model optimization

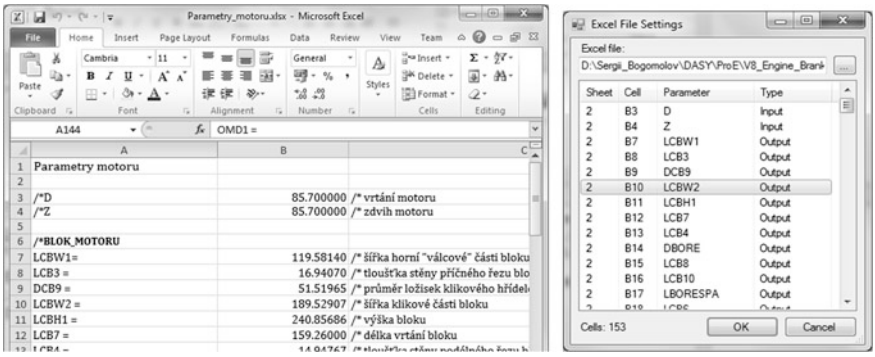

Fig. 9 Excel sheet with variables (on the *left*) and its location in DASY (on the *right*)

5 CAD and DASY

DASY may also interact with parametric CAD models. The example shown

- Excel file as a data source and as a calculations tool,
- Pro Engineer as a 3D modeler.

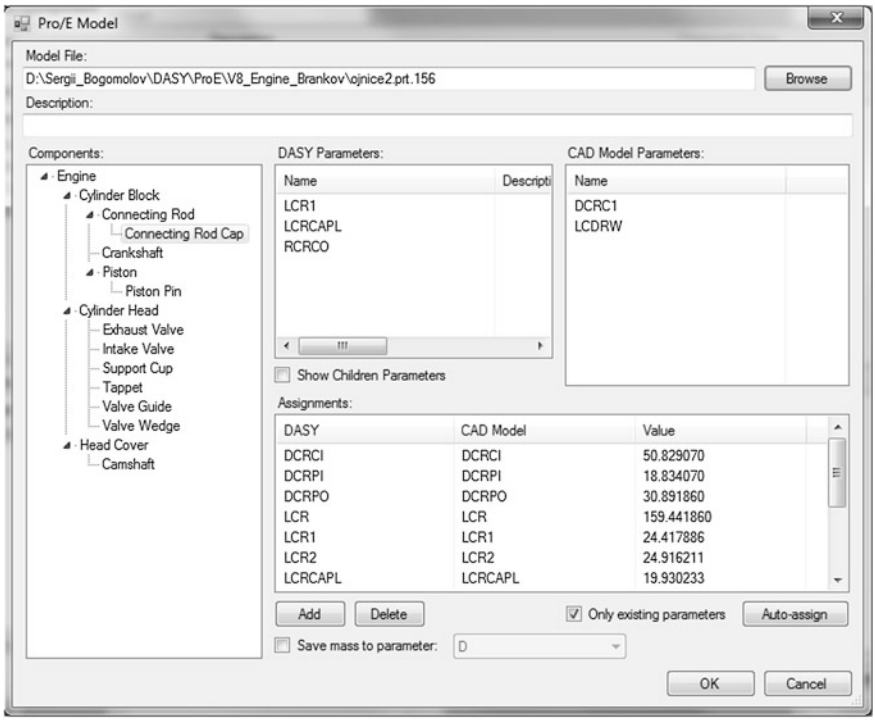

Fig. 10 ProEngineer 3D model structure in the DASY

On the basis of source data DASY does optimization in cooperation with excel and next transmit final data to the Pro Engineer for 3D modification. In next example, is optimization of model of engine (Figs. 8, 9, 10).

6 Conclusions

DASY will be gradually supplemented by knowledge of research of the research center members. The result will be a knowledge-based system for the design and optimization of powertrain especially cars.

Acknowledgments This research has been realized using the support of Technological Agency, Czech Republic, programme Centres of Competence, project # TE01020020 Josef Božek Competence Centre for Automotive Industry. This support is gratefully acknowledged.

Contribution has been done in connection with project Increasing of Professional Skills by Practical Acquirements and Knowledge, reg. no. CZ.1.07/2.4.00/17.0082.

Reference

1. Bogomolov S (2013) Design assistance system (DASY). Presentation on DASY workshop, Roztoky, 2013, FMU CTU in Prague, Prag

Device Providing a Continuous Process and Increasing the Efficiency of Inorganic Nanofibers Production

R. Kovář and D. Vejrych

Abstract At present, there are several methods of inorganic nanofibers production. One of them is spinning from a roller to a rotating brush. When correct settings are used, we can call this option the continuous process of nanofibers production. There is a theory that we can carry on more than one process of electrospinning in a closed space. Changing the condition settings can improve the efficiency of electrospinning. Therefore, an experimental device with four areas for processing was built.

Keywords Nanofibers · Electrospinning · Efficiency · Continuous process

1 Introduction

Implementation of the continuous process of nanofibers production leads to the reduction of process time and cost savings. One possibility of electrospinning is to use the rotating roller as a spinning electrode and the rotating brush as a collector. For pulling down a layer of nanofibers from the rotation brush some mechanism allowing it must be used. Another part that is needed to continual operation is some exhaust. This unit can remove all nanofibers from the "pulling down" mechanism. Together they carry out the conditions for continuous process of nanofibers production.

A machine was designed to verify the functionality of these theories. This machine contained four separate units. Each unit contained elements required for

R. Kovář (✉) · D. Vejrych
Technical University of Liberec, Liberec, Czech Republic
e-mail: radovan.kovar@tul.cz

D. Vejrych
e-mail: david.vejrych@tul.cz

L. Ševčík et al. (eds.), *Modern Methods of Construction Design*,
Lecture Notes in Mechanical Engineering, DOI: 10.1007/978-3-319-05203-8_68,

the process. There were combined different elements like: a spinning electrode, a collector, a "pull down" mechanism, an exhaust mechanism and a tub. So, in each unit could be a self-operated electrospinning process. Different elements may have effect on the efficiency of electrospinning. The machine was designed modularly for the maximum number of possible arrangements of elements.

2 Nanospinning Continuous Process

The most widespread way to produce nanofibers on an industrial scale is based on the principle of electrospinning from a "roller". A device allowing the production of nanofibres this way is called Nanospider. It is a laboratory device made of insulating materials. Inside the device there is an empty space in which the process of spinning is carried out. The size of this area is variable. The smallest ones are only for a tub with a collector. Into larger ones there may get a bigger experimental device. There are two high voltage generators anchored to a device construction. Each of them can supply high-voltage up to 100 kV to the process area. The airflow through the chamber, as well as the temperature and humidity, plays a significant role in the successful run of the process. In the middle of the chamber there is placed the tub. It is filled with a polymer. It can be used for both organic and inorganic plastic solutions. The spinning electrode, less than half-immersed in a polymer, rotates in the tub. The high voltage source is applied to the electrode. Above it there is the grounded collector through which runs a spunbond. It serves as a supporting material that allows the fibers to be removed from the chamber. Rotation of the electrode is secured by an electric motor, which is mounted to the construction outside the area, where the process of electrospinning runs. Torque is applied to the electrode over the motor shaft and bevel gears. Schematic diagram of Nanospider function is illustrated in Fig. 1.

A disadvantage of the prior solutions is the production of fibers carried by other element, in this case using a spunbond. The idea of the introduction of continuous operation consists in obtaining separate threads for the possibility of further modifications. For the continuous process a rotating cylindrical brush can be used as a collector. It is also able to provide the continuous process for producing nanofibers (Angammana and Jayaram 2011; Petrů et al. 2012; Lukáš et al. 2009; Jirsák 2004).

2.1 Optimization of the Continuous Process

Rotating cylindrical brush is used to replace the collector. The principle of the process of spinning on the rotating cylindrical brush is shown in Fig. 2. Charged spinning fiber electrodes are attracted to the grounded brush. The rotation of the brush depends on its radius. Speed of rotation is between 1 rotation in 5 min

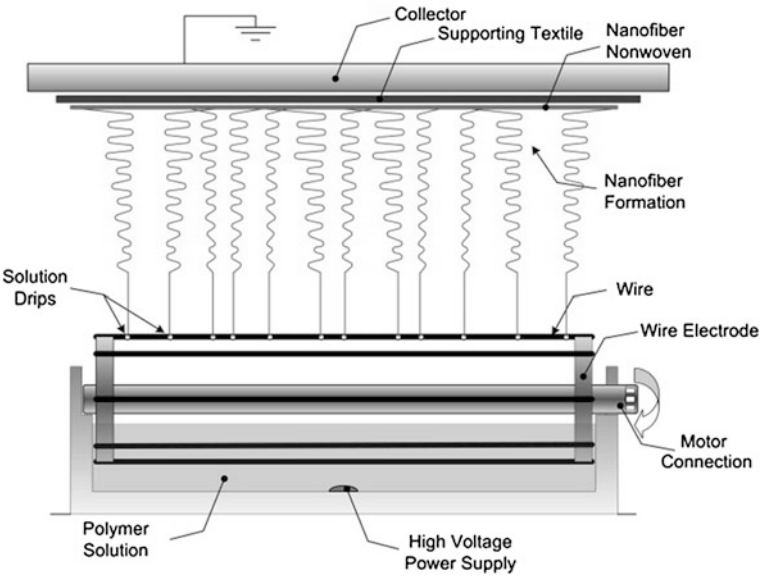

Fig. 1 Schematic diagram of Nanospider

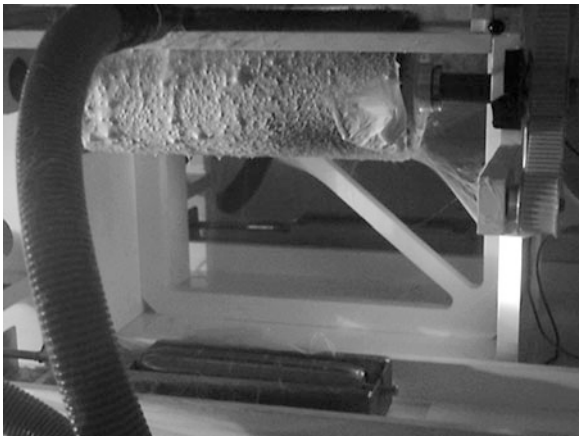

Fig. 2 Electrospinning using a cylindrical brush as a collector

and 1 rotation in 10 min. During one rotation the one half of the brush is coated with fibers while on the other hand leads to entrainment of fibers from brush surface. At the beginning of the second rotation clean surface is getting in the area of spinning. To maintain the continuous process, accumulated fibers must be removed from the surface of the brush. Therefore, the "pull down" system with a mechanical or pneumatic element is integrated in. Fibers that are pulled down leave the spinning area through the exhaust system. Due to the high voltage inside the chamber of the machine only pneumatic power systems can be used.

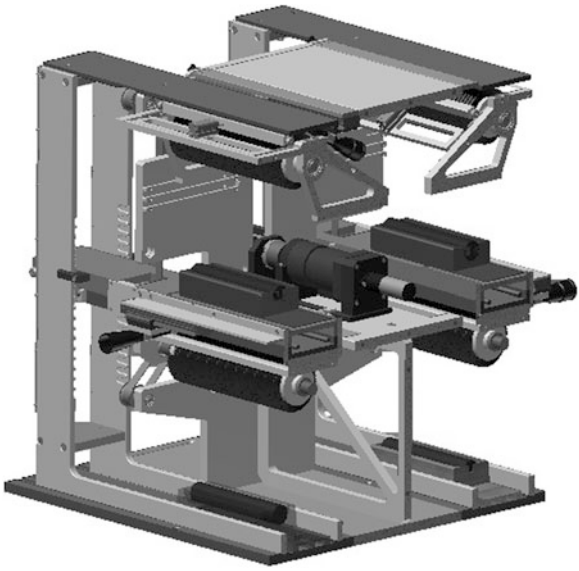

Fig. 3 Electrospinning using a cylindrical brush as a collector

3 Design of the Machine

To test the principle in the real scale a machine was designed to test the equipment. The machine is divided into four parts. In each part there is the actual process of electrospinning. Individual processes are independent of each other. There are four spinning electrodes and four brushes as collectors in the machine. The electrodes are the same in all cases, but the tubs, in which the electrodes are inserted and also into which is poured polymer solution prepared for spinning, are different. Each tub is made of a different material and is produced by another technology. As tub materials are used: glass, wood, metal plate with a plasma modification of its properties, plastic. One of "pull down" systems for removal of fibers is applied to each brush. The machine structure was designed with functionality, simplicity and flexibility in mind. Emphasis was placed on ease of exchange of brushes and tubs with each other. Figure 3 shows a modular design structure. As the module can be meaning: drive of brushes, tubs, brushes, exhaust.

The main task was to secure the drive of brushes using belt transmission. All of the four brushes had to be connected to one drive. All drive elements except spinning electrodes must not be driven electrically. Therefore, a pneumatic motor was applied to drive the brushes and "pull down" systems. Torque had to be applied to each electrode placed in the tub. It was implemented as a single electric motor. It had to be placed outside of the spinning chamber and it was shielded from it. Each section was thus formed with the polymer tub, the spinning electrode, the brush with "pull down" system and the exhaust. Spinning process depends on many factors. One of them is the distance between the electrode and the brush. The ideal value for the inorganic fiber spinning solution is 180 mm.

For the possibility of testing values were selected ranging between 160 and 200 mm in increments of 20 mm. It was therefore possible to test in all four spinning areas at maximum or minimum distance at the same time.

3.1 Brush

Because the rotating cylindrical brush replaces one of the electrodes the entire surface must as conductive as possible. Therefore, when choosing the materials from which wire brushes are made, the emphasis is on high conductivity values. The first type is the cylindrical spiral brush when wires are attached to the sheet metal. Then it is rolled into a spiral, this way it is holding the required dimensions. The conductivity of the wire is secured with sheet metal, that is connected to the charge. In the second type of the brush there are bunches of wires inserted into the plastic core. We can call it the "core" brush. Charge is led with a use of wire that is interwoven between bunches. The pitch of the brunches is between 8 and 16 mm. The brush length must be greater than the length of the spinning electrode. In our case, the selected brush length is 340 mm and length of the spinning electrode is 250 mm. There were the limiting factor dimensions of the chamber, because the distance between the electrode surface and the collector should be 180 mm for optimum start of the process of polymer testing.

3.2 "Pull Down" System

If we use the brush with appropriately selected parameters, its surface will be completely covered with a thicker layer of nanofibers. For continuous process it is necessary to pull down the layer so that the surface of the brush will be completely free of fibers. It is possible to pull down the fibers through contact or contactless manipulation. The contact manipulation is when external tools are used, which disrupts the bond between the fibers and the end of the wire brush. The contactless method can be thought of as an exhaust air flow. Steel wire with a length of 20 mm and a diameter of 0.2 mm has smaller elasticity then the plastic line and does not deform over the comb. It is inserted tangentially to the surface of the brush to a depth of 2 mm and makes reciprocating movement perpendicular to the axis of the brush. The system is complemented by an exhaust, which is to ensure extraction of fibers collected on the comb. "Pull down" system starts when a continuous layer of fibers is created. Complete system of extraction of nanofibers from the comb is shown in Figs. 4 and 5 (Kovář 2012).

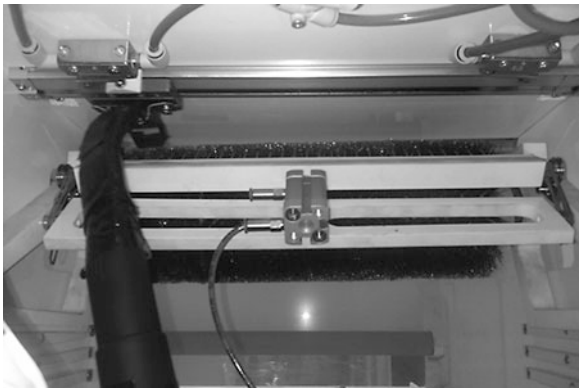

Fig. 4 Exhaust layer of fibers from a comb

Fig. 5 Pulled down layer of fibers

4 The Experiment

For the continuous operation all combinations of elements were tested. Thus, each of the described brushes was tested with all variants of "pull down" systems and all types of the tubs. Test conditions were the same for all the experiments. Special attention was given to the climate of the test area, the distance between the electrode and the collector, the rotation speed of the electrode and the collector. Inorganic polymers, specifically titanium oxide, were used for the tests. Voltage values ranged from 70,000 to 80,000 V. For the continuous operation it is best to use a brush with spiral steel wires with a diameter of 0.15–0.25 mm. During the experiment it showed the highest efficiency in combination with glass tug. Comparison the efficiency of all types of tugs with a brush with spiral steel wires is shown in the Fig. 6. During one rotation of the brush was measured at the largest fiber layer on a spiral brush with metal wires.

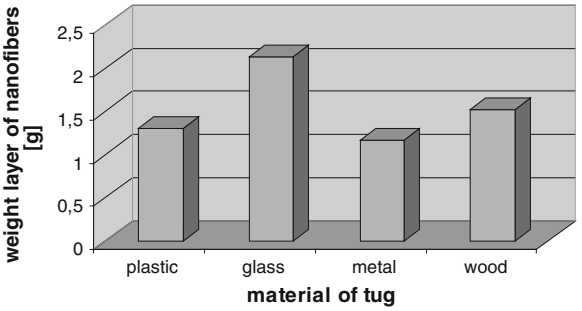

Fig. 6 Spinning efficiency depending on the type of tug

5 Conclusion

An experimental machine was built for the test. It was tested on a combination of brushes, tugs and "pull down" mechanisms. The best resolution is the spiral brush with metal wires in combination with the glass tug and "pull down" mechanism with an exhaust. So, there is a possibility of continuous production of nanofibers. This alternative solution showed an almost perfect ability to clean the nanofibers from the surface of the brush and remove them from the workspace.

This work was supported by the Ministry of Education of the Czech Republic within the SGS project no. 28007 on the Technical University of Liberec.

References

Angammana CJ, Jayaram SH (2011) The effects of electric field on the multi-jet electrospinning process and fiber morphology. IEEE Trans Ind Appl 47(2):1028–1035

Jirsák O (2004) Method of nanofibres production from a polymer solution using electrostatic spinning and a device for carrying out the method. Patent, WO 0127365

Kovář R (2012) Ways to pull down spinning nanofibers from the rotating brush in high voltage area. In: Proceedings 53rd international conference of Machine Design Departments, Brno, pp 141–144

Lukáš D, Sakar A, Martinová L, Vodseďálková K, Lubasová D, Chaloupek J, Pokorný P, Mikeš P, Chvojka J, Komárek M (2009) Physical principles of electrospinning (Electrospinning as a nano-scale technology of the twenty-first century). Text Prog 41:59–140

Petrů M, Novák O, Lepšík P (2012) Increase of the efficiency of the production lines for the spinning of inorganic nanofibers by the electrostatic field intensity optimization. MM Sci J 4:382–385

Dynamic Analysis of Lifting Platform Construction for Car Relocation

M. Petrů, L. Ševčík, I. Mašín, P. Lepšík, A. Lufinka and O. Novak

Abstract For a force assessment which acts in individual parts of a scissor lift platform for moving of cars from the production line a dynamic analysis and experimental studies were performed. The analysis of loads show that immediate loading of platforms by the car causes additional bending moment that must be captured in a scissor mechanism. Initially experimental measurements were carried out on the real platform for obtaining of trajectory, velocity and acceleration. Subsequently, model analysis of the lifting platform using four point Runge-Kutta method, were assembled. The model analyzes found that a step loading during acceleration and deceleration of the platforms leads to a dynamic impact that are unsafe due to long term use. The consequence of said is repeated overloading of pivots, bearings, fittings and other parts. Also the dynamic stress may be accompanied by the resonances.

Keywords Lift platform · Scissor mechanism · Construction parts · Dynamic analysis · Impact

M. Petrů (✉) · L. Ševčík · I. Mašín · P. Lepšík
Department of Design of Machine Elements and Mechanism, Faculty of Mechanical Engineering, Technical University of Liberec, Liberec, Czech Republic
e-mail: michal.petru@tul.cz

L. Ševčík
e-mail: ladislav.sevcik@tul.cz

I. Mašín
e-mail: ivan.masin@tul.cz

P. Lepšík
e-mail: petr.lepsik@tul.cz

A. Lufinka · O. Novak
Technical University of Liberec, Liberec, Czech Republic
e-mail: ales.lufinka@tul.cz

O. Novak
e-mail: novak.ondra1@seznam.cz

L. Ševčík et al. (eds.), *Modern Methods of Construction Design*,
Lecture Notes in Mechanical Engineering, DOI: 10.1007/978-3-319-05203-8_69,

1 Introduction

Currently, lifting platforms in large production lines are used especially in the automotive industry, and they provide the desired logistics and layout of the production process. This paper deals with a platform lift, which is used for moving the car with the base from the upper level to the lower level of the production hall. The platform (Fig. 1) consists of a frame profile stand firmly anchored to the floor, on which is placed a scissor mechanism with traversing members (wheels are mounted on the frames). This platform moves from the top position to bottom position for 10 seconds approximately. The aim is to assess the components, which are most loaded by dynamic loading which is caused by the movement of the platform. For complicated construction, like this, would be very complicated to use analytical calculations, so it is appropriate to establish a model that uses numerical methods for the study of movements and loads. That is why the numerical analysis are very suitable tool for the study and optimization of various structures (Bosnjak et al. 2009; Affolter et al. 2011; Liu and Yan 2012; Szweda et al. 2010; Petrů et al. 2012; Pesik and Vancura 2009; Dekys and Broncek 2012). Also, it can be very suitable, when it can not be used analytical relationships, or for their refinement (Dong et al. 2013; Petru et al. 2012, 2013; Herak et al. 2013).

2 Materials and Methods

2.1 Experimental Analysis of Dynamic Loading of Platform

The platform moves on the given trajectory and time by the certain velocity. On a start and the end of the moving a step change of velocity appears (it is connected with extreme acceleration). It was therefore necessary for an evaluation of the trajectory to measure the velocity and acceleration of the real platform during operation of line directly in factory. The principle of measurement and a placement of the sensors are shown schematically in Fig. 2. Starting position for measurement was always of the highest and lowest position of the platform. In between these positions acceleration and position were measured. When moving down the platform was loaded by the stand with the car, when moving up without load, which corresponds to real use. Used biaxial accelerometer Analog Devices ADXL 203 EB measured acceleration and static acceleration (gravity). At the beginning of each measurement the static acceleration (gravity = 9.81 m/s^2) was reset to zero, therefore in the vertical direction the acceleration was equal to 0. Therefore results of acceleration measuring shown as immediate acceleration of the platform without gravity. Displacement was measured cable reverse sensor

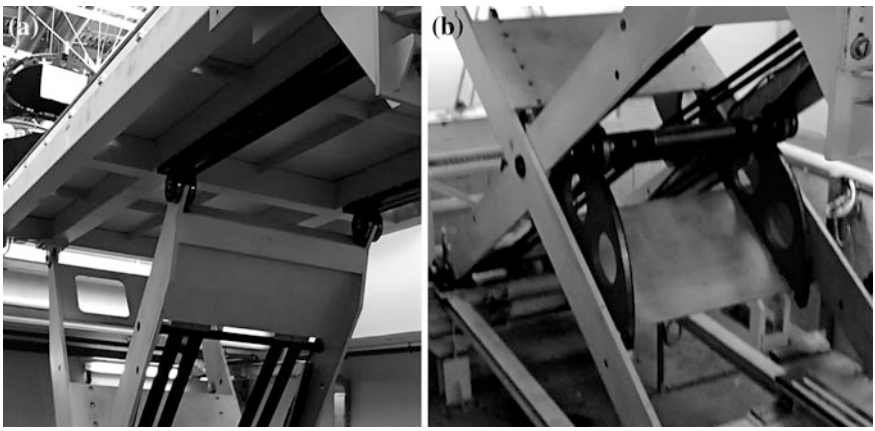

Fig. 1 Lift platform for transportation of cars

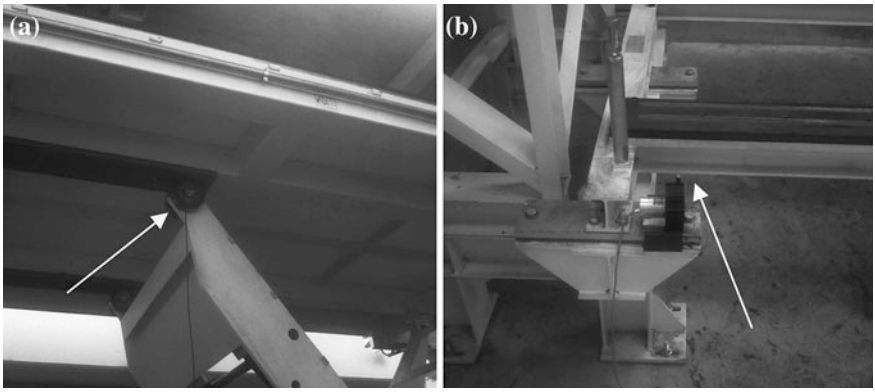

Fig. 2 Scheme of measurement of the platform dynamic movement: **a** placement of acceleration sensor, **b** placement of trajectory sensor

Michro Epsilon-WDS-4000-P115-CA-P and recorded in the data logger Dewetron DEWE 5000 with software Dewesoft 7.03. The resulting data was processed in the software Datel 08.01.

2.2 Numerical Analysis of Platform Dynamic Loading

Numerical analysis of dynamic load of technical assessment of the construction nodes of the platform was based on CAD data (Fig. 3). For model dynamic analysis of platform were used only data of parts and components that contribute to

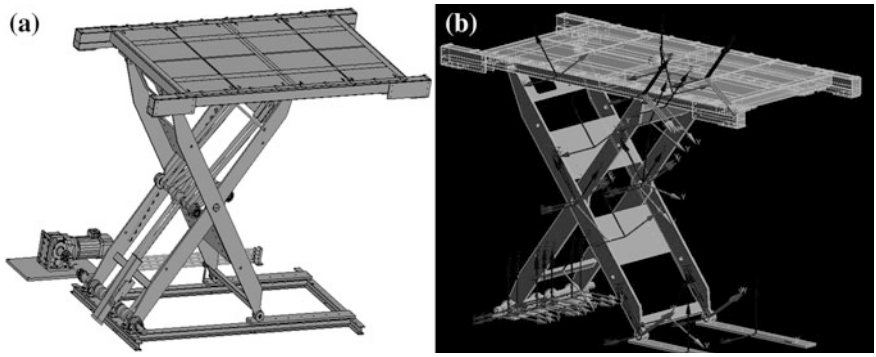

Fig. 3 CAD model of platform (*left*), numerical model for dynamical analyses (*right*)

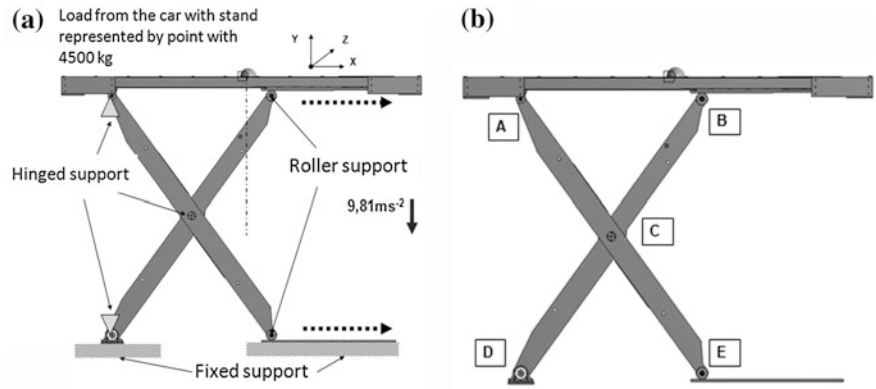

Fig. 4 **a** Scheme of links applied in the model, **b** evaluated nodes of the platform

transformation of dynamic loads, such as construction platforms, storage, cogs, wheels. Other parts such as the drive coupling parts (screws, washers, bearings…) were removed from the model. Dynamic analyzes were performed to assess the loading course of platform and its scissor mechanism on which the upper part of platform, stand and car acts. This geometry was imported into ANSYS preprocessor for kinematic and dynamic analysis of the forces. Then kinematic model of the links among different parts (Fig. 3), forces (defining of the material model, the weight of individual components, platform load) and initial and boundary conditions were defined (Fig. 4).

Dynamic analysis was performed using the numerical solver using the 4th order Runge-Kutta method (1).

$$x_{n+1} = x_n + \sum_{i=1}^{p} \psi_i k_i, \quad k_i = f\left(t + \alpha_i h, y_n + h \sum_{j=1}^{i-1} \beta_{ij} k_j\right) \tag{1}$$

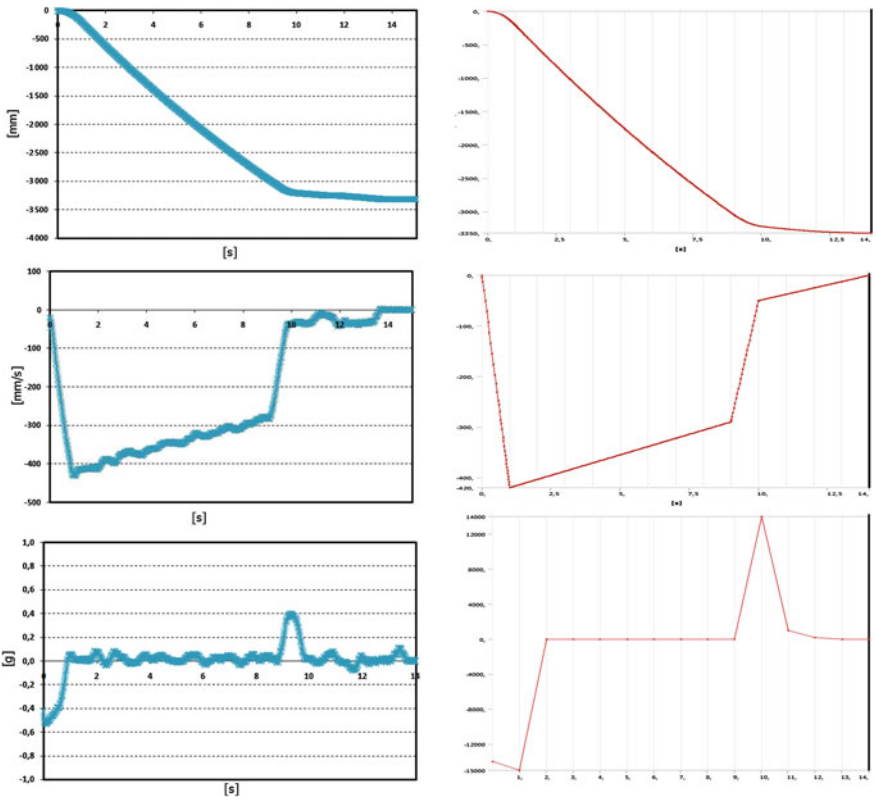

Fig. 5 Course of displacement, velocity and acceleration for individual time: measurement (*left*), simulation (*right*)

where the individual coefficients are calculated so that the method order p correspond to Taylor polynomial function x(t) for 4 orders.

3 Results and Discussion

The resulting courses of track, velocity and acceleration measurements obtained on a real platform are shown in Fig. 5 on the left. The course of the trajectory, in other words the displacement of the platform is constant in the whole range (time $0 \sim 14$ s). The velocity course the platform is characterized by a steep increase at time 0–1 s, constant course at time 2–9 s, and when braking steep deceleration at

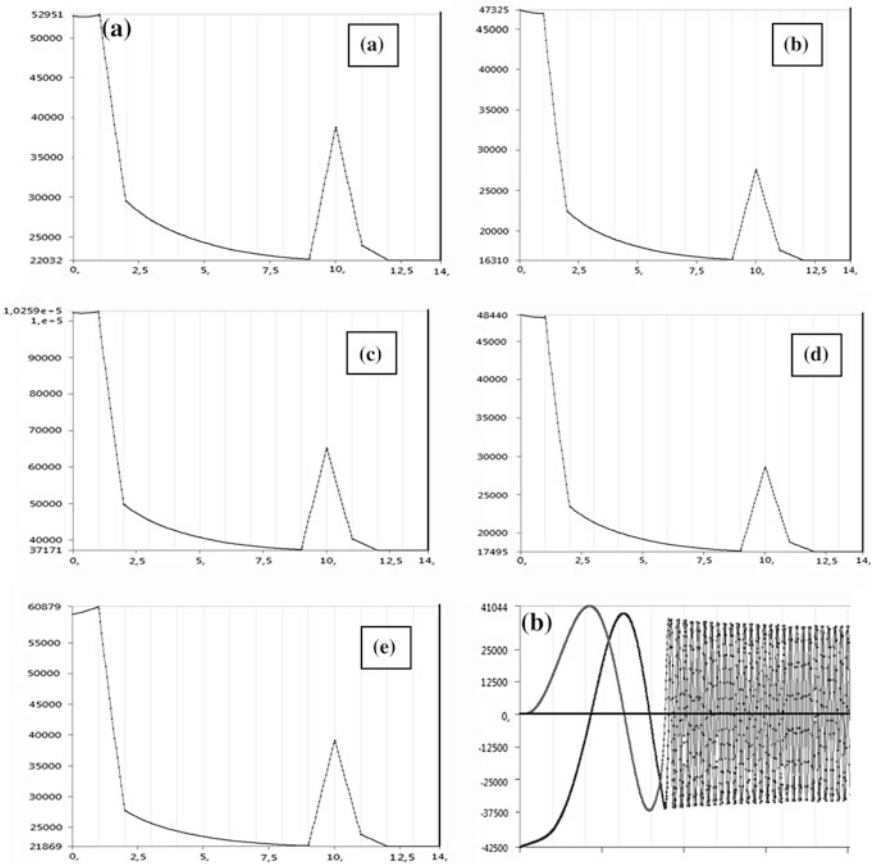

Fig. 6 **a** Load values in the exposed places A–E, **b** course of initial oscillation

the time of 9–10 s occurs. The acceleration of platform in the range of about 1–9 s is approximately constant with a value of 1 g = 9.81 m/s^2. The results show that when the move of platform starting (t = 0–1 s) the acceleration is 1 + 0.5 g ($\sim$15 m/s^2) and when platform stops (t = 9–10 s) the deceleration is 1 + 0.4 g, thus resulting acceleration is −1.4 g ($\sim$−14 m/s^2). The resulting acceleration courses obtained from numerical analysis are shown in Fig. 5 on right side.

The resulting courses of forces of the individual components in nodes A-E are shown in Fig. 5. The course is characterized by a start and end thrust, which apparently causes the initial oscillations (Fig. 6). The maximum load values in the most exposed places A–E are listed in Table 1.

Table 1 Results of numerical analysis of loaded construction nodes of the platform

Construction node	A	B	C	D	E
Force (N)	52,951	47,325	102,590	48,440	60,879
Indentation stress (MPa)	38.9	52.5	56.9	18.1	67.75
Bending stress (MPa)	124.3	374.9	193.5	31.4	483.1
Shear stress (MPa)	42.1	66.9	36.3	7.6	86.2

4 Conclusions

The article dealt with the studies and model analyzes of construction nodes of dynamically loaded platform for lifting a car put on the stand. From results of measurements on a real platform is obvious initial step acceleration caused by starting and braking of the platform. There is the oscillation and shock load of bearing parts of construction. According to model simulations it causes high stress and strain in construction nodes A–E. Overall, the mass of the car with stand causes additional bending moment that must be captured in the scissor mechanism. Shock loading is due to the long term operation dangerous because repeatedly loads not only construction parts such as pivots, but also other part—bearings and connecting members. Also resonances in construction can develop. The optimization of the platform can be realized by suitable guides that avoids especially transverse stresses and shocks.

Acknowledgments The research reported in this paper was supported in part by the Project OP VaVpI Centre for Nanomaterials, Advanced Technologies and Innovation CZ.1.05/2.1.00/01.0005 which has been financed by The Ministry of Industry and Trade of the Czech Republic and Project Development of Research Teams of R&D Projects at the Technical university of Liberec CZ.1.07/2.3.00/30.0024 and the project of CREATex (CZ.1.07/2.2.00/28.0321), which has been financed by Europen Social Fund and The Ministry of Education, Youth and Sports of the Czech Republic.

References

Affolter Ch, Piskoty G, Weisse B (2011) Failure of a bus hoisting platform due to unexpected system behaviour. Eng Fail Anal 18(7):1742–1749

Bosnjak S, Petkovic Z, Zrnic N, Simic G, Simonovic A (2009) Cracks, repair and reconstruction of bucket wheel excavator slewing platform. Eng Fail Anal 16(5):1631–1642

Dekys M, Broncek O (2012) Measuring strain of the lattice towers. Commun: Sci Lett Univ Zilina 14(3):39–42. http://www.uniza.sk/komunikacie/archiv/2012/3/3_2012en.pdf

Dong W, Du Z, Xiao Y, Chen X (2013) Development of a parallel kinematic motion simulator platform. Mechatronics 23(1):154–161

Herak D, Kabutey A, Divisova M, Simanjuntak S (2013) Mathematical model of the mechanical behavior of *Jatropha curcas* L. seed under compression loading. Biosyst Eng 114(3):279–288

Liu XM, Yan HY (2012) Dynamic analysis of 6-DOF large displacement composite simulation platform. Appl Mech Mater 233:181–185

Pesik L, Vancura M (2009) Vibration isolation support of machine with flexible frame. In: Proceedings of 50th international conference of machine design departments, p 46

Petru M, Novak O, Herak D, Simanjuntak S (2012) Finite element method model of the mechanical behavior of *Jatropha curcas* L. seed under compression loading. Biosyst Eng 111(4):412–421

Petru M, Novak O, Vejrych D, Lepsik P (2013) FEM study of the strain kinematics in the 3D nanofibrous structure prepared by the electrospinning process. Appl Math 4(5a):80–90

Petrů M, Novák O, Lufinka A (2012) Study and analysis of transmissibility of car seat with non polyurethane material. In: Proceedings of 50th annual conference on experimental stress analysis (EAN), pp 321–326

Szweda J, Poruba Z, Sikora R, Bilosova A (2010) Dynamical analysis of lifting platform, TRANSACTIONS of the VŠB—Technical University of Ostrava—Mechanical Series

The Simulating Model of a Supercharged Hydrogen Engine

J. Popelka

Abstract In this paper I am dealing with a design of the simulating model of the supercharged hydrogen engine. The simulating model is designed so that it would be possible to simulate the engine behaviour by various A/F ratios and various configurations on the supercharger side. The results received by this simulation contribute to the optimal configuration of the engine, which will be tested on the test bed.

Keywords Hydrogen · Supercharging · Lean mixture

1 Introduction

In using hydrogen as fuel for the combustion engines is necessary to take in account its qualities and to try to use them maximally. The most important matter is to focus on burning the hydrogen mixture with air and to optimize the running of the combustion procedure to receive as high efficiency and safety of the engine running as possible. From the collected results of research focused on hydrogen combustion as the fuel is seen that hydrogen is from the energetically, ecological and technological point of view possible to be managed and it can be used as the source of energy for combustion engines (Kovář et al. 2002). Despite of all success in this research sphere there are still some matters which aren't absolutely clear and reserves, which have to be dealt with continuously.

The hydrogen combustion engines we can divide into two categories. The first one is the engines with external creation of the mixture, where the fuel injector is placed directly in the intake tract of the engine. By this conception there often

J. Popelka (✉)
Technical University of Liberec, Liberec, Czech Republic
e-mail: josef.popelka@tul.cz

L. Ševčík et al. (eds.), *Modern Methods of Construction Design*,
Lecture Notes in Mechanical Engineering, DOI: 10.1007/978-3-319-05203-8_70,

appear some unwanted phenomena and also it isn't possible to use the very lean mixture, because there a rises a problem with its ignition. The other possibility is the internal creation of mixture, so called the direct fuel injection into the combustion space (Popelka 2010).

2 Description of the Lean Hydrogen Mixture Burning Problems

By burning of extremely lean mixtures ($\lambda > 2$) apart from significant reduction of NO_x production, also significant power reduction appears. The aim of hydrogen engines supercharging is to receive higher power. However, this procedure is limited by conditioned formation of NO_x emission pollutants. Problems of the hydrogen engine supercharging is described in works (Kovář et al. 2002; Scholz et al. 2002, 2003).

For receiving the needed lean mixture, it necessary to reach for the blower to be able to provide supply a sufficient amount of air to the engine by the required compression. It has to be in the widest possible range of operated revolutions. These aspect results in requirement on the blower power, which on the other hand must be supplied by the turbine. The turbine operation depends on the mass flow, running through the turbine, pressure gradient and exhaust gases temperature. From this point of view it is necessary to choose the turbine case, which is as small as possible, so that high turbine and consequently of the all machinery—turns can be reached. By choosing of the turbine case is necessary to consider the turbine through put, so that no overloading and consequent choking of the canal and blades on the revolving wheel appears. The turbine throughput is expressed as the dependence of pressure ratio on the turbine and the total mass flowing through the turbine.

For receiving the required engine power by the particular regime, it is necessary to supply a sufficient fuel amount to the procedure.

For the fuel burning it is necessary to supply enough air to the system. For receiving the required A/F ratio it is necessary for the blower to supply large amount of air into the engine. Blower operating in the regime, when it supplies the large amount of air, is very power—intensive. In our case, when the very lean mixture is burned in the engine, no large amount of thermal energy is released by the burning procedure. Operations inside the cylinder run by lower temperatures and also the burning products have lower temperature. For this reason it is possible, that the turbine, in which the thermal energy is converted into the kinetic energy, won't have a sufficient gradient and won't be able to supply the needed power to the blower. On conditions of that we can say, that the blower power depends on the energy of exhaust gases. By the designing and following optimizing of the whole system it is necessary to consider the engine construction.

3 Description of the Engine and Supercharging System

The engine structurally initiates from the series three cylinder-engine with volume of 1,200 ccm, which was adjusted for the needs of direct fuel injection. The main adjustment meant the suitable injection placement in the cylinder head, so that cooling and valve systems function can't be influenced (Fig. 1).

The supercharging system is constructed with the supercharger Garet GT 1241, which i suitable not only for its development dimension. The supercharging system is equipped with the multi component regulation. The turbine is regulated by the by-pass valve Waste-gate, which drains exhaust gases from the space in front of the turbine. The flow rate drop through the turbine results in drop, let us say consolidation of filling pressure from the compressor side. Due to the fact, that it is a spark ignition engine with quantitative regulation by the help of the throttle valve following situation may appear. By the throttle valve closing the pressure in front of the throttle valve may increase and because of that, the compressor blading wheel may stop. These phenomena can happen, for example, by engine braking. The supercharging system is equipped with a valve, which follows pressure in front of the throttle valve and in case of necessity it drains that pressure into the compressor intake.

4 Mathematical Model of the Supercharged Engine

For the design of a mathematical model of the supercharging system the program Wave by Ricardo Company was used. In the wave program environment it is generally possible to model the engine and its basic parameters 0-D and the engine pipes can be designed with 1-D access. The 0-D engine simulations are used especially for finding out the engine parameters by various settings and regimes without the necessity to test the engine in real operation or to chance its construction parameters expensively. Although the engine uses 0-D or 1-D models, in some parts of the calculation program settings it is possible to create directly a 3-D model. It is also possible to transform real 3-D models created in CAD system into 1-D model, which is suitable for calculation in Wave environment. This procedure can be done in an easy way. To be able to create a simulating model, we must know not only geometrical parameters (drilling, stroke, compression ratio, intake and exhaust pipes dimensions, injector parameters and valve timing), but also thermodynamic qualities of materials and basic data about burning procedure. The burning procedure in this case is described with the help of Vibe burning law, the course of which is displayed in Fig. 2.

The vibe law course is featured with the help of 10, 50 and 90 % amounts of burnt fuel, dependently on the crankshaft turning aside. These values have to be measured in a real experiment. For primary finding of model functionality I used the fuel burning values from measuring on the atmospheric engine.

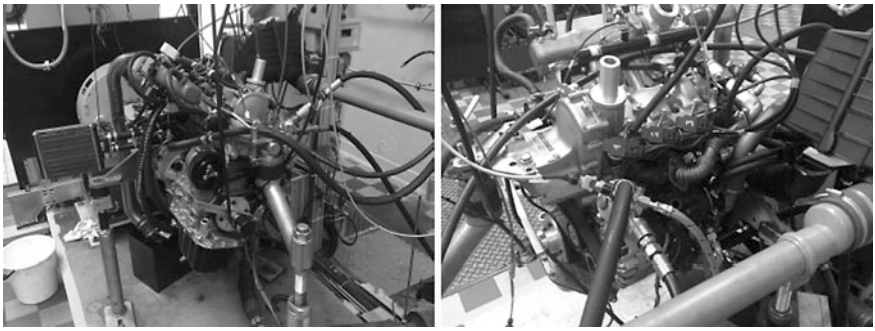

Fig. 1 The view on the test bed with supercharged hydrogen engine

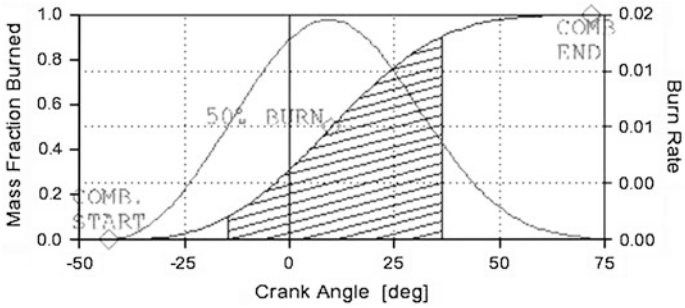

Fig. 2 The Vibe burning law

Table 1 Values of air/fuel ratio

n_m (ot/min)	2,500			3,000		
λ (−)	1.8	2	2.1	1.8	1.9	2

5 Simulation of Various Operating Engine Regimes

Due to the fact that it wasn't possible to find out the burning law values I used for the simulation values measured on the atmospheric engine, which was operated in two revolution regimes with the changeable A/F ratio and full engine loading (Table 1).

During simulating i found out, that the calculation is very sensitive on these values. Unless we have measured them, they are very difficult to guess (Figs. 3, 4) (Table 2).

From the results we can find out, that the compressor is able to work properly in both revolution regimes.

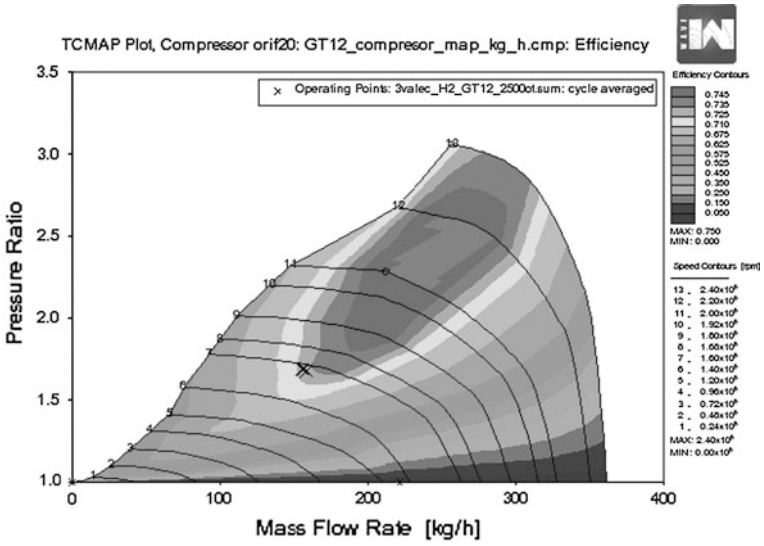

Fig. 3 Operating points of the compressor Garet GT 1241 for 2,500 RPM

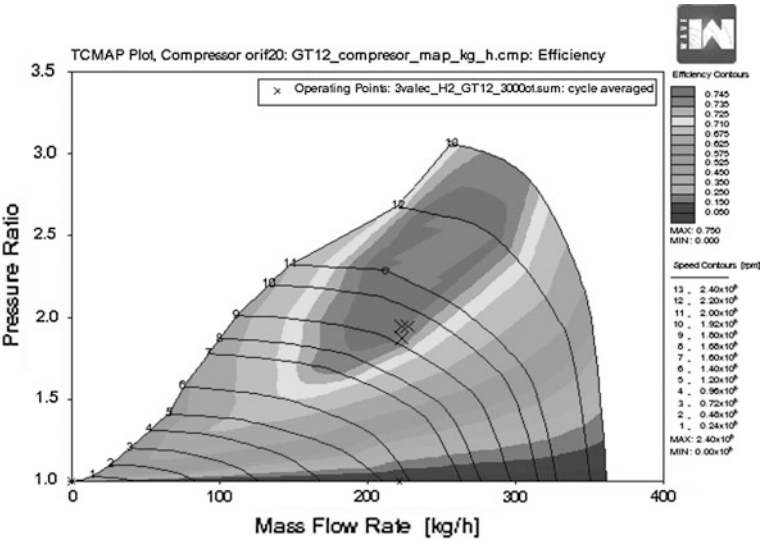

Fig. 4 Operating points of the compressor Garet GT 1241 for 3,000 RPM

Table 2 Powers parameters of supercharged engine

Supercharger Garet GT 1241							
n_m	(ot/min)	2,500			3,000		
λ	(−)	1.8	2	2.1	1.8	1.9	2
P_m	(kW)	28.3	25.9	24.6	36.6	36.5	34
M_m	(Nm)	108	98.9	94	116.5	116	108

6 Conclusions

The simulating model, presented in this article, proved a reasonable correspondence by verifying with the calculation. Unfortunately, it hasn't been possible to verify it on the engine on the test bed yet. The reason is that engine itself is damaged.

From simulations it is obvious, that both the turbine and the compressor move in the area with high efficiency. The engine with supercharger Garet achieves high power and at the same time the Air/Fuel ratio is kept. Dates from other supercharger types were experimentally put into simulations and for this designed configuration the best one the original type GT 1241.

The optimal parallel action of the engine and supercharger is explained by its construction and size. The turbine is able to supply sufficient compressor power also by very lean mixtures burning. On the other hand, the compressor is able to supply sufficient air amount so that the required Air/Fuel ratio amount so that required mixing ratio is kept. The model, designed in this way, is prepared for other research work with possible verification on the real engine.

Acknowledgments Published results were acquired targeted using the support for specific university research within the student grant competition TUL. Internal project number 28009.

References

Kovář Z, Beroun S, Scholz C, Blažek J, Drozda H, Salhab Z (2002) Study of the combustion of hydrogen lean mixture in experimental direct injection SI engine. In: FISITA 2002, World Automotive Congress, Helsinki

Popelka J (2010) Přeplňovaný vodíkový motor 1, 2 HYTD, diplomová práce, KSD_DP_629, Liberec 2010

Scholz C, Beroun S, Drozda H, Blažek J (2002) Vodík—palivo pístových spalovacích motorů. AUTOSYMPO 2002, Brno

Scholz C, Kovář Z, Beroun S, Drozda H, Blažek J (2003) Pístový motor pro spalování vodíku. TUL, Liberec

Different Approaches to Calculation of Rotating Ring Deformations of Wrapping Machine

F. Starý, J. Mrázek, P. Kříbala and J. Kamenický

Abstract The article describes different approaches to calculation of rotating ring deformations of wrapping machine and compares results gained by different types of calculations and evaluates precision of results to measured value and difficulty of calculation.

Keywords Wrapping machine · Stress · FEM · Comparison

1 Introduction

During design of machines and mechanisms we can choose from many ways, how to calculate loading and deformations of designed components. Each calculation method has its pros and cons. The methods differ in demands on accuracy of mechanism behavior description and amount of consumed time to create model of mechanism behavior. In most cases the methods with more time-consuming model creation attain more accurate calculation results. The problem is that almost in every calculation of complex mechanism we have to use some simplifications that can bring error in calculation.

F. Starý (✉) · J. Mrázek · P. Kříbala · J. Kamenický
Czech Technical University in Prague, Prague, Czech Republic
e-mail: frantisek.stary@fs.cvut.cz

J. Mrázek
e-mail: jiri.mrazek@fs.cvut.cz

P. Kříbala
e-mail: petr.kribala@fs.cvut.cz

J. Kamenický
e-mail: josef.kamenicky@fs.cvut.cz

L. Ševčík et al. (eds.), *Modern Methods of Construction Design*,
Lecture Notes in Mechanical Engineering, DOI: 10.1007/978-3-319-05203-8_71,

The purpose of this article is to compare demands on behavior description and accuracy of reached results on rotating ring of wrapping machine (Starý and Mrázek 2012). Compared methods are following: Analytical method, FEM calculation of wire model, simplified solid model with boxes, FEM model of real parts without and with modeled welds.

2 Analytical Method

For determination of stress in rotating ring is used calculation for curved beam, where boundary conditions makes from opened beam closed beam. Description of model is visible in Fig. 1 (Kamenický 2013). Forces acting on beam correspond to centrifugal forces from two opposite positioned prestretch devices (FO) and two opposite positioned switchboards (FR). Continuous load (qo) corresponds to centrifugal force of rotating ring. In calculation is mass of inertia of switchboards and prestretch devices moved to the center of beam which causes that torque moments on beam from these parts are ignored. This model further ignores forces from gravity.

Results of analytical calculations are shown in Fig. 2 for rotational speed from 0 to 60 rpm. It is evident from figure that peak values do not respect reinforcements of rotating ring by flanges for screwing switchboards and prestretch devices and on real model will be smaller.

3 FEM Calculations

FEM calculations enable to calculate stress in more complex mechanisms than analytical methods. Accuracy of results is affected with used simplifications and amount of input parameters. 100 % correspondence cannot be achieved for complex structures. For our purposes maximal deviation from experimental measured value was set to 20 %. With increasing number of input condition increases computing time and in calculation cannot be captured accuracy of manufacture of components and deformations introduces during assembly.

3.1 Wire Model

The wire model corresponds with its input parameters and behavior to analytical model. Scheme of this model is shown in Fig. 3. The wire is loaded by four centrifugal forces from switchboards and prestretch devices and centrifugal force of rotating ring. Centrifugal forces of switchboards and prestretch devices are set manually according to calculated speed. Centrifugal force of rotating ring is

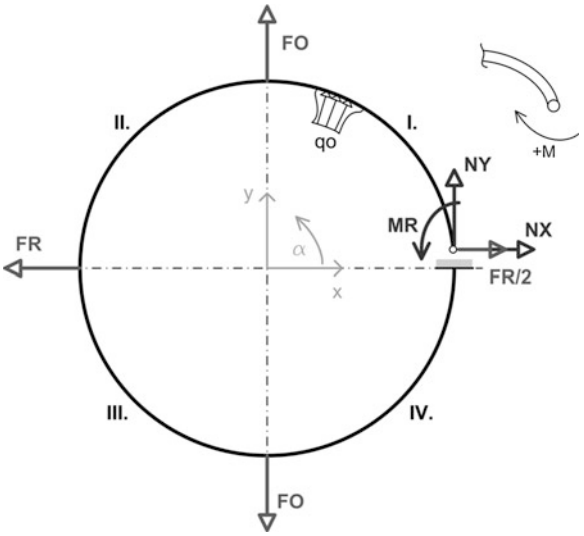

Fig. 1 Forces and bending moments acting on beam

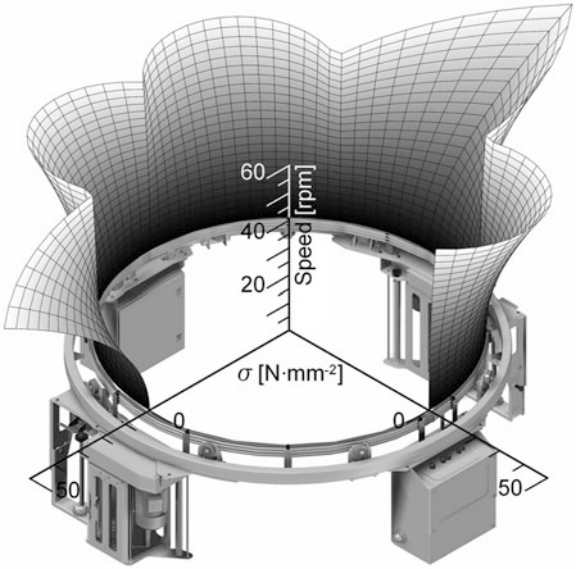

Fig. 2 Behavior of bending moment for rotational speed 0–60 rpm

calculated automatically from rotational speed. Wire is coupled with central point by coupling-continuum distributing which has zero displacement in all three directions and there are also zero angles in this point.

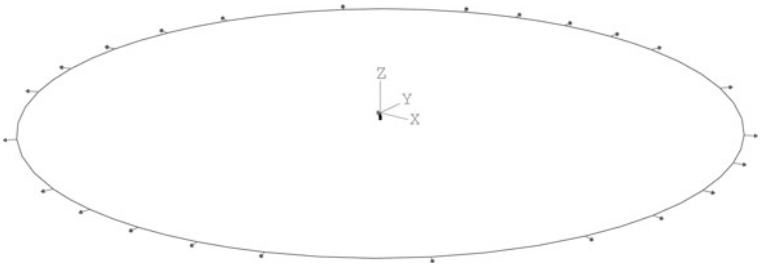

Fig. 3 Wire model of rotating ring for FEM calculation

3.2 Simplified Solid Model

Solid model of rotating ring with switchboards and prestretch devices replaced with boxes is shown in Fig. 4. This model is already affected by deformations from torsional forces. Devices mounted on rotating ring are replaced with boxes, that are of the same weight and has same position of center of mass. It is a very simple model with minimal elaborateness. Advantage of this model is quick determination of boundary conditions. Disadvantage of this model is that reinforcements of rotating ring by flanges for screwing switchboards and prestretch devices are not respected.

3.3 FEM Model with Real Parts

Model with real components was made in two levels of elaborateness (Kříbala 2013). First variant has no welds and second has modeled welds. Model for both variants is shown in Fig. 5.

3.3.1 FEM Model Without Modeled Welds

In model of real machine welded flanges and supports for switchboards are added. The mass of devices is distributed to particular components as much as possible. The rotating ring is not coupled to central point as in previous models. Movement of ring is limited through pulleys (8 radial and 8 axial). The welds are not modeled. Components are connected via bonded contacts in points of contact.

3.3.2 FEM Model with Modeled Welds

In this model are welds modeled according to real machine and joined via bonded contact. Steel sheets that were bonded in previous model can now separate.

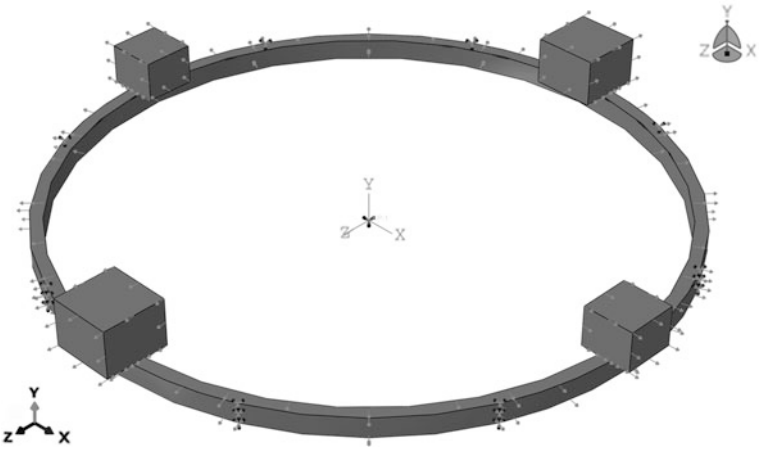

Fig. 4 Model of rotating ring with switchboards and prestretch devices replaced with boxes

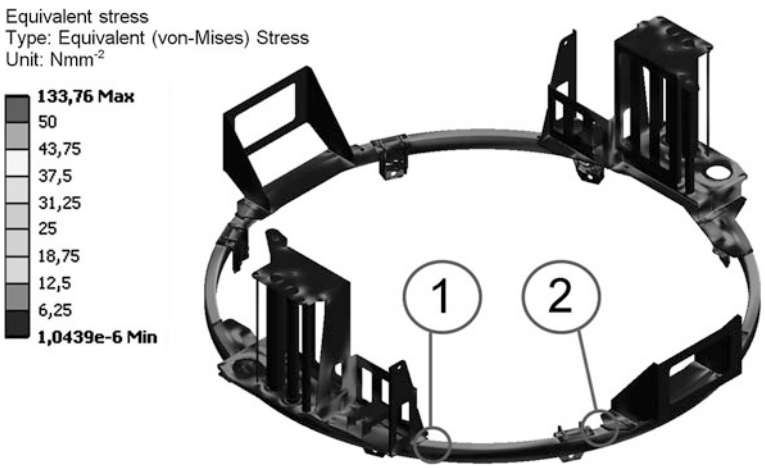

Fig. 5 FEM model of real rotating ring

4 Conclusion

Most simple methods for putting behavior together with short time of calculation are wire model, analytical model and simplified solid model. Behavior along rotating ring circumference is shown in Fig. 6. Accuracy of calculation for all methods is shown in Table 1. First three methods do not satisfy demanded accuracy. Accuracy of these calculations could be improved by adding flanges to calculation, but the calculation would be more difficult. Both FEM calculations with real components meet requirements on deviation under 20 %. Reason for

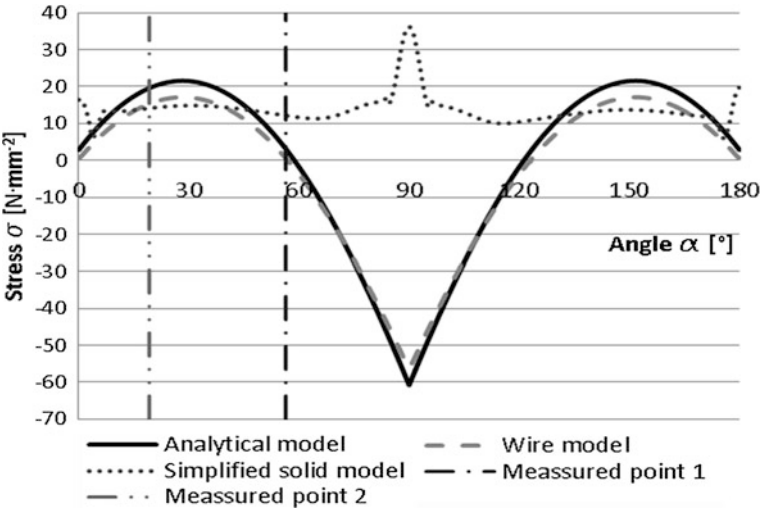

Fig. 6 Behavior of stress along half of rotating ring circumference

Table 1 Comparison of calculated values to measured values in points 1 and 2

Method	Stress in point 1 (N mm^{-2})	Deviation from measurement (%)	Stress in point 2 (N mm^{-2})	Deviation from measurement (%)
Analytical	3.1	94.2	19.6	36.0
FEM—wire	0.6	98.9	15.3	50.0
FEM—simpl. solid	12.1	77.3	14.1	53.9
FEM—no welds	54.6	2.6	26.8	12.4
FEM—with welds	60.0	12.8	30.1	1.6
Measured value	53.2	0	30.6	0

creating model with welds is to achieve better accuracy on prestretch devices, because model without welds is more rigid.

Acknowledgments The research work reported here was made possible by Ministry of Industry and Trade of the Czech Republic grant No. FR-TI3/281. This project runs in cooperation with company Pragometal, s.r.o.

References

Kamenický J (2013) Mathematical and experimental stress analysis of the rotating ring of wrapping machine. Student's conference STC 2013, ISBN-978-80-01-05232-7, Available via STC. http://stc.fs.cvut.cz/pdf13/2592.pdf

Kříbala P (2013) FEM Analysis of construction parts of wrapping machine. Student's conference STC 2013, ISBN-978-80-01-05232-7, Available via STC. http://stc.fs.cvut.cz/pdf13/2591.pdf

Starý F, Mrázek J (2012) Design of the wrapping machine with integrated manipulator. In: Proceedings of 53rd international conference of machine design departments, pp 275–280, ISBN 978-80-214-4533-8

HCR Gearing Geometry Optimization by Using of Generalized Particle Swarm Algorithm

M. Vereš, Ž. Kanović and M. Rackov

Abstract Pitting and temperature scuffing evidenced by damage to teeth flanks of gears are the most important problems needing to be solved in the process of gearing design and calculation. According to current valid standards, such calculations can be resolved with a high level of reliability for all the usual gearing types. However, suitable calculations for High Contact Ratio (HCR) gears have not been adequately researched to date. It has been identified that in HCR gears some different process of scuffing and pitting formation occurs during the gear's operation. Therefore it is actual to deal with optimization of HCR gearing just from these kinds of teeth flanks damages. In article, the authors describe a new method for finding optimal solutions for geometrical parameters h_{a1}^{*}, h_{a2}^{*} and $x_{1,}$ using a Generalized Particle Swarm Optimization Algorithm for both above mentioned optimization tasks.

Keywords HCR gearing · Optimization · Scuffing load capacity · Pitting damage resistance

M. Vereš (✉)
Slovak University of Technology, Staré Mesto, Slovakia
e-mail: miroslav.veres@stuba.sk

Ž. Kanović · M. Rackov
University of Novi Sad, Novi Sad, Serbia
e-mail: kanovic@uns.ac.rs

M. Rackov
e-mail: eng.milan.rackov@gmail.com

L. Ševčík et al. (eds.), *Modern Methods of Construction Design*,
Lecture Notes in Mechanical Engineering, DOI: 10.1007/978-3-319-05203-8_72,

1 Introduction

The High Contact Ratio (HCR) gearing is nowadays commonly used in the automotive gearboxes. Advantage of using such gears just in the transport vehicles transmissions is that this art of gearing has, with comparison to standard involute teeth profiles, low noise and also low load distribution along the path of contact during the whole teeth mesh. Lower load means greater resistance to pitting damage. On the other hand, longer contact line causes an increase in specific sliding and thus increased risk of thermal scuffing formation on the teeth flanks. Moreover, in order to get a further reduction of the vibration and in order to increase the resistance of teeth flanks against the pitting and temperature scuffing damages, HCR gear profiles have to be optimized.

2 High Contact Ratio (HCR) Gearing

The correct working of the gear will be assured if the value of the contact line is higher than that of the base pitch (Fig. 1).

The ratio between the line of contact length g_a, and pitch on the base cylinder p_{bt} (transverse contact ratio) is given by the formula

$$\varepsilon_\alpha = \frac{g_a}{p_{bt}} = \frac{\sqrt{r_{a1}^2 - r_{b1}^2} + \sqrt{r_{a2}^2 - r_{b2}^2} - a_w \sin \alpha_{wt}}{p_{bt}} \tag{1}$$

It is called the transverse contact ratio. Contact ratios for conventional gearing are generally in the range 1.4–1.6; so the number of tooth engagements is either one or two. One special kind of involute, non-standard gearing is called high contact ratio (HCR) gearing, where the contact ratio is higher, and there are always at least two pairs of teeth in contact ($\varepsilon_\alpha \geq 2$).

2.1 Possibilities of HCR Geometrical Parameters Optimization

The most favorable solution how to increase in contact ratio is obtained by increasing addendum height, however there are a lot of geometrical and manufacturing constraints which limit the possibilities of increasing it. Equation (1) shows that $\varepsilon_\alpha = f(g_a, p_{bt})$. The greatest value of the contact ratio ε_α has to be obtained through the greatest possible increase in the length of the line of action g_a. The length of the contact line g_a is calculated in Eq. (2)

$$g_a = \sqrt{r_{a1}^2 - r_{b1}^2} + \sqrt{r_{a2}^2 - r_{b2}^2} - a_w \sin \alpha_{wt} \tag{2}$$

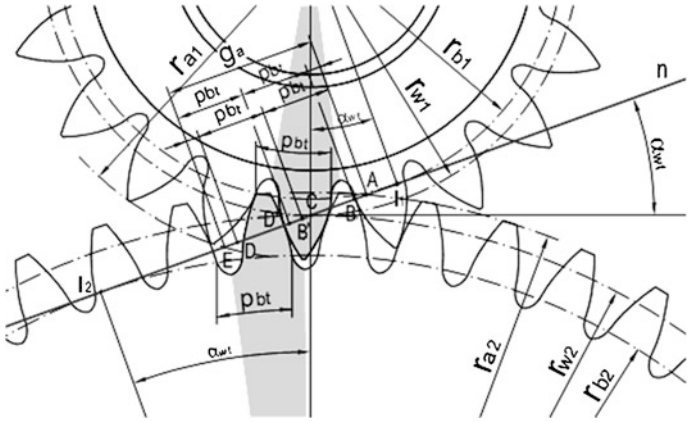

Fig. 1 Geometry and load distribution in HCR gearing

where the tip diameters of the pinion and gear wheel are as follows:

$$r_{a1} = r_1 + \left(h^*_{a1} + x_1\right) \cdot m_n, \quad r_{a2} = r_2 + \left(h^*_{a2} + x_2\right) \cdot m_n \tag{3}$$

From Eqs. (2) and (3), it is clear that the length of the contact line g_a is directly dependent on the addendum height factors h^*_{a1}, h^*_{a2} and the addendum modification factors x_1, x_2. For a given distance between the centers of the wheels, $x_c = x_1 + x_2$ can be expressed as a function of a_w. That means that the contact ratio is the function of both addendum heights and the addendum modification factor of the pinion $\varepsilon_\alpha = f(h^*_{a1}, h^*_{a2}, x_1)$, i.e. optimization parameters h^*_{a1}, h^*_{a2}, x_1 make a non-linear optimization of triple parameters, with limitation requirements defined for:

- removal of primary production and meshing interferences,
- minimum arc thickness of the tooth tip $s_{a1,2}$,
- distribution x_c to x_1, x_2 has to be effected by balancing the slip ratios, strength, or, compromising the conditions of their combinations.

Based on preliminary theoretical considerations optimization task with main objective functions for maximum resistance against pitting damage (Vereš et al. 2012; Rackov et al. 2013) can be defined as

$$\sigma_{HX} = \sqrt{\frac{F_{b_{nX}}}{\rho_r \, \pi . b} \cdot \frac{1}{\left(\frac{1-\frac{1}{\mu_1^2}}{E_1} + \frac{1-\frac{1}{\mu_2^2}}{E_2}\right)}} = \min \tag{4}$$

and on the same way it is possible to define the objective function for maximum resistance against temperature scuffing formation by the formula

$$\vartheta_{BlE} = 0.62\mu\, w_{b_{tE}}^{0,75}\left(\frac{1}{\rho_{r_E}}\right)^{0,25} X_M\left(\sqrt{|v_{\rho_{1E}}|} - \sqrt{|v_{\rho_{2E}}|}\right) = f\left(\frac{\sqrt{|v_{\rho_{1E}}|} - \sqrt{|v_{\rho_{2E}}|}}{\left(\rho_{r_E}\right)^{0,25}}\right) = \min \tag{5}$$

or demand for the contact ratio values $\varepsilon_\alpha = 2$ or $\varepsilon_\alpha = \max$

Of course, these tasks can be combined and defined as multicriteria optimization tasks.

It is clear, that the all above equations can be expressed as functions of pinion and wheel addendum coefficients and addendum modification factor of pinion $(h_{a1}^*, h_{a2}^*, x_1)$. Than as optimization parameters of these optimization tasks we can assume addendum h_{a1}, h_{a2}, and addendum modifications coefficients x_1 and x_2. Generally we can assume also α_n but this is not advisable because this would mean decrease of value α_n, what means also decrease of gearing resistance against fatigue failure in tooth dedendum. For given value of centre distance a_w is known x_c and expressly defined relation between x_1 and x_2. Than the objective functions can be express in the form $\sigma_{HX} = f\left(h_{a1}^*, h_{a2}^*, x_1\right) = \min$, $\vartheta_{BlE} = f\left(h_{a1}^*, h_{a2}^*, x_1\right) = \min$ $\varepsilon_\alpha = f\left(h_{a1}^*, h_{a2}^*, x_1\right) = 2$ or $\varepsilon_\alpha = f\left(h_{a1}^*, h_{a2}^*, x_1\right) = \max$ with constrains of minimum top land width $sa \geq 0.4m_n$, elimination of manufacturing and mesh interferences and slip ratio on the begin and the end of mesh equalization. Solution of these tasks can be realized by different methods. Further is described the originally modified PSO algorithm, which the authors used to solve the above described optimization problems.

3 Generalized Particle Swarm Optimization Algorithm

The optimization method used in this paper is a relatively new method called the Generalized Particle Swarm Optimization Algorithm (GPSO). The algorithm was implemented as a function which allows the user to specify the values of all the adjustable parameters and to define many available algorithm options. Successful optimizers are often inspired by natural processes and phenomena. Indeed, the natural world is extraordinarily complex, but it provides us with remarkably elegant and robust solutions to even the most difficult problems. Compared to other evolutionary techniques, PSO has only a few adjustable parameters, and it is computationally inexpensive and very easy to implement. PSO uses a set of particles called swarm to investigate the search space. Each particle is described by its position (x) and velocity (v). The position of each particle is a potential solution, and the best position that each particle achieved during the entire optimization process is memorized (p). The swarm as a whole memorizes the best position ever achieved by any of its particles (g). The position and the velocity of each particle in the k-th iteration are updated as

$$\begin{aligned} v[k+1] &= w \cdot v[k] + cp \cdot rp[k] \cdot (p[k] - x[k]) + cg \cdot rg[k] \cdot (g[k] - x[k]) \\ x[k+1] &= x[k] + v[k+1] \end{aligned} \tag{6}$$

Acceleration factors *cp* and *cg* control the relative impact of the personal (local) and common (global) knowledge on the movement of each particle. Inertia factor *w*, which was introduced for the first time in (Schutte and Groenwold 2005), keeps the swarm together and prevents it from diversifying excessively and therefore diminishing PSO into a pure random search. Random numbers *rp* and *rg* are mutually independent and uniformly distributed on the range [0, 1]. Particle swarm, however, has also some disadvantages. Most important of them is its inability to independently control various aspects of the search, such as stability, oscillation frequency and the impact of personal and global knowledge. The new algorithm, named Generalized PSO (GPSO), which is described and analyzed in details in (Shi and Eberhart 1999), overcomes the above mentioned flaw. It considers each particle within the swarm as a second-order linear stochastic system with two inputs and one output. The output of such a system is the current position of the particle (x), while its inputs are personal and global best positions (p and g, respectively). The stability and response properties of such a system can be directly related to its performance as an optimizer, i.e., its explorative and exploitative properties. This way, the above mentioned flaw of PSO can be overcome. GPSO uses canonical equation, used in control theory:

$$x[k+1] - 2\zeta\rho x[k] + \rho^2 x[k-1] = \left(1 - 2\zeta\rho + \rho^2\right)(c \cdot p[k] + (1-c) \cdot g[k]) \tag{7}$$

where ρ is the eigenvalues module, and ζ is the cosine of their arguments. Parameter c is introduced to replace both b_p and b_g. The parameters in this equation allow a more direct and independent control of the various aspects of the search procedure.

Based on many analyses of PSO and its parameters, two parameters adjusting schemes, GPSO1 and GPSO2 were proposed in (Shi and Eberhart 1999). In both of them, it is recommended to linearly decrease ρ from about 0.95 to about 0.6, and c from about 0.8 to approximately 0.2. In the first scheme (GPSO1), ζ was adopted as a stochastic parameter with uniform distribution ranging from -0.9 to 0.2, while in the second scheme (GPSO2), ζ was uniformly distributed in the range $[-0.9, 0.6]$.

Using GPSO algorithm, solution of HCR value is obtained in a very short time, less than one second. This solution is very accurate, and it goes till 10^{-15} accuracy. Obtained results calculated by this method are presented in (Kanović et al. 2011; Vereš et al. 2011; Kuzmanović et al. 2012) and shortly further in conclusions.

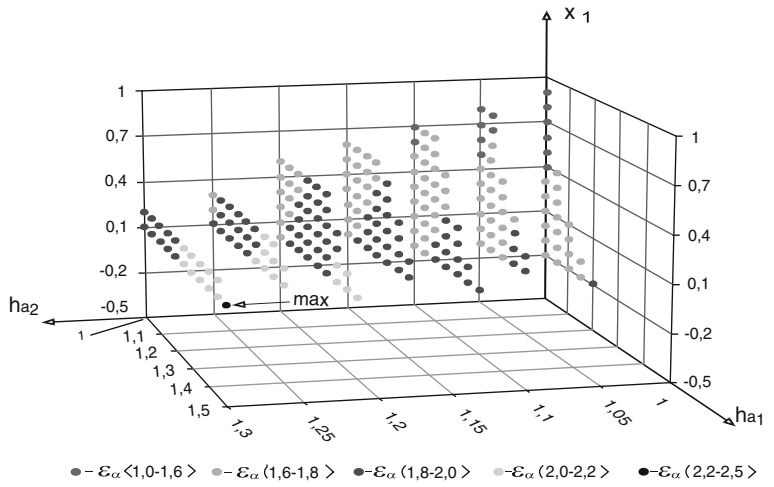

Fig. 2 Optimal values h_{a1}^*, h_{a2}^*, x_1 for objective function defined by expressions (4) and (5)

4 Conclusions

According to the results obtained and their analysis, it is possible to state that the optimization of HCR gearing geometry from the point of view of minimizing temperature scuffing damage and pitting damage are important tasks in transmission design. There on the Fig. 2 are displayed results of such optimization task for concrete transmissions parameters ($a_w = 144$ mm, $z_1 = 21$, $z_2 = 51$, $mn = 4$ mm).

Optimizing the results to fully meet the requirements stated in the objective functions, when the results meet the defined conditions, demonstrates that the whole process to find the optimal vector $(h_{a1}^*, h_{a2}^*, x_1)$ is limited by the small number of suitable combinations of optimizing parameters. However, swarm-based methods in general, and PSO in particular, provide us with powerful and robust tools for tackling the global optimization problems encountered in science and engineering.

As a result of incorporating requirements of the properties of exploration and exploitation which were formerly usually connected to linear control theory, GPSO has recently been proposed as a method for addressing optimization issues. PSO however has some disadvantages. The key disadvantage is its inability to independently control various aspects of the search, such as the stability, oscillation frequency and the impact of personal and global knowledge.

The new algorithm named Generalized PSO (GPSO), overcomes the above mentioned flaw. The method presented here of finding optimal solutions for h_{a1}^*, h_{a2}^* and x_1 uses the GPSO Algorithm and MATLAB as a program for optimization. This GPS optimization is a very fast and reliable method. Using this

method provides an infinite number of very precise solutions to the transcendental equation defined in the objective function for HCR geometry optimization.

Acknowledgments This contribution has been developed as a result of Project 1/0277/12 subtask, supported by the Slovak VEGA Grant Agency.

References

Kanović Ž, Rapaić MR, Jeličić ZD (2011) Generalized particle swarm optimization algorithm—theoretical and empirical analysis with application in fault detection. Appl Math Comput 217:10175–10186

Kuzmanović S, Vereš M, Rackov M (2012) Generalized particle swarm algorithm for HCR gearing geometry optimization. In: Scientific Proceedings FME, pp 119–126. ISSN 1338-1954

Rackov M, Vereš M, Kanović Ž, Kuzmanović S (2013) HCR gearing and optimization of its geometry. Adv Mater Res 633:117–132

Schutte JC, Groenwold AA (2005) A study of global optimization using particle swarms. J Global Optim 31:93–108

Shi Y, Eberhart RC (1999) Empirical study of particle swarm optimization. In: Proceedings of IEEE international congress on evolutionary computation, vol 3 pp 101–106

Vereš M, Bošanský M, Rackov M (2011) Theoretical and experimental research of the HCR gear's contact strength. Mach Des 3(2):105–108 (ISSN 1821-1259)

Vereš M, Kuzmanović S, Rackov M (2012) Experimental research of HCR gearing from pitting damage point of view. In: Proceedings of 7th international symposium about mechanical and industrial engineering, KOD 2012, pp 317–320. ISBN 978-86-7892-399-9

Part VI
Modern Material and Technology

Mustafa M. Abdulgadir, R. Bašťovanský, S. Poljak, T. Donič, P. Bocko, O. Marada, T. Bouda, J. Ilčík, D. Koutný, D. Paloušek, M. Matuszak, P. Kochmański, B. Powalka and J. Petřík

Part VI—Without exaggeration we can say that the twentieth and twenty-first centuries may be considered as the century of modern materials and technologies. This is primarily due to the development of knowledge in the field of material science and application of new materials that bring new, unique properties such as high strength and toughness at low weight, extreme hardness, etc. These materials increase the added value of the product, comfort of use, product life, and also reduce production costs. Obviously, these materials require innovative working procedures including testing and consequential evaluation and interpretation of obtained results. This section contains six articles on this topic that bring new insights and knowledge into areas of machining, cutting, testing, and simulation properties.

Cutting Forces Analysis During High Speed Milling of Hardened Tool Steel

Mustafa M. Abdulgadir

Abstract The paper presents an experimental investigation of high speed milling of a hardened tool steel when machining sculptured and flat surfaces from the point view of a tool load. The experiments were performed on a hardened tool steel (DIN 1.2080) of 52 HRc hardness using index able insert toroidal cutter employing coated carbide bits. The effect of different tool paths, process parameters and rates of a tool wear on the cutting forces induced was investigated. The cutting parameters involved were cutting speeds ranging from 150 to 430 m/min, constant feed rate 0.1 mm/tooth and axial-radial depths of cut 0.5 mm. The optimum cutting conditions were specified based on the cutting forces induced.

Keywords High speed milling (HSM) · Tool steel · Process parameters · Tool path · Cutting forces

1 Introduction

Recent development in cutting tool materials, coating techniques, machine tools and CAD/CAM systems, have resulted in a wide spread of high speed cutting (HSC) technology (Schulz 2001). The most significant benefit of its use can be observed in a die and mould industry, where the savings in manufacture of hardened steel components are substantial especially in terms of reduced machining cost and time consumption in comparison with the traditional way. Milling of molds and dies with structured surfaces may be performed in a different way causing changes in a cutting tool force load. Especially in finishing milling this may cause problems in achieving high precision of surfaces being machined.

M. M. Abdulgadir (✉)
Libyan Arab Jamahyriya, The Higher Technical Institute, Elgubba, Libya
e-mail: elgubba2008@yahoo.com

L. Ševčík et al. (eds.), *Modern Methods of Construction Design*,
Lecture Notes in Mechanical Engineering, DOI: 10.1007/978-3-319-05203-8_73,

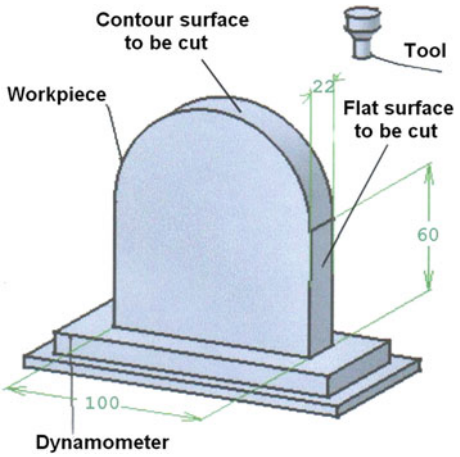

Fig. 1 Work piece shape and a measurement set-up

On a workpiece with a combination of flat and round surfaces using different ways of cutting, state of a tool wedge wear, the cutting forces were measured in the regime of HSM to reveal the cutting forces and the tool force load changes.

2 Experimental Procedures

2.1 Work Piece Material, Tooling and Equipment Used

The work piece material was high-alloyed tool steel, heat treated to 52 HRc, DIN 1.2080, with chemical composition in [%] (C 1.80–2.05, Si 0.20–0.45, Mn 0.20–0.45, P $\leq$ 0.030, S $\leq$ 0.035, Cr 11.0–12.5 and Ni $\leq$ 0.50). The work piece was prepared to allow both flat and contour surface machining to imitate die and mould machining, see Fig. 1.

For the experiments, 25 mm diameter index able insert torodial cutter was used, with only one screwed mounted insert to avoid the effect of a bit run-out. According to ISCAR the tool making company, sintered carbide of a new generation IC908 was used for high speed milling purposes. This insert was coated with a TiAlN layer, 4 μm thick. The assembly was provided with a rake angle of +8° and a primary relief angle of +19°. Chamfered edge was 0.160 mm wide and the corner radius was 6.2 mm. Cutting experiments were performed on a MCV 750 A, vertical 3-axis CNC milling centre with maximum spindle speed of 14,000 rev/min, and power output of 36 kW. The cutting force components (Fx, Fy, Fz)

were measured using a Kistler piezoelectric dynamometer (type 9,255 A) and charge amplifier (type 5007) connected to a PC with a measuring and analyzing software (Labview 6.1). Tool wear measurements were performed using a CCD video microscope system provided with a 150× magnification lens.

Operating parameters and tests procedure:

Two types of tests were performed according to the type of a milling operation.

2.1.1 Flat Surface High Speed Milling

Down and Up High Speed Milling was employed with tests performed without a coolant (Urbanski et al. 2000). Cutting tool axis was oriented normal to the workpiece surface with 50 mm of a cut length for each tool pass. The operating conditions were applied as typical for semi-finishing. Three different cutting speeds were tested (150, 300, 430 m/min) with an unworn insert and with a worn one (the worn insert was with VB = 0.25–0.30 mm). Fixed parameters were the axial depth of cut of 0.5 mm, the radial depth of cut (step over) of 0.5 mm and the feed of 0.1 mm/tooth Elbestavi et al. (1997).

2.1.2 Contour Surface High Speed Milling

The same cutting conditions were used on a contour surface of 100 mm in diameter and a width of 22 mm, using unworn and worn inserts as well. The worn one was with a flank wear VB = 0.25–0.30 mm. Each cutting speed was employed in down and up dry High Speed Milling. In addition, three different machining ways were tested the upward, the plane, and the downward machining. The cutting speed was not constant along the machining path, because of the changing lag angle (β_i) which is not constant in such machining operations (this angle is defined as an angle between the tool axis and the surface normal) (Koshy et al. 2002). According to the changes in lag angle, the effective tool diameter is changing too, from the maximum value at the engagement beginning to the minimum value at the top of the workpiece, Fig. 2.

Figure 3. Shows the cutting force component directions taken according to the axes of the machine tool,used in this work.

3 Results

Under the conditions specified in the previous chapters, the experiments were run, the results of them are shown in Table 1a–c. From the components the resultant force F_r was calculated (Table 1d–f) and plotted in Fig. 4a–d.

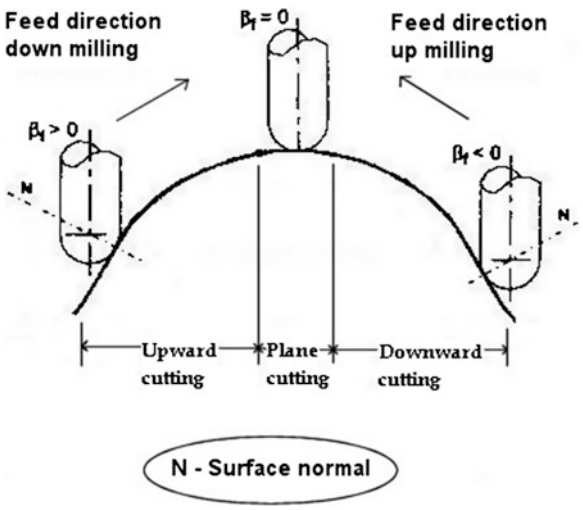

Fig. 2 Three cutting types applied in a contour surface High Speed Milling, and a change of the *lag angle*

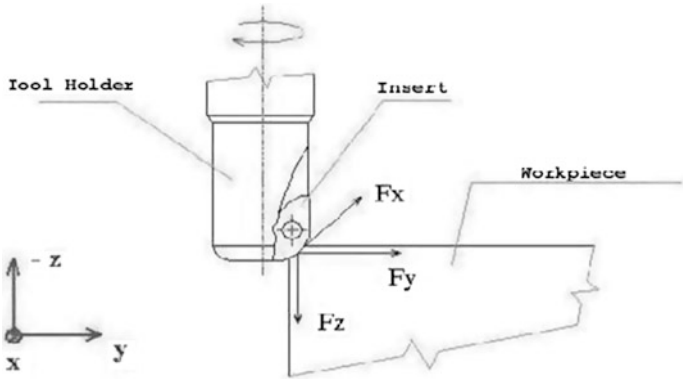

Fig. 3 Cutting force components directions according to the machine tool

4 Conclusion

4.1 Milling of a Flat Surface

As shown in Table 1a–c the highest force component is the axial thrust force F_z ranging between 711–812 N for up and down milling while the other two components are much lower and vary between 150–363 N. Up milling in case of cutting a hardened tool steel may have larger negative influence on a tool life

Table 1 a Force components results obtained at $V_c = 150$ m/min, f = 0.1 mm/tooth, ap = 0.5 mm and ae = 0.5 mm. b Force components results obtained at $V_c = 300$ m/min, f = 0.1 mm/tooth, ap = 0.5 mm and ae = 0.5 mm. c Force components results obtained at Vc = 430 m/min, f = 0.1mm/tooth, ap = 0,5 mm and e = 0.5 mm. d Force resultant obtained at $V_c = 150$ m/min, f = 0.1 mm/tooth, ap = 0.5 mm and ae = 0.5 mm. e Force resultant obtained at $V_c = 300$ m/min, f = 0.1 mm/tooth, ap = 0.5 mm and ae = 0.5 mm. f Force resultant obtained at $V_c = 430$ m/min, f = 0.1 mm/tooth, ap = 0.5 mm and ae = 0.5 mm

Operation type	Insert	Force (N)	Flat surface	Contour surface		
				Upward	Plane	Downward
a						
Up milling	Unworn insert	F_x	182	217	194	40
		F_y	183	50	170	192
		F_z	791	230	610	245
	Worn insert	F_x	356	406	225	197
		F_y	364	102	262	319
		F_z	1,556	510	836	419
Down milling	Unworn insert	F_x	273	199	199	242
		F_y	193	181	186	147
		F_z	744	226	752	151
	Worn insert	F_x	408	351	243	293
		F_y	354	315	251	95
		F_z	1,530	421	903	520
b						
Up milling	Unworn insert	F_x	235	168	325	240
		F_y	150	101	363	60
		F_z	707	188	535	80
	Worn insert	F_x	405	291	343	358
		F_y	276	182	447	133
		F_z	1,316	296	710	203
Down milling	Unworn insert	F_x	363	160	186	183
		F_y	194	157	351	118
		F_z	812	231	520	146
	Worn insert	F_x	407	230	245	273
		F_y	410	225	463	183
		F_z	1,427	365	774	252
c						
Up milling	Unworn insert	F_x	195	135	226	107
		F_y	168	116	354	265
		F_z	711	195	906	490
	Worn insert	F_x	312	190	306	195
		F_y	300	194	496	352
		F_z	1,094	360	1,076	596
Down milling	Unworn insert	F_x	309	109	158	109
		F_y	213	259	367	150
		F_z	807	479	982	287
	Worn insert	F_x	405	180	220	197
		F_y	377	361	502	214
		F_z	1,116	601	1,176	376

(continued)

Table 1 (continued)

Operation type	Insert	Force (N)	Flat surface	Contour surface		
				Upward	Plane	Downward
d						
Up milling	Unworn insert	F_r	832	320	662	314
	Worn insert	F_r	1,637	660	905	562
Down milling	Unworn insert	F_r	816	351	800	321
	Worn insert	F_r	1,622	532	968	604
e						
Up milling	Unworn insert	F_r	760	272	724	260
	Worn insert	F_r	1,404	453	906	433
Down milling	Unworn insert	F_r	910	322	654	262
	Worn insert	F_r	1,540	487	935	414
f						
Up milling	Unworn insert	F_r	756	264	999	567
	Worn insert	F_r	1,177	451	1,224	719
Down milling	Unworn insert	F_r	890	555	1,060	342
	Worn insert	F_r	1,246	724	1,297	475

because of larger friction at the beginning of cut before minimal chip thickness is reached. Its influence has not been evaluated. The influence of a changing cutting velocity is shown for the resultant force F_r. A relatively low tool wear (VB = 0.25–0.3 mm) may increase the cutting force components substantially, especially the thrust force F_z.

4.2 Milling of a Contour Surface

Three machining types (upward, plane and downward) were performed on a contour surface, Fig. 2. For the two machining types (upward and downward), no substantial differences in all cutting force components were found for both cases in up and down milling. The thrust force F_z does not exceed substantially the other two components. Also a tool wear has a lower influence on a force increase than in case of flat surface milling. Milling of the short part on the top of the workpiece (marked as plane milling) seems to be very close to flat surface milling with the thrust force F_z the highest (Metal Handbook 1989). To reveal influence of the cutting velocity on a tool load the cutting force resultant F_r was calculated. Figure 4b–d are of the same character indicating the cutting velocity around $V_c = 300$ m/min to be the optimal one for practical use. Diagrams also show the influence of a tool wear which is important to count with in case of a tool low rigidity. The presented study shows differences in a tool load especially when a

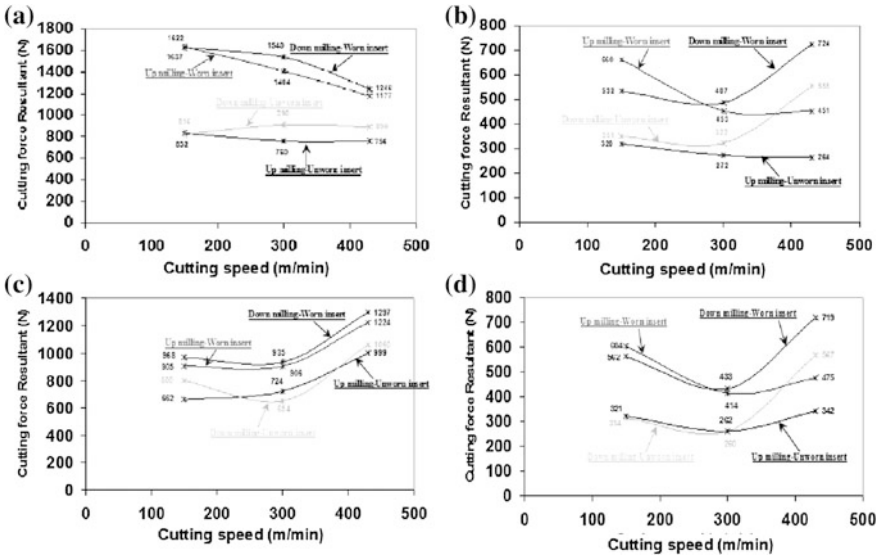

Fig. 4 **a** Cutting forces versus cutting speeds; f=0.1mm/tooth, ap = 0.5 mm and ae = 0.5 mm, flat surface **b** Cutting forces versus cutting speeds; f = 0.1 mm/tooth, ap= 0.5 mm and ae = 0.5 mm, Contour surface *Upward* cutting, **c** Cutting forces versus cutting speeds; f = 0.1mm /tooth, ap = 0.5 mm and ae = 0.5 mm, Contour surface *plane* cutting, d) Cutting forces versus cutting speeds; f = 0.1 mm/tooth, ap = 0.5 mm and ae = 0.5 mm, Contour surface *downward* cutting (Baptista and Antune Simoes 1999)

tool crosses from one surface to another one following the required surface line. Of a less importance proved to be the way of milling (up and down) or whether the tool moves downwards or upwards the contour surface.

References

1. Metal Handbook (1989) Volume 16 machining. Prepared under the direction of the ASM. International handbook committee, ASM International, USA
2. Schulz H (2001) Scientific Fundamentals of HSC. C. Hanser V, Munchen
3. Productive Metal Cutting (1997) Sandvik Coromant, Technical Editorial Dept, Sweden
4. Urbanski JP, Koshy P, Dewes RC (2000) High speed machining of moulds and dies for net shape manufacture. The University of Birmingham, Edgbaston, Birmingham, UK
5. Elbestavi MA, Chen L, Becze CE (1997) High speed milling of dies and moulds in their hardened state. Intelligent machine and manufacturing research center, McMaster University, Hamilton, Ont, Canada, 9 Jan 1997
6. Koshy P, Dewes RC, Aspinwal DK (2002) High speed end milling of hardened tool steel.school of engineering. University of Birmingham, Edgbaston, Birmingham, UK
7. Baptista R, Antune Simoes JF (1999) Three and five axes milling of sculptured surfaces. School of technology/polytechnic institute of Setubal, Setubal, 17 Dec 1999

Rotary-Die ECAP System: Static and Dynamic

R. Bašťovanský, S. Poljak and T. Donič

Abstract For the purpose of creating nanostructures in the metallic materials was designed a special experimental system. This system has a very simple way to ensure repeat deformation group procedure that functional part of the system is able to rotate. Blanks for the experimental work was 99.9 % aluminium powder, which was compressed pressure of 600 MPa, then the forward extruded and that sample was then used in ECAP system. Universal deformation system Rotary Die ECAP was used in the process of static deforming—hydraulic press, but also at higher speeds on Cam plastometer and also for high-speed deformation—HILTI system. Metallographic analysis of products derived from these types of deformation were analyzed in detail.

Keywords Forward extrusion · High strain rate · ECAP · Ultra-fine powder

1 Introduction

A new ECAP process method called the rotary—die equal channel angular processing (RD—ECAP) method was developed at Japan's National Institute of Advanced Industrial Science and Technology of Nagoya to form fine—grained bulk materials such as aluminum alloys, aluminum composites, magnesium alloys and titanium. In this paper, the RD—ECAP process is explained and it is use in the

R. Bašťovanský (✉) · S. Poljak · T. Donič
University of Žilina, Žilina, Slovakia
e-mail: bastovanskyr@fstroj.uniza.sk

S. Poljak
e-mail: poljaks@fstroj.uniza.sk

T. Donič
e-mail: donict@fstroj.uniza.sk

L. Ševčík et al. (eds.), *Modern Methods of Construction Design*,
Lecture Notes in Mechanical Engineering, DOI: 10.1007/978-3-319-05203-8_74,

processing static and dynamic deformation conditions of aluminum powder of size particles 1 μm. However, in conventional ECAP method, the billet must be removed from the die and reinserted back for the next processing, making the process inefficient. Using the RD—ECAP method, up to 4 passes of ECAP—style severe plastic deformation is possible without billet removal.

Schematic diagrams of the RD—ECAP method are shown in Fig. 1. It consists of four cylindrical channels meeting at the center of the rotary die and four punches in the corresponding channels. The sample is set into the center of the hole. Then, the four punches are placed into the holes from the four directions and the die is set on a die holder. The sample is extruded to the left direction because the right punch and the bottom punch are locked in place due to contact with the die holder. After this extrusion, the die is rotated clockwise 90° to the initial configuration with the exposed punch at the top, and a second pressing is performed (Petrů et al. 2013).

2 Virtual 3D Model of New RD—ECAP

For construction of deformation system RD—ECAP was necessary to propose mathematical models that respect the basic design requirement.

Virtual models must comply with design and technological requirements for the production of this experimental system. The construction must ensure the conditions of universality, that is operative confusion functional parts of the tool. The creation options for the deformation of samples of different diameters to 12 mm in diameter, of course other shapes.

The basic presentation of the mathematical model of RD—ECAP is shown in Fig. 2.

Deformation system RD—ECAP is predominantly loaded by extreme tensile stresses, which spread from the center of plastic deformation, in the centre, where the deformation of the channels cross.

Solid fixation of the central zone of deformation in two spherical shaped blanking elements of fortification is very advantageous term provides a great shape and stiffness of RD—ECAP, Fig. 3.

The different stages of decomposition of the RD—ECAP are shown in Fig. 4.

The experimental material for verifying the functionality of the new RD—ECAP has an aluminium powder with a particle size 1 μm. Verification the RD—ECAP was carried out under static conditions—Heckert system as well as in dynamic conditions of cam plastometer—Fig. 5 and explosive devices HILTI—Fig. 6. Deformation Speed cam plastometer to be in the range 2–10 m/s for HILTI 800–1,200 m/s.

These systems are compact deformation associated with the registration firm Kistler Electric system and recording digital oscilloscope Tektronix TDS 3034. Registration worked very dynamic, crushing forces was smooth. Tightness of the crumple zone was intact, specimens were geometrically perfect.

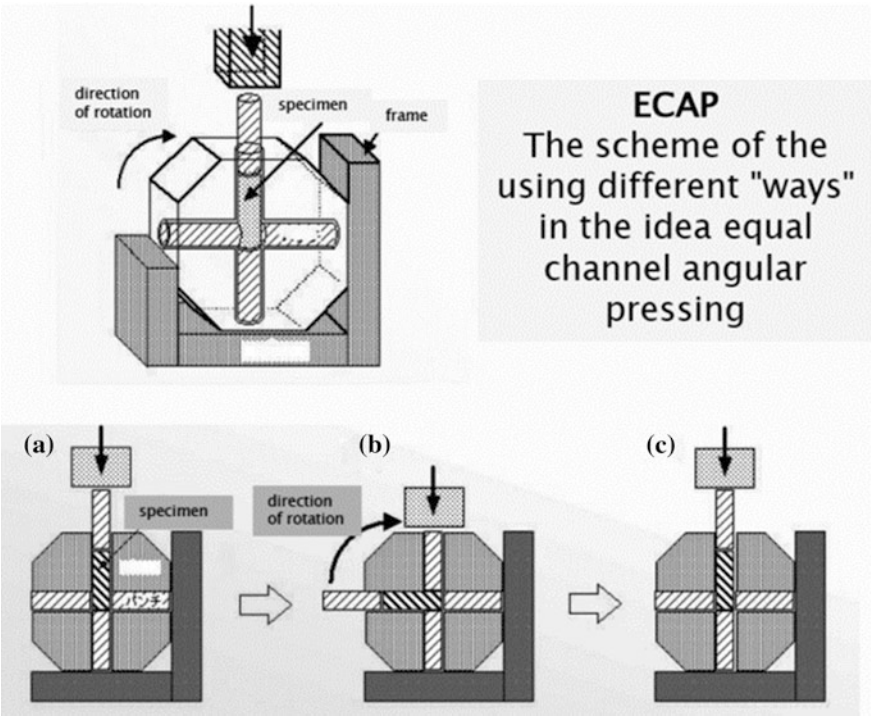

Fig. 1 Schematic diagram of rotary—die equal channel angular processing. Initial state (**a**), offer the pass (**b**), after 90° die rotation (**c**) (Nishida et al. 2001)

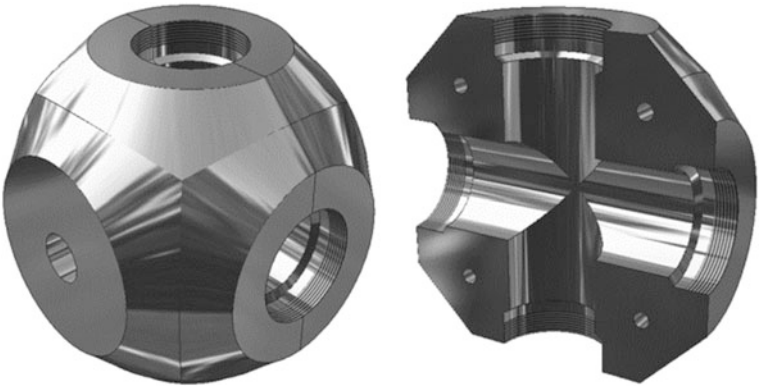

Fig. 2 Virtual 3D model of new RD—ECAP system

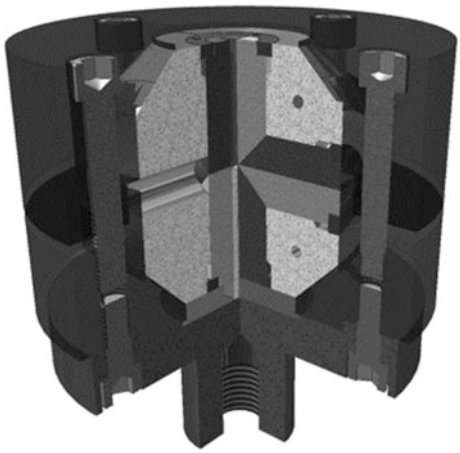

Fig. 3 The core RD—ECAP system located between two blanking elements

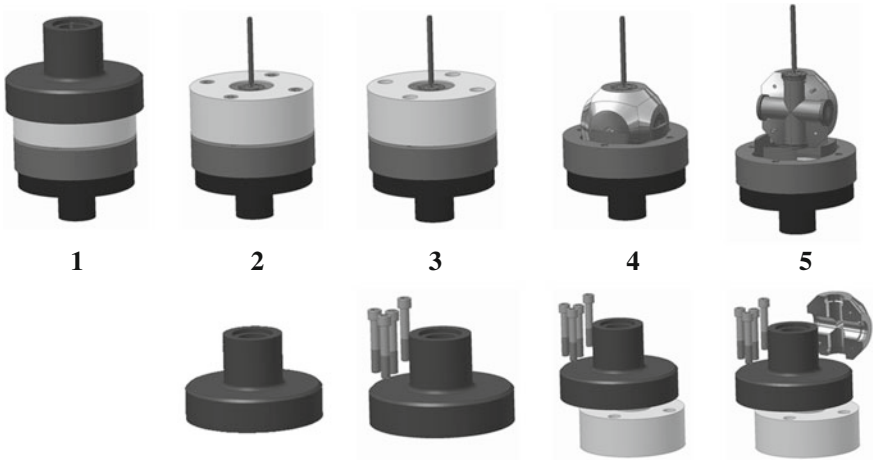

Fig. 4 Different stages of decomposition RD—ECAP

3 Experimental Verification of the RD—ECAP

Detail of the dismantling of functional RD—ECAP after deformation is shown in Fig. 7 Specimen this case to 3 mm diameter.

Detail of the microstructure of aluminum powder with a particle size of 1 μm in the zone of maximum shear deformation is presented in Fig. 8.

The zone of deformation identified areas where very likely there was a strong diffusion process of the accumulated strain energy obtained from dynamic shock action. Grain size was below 1 μm.

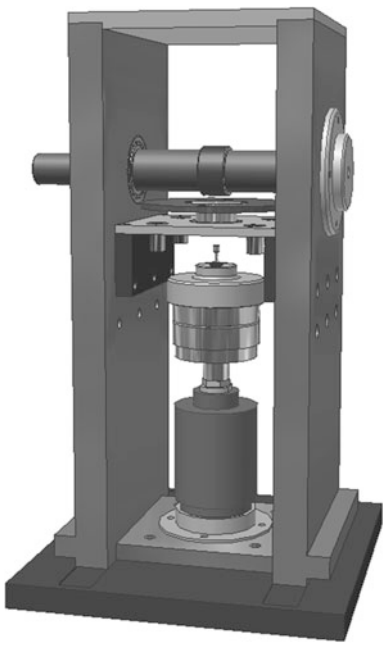

Fig. 5 Experimental dynamic cam plastometer

Fig. 6 Experimental high speed system HILTI

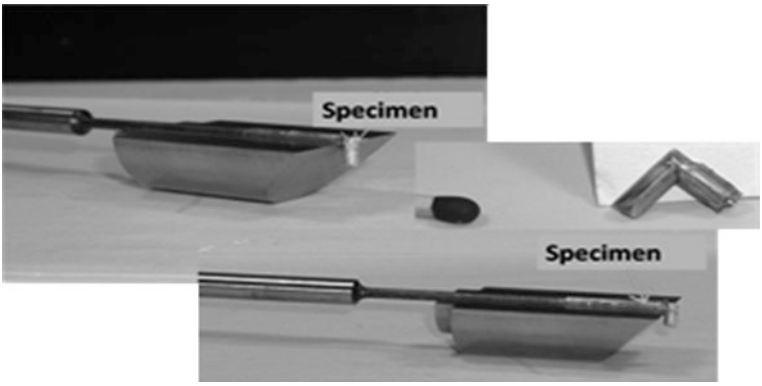

Fig. 7 Decomposition of core RD—ECAP system, specimen 99.99 % aluminum powder, particle size 1 μm

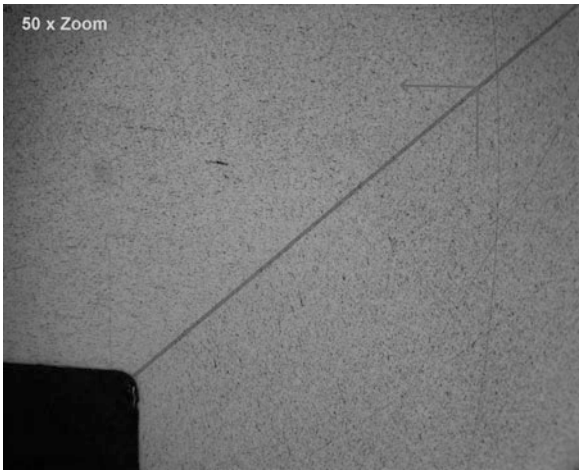

Fig. 8 Microstructure of compaction of aluminum powder in the zone of maximum shear stress of RD—ECAP

The experimentally obtained load—displacement curves of the plunger for the rotary die equal channel angular pressing is presented in Fig. 9. Experimental material is aluminum 99.99 % powder, size particles 1 μm.

The functional dependencies presented in Fig. 9 may be made the following conclusions:

- Character, hence the shape of functional dependencies $F = f(h)$ static and dynamic is vastly different.
- Incremental increase in dynamic power per unit of time compared to the analogues static change is much more.
- Dynamic functional dependency $F = f(h)$ has not monotonous character as the same functional dependence of static.

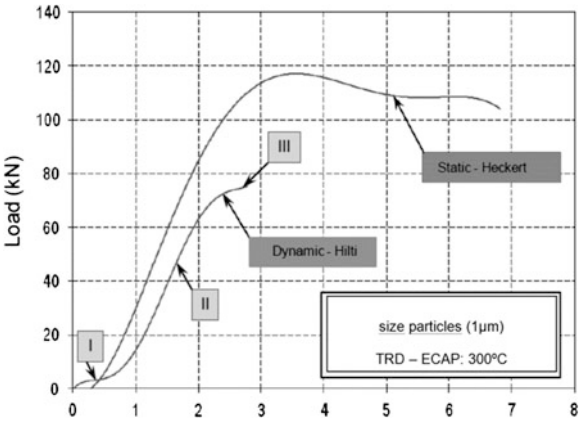

Fig. 9 Experimentally obtained load—displacement curves of the plunger for the rotary—die equal channel angular pressing at 300 °C, aluminum 99.99 % powder, size partials 1 μm

- On functional dependence of the dynamic F = f(h) it is possible to identify at least three distinctive areas, where the first derivate of the path by time i.e. velocity, that rate has different values of acceleration—I, the stable compaction deformation—II and the stead braking—III.

4 Conclusions

Because the samples before the actual process of ECAP—Rotary Die, were not individual particles and sintered aluminium powder was substantially covered with oxide layer and in the operation of forward extrusion, the oxide layer is not perfect destructed and consequently the process of self diffusion of pure aluminium material is very limited. This shortcoming could not be eliminated by the operation nor ECAP Rotary Die as demonstrably proven by metallographic analysis. Upgrade of Rotary Die ECAP with the possibility of heating the functional parts would be a promising procedure for the procedure diffusion activation between aluminium particles which would result in a homogenous ultra fine metal aluminium structure.

- Presented RD ECAP system fulfill extreme requirements on internal and external universality of forming construction—system.
- RD ECAP is possible implemented into three experimental load systems—HECKERT, HILTY and CAM Plastometer.
- The heating system module is independent part of system RD ECAP and arrange heating samples up to 700 °C.
- RD ECAP system is possible used for circle and square shape of specimens.

Acknowledgments This work was created by the implementation of the "Reengineering of the product portfolio of VIPO a.s.", "ITMS: 26220220091" to support the Operational Programme Research and Development financed by the European Fund for Regional Development.

References

Nishida Y et al (2001) Rotary-die equal-channel angular pressing of an Al–7 mass % Si–0.35 mass % Mg alloy. Scr Mater 45:261–266. www.elsevier.com/locate/scriptamat

Petrů M et al (2013) FEM study of the strain kinematics in the 3D nanofibrous structure prepared by the electrospinning process. Appl Math 4:80–90. www.scirp.org/jornal/am

Material and Component Testing of Conveyor Belts and its Numerical Analyses

P. Bocko, O. Marada and T. Bouda

Abstract This paper contains information about complex material and component testing of conveyor belts which are used for its numerical analyses. Paper also contains description of methods used for calibration of user defined material models and building of numerical models. Material tests include determining of mechanical properties of rubber cover plies, textile reinforcements and textile plies with adjacent rubber. Component tests include uniaxial tension, biaxial tension, bending and impact tests of complete conveyor belts. This solution is part of complex research of conveyor belts affected especially by impact loading in brown coal surface mine. Bergström–Boyce material model and chain strain multiaxial failure criterion is used for rubber plies numerical simulations in Abaqus Standard and Explicit. Internal failures of conveyor belts caused by impact tests are evaluated on the basis of computer tomography.

Keywords Conveyor belt simulation · Rubber · Bergström–Boyce · Multiaxial mechanical behavior · Impact damage

1 Introduction

Numerical simulation of conveyor belts is important for optimization of impact area of return stations, especially distribution and type of rollers. This solution is part of complex research of conveyor belts affected especially by impact loading in

P. Bocko (✉) · O. Marada
IDIADA CZ a.s., Mladá Boleslav, Czech Republic
e-mail: peter.bocko@idiada.cz

O. Marada
e-mail: ondrej.marada@idiada.cz

T. Bouda
Czech Technical University in Prague, Prague, Czech Republic
e-mail: bouda.tom@gmail.com

L. Ševčík et al. (eds.), *Modern Methods of Construction Design*,
Lecture Notes in Mechanical Engineering, DOI: 10.1007/978-3-319-05203-8_75,

brown coal surface mine. The main task of this project is to increase working life of conveyor belt based on optimization of size and shape of transported parts, dropping height, design of the belt and impact area. Project contains theoretical, experimental and numerical analyses and it is solved in cooperation with IDIADA CZ, TU of Liberec and Severočeské doly a.s. Project is oriented especially to optimization of drive and return stations using of detailed numerical models, new design concepts and materials (Bocko et al. 2012).

2 Material and Component Tests

The first important input for numerical model is material model of rubber cover plies. The second important input is material model for each breaker and carcass plies made by tests of those separate plies—uniaxial and biaxial tension tests. Smaller parts of all plies could be easily separated for testing specimen. Bigger specimens of rubber cover could be made from raw cover plies used for renovations. An independent test of textile reinforcements was also part of this project (Fig. 1).

Testing of rubber specimens for Bergström–Boyce model definition: (Table 1)

(a) Stress–strain test—curves for the first five load cycles, five different strain levels, Mullins softening (Fig. 2) (Bergstrom and Boyce 1998),
(b) Stress–strain test—three strain levels with relaxation (Fig. 3) (Bergstrom and Boyce 1998),
(c) Stress–strain test—curves for the same strain levels, independent tests at different strain levels (e.g. 10 cycles at true strain at level-1),
(d) Elongation at break including optical recording of breaking,
(e) Additional tests (friction, hardness, etc.) (Petrikova et al. 2013).

3 Tests of Complete Conveyor Belts

As a third step, the complete conveyor belts multiaxial behavior and impact tests are necessary for numerical model validation. Uniaxial and biaxial tests are realized in biaxial testing machine using tension force measurement and optical monitoring of deformation (Pesek 2006). Four different shapes of testing specimens were tested—rectangle, two widths of Greek and one Pattée cross. Different combinations of longitudinal and lateral forces and its magnitudes were tested (e.g. 100 % nominal pretension force in longitudinal direction and 0 % in lateral direction—both directions fixed). Strains in different specimen locations are outputs from this test. Additionally the 3 point bending tests were realized (Petrikova et al. 2013) (Fig. 4).

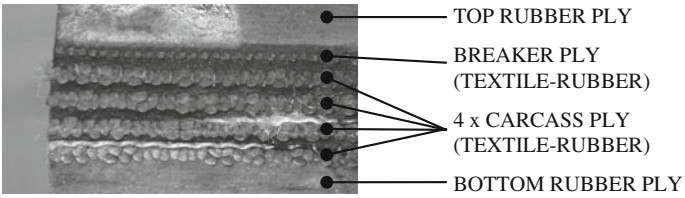

Fig. 1 Plies of conveyor belt P2500 4+1; 8+4 A

Table 1 True strain and elongation

True strain	Elongation (%)	Elongation/elongation at break (%)
−0.2	**22.1**	**4.9**
−0.4	**49.2**	**10.9**
−0.6	**82.2**	**18.3**
−0.8	**122.6**	**27.2**
−1	**171.8**	**38.2**
−1.2	232.0	51.6
−1.4	305.5	67.9
−1.6	395.3	87.8
−1.8	505.0	112.2

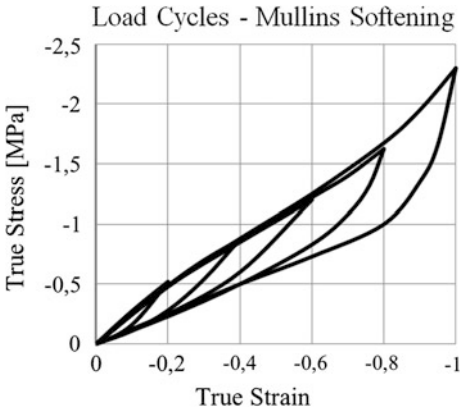

Fig. 2 Stress–strain curves for the first five load cycles (elongation at break is 450 %)

Impact tests are realized in impact testing machine (Fedorko et al. 2013a). Specimen pretension, dropping height and impact forces are continuously registered by measurement system. Dropping height is between 0 and 260 cm. Impactor weight could be 50–100 kg. Six types of impactors are available. Two types are used for project—normalized impactor with radius 25 mm and user defined pyramid with angle 74°. Pyramidal impactor 74° could break through the strengthen conveyor belt P2500 used in project. Breaking and internal failures from impact

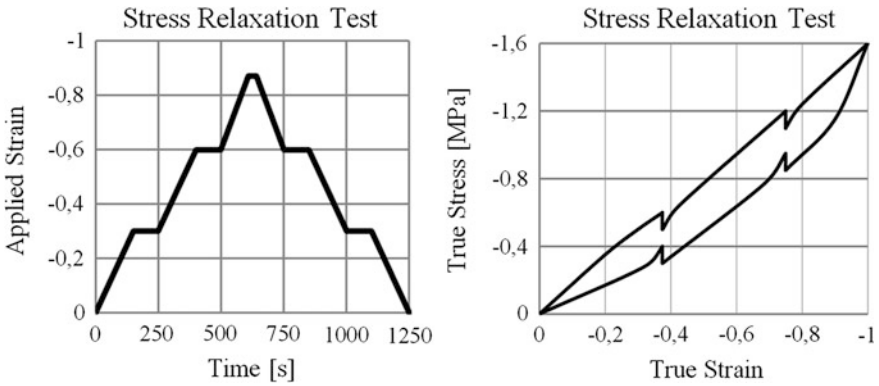

Fig. 3 Stress–strain test with relaxation—loading scheme

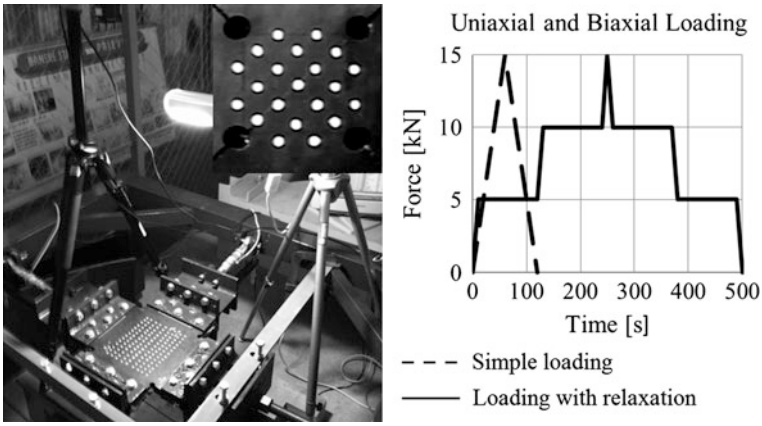

Fig. 4 Uniaxial and biaxial testing (detail of Patée cross) device and loading scheme

test are used also for comparison of different conveyor belt types. Internal failures are analyzed by Carl Zeiss Metrotom 1500 CT-based coordinate measuring machine (Fedorko et al. 2013b) (Figs. 5, 6, 7).

Size of the kinetic energy needed to break through the P2500 belt is approximately 1,600 J with sharpest pyramid impactor 74°. However, the internal failure occurs at much lower energies, even when using impactor with radius 25 mm (Fig. 8).

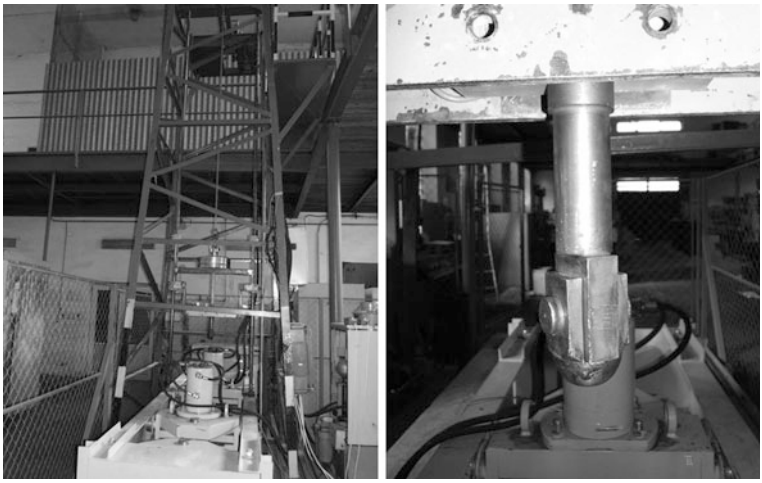

Fig. 5 Impact testing machine with impactor R = 25 mm

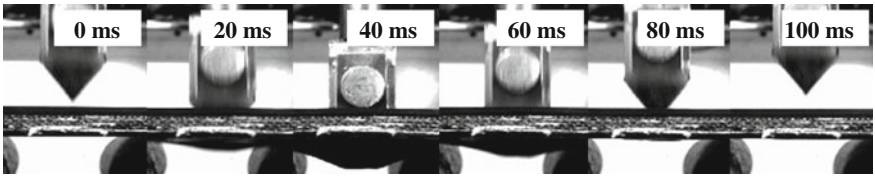

Fig. 6 Impact test sequence of conveyor belt P2500—impactor weight 82 kg, drop height 190 cm

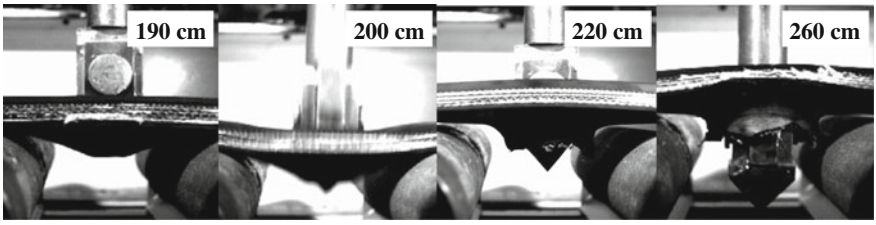

Fig. 7 Impact test of conveyor belt P2500—maximal deformation, impactor weight 82 kg, drop heights *190*, *200*, *220* cm (break through), *260* cm (break through)

4 Material Models and Numerical Models

Rubber cover material model is an essential input for the numerical model of the conveyor belt. Second input is the component (material) model of plies. Strain and deformation results of complete conveyor belt are used for tuning of numerical

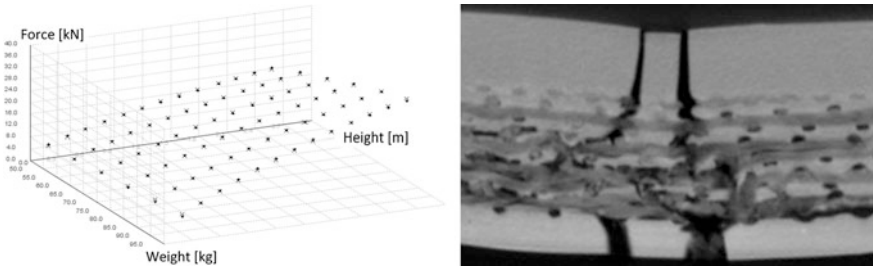

Fig. 8 Impact test postprocessing—graph of impact forces depending on the dropping height and impactor weight (*left*), CT scan of testing specimen (*right*)

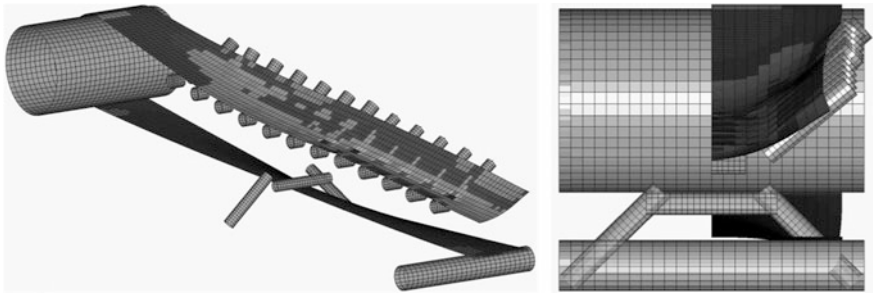

Fig. 9 Numerical analysis of return station Noen DPD 1800 with conveyor belt in Abaqus

models. Numerical models are developed for Abaqus Standard and Explicit solvers. User defined Bergström–Boyce numerical model of rubber was developed especially for rubber cover plies. This model could simulate hardening of the polymeric material in the region close to the final elongation of chains. It can also simulate rate-dependent phenomenon (creep, strain relaxation, stress–strain response dependent on deformation speed) and hysteresis during cycling loading (Bergstrom and Boyce 1998). Bergström–Boyce is implemented using Arruda–Boyce model + keyword *HYSTERESIS to Abaqus Standard and by VUMAT subroutine in Fortran to Abaqus Explicit. Chain Strain criterion which can simulate breaking of numerical model during impact is implemented using UVARM subroutine to Abaqus Standard and VUMAT subroutine to Abaqus Explicit. The most complicated part of material model definition is its calibration to results of different material tests. Four types of approaches were considered—Abaqus Insight (FEM based optimization, license needed), Veryst MCalibration (license needed), Octave (open-source) and Python + SciPy (open-source). Python + SciPy (library for scientific computing) was finally selected as one of the best method. The output of calibration is set the material models parameters to fit all material tests (Fig. 9).

5 Conclusions

The impact tests of first about 50 conveyor belts specimens shows very interesting results comparing new, old and wearing belts. Based on preliminary data, age of carcass plies and the associated hardness has a significant effect on the impact endurance and top cover ply has negligible effect to this endurance. This issue will be deeply analyzed in 2013 by more than 200 impact tests. Results of impact tests help to assess the influence of dropping height changes in surface mine and also helps to tune the dynamic behavior of numerical model. A new approach using non-destructive analyses brought new opportunities in evaluation of breaker and carcass plies failures. Working life of conveyor belts is complex problem and impact resistance is only one of the important parameters. Numerical models of return stations will be used for optimization of its components. Bergström–Boyce material models with Chain Strain criterion were developed for Abaqus Standard and Explicit using user subroutines. All input data needed for tuning the material models will be available in 2013.

Acknowledgments The research work reported here was supported by the subvention from Ministry of Trade and Industry under contract code FR-TI4/310.

References

Bergstrom J, Boyce MC (1998) Constitutive modeling of the large strain time-dependent behavior of elastomers. J Mech Phys Solids 46(5):931. doi:10.1016/S0022-5096(97)00075-6 ISSN 00225096

Bocko P, Petrikova I, Kraus V, Marvalova B, Blekta J, Skarolek A (2012) Increasing of working life of conveyor belts affected by shocks. Proceedings of the international journal of transport and logistics, ISSN 1451-107X

Fedorko G, Molnar V, Zivcak J, Dovica M, Husakova N (2013a) Failure analysis of textile rubber conveyor belt damaged by dynamic wear. In: Engineering failure analysis, vol 28, pp 103–114. ISSN 1350-6307

Fedorko G, Molnar V, Dovica M, Zivcak J, Weiszer M (2013b) Metrotomography: a progressive method for conveyor belt analysis. In: Bulk solids handling, vol 33(1), pp 56–60. ISSN 0173-9980

Pesek L (2006) Possibilities of videoextensometry for analysis of local deformations of sheetmetals. In: Proceedings of 3. česko – slovenský seminář "Lokální mechanické vlastnosti 2006 – Možnosti aplikace výsledků měření", Plzeň – Nečtiny, ZČU v Plzni, 8.-10.11.2006, s. 116–125, ISBN 80-7043-512-7

Petrikova I, Marvalova B, Tuan HS (2013) Experimental evaluation of mechanical properties of belt conveyor with textile reinforcement and numerical simulation of its behaviour. In: Proceedings of the 8th European conference on constitutive models of rubbers (ECCMR VIII), San Sebastian, 25–28 June 2013. ISBN 978-1-138-00072-8

Geometrical Accuracy of the Metal Parts Produced by Selective Laser Melting: Initial Tests

J. Ilčík, D. Koutný and D. Paloušek

Abstract The paper deals with the inspection of the geometric accuracy of the parts produced by additive manufacturing. Tested parts were produced on commercial machine SLM280HL based on selective laser melting technology. Tests were focused on determination of the geometric precision of building process and dimensional variations within the machine's platform. The results shows change in surface quality at different wall angles and large variation of part outer dimensions. The tests of different settings of laser power and scanning speed are also presented.

Keywords Selective laser melting · Additive layered manufacturing · Geometrical accuracy

1 Introduction

Additive layer manufacturing (ALM) allows creation of complex three dimensional parts directly from the CAD data. One of the most progressive techniques is the selective laser melting (SLM), which uses laser beam to melt the metal powder for building the functional prototype or even the series of final products (Fig. 1). So far, there are no standards for evaluation of the ALM machines' performance, whereas there are many influencing variables affecting mechanical properties,

J. Ilčík · D. Koutný (✉) · D. Paloušek
FSI VUT v Brně, Ústav konstruování, Brno, Czech Republic
e-mail: koutny@fme.vutbr.cz

J. Ilčík
e-mail: y115622@stud.fme.vutbr.cz

D. Paloušek
e-mail: palousek@fme.vutbr.cz

L. Ševčík et al. (eds.), *Modern Methods of Construction Design*,
Lecture Notes in Mechanical Engineering, DOI: 10.1007/978-3-319-05203-8_76,

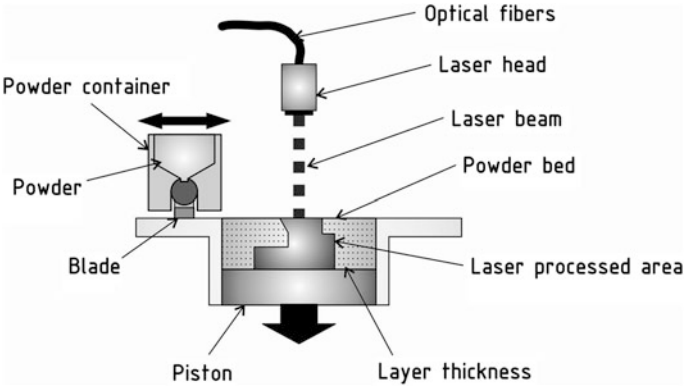

Fig. 1 SLM principle schema

density, surface quality and accuracy of the produced parts. This paper focuses on the initial tests of surface quality and geometrical accuracy.

Process quality and optimization of the influencing parameters were investigated by Kruth et al. (2007), Yasa et al. (2009). They studied the melting process of the powder and heat dissipation of the whole piece. There was evidence, that support structures or already built piece of the object is used to remove heat from the melted area to the platform. If a fixed laser power and scan speed was set, the use of the supports was necessary. However using developed feedback system, it was possible to achieve similar quality of overhanging elements without the use of supports.

Another investigated parameters of the building process were the density of the part and its surface roughness (Yasa et al. 2009, 2011). Those can be improved for example by reprocessing of single layer. After laser processing of the powder, there was no application of a new powder layer, but another re-melting by the laser. The negative effect of this method is an extension of building time to almost double.

Several authors (Van Bael et al. 2012; Parthasarathy et al. 2011), have been studied accuracy of the structured parts for biomedical applications, such as replacements of bones or teeth. Van Bael et al. (2012) evaluated the building precision of lattice structures with different size and shape of the pores. Using a laboratory machine, pore size and strength of built bars were evaluated.

Only limited number of authors devoted their interest to the evaluation of geometrical accuracy of the SLM machines. Kruth et al. (2005) deals with a comparison of parts built on machines from different manufacturers. Building accuracy and capabilities of each machine depending on the economic performance were reviewed. Similar tests were performed at the National Institute of Standards and Technology, Gaithersburg, USA (Cooke and Soons 2010). The parts built using AM were tested and compared with same part produced by standard machining.

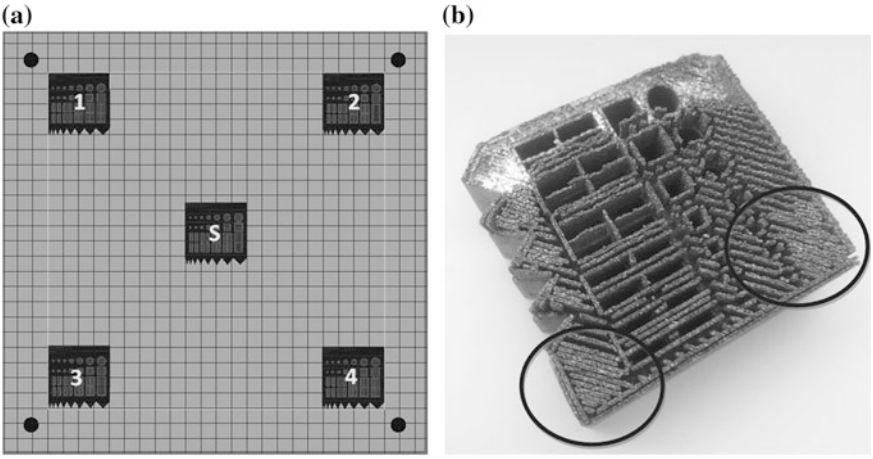

Fig. 2 **a** Position of test parts on the platform. **b** Strengthened support structures

2 Materials and Methods

In this study, all samples were produced on SLM 280HL machine (SLM Solutions GmbH, Germany). Machine is equipped with 400 W YLR fiber laser with variable beam focus from 170 till 700 μm. Parts can be built under argon or nitrogen inert atmosphere in the chamber with dimensions up to 280 × 280 × 350 mm.

For the production of the test parts an aluminum alloy AlSi12 was used in the form of fine metal powder. The distribution of the metal powder particles is typically Gaussian with a particle size range from 20 μm (10 % quantile) till 63 μm (90 % quantile). For the processing of aluminum powder a nitrogen inert atmosphere with maximum oxygen content of 0.2 % was used.

2.1 Geometry of Test Parts

For the testing of building parameters a three types of test parts were used. The first part of the test was designed to determine the surface roughness at different slope angles to the machine platform. For these purposes a test part was designed with 10° inclination of stepped surfaces (Fig. 3). With such designed surfaces a surface roughness of almost the entire angular range could be obtained using only one test piece.

The second test piece was used to determine the dimensional accuracy of the building process. For these purposes a part comprising a hole with a circular (denoted as C) and a square (S) cross-section, the thin wall (T), the radius and

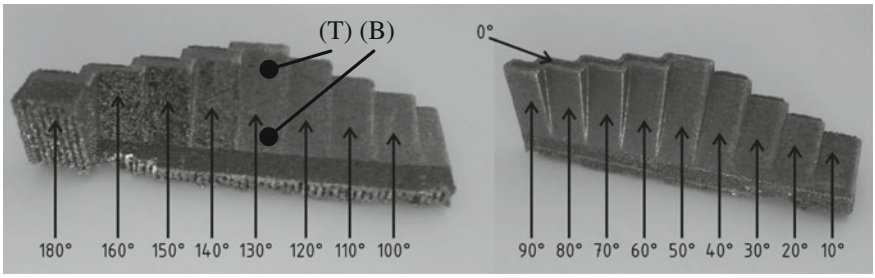

Fig. 3 Identification of the angled surfaces

angular surfaces has been designed. Geometrical elements were constructed in the range of 0.5–5 mm for holes and 0.25–2 mm for thin walls.

The third part was designed to test various parameters of the building process. For these purposes a cylinder with height and diameter of 10 mm was used. The parameters studied part were the surface roughness in the axial direction and the dimension in the XY plane.

2.2 Building Parameters of Test Parts

Test parts were prepared in Autofab software (Marcam Engineering, Germany), where the laser parameters were set, support structures were prepared and 2D slices were generated. The line supports were chosen for all test parts to ensure strong fixation of the part to the base platform. The thickness of the line supports was set to 0.3 mm and the distance between supports to 1 mm. The supports were condensed in the corners of the part, where the tear-off from the base platform usually occurs (Fig. 2b).

Test parts for dimensional inspection were placed in the center of the platform and at each corner (Fig. 2a). Altogether five parts were built during a single machine setting. During the tests a change in the calibration of the machine were done, therefore the building was repeated two times.

The cylindrical test parts were produced as a test series with 25 variants with different laser scan speed and laser power. Change of this two parameters was separately defined for the outer contour and for the internal volume of the test part. The variation of these parameters within the test series is shown in Tables 1 and 2.

2.3 Measurement

To measure the surface roughness a 3D optical profilometer ContourGT-X8 was used. The surface roughness was measured at two points of each angled area.

Table 1 Laser scan speed (mm/s)

Build phase	A	B	C	D	E
Part contour	400	450	500	550	600
Part volume	744	837	930	1,023	1,116

Table 2 Laser power (W)

Build phase	1	2	3	4	5
Part contour/volume	280	315	350	385	400

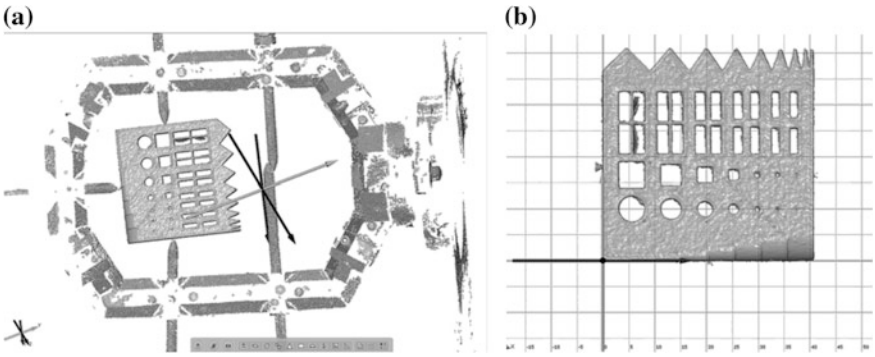

Fig. 4 Data processing in ATOS software. **a** Unwanted geometry of supporting scanning tool. **b** Aligned axis system

At the place closer the platform (B) and at the place with maximum distance from the platform (T). Areas have been identified depending on the angle between surface normal and normal of the platform, as can be seen on Fig. 3.

For determination of the dimensions of the parts and evaluation of geometric accuracy a 3D optical system (ATOS III TripleScan, GOM, Germany) based on active triangulation was used. Before the optical digitization process, it was necessary to use titanium powder for matting the surfaces of the test parts. The maximum thickness of the titanium coating is 6 ± 3 μm. The measured dimensions of the test parts were evaluated in hundredths of a millimeter, therefore additional thickness of matting of the surfaces was neglected.

Scanned point cloud of each test part was separately processed using the ATOS software (GOM, Germany). From the resulting polygonal mesh all unwanted geometry was removed (Fig. 4a) and a coordinate system was created (Fig. 4b). The GOM Inspect software (GOM, Germany) was used for the measurement and evaluation of the individual test part features.

Some dimensions were measured directly on the 3D data, while others were measured in sections. For larger features each measuring distance was measured five times. For some cases of smaller geometric features a sufficiently large

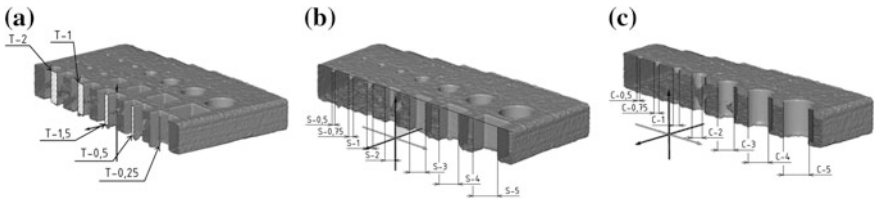

Fig. 5 **a** Thin walls, **b** rectangular holes and **c** cylindrical holes identification

Table 3 Comparison of dimensional accuracy—outer dimensions (mm)

	Nominal	First batch	Second batch
X	40.25	39.69 ± 0.53	40.07 ± 0.71
Y	41.00	40.14 ± 0.55	40.89 ± 0.24

volume of data were not digitized, therefore there were fewer measurements, or it was not measured at all. To evaluate the size of the cylindrical features it was necessary to create fitting geometrical primitives on the polygonal mesh, which were then measured. For square holes and thin walls a measurement between two points on parallel walls in the desired X or Y direction were used. From the measured values a mean size, variation and deviation from the nominal were calculated.

3 Results

For surfaces having an angle of 140°–160° the surface roughness was high. The value of the arithmetical mean deviation Ra of these surfaces ranged from 27.8 to 72.2 microns. For surface with angle 180° it was not possible to determine surface roughness, because of the presence of a support material. The surface roughness of the surfaces with angle from 10° till 130° did not differ significantly. Arithmetical mean deviation Ra of these surfaces ranged from 4.2 to 6.8 microns. The surface with 0° angle was identified with Ra value of 11.4 microns. The higher roughness was mainly caused by distinct laser pathways. To achieve good surface quality for surfaces with angles of 140°–180° post-processing is necessary. Due to the necessity of post-processing for such surfaces, it is suitable to use support structures in these areas.

Evaluation of dimensional accuracy was carried out on all test parts. The main reason was to compare building accuracy in different positions of the base platform. At the first build a high inaccuracies were found in the XY plane. All outer dimensions were built smaller than it was designed (Table 3). Interior dimensions were built with maximum inaccuracy of 0.13 mm. However, in most cases the deviation from the designed size ranged within hundredths of a millimeters.

Table 4 Comparison of dimensional accuracy—thin walls (mm), Fig. 5a

	Axis	First batch	Second batch
T-0.25	X	0.23 ± 0.03	0.41 ± 0.05
	Y	0.25 ± 0.04	0.41 ± 0.06
T-0.5	X	0.50 ± 0.06	0.56 ± 0.03
	Y	0.49 ± 0.05	0.56 ± 0.08
T-1	X	0.94 ± 0.03	1.05 ± 0.03
	Y	0.93 ± 0.05	1.04 ± 0.04
T-1.5	X	1.42 ± 0.05	1.53 ± 0.05
	Y	1.41 ± 0.04	1.53 ± 0.04
T-2	X	1.90 ± 0.05	2.03 ± 0.05
	Y	1.92 ± 0.04	2.05 ± 0.06

Table 5 Comparison of dimensional accuracy—rectangular holes (mm), Fig. 5b

	Axis	First batch	Second batch
S-0.5	X	DNM	DNM
	Y	DNM	DNM
S-0.75	X	0.77 ± 0.02	0.63 ± 0.06
	Y	0.78 ± 0.03	0.64 ± 0.03
S-1	X	1.04 ± 0.13	0.92 ± 0.05
	Y	1.05 ± 0.07	0.92 ± 0.05
S-2	X	2.03 ± 0.09	1.95 ± 0.08
	Y	2.03 ± 0.08	1.96 ± 0.07
S-3	X	3.02 ± 0.13	2.95 ± 0.12
	Y	3.04 ± 0.09	2.96 ± 0.06
S-4	X	4.01 ± 0.09	3.96 ± 0.10
	Y	4.03 ± 0.09	3.97 ± 0.05
S-5	X	4.99 ± 0.11	4.96 ± 0.12
	Y	5.02 ± 0.09	4.96 ± 0.05

These inaccuracies have been addressed with the machine vendor and were subsequently compensated by adjustment of the machine settings. This optical bench recalibration led to an increase in the building quality as well as the dimensional and surface quality (Tables 3, 4, 5, 6). The most significant changes in size, was achieved in the Y-direction. With regard to surface quality, this setting has led to significant improvements in the z-axis accuracy. Regarding the position on the platform, best results was reached between the center and right part of the platform.

At the first test build a large disparities in the direction of the Z axis were evident at all parts (Fig. 6). In subsequent builds these inequalities have been eliminated by calibration and tooth surface was compact.

Building of test parts with different parameters gave the following results. The surface roughness was not found significant changes in surface quality and overall scope of the arithmetical mean deviation of the surface ranged within

Table 6 Comparison of dimensional accuracy—cylindrical holes (mm), Fig. 5c

	First batch	Second batch
C-5	4.97 ± 0.07	4.34 ± 0.09
C-4	3.97 ± 0.05	3.93 ± 0.08
C-3	2.98 ± 0.04	2.94 ± 0.09
C-2	1.98 ± 0.03	1.90 ± 0.09
C-1	0.96 ± 0.02	0.95 ± 0.07
C-0.75	0.73 ± 0.05	0.72 ± 0.08
C-0.5	DNM	DNM

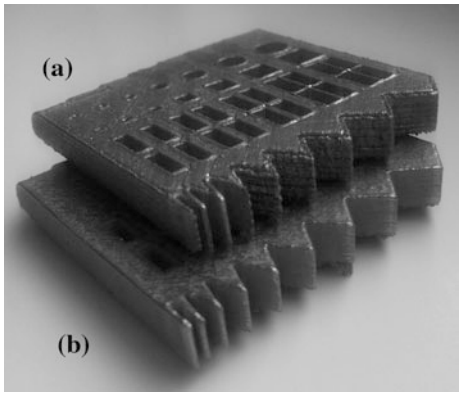

Fig. 6 Comparison of test parts. **a** First batch test part. **b** Second batch test part

±0.25 microns. The dimensional inspection found that the change of the laser parameters affects the part accuracy in significant way. Best geometrical accuracy with deviation of 0.02 mm was achieved at test part A5, which had the minimal laser scan speed and maximum laser power. The test part E1 with reversed settings shows exactly opposite results with the worst quality (Fig. 7).

4 Discussion

The first batch of test parts was manufactured with the calibration which did not fully met the required production quality. Most of these deficiencies were successfully compensated through subsequent calibration. Manufacturing of test parts showed that the attachment of the test piece to the platform is very important. Therefore it is necessary to make the supports in critical areas strongest as possible. With use of more dense support structures build quality is better and no tearing and warping occurs. However, adding large amounts of supports increase material costs. Therefore it is necessary to choose an appropriate support type and density particularly at the areas with higher thermal stresses. Further investigation

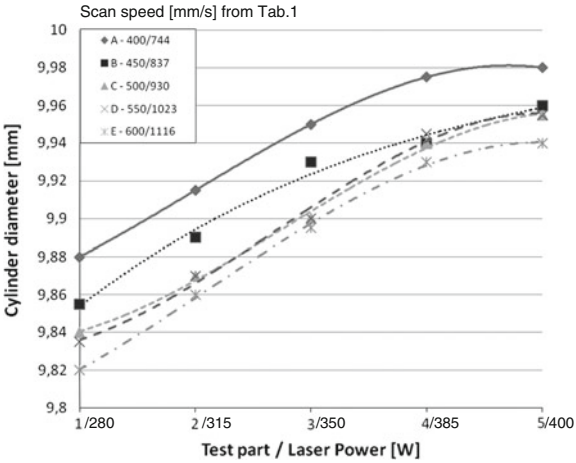

Fig. 7 Influence of laser settings on geometrical accuracy

needs to be done to find some prediction of highly stressed places and recommendation of optimal support structures.

The measured surface roughness of the test parts can be divided into three groups. Surfaces with angle 10°–90°, where the surface roughness did not significantly change. Surfaces with angle 100°–130°, that lies on the material and surface roughness increases with its increasing inclination. And surfaces, which surface roughness cannot be measured or is too high, those are with angle 140°–180°. Due to excessive roughness and the necessity of subsequent machining it is suitable to use supports at all surfaces with angle of 140°–180°.

For internal geometrical features (Fig. 5), holes with squared and circular cross-section and thin walls, a high geometrical precision was evaluated. Inner features were not significantly affected by the calibration of the machine or by the location of the test part at the platform.

In terms of precision of test part's outer size, further calibration needs to be done, to compensate the laser focus evenly over the platform. To achieve the smallest deviation of the resulting part, it is suitable to modify the parameters of the laser power and scan speed. The measurement shows, that it is best to set the laser scan speed to 400 mm/s and laser power to 400 W. Laser scan speed is therefore reduced by 20 %, while the laser power is increased by 20 % in comparison with standard setup.

5 Conclusions

This paper has presented initial tests of geometrical accuracy of commercially available machine for additive layered manufacturing of metal parts. A test parts were designed and built repeatedly. Manufactured test parts were digitized by

optical 3D scanner and its dimensions were analyzed to verify the process accuracy and precision of specific geometrical features.

During the testing, an unsatisfactory results were observed regarding surface quality and shape accuracy. After calibration of optical bench the surface quality and geometrical accuracy were improved significantly. Although the internal features showed good accuracy and low variation in size, the outer dimensions still needs to be optimized by recalibration. Overall work greatly contributed to better quality of the resulting prototype parts.

Acknowledgements The work was supported by European Regional Development Fund in the framework of the research project NETME Centre under the Operational Programme Research and Development for Innovation. Reg. Nr. CZ.1.05/2.1.00/01.0002, id code: ED0002/01/01, project name: NETME Centre—New Technologies for Mechanical Engineering and project of specific research FSI-S-11-30/1454.

References

Cooke AL, Soons JA (2010) Variability in the geometric accuracy of additively manufactured test parts. In: 21st annual international solid freeform fabrication symposium, Austin, Texas, USA, pp 1–12

Kruth J-P, Vandenbroucke B, Van Vaerenbergh J, Mercelis P (2005) Benchmarking of different SLS/SLM processes as rapid manufacturing techniques. In: Proceedings of the international conference polymers and moulds innovations PMI 2005, paper 525

Kruth JP, Mercelis P, Van Vaerenbergh J, Craeghs T (2007) Feedback control of selective laser melting. In: Proceedings of the 3rd international conference on advanced research in virtual and rapid prototyping, pp 521–527

Parthasarathy J, Starly B, Raman S, Moesen M, Kerckhofs G, Van Oosterwyck H, Kruth J-P, Schrooten J (2011) A design for the additive manufacture of functionally graded porous structures with tailored mechanical properties for biomedical applications. J Manuf Process 13(2):160–170. doi:10.1016/j.jmapro.2011.01.004

Van Bael S, Chai YC, Truscello S, Moesen M, Kerckhofs G, Van Oosterwyck H, Kruth J-P, Schrooten J (2012) The effect of pore geometry on the in vitro biological behavior of human periosteum-derived cells seeded on selective laser-melted Ti6Al4V bone scaffolds. Acta Biomater 8(7):2824–2834. doi:10.1016/j.actbio.2012.04.001

Yasa E, Craeghs T, Badrossamay M, Kruth J-P (2009) Rapid manufacturing research at the Catholic University of Leuven. In: US Turkey workshop on rapid technologies, Istanbul, p 10

Yasa E, Deckers J, Kruth J-P (2011) The investigation of the influence of laser re-melting on density, surface quality and microstructure of selective laser melting parts. Rapid Prototyping J 17(5):312–327. doi:10.1108/13552541111156450

Workpiece Grain Size Influence on the Vibration in Micro-Milling

M. Matuszak, P. Kochmański and B. Powałka

Abstract The vibration occurring during a micro-milling process can have impact on the surface quality. Usually the main influence on a vibration occurring during milling have cutting parameters (feed rate, cutting speed, depth of cut), workpiece material and type of milling tool. However in micro scale different phenomena can also affect on a vibration occurring during the micro-milling. In some cases repetition of experiment results is challenging. One of factors that is commonly neglected is material structure. The paper describes influence of the workpiece material (C45 steel) grain size on the vibration occurring during micro-milling. The experiment shown that for the same material, tool and cutting parameters vibration can occur or not. Only difference between two workpieces was their grain size. This leads to the conclusion that the workpiece grain size can decide if vibration occurs during micro-milling.

Keywords Micro-milling · Vibration · Grain size · Dynamics

1 Introduction

Investigation under the phenomena of vibration occurring during milling both in macro and micro scale was performed by many researchers. Due to ploughing and elastic recovery macro scale models cannot be applied directly into micro

M. Matuszak (✉) · P. Kochmański · B. Powałka
Szczecin University of Technology, Szczecin, Poland
e-mail: marcin.matuszak@zut.edu.pl

P. Kochmański
e-mail: pawel.kochmanski@zut.edu.pl

B. Powałka
e-mail: bartosz.powalka@zut.edu.pl

L. Ševčík et al. (eds.), *Modern Methods of Construction Design*,
Lecture Notes in Mechanical Engineering, DOI: 10.1007/978-3-319-05203-8_77,

scale (Jun et al. 2006; Filliz and Ozdoganalar 2008). Moreover in the micro-milling process factors that can be neglected in a macro scale might have impact on vibration.

Some researchers are focused on chip formation n micro scale milling considering cutting edge radius. Usually they propose finite elements method (FEM) on chip formation modeling and cutting forces analysis (Ducobu et al. 2009a, b; Liu and Melkote 2007; Woon et al. 2008). Material in this cases is considered as homogenous. Other researchers analyzed impact of workpiece structure in non homogenous materials on micro-milling cutting forces in micro scale using FEM models (Wang et al. 2008; Simoneau et al. 2006; Vogler et al. 2003).

There is a lack of research works considering material structure influence on vibration occurring during micro-milling process. In the ferrous materials can exist different non homologeus structures e.g. in not hardened steel there is ferrite and perlite. Gran size of perlite can be various and affect micro-milling process. Typical feed rate in micro-milling is between 1 and 10 μm per tooth. Grain size in C45 steel can be between 5 and 150 μm. Influence of grain size can be usually neglected in macro scale, but can be significant in micro-milling.

To become familiar with steel grain size influence on vibration in micro-milling process experiment was performed. Two steel samples with the same carbon content but different average grain size were used. Milling parameters were selected in order to achieve vibration.

2 Milling Experiment

Milling experiment was performed on prototype micro-milling machine which was built in West Pomeranian University of Technology (Broel-Plater et al. 2011; Matuszak 2011; Matuszak and Waszczuk 2012). During experiment machine was equipped with Kistler 9256C1 three axial dynamometer, PCB Piezotronics 352B10 accelerometers mounted both on workpiece and machine spindle. Signals were recorded with National Instrument CompactRIO. Experiment was performed for two C45 steel workpieces (further called workpiece 1 and workpiece 2). Kyocera 2FESM010-025-04 (diameter 1 mm) tool was used for milling both workpieces.

Cutting parameters during experiment are presented in Table 1. The same parameters were used for workpiece 1 and 2. The milling tool used for milling workpiece 1 and 2 was the same moreover experiment was repeated with new and worn tool and results were similar.

In order to detect vibration acceleration signals can be used (Matuszak 2011). Previous research showed that vibration can be detected mostly on accelerometer mounted near micro-milling machine spindle. Acceleration signal from Y (cross feed) direction is used for further analysis. In order to achieve displacement signal acceleration signal was double integrated. The displacement signal was then transferred into frequency domain with fast Fourier transformation.

Table 1 Cutting parameters during milling experiment

Depth of cut (μm)	Rotational speed (RPM)	Feed (μm/tooth)
10	30,000	2
25	30,000	2
40	30,000	2

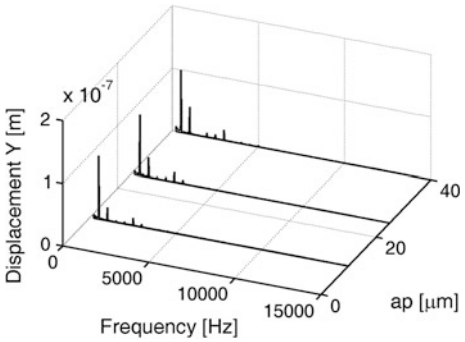

Fig. 1 Fast Fourier transform of displacement signals on machine spindle for workpiece no. 1 at 30,000 RPM, 2 μm/tooth

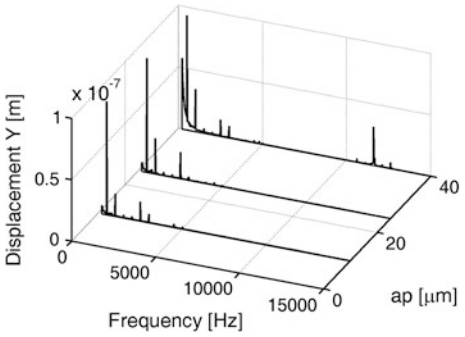

Fig. 2 Fast Fourier transform of displacement signals on machine spindle for workpiece no. 2 at 30,000 RPM, 2 μm/tooth

Fast Fourier transform of displacement signal for variable depth of cut (a_p) and workpiece 1 is presented on Fig. 1. There can be seen only frequencies that are connected with tool teeth immersion frequency and its harmonics.

Figure 2 shows Fast Fourier transform of displacement signal for variable depth of cut (a_p) and workpiece 2. There can be seen not only frequencies that are connected with tool teeth immersion frequency and its harmonics. There is also resonance about 11 kHz, which corresponds with tool own vibration frequency.

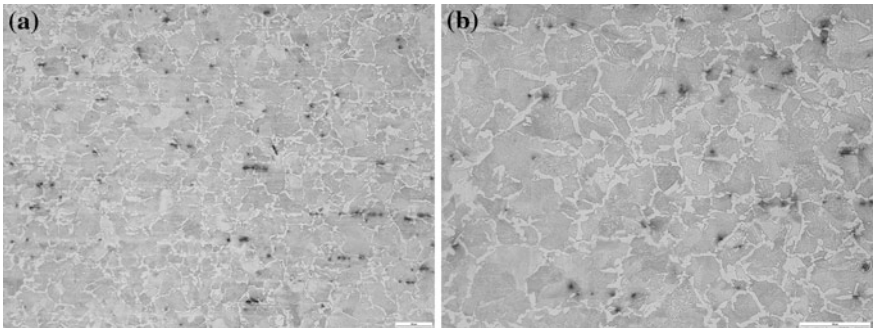

Fig. 3 Workpiece 1 structure: **a** 10× magnification, **b** 40× magnification

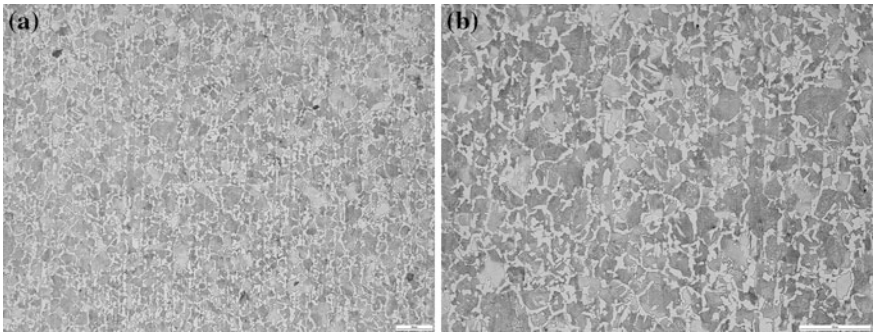

Fig. 4 Workpiece 2 structure: **a** 10× magnification, **b** 40× magnification

Table 2 Average grain size in workpiece 1 and 2

Grain size workpiece 1	Grain size workpiece 2
52 µm	29 µm
6 ASTM	7 ASTM

3 Workpiece Structure

Both workpieces were expected to be identical, as they were made from C45 steel and they had the same carbon content and no alloy additions. Since workpiece material, cutting parameters and milling tool were the same there must be difference in material structure between workpiece 1 and 2.

Workpiece 1 material structure is shown on Fig. 3 with 10× (Fig. 3a) and 40× (Fig. 3b) magnification. Workpiece 2 material structure is shown on Fig. 4 with 10× (Fig. 4a) and 40× (Fig. 4b) magnification. There can be seen significant difference in perlite grain size between workpiece 1 and 2.

Average grain size for workpiece 1 and workpiece 2 are shown in Table 2. Grain size is assigned to ASTM (American Society for Testing Materials) size group. Perlite grain size measurement confirms difference between material 1 and 2.

4 Conclusions

Experiment shown that material grain size can have influence on vibration occurring during micro-milling process. Vibration occurred during milling in workpiece with smaller grain size (29 μm) but it did not occurred during milling in workpiece with larger grain (52 μm).

The main problem in micro-milling process investigation is repeatability of experiment. In comparison to macro scale more factors can affect on micro-milling process. Further research will be focused exploration of wider grain size range influence for vibration in micro-milling. There is also a need for construction of a model that will explain influence of grain size on the vibration in micro-milling. Another aspect is hardness of the workpiece material that could have impact on micro-milling process. Milling in one phase material e.g. perlite steel is also interesting aspect and could ensure high repeatability of micro-milling experiments.

Acknowledgments The work is co financed by the European Union under the European Social Fund and the State Budget, Operational Programme Human Capital Priority VIII, Activity 8.2 Sub-activity 8.2.2 Transfer of knowledge "Regional Innovation Strategies", the system project implemented by the Regional Labour Office in Szczecin An investment in knowledge engine of growth innovation in the region—second edition.

References

Broel-Plater P, Waszczuk P, Kobyłkiewicz A (2011) System diagnostyki procesu mikroskrawania. Napędy i sterowanie, 6/2011:32–35

Ducobu F, Filippi E, Rivière-Lorphèvre E (2009a) Investigations on chip formation in micro-milling. In: Proceedings of the 8th national congress on theoretical and applied mechanics, pp 333–339

Ducobu F, Filippi E, Rivière-Lorphèvre E (2009b) Chip formation and minimum chip thickness in micro-milling. In: Proceedings of the 12th CIRP conference on modeling of machining operations, pp 339–346

Filliz S, Ozdoganalar O (2008) Microendmill dynamics including the actual fluted geometry and setup errors—part I: model development and numerical solution. J Manuf Sci Eng 130:031119-1–031119-10

Jun MBG, Liu X, DeVor RE, Kapoor SG (2006) Investigation of the dynamics of microend milling—part I: model development. J Manuf Sci Eng 128:893–900

Liu K, Melkote SN (2007) Finite element analysis of the influence of tool edge radius on size effect in orthogonal micro-cutting process. Int J Mech Sci 49:650–660

Matuszak M (2011) Charakterystyka systemów pomiarowych do badań parametrów dynamicznych procesów mikrofrezowania, Automatyka, tom 15, zeszyt 2:327–333

Matuszak M, Waszczuk P (2012) Experimental sensor system implementation for selected micromilling-related parameters. Zeszyty Naukowe Akademii Morskiej w Szczecinie, 31(103):134–139

Simoneau A, Ng E, Elbestawi MA (2006) Chip formation during microscale cutting of a medium carbon steel. Int J Mach Tools Manuf 46:467–481

Vogler MP, DeVor RE, Kapoor SG (2003) Microstructure-level force prediction model for micro-milling of multi-phase materials. J Manuf Sci Eng 125(2):202–209

Wang JS, Gong YD, Abba G, Chen K, Shi JS, Cai GQ (2008) Surface generation analysis in micro end-milling considering the influences of grain. Microsyst Technol 14:937–942

Woon KS, Rahman M, Fang FZ, Neo KS, Liu K (2008) Investigations of tool edge radius effect in micromachining: a FEM simulation approach. J Mater Process Technol 195:204–211

Simulation of Laminated Composite Loading

J. Petřík

Abstract In the present development of automotive industry and other industries is the main trend to decrease the weight of miscellaneous designs. Transportation vehicles are responsible for around 12 % of total EU emissions of carbon dioxide (CO_2). The long time target for CO_2 per kilometer decreases significantly and the target for year 2020 represent 40 % reduction of emissions from the year 2007. The light weight designs based on metallic material are close to the limit and there is the area for new materials. The composite materials based on poly-ester matric with glass fibers represent the "low cost" composite materials and this article describes the material model approach of this laminate used for virtual testing and validation. Thickness of the laminated composite plies is optimized for the comparison to steel plate with same mechanical stiffness.

Keywords Emission · Composite · Laminate · Loading

1 Introduction

The mass reduction directly reduces the fuel consumption, hence the related CO_2 emissions, because the energy required to move a vehicle is directly proportional to its mass during the entire life cycle. The target for year 2020 is 95 g of CO_2 per kilometer. It is approximately equivalent to 4.1 l/100 km of petrol or 3.6 l/100 km of diesel (Lutsey 2010). The reduced vehicle mass enables significant safety improvements as well as better driving performance and higher comfort. The major mass reductions from different approaches are steel design which represents around 15–40 % reduction like optimization of the design and using of high

J. Petřík (✉)
Technical University of Liberec, Liberec, Czech Republic
e-mail: jan.petrik@tul.cz

L. Ševčík et al. (eds.), *Modern Methods of Construction Design*,
Lecture Notes in Mechanical Engineering, DOI: 10.1007/978-3-319-05203-8_78,

strength steel for miscellaneous designs. The aluminum, carbon and multi-material design represents 30–60 % mass reduction like replacement of the steel parts by another material. The disadvantage of this method is the price of those materials and also the production and manufacturing technology but the mass reduction is more effective. The using of composite material with poly-ester matric and glass fibers enables the effective mass reduction for some parts of car body or other structures like side and back doors, seat frames, interior assembly or safety equipment etc. Based on knowledge of poly-ester composite with glass fibers was done the initial stiffness deliberation of using the composite possibilities. The common composite profiled manufactured by pultrusion ale available in varied shapes and profiles but thanks to their strong orthotropic behavior is not possible to replace low anisotropic steel plate. The other possibility with lower orthotropic behavior is the composite with fabric structure of glass fibers. Thanks to included fabric structure inside the matrix has this type of composite lower stiffness around 3/8 of profile from one direction pultrusion. The replacement of steel plates might be represented by laminate composite. The minimal count of laminate plies is 5 layers cause of delamination effects. The laminate material improves the better stiffness and lower orthotropic effect than one layer composite plates. The material model describes the behavior of all layers and enables the physical orthotropic approach (Gibson 2012).

2 Material Model of Layered Composite

Material model correspond to multi-layered and multi-material shell model. The model is divided to each layer with each mechanical property. There are two approaches to describe the individual layer. The first approach is based on describing of the matrix and fibers as particular mechanical behavior. The disadvantage of this approach might be the non-relevant physical interaction between poly-ester matrix and fibers. This methodology is used only if is known the precise form of the composite structure. The second approach is based on the global point of view. Instead the composite ply is described using homogenous continuum mechanics. This method might be more suitable for the material model validation from experimental measurement. The individual layer of the composite might be analyzed before the lamination with the same methodology as in virtual material model. In our case is more suitable to use cause of measurement possibilities and for the initial analysis might be satisfactory (Barbero 2012).

The minimum count for lamination is three layers to prevent the delamination effects. The individual layer has glass fibers only in one direction and is manufactured by common pultrusion. The orientation of fibers in each layer is optimized for minimalize the orthotropic behavior. The optimal count to use lamination is five layers to prevent the delamination effect and the orthotropic behavior. The orientations of fibers are described on Fig. 1. The orthotropic behavior is also caused by only one layer with orientation of fibers with 0°. It is possible to change

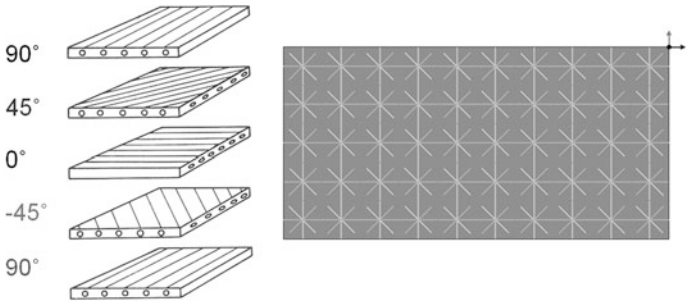

Fig. 1 Individual layers with fiber orientation and the composite plate

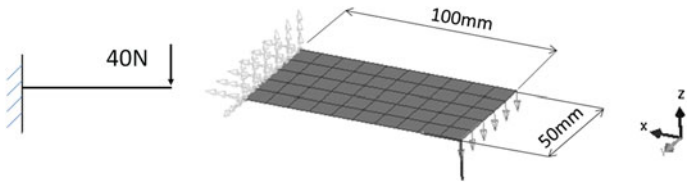

Fig. 2 Description of the first loading case

the fiber orientation and choose the lower stiffness direction (only one layer with 0° fiber orientation) to comparison with steel plate. The main aim is to compare with the lower stiffness oriented composite to completely replace the material with the same mechanical properties and the stiffer direction should be the positive benefit of replacing (Hyer 2009).

3 Loading Cases

The comparison with steel was done on two loading cases. Both of them are based on the mechanical loading of the plate. The first is the bending of the plate by the 40 N force. The plate is fixed on the left side edge in all displacement and rotation and on the right side edge is loaded by the force in z direction (Fig. 2).

The second loading case is based on the bending of the plate by the cylinder. The plate is fixed on the left side edge in all displacement and rotation and on the right side edge has only one degree of freedom—displacement in x direction. The plate is bending by the cylinder (radius 20 mm) in the middle by 300 N force (Fig. 3).

The differences between composite plate 1 and 2 is in direction of glass fibers in first and fifth layer (Fig. 4).

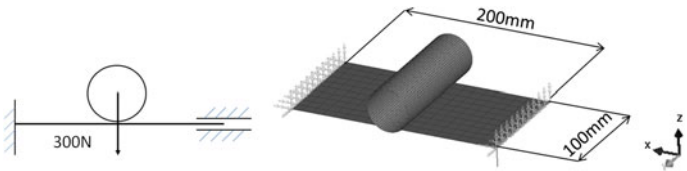

Fig. 3 Description of the second loading case

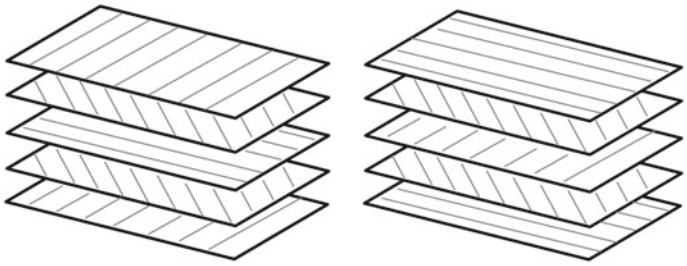

Fig. 4 Description of glass fibers orientation on composite plate *1* and *2*

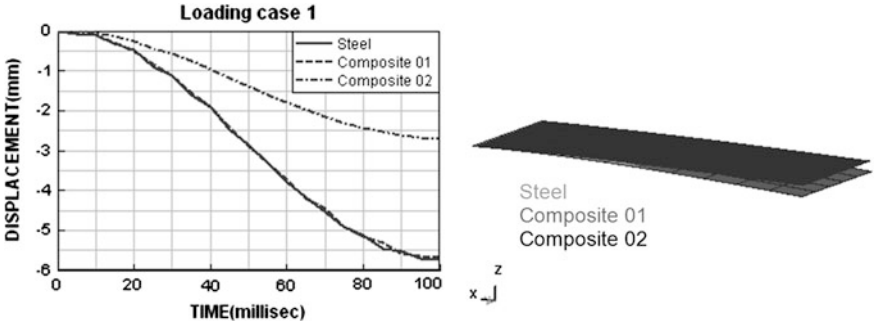

Fig. 5 Simulation results of loading case 1

4 Results

The loading case 1 results are shown on Fig. 5. The thickness of composite plate 1 and 2 is the same. The thickness is optimized in term of same mechanical property as steel plate for composite plate 1. The curves and results states for steel plate and composite plate 1 are overlapped.

The mass reduction of the used composite with thickness 5 mm is shown on Table 1.

Table 1 Mass reduction for loading case 1

Plate for loading case 1	Mass (kg)	Thickness (mm)	MAX strain (mm)
Steel	0.053	1.35	5.69
Composite 01	0.037	5	5.71
Composite 02	0.037	5	2.63

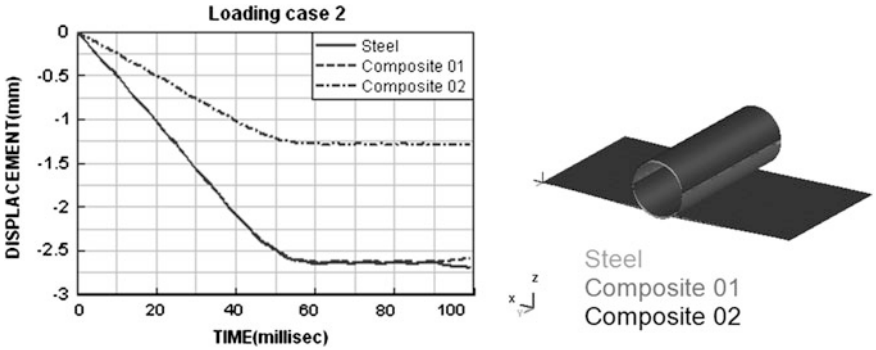

Fig. 6 Simulation results of loading case 2

Table 2 Mass reduction for loading case 2

Plate for loading case 2	Mass (kg)	Thickness (mm)	MAX Strain (mm)
Steel	0.212	1.35	2.65
Composite 01	0.150	5	2.55
Composite 02	0.150	5	1.255

Composite plate 2 is stiffer during loading case 1 cause of optimal fiber direction (Fig. 6).

The force limit for loading cases is chosen on the basis of the stress analysis for the steel plate. The maximum bending stress is close to the yield stress for the used steel material. The mass reduction for the composite plate is around 30 % with the positive trend for the stiffer fiber orientation for composite plate 2 (Table 2).

5 Conclusions

The methodology of optimization of the composite plate thickness will be used in experimental environment to validate the results. The validation of the material model of the composite plate is necessary to do before this optimization with the individual layer of the plate with one direction of glass fiber. Next step is the simulation of loading cases to optimize the thickness of composite material in

comparison with steel plate. This optimization is possible to use for common steel material and composite and is possible to extend by other loading cases (torsion, shear etc.). The main aim is to replace the steel material and optimize the mechanical properties of new material to fulfill the same stiffness properties. The mass reduction is significant in term of static loading cases. To relevant replacement of the composite material is necessary to validate in dynamic loading cases like crash impact to analyze the strain rate characteristic and failure criterion. The failure criterion is very important and is possible to include to the material model of the composite. The mass reduction enables to saving the energy needed for the movement of the vehicle and brings the lower emissions of CO_2. To completely replace the steel material is necessary to solve the technology of mounting which is not the topic of this article. The steel replacement is present important topic and thanks to the virtual environment is possible to separate the non-relevant cases of using new composite material.

References

Barbero EJ (2012) Introduction to composite materials design. CRC Press, Boca Raton
Gibson RF (2012) Principles of composite material mechanics. CRC Press, Boca Raton
Hyer MW (2009) Stress analysis of fiber-reinforced composite materials, DEStech Publications
Lutsey N (2010) Survey of vehicle mass-reduction technology trends and prospects. http://www.arb.ca.gov/msprog/levprog/leviii/meetings/051810/lutsey_its_may18_final.pdf

Part VII
Tribology

J. Broncek, M. Dzimko, M. Kovalicek, Y. Takeichi, M. Leitman, R. Bastovansky, S. Poljak, D. Necas, M. Vrbka, P. Sperka, M. Druckmuller, P. Skladal, P. Starha, I. Krupka, M. Hartl, D. Smejkal and M. Omasta

The shows of a friction we meet practically in all machine parts and mechanisms. The reciprocal movement of two or more materials or interaction of the material with the environment leads to loss of the material from the surface. This process is known as wear. The main types of wear are abrasion, friction (adhesion and cohesion), erosion, and corrosion. Wear can be minimized by coating of solids or use of lubricants (for slide or roller wear). Tribology is a science that deals with the behavior of touching surfaces in relative motion or when trying to move. This movement can be generally sliding, rolling, impact, or oscillating. Studies and research on the problems of friction are applied in the design of bearings, engines, and other machinery and equipments, but it also extends to other sectors of modern technologies such as artificial joints in biomechanics. Correctly selected surface treatment and lubrication reduces friction of solids to a minimum, which minimizes wear and reduces energy consumption. The authors of Part VII—*Tribology* state in their contributions new knowledge about the friction between surfaces and also show measurement methodologies gained through the study and research of this issue.

Friction Characteristic of CrN/DLC2 Layer Deposited on AISI 304 in Contact with Al_2O_3 Ball Examined Under Atmospheric and Vacuum Conditions

J. Bronček, M. Dzimko, M. Kovalíček and Y. Takeichi

Abstract The results of "ball on disc" tests for determination of the friction coefficient under the specific conditions of low and high vacuum are presented. Advanced nanocomposite coating CrN/DLC2 was deposited by plasma assisted chemical vapour deposition PACVD on AISI 304 (STN 41 7241) stainless steel plates. Friction pairs—composed from coating surface and Al_2O_3 ball examined under low vacuum reached during the tribological tests significant lower friction coefficient values than those worked under atmospheric conditions.

Keywords Friction · CrN/DLC2 layer · Testing device

1 Introduction

Development of laboratory test equipment for tribology science area is closely linked with the explanation of friction and wear mechanisms theories. Within the grant projects in tribological laboratory an experimental test was developed for tribometer device which allows the microscopic and submicroscopic examination of friction and wear in controlled environments (Vidiečan et al. 2011).

Acquired knowledge of present research on the active adhesive surfaces in high vacuum environments enables better describing and understanding the processes going on the surfaces of components working in the specific conditions of high vacuum. In the experimental device, according to principle of "Ball on Disk",

J. Bronček (✉) · M. Dzimko · M. Kovalíček
University of Žilina, Žilina, Slovakia
e-mail: jozef.broncek@fstroj.uniza.sk

Y. Takeichi
Toyohashi University of Technology, Toyohashi, Japan
e-mail: takeichi@mech.tut.ac.jp

L. Ševčík et al. (eds.), *Modern Methods of Construction Design*,
Lecture Notes in Mechanical Engineering, DOI: 10.1007/978-3-319-05203-8_79,

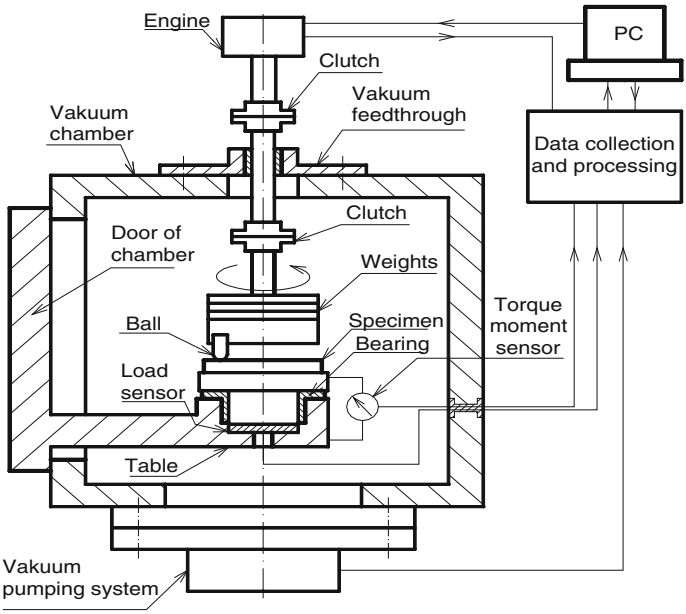

Fig. 1 Schematic illustration of vacuum tribometer device

chosen samples were tested. Progressive nanocrystalline PVD coatings represent revolutionary solution of hard and super hard wear resistant surfaces. Tested CrN/DLC2 (CROMVIc2-designation by the producer) coating can be widely used for high quality machine components like: medical devices, cutting tools, aerospace components etc. Diamond-like carbon (DLC) is a metastable form of amorphous carbon containing a significant fraction of sp. bonds. It can have high mechanical hardness, chemical inertness, and optical transparency smooth surface and low friction behaviour.

2 Vacuum Tribometer Device

A tribometer for tests under vacuum conditions consist of a vacuum chamber which contains the dynamic contact and surrounding ancillary equipment such as vacuum pumps and drive system. A schematic illustration of tribometer for vacuum operation is shown in Fig. 1. There is a one point contact between the rotating ball and plane sample which allows use of "Ball on Disc" principles.

Specific design of equipment allows examinations of friction pairs in environment of the pressure up to $p = 10^{-5}$ Pa. Operation requires keeping and maintaining a high degree of purity, not only of the environment but also the

samples themselves. The Fig. 1 shows clearly the principle and the location of individual components and is accomplished by the scheme of operation.

The rotating shaft is connected with a loading head with a support of a special linear bearing. This transmits the torque and allows vertical movement of the head along the shaft in the direction of the z-axis at the same time. A pin with a ball fixed on its end is connected with loading head. In the described construction arrangement the friction force is generated in the friction pair created by ball and tested coated disc. The rotating ball is being pressed against the stationary plane sample fixed to the holder. The value of the friction force F_T or friction moment M_T is determined by strain gage measurements applied on flat spring deformation. The values of the friction coefficient are calculated from the obtained F_T and F_N.

3 Samples and Experiments

The tested coating was applied on stainless steel of 2 mm thickness. Double coating CROMVIc2® with nanogradient structure was deposited by using PACVD (Plasma Assisted Chemical Vapour Deposition) and reaches thickness about 2 μm. Imagine of SEM view of CrN/DLC2 coating is shown in Fig. 2 (http://platit.com/coatings-structures/dlc-coating?page=0%2C2).

The substrate material of the fixed sample is stainless steel AISI 304 with a Brinell hardness of HRB = 70. Basic properties of the coating applied, given by the coatings manufacturer LISS (http://platit.com/coatings-structures/dlc-coating?page=0%2C2) are: micro-hardness = 25 GPa, thermal stability up to ~450 °C and the coefficient of friction against steel f = 0.1, where the second friction element is made of steel ball. The active surfaces of tested samples were prepared by conventional metallographic procedure to reach the stage of perfect polishing. Micro geometry surface was determined according to EN ISO 4287 that is represented by an arithmetic mean deviation of the profile *R*a and maximum height roughness *R*z, which were measured before and after deposition. The values are shown in Table 1.

Sliding pair consists of AL_2O_3 ball, with 3,175 mm diameter, and square shaped plane sample with a edge length of 30 mm. For the objective comparison, coefficient of friction as a function of time under normal atmospheric conditions was measured. Initial level of low vacuum was set from 1.0×10^{-1} Pa and during the experiment value of higher vacuum 5.6×10^{-4} Pa was reached. The experimental time was set to 4,980 s (resulting from the sliding length), the applied constant load was $F_N = 1$ N, and constant sliding speed $v = 0.02$ ms^{-1}. The diameter of tribological track was 22 mm, and sliding trajectory length of each sample was set to 100 m.

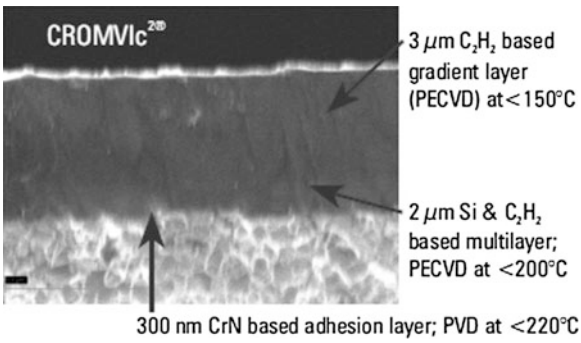

Fig. 2 SEM view of CROMVIc2 (CrN/DLC2) coating (http://platit.com/coatings-structures/dlc-coating?page=0%2C2)

Table 1 Specimens roughness *R*a and *R*z before and after deposition of CrN/DLC2

Samples		*Ra* (μm)	*Rz* (μm)
CrN/DLC2 coating	Before deposition	0.01–0.02	0.07–0.14
	After deposition	0.08–0.12	1.2–1.9

4 Results and Discussion

4.1 Friction Test and Analysis

Experimental measurements were performed according to the methodology described above and representative values are graphically elaborated in next figures.

The recorded curves of friction coefficient progress for samples without coating as with coating CrN/DLC2 (CROMVIc2®) under atmospheric conditions as well as in vacuum are shown in Figs. 3 and 4. From the gradient of the friction coefficients, obtained under atmospheric environmental conditions (Fig. 3) can be seen that the value of non-coated surface of the stainless steel sample reached the friction coefficient within the range from 0.25 to 0.35. For the same conditions but using the coated surface value of coefficient of friction reached about 0.06.

The curves of friction coefficients for 10^{-4} Pa pressure (Fig. 4) express unstable course of the friction coefficient for uncoated surface chrome-nickel samples. Value at the end of the test oscillates around the value $\sim$0.5 (max. value of 0.7 and min. 0.35 value). Friction coefficient values of coated samples (after running in) are low and stable and oscillate around a value of 0.05. In both cases, no break of the coated surfaces has been recorded.

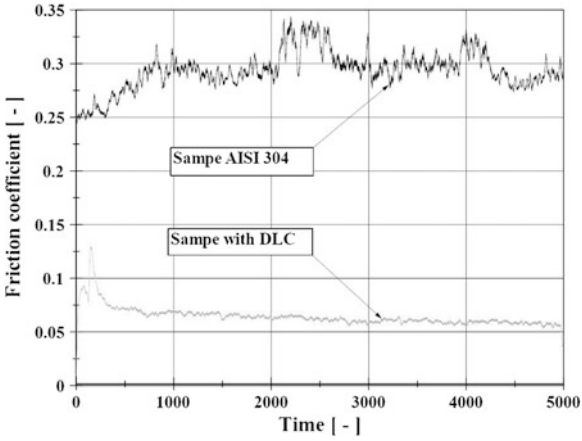

Fig. 3 The friction coefficient as a function of time between AL_2O_3 ball and uncoated surface and CrN/DLC2 surface and AL_2O_3 in atmospheric conditions

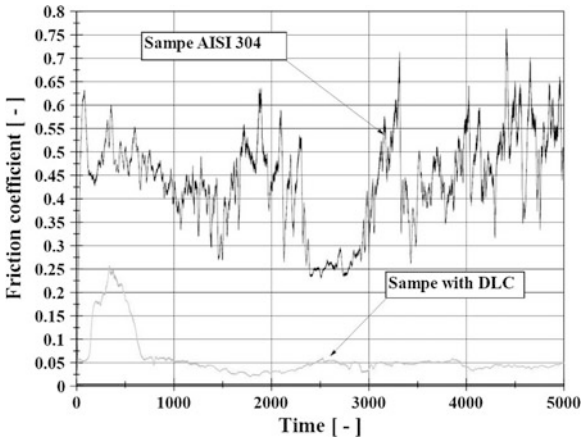

Fig. 4 The friction coefficient as a function of time between AL_2O_3 ball and CrN/DLC2 coating deposited or uncoated surface in high vacuum conditions on level of 10–4 Pa

4.2 Evaluation of Surface Topography

For better understanding of tribological processes—specifically wear—it is appropriate to undertake an evaluation of a topology of coating. The listed values of the parameters in Table 1 indicate that after applying the coating to the substrate, the average roughness given by *R*a value increased approximately 6-times and while the value of *R*z is increased nearly 1.5 times.

Wear rate evaluation through the use of friction track width was done by stereomicroscope Nikon AZ100 and AFM microscope SOLVER NEXT. Figure 5 shows tribological trace created during the test with CrN/DLC2 coating. The wear trace is nearly 100 μm wide. There is also no coating abrasion created during the testing. For illustration the Fig. 6 shows the coating of AL_2O_3 ball after completed tests.

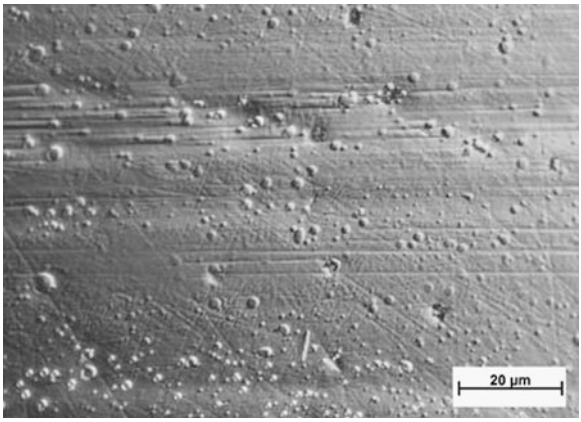

Fig. 5 The microscopic image of worn surface for DLC coating CROMVIc2®

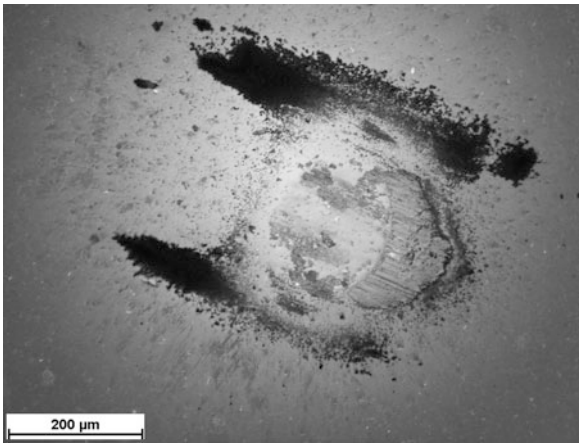

Fig. 6 The microscopic image of the friction scar on the AL_2O_3 ball in vacuum

The abrasion of the ball coating is more significant as in the case of the disc sample. There was also progressive displacement of the ball′s material to the edge of the ball′s abrasion area during the testing.

Figure 8 shows 3D image of unworn surface for CrN/DLC2 coating and Fig. 7 shows 3D image of worn uncoated surface.

In coating surface the microscopic droplets of vaporized metal are built in. This creates asperities emerging from the coating surface as shown in Fig. 9. This phenomenon has influence on some of tribological important features, such as surface roughness, coefficient of friction, corrosion resistance (Brezničan et al. 2011; Petru et al. 2012).

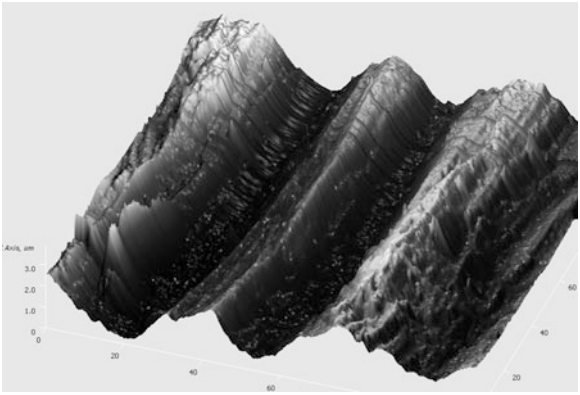

Fig. 7 3D image of worn surface for uncoated surface in vacuum

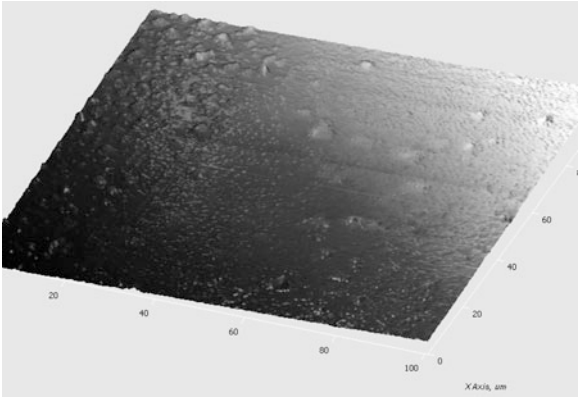

Fig. 8 3D image of worn surface for CROMVIc2 (CrN/DLC2) coating CROMVIc2® in vacuum

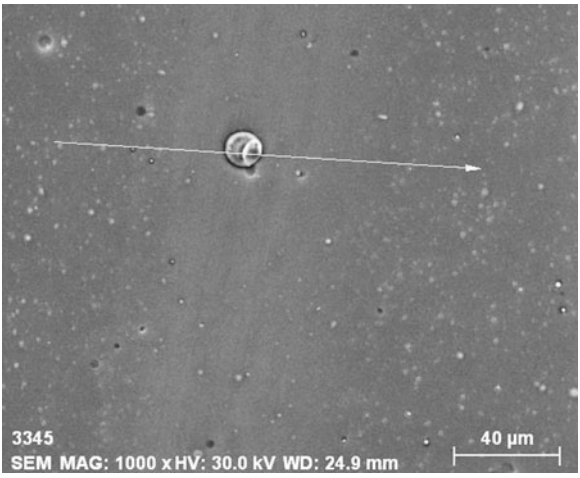

Fig. 9 SEM image of the coating surface

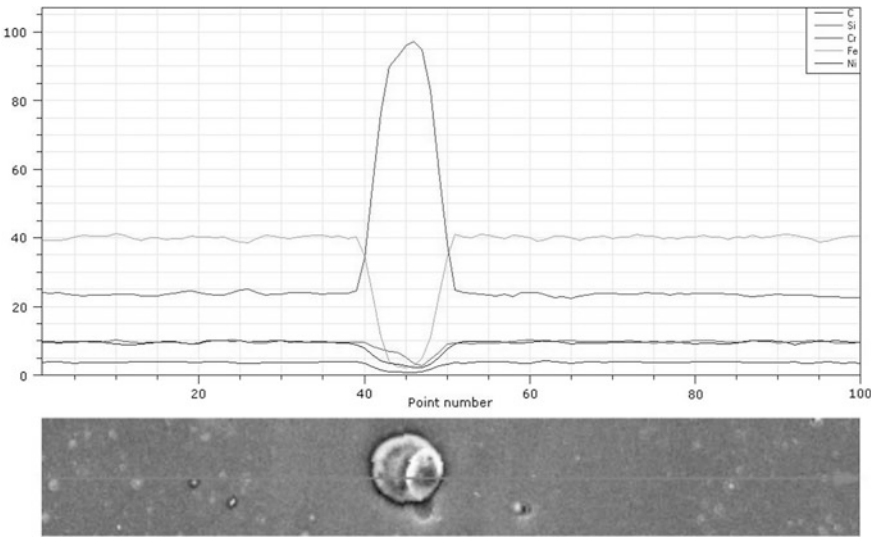

Fig. 10 Results of line EDX analysis

Using the EDX analysis (Fig. 10), we found that it is a particle based on chrome element that emerged during the process of coating by the PACVD method. The presence of these "micro beads" embedded in the surface layer is directly reflected in the increase of surface roughness parameters *R*a and *R*z.

5 Conclusions

The friction behaviour of hard coatings in vacuum can be explained by formation of low shear strength microfilms on the hard coating or on the asperity tips of the coatings and reduction in the real contact.

After the carried out investigations, the following conclusions can be drawn:

- Friction pairs worked under low vacuum reached during the tribological tests 4 times lower friction coefficient values than pairs worked under atmospheric conditions.
- A transferred layer is often formed on steel surface when it slides over a diamond-like coating and the process of layer formation has a crucial influence on the friction and wear.
- Technological conditions of the deposition of thin layers influence the microgeometry of the surface.

For the application of hard coatings with aim to improve performance and to reduce mechanical friction losses is necessary to take into account a broader range

of tribological requirements. Tribology parameters to be considered are mainly: the value of contact pressure, sliding speed, lubricant type, effect of temperature, pollution and contamination of the surface with impurities, also the effect of cyclic and dynamic loading, and so on.

Acknowledgments The work has been supported by the grant project VEGA V-1/1049/11, VEGA V-1/0582/12, and DAAD exchange service program.

References

Brezničan M, Fabian P, Meško J (2011) Formations of special steels after vacuum quenching. In: Strojírenská technologie: Časopis pro vědu, výzkum a výrobu, Roč. 16, č. 2, ISSN 1211-4162, pp 7–11

Petru M, Novak O, Herák D, Simanjuntak S (2012) Finite element method model of the mechanical behavior of *Jatropha curcas L.* seed under compression loading. Biosyst Eng 111:412–421 www.elsevier.com/locate/issn/15375110

Vidiečan J, Bronček J, Radek N (2011) Design of the test system working in high vacuum, *Terotechnologia 2011*. PL ISSN 1897–2683:200–205

Tribological Application with Non-metallic Coatings

M. Leitman, R. Bašťovanský and S. Poljak

Abstract Non-metallic coating used in the tribological junctions are progressive, modern way to increase its resilience and durability in demanding operating conditions. The authors describe in this paper an overview of suitable pairs of tribological properties under evaluation for selected applications. The results of the measurements and experiments show the correctness of the assessment methodology. Use non-metallic coating is subject to the level of technology introduced in practice.

Keywords Tribology · A pair of friction · Bearing friction coefficient

1 Introduction

To prolong the life of artificial and biological systems, increase efficiency, saving materials and energy and increase security considerations constantly increasing demands on monitoring and control processes of friction and wear These objectives were achieved by changing the design, choice of materials and refining new techniques lubrication. Changes and developments in materials brought applications of ceramics or polymers. Lubrication systems allow the use of mineral and synthetic oils, special lubrication systems, application of solid lubricants and the like.

M. Leitman (✉) · R. Bašťovanský · S. Poljak
Faculty of Mechanical Engineering, Department of Mechanical Parts, University of Žilina, Žilina, Slovakia
e-mail: marian.leitman@fstroj.uniza.sk

R. Bašťovanský
e-mail: silvester.poljak@fstroj.uniza.sk

S. Poljak
e-mail: ronald.bastovansky@fstroj.uniza.sk

L. Ševčík et al. (eds.), *Modern Methods of Construction Design*,
Lecture Notes in Mechanical Engineering, DOI: 10.1007/978-3-319-05203-8_80,

The use of surface treatments and coatings has been designed to achieve the desired tribological parameters of structural components and systems. Thus the area of application of intentionally—applied thin layers of the base material for the purpose of modifying the friction and wear. Their share of this development are new kinds of layers and methods of their application, which affect the mode of friction and wear, and also the fact that engineering practice appeared and acknowledged that it is the quality and choice of the type of surface engineering components and systems to ensure tribotechnical functions and have their irreplaceable role in designing and manufacturing. The use of surface treatments and coatings enables the development of new technical and technological structures for which the required properties are controlled by a pair of contact at a particular location in a given quantity and quality.

2 Frictional Wear

Wear of the functional surfaces of critical structural components or nodes plant and machinery has in most cases affected the life and reliability of machinery and equipment. Wear process usually leads to progressive deterioration of technical and economic parameters, and therefore he pays in practice much less attention than the process of sudden breach components such as fatigue fractures. However, surveys show that in 80 % of cases, the primary cause of the disposal of machinery and installations are wearing. Designers can design machine nodes with complicated load, but usually not enough materials for the construction of mechanisms with friction knots. Therefore, materials are selected on the basis of past experience, which may not always lead to optimal results. Wear processes are also the main cause of decommissioning tools, however, does not occur until its sudden destruction in extreme strength and thermal stress caused by wrong choice of ballast parameters (Dzimko et al. 1995).

Requirements to improve the tribological characteristics have their limits. New options provide example. Composite materials that combine the characteristics of the metallic material (strength, plasticity, thermal and electrical conductivity), and ceramics (strength, hardness, thermal stability), or polymeric materials (toughness, good tribological characteristics, resistance to chemical agents, etc.). One of the widely used composite systems is thin wear resistant coatings or coating on the functional surface of metal parts. The thickness of thin coatings or modified surface layers is <20 microns. In these coatings reduce composites that combine bulk properties of the base material (strength, toughness) with specified surface layer or covering (wear resistance, resistance to chemical, physical and thermal effects of the environment, etc.) (Suchánek 1989).

3 Surface Modification Conditions for Friction and Wear

Surface treatments that improve the tribological characteristics of metallic materials (coefficient of friction and resistance to wear different types) can in principle be divided into two basic groups:

1. *Coatings and coatings with high hardness*

For hard surfaces will greatly reduce the amount of plastic in contact microdeformation of inequality and the depth of penetration tip and cutting edges of abrasive particles. Coefficient of friction is reduced in cases where the interaction occurs through friction surface without lubricant, as well as to reduce creasing adhesive component of friction. Reduces the thermal and mechanical stresses in the contact area, resulting in a decreasing intensity of degradation processes or change the dominant wear mechanism. When the adhesive wear at low roughness friction and good adhesion of the coating to the substrate surfaces may violate High-cycle fatigue mechanism, which has a very low intensity.

2. *Soft and tough coatings and coatings*

When these coatings are shear deformation and breach localized in a thin layer of high plasticity. Higher strength material under the surface layer modifies the stress field and deformation and prevents the development of plastic microdeformation and thus violations of the material in greater depth (Figs. 1, 2).

4 Technological Process Preparation Surface Layers

When mechanical processes improves the surface roughness and strength characteristics of surface layers by cold plastic deformation (shot peening, roller, blasting, calibration, detonation hardening) or special Technology machining (polishing, friction under special conditions, particles rubbing, stroking). Improved surface topography and surface layers of reinforcement affect a particular phase of running sliding knot.In many cases, improve the tribological characteristics using mechanical processes only a secondary phenomenon. The main objective of horsehair processes to improve fatigue strength of machine parts. Ion implantation used to modify the effects of thin surface layers of high energy ions. The process takes place in a vacuum 104 Pa, the source sends the bundle of electrically accelerated ions selected elements that enter into under surface layers, which generate a variety of instant I or late phenomena. The incident ions with energies of 50–200 keV affect the structure and substructure of thin surface layers, while particles of extracting material from the surface of the implanted material. Dose of incident ions to the metal surface are in the range 1,016–1,018 ionts.cm^{-2} Allow to create unique structures that cannot be obtained by conventional methods, for

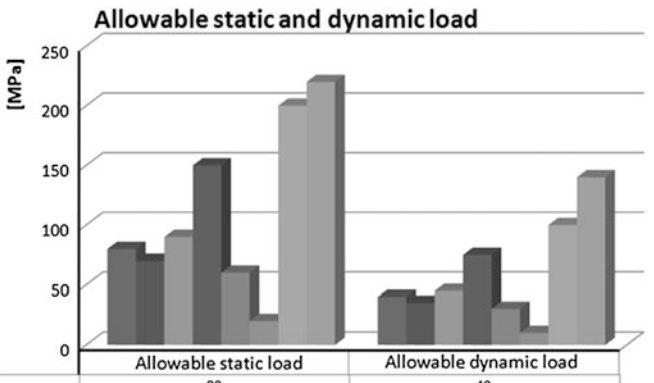

	Allowable static load	Allowable dynamic load
PA 66T+PTFE+glass fibre+graphit	80	40
PBT+PTFE+bronze powder	70	35
PBT+PTFE+bronze powder+glass fibre	90	45
PEEK+PTFE+graphit+carbon fibre	150	75
POM-C+PTFE	60	30
POM-C	20	10
PTFE+PA+wound glass fiber+polymeric bond	200	100
PTFE+PBT+wound glass fiber+polymeric bond	220	140

Fig. 1 Allowable static and dynamic load

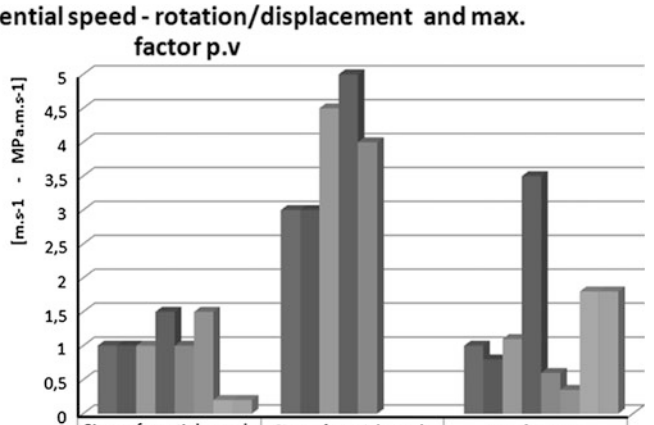

	Circumferential speed - rotation	Circumferential speed - displacement	Max. factor p.v
PA 66T+PTFE+glass fibre+graphit	1	3	1
PBT+PTFE+bronze powder	1	3	0,8
PBT+PTFE+bronze powder+glass fibre	1	4,5	1,1
PEEK+PTFE+graphit+carbon fibre	1,5	5	3,5
POM-C+PTFE	1	4	0,6
POM-C	1,5		0,35
PTFE+PA+wound glass fiber+polymeric bond	0,2		1,8
PTFE+PBT+wound glass fiber+polymeric bond	0,2		1,8

Fig. 2 Circumferential speed—rotation /displacement and max. factor p.v

Table 1 Coatings—thermal spraying

Industrial applications	Coating	Function
Automotive	Mo, WC–Co, Al_2O_3–TiO_2, Si_3N_4, Cr_2O_3	Wear resistance
	Mo, MoS_2, Si_3N_4	Bonded coatings
Chemical	Ni-Al, TrB_2, Ta	Resistance to aggressive environment
Electrical	Al_2O_3	Electro isolation
Aerospace	ZrO_2–CeO_2, ZrO_2–Yb_2	Thermal isolation
	O_3 Cr_2C_3–NiCr	Wear resistance
	BN–Al, Ni–graphite	Gaskets and seals
Medical	$Ca_5(PO_3)3x$(x=F, Cl,OH)	Biocompatibility
Textile	Al_2O_3–TiO_2, Cr_2O_3	

instance. metastable phase elements are insoluble or amorphous surfaces with extraordinary properties. The advantages of ion implantation are that the process is deformation-free, universally applicable, does not change the size and improves the original surface topography (Table 1).

The disadvantages are the high investment demands, the need for high vacuum, high demands on surface quality and highly complex system of manipulation tools or components for ion implantation of intricate surfaces. While the most common use ion implantation of nitrogen (light gas ionization) (Table 2).

5 Results and Discussion

Friction coefficient calculated from the measured values are compared with the values determined analytically by the formula

$$\mu_{ad} = \frac{\tau_s A_{el}}{W} = \frac{\pi \tau_s}{W^{1/3}} \left[\frac{3R_1}{4E_{red}}\right]^{2/3} \quad (1)$$

The statistics for a sufficient number of experiments and analytical results showed that between them there is a marked difference in the values of the friction coefficient obtained experimentally are in both cases higher, than those obtained according to the above analytical formula. Friction coefficient decreased with increasing normal load to the minimum value of about = 0.26. After reaching her grow as a continuing increase in the load, as well as in his subsequent lightening. The course of the friction coefficient with increasing and decreasing burdened not identical (oscillated around a value of about = 0.32) and creates the characteristic curve in the shape of "fish". This phenomenon is attributed to the ongoing changes in the size of the real contact area, those carrying the material PVD coating layer front part of the bullet, which persisted even after the running-in phase.

Table 2 The technology of coatings

Technology	Flame	HVOF	Plasma	Electric arc
Flame temperature (°C)	2,700–3,000	3,000	5,000–2,500	3,000–6,000
Speed of particles ($m.s^{-1}$)	80–100	400–800	80–300	50–150
Typical materials	Metals, alloys, plastics	Metals, alloys, cermets	Ceramic	Metals, alloys, cermets
Surface properties	Higher porosity and oxide content	United density, excellent adhesion, compressive stress	porous ceramics	Higher thickness, high density
Applications	Classical metallization, less demanding applications	Protection against wear and corrosion	Thermal isolation, isolators	Wear resistant coatings, renovation

Investigation of the friction surfaces at the end of measurement, it was found that the contact area involved in the adhesive component of the friction coefficient is significantly higher (up to 30 times) than the area given by calculation according to the Hertz theory. This phenomenon can be explained by the emergence of "optimal" coating thickness. By using new balls and original plates remain in the friction track extremely thin layer. New samples need to overcome resistance to motion compensate only shear forces resulting from the division of adhesive connections and plastic deformation involved in the friction is suppressed to a minimum. In addition, the actual area of adhesive connection is smaller. The second is almost identical, constant progress of the friction coefficient in the range of 0.20–0.60 N in the upward and downward axial load, which is also explained by "optimal" thick layer formed from deposited material.

6 Conclusions

Experimental results confirm the hypothesis that in the case of an extremely soft thin film deposited on a hard surface, the impact of plastic deformation on the coefficient of friction at the end of the initial phase of the process is negligible friction. The predominant mechanism of friction generated and acting in touch can be reasonably characterized as an adhesive. In the case of new steel balls and being equal Si-plates has a coefficient of friction course characterized decrease with increasing loads and constancy in the subsequent reduction of the normal load. The tribological behavior of the pair can be characterized and described so. Coulomb friction law. Surface analysis confirmed the postulated that even when applied at

high pressure Hertz contact, the surface remains even after the initial phase of the friction process extremely thin layer initially deposited film, which significantly affects the size of the friction coefficient and determines the nature of the dominant friction mechanism. The thickness of the remaining layer is in the range of fractions of nanometers and its impact persists, which is documented by the results of extensive experimental research. Your manuscript must be uploaded at the conference website. Please respect the deadlines.

Acknowledgments This work was created by the implementation of the project support V-11-012-00 Research on tribological performance of coated and solid technical and biomechanical systems with nanoparticles and nanostructures.

References

Dzimko M, Kimura Y, Uemura M (1995) Progresívne smery v tribotechnike, In: Zborník kurzu tribotechnik, Stará Lesná, Sept 1995, Dom Techniky ZTVS Bratislava

Suchánek J (1989) Tribologické charakteristiky otěruvzdorných vrstev a povlaků. Sborník mezinárodní konference Vrstvy odolné proti opotřebení, DT ČSVTS Praha, 1989, svaz. 1, str.4

Qualitative Analysis of Film Thickness in Rolling EHD Contact by Fluorescence Technique

D. Nečas, M. Vrbka, P. Šperka, M. Druckmüller, P. Skládal, P. Štarha, I. Křupka and M. Hartl

Abstract Nowadays, it is well known that tribological processes play a significant role in a daily life. The elastohydrodynamic (EHD) regime of lubrication occurs in many applications including both technical and biological points of view. During the last fifty years there was a rapid evolution in experimental methods which help to better understand friction, lubrication and wear. In this study, mercury lamp induced fluorescence is employed to qualitative assess the film thickness in rolling EHD contact created by a steel ball and glass disk. Several experiments were performed to confirm the theory that the dependence between film thickness and entrainment speed should be linear in logarithmic. The results show satisfactory agreement with this prediction, so the method is correct and suitable for further research in the area of EHD contacts. This method also allows analyzing of compliant non-reflective contacts, which will be described in the next paper.

Keywords EHD · Fluorescence · Film thickness · Tribology

D. Nečas (✉) · M. Vrbka · P. Šperka · M. Druckmüller · P. Štarha · I. Křupka · M. Hartl
Faculty of Mechanical Engineering, Brno University of Technology, Brno, Czech Republic
e-mail: Mieke.vanderfluit@springer.com

P. Skládal
Faculty of Science, Masaryk University, Brno, Czech Republic

M. Vrbka · P. Šperka · I. Křupka
Central European Institute of Technology, Brno University of Technology, Brno, Czech Republic

P. Skládal
Central European Institute of Technology, Masaryk University, Brno, Czech Republic

D. Nečas · M. Hartl
New Technologies for Mechanical Engineering, Brno University of Technology, Brno, Czech Republic

L. Ševčík et al. (eds.), *Modern Methods of Construction Design*, Lecture Notes in Mechanical Engineering, DOI: 10.1007/978-3-319-05203-8_81,

1 Introduction

In the world of today, the understanding of tribological phenomenon is of a great importance. The rubbing surfaces are present in many applications of daily life, from technical point of view such as seals or bearings, to biological processes, for example in synovial joints, contact between eye and lens, friction between skin and dress and so on.

The basics of EHD lubrication theory were defined by Dowson and Higginson (1959) and Hamrock and Dowson (1976). One of the characteristics of EHD contact is that contact pressure causes substantial elastic deformation of surfaces; also, increasing pressure leads to change in lubricant viscosity (Esfhanian and Hamrock 1991). EHD lubrication regime is typical for contact between non-conformal surfaces.

Firstly, at the beginning of EHD, there was a lack of experimentalists who could verify the numerical predictions. Over the years many experimental techniques were developed for analyzing the processes in tribology. These methods can be divided into several groups. Firstly, the electrical techniques (contact resistance, capacitance, magnetic reluctance); secondly the optical methods (interferometry, optical densitometry, Raman spectroscopy, x-ray transmittance, fluorescence), and finally the other techniques (pressure tapping, direct displacement). For more details see Spikes (1999), Poll and Gabelli (1992). In the 1990s, the experimental approaches enabled to fully cover the predictions and, in addition, to overcome them in many cases (Spikes 1999).

While using the experimental method, it is necessary to carefully study the capabilities of the technique. The main attention should be paid to the type of the contact which has a critical importance. There are two main types of the contacts; rigid and compliant. Usually it is not a problem to study rigid contacts, however it is documented that the mostly used methods (optical interferometry, contact resistance and capacitance technique) are not suitable for studying compliant contacts (Spikes 1999; Myant et al. 2010). The compliant contacts can be characterized in several points (Poll and Gabelli 1992; Myant et al. 2010):

- The value of lubricant film thickness covers a wide range (from fractions of microns to hundreds microns).
- The contact area is significantly larger than in rigid contacts.
- Compliant contacts are often made by elastomeric and tissue materials, which have poor reflectivity and low electrical conductivity.
- It is not easy to coat these materials, because the coating layers tend to prone to wear and also influence the elastic properties of the base material.
- The polishing of compliant materials is the problem too because of the high roughness of surfaces.

The most appropriate method is the fluorescence technique, which is also used in this study. Fluorescence was firstly used in tribology by Smart and Ford (1974) and Ford and Foord (1978) for determining the film thickness. In the next years,

the method has been improved and was used in several ways. Accurate film thickness measurement by dual emission laser induced fluorescence (Hidrovo and Hart 2000, 2001), film thickness measurement in industrial processes (Azushima 2005, 2006), in rotary seals (Poll and Gabelli 1992; Poll et al. 1992) and in automotive (Ting 1980; Shaw et al. 1992; Inagaki et al. 1997), or formation of lubricant film (Poll and Gabelli 1992; Reddyhoff et al. 2010).

The aim of this study is to verify the correctness of newly used method based on fluorescence microscopy. It was predicted by Hamrock and Dowson (1978), that the dependence between the film thickness and entrainment speed should be linear in logarithmic coordinates. Azushima (2005, 2006) showed also linear dependence between fluorescence intensity and film thickness. This leads to possibility of analyzing film thickness, which is equal to fluorescent intensity in a qualitative way.

2 Materials and Methods

The optical method based on the fluorescence microscopy was employed to study film thickness in rolling contact. The phenomenon of fluorescence was described by Haugland et al. (1996) and occurs in three phases:

- *Excitation*—A photon is supplied by an external source such as an incandescent lamp or a laser and it is adsorbed by a fluorophore, creating an excited electronic singlet state.
- *Excited-State lifetime*—The excited state exists for a finite time (1–10 ns). During this time, the fluorophore may undergo relaxation (energy dissipation), then the molecule may emit fluorescence.
- *Fluorescence emission*—The photon of energy is emitted, while the fluorophore returns to its ground state. Due to dissipation of energy during the excited-state lifetime, the photon has a lower energy and therefore longer wavelength. This difference in wavelengths is called as Stokes shift. This phenomenon is necessary for using fluorescence because it allows separation of the measured emission from excitation.

The schematic of the fluorescence technique can be seen in Fig. 1.

2.1 Experimental Setup

The experimental apparatus utilized in this study is routine ball-on-disk tribometer which consists of optical system and contact simulator, see Fig. 2. Notwithstanding it was mentioned above that fluorescence method enables to study compliant materials, these days the method is being in process of tuning, so it was decided to perform experiments with rigid contact firstly.

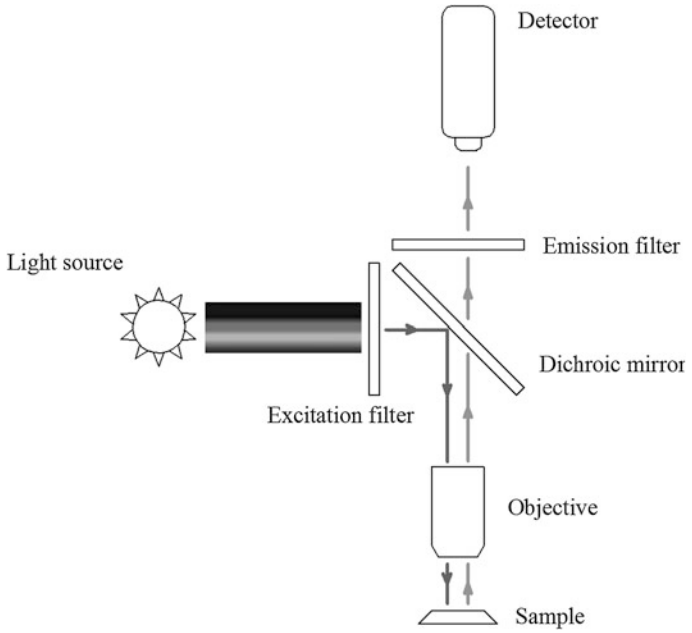

Fig. 1 Schematic of the optical setup

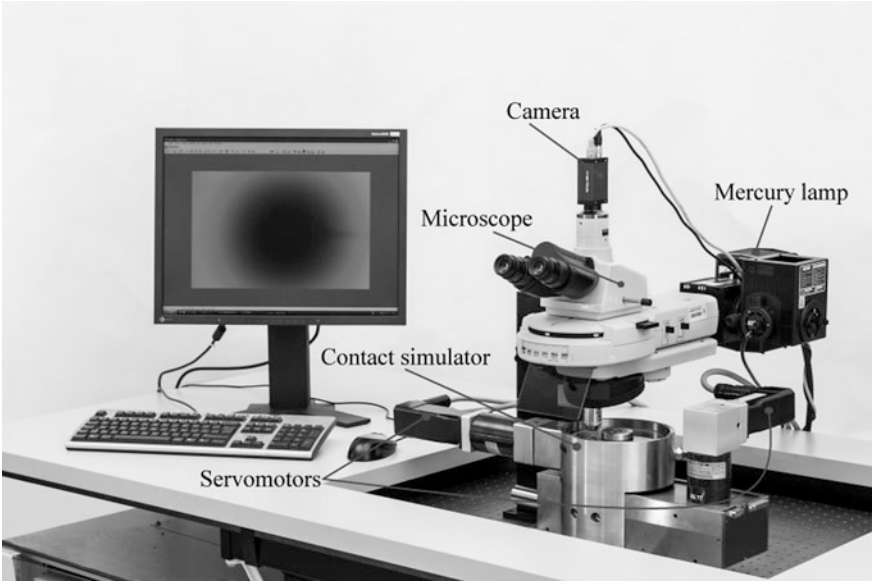

Fig. 2 Experimental apparatus

Fig. 3 Detail of the contact between steel ball and glass disk

Five different entrainment speeds were used to confirm theories made by Hamrock and Dowson (1978) and Azushima (2005, 2006) mentioned above. The values of the speeds were: $U_1 = 10$ mm/s, $U_2 = 20$ mm/s, $U_3 = 40$ mm/s, $U_4 = 60$ mm/s, $U_5 = 100$ mm/s.

If the method should provide reliable results, the correct light source, light direction and filtering are crucial (Gabelli and Poll 1992). As the light source it is possible to use laser, halogen, xenon, or mercury lamp (Poll et al. 1992). The laser brings the most benefits, but disadvantage is a price. In this study, 100 W mercury lamp was chosen for illumination.

For observation the contact, fluorescent microscope (NIKON) was used and the contact area was captured via GigE Vision camera Manta G146B.

2.2 Test Specimens and Lubricants

The non-conformal contact is formed between the steel ball of diameter 28 mm and pure glass disk of diameter 150 mm. The detail of the contact just before measurement is shown in Fig. 3. The elastic modulus of steel ball and glass disk was 212, 81 GPa, respectively. Both parts of the contact can be driven independently by their own servomotors.

As a lubricant, oil Spectrasyn 6 with dynamic viscosity 0.181 Pa · s was used. The oil was doped by a fluorescent dye Eosin (Sigma Aldrich). This dye was selected because of its satisfactory solubility in many liquids. The dye was also used by Myant et al. (2010) and Reddyhoff et al. (2010). These authors used a laser for the illumination. Due to this fact, very low concentration of fluorescent dye

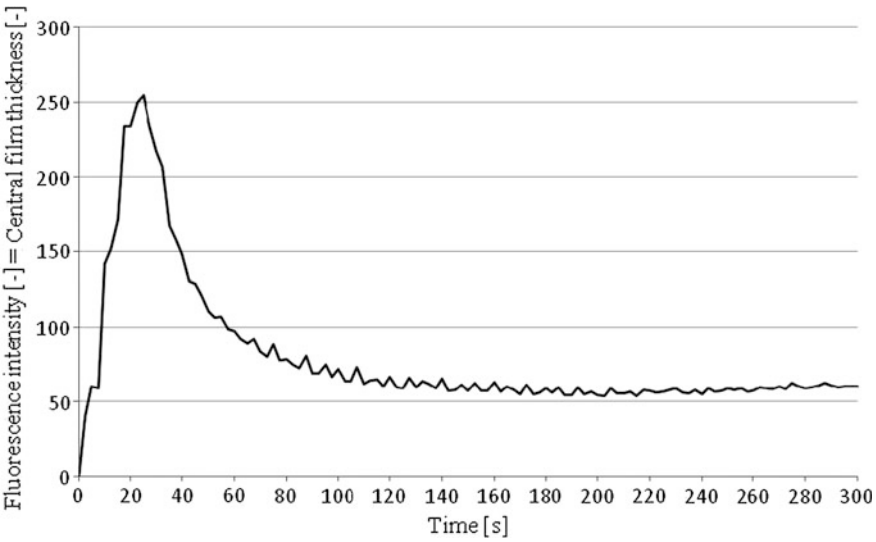

Fig. 4 Time course of central film thickness for entrainment speed $U_1 = 10$ mm/s

could be used; 0.04 % by mass (Reddyhoff et al. 2010). In our case, after several tests, we have decided to utilize different concentration by one order. So the concentration of Eosin was 0.4 % by mass. The total amount of lubricant was 10.5 ml and it was uniformly supplied into the contact for 3 min. Every measurement took 5 min in total.

3 Results

The evaluation of measurement is a process connected with image processing. Quite easy software, for determination the intensity of selected circular area in arbitrary number of images, was created.

Figure 4 shows the film thickness profile during the experiment for entrainment speed $U_1 = 10$ mm/s. The character of forming the lubricant film was almost the same for all measurements. There is a rapid increase of film thickness in first approximately 30 s. After next few tens of seconds, the film thickness decreases slightly and converges to a constant value.

In Fig. 5, there can be seen the dependence between film thickness and entrainment speed in a logarithmic. Even if the approximation is not perfectly linear, it can be considered as a quite good agreement with predictions made by Hamrock and Dowson (1978). This proves convenience of described technique for research in the area of EHD contacts.

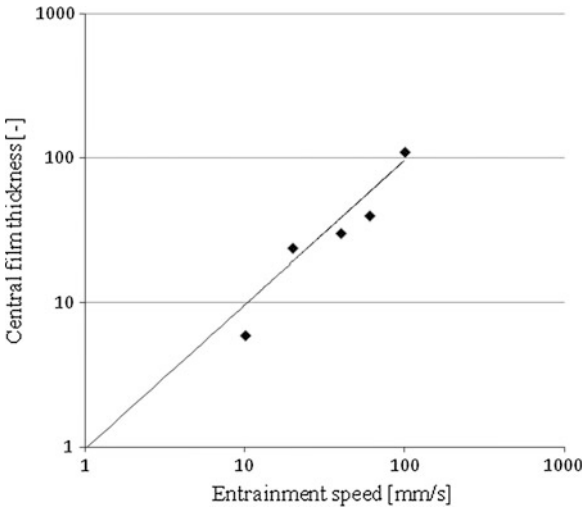

Fig. 5 Central film thickness for different entrainment speeds

4 Discussion

The new optical method based on the fluorescence microscopy was employed to observe the rolling EHD contact between steel ball and pure glass disk. The paper was focused on the qualitative analysis of film thickness, which is equal to emitted radiation of fluorescent dye.

The next step of research is going to focus on a quantitative evaluation of film thickness. A several problems have to be solved. Firstly, a mercury lamp seems to be insufficient for higher entrainment speeds. It would be much better to use laser in a pulse regime for excitation. Secondly, while studying reflective surfaces, there is a significant problem with calibration because of interference. This was also mentioned by Sugimura et al. (2000), who solved this undesirable phenomenon by using glass lens /glass disk configuration for calibration. Finally, it was found out that there could be a problem with durability of fluorescent dye. Eosin, which was used in this study is not appropriate for long-standing measurement, especially when is illuminated continuously, because it losses ability to fluoresce.

When the method will be tuned fully, the authors plan to extend the tribology research on compliant contacts in technical and also biological applications.

Acknowledgement This research was supported by Specific Research project FSI-J-13-2096.

References

Azushima A (2005) In lubro 3D measurement of oil film thickness at the interface between tool and workpiece in sheet drawing using a fluorescence microscope. Tribol Int 38(2):105–112. doi:10.1016/j.triboint.2004.04.006

Azushima A (2006) In situ 3D measurement of lubrication behavior at interface between tool and workpiece by direct fluorescence observation technique. Wear 260(3):243–248. doi:10.1016/j.wear.2005.01.053

Dowson D, Higginson GR (1959) A numerical solution to the elastohydrodynamic problem. J Mech Engi Sci 1:6–15

Esfhanian M, Hamrock BJ (1991) Fluid-film Lubrication regimes revisited. Tribol Trans 34(4):628–632. doi:10.1080/10402009108982081

Ford RAJ, Foord CA (1978) Laser-based fluorescence techniques for measuring thin liquid films. Wear 51(2):289–297. doi:10.1016/0043-1648(78)90267-3

Gabelli A, Poll G (1992) Formation of lubricant film in rotary sealing contacts: part I: lubricant film modeling. J Tribol 114(2):280. doi:10.1115/1.2920885

Hamrock BJ, Dowson D (1976) Isothermal EHL of point contacts: fully flooded results. ASME Trans J Lubr Technol 93:264–277

Hamrock BJ, Dowson D (1978) Elastohydrodynamic lubrication of elliptical contacts for materials of low elastic modulus I—fully flooded conjunction. J Lubr Technol 100(2):236. doi:10.1115/1.3453152

Haugland RP, Spence MT, Johnson ID (1996) Handbook of fluorescent probes and research chemicals, 6th edn. Molecular Probes, Eugene, xii, 680 p. ISBN 09-652-2400-7

Hidrovo CH, Hart DP (2000) Dual emission laser induced fluorescence technique (DELIF) for oil film thickness and temperature measurement. In: FED 2000, pp 175–182. ISSN 0888-8116

Hidrovo CH, Hart DP (2001) Emission reabsorption laser induced fluorescence (ERLIF) film thickness measurement. Measure Sci Technol 12(4):467–477. doi:10.1088/0957-0233/12/4/310

Inagaki H, Saito A, Murakami M, Konomi T (1997) Measurement of oil film thickness distribution on piston surface using the fluorescence method (development of measurement system). JSME Int J Ser B-Fluids Therm Eng 40:487–493

Myant C, Reddyhoff a T, Spikes HA (2010a) Laser-induced fluorescence for film thickness mapping in pure sliding lubricated, compliant, contacts. Tribol Int 43(11):1960–1969. doi:10.1016/j.triboint.2010.03.013

Myant C, Fowell M, Spikes HA, Stokes JR (2010b) An investigation of lubricant film thickness in sliding compliant contacts. Tribol Trans 53(5):684–694. doi:10.1080/10402001003693109

Poll G, Gabelli A (1992) Formation of lubricant film in rotary sealing contacts: Part II: a new measuring principle for lubricant film thickness. J Tribol 114(2):290

Poll G, Gabelli A, Binnington PG, Qu J (1992) Dynamic mapping of rotary lip seal lubricant films by fluorescent image processing. In: Nau B (ed) Fluid sealing. Kluwer Academic Publishers, Boston. ISBN 079231669x

Reddyhoff T, Choo JH, Spikes HA, Glovnea RP (2010) Lubricant flow in an elastohydrodynamic contact using fluorescence. Tribol Lett 38(3):207–215. doi:10.1007/s11249-010-9592-6

Shaw B, Hoult D, Wong V (1992) Development of engine lubricant film thickness diagnostics using fiber optics and laser fluorescence. In: SAE international, pp 1–10

Smart AE, Ford RAJ (1974) Measurement of thin liquid films by a fluorescence technique. Wear 29(1):41–47. doi:10.1016/0043-1648(74)90132-x

Spikes HA (1999) Thin films in elastohydrodynamic lubrication: the contribution of experiment. Proc Inst Mech Eng Part J: J Eng Tribol 213(5):335–352. doi:10.1243/1350650991542712

Sugimura J, Hashimoto M, Yamamoto Y (2000) Study of elastohydrodynamic contacts with fluorescence microscope. Tribol Ser 38:609. doi:10.1016/S0167-8922(00)80165-0

Ting LL (1980) Development of a laser fluorescence technique for measuring piston ring oilfilm thickness. J Lubr Technol Trans ASME 102:165–171

An Experimental Investigation of the Adhesion Behavior Between Wheel and Rail under Oil, Water and Sanding Conditions

D. Smejkal, M. Omasta and M. Hartl

Abstract The aim of this paper is to investigate the adhesion behavior under poor condition in presence of the debris particles, oil, water and sanding conditions. Experimental data are obtained with an experimental device that simulates sliding velocity, the adhesion coefficient, the load per wheel. respectively Hertzian pressure by using specimens made with similar mechanical properties like a real rail wheel and a rail. The wheel and the rail are simulated by the twin disk mechanism. The first result shows that traction curve has similar shape like theoretical one. In wet and oil conditions the adhesion coefficient decreases compare to dry condition. Sanding can increase the adhesion coefficient, however using this modification leads to damage of the wheel to rail contact surface. The saturation point differs for each condition applied. An ability to hold enough traction is better for dry contact.

Keywords Wheel/rail · Adhesion · Oil · Water · Sand

1 Introduction

One of the most important factors in the railway transportation is contact between the wheel and the rail which transfers all energy. The amount of transferred kinetic energy depends on the adhesion in contact especially during acceleration and braking phase. Losses in adhesion coefficient might cause many serious problems, particularly during braking and acceleration. During such process the wheel is sliding on the rail surface what increases wear and surface damage of wheel/rail materials. Another serious problem during braking with low adhesion is extended

D. Smejkal (✉) · M. Omasta · M. Hartl
Brno University of Technology, Brno, Czech Republic
e-mail: smejkal@fme.vutbr.cz

L. Ševčík et al. (eds.), *Modern Methods of Construction Design*,
Lecture Notes in Mechanical Engineering, DOI: 10.1007/978-3-319-05203-8_82,

braking distance (Rail Accident Investigation Branch 2005; Arias-Cuavas and Li 2011). It is an unpredictable process therefore it is problem of safety and also time delay. The exploration executed by Rail Accident Investigation Branch X (Wang et al. 2011) observed the amount of serious problems connected with low adhesion in autumn between years 2000–2005. The results show approximately 350 problems related to station overruns and signal passed at danger per one year. Most of them were caused by low adhesion due to dirty and leaf—covered rails. In case of acceleration, there are problems with time delay and it relates to the comfort and satisfaction of passengers. Therefore, managing of adhesion coefficient in railway transportation is clearly advantageous (Lewis and Olofsson 2009).

Recently many studies have been carried out on field research to investigate causes and mechanism of adhesion loss between the wheel and the rail using experimental and theoretical approaches, specifically (Olofsson 2007; Clayton 1996). Results indicate rapid decrease of adhesion coefficient affected by wet, oil contamination, dew and leaves. Extensive investigation of the change of friction at wheel/rail interface was made by British rail research in the 1970s (Broster et al. 1974; Pritchard 1980). It was found that the rail is covered by third body layer consisting of oil, leaves, water and solid materials. They came to conclusion that water has the significant influence on loss wheel/rail adhesion. During the dry period a dust layer consisting of natural dust, fragments from brakes, particles of metal from the wheel and the rail are created. Moisture, fog or light rain are mixed with the dry layer and create a thin lubrication film with high level of viscosity. This substrate is resistant to removal from the contact band and provides elasto-hydrodynamic lubrication with friction coefficient about 0.015. For example heavy rain gives higher consistent adhesion level of 0.2.

In poor condition when adhesion of wheel/rail is low the sanding can be used to improve traction abilities. The disadvantage of sanding method is excessive abrasive wear of wheel and rail during the application. Various methods have been investigated to decrease effects of low adhesion (Dobs 1970; Zobel 1975), all without significant success (Clayton 1996).

At present many methods have been used to explore the adhesion characteristic of wheel/rail. Experimental devices like pin-on-disk, disk-on-flat and twin disk have been introduced (Lewis et al. 2011). Twin disk experimental device is used for investigation of creep characteristic between the wheel and the rail. Some devices are fully scaled some of them are scaled. A scaled one explains behavior and basic principles well. The disadvantage is a shape and a size of a contact zone. Results may be taken into account only as a guide for interface understanding. Fully scaled model, in contrast, can describe the real behavior of wheel/rail interface but this approach can be very expensive when applied to larger projects.

In this paper experimental device in small scale was designed to simulate and evaluate the adhesion characteristics. The aim of this work was to investigate traction characteristics under dry, wet and oil conditions and to verify influence of sanding in wheel/rail contact (Fig. 1).

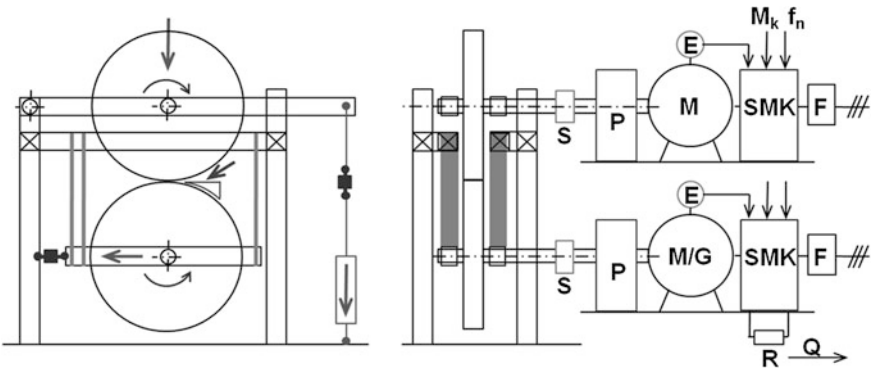

Fig. 1 Scheme of the roller test rig

2 Experimental Details

2.1 Apparatus

An experimental roller test rig based on twin disk principle was designed. This machine was used for wheel/rail contact simulation during rolling and sliding conditions. The test apparatus was constructed on Institute of Mechanical Design. Schematic principle is shown on Fig. 2. The rig consists of two independent driven disks. Each disk has its own transmission, motor and frequency converter so the power (traction or brake force) imposed on the rail wheel can be controlled accurately. The software was developed specially for this application and it allows to set up certain velocity (revolutions) and slip. A load is applied on the wheel using lever mechanism. Particular load is controlled by screw on the end of the lever. Vibration instabilities during the rotation are absorbed by mechanism with spring. Friction force is recorded by strain gauge. The diameter of wheel and rail roller is 320 mm (Fig. 3). Both disks are made from material C45 however each of them has different hardness according real rail and wheel parameters. Twin disk is designed in scale of 1:3 thus contact zone and all dimensions are scaled however the load corresponds to the real wheel/rail contact (Gallardo-Hernandez 2008).

The load in position of loading mechanism is 1.2 kN, in disk to disk contact it is approximately 3.2 kN what producing a Hertzian pressure 1 GPa in contact zone. This configuration represents contact between wheel and rail of passing tram in traffic. The test rig contains hermetically closed chamber which covers the rollers and devices for water and sand application without any influence of laboratory pollution.

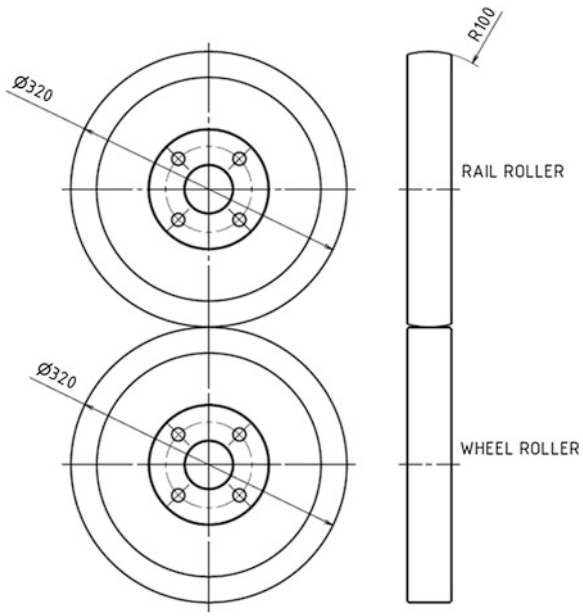

Fig. 2 Scheme of the wheel and rail rollers

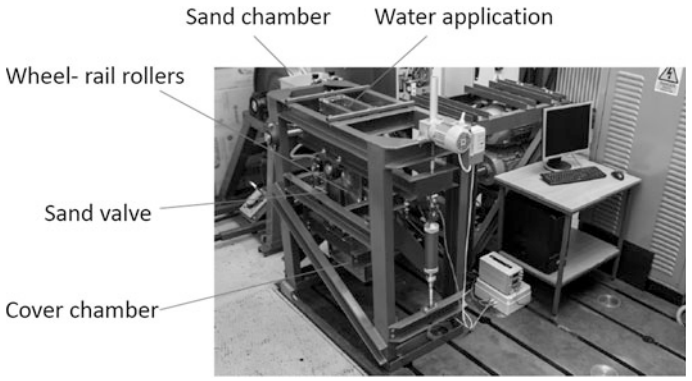

Fig. 3 The test rig

2.2 Test Procedure

Sets of rolling and sliding tests were conducted on the experimental apparatus. In each of set adhesion characteristics were constructed base on measurement of adhesion coefficient for different conditions. Before each test rollers were wiped to remove dirt and grease. Hertzian contact pressure of 0.8 GPa was applied. The

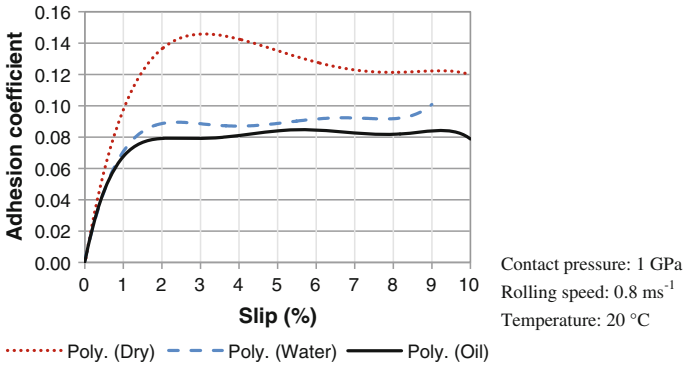

Fig. 4 Influence of contaminants on the adhesion coefficient

speed was set up to 0.8 m s^{-1} and slip was varying from 1 to 10 % by 1 % step The friction force was measured in each step, based on these data the adhesion coefficient was calculated. Tests were carried out in dry condition and others with application of water and oil. Adhesion coefficient during sanding and 4 % slip with the same load and speed settings was measured during the last test.

3 Results

Adhesion performance of four different conditions was investigated. First test was performed with expected the lowest values of adhesion coefficient. There were applied continuous layers of oil. The traction curve was constructed. At very beginning the adhesion coefficient in saturation point was under 0.08 and the slip of 1 %., After this rapid coefficient value change trend of curve stabilized. Next test were performed with use of contamination of water. The results show increase of adhesion coefficient however the gradient of this curve against the adhesion curve under oil does not reach growth rapidly. The trend has constant value during the phase of negative friction it is similar process like in oil condition. Last complete test was performed under the dry condition. The curve shows the most stable trend. In point of saturation where the curve changes from stable to non-stable the coefficient of adhesion is 0.15 and the slip 3 %. After the point of saturation the adhesion coefficient decrease and the trend of curve falls in parabolic manner. Adhesion coefficient stabilized on the value of 0.12.

When sand was applied to the wheel/rail interface during the application of water the particles of sand were crushed and abrasively wear discs. The noise had been higher in compare to non-use of sand. Coefficient of adhesion during the sanding in 4 % slip was 0.14. Compare to the non-sanding conditions the coefficient of adhesion increased to 0.05 (Fig. 4).

4 Discussion

The adhesion behavior in wheel/rail interface is complicated tribological process. Coefficient adhesion is influenced by many factors. In this paper Adhesion characteristics in wheel/rail interface in pure conditions were measured. Laboratory results measured on test rig indicate that changed tendency of adhesion curves of the wheel/rail interface is very similar with previous experimental results. Results show that different condition has impact on adhesion in contact. Adhesion coefficient drop under dry condition rapidly. Difference between water and oil is not so significant. The oil shows less than 10 % decrease against water condition. In dry condition increase of adhesion coefficient from 0.09 to 0.15 in point of saturation has been observed. Measured values in traction curves are not similar like in other experimental research what might be causes by many factors in measured chain. The experimental device is in phase of calibration and debugging.

Acknowledgement The work is supported by Specific Research project FSI-J-13-2096.

References

Arias-Cuavas O, Li Z (2011) Field investigations into the performance of magnetic track brakes of an electrical multiple unit against slippery tracks. J Rail Rapid Transit Adhesion Improve 225:613–636

Broster M, Pritchard C, Smith DA (1974) Wheel/rail adhesion: its relation to rail contamination on british railways. Wear 29(3):309–321

Clayton P (1996) Tribological aspects of wheel-rail contact: a review of recent experimental research. Wear 191(1–2):170–183

Dobs DJ (1970) Evaluation plasma torch. Federal Railroad Administration Report FRA-RT-70-27, Jan 1970

Gallardo-Hernandez EA, Lewis R, Olofsson U (2008) Twin disc assessment of wheel/rail adhesion: its relation to rail contamination on British railways. Wear 265:9–10

Lewis R, Olofsson U (2009) Wheel-rail interface handbook. Woodhead Publishing in Mechanical Engineering, Cambridge, xxii, 842 p. ISBN 978-1-84569-412-8

Lewis SR, Lewis R, Olofsson U (2011) An alternative method for the assessment of railhead traction: its relation to rail contamination on British railways. Wear 271(1–2):62–70

Olofsson U (2007) A multi-layer model of low adhesion between railway wheel and rail. Proc Inst Mech Eng Part F: J Rail Rapid Transit 221(3):385–389

Pritchard C (1980) Traction between rolling steel surfaces: a survey of railway and laboratory experiments. In: Proceedings of 7th leeds-lyon symposium on tribology, MEP

Rail Accident Investigation Branch (2005) Rail accident report: autumn adhesion investigation Part 3: review of adhesion-related incidents Autumn 2005. Report 25 (Part3)/2006. Jan 2007

Wang WJ, Shen P, Song JH, Guo J, Liu QY, Jin XS (2011) Experimental study on adhesion behavior of wheel/rail under dry and water conditions. Wear 271(9–10):2699–2705. ISSN 0043-1648. doi. 10.1016/j.wear.2011.01.070

Zobel FGR (1975) Development of remedies for poor adhesion. Railway Eng J 4(4):14–27

Author Index

L. Ševčík et al. (eds.), *Modern Methods of Construction Design*,
Lecture Notes in Mechanical Engineering, DOI: 10.1007/978-3-319-05203-8,